

EAS Publications Series, Volume 61, 2013



Gamma-ray Bursts: 15 Years of GRB Afterglows Progenitors, Environments and Host Galaxies from the Nearby to the Early Universe

Marbella (Málaga), Spain, October 8–12, 2012

Edited by: *A.J. Castro-Tirado, J. Gorosabel and I.H. Park*



17 avenue du Hoggar, PA de Courtabœuf, B.P. 112, 91944 Les Ulis cedex A, France

First pages of all issues in the series and full-text articles

in PDF format are available to registered users at:

<http://www.eas-journal.org>

Cover Figure

Artist's view of a gamma-ray burst being observed by UFFO aboard *Lomonosov*. The spacecraft is crossing the heavens above Marbella's Sierra Blanca and Playa de El Ancón, in Málaga (Costa del Sol). Design by I. Guziy, picture by Marbella Town Hall and graphics by the UFFO/*Lomonosov* team and ESO (Y. Beletsky and A. Roquette).

Indexed in: ADS, Current Contents Proceedings – Engineering & Physical Sciences, ISTP®/ISI Proceedings, ISTP/ISI CDROM Proceedings.

ISBN 978-2-7598-1002-4 EDP Sciences Les Ulis
ISSN 1633-4760
e-ISSN 1638-1963

This work is subject to copyright. All rights are reserved, whether the whole or part of the material is concerned, specifically the rights of translation, reprinting, re-use of illustrations, recitation, broad-casting, reproduction on microfilms or in other ways, and storage in data banks. Duplication of this publication or parts thereof is only permitted under the provisions of the French Copyright law of March 11, 1957. Violations fall under the prosecution act of the French Copyright Law.



1 Ripa
 2 Connell
 3 Troja
 4 Omodei
 5 Kann
 6 Guiriec
 7 Meli
 8 Brandt
 9 Perley
 10 Vedenkin
 11 Svertilov
 12 Amelyushkin
 13 Pandey
 14 Jakobsson
 15 Rossi
 16 Metzger
 26 27 28 29 30
 31 32 33 34 35
 36 37 38 39 40
 41 42 43 44 45
 46 47 48 49 50
 51 52 53 54 55
 56 57 58 59 60
 61 62 63 64 65
 66 67 68 69 70
 71 72 73 74 75
 76 77 78 79 80
 81 82 83 84 85
 86 87 88 89 90
 91 92 93 94 95
 96 97 98 99 100
 101 102 103 104
 105 106 107 108
 109 110 111 112

94
 95
 96
 97
 98
 99
 100
 101
 102
 103
 104
 105
 106
 107
 108
 109
 110
 111
 112

1 Ripa	17 Filgas	33 Hurley	49 Grossan	65 Zhao	81 Vergani	97 Page
2 Connell	18 Greiner	34 Simon	50 Jelínek	66 Osborne	82 Bogomolov	98 Sánchez-Ramírez
3 Troja	19 Savaglio	35 Lara-Gil	51 Topinka	67 Granot	83 Sokolova	99 Llorente
4 Omodei	20 Kubánek	36 D'Elia	52 Pérez-Rendón	68 Secr. de Sala	84 Vohnova	100 Bhat
5 Kann	21 Asano	37 Tagliaferri	53 Huang	69 Nishikawa	85 Bersten	101 Castro-Tirado
6 Guiriec	22 López-Cámara	38 Covino	54 Yashin	70 Mizuno	86 Lim	102 Sokolov
7 Meli	23 Bromberg	39 Tanvir	55 Fishman	71 Pérez-Álvarez	87 Jeong	103 Arsentieva
8 Brandt	24 De Pasquale	40 Costa	56 Aptekar	72 Karpov	88 Kocevski	104 Minaev
9 Perley	25 Palazzi	41 Piranomonte	57 Battai	73 Nousek	89 Jung	105 Shlyapnikov
10 Vedenkin	26 Klose	42 Rowlinson	58 Graham	74 Chernenko	90 Serino	106 Pavlenko
11 Svertilov	27 Barniol-Durán	43 Moskvitin	59 Gehrels	75 Tiarchuk	91 Fruchter	107 Pozzanenko
12 Amelyushkin	28 Daigne	44 Bjornsson	60 Sacahui	76 Connaughton	92 Pérez-García	108 Hudec
13 Pandey	29 Izzo	45 Corsi	61 F.-W.Zhang	77 Frederiks	93 Manckiewicz	109 Mirabel
14 Jakobsson	30 Flores	46 Wiersma	62 Liu	78 Inoue	94 Nam	110 Park
15 Rossi	31 Lund	47 Petrov	63 Bing Zhang	79 Niño	95 Lee	111 Sari
16 Metzger	32 Tello	48 Oates	64 Sapountzis	80 Campana	96 Guzy	112 Castro-T. M.



List of Participants

- Alexander AMELYUSHKIN (Lomonosov Moscow St. Univ Skobeltsyn Inst. of Nuclear Physics (MSU SINP), Russia)
- Raphail APTEKAR (Ioffe Institute of Russian Academy of Sciences, Russia)
- Katsuaki ASANO (Tokyo Institute of Technology, Japan)
- Magnus AXELSSON (Royal Institute of Technology (KTH), Stockholm, Sweden)
- Rodolfo BARNIOL-DURÁN (Hebrew University of Jerusalem, Israel)
- Aldo BATTA (Instituto de Astronomía, UNAM, México)
- Melina BERSTEN (Kavli Institute for the Physics and Mathematics of the Universe (IMPU), Japan)
- Gregory BESKIN (Special Astrophysical Observatory (SAO-RAS), Russia)
- Narayana BHAT (University of Alabama in Huntsville, USA)
- Vitaly BOGOMOLOV (Lomonosov Moscow St. Univ Skobeltsyn Inst. of Nuclear Physics (MSU SINP) Russia)
- Gunnlaugur BJÖRNSSON (Centre for Astrophysics and Cosmology, University of Iceland)
- Søren BRANDT (Danish Technical University (DTU) Space, Denmark)
- Antoine Claude BRET (Universidad de Castilla La Mancha, Ciudad Real, Spain)
- Omer BROMBERG (Hebrew University of Jerusalem, Israel)
- Volker BROMM (University of Texas, USA)
- Michael BURGESS (University of Alabama in Huntsville, USA)
- Sergio CAMPANA (Osservatorio Astronomico di Brera (INAF-OAB), Italy)
- Alberto J. CASTRO-TIRADO (Instituto de Astrofísica de Andalucía (IAA-CSIC) Granada, Spain)
- Pisin CHEN (LeCosPA, National Taiwan University, Taiwan)
- Anton CHERNENKO (Space Research Institute (IKI-RAS), Russia)
- Valerie CONNAUGHTON (University of Alabama in Huntsville, USA)
- Paul CONNELL (Universidad de Valencia, Spain)
- Alessandra CORSI (The George Town University, USA)
- Enrico COSTA (Istituto di Astrofisica e Planetologia Spaziali (INAF-IAPS), Roma, Italy)
- Stefano COVINO (Osservatorio Astronomico di Brera (INAF-OAB), Italy)
- Ronan CUNNIFFE (Instituto de Astrofísica de Andalucía (IAA-CSIC), Granada, Spain)
- Frederic DAIGNE (Institut d'Astrophysique de Paris, France)
- Simone DALL'OSO (Racah Institute for Physics, The Hebrew University of Jerusalem, Israel)

Arnon DAR (Technion, Haifa, Israel)

Valerio D'ELIA (Osservatorio Astronomico di Roma (INAF-OAR) and
ASI-ASDC Italy)

Massimiliano DE PASQUALE (Mullard Space Science Laboratory
(MSSL-UCL), Surrey, UK)

Robert FILGAS (Institute of Experimental and Applied Physics (IEAP-CTU),
Prague, Czech Republic)

Jerry FISHMAN (NASA-Marshall Space Flight Center (ESSSA), USA)

Dmitry FREDERICS (Ioffe Institute of Russian Academy of Sciences, Russia)

Andrew FRUCHTER (Space Telescope Science Institute, USA)

Neil GEHRELS (NASA-Goddard Space Flight Center, USA)

John GRAHAM (Space Telescope Science Institute and Johns Hopkins
University, USA)

Jonathan GRANOT (Hebrew University and Tel Aviv University, Israel and
U. of Hertfordshire, UK)

Jochen GREINER (Max-Planck-Institute for Extraterrestrial Physics (MPE)
Garching, Germany)

Javier GOROSABEL (Instituto de Astrofísica de Andalucía (IAA-CSIC), Granada,
& ETSI (UPV/EHU) Bilbao, Spain)

Bruce GROSSAN (UC Berkeley Space Science Lab, USA)

Sylvain GUIRIC (NASA Goddard Space Flight Center / NPP, USA)

Sergey GUZIY (Astronomical Observatory of Nikolaev National University,
Ukraine)

Paul HANCOCK (SIfA/CAASTRO – The University of Sydney, Australia)

Ming-Huey A. HUANG (National United University & LeCosPA, National
Taiwan University)

René HUDEC (Astronomical Institute (ASU AV CR) and CVUT FEL, Czech
Republic)

Kevin HURLEY (Univ. of California (UC) Berkeley, USA)

Susumu IONUE (Max-Planck Institute for Physics)

Luca IZZO (Sapienza University of Rome and ICRA-Net, Italy)

Palli JAKOBSSON (Centre for Astrophysics and Cosmologic, University of
Iceland)

Mates JELINEK (Instituto de Astrofísica de Andalucía (IAA-CSIC) Granada,
Spain)

Sooming JEONG (Sungkyunkwan University, Suwon, Korea)

Aera JUNG (Sungkyunkwan University, Suwon, Korea)

Alexander KANN (Thüringer Landessternwarte Tautenburg, Germany)

Sergey KARPOV (Special Astrophysical Observatory of Russian Academy of Sciences, Russia)

Sylvio KLOSE (Thüringer Landessternwarte Tautenburg, Germany)

Daniel KOCEVSKI (Stanford University, USA)

Petr KUBÁNEK (Institute of Physics, AS CR, Czech Republic)

Oscar LARA-GIL (Instituto de Astrofísica de Andalucía (IAA-CSIC) Granada, Spain)

Jik LEE (Sungkyunkwan University, Suwon, Korea)

Heuijin LIM (Ewha Womans University, Korea)

Tong LIU Xiamen University, China)

Niels LUND (Danish Technical University (DTU) Space, Denmark)

Alvaro LLORENTE (Ingeniería de Software Avanzado (INSA), Madrid, Spain)

Daniel LÓPEZ-CÁMARA (North Carolina State University, USA)

Lech MANCKIEWICZ (Center for Theoretical Physics PAN, Poland)

Athina MELI (University of Liege, Belgium)

Brian METZGER (Princeton University, USA)

Pavel MINAEV (Space Research Institute (IKI-RAS) Moscow, Russia)

Felix MIRABEL (Service d'Astrophysique, CEA-Saclay, France)

Yosuke MIZUNO (National Tsing-Hua University, Taiwan)

Alexander MOSKVITIN (Special Astrophysical Observatory (SAO-RAS), Russia)

Jiwoo NAM (National Taiwan University)

Ana María NICUESA (Thüringer Landessternwarte Tautenburg, Germany)

Yuu NIINO (NAOJ, Japan)

Ken-ichi NISHIKAWA (University of Alabama in Huntsville, USA)

John NOUSEK (Penn State University, USA)

Samantha OATES (Mullard Space Science Laboratory (MSSL-UCL), Surrey, UK)

Paul O'BRIEN (University of Leicester, UK)

Nicola OMODEI (Stanford University, USA)

Julian OSBORNE (University of Leicester, UK)

Kim PAGE (University of Leicester, UK)

Eliana PALAZZI (Istituto di Astrofisica Spaziale (INAF-IASF) Bologna, Italy)

Shashi B. PANDEY (ARIES, Nainital, India, India)

I.H. PARK (Sungkyunkwan University, Suwon, Korea)

Elena P. PAVLENKO (Crimean Astrophysical Observatory, Ukraine)

Asaf PE'ER (Crimean Astrophysical Observatory, America)

Erica PÉREZ-ÁLVARO (Universidad de Castilla-La Mancha, Ciudad Real, Spain)

María Ángeles PÉREZ-GARCÍA (University of Salamanca, Spain)
 Brenda PÉREZ-RENDÓN (Departamento de Investigación en Física,
 Universidad de Sonora, Mexico)
 Dolores PÉREZ-RAMÍREZ (University of Jaén, Spain)
 Daniel PERLEY (The California Institute of Technology (Caltech), USA)
 Vasily PETROV (Lomonosov Moscow St Univ. Skobeltsyn Inst. of Nuclear
 Physics (MSU SINP), Russia)
 Silvia PIRANOMONTE (Osservatorio Astronomico di Roma (INAF-OAR),
 Italy)
 Alexander POZANENKO (Space Research Institute (IKI-RAS), Russia)

Victor REGLERO (University of Valencia)
 Jakub RIPA (Sungkyunkwan University, Suwon, Korea)
 Antonia ROWLINSON (University of Ámsterdam, The Netherlands)
 Andrea ROSSI (Thüringer Landessternwarte Tautenburg, Germany)

José SACAHUI (Instituto de Astronomía, Universidad Nacional Autónoma de
 México)
 Rubén SÁNCHEZ-RAMÍREZ (Instituto de Astrofísica de Andalucía
 (IAA-CSIC) Granada, Spain)
 Kostas SAPOUNTZIS (National University of Athens, Greece)
 Re'em SARI (Hebrew University of Jerusalem, Israel)
 Sandra SAVAGLIO (Max-Planck Institute for Extraterrestrial Physics (MPE)
 Garching, Germany)
 Motoko SERINO (RIKEN, Japan)
 Vojtech SIMON (Astronomical Institute AS CR, Ondrejov, Czech Republic)
 Aleksey SHLYAPNIKOV (Crimean Astrophysical Observatory, Ukraine)
 Ilya SOKOLOV (Institute of Astronomy of Russian Academy of Sciences,
 Russia)
 Tatyana SOKOLOVA (Special Astrophysical Observatory of Russian Academy
 of Sciences, Russia)
 Sergey SVERTILOV (Lomonosov Moscow St Univ. Skobeltsyn Inst. of Nuclear
 Physics (MSU SINP), Russia)

Gianpiero TAGLIAFERRI (Osservatorio Astronomico di Brera (INAF-OAB),
 Italy)
 Pak Hin Thomas TAM (National Tsing Hua University, Taiwan)
 Nial TANVIR (University of Leicester, UK)
 Juan Carlos TELLO (Instituto de Astrofísica de Andalucía (IAA-CSIC) Granada,
 Spain)
 Kim TIBBETS-HARLOW (University of Leicester, UK)
 Lev TITARCHUK (University of Ferrara, Italy)
 Martin TOPINKA (University College Dublin, Ireland)

Eleonora TROJA (NASA-Goddard Space Flight Center, USA)

Nikolay VEDENKIN (Lomonosov Moscow St. Univ Skobeltsyn Inst. of Nuclear Physics (MSU SINP), Russia)

Susanna VERGANI (Osservatorio Astronomico di Brera (INAF-OAB), Italy)

Alina VOLNOVA (Sternberg Astronomical Institute of Moscow State University (SAI MSU), Russia)

Klaas WIERSEMA (University of Leicester, UK)

Ivan YASHIN (Lomonosov Moscow St. Univ Skobeltsyn Inst. of Nuclear Physics (MSU SINP), Russia)

Bing ZHANG (University of Nevada-Las Vegas, USA)

Fu-Wen ZHANG (Purple Mountain Observatory, China)

Xiaohong ZHAO (Yunnan Astronomicañ Observatory, China)

Contents

<i>List of participants</i>	VII
-----------------------------------	-----

Editorial	1
-----------------	---

Chapter I: Historical Remarks

The History of BATSE G.J. Fishman	5
Early Danish GRB Experiments – and some for the Future? N. Lund	15
Ioffe Institute GRB Experiments: Past, Present and Future R.L. Aptekar, S.V. Golenetskii, D.D. Frederiks, E.P. Mazets and V.D. Palshin	27

Chapter II: Prompt Emission-I Observations

<i>Fermi</i> and <i>Swift</i> Observations of Short GRBs E. Troja	39
Temporal Decomposition Studies of GRB Lightcurves N.P. Bhat	45
Photospheric Emission from Gamma-Ray Bursts M. Axelsson	53
GRBs Observed by MAXI M. Serino, T. Sakamoto, A. Yoshida, N. Kawai, M. Morii, M. Sugizaki, S. Nakahira, H. Negoro, T. Mihara, Y. Nishimura, Y. Ogawa and M. Matsuoka	59
Searching for Galactic Sources in the <i>Swift</i> GRB Catalog J.C. Tello, A.J. Castro-Tirado, J. Gorosabel, D. Pérez-Ramírez, S. Guziy, R. Sánchez, M. Jelínek, P. Veres and Z. Bagoly	65

<i>Konus-WIND</i> Observation of the Ultra-Luminous GRB 110918A D. Frederiks, D. Svinkin, R. Aptekar, S. Golenetskii, E. Mazets, P. Oleynik, V. Pal'shin, A. Tsvetkova, M. Ulanov and T. Cline.....	71
Gamma-Ray Bursts: The Dependence of the Spectral Lag on the Energy P. Minaev, A. Pozanenko, S. Grebenev and S. Molkov	75
On the Properties of Spectral Lags and Peak-Count Rates of RHESSI Gamma-Ray Bursts J. Řípa, A. Mészáros, P. Veres and I.H. Park	79
<i>Fermi</i> /LAT Observations of GRB 110625A P.H.T. Tam, A.K.H. Kong and Y.-Z. Fan	83
Intrinsic Properties of <i>Swift</i> Long Gamma-Ray Bursts F.-W. Zhang	87
The Multi-Band Emission Profile in GRB X.-H. Zhao and J.-M. Bai	91
On the Prompt Signals of Gamma Ray Bursts P. Chen, T. Tajima and Y. Takahashi	95

Chapter III: Prompt Emission-II Theory

Radiative Mechanisms in GRB Prompt Emission A. Pe'er	105
Wide-Band Spectra of Prompt Emission K. Asano	115
Global Properties of High-Energy Emission from Gamma-Ray Bursts N. Omodei, G. Vianello, F. Piron, V. Vasileiou, S. Razzaque and the Fermi Large Area Telescope collaboration	123
On Amati Relation For GRB Prompt Emission L. Titarchuk and R. Farinelli	129
Relativistic Filamentation Instability in an Arbitrarily Oriented Magnetic Field E. Pérez-Álvaro and A. Bret	135

Chapter IV: Jet Dynamics

Gamma-Ray Burst Jet Dynamics J. Granot	141
Cooling-Induced Structures in Collapsar Accretion Disks A. Batta and W.H. Lee	153
3D GRB Jets Drilling Through the Progenitor D. López-Cámara	159
Radio Afterglow of the Jetted Tidal Disruption Event <i>Swift</i> J1644+57 B.D. Metzger, D. Giannios and P. Mimica	165
Magnetic Field Amplification and Saturation by Turbulence in a Relativistic Shock Propagating through an Inhomogeneous Medium Y. Mizuno, M. Pohl, J. Niemiec, B. Zhang, K.-I. Nishikawa and P.E. Hardee	173
Radiation from Accelerated Particles in Relativistic Jets with Shocks, Shear-Flow, and Reconnection K.-I. Nishikawa, B. Zhang, I. Dutan, M. Medvedev, P. Hardee, E.J. Choi, K.W. Min, J. Niemiec, Y. Mizuno, A. Nordlund, J.T. Frederiksen, H. Sol, M. Pohl and D.H. Hartmann	177
Acceleration of Magnetized Collapsar Jets After Breakout K. Sapountzis and N. Vlahakis	181
GRB Prompt Emission and the Physics of Ultra-Relativistic Outflows F. Daigne	185

Chapter V: Afterglow Emission-I Long GRBs (Observations)

Linear and Circular Polarimetry Observations of Gamma-Ray Burst Afterglows K. Wiersema	195
Implications of Early Time Observations of Optical Afterglows of GRBs S.B. Pandey and W. Zheng	203

An Intrinsic Correlation Between GRB Optical/UV Afterglow Brightness and Decay Rate S.R. Oates, M.J. Page, M. De Pasquale, P. Schady, A.A. Breeveld, S.T. Holland, N.P.M. Kuin and F.E. Marshall	211
Physical Properties of Rapidly Decaying Afterglows M. De Pasquale, S. Schulze, D.A. Kann, S. Oates and B. Zhang	217
Tackling the Afterglow Forward-Shock Model with GROND R. Filgas	223
A Complete Sample of Long Bright <i>Swift</i> GRBs G. Tagliaferri, R. Salvaterra, S. Campana, S. Covino, P. D'Avanzo, D. Fugazza, G. Ghirlanda, G. Ghisellini, A. Melandri, B. Sbarufatti, S. Vergani and L. Nava	229
Observing GRB Afterglows, SNe and their Host Galaxies with the 10.4 m Gran Telescopio Canarias (GTC) J. Gorosabel, A.J. Castro-Tirado, A. de Ugarte Postigo, C.C. Thöne, R. Sánchez-Ramírez, D. Pérez-Ramírez, J.C. Tello, M. Jelínek and S. Guziy	235
Statistical Properties of GRB Afterglow Parameters as Evidence of Cosmological Evolution of Host Galaxies G. Beskin, G. Oganesyan, G. Greco and S. Karpov	241
VLT/X-Shooter Absorption Spectroscopy of the GRB 120327A Afterglow V. D'Elia	247
GRBS Followed-Up by the Bootes Network S. Guziy, A. Castro-Tirado, M. Jelínek, J. Gorosabel, P. Kubánek, R. Cunniffe, O. Lara-Gil, O. Rabaza-Castillo, A. de Ugarte Postigo, R. Sánchez-Ramírez, J. Tello, C. Pérez del Pulgar, S. Castillo-Carrión, J. Castro Cerón, T. de J. Mateo Sanguino, R. Hudec, S. Vitek, B. de la Morena Carretero, J. Díaz Andreu, R. Fernández-Muñoz, D. Pérez-Ramírez, P. Yock, W. Allen, I. Bond, I. Kheyfets, G. Christie, L. Sabau-Graziati, C. Cui, Y. Fan and I.H. Park	251
Cataclysmic Variables and Gamma-Ray Sources E. Pavlenko, V. Malanushenko, S. Shugarov and D. Chochol	255

Gamma-Ray Burst Observations with ISON Network A. Pozanenko, L. Elenin, E. Litvinenko, A. Volnova, A. Erofeeva, A. Matkin, A. Ivanov, V. Ivanov, D. Varda, E. Sinyakov, V. Nevski, Yu. Krugly, A. Erofeev, N. Tungalag, R. Inasaridze, O. Kvaratskhelia, V. Kouprianov and I. Molotov	259
Managing GRB Afterglows Optical/IR Observations in the Web 2.0 Era D. Ricci and L. Nicastro	263
GRB 110715A: Multiwavelength Study of the First Gamma-Ray Burst Observed with ALMA R. Sánchez-Ramírez, P. Hancock, T. Murphy, A. de Ugarte Postigo, J. Gorosabel, D.A. Kann, C.C. Thöne, A. Lundgren, A. Kamble, S.R. Oates, J.P.U. Fynbo, I. de Gregorio Monsalvo, D. García-Appadoo, S. Martín, N.P.M. Kuin, J. Greiner and A.J. Castro-Tirado	267
Color Indices of Optical Afterglows of Long GRBs in the <i>Swift</i> Era V. Šimon, G. Pizzichini and R. Hudec	271
A Case Study of Dark GRB 051008 A. Volnova, A. Pozanenko, J. Gorosabel, D. Perley, D.A. Kann, D. Frederiks, V. Rumyantsev, A.J. Castro-Tirado and P. Minaev	275
Millimetre Observations of Gamma-Ray Bursts at IRAM A.J. Castro-Tirado, M. Bremer, J.M. Winters, J.C. Tello, S.B. Pandey, A. de Ugarte Postigo, J. Gorosabel, S. Guziy, M. Jelinek, R. Sánchez-Ramírez, D. Pérez-Ramírez and J.M. Castro Cerón	279

Chapter VI: Afterglow Emission-II (Theory)

GRB Afterglow B. Zhang	285
Theoretical Aspects of the Fireball Scenario A. Bret, A. Stockem, E. Pérez-Álvaro, F. Fiúza, C. Ruyer, L. Gremillet, R. Narayan and L.O. Silva	295
Similarities: GRB 940217, GBR 090926A and GRB 980923 J.R. Sacahui, M.M. González, N. Fraija, J.L. Ramirez and W.H. Lee	301

Chapter VII: Short GRBs

Multi-Wavelength Observations of Short-Duration Gamma-Ray Bursts: Recent Results D.A. Kann	309
Short Duration Gamma-Ray Burst with Extended Emission A. Pozanenko and M. Barkov.....	319
Short GRB Afterglows Observed with GROND A. Nicuesa Guelbenzu, S. Klose, A. Rossi, S. Schmidl, J. Greiner, D.A. Kann, J. Elliott, F. Olivares E., A. Rau, P. Schady, V. Sudilovsky, T. Krühler, P. Ferrero, S. Schulze, P.M.J. Afonso, R. Filgas and M. Nardini.....	325
GRB Emission in Neutron Star Transitions M.A. Pérez-García, F. Daigne and J. Silk.....	331
Spectral Evolution of Short GRBS on Sub-Millisecond Time Scale A. Chernenko	337
Nucleosynthesis from LGRB-Type Accretion Disks T. Liu, L. Xue, W.-M. Gu and J.-F. Lu.....	341
A GTC Study of the Afterglow and Host Galaxy of the Short-Duration GRB 100816A D. Pérez-Ramírez, J.P. Norris, J. Gorosabel, A.J. Castro-Tirado, L. Hernández-García, A. de Ugarte Postigo, S. Guziy, J.C. Tello, R. Sánchez-Ramírez and P. Ferrero.....	345
High-Energy Emission in Short GRBs and the Role of Magnetar Central Engines A. Rowlinson and P.T. O'Brien.....	351

Chapter VIII: Progenitors and Environments

Dissecting the GRB Environment with Optical and X-Ray Observations S. Campana	359
Early UV/Optical Emission of the Type IB SN 2008D M.C. Bersten.....	367

The Circumstellar Medium Surrounding Rotating Massive Stars as GRB Precursors B. Pérez-Rendón, J. Higuera, G. García-Segura, A. Santillán and L. Hernández-Cervantes	371
---	-----

GRB Afterglows: A Story Yet to be Written S. Covino	375
--	-----

Chapter IX: Host Galaxies

The Cosmic Evolution of Gamma-Ray Burst Host Galaxies S. Savaglio	381
Keck Observations of 160 Gamma-Ray Burst Host Galaxies D.A. Perley, J.S. Bloom and J.X. Prochaska	391
The Redshift Distribution of the Tough Survey P. Jakobsson, J. Hjorth, D. Malesani, J.P.U. Fynbo, N.R. Tanvir, B. Milvang-Jensen and T. Krühler	397
GRB–SN Connection in SAO RAS Observations A.S. Moskvitin, V.V. Sokolov, V.N. Komarova <i>et al.</i>	403
X-Shooter Slit Observations of GRB Host Galaxies S.D. Vergani	407
On the Metal Aversion of LGRBs J.F. Graham and A.S. Fruchter	413
Probing Galaxy Evolution with Gamma-Ray Bursts N.R. Tanvir	421
The Mass-SFR-Metallicity Relation of Star Forming Galaxies and its Evolution: Implications for GRB/SN Host Galaxies Y. Niino	427
A Deep Search for the Host Galaxies of GRBs with no Detected Optical Afterglow A. Rossi, S. Klose, P. Ferrero, J. Greiner, A. Updike, D.A. Kann, T. Krühler and A. Nicuesa Guelbenzu	431
Study of BTA, Hubble, and Spitzer GRB 021004 Deep Fields I.V. Sokolov, O.J.A. Bravo Calle and Yu.V. Baryshev	435

The Multi-Band Study of the Environment of the RC J0311+0507
 Radio Galaxy: A Step Forward to Understand Massive Stellar
 System Formation at $Z > 4$

Yu.N. Parijskij, O.P. Zhelenkova, P. Thomasson, A.I. Kopylov, A.V. Temirova, I.V. Sokolov, V.N. Komarova and O.J.A. Bravo Calle.....	439
--	-----

GRB Host Galaxies: A Fascinating Research Field

S. Klose	443
----------------	-----

**Chapter X: Instrumentation and Techniques-I
 (Ongoing Projects)**

Recent Progress on GRBs with *Swift*

N. Gehrels and J.K. Cannizzo	449
------------------------------------	-----

The Interplanetary Network

K. Hurley, I.G. Mitrofanov, D. Golovin, M.L. Litvak, A.B. Sanin, W. Boynton, C. Fellows, K. Harshman, R. Starr, S. Golenetskii, R. Aptekar, E. Mazets, V. Pal'shin, D. Frederiks, D. Svinkin, D.M. Smith, W. Hajdas, A. von Kienlin, X. Zhang, A. Rau, K. Yamaoka, T. Takahashi, M. Ohno, Y. Hanabata, Y. Fukazawa, M. Tashiro, Y. Terada, T. Murakami, K. Makishima, T. Cline, S. Barthelmy, J. Cummings, N. Gehrels, H. Krimm, D. Palmer, J. Goldsten, E. Del Monte, M. Feroci, M. Marisaldi, V. Connaughton, M.S. Briggs and C. Meegan.....	459
--	-----

Status and Perspectives of Mini-MegaTORTORA Wide-Field
 Monitoring System with High Temporal Resolution

S. Karpov, G. Beskin, S. Bondar, A. Perkov, E. Ivanov, A. Guarnieri, C. Bartolini, G. Greco, A. Shearer and V. Sasyuk	465
--	-----

Status of the BOOTES-IR Project at OSN for GRB near-IR
 Follow-Up

R. Cunniffe, A.J. Castro-Tirado, M. Jelínek, J. Gorosabel, B. Moliné and F. García-Segura	471
--	-----

Photometric Observations of GRB 080605 by BOOTES-1B
 and BOOTES-2

M. Jelínek, E. Gómez Gauna, A.J. Castro-Tirado and J. Gorosabel, on behalf of the BOOTES Collaboration	475
---	-----

Status of Pi of the Sky Telescopes in Spain and Chile T. Batsch, H. Czyrkowski, M. Cwiok, R. Dabrowski, G. Kasprowicz, A. Majcher, A. Majczyna, K. Malek, L. Mankiewicz, K. Nawrocki, R. Opiela, L.W. Piotrowski, M. Siudek, M. Sokolowski, R. Wawrzaszek, G. Wrochna, M. Zaremba and A.F. Żarnecki	479
GLORIA - the GLObal Robotic Telescopes Intelligent Array for E-Science L. Mankiewicz and on behalf of the GLORIA collaboration	483
Status Update of the Watcher Robotic Telescope M. Topinka, S. Meehan, L. Hanlon, P. Tisdall, H. van Heerden, P. Meintjes, M. Hoffman, M. Jelínek and P. Kubánek	487
<i>Swift</i> Publication Statistics and the Comparison with Other Major Observatories S. Savaglio and U. Grothkopf	491
Astronomical Hosting in Central Asia A. Pozanenko, A. Volnova, S. Guziy, N. Tungalag, E. Klunko and I. Molotov	495

Chapter XI: Instrumentation & Techniques-II (*Lomonosov/UFFO*)

Ultra-Fast Flash Observatory: Fast Response Space Missions for Early
Time Phase of Gamma Ray Bursts

I.H. Park, S. Ahmad, P. Barrillon, S. Brandt, C. Budtz-Jørgensen, A.J. Castro-Tirado, P. Chen, J.N. Choi, Y.J. Choi, P. Connell, S. Dagoret-Campagne, C. Eyles, B. Grossan, M.-H.A. Huang, A. Jung, S. Jeong, J.E. Kim, M.B. Kim, S.-W. Kim, Y.W. Kim, A.S. Krasnov, J. Lee, H. Lim, E.V. Linder, T.-C. Liu, K.W. Min, G.W. Na, J.W. Nam, M.I. Panasyuk, H.W. Park, J. Ripa, V. Reglero, J.M. Rodrigo, G.F. Smoot, S. Svertilov, N. Vedenkin, M.-Z. Wang and I. Yashin	501
--	-----

The Ultra Fast Flash Observatory Pathfinder – UFFO-p GRB Imaging
and Location with its Coded Mask X-Ray Imager UBAT

P.H. Connell and V. Reglero, on behalf of the UFFO collaboration	517
---	-----

Design, Construction and Performance of the Detector for UFFO Burst Alert & Trigger Telescope

- J. Lee, S. Jeong, J.E. Kim, Y.W. Kim, G.W. Na, J.E. Suh, M. Kim, H. Lim, I.H. Park, J. Ripa, J.N. Choi, S.-W. Kim, Y.J. Choi, K.W. Min, P. Chen, J.J. Huang, T.-C. Liu, J.W. Nam, M.-Z. Wang, M.-H.A. Huang, P. Connell, C. Eyles, V. Reglero, J.M. Rodrigo and A.J. Castro-Tirado 525

The Calibration and Simulation of the GRB Trigger Detector of the Ultra Fast Flash Observatory

- M.-H.A. Huang, S. Ahmad, P. Barrillon, S. Brandt, C. Budtz-Jørgensen, A.J. Castro-Tirado, S.-H. Chang, Y.-Y. Chang, C.R. Chen, P. Chen, H.S. Choi, Y.J. Choi, P. Connell, S. Dagoret-Campagne, C. Eyles, B. Grossan, J.J. Huang, S. Jeong, A. Jung, J.-E. Kim, M.-B. Kim, S.-W. Kim, Y.-W. Kim, A.S. Krasnov, J. Lee, H. Lim, C.-Y. Lin, E.V. Linder, T.-C. Liu, N. Lund, K.W. Min, G.-W. Na, J.-W. Nam, M.I. Panasyuk, I.H. Park, V. Reglero, J. Řípa, J.M. Rodrigo, G.F. Smoot, J.-E. Suh, S. Svertilov, N. Vedenkin, M.-Z. Wang and I. Yashin 531

The Slewing Mirror Telescope and the Data-Acquisition System for the UFFO-Pathfinder

- H. Lim, S. Ahmad, P. Barrillon, S. Brandt, C. Budtz-Jørgensen, A.J. Castro-Tirado, P. Chen, Y.J. Choi, P. Connell, S. Dagoret-Campagne, C. Eyles, B. Grossan, M.-H.A. Huang, A. Jung, S. Jeong, J.E. Kim, M.B. Kim, S.-W. Kim, Y.W. Kim, A.S. Krasnov, J. Lee, E.V. Linder, T.-C. Liu, N. Lund, K.W. Min, G.W. Na, J.W. Nam, M.I. Panasyuk, I.H. Park, J. Ripa, V. Reglero, J.M. Rodrigo, G.F. Smoot, J.E. Suh, S. Svertilov, N. Vedenkin, M.-Z. Wang and I. Yashin 537

Space Experiments On-Board of *Lomonosov* Mission to Study Gamma-Ray Bursts and UHECRS

- A.M. Amelushkin, V.V. Bogomolov, V.V. Benghin, G.K. Garipov, E.S. Gorbovskoy, B. Grossan, P.A. Klimov, B.A. Khrenov, J. Lee, V.M. Lipunov, G. Na, M.I. Panasyuk, I.H. Park, V.L. Petrov, G.F. Smoot, S.I. Svertilov, Yu. Shprits, N.N. Vedenkin and I.V. Yashin 545

BDRG and Shok Instruments for Study of GRB Prompt Emission in Michaylo *Lomonosov* Space Mission

- A.M. Amelushkin, V.V. Bogomolov, V.I. Galkin, B.V. Goncharov, E.S. Gorbovskoy, V.G. Kornilov, V.M. Lipunov, M.I. Panasyuk, V.L. Petrov, G.F. Smoot, S.I. Svertilov, N.N. Vedenkin and I.V. Yashin 553

Development of Slewing Mirror Telescope Optical System
for the UFFO-Pathfinder

S. Jeong, J.W. Nam, K.-B. Ahn, I.H. Park, S.-W. Kim, J. Lee,
H. Lim, S. Brandt, C. Budtz-Jørgensen, A.J. Castro-Tirado,
P. Chen, M.H. Cho, J.N. Choi, B. Grossan, M.A. Huang, A. Jung,
J.E. Kim, M.B. Kim, Y.W. Kim, E.V. Linder, K.W. Min, G.W. Na,
M.I. Panasyuk, J. Ripa, V. Reglero, G.F. Smoot, J.E. Suh,
S. Svertilov, N. Vedenkin and I. Yashin

561

Design and Implementation of Electronics and Data Acquisition System
for Ultra-Fast Flash Observatory

A. Jung, S. Ahmad, P. Barrillon, S. Brandt, C. Budtz-Jørgensen,
A.J. Castro-Tirado, S.-H. Chang, Y.-Y. Chang, C.R. Chen, P. Chen,
H.S. Choi, Y.J. Choi, P. Connell, S. Dagoret-Campagne, C. Eyles,
B. Grossan, J.J. Huang, M.-H.A. Huang, S. Jeong, J.E. Kim,
M. Kim, S.-W. Kim, Y.W. Kim, A.S. Krasnov, J. Lee, H. Lim,
C.-Y. Lin, E.V. Linder, T.-C. Liu, N. Lund, J.W. Nam, K.W. Min,
G.W. Na, M.I. Panasyuk, I.H. Park, V. Reglero, J. Ripa,
J.M. Rodrigo, G.F. Smoot, J.E. Suh, S. Svertilov, N. Vedenkin,
M.-Z. Wang and I. Yashin, on behalf of the UFFO collaboration.....

567

Development of Motorized Slewing Mirror Stage for the UFFO Project

J. Nam, for the UFFO Collaboration, K.B. Ahn, M. Cho, S. Jeong,
J.E. Kim, S. Ahmad, P. Barrillon, S. Brandt, C. Budtz-Jørgensen,
A.J. Castro-Tirado, C.-H. Chang, C.-Y. Chang, Y.Y. Chang,
C.R. Chen, P. Chen, H.S. Choi, Y.J. Choi, P. Connell,
S. Dagoret-Campagne, C. Eyles, B. Grossan, J.J. Huang,
M.-H.A. Huang, A. Jung, M.B. Kim, S.-W. Kim, Y.W. Kim,
A.S. Krasnov, J. Lee, H. Lim, E.V. Linder, T.-C. Liu, N. Lund,
K.W. Min, G.W. Na, M.I. Panasyuk, I.H. Park, V. Reglero,
J. Ripa, J.M. Rodrigo, G.F. Smoot, J.E. Suh, S. Svertilov,
N. Vedenkin, M.-Z. Wang and I. Yashin

573

In-Flight Calibrations of UFFO-Pathfinder

J. Řípa, S. Ahmad, P. Barrillon, S. Brandt, C. Budtz-Jørgensen,
A.J. Castro-Tirado, S.-H. Chang, Y.-Y. Chang, C.R. Chen, P. Chen,
H.S. Choi, Y.J. Choi, P. Connell, S. Dagoret-Campagne, C. Eyles,
B. Grossan, J.J. Huang, M.-H.A. Huang, S. Jeong, A. Jung,
J.-E. Kim, M.-B. Kim, S.-W. Kim, Y.-W. Kim, A.S. Krasnov,
J. Lee, H. Lim, C.-Y. Lin, E.V. Linder, T.-C. Liu, N. Lund,
K.W. Min, G.-W. Na, J.-W. Nam, M.I. Panasyuk, I.H. Park,
V. Reglero, J.M. Rodrigo, G.F. Smoot, J.-E. Suh, S. Svertilov,
N. Vedenkin, M.-Z. Wang, I. Yashin and others from the UFFO
collaboration

579

Chapter XII: Cosmology and Early Universe

Gamma-Ray Bursts and the First Stars V. Bromm	585
A Common Behavior in the Late X-Ray Afterglow of Energetic GRB-SN Systems L. Izzo, G.B. Pisani, M. Muccino, J.A. Rueda, Y. Wang, C.L. Bianco, A.V. Penacchioni and R. Ruffini	595

Chapter XIII: Instrumentation & Techniques-III Future Projects

X-Ray and Gamma-Ray Polarimetry of GRBs E. Costa	601
GRBs and Lobster Eye X-Ray Telescopes R. Hudec, L. Pina, V. Marsikova and A. Inneman.....	611
Observing GRBs with the <i>LOFT</i> Wide Field Monitor S. Brandt, M. Hernanz, M. Feroci, L. Amati, Alvarez, P. Azzarello, D. Barret, E. Bozzo, C. Budtz-Jørgensen, R. Campana, A. Castro-Tirado, A. Cros, E. Del Monte, I. Donnarumma, Y. Evangelista, J.L. Galvez Sanchez, D. Götz, F. Hansen, J.W. den Herder, A. Hornstrup, R. Hudec, D. Kareljin, M. van der Klis, S. Korpela, I. Kuvvetli, N. Lund, P. Orleanski, M. Pohl, A. Rachevski, A. Santangelo, S. Schanne, C. Schmid, L. Stella, S. Suchy, C. Tenzer, A. Vacchi, J. Wilms, N. Zampa, J.J.M. in't Zand and A. Zdziarski	617
<i>A-STAR</i> : The All-Sky Transient Astrophysics Reporter J.P. Osborne, P. O'Brien, P. Evans, G.W. Fraser, A. Martindale, J.-L. Atteia, B. Cordier and S. Mereghetti	625
Feasibility of a Small, Rapid Optical/IR Response, Next Generation Gamma-Ray Burst Mission B. Grossan, G.F. Smoot, V.V. Bogomolov, S.I. Svertilov, N.N. Vedenkin, M. Panasyuk, B. Goncharov, G. Rozhkov, K. Saleev, E. Grobovskoj, A.S. Krasnov, V.S. Morozenko, V.I. Osedlo, E. Rogkov, T.V. Vachenko and E.V. Linder	633
GRB Potential of ESA <i>Gaia</i> R. Hudec and V. Šimon	639

Chapter XIV: Non Electromagnetics, VHE and UHE Emission

Constraining GRB as Source for UHE Cosmic Rays through Neutrino Observations P. Chen	647
<i>Fermi</i> GBM Capabilities for Multi-Messenger Time-Domain Astronomy V. Connaughton, V. Pelassa, M.S. Briggs, P. Jenke, E. Troja, J.E. McEnery and L. Blackburn	657
Cosmic-Rays and Gamma Ray Bursts A. Meli.....	663
Concluding Remarks L. Mankiewicz	667
Author Index	671

Editorial

A.J. Castro-Tirado¹, J. Gorosabel^{1,2,3} and I.H. Park⁴

Many of us started our research in the gamma-ray burst field in the 1990's, and we still remember the Hunstville GRB Symposium in 1991 where the first BATSE results were presented showing the isotropic distribution of the bursts, confirming the earlier hints provided by the *VENERA* satellites, besides the first "accurate" GRB localizations by WATCH onboard *Granat*. And then, 15 yrs ago, *BeppoSAX* allowed the detection of the first GRB X-ray afterglow, leading to the detection of afterglows at other wavelengths (optical, radio) in the years to come, probing the cosmological distance scale. We do appreciate that Jerry Fishman, Niels Lund and Raphail Aptekar could make it to this Conference. They inspired the work from many other colleagues and friends too who are also here in the audience.

But now we should concentrate in the future. There are still many other open issues which we still should address, regarding both theoretical and observational aspects: prompt emission and afterglow physics, progenitors (including Pop III stars), host galaxies, multi messenger information, etc. The manuscripts published in this Volume of the European Astronomical Society Conference Series are the fruit of the Fall 2012 Gamma-ray Burst Symposium held in Málaga (Spain) on 8-12 Oct., 2012.

The Scientific Organizing Committee prepared a very comprehensive scientific program which covered many fields. We heard from the new technical developments on ground and on the future experiments and missions, like the forthcoming *Lomonosov* satellite carrying the Ultra-Fast Flash Observatory (UFFO) experiment onboard, which will be launched end of this year. The research in the field is still very exciting for the new generation of young astronomers, which we expect will be as enthusiastic as we were 15 yr ago, when the first GRB afterglow was discovered.

The Symposium was organized by both the Instituto de Astrofísica de Andalucía of the Spanish Research Council (IAA-CSIC) and the Department of System Engineering and Automatics at Universidad de Málaga (UMA), the Ewha Womans University in Seoul and the LeCospa Center in Taiwan. We want to thank the members of the Scientific Organizing Committee (SOC): S. Brandt, A.J. Castro-Tirado (chair), V. Connaughton, S. Covino, F. Daigne, K. Hurley,

¹ Instituto de Astrofísica de Andalucía (IAA-CSIC), Granada, Spain

² Unidad Asociada Grupo Ciencia Planetarias UPV/EHU-IAA/CSIC, Departamento de Física Aplicada I, E.T.S. Ingeniería, Universidad del País Vasco UPV/EHU, Bilbao, Spain

³ Ikerbasque, Basque Foundation for Science, Bilbao, Spain

⁴ Department of Physics, Sungkyunkwan University, Suwon, Korea

N. Kawai, S. Klose, K. Page, S.B. Pandey, I.H. Park, G.F. Smoot, V. Sokolov and T. Piran for arranging an excellent scientific programme, and thanks all the chairman/chairwomen who accepted to lead the 14 sessions. We also want to express our gratitude to the members of the Local Organizing Committee (LOC): A. Castro, R. Cunniffe, J. Gorosabel (chair), M. Jelinek, O. Lara-Gil, S. Guziy, V. Muñoz-Fernández, C. Pérez del Pulgar, M. Pérez-Ramírez, R. Sánchez-Ramírez and J.C. Tello. We thank Irina Guziy for designing the nice Conference announcement poster, Oscar Lara-Gil for acting as a careful website (grb2012.iaa.es) curator also taking care of the 741 pictures (thanks to all contributors!) available to all attendants, and Sergey Guziy for editing the “official” post-conference videoclip (25 min 49 s) (also available at the site) depicting not only the Conference itself but also the many social events carried out during the unforgettable five days.

Finally, some of us (AJCT & JGU) managed a long-awaited dream: the first GRB Symposium ever host in Spain. Moreover, the event was hosted in “Málaga-Costa del Sol” region, which includes Marbella, 50 km away from Málaga, AJCT’s home town. This region is the product of the mixing of many civilizations. Málaga was funded by the Phoenicians more than 3.000 yr ago and Carthaginians, Romans, Moorish and Jewish populated this land over the last two millennia. Mathematics and astronomy amongst other disciplines flourished in Málaga (and in all over Al-Andalus, Andalucia) 1.000 yr ago, thanks to the Moorish heritage, which was revealed on Wednesday afternoon during the guided visit to Málaga and the Conference Dinner near the Moorish Gibralfaro Castle. Visiting to Granada or Tanger (Morocco, across Gibraltar Straight) on Friday (the whole day!) led the participants to check this splendour.

Marbella (meaning Beautiful Sea) was also a Phoenician settlement 2.700 years ago. 45 years ago Marbella was an agricultural town with a mining industry and some 10.000 inhabitants. Today there are more than 100.000 inhabitants with many of them being from all over the world, hence Marbella is recognized nowadays as a “Universal City” and probably the most famous turistic destination all over Spain. In this respect, the Local Organizing Committee tried to complete the Scientific Program with social events for attendants and accompanying persons to get acquainted around Marbella and we do believe that all participants enjoyed the staying too (in spite of the non-optimal wifi connection within the Auditorium which allowed attendants to concentrate on the talks; not a bad idea after all). Swimming at night in the sea was also possible due to the mild temperatures in October, even after the Flamenco Dance dinner and show on Thursday!

To conclude, we want to express our deepest thanks to both the Marbella Town Hall and Hotel Spa Senator Marbella (wonderful Jacuzzi free of charge for participants!) for a charming atmosphere all over, an to the University of Málaga, the Spanish Research Council, the Fundación Málaga, Sungkyunkwan University in Korea and the LeCospa Center in Taiwan for their support to arrange this Symposium.

Thanks / Gracias /감사합니다.

A.J. Castro-Tirado, J. Gorosabel, and I.H. Park, in Málaga, on 21 March 2013.

Chapter I.

Historical Remarks

THE HISTORY OF BATSE

G.J. Fishman¹

Abstract. The BATSE experiment on the Compton Gamma-ray Observatory was the first large detector system designed for the study of gamma-ray bursts. The eight large-area detectors allowed full-sky coverage and were optimized to operate in the primary energy region of emission of most GRBs. BATSE provided detailed observations of the temporal and spectral characteristics of several thousand GRBs, and it was the first experiment to provide rapid notifications of the coarse location of many them. It also provided strong evidence for the cosmological distances to GRBs through the observation of the sky distribution and intensity distribution of numerous GRBs. The large number of GRBs observed with the high-sensitivity BATSE detectors continues to provide a database of GRB spectral and temporal properties in the primary energy range of GRB emission that will likely not be exceeded for at least another decade. The origin and development of the BATSE experiment, some highlights from the mission and its continuing legacy are described in this paper.

1 How BATSE began

Soon after the announcement of the discovery of GRBs by the Los Alamos Group with the Vela satellites (Klebesadel *et al.* 1973) it was realized that balloon flight observations of them were possible by means of sufficiently large area, sensitive detectors. An extrapolation of a $-3/2$ power law intensity distribution of them, expected for a homogeneous, three-dimensional distribution of GRB sources to lower intensities would yield a GRB rate of several dozen per day over the full sky. Thus, a balloon-borne detector system with an effective area of $\sim 1 \text{ m}^2$ had a good chance of observing ~ 10 GRBs during a balloon flight of reasonable duration.

Using the cosmic ray research facilities and personnel kindly made available by T. Parnell at the NASA-Marshall Space Flight Center (MSFC), I decided to begin a modest balloon flight program aimed at observing GRBs that were considerably

¹ ZP12, NASA-Marshall Space Flight Center, Huntsville, AL, 35812 USA;
e-mail: jerry.fishman@nasa.gov

weaker than those observed by the Vela spacecraft and by other small, space-borne detectors. Large-area crystal scintillation detectors were fabricated using cheap, scrap pieces of thallium-activated sodium iodide scintillator crystals, NaI(Tl), immersed in clear mineral oil (Fishman 1974; Fishman & Austin 1976), as seen in Figure 1. These hermetically-sealed detectors had a crystal thickness of ~ 2 cm, with a high detection efficiency for gamma radiation up to a few hundred keV. Two balloon flights with a total duration of 28 hours were carried out in 1975 and 1977 from Palestine, Texas using an array of these detectors on a balloon payload similar to that shown in Figure 2. These observations resulted in an observed GRB rate that was well below that expected for a homogeneous, nearby distribution of GRBs (Fishman *et al.* 1978).

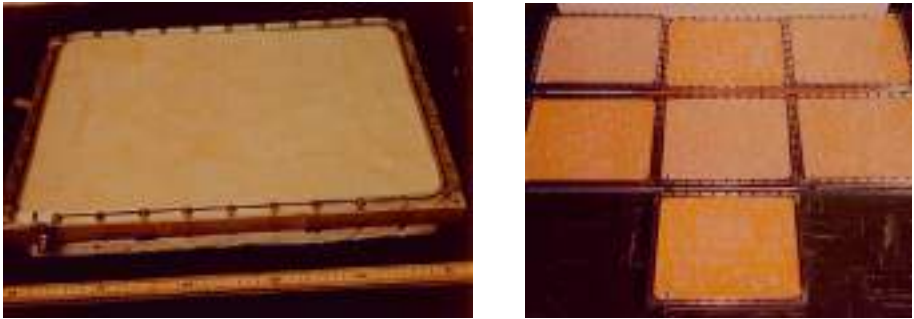


Fig. 1. *Left:* a single large area detector tray made from NaI(Tl) scintillation crystal pieces. *Right:* a group of seven NaI(Tl) detector trays developed for balloon flight observations of GRBs. Notice the variation in the amount of hydration (yellow color) of the crystals in the different trays. This hydration was largely reversible by pumping the interior of the trays for long periods and removing the moisture.

2 The BATSE proposal

NASA Headquarters issued an Announcement of Opportunity (AO) in 1977, soliciting proposals for instruments for a large Gamma-Ray Observatory (GRO), originally scheduled for launch in 1985. This spacecraft was intended to be the second of the four “Great Observatories in Space” that NASA planned to launch with the Space Shuttle in the 1980s (Hubble was the first of the series; Chandra was the third; Spitzer was the forth). Initially, our balloon group in Huntsville had not planned to submit a proposal, but at the suggestion of Tom Cline and with the encouragement of Tom Parnell, a proposal was submitted with myself (G. Fishman) as the Principal Investigator (P.I.). Chip Meegan and Tom Parnell were Co-Investigators.

The objectives of the experiment were to observe the coarse sky distribution and the intensity distribution of GRBs, along with the spectral and high-time-resolution properties of a large number of them. In addition, this experiment

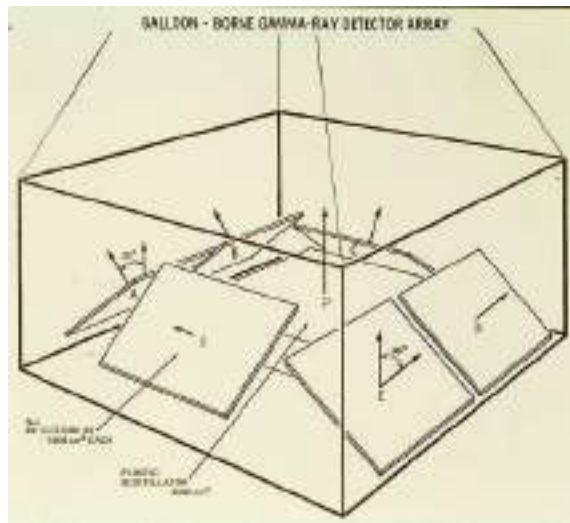


Fig. 2. A balloon flight array of scintillation detectors comprised of a number of individual detectors, pointed in different directions.

would provide a “trigger signal” to the other GRO instruments, so that their wide-field, secondary detectors could also respond to GRBs detected by our instrument. This was a key element of our proposal; it was to be a “service” to the other, larger experiments that had GRB observations as a secondary objective of their proposals. These experiments were not optimized for GRB observations and they did not have full-sky coverage. This strategy was suggested by Tom Cline.

The principal design philosophy for the BATSE detectors was to maximize the collecting area and monitor the entire sky for GRBs, while providing a rough location for them. A high time resolution, versatile (re-programmable) data system with multiple data types was also important, as it was recognized from the Konus catalogs of the St. Petersburg group (and other space-borne observations) that GRBs had extremely diverse and chaotic time profiles. Background reduction and good energy resolution were of less importance for the instrument.

3 Developing GRO and launch into orbit

Originally, five instruments were selected to be on the GRO spacecraft. An early, conceptual design of the configuration of these five instruments on the spacecraft is shown in Figure 3. In 1980, it was determined that one of these five instruments had to be removed. This difficult decision arose from a combination of limitations of GRO to accomodate the required mass and volume, and also for cost considerations. A review panel was convened to provide input to NASA Headquarters, which made the final decision of which of the five instruments would be removed. In 1981, it was determined that the Gamma-ray Spectrometer Experiment (GRSE)

would not be part of the GRO spacecraft. BATSE was the smallest, lightest, had the lowest data rate, and was the least expensive of the instruments that were selected for GRO in 1978. It was primarily considered as a “monitor”, rather than an “experiment”.

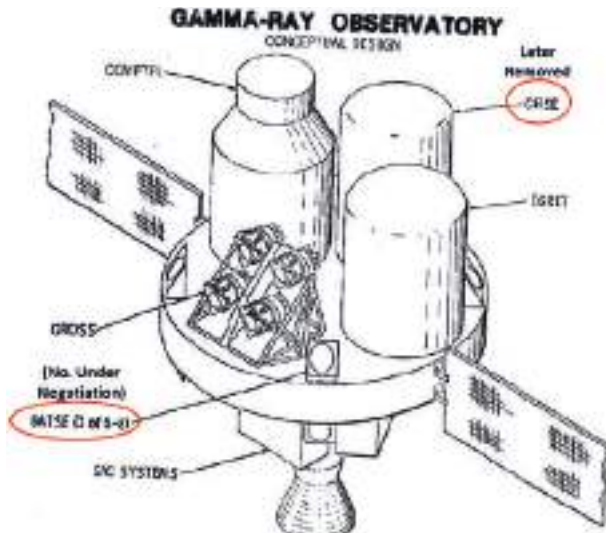


Fig. 3. An early conceptual design of the GRO spacecraft. At the time this drawing was made, it was not yet decided whether there would be six or eight BATSE detector modules on the spacecraft. Also at this time, there were five instruments. The GRSE high-resolution gamma-ray spectrometer instrument was removed from the spacecraft, as described in the text. That instrument had similar scientific objectives as the SPI instrument on the *Integral* spacecraft. The original name for the OSSE instrument was the acronym “GROSS”.

Balloon flights of prototypes of the BATSE detectors and associated instrumentation were carried out in 1980 and 1982. These flights used arrays of more expensive, single-crystal detectors with a much higher light output than those shown in Figure 1. This resulted in better measurements of the rate of weak GRBs than the initial balloon flight measurements (Meegan *et al.* 1985). A example of a BATSE Large Area Detector (LAD) crystal, sealed with its fused silica optical window is shown in Figure 4.

After the elimination of the GRSE instrument from GRO, it was recognized that the spacecraft would not have the capability for wide-field, high-spectral resolution observations of GRBs. At that time, spectral lines from GRBs were reportedly observed by several groups; these were deemed to be high scientific priority capability for the GRO mission. These reported lines were believed to arise from positron annihilation, cyclotron line production, and/or redshifted nuclear excitation lines in the gravitational field of Galactic neutron stars, at that time

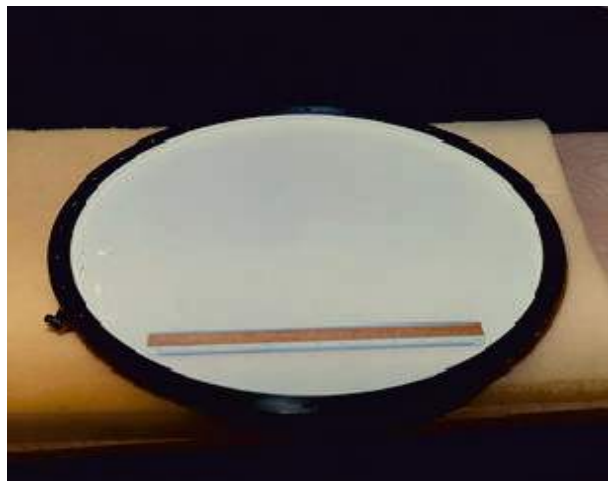


Fig. 4. The scintillation detector element of a Large Area Detector (LAD) for BATSE. The design and dimensions are similar to those manufactured for medical diagnostic purposes in devices known as Anger cameras. It consists of a circular, hermetically-sealed disc of NaI(Tl), optically-coupled to a thick, fused silica optical window. The crystal had a thickness of 1.27 cm and a surface area of 2025 cm^2 . Details of the design, development and testing of the BATSE flight system are contained in the comprehensive publication by Horack (1991).

presumed to be the source of GRBs. An appeal was made to NASA Headquarters by a group of GRB theorists to include a capability for these observations by an instrument on GRO. After a study of the impact to the mission, NASA agreed to include this capability. In response, the BATSE team (with additional investigators from UCSD and GSFC) submitted a proposal to include an additional detector in each of the eight BATSE modules, smaller than the LAD, but thicker and with better energy resolution. It would cover a broader energy range (both higher and lower) than the LAD. These detectors were termed the Spectroscopy Detectors (SDs). This proposal was accepted by NASA Headquarters.

Although the BATSE SDs had considerably better energy resolution than the LADs, their sensitivity was much less than that of the LADs in the energy region from ~ 30 keV to ~ 600 keV. However, at lower and at higher energies, the SDs had greater sensitive area than the LADs for the following reasons: Below 30 keV, the LAD efficiency dropped sharply due to absorbing material in front of the detector and above 600 keV, the LAD efficiency decreased due to the transparency of the relatively thin NaI detector. The final design of the GRO spacecraft, showing the placement of the four main instruments and the eight BATSE detector modules at the corners of the spacecraft is shown in Figure 5. The faces of the BASE LAD detectors are aligned to be parallel to the faces of a regular octahedron; the three axes of this octahedron are parallel to the spacecraft axes.

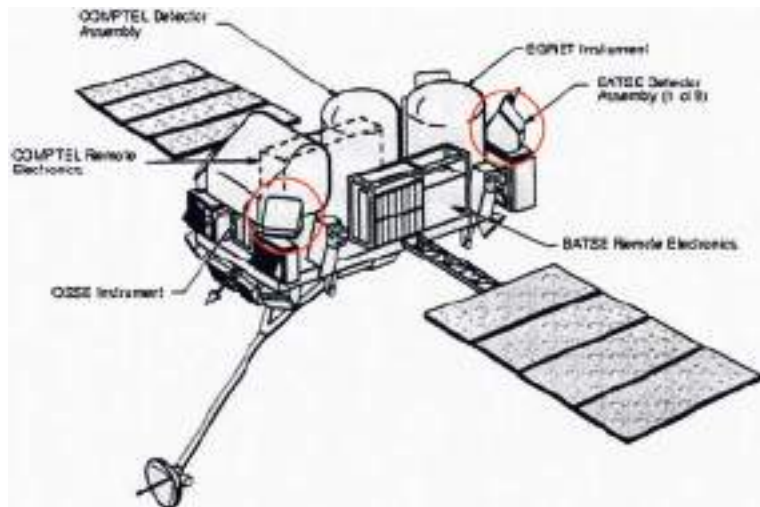


Fig. 5. The final configuration of the CGRO spacecraft with eight BATSE detector modules at the corners of the spacecraft. Each module had nearly a clear forward field-of-view. Two of the BATSE Modules are circled in red.

The majority of the design, development and testing of the BATSE instrumentation was performed at NASA-MSFC in the timeframe from 1982 to 1988 (Fig. 6). In late 1988, the BATSE flight system was delivered to the facilities of the spacecraft contractor, TRW Inc., in Redondo Beach, California. BATSE underwent two years of integration and testing with the GRO spacecraft. It was then shipped to the Kennedy Space Flight Center (KSC) for integration and testing with the Space Shuttle Atlantis. GRO was launched and deployed into an initial orbit of ~ 450 km in April 1991 (Fig. 7). When it became operational about a month later, it was re-named the Compton Gamma-ray Observatory (CGRO), in honor of Arthur Holly Compton. He was awarded the Nobel Prize in Physics in 1927 for discovering what became known as the Compton scattering of gamma rays. The CGRO spacecraft was re-boostered twice by an on-board propulsion system, following the expected, slow decay of its orbit. It operated extremely well up during its lifetime; it was de-orbited into the Pacific Ocean in June 2000.

4 Primary GRB results from BATSE

Before the end of its first year in orbit, the BATSE-observed isotropic sky distribution, together with the intensity distribution of GRBs, showed with high significance that their origin was unlike that of any known Galactic distribution of objects (Meegan *et al.* 1992). Furthermore, they were not associated with any nearby galaxies, or clusters of galaxies. Over the next few years, as the statistical measurements of these distributions became more accurate, workers in the



Fig. 6. A group of four BATSE detector modules undergoing assembly and testing at the NASA-Marshall Space Flight Center (MSFC) in Huntsville.



Fig. 7. The GRO spacecraft (later re-named the CGRO) during deployment from the payload bay of the Space Shuttle Atlantis in April 1991.

GRB field were abandoning models of GRBs originating from Galactic neutron stars. At that time, these were thought to have been their origin. The most likely explanation was that the GRBs originated from cosmological distances. The final BATSE sky distribution of GRBs after nine years of observations is shown in Figure 8. The definitive recognition of the cosmological distances of GRBs had to

wait for the BeppoSAX observations in 1997 and 1998 which provided precise and rapid GRB locations. Along with this breakthrough came rapid follow-up X-ray and optical observations of GRB afterglows and the redshift measurements of their host galaxies and/or that of intervening matter.

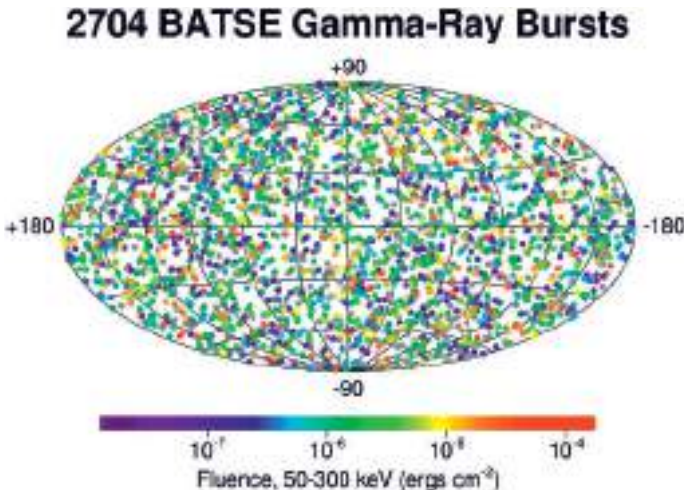


Fig. 8. The BATSE sky distribution of GRBs observed over nine years of observation by BATSE-CGRO, plotted in Galactic coordinates. This distribution has not been corrected for sky exposure. The color of each GRB corresponds to the indicated fluence of the burst.

There are generally accepted to be two classes of GRBs, short and long; the usual dividing line between long and short GRBs is ~ 2 s, although there is significant overlap between these classes. Prior to BATSE, it had been suspected that the shorter GRBs had harder spectra than the longer ones. BATSE data showed the definitive separation between the short/hard and the long/soft classes with very good statistics, as shown in Figure 9.

Data from BATSE triggered GRBs are available online (<http://heasarc.gsfc.nasa.gov/>); they are described by Paciesas *et al.* (1999). Limits to gamma-ray lines from GRBs using the BATSE spectroscopy detectors were found to be below those of line fluxes reported previously (Briggs *et al.* 1999). In an effort to find additional (primarily weaker) GRBs that were not part of the standard BATSE GRB catalogs, several investigators compiled catalogs of un-triggered BATSE GRBs, using the so-called “continuous” data stream.

In 1993, a system known as BACODINE (for BATSE Coordinates Distribution Network) was implemented at GSFC. This system was made possible due to the deterioration of the CGRO tape recorders during the first year of its mission and the need for real-time data from the spacecraft caused by the resulting lack of on-board data storage. The design and implementation of BACODINE was the work of Scott Barthelmy and colleagues from NASA-GSFC (Barthelmy *et al.* 1995) to take advantage of this unplanned opportunity. It used the near real-time

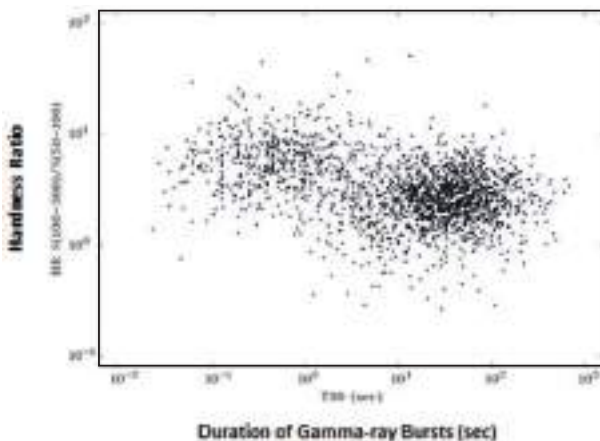


Fig. 9. Two classes of GRBs, as observed with BATSE: Short-Hard and Long-Soft (Kouveliotou *et al.* 1993). They are seen to have overlapping distributions.

BATSE data to compute a coarse GRB location when an on-board burst trigger occurred. Automated GRB location messages were made available to users for rapid GRB follow-up observations. Even though these locations were usually of the order of several square degrees, they were useful for wide-field optical cameras. Several optical systems were constructed specifically for this purpose. One of these robotic systems was able to observe the optical emission from the intense burst GRB 990123 while the burst was in progress (Akerlof *et al.* 1999). As other spacecraft with GRB capabilities were placed into orbit, their data were also distributed to the GRB community over this same network. The BACODINE system evolved into a more general system, the GRB Coordinates Network (GCN), which distributes data from many spacecraft and ground-based observatories. It is used today by hundreds of observers world-wide and has become an invaluable service for the GRB community.

The large number of GRBs observed with BATSE, afforded by its sensitive area and long duration in orbit, allowed observations of the temporal and spectral properties of GRBs in more detail than those previously. Over a thousand of papers have been published describing the BATSE-observed properties of GRBs and the theoretical implications derived from them. Observations with BATSE afforded an unsurpassed study of many of the fine points of the gamma-ray emission in the energy region where the major fraction of energy is emitted during the prompt phase. The GRBs observed with a single instrument has provided a large, homogeneous dataset of GRBs, without the difficulties associated with cross-calibration between different instruments. This capability will likely not be exceeded for many years. An overview of many more of the GRB and scientific results made possible through BATSE observations, but not covered here, are summarized in a chapter entitled “The BATSE Era”, in a recently-published book (Fishman & Meegan 2012).

References

- Akerlof, C., Balsano, R., Barthelmy, S., *et al.*, 1999, Nature, 398, 400
Barthelmy, S.D., Butterworth, P., Cline, T.L., *et al.*, 1995, Ap&SS, 231, 235
Briggs, M.S., Band, D.L., Preece, R.D., *et al.*, 1999, ApL, 39, 237
Fishman, G.J., & Meegan, C.A., 2012, "The BATSE Era", Chapter 3, in Gamma-ray Bursts, ed. C. Kouveliotou, *et al.* (Cambridge Univ. Press)
Fishman, G.J., 1974 "Radiation Detectors Using Multiple Scintillation Crystal Pieces", U.S. Patent #3,835, 325
Fishman, G.J., & Austin, R.W., 1976, Nucl. Inst. Meth., 140, 193
Fishman, G.J., Meegan, C.A., Watts, J.W., Jr., & Derrickson, J.H., 1978, ApJ, 223, L13
Horack, J.M., 1991, "Development of the Burst and Transient Source Experiment", NASA Reference Publication 1268 (Washington: NASA)
Klebesadel, R.W., Strong, I.B., & Olson, R.A., 1973, ApJ, 182, L85
Kouveliotou, C., Meegan, C.A., Fishman, G.J., Bhat, N.P., *et al.*, 1993, ApJ, 413, L101
Meegan, C.A., Fishman, G.J., & Wilson, R.B., 1985, ApJ, 291, 479
Meegan, C.A., Fishman, G.J., Wilson, R., *et al.*, 1992, Nature, 355, 143
Paciesas, W.S., Meegan, C.A., Pendleton, G.N., *et al.*, 1999, ApJS, 122, 465

EARLY DANISH GRB EXPERIMENTS – AND SOME FOR THE FUTURE?

N. Lund¹

Abstract. By 1975 the hunt for GRB counterparts had been on for almost ten years without success. Gamma burst instruments of that day provided little or no directional data in themselves. Positions could be extracted only using the time delay technique – potentially accurate but very slow. Triggered by a Japanese report of a balloon instrument for GRB studies based on a Rotation Modulation Collimator we at the Danish Space Research Institute started the development of an RMC detector for GRBs, the WATCH wide field monitor.

Four WATCH units were flown on the Soviet Granat satellites, and one on ESA's EURECA satellite. The design and results will be summarized. Now, 35 years later, recent detector developments may allow the construction of WATCH-type instruments able to fit weight, power and data-wise into 1 kg cubesats. This could provide the basis for a true all-sky monitor with 100 percent duty cycle for rare, bright events.

1 Introduction

The Danish Space Research Institute (DSRI) was set up in 1968 to provide a national focal point for a national participation in the European Space Research Organisation, ESRO. Prior to the formation of DSRI the national efforts in space had been directed towards the ionosphere because of the importance of this atmospheric region for radio communications with Greenland. The first director of DSRI was Bernard Peters, a well known figure in the post war cosmic ray research. Not surprisingly, the first astrophysics project was a cosmic ray isotope experiment, constructed in collaboration with Centre d'Etudes Nucléaire, Saclay in France. This experiment was launched in 1979 on the NASA satellite HEAO-3. With a weight of 350 kg the HEAO-3 experiment was very large for its time, and even before the launch it was clear that DSRI had to find a new future research

¹ DTU Space, Elektrovej Building 327, 2800 Lyngby, Denmark

theme for its astrophysics group, we could not dream of building anything larger or more complex to improve on the HEAO-3 results.

At that time the Cosmic Gamma-Ray Bursts were the big mystery which intrigued astrophysicists all over the world. Why had nobody succeeded in finding any counterparts? How could these events be so luminous in X- and gamma-rays, yet so completely absent at other wave-lengths? The distribution across the sky was peculiar to say the least – no hint of an origin within our Galaxy, yet it seemed obvious that such extraordinary flashes had to have a relatively local origin? A few good positions had been obtained from the early InterPlanetary Network (IPN), but nothing conspicuous was visible within the small IPN error boxes. Figure 1. In the early days it took quite a while to finalize the IPN positions – clock synchronization is not trivial! Therefore it was obvious that what was needed was an instrument which by itself could determine the burst position in near real time so ground based follow-up could start within hours or days rather than months. For the follow-up we planned to use classical astronomical search procedures – blinking Schmidt-plates, so we expected that a position accuracy better than 1 degree would be adequate – at least it would be far better than anything done in near real time on GRB's up to that point.

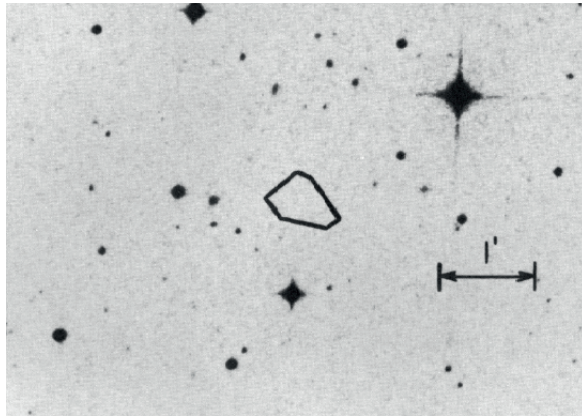


Fig. 1. Error box for GRB 790406 derived by the Interplanetary Network (Evans *et al.* 1980).

2 Instrument design

For our instrument design we were inspired by a Japanese balloon experiment employing Rotation Modulation Collimators (RMC's), Nishimura *et al.* (1976). RMC's were originally developed by Mertz (1968), actually to be used for electronic read-out of optical Schmidt telescopes. However, it was in X-ray astronomy that the RMC technique really made its mark, with experiments on the British ARIEL V and the US SAS-3 satellites.

Nishimuras balloon experiment, specifically designed for GRB studies, employed 3 detectors, two RMC detectors with orthogonal grid orientations and one “monitor counter” to provide an unmodulated time history of the burst. Figure 2. In the RMC technique the source positions are derived by an analysis of the “modulation pattern” arising through the rotation of the double grid structure. Figure 3.

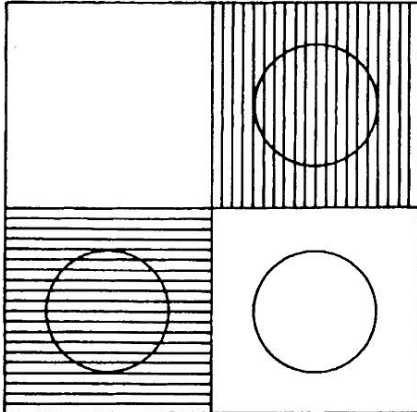


Fig. 2. Detector configuration of Nishimuras balloon payload. Two orthogonal RMC detectors and one monitor counter.

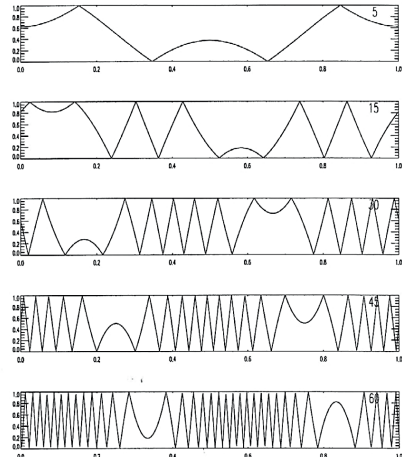


Fig. 3. Modulation patterns corresponding to different off-axis and phase angles. Off-axis: 10° , 20° , 30° , 40° and 50° .

The Japanese design with the monitor counter took into account that GRB's were known to have unpredictable time structures, and the derivation of the instrument modulation would be uncertain without an independent measurement of the true light curve. Two orthogonal RMC-units were used because the balloon payload rotated relatively slowly (two revolutions per minute) and many GRB's would only last for a small fraction of a revolution.

We realized that by suitable modifications of the RMC detector we could dispense with the monitor counter and achieve with one detector what was done with three in the balloon.

The design of our WATCH (Wide Angle Telescope for Cosmic Hard X-rays) detector is shown together with the classical RMC in Figure 4. We eliminated the lower shadow grid and replaced it by two interleaved grid detectors with the same pitch as the top shadow grid. Now we can derive the un-modulated time history of a burst by adding the signals from the two detectors, and we can derive the instrument modulation of the signal independent of the signal amplitude from the ratio of the time history from one of the detectors to the un-modulated time history.

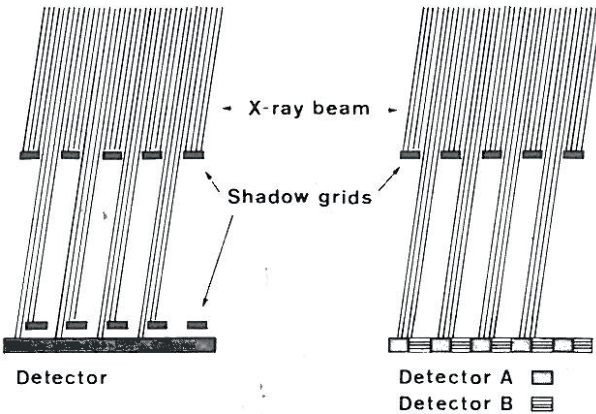


Fig. 4. Comparison of classical RMC (*left*) and WATCH design (*right*). The classical RMC uses two 50% open grids rotating synchronously and a single, large area detector which observes the time pattern of light and shadow as the grids rotate. WATCH uses only one shadow grid, but the co-rotating detector is now more complex with two interleaved grid-detectors.

We also opted for a high spin rate of our detector: 60 revolutions per minute. More details on the design of the original WATCH instruments can be found in (Lund 1981 & Brandt *et al.* 1990).

It should be noted that unlike most other GRB-instruments WATCH did not rely on the “burst”-nature of the GRBs to observe and localize them. WATCH performs equally well on persistent X-ray sources, it is a true wide field monitor.

We build prototypes of the instrument and flew them in balloons from Spitzbergen in 1979 and 1980. Figure 5. No gamma bursts were observed during these flights but the design was proven and on this basis we got the instrument accepted for flight on ESA’s EURECA (EUropean REtrievable CArrier), a microgravity satellite with a planned launch in 1988.

The main characteristics of the original WATCH instrument (Fig. 7) and the expected characteristics of a modern version of the instrument can be found in Table 1 of Section 5.

3 The challenger disaster and a new opportunity

The construction of the WATCH flight model was well underway when in January 1986 the Challenger accident put a halt to the US shuttle program. For more than a year it was undecided whether EURECA would ever fly – in the aftermath of the disaster NASA had decided to transfer all future satellite launches back to expendable launchers, the Shuttle would only be used for manned flights – with a few exceptions.

In the summer of 1986, in the middle of this limbo I was fortunate to meet Rashid Sunyaev from the Moscow at a COSPAR meeting in Toulouse. We both made a presentation in a session devoted to future X-ray satellite missions.

Rashid presented “Granat”, a Russian-French mission with a large French gamma-ray instrument, Sigma, and a cluster of Russian X-ray telescopes, ART-P and ART-S. In addition Granat carried two gamma-burst instruments, the French Phebus and the Russian Konus with an associated rapid moving platform, “Tournesol” with X-ray and optical cameras. (Unfortunately the downlink data connection to the entire Russian GRB instrument complex was lost soon after launch – otherwise the GRB afterglows may have been discovered with Granat in 1990 rather than with SAX in 1997.) In his presentation Rashid expressed regret that Granat did not carry an all-sky monitor. Such an instrument had been foreseen, there was room for it as well as excess payload mass, but the instrument development had been delayed.

Immediately after this I presented WATCH – an all-sky monitor which now appeared to be homeless!

This was too much of a coincidence to be neglected. After the session Rashid and I met and after a good bottle of French red wine I could go back to Copenhagen with an offer from Rashid to fly four WATCH units on Granat – delivery of the flight units to be executed within a year! Of course we did not succeed to build four flight units adapted for Granat within a year, but the delivery of the flight units began in 1988.

A few stones had to be cleared during the adaptation – Granat had room and mass to accommodate four WATCH units, but no data storage and very little power. We had to modify the on-board software to allow the storage of data for four days (the Granat orbital period) inside the 512 kByte RAM memory of each instrument – and we had to negotiate directly with the spacecraft builder, Lavotchkine, to pay for a special WATCH solar panel to be fitted to the spacecraft. (The Granat spacecraft was the 25th and last copy of the Russian “Venera”-probes handed over to IKI to be used for X- and gamma-ray astronomy on the condition that there would be absolutely no modification on the spacecraft systems! All final decisions can be revoked under suitable temptation!)

Granat was launched in December 1989 carrying four WATCH units. Unfortunately one of the units did not survive the launch, a thin aluminium foil used as an entrance window for the scintillator broke, probably due to air trapped behind the foil. So we had to contend ourselves with a monitor for 75% of the sky rather than 100%. But even the 75% gave us plenty of data between 1990 and 1994 as will be discussed below.

By 1989 it had also become clear that NASA would stick to the agreement with ESA: EURECA would be launched and retrieved by the shuttle system. So the EURECA programme began to move forward again. The EURECA WATCH did incorporate a number of improvements relatively to the Granat version, not the least a Beryllium X-ray entrance window as replacement for the less reliable aluminium foil. But also an important modification of the scintillator mosaic which reduced the artefacts present in the Granat RMC correlation images. EURECA was

launched by the space shuttle Atlantis in July 1992 and retrieved after 11 month in orbit by the Endeavour shuttle in June of 1993.

4 WATCH results

The original inspiration for WATCH was the enigma of the gamma-ray bursts. And GRBs were detected and localized. But as will be illustrated it was as an X-ray all-sky monitor WATCH made its most significant discoveries.

4.1 Gamma-ray bursts

A total of 47 bursts were localized by Granat WATCH between January 1990 and September 1994 (Sazonov *et al.* 1997). For the first time GRBs were imaged in real time, and for the brightest of the bursts the source position was even derived on-board within seconds. But the precision of the localization, 0.2 to 1 degree error radius – although far better than anything previously obtained – was inadequate for the facilities available on the ground in those days. Only Schmidt telescopes could cover the error boxes, and their photographic recording system was lacking in sensitivity. But probably the primary obstacle was the slowness of the communication systems. Data was only retrieved from Granat once every four days, so most GRB detections were “out of date” already by the time the data was retrieved – this can be said today! Data analysis on the ground station in Crimea would add another few hours, and then any messages would have to go to Copenhagen via slow telephone systems under tight security control. From Copenhagen things would go easier, but the rescheduling of a Schmidt telescope observation plan to make room for the seventeenth fruitless attempt to find a GRB counterpart would at that time not make many astronomers jump in excitement to their feet.

12 GRBs were localized during EURECAs 11 month lifetime (Brandt *et al.* 1995). The communications with EURECA WATCH was easier, and the orbital period was shorter, only 90 minutes. But the ground data transfer and analysis would still add a couple of hours. And the scheduling bottleneck at the ground observatories remained. It must be remembered that in 1992 nobody could know what to expect and what to look for.

One important result which came out of the WATCH GRB positions was that it allowed an independent test of the positions coming from the Interplanetary Network and later the BATSE experiment, as illustrated in Figure 5 for GRB 921022.

WATCH also detected some unusual bursts, the light curve of GRB 921022 (Fig. 6), is a fascinating example of a single burst exhibiting simultaneously the characteristics of a short and a long GRB. The initial spike in this burst was resolved in the raw detector data with a FWHM duration of about 10 ms, whereas the second pulse evolves over a time scale about 2000 times longer than that of the spike.

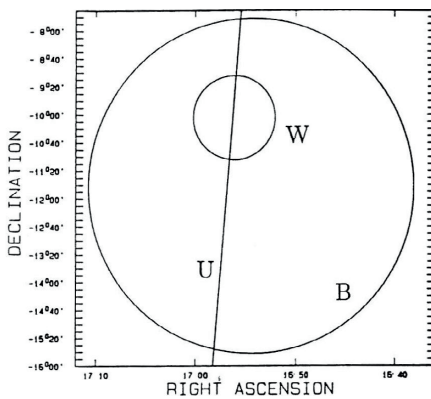


Fig. 5. IPN (U), BATSE (B) and WATCH (W) localizations of GRB 901022.

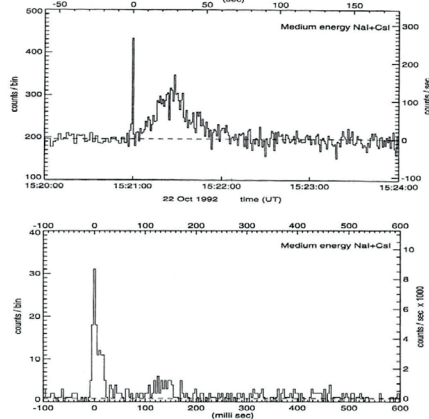


Fig. 6. *Top:* full light curve, 0.9 s/bin.
Bottom: initial spike, 0.0035 s/bin.

4.2 X-ray Novae

WATCH made real headlines (even in the newspaper *Известия*) with the discovery and localization of the X-ray transient Nova Musca 1991 (Lund & Brandt 1991). This transient was later observed in detail with the Sigma telescope on Granat and in a brief episode a transient gamma ray line was observed near 500 keV (Gilfanov *et al.* 1991).

Another X-ray nova highlight is GRO J0411+22 (Nova Persei 1992). This transient was discovered by the BATSE experiment on GRO during a period where Granat was off. But as soon as the Granat observations were resumed the source was detected and localized accurately. Armed with the WATCH position our conference host, Alberto, went off from Evpatoria to the nearby Crimean Astrophysical Observatory and there he managed against all odds, with a small telescope – but some very helpful local astronomers – to identify the optical counterpart! (Castro-Tirado *et al.* 1992a).

4.3 GRS 1915+105

After successfully identifying the optical counterpart of the Persei nova Alberto returned to Evpatoria, and immediately noted another transient: GRS 1915+105! (Castro-Tirado *et al.* 1992b). Off again to the observatory, but this time: no luck! GRS 1915+105 was not visible in the optical. But apart from that, GRS 1915+105 is probably the most significant discovery from the WATCH instruments. It was soon found to be a radio source and it was the first Galactic source observed to exhibit the characteristics of a microquasar (Mirabel *et al.* 1993).

4.4 Solar flare observations

One of the WATCH units on Granat was always observing in the direction of the Sun. Normally the Sun was completely invisible (the lower energy threshold of WATCH was about 6 keV). But when a flare erupts the Sun becomes bright – sometimes even extremely bright. It so happened that Granat was launched only one month after the demise of the Solar Max Satellite – and the next Solar observatory was only launched in 1994. So the WATCH data came as a very welcome bridging data set between these two Solar observatories (Crosby *et al.* 1998).

5 A WATCH concept for the future?

It is now more than 30 years since the WATCH concept was developed and it may be reasonable to question whether the instrument today can be of more than historic interest? But I think it is, and I shall describe why.

First of all, there is a continuing interest in keeping an eye on the transient X-ray sky. In the 50 years of X-ray astronomy nature has entertained us with ever new forms of variable X-ray sources, and it would not be wise to suppose that by now we have seen all. In particular because the understanding of even the well known transients is still incomplete – not the least in the case of gamma-ray bursts.



Fig. 7. Original WATCH detector.

But why should we revert to the old-fashioned technique of the rotation modulation collimator when so much more advanced and powerful techniques like the coded mask telescopes have been developed? I will argue that we should revive the RMC technique considering three facts:

- The RMC, technically and data-wise, is much simpler than the coded mask.
- The RMC can be installed on a simple, spinning satellite platform.
- A wonderful new detector, exactly matching the RMC, has been developed.

Therefore, if your wish is to produce a (cluster of) low cost satellite(s) to keep an eye on the X-ray sky, the RMC is the best choice.

I have already mentioned that WATCH on both Granat and EURECA was working on a very meagre telemetry budget, 37 bits/s per WATCH unit for Granat and 120 bits/s for EURECA. I should hope that by today we can do better even on a 1 kg Cubesat, but if we need to survive on 100 bits/s we know it can be done. The attitude control for a spinning satellite is much simpler than for a 3-axis stabilized satellite, both regarding the sensors and the actuators. Considering the on-board software we can now do much better than we did in 1989, we will be able to make a better selection of the important data and localize on-board a much larger fraction than we did 20 years ago. And today the ground based astronomers know what to look for, and they are aware of the importance of being fast!

But the real crux is the emergence of the Silicon Drift Detectors, the SDDs (Vacchi *et al.* 1991; Rashevsky *et al.* 2002). The SDDs are now vigorously being developed and space qualified as X-ray detectors for the LOFT mission – one of the candidates for the M3-slot in the ESA programme (Feroci *et al.* 2012). Their key advantages for WATCH is the low weight and the low energy threshold, 2 keV, giving the new instrument access to a much richer sky – and provide better opportunities for analysis of emission temperatures and radiation transfer parameters of the sources.

The SDD is an ideal match for an RMC. Through the string of point-like anodes (Fig. 8) which assures the very low read-out noise of the SDD this detector is born with one dimensional position sensitivity. This comes “for free”, and this exactly what is needed for an RMC.

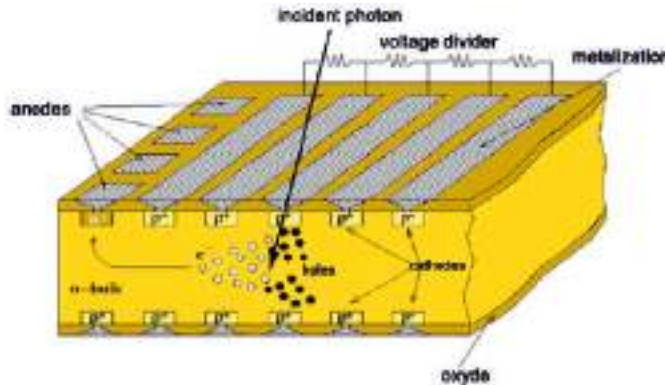


Fig. 8. The electrical structure and working principle of the Silicon Drift Detector. Note the string of small anode pads on the left edge providing 1-D position sensitivity.

Table 1 compares the original WATCH parameters with the parameters for a “CubeWATCH”, a minimal proof of concept instrument matched to a $10 \times 10 \times 10$ cm³ cubesat. Initial studies have been carried out at DTU Space which have demonstrated that the required attitude control stability can be achieved with

Table 1. Main characteristics of original and modern WATCH instruments.

	Original WATCH	CubeWATCH
Energy range	6 to 80 keV	2 to 20 keV
Energy resolution	25% @ 60 keV	1% at 6 keV
Field of view	3 steradian	3 steradian
Localization error	0.3°	0.1°
Point spread function	5°	2°
Sensitive area (through mask)	45 cm ²	25 cm ²
Detector	NaI(Tl)/CsI(Na) scintillator mosaic	Silicon Drift
RMC spin rate	60 rpm	60 rpm
Burst-trigger energy bands	6 to 10 keV NaI 10 to 60 keV NaI and CsI	2 to 5 keV 5 to 20 keV
Time resolution Burst data	4 ms (1/256 spin period) 4 s (spin periods)	4 ms (1/256 spin period) 1 s (spin period)
Count rates (2 ch.)	256 s (spin periods)	256 s (spin periods)
2 channel data	4096 s (spin periods)	2048 s (spin periods)
16 channel data		
Background count rate	400 cps	~1000 cps
Data rate	37 bits/s (Granat) 120 bits/s (EURECA)	200 bits/s
Weight	11 kg	0.4 kg
Power	12 W	0.3 W
Dimensions	27 × 28 × 29 cm ³	9.5 × 9.5 × 3 cm ³

existing sensors and actuators for a fast spinning cubesat. A project is underway to develop a special SDD matched to the specific cubesat requirements.

6 Discussion

The WATCH wide field monitor was originally developed to identify the sources of the cosmic gamma ray bursts. Although the instrument performed according to expectations on two space missions the primary goal was not achieved. With present day knowledge about the GRB optical afterglows we can see that the limited precision of the burst localizations and the limited possibilities at the time for very rapid follow-up from ground based telescopes with adequate sensitivity conspired to make a successful identification of a gamma-burst host from WATCH data very unlikely. However WATCH performed very well as an all-sky monitor, and particularly for the Granat mission this allowed to make important discoveries using the pointed instruments.

The usefulness of permanently keeping the sky under surveillance to detect new or rare phenomena has been demonstrated time and again in X-ray astronomy.

The RMC technology offers a relatively simple way to realize this goal and the recent development of X-ray sensitive Silicon Drift Detectors opens the possibility to build ultra light versions of WATCH (<0.5 kg) with a sensitivity fully matching the original units. If realized this would allow to launch an all-sky monitoring swarm of minisatellites for a moderate cost.

The original development of WATCH was supported by the Danish Natural Sciences Research Council and by the Danish Space Board. The author gratefully acknowledges the support from the University of Granada to participate in the conference.

References

- Brandt, S., Lund, N., & Rao, R.A., 1990, ICRC, 4, 145B
Brandt, S., Lund, N., & Castro-Tirado, A.J., 1995, AdSpR, 16, 43
Castro-Tirado, A.J., Brandt, S., Lund, N., *et al.*, 1992a, IAUC 5587
Castro-Tirado, A.J., Pavlenko, P., Salyapikov, A., *et al.*, 1992b, IAUC 5588
Crosby, N., Vilmer, N., Lund, N., & Sunyaev, R., 1998, A&A, 334, 299
Evans, W.D., Klebesadel, R.W., Laros, J.G., *et al.*, 1980, ApJ, 237, L7
Feroci, M., Stella, L., van der Klis, M., *et al.*, 2012, ExpA, 34, 415
Gilfanov, M., Sunyaev, R., Churazov, E., *et al.*, 1991, SovAL, 17, 437
Lund, N., 1981, Ap&SS, 75, 145
Lund, N., 1986, ed. Culhane J.L., SPIE Proc., 597, 95
Lund, N., & Brandt, S., 1991, IAUC 5161
Mertz, L., 1967, Modern Optics (New York, Brooklyn Polytechnic Press), 787
Mirabel, I.F., Rodriguez, L.F., Marti, J., *et al.*, 1993, IAUC 5773
Nishimura, J., Fujii, M., Tawara, Y., *et al.*, 1978, Nature, 272, 337
Rashevsky, A., Bonvicini, V., Burger, P., *et al.*, 2002, NIM, A485, 54
Sazonov, S.Y., Sunyaev, R.A., Terekhov, O.V., *et al.*, 1998, A&AS, 129, 1
Vacchi, A., Castoldi, A., Chinnici, S., *et al.*, 1991, NIM, A306, 187

IOFFE INSTITUTE GRB EXPERIMENTS: PAST, PRESENT AND FUTURE

R.L. Aptekar¹, S.V. Golenetskii¹, D.D. Frederiks¹, E.P. Mazets¹
and V.D. Palshin¹

Abstract. The short review of GRB studies performed for many years by Ioffe Institute is presented. An important breakthrough in GRB studies became possible owing to four Konus experiments carried out by the Ioffe Institute onboard the Venera 11 to 14 interplanetary missions from 1978 to 1983. The joint Russian-American Konus-Wind experiment, which has already been operating for more than 18 years, provides important and often unique data regarding GRB characteristics in 20 keV – 15 MeV energy range. These investigations were complemented by several Konus and Helicon experiments onboard Russian near-Earth spacecraft. A short description of future Konus-UF and Konus-M experiments are also given.

1 Introduction

Cosmic gamma-ray bursts were discovered in 1967-1973 by the U.S. Vela satellites (Klebesadel *et al.* 1973). One of the first confirmations of the discovery of this new astrophysical phenomenon was provided by observations of the Ioffe Institute made on board Kosmos-461 satellite (Mazets *et al.* 1974). We present the results of many years' study of GRBs, performed by Ioffe Institute onboard interplanetary space missions and near-Earth satellites. Many of the basic characteristic of GRBs, such as their time profiles and energy spectra, and the first all-sky map of their source distribution on the celestial sphere, were determined using early Konus experiments onboard the Venera-11, -12, -13, and -14 deep space missions in 1978-1983. As a result of the observations of the giant flare on March 5, 1979, and a series of short repeated burst from its source the new class of rare astrophysical phenomena was discovered. In the somewhat later, these sources were named soft gamma repeaters (SGRs). In the subsequent Konus and Helicon experiments studies of GRBs and SGRs were continued, new SGR sources were found, and other

¹ Ioffe Physico-Technical Institute, St. Petersburg 194021, Russia

SGR-related giant flares were also observed. Recently and most notable, Konus measurements have been central in finding SGR sources in the galaxies M81/M82 and M31, far outside our own Milky Way system. In the modern epoch of multi-wave studies of cosmic gamma-ray bursts, the joint Russian-American Konus-Wind experiment, which has already been operating for more than 18 years, provides important and frequently unique data regarding temporal and spectral parameters of GRBs though the 20 keV to 15 MeV energy range. A short description of future Konus-UF and Konus-M experiments are also given.

2 Study of GRBs from the Venera interplanetary missions in 1978-1983

An important breakthrough in studies of GRBs was made possible owing to four Konus experiments carried out by the Ioffe Institute on board the Venera 11, 12, 13 &14 deep space missions in 1978-1983. Each Konus instrument consisted of six scintillation detectors with close to cosine angular sensitivity; detectors were arranged along six axes of the spacecraft. It gave an opportunity to determine the direction towards GRB sources independently using single spacecraft data. The second approach to localize GRB source position in the Konus experiments was a triangulation method. The Venera interplanetary missions were launched in pairs and separated each from other by distance measured by several tens million kilometers. Such large distance between missions provided a high accuracy for GRB source localization on the celestial hemisphere. Therefore the Konus experiments had two independent methods for GRB source localization: the autonomous approach based on the data from detectors with an anisotropic angular sensitivity and the triangulation method using large distances between Venera missions.

The Konus observations of the temporal structures of GRBs had revealed for the first time the existence of a separate class of short bursts, demonstrating the so-called “bimodal” duration distribution (Mazets *et al.* 1981) (Fig. 1). It had been for the first time established that GRBs were randomly distributed over the celestial sphere (Mazets & Golenetskii 1988) (Fig. 2).

Later, these findings were confirmed with an even larger number of events in the well-known BATSE experiment on board NASA’s Compton Gamma-Ray Observatory (Paciesas W.S. *et al.* 1999).

Another key result of the Konus experiments onboard Venera missions came from the observations of the giant flare on March 5, 1979 (Fig. 3) and a series of short repeated burst from its source (Fig. 4). As a result, a new class of rare astrophysical phenomena was discovered (Mazets *et al.* 1979; Golenetskii *et al.* 1983), which somewhat later were named soft gamma-ray repeaters (SGRs).

3 The Konus-Wind experiment

A new and important chapter in the research of GRBs and SGRs carried out by the Ioffe Institute is associated with a joint Russian-American experiment which is being conducted using the Russian Konus scientific instrument onboard the

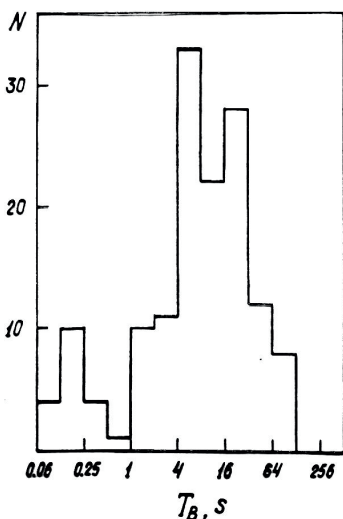


Fig. 1. Konus observations of the GRBs temporal structures revealed the existence of a separate class of short bursts (Mazets *et al.* 1981).

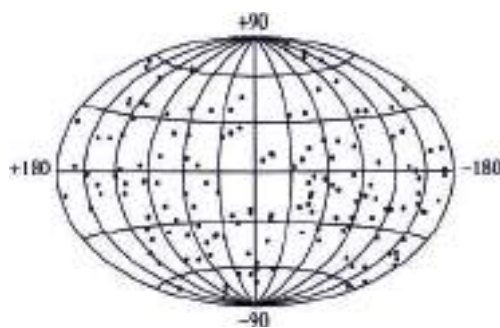


Fig. 2. Localizations of GRB sources demonstrated their isotropic distribution on the celestial sphere (Mazets & Golenetskii 1988).

U.S. Wind spacecraft. The trajectory of the Wind spacecraft is maintained in the vicinity of the L1 Lagrangian point and the instrument has up to 5 light-seconds lag from the near-Earth GRB observing missions. Remote from the Earth and Moon, its exposure to entire celestial sphere is exceedingly favorable for studies of unpredictable and transient sources. Two high-sensitivity scintillation detectors of Konus-Wind gamma-spectrometer permanently observe the entire celestial sphere, so that no energetic event important to the astrophysics of GRBs and SGRs has yet been missed by the Konus-Wind experiment during all its 18 years of successful observations.

The Konus-Wind instrument is a scintillation gamma-ray spectrometer consisting of two identical spectrometric detectors of gamma-ray photons and the electronics unit (Aptekar *et al.* 1995). Each detector includes a NaI(Tl) crystal with a diameter of 130 mm and height of 75 mm placed in a thin-walled aluminum container with a beryllium entrance window. A highly-transparent lead-glass exit window is used to protect the detectors from the spacecraft background in the soft spectral region. Such detector provides a low energy threshold for recording radiation of 10–12 keV, the photon registration range up to 15 MeV and the burst detection sensitivity at the $\sim 10^{-7}$ erg cm $^{-2}$ level. These detectors have no analogue in the GRB observations with respect to the wide energy range and degree of protection from the spacecraft background. The detectors are located on the spacecraft stabilized by rotation in such a way that they constantly observe the northern and southern ecliptic hemispheres.

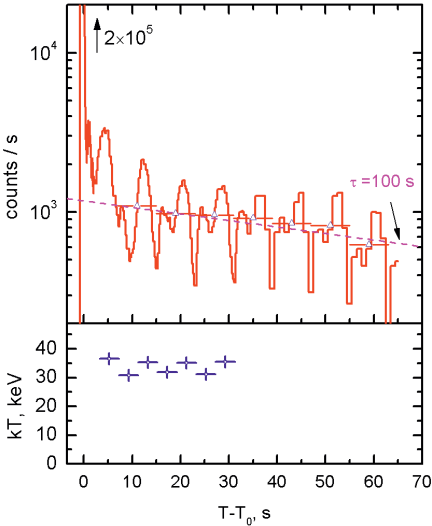


Fig. 3. Giant flare of SGR 0526-66 was observed on March 5, 1979 (Mazets *et al.* 1979).

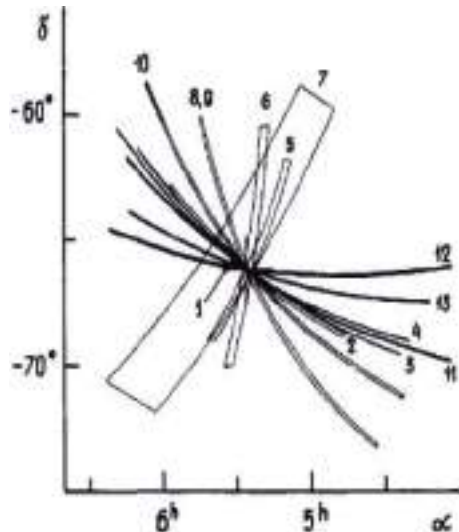


Fig. 4. Repeated bursts from SGR 0526-66 (Golenetskii *et al.* 1983).

The instrument operates in two distinct modes: the triggered burst detection and the background measurement. In the triggered mode, burst time profiles are recorded, in the current calibration, in the 20–80, 80–300, and 300–1200 keV energy bands with the time resolution varying from 2 ms to 256 ms and total duration of registration lasting ~ 230 s. The standard program for recording an event time profile makes it possible to maintain a time resolution of 2 ms during the first 0.5 s of burst and for 0.5 s before burst. The instrument also has two special time analyzers (so called time “verniers”), which allow one to record with a high time resolution (2 ms) any light curve’s section with sufficient increase in count rates. Two multichannel amplitude analyzers with quasi-logarithmic scales covering two energy intervals (20–1100 keV and 350 keV–15 Mev) are used to measure event energy spectra. The accumulation time for each spectrum is automatically adjusted to the current burst intensity within a range from 64 ms to 8.192 s.

The instrument calibrations and a method for reconstructing an initial gamma-ray spectrum from the instrumental spectrum recorded with Konus-Wind instrument is considered in (Terekhov *et al.* 1998). This technique was improved later by using a more advanced version of the program for calculating the detector response matrix (based on GEANT4) and the XSPEC12 package for modeling measured GRB spectra.

The possibility to continuously observe the entire celestial sphere and the wide energy range of observations in combination with the optimal program for recording GRB spectral characteristics are the main advantages of the Konus-Wind experiment. For this reason, the data of Konus-Wind experiment are widely used

in present day multi-wave GRB observations. The Konus-Wind experiment is also an important vertex of the interplanetary network (IPN) of spacecraft with gamma-ray detectors, which localizes GRB sources by the triangulation method (for details see Pal'shin *et al.* 2013).

The famous “naked-eye” GRB 080319B studies illustrate the effective participation of the Konus-Wind experiment in multi-wave observations. The extraordinary optical brightness of this burst reached at a maximum 5.3 m (Racusin *et al.* 2008). The Konus-Wind instrument recorded detailed light curves of the bursts in the gamma-ray range from 18 keV to 1160 keV; Figure 5 presents these measurements together with the data from two optical monitors.

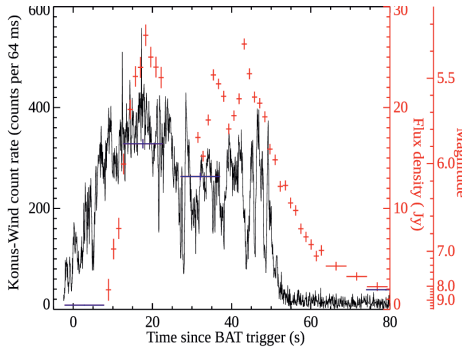


Fig. 5. Light curve of the GRB 090319B in the 18–1160 keV energy range according to the Konus-Wind experiments and optical monitors (Racusin *et al.* 2008).

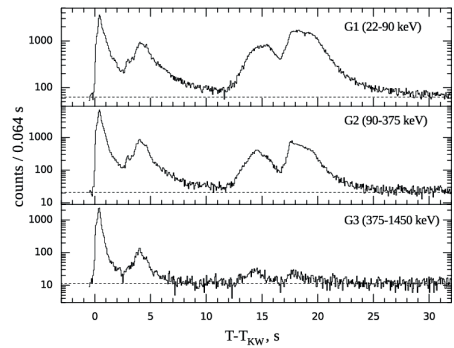


Fig. 6. The Konus-Wind light curves of the extremely bright GRB 110918A (Frederiks *et al.* 2013).

The gamma-ray light curve of this burst demonstrates multiple short spikes that do not correlate with the peaks in the optical range. Nevertheless, the gamma-rays and the optical emission of the burst source start and end at almost the same time, what evidently demonstrates that these radiations come from the same spatial region. The energy spectra of the GRB were studied in detail in the Konus-Wind experiment in the 20 keV – 7 MeV range. These spectra demonstrate a strong spectral evolution in the form of pronounced radiation softening by the end of the main burst phase recorded in gamma-rays. According to the Konus-Wind data, this burst had a peak gamma-ray flux of $(3.26 \pm 0.21) \times 10^{-5}$ erg cm $^{-2}$ s $^{-1}$ in the 20 keV – 7 MeV range, an integral energy flux of $(6.23 \pm 0.13) \times 10^{-4}$ erg cm $^{-2}$ in the same range, and an isotropic equivalent energy release in gamma-rays of 1.3×10^{54} erg (at $z = 0.937$) which places GRB 080319B among several gamma-ray bursts with the highest released energy.

One more GRB with an exceptional luminosity happened on September 18, 2011 was studied in detail in the Konus-Wind experiment. The long GRB 110918A was discovered by several GRB observing missions: INTEGRAL (SPI-ACS), Konus-WIND, Mars Odyssey (HEND), and MESSENGER (GRNS). This GRB was localized by the IPN and its bright X-ray counterpart was found close to

the IPN box in the Swift/XRT follow-up observations starting 1.2 days after the trigger. The optical afterglow was discovered by the Isaac Newton Telescope and its spectroscopic redshift $z = 0.982$ was measured with the GMOS spectrograph mounted on the Gemini-N telescope (Levan *et al.* 2011). GRB 110918A is the brightest burst detected by Konus-WIND for more than 18 years of its continuous observations. The instrument's light curves in three energy bands covering the 22 – 1450 keV range (Fig. 6) show an extremely bright, short, hard pulse followed by three weaker, softer, partly overlapping pulses within next 25 seconds. A spectral lag between the light-curves is determined, showing a substantial increase in the course of the burst. The emission is detected up to 12 MeV. Modeling the time-integrated energy spectrum with the Band function yields a moderate value of $E_{\text{peak}} = 340$ keV, while the time-resolved spectral analysis reveals strong hardness-intensity correlation and a hard-to-soft evolution of the emission: E_{peak} falls from ~ 2.3 MeV at the onset of the huge initial pulse to ~ 50 keV at the final stage of the burst (Fig. 7). The total 20 keV – 10 MeV energy fluence amounts to $(7.8 \pm 0.4) \times 10^{-4}$ erg cm $^{-2}$ and a 64-ms peak flux is $(9.2 \pm 0.4) \times 10^{-4}$ erg cm $^{-2}$ s $^{-1}$, what corresponds to a huge isotropic-equivalent energy release of $(2.1 \pm 0.1) \times 10^{54}$ erg and the record-breaking peak luminosity of $(4.7 \pm 0.2) \times 10^{54}$ erg s $^{-1}$. The Konus-WIND results on GRB 110918A as well as the detailed coverage of the IPN localization, the X-ray afterglow observations with Swift/XRT, and the optical monitoring with Swift/UVOT can be found in the forthcoming paper (Frederiks, Hurley *et al.* in preparation).

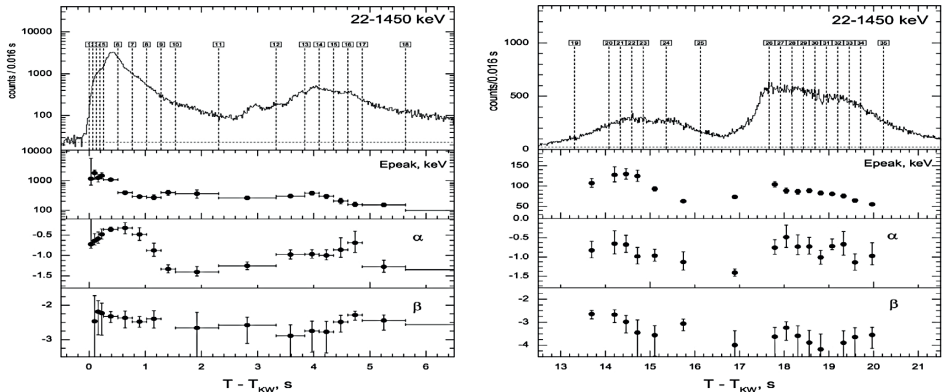


Fig. 7. Time-resolved spectral fits of GRB 110918A. The spectra are well described by the Band GRB function with the model parameters α , β , and E_p (Frederiks *et al.* 2013).

Thus, during the present-day epoch of intense multi-wave studies of cosmic gamma-ray bursts, the Konus-Wind experiment presents an important and often unique data on the time and energy properties of burst radiation in the 20 keV – 15 MeV range.

A very important and unusual result was obtained during simultaneous observations of the giant flare from SGR 1806-20 on December 27, 2004 by Konus-Wind

and by another Ioffe Institute's instrument Helicon onboard Russian near-Earth solar space observatory CORONAS-F (Frederiks *et al.* 2007a). The photon counting rate of gamma-rays in the initial pulse of a giant SGR flare is always so great that sensitive detectors are fully overloaded ("saturated") in such a way that precise measurements of the initial pulse become difficult and only rough lower-bound estimates are possible. Positions of the spacecraft at the time of detection of this burst are shown schematically in Figure 8. The detectors of the Helicon instrument were screened by Earth from direct exposure to the initial pulse of the giant flare from gamma-repeater, but clearly recorded its reflection from the Moon's surface. This reduction in intensity allowed, for the first time, reliably reconstructing the temporal profile of the initial pulse of the giant flare (Fig. 6) and determining its energy parameters: the full isotropic energy release of 2.3×10^{46} erg and the peak luminosity of 3.5×10^{47} erg s $^{-1}$ [15]. This detection of the 27 December 2004 giant flare became the first example of studying Moon-reflected X-ray and gamma-radiation coming from a source outside the Solar System.

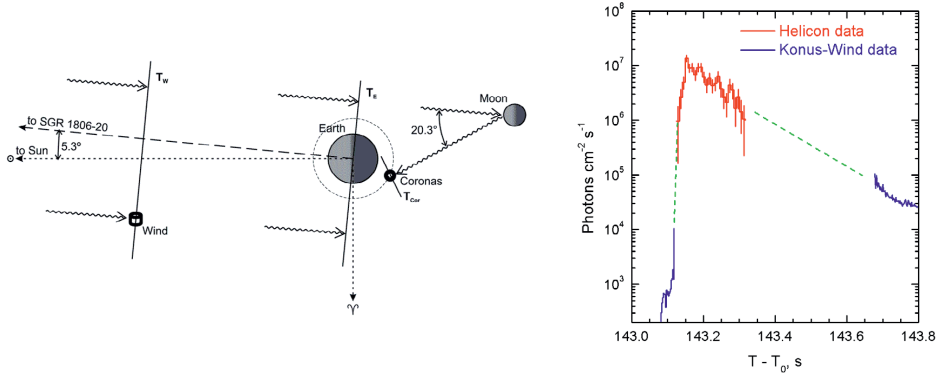


Fig. 8. Reflection of the initial pulse of the giant flare from SGR 1806-20 by the Moon and its detection by Konus-Wind and Helicon instruments (Frederiks *et al.* 2007a).

Recently, Konus-Wind measurements have been central in finding SGR sources in the galaxies M81/M82 and M31, first time far outside our own Milky Way system (Frederiks *et al.* 2007b; Mazets *et al.* 2008).

4 The future Ioffe Institute experiments in the field of GRB study

One of the future experiments is the Konus-UF instrument which is planned to install on board Russian Spectr-UF mission with the second name the World Space Observatory. The Konus-UF instrument consists of two detectors and an electronics unit. The Konus-UF detectors are built on NaI(Tl) scintillation crystals with dimensions like the Konus-Wind detectors have. The detectors will be allocated on the spacecraft body in such a manner as to observe a hemisphere (Fig. 9). The instrument is going to have a detailed program for measuring the temporal and

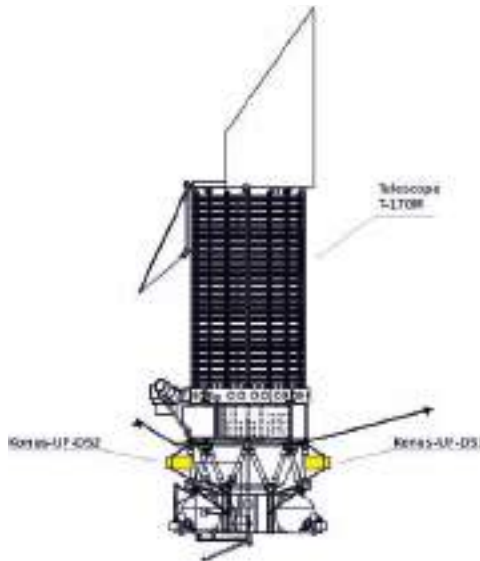


Fig. 9. Allocation of the Konus-UF detectors onboard the Spectrum-UF mission.

spectral characteristics of GRBs in the 10 keV to 15 MeV energy range. It is planned that the Spectr-UF mission is being launched in 2016 to a high-apogee orbit.

The second experiment is the Konus-M. It is planned that this experiment will be launched onboard a Small-size Scientific Spacecraft #3 which is built by Lavochkin Assosiation in the frame of Program of small scientific spacecraft for fundamental space research. The spacecraft is planned to launch into a high-apogee orbit by the end of 2014.

Two sets of detectors are planed to use in the Konus-M experiment. The first one is a four-detector Konus-M-DN GRB localization system. Each Konus-M-DN detector includes a NaI(Tl) crystal with a diameter of 130 mm and a height of 15 mm in a thin-walled aluminum container with a beryllium entrance window and a high-transmission lead-glass exit window. These detectors have a passive shielding of their lateral surface and an anisotropic cosine-like angular sensitivity. Their placement on the spacecraft is shown in Figure 10. The axes of these four detectors are inclined to the spacecraft symmetry axis by 30° and are separated in azimuth by 90°. Such system of Konus-M-DN detectors provides a GRBs source localization capability with an accuracy of 0.5 – 2.0 degree depending on a burst intensity.

These detectors will observe a celestial hemisphere in the direction of +X of the spacecraft. Such a system of detectors was successfully used in the Ioffe Institute's Konus-A experiment on board Cosmos-2326 (Aptekar *et al.* 1998). The other set contains two spectrometric detectors (Konus-M-DS-1 and Konus-M-DS-2) which are similar to the Konus-Wind detectors. The axes of these detectors aligned

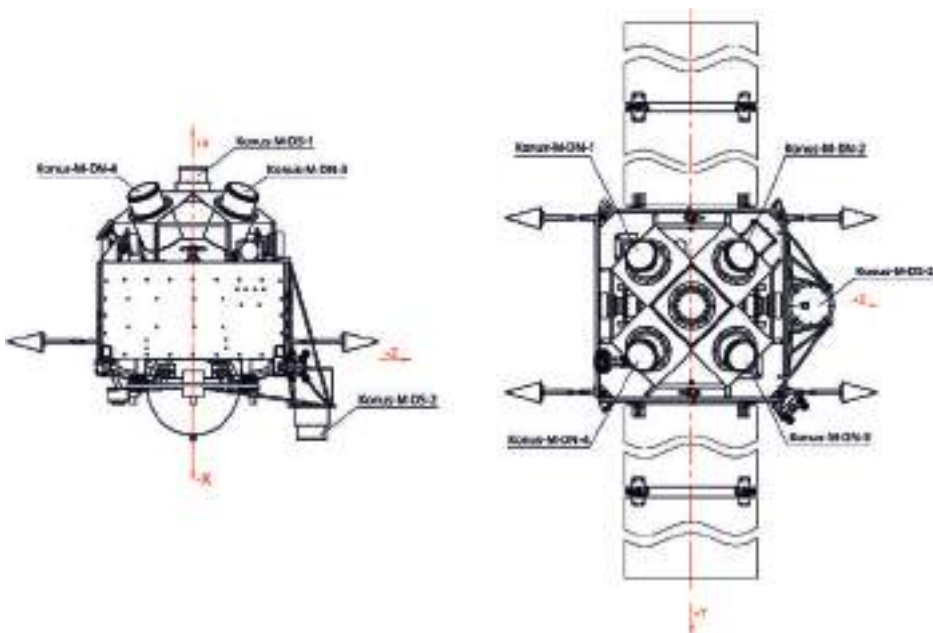


Fig. 10. The schematic arrangement of Konus-M detectors onboard spacecraft.

along the $+X$ and $-X$ axes of the spacecraft (Fig. 10). Thereby the Konus-M experiment will have a capability to constantly observe the whole celestial sphere and to obtain information about a GRB position simultaneously with temporal and spectral characteristics of bursts coming from a half of the sky.

5 Conclusions

The Ioffe Institute Konus experiments onboard Venera 11–14 interplanetary missions had for the first time investigated many of the basic characteristic of GRBs. The joint Russian-American Konus-Wind experiment, which has already been operated for more than 18 years, provides important and often unique data regarding the various characteristics of GRBs in the 20 keV to 15 MeV energy range. The future Ioffe Institute experiments will give us an opportunity to continue effective research of the extremely-explosive phenomena in the Universe.

Our work is supported by the state contract of the Federal Space Agency and Russian Foundation for Basic Research (projects numbers 11-02-12082-ofi-m and 12-02-000320-a).

References

- Aptekar, R.L., Frederiks, D.D., Golenetskii, S.V., *et al.*, 1995, Space Sci. Rev., 71, 265
- Aptekar, R.L., Butterworth, P.S., Cline, T.L., *et al.*, 1998, ApJ, 493, 404

- Frederiks, D.D., *et al.*, this proceedings
- Frederiks, D.D., Golenetskii, S.V., Palshin, V.D., *et al.*, 2007a, Astron. Lett., 33, 1
- Frederiks, D.D., Palshin, V.D., Aptekar, R.L., *et al.*, 2007b, Astron. Lett., 33, 19
- Golenetskii, S.V., Il'inskii, V.N., & Mazets, E.P., 1984, Nature, 307, 41
- Klebesadel, R.W., Strong, I.B., & Olson, R.A., 1973, ApJ, 182, L85
- Levan, A.J., Tanvir, N.R., & Wiersema, K., 2011, GCN Circular, 12368
- Mazets, E.P., Golenetskii, S.V., & Il'inskii, V.N., 1974, JETP Letters, 19, 77
- Mazets, E.P., Golenetskii, S.V., Il'inskii, V.N., Aptekar, R.L., & Guryan, Yu. A., 1979, Nature, 282, 587
- Mazets, E.P., Golenetskii, S.V., Il'inskii, V.N., *et al.*, 1981, Ap&SS, 80, 3
- Mazets, E.P., & Golenetskii S.V., 1988, Observations of cosmic gamma-ray bursts, Sov. Sci. Rev., Sect. E, 6, 283
- Mazets, E.P., Aptekar, R.L., Cline, T.L., *et al.*, 2008, ApJ, 680, 545
- Pal'shin, V.D., *et al.*, 2013, in press
- Racusin, J.L., Karpov, S.V., Sokolowski, M., *et al.*, 2008, Nature, 455, 183
- Terekhov, M.M., *et al.*, 1998, AIP Conf. Proc., 428, 894

Chapter II.

Prompt Emission-I Observations

FERMI AND SWIFT OBSERVATIONS OF SHORT GRBS

E. Troja¹

Abstract. The *Fermi* and *Swift* satellites offer unique, and complementary capabilities for the study of short GRBs. Here, I briefly summarize the current status of *Fermi* and *Swift* observations of short GRBs, and outline some highlights, focusing on the prompt emission phase.

1 Fermi observations of short GRBs

1.1 GBM observations: Spectral properties of the prompt phase

The Gamma-Ray Burst Monitor (GBM; Meegan *et al.* 2009) is the secondary instrument on board the *Fermi* Gamma-ray Space Telescope. It is composed of 14 scintillators, twelve Sodium Iodide (NaI) detectors, sensitive between 8 keV and 1 MeV, and two Bismuth Germanate (BGO) detectors, sensitive between 150 keV and 40 MeV. Thanks to its wide field of view (~ 8 sr), broad energy bandpass (8 keV–40 MeV), and sophisticated trigger algorithms, the Gamma-Ray Burst Monitor (GBM) on-board *Fermi* is currently the most prolific detector of short hard bursts (~ 45 events yr^{-1}). By using the relative ratios of the fluxes received by the NaI detectors, a burst detected by the GBM can be localized to an accuracy of a few degrees on the sky. While the typical positional uncertainty of GBM bursts is adequate for multi-messenger searches (*e.g.* neutrino or GW signal; Abbasi *et al.* 2012; Abadie *et al.* 2012), it hampers follow-up observations, thus preventing the localization of the GRB afterglow. In fact, thus far the redshift of a GBM short burst has been measured only in the case of a simultaneous *Swift* trigger.

One of the main strengths of the GBM is its broadband spectral coverage, which enables detailed spectral and temporal studies of the brightest short GRBs. GBM spectral studies confirm that short GRBs are characterized by harder spectra than long GRBs, mainly due to their higher peak energies ($\langle E_{\text{pk}} \rangle \sim 490$ keV; Nava *et al.* 2011; Goldstein *et al.* 2012). Time-resolved spectroscopy shows that the peak energy mostly tracks the light curve evolution, following a hardness-intensity

¹ NASA GSFC & CRESST, 8800 Greenbelt Rd, 20771 Greenbelt, MD, USA

correlation already observed in long GRBs (Guiriec *et al.* 2010). These results suggests that the observed prompt gamma-ray emission of short and long GRBs is produced by a similar physical mechanism, independent of the progenitor system (Ghirlanda *et al.* 2011).

Fermi/GBM observations continue to provide growing evidence of spectral deviations from the canonical Band function (Band *et al.* 1993). Such spectral “humps” are interpreted as evidence of photospheric emission from the expanding hot fireball (*e.g.* Ryde *et al.* 2010). Lazzati *et al.* (2009) found that the interaction of the relativistic outflow with the progenitor star might enhance the efficiency of the photospheric emission, thus explaining the bright photospheric components observed in some long GRBs. The possible detection of photospheric emission in the bright short GRB 120323A (Guiriec *et al.* 2012) complicates this picture, suggesting that another mechanism, not related to the progenitor type, drives the evolution of the relativistic jet.

1.2 LAT observations: High-energy emission from short GRBs

The Large Area Telescope (LAT; Atwood *et al.* 2009) is a pair production telescope sensitive to gamma-rays in the 20 MeV – 300 GeV energy range. In its first four years of operations LAT detected six short GRBs, but only half of them were significantly detected at energies above >100 MeV (GRB 081024B, GRB 090510, and GRB 120830A).

Despite the low rate of detections, LAT observations provided an unique insight into the jet physics of short GRBs. Before the advent of *Fermi*, GeV emission had been detected from several long BATSE GRBs (Dingus 1995). Little was known about short GRBs, their radiation physics, and whether they could produce such high-energy emission. LAT observations shows that the GeV emission of short bursts closely resemble the properties observed in long duration bursts. The high-energy (>100 MeV) emission shows a delayed onset with respect to the lower energy (<1 MeV) one, and a significantly longer duration (see Fig. 1). The bright short GRB 090510 further shows evidence of a distinct spectral component, modeled as a power-law, which dominates above 100 MeV. This is consistent with the behavior of several bright long GRBs at GeV energies.

Several GeV photons were detected by the *Fermi*/LAT during the prompt phase of GRB 090510, the highest energy one at \sim 31 GeV (see Fig. 1, bottom panel). By using simple $\gamma\gamma$ opacity arguments, Ackermann *et al.* (2010) used the detection of GeV emission to constrain the outflow Lorentz factor of a short GRB for the first time. The lower limit derived for GRB 090510, $\Gamma > 1200$, is comparable to the values derived for other bright long GRBs, showing that the outflows powering short GRBs are at least as relativistic as those of long GRBs.

2 Swift observations of short GRBs

The Burst Alert Telescope (BAT) on-board *Swift* detects only a few short bursts (\sim 8–9 events yr^{-1}), but provides more accurate localizations (\sim 3 arcmin), enabling

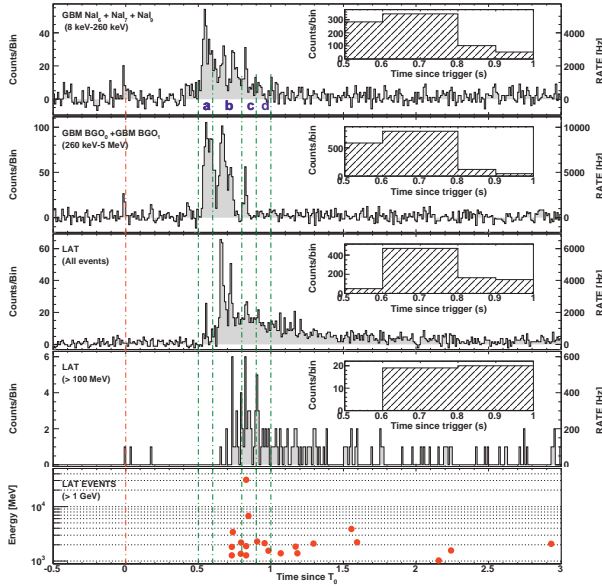


Fig. 1. *Fermi* GBM and LAT light curves of GRB 090510. The *bottom panel* reports the individual photon energies as a function of time. From Ackermann *et al.* (2010). Similar to long GRBs, the high-energy (>100 MeV) of short GRBs displays a delayed onset, and a longer duration than the sub-MeV emission.

rapid follow-up observations of their afterglows. Approximately 65% of the *Swift* short GRBs have a detected X-ray afterglow, and $\sim 30\%$ have optical/infrared afterglow detection, usually from ground-based observatories. Thanks to its higher sensitivity, and soft energy bandpass (15–150 keV), the *Swift*/BAT revealed the presence of a relatively long duration (~ 100 s), spectrally soft tail of the prompt emission, observed in ~ 15 – 20% of short bursts. The presence of this new emission component represents a main challenge for an understanding of the mechanism, and progenitors of short duration GRBs.

2.1 Short GRBs with extended emission

An example of short GRBs with extended emission components is shown in Figure 2 (bottom panel): they are characterized by a short duration (< 2 s) spike followed by a period of quiescence of 3–10 s, then an extended period (~ 100 s) of spectrally softer emission. Such tail of emission is usually very faint, but in some rare cases (*e.g.* 080503) it dominates the prompt emission, being 30 times more energetic than the initial short spike.

Hints of a temporally extended emission were first found by Lazzati *et al.* (2001), in the summed BATSE lightcurves of 76 short gamma-ray bursts. The observed excess in the average temporal evolution was interpreted as the onset of the

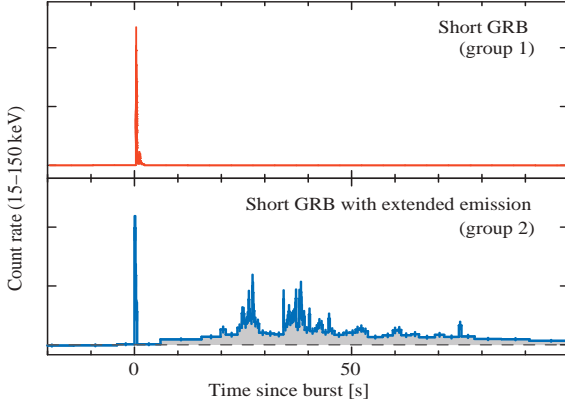


Fig. 2. *Swift* light curves of a short GRB (*top panel*), and a short GRB with a bright temporally extended emission (*bottom panel*). A soft tail of emission is seen in \sim 15–20% of short GRBs. At difference with the BATSE data, the stacked analysis of *Swift* short GRB light curves does not reveal any significant excess, suggesting that only some short GRBs are accompanied by this new, longer-lasting emission component.

afterglow emission. Though an afterglow origin may accommodate some of the *Swift* observations, the brightest extended tails display large and rapid luminosity fluctuations. These features are hard to accommodate within the standard afterglow theory, and instead they are suggestive of a long-lasting (\sim 100 s) central engine activity (Norris & Bonnell 2006). Such activity has fundamental implications for all short GRB progenitor models. For instance, the time-scales of a GRB, *i.e.* its variability and its duration, are set by the dynamical and the viscous time of the accretion disc created in the merger. The viscous lifetime of such accretion disc is \approx 0.1 s, far too short to be the power source of the prolonged engine activity. Durations of $>$ 100 s are indeed not expected, unless an additional mechanism accretes mass onto the disc over longer timescales. Addressing the nature of this mechanism is therefore a crucial step towards understanding the progenitors of short GRBs and the extreme physical processes that take place around the newly formed black hole.

References

- Meegan, C., Lichti, G., Bhat, P.N., *et al.*, 2009, ApJ, 702, 791
- Abbasi, R., Abdou, Y., Abu-Zayyad, T., *et al.*, 2012, Nature, 484, 351
- Abadie, J., Abbott, B.P., Abbott, R., *et al.*, 2012, ApJ, 760, 12
- Nava, L., Ghirlanda, G., Ghisellini, G., & Celotti, A., 2011, A&A, 530, A21
- Goldstein, A., Burgess, J.M., Preece, R.D., *et al.*, 2012, ApJS, 199, 19
- Guiriec, S., Briggs, M.S., Connaughton, V., *et al.*, 2010, ApJ, 725, 225
- Ghirlanda, G., Ghisellini, G., & Nava, L., 2011, MNRAS, 418, L109

- Band, D., Matteson, J., Ford, L., *et al.*, 1993, ApJ, 413, 281
Ryde, F., Axelsson, M., Zhang, B.B., *et al.*, 2010, ApJ, 709, L172
Lazzati, D., Morsony, B.J., & Begelman, M.C., 2009, ApJ, 700, L47
Guiriec, S., Daigne, F., Hascoët, R., *et al.*, 2012 [[arXiv:1210.7252](https://arxiv.org/abs/1210.7252)]
Atwood, W.B., Abdo, A.A., Ackermann, M., *et al.*, 2009, ApJ, 697, 1071
Dingus, B.L., 1995, Ap&SS, 231, 187
Ackermann, M., Asano, K., Atwood, W.B., *et al.*, 2010, ApJ, 716, 1178
Lazzati, D., Ramirez-Ruiz, E., & Ghisellini, G., 2001, A&A, 379, L39
Norris, J.P., & Bonnell, J.T., 2006, ApJ, 643, 266

TEMPORAL DECOMPOSITION STUDIES OF GRB LIGHTCURVES

N.P. Bhat¹

Abstract. Gamma-ray bursts (GRB) are extremely energetic events and produce highly diverse light curves. Light curves are believed to be resulting from internal shocks reflecting the activities of the GRB central engine. Hence their temporal studies can potentially lead to the understanding of the GRB central engine and its evolution. The light curve variability time scale is an interesting parameter which most models attribute to a physical origin *e.g.*, central engine activity, clumpy circum-burst medium, or relativistic turbulence. We develop a statistical method to estimate the GRB minimum variability time scale (MVT) for long and short GRBs detected by GBM. We find that the MVT of short bursts is distinctly shorter than that for long GRBs supporting the possibility of a more compact central engine of the former. We find that MVT estimated by this method is consistent with the shortest rise time of the fitted pulses. Hence we use the fitted pulse rise times to study the evolution of burst variability time scale. Variability time is in turn related to the minimum bulk Lorentz factor. Using this we relate the GRB spectral evolution to the evolution of the variability time scale.

1 Introduction

Gamma-ray bursts (GRBs) are short, intense and distant flashes of γ -rays that occur at random locations in the sky with their peak power in the 200–500 keV range. During their appearance, they often outshine all other sources in the γ -ray sky combined. The temporal structure of GRBs exhibits diverse morphologies. They can vary from a single smooth pulse to extremely complex light curves with many erratic pulses with different durations, amplitudes, and fine structures. Physically, several mechanisms have been invoked to interpret GRB temporal variability. The leading scenario is to attribute the light curve variability to the activity of the

¹ University of Alabama in Huntsville, 301 Sparkman Dr. Huntsville 35899, AL, USA

central engine (Rees & Mészáros 1994; Sari & Piran 1997). There are no direct observations of the central engine. Most of the bursts exhibit variability on time scales that are much shorter than the burst durations. According to internal shock model of GRBs, the γ -ray light curves result from collisions between shells with different values of the bulk Lorentz factor Γ . Within such a scenario, the observed light curves can be directly connected to the behavior of the central engine (Lei 2007; Lu *et al.* 2008).

One approach for probing light curves which has received attention (Norris *et al.* 2005; Bhat *et al.* 2012) is to express them as a series of displaced pulses, each with a parametric form. There is an appeal to this approach because fitting routines are well-understood and interpretations of rise time, decay time, full width at half max, etc., are possible.

GRB light curves exhibit variability on various time scales. In this paper we present a new statistical method of estimating the minimum value of such variability time scales of a GRB and relate it to the minimum value of the fitted pulse rise time. This in turn can be related to the minimum Lorentz factor of the relativistic shells emitted by the central engine. The evolution of the minimum Lorentz factor is then related to the spectral evolution of the GRBs.

2 Minimum variability time-scale in GRBs

GRB light curves are generally binned in to narrow time bins. Such light curves with high variability at low power may show variations which are not statistically significant. While statistically significant variability could become statistically insignificant at finer bin-widths and significant variability could vanish if the bin-widths are too coarse. By a comparison of the GRB prompt emission variability with the purely statistical variability of the background region we derive an optimum bin-width when the non-statistical variability in the light curve becomes significant.

We identify the prompt emission duration and an equal duration of background region. We then derive a differential of each light curve and compute the ratio of the variances of the GRB and the background. This ratio divided by the bin-width is plotted as a function of bin-width in Figure 1. As can be seen at very fine bin-widths the ratio falls monotonically with increasing bin-width signifying that at such fine bin-widths the variations in the background and burst regions are statistically identical. In other words the signal in the burst light curve is indistinguishable from Poissonian fluctuations. Later at certain bin-width the variation starts deviating from the $\frac{1}{\text{bin-width}}$ behavior. We measure the bin-width at this valley by fitting a parabola and the bin-width at the minimum of the parabola is called the optimum bin-width t_b . t_b is also interpreted as the minimum variability time scale of the GRB t_v . At this bin-width the variability in the GRB light curve becomes detectable compared to the normal fluctuations seen in the background. We are therefore confident that the short-term variability is real and is not an artifact of data reduction or statistical fluctuations.

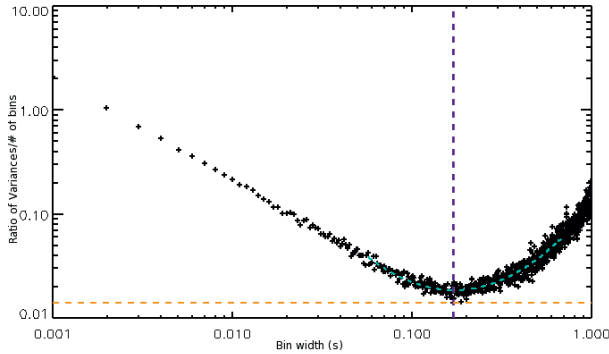


Fig. 1. Variation of the ratio of the variances per bin to the histogram bin-width. At very fine bin-widths the GRB signal is indistinguishable from background fluctuations and hence the ratio decreases monotonically with increasing bin-width. At larger bin-widths the signal is clearly visible from the background and hence the ratio per bin starts increasing. The turn over bin-width is defined as the minimum variability time scale where the bin-width is optimum. Cyan dashed line shows a fitted parabola around the minimum that has a minimum at a bin-width indicated by the vertical dashed line in blue. See text for more details.

Another possibility is that t_b could be a function of the signal-to-noise ratio of the GRB rather than an intrinsic feature of the GRB light curve. For this we generated synthetic light curves of the same GRB by adding Poisson noise to the fitted lognormal pulses and adding them to the fitted background with added noise. The optimum bin-width was estimated for each of the synthetic light curve derived by varying the signal-to-noise ratio over a few orders of magnitude. It was found that the value of t_b is not a strong function of the signal-to-noise ratio.

Recently the minimum variability time scales were estimated for long and short GRBs by a model independent method based on a wavelet decomposition technique (MacLachlan *et al.* 2012). In Figure 2 we compare the minimum variability time scales estimated by MacLachlan *et al.* (2012) with those estimated by the present method for the same GRBs. The blue line shows the ideal case when the two quantities are equal. The figure shows that the minimum variability time scales estimated by two different techniques are statistically consistent with each other. Hence we conclude that the present method indeed estimates the minimum variability time scale of a given GRB. MacLachlan *et al.* (2012) also demonstrate that the minimum variability time scale estimated by the wavelet decomposition technique is also consistent with the minimum of the rise-times of the fitted pulses using the lognormal shape for the individual pulses (Bhat *et al.* 2012).

2.1 Minimum variability time-scale as a GRB type identifier

GRBs are generally classified as long or short depending on their duration T_{90} and their hardness ratios. Long GRBs ($T_{90} > 2$ s) are generally soft and short

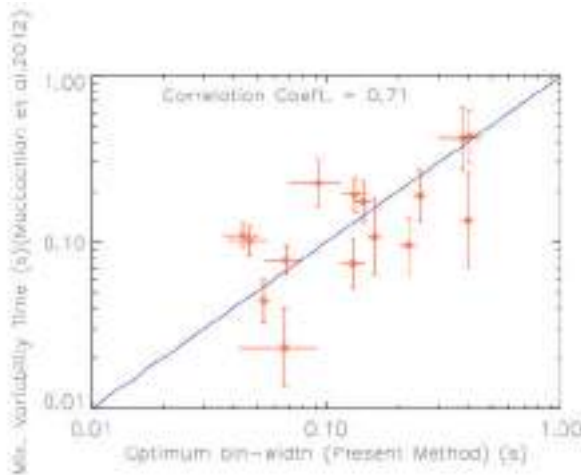


Fig. 2. A comparison of the minimum variability time scale estimated by McLachlan *et al.* (2012) with the optimum bin-width estimated by the present method. They seem to correlate well.

GRBs ($T_{90} < 2$ s) are generally hard. They are considered to form two different GRB classes (Kouveliotou *et al.* 1993). The measurement of spectral lags is another tool in the study of GRBs and their classification since short GRBs exhibit negligible lags. However classification schemes based on any or all of these parameters result in significant overlap of GRBs of either type. Hence we need more such identifying parameters to uniquely identify a GRB type. Here we have another parameter, t_v , to add to that list. Figure 3 shows a distribution of minimum rise-times for long and short GRBs. The minimum pulse rise-times of short GRBs are distinctly shorter (at least by a factor of 15) than that of long GRBs. In other words the minimum variability time scale, t_v , can be used as another parameter to identify short GRBs.

3 Minimum variability time scale and minimum Lorentz factor

While t_v has been shown to be consistent with the minimum rise-time of fitted pulses, the rise-times of the fitted pulses to the prompt emission light curve can be used to trace the evolution of the variability time scale at any time during the GRB prompt emission. One can also derive a lower limit on the bulk Lorentz factor (Γ_{min}) given the variability timescales and observations of the highest energy photons at any time during a burst. Constraining the bulk Lorentz factor, Γ , of the jet is a major challenge in understanding the GRB physics, the mechanism for launching the jet as well as high-energy emission. High-energy γ -rays produced and emitted from the GRB jet are subject to $\gamma\gamma \rightarrow e^+e^-$ pair production process with soft target photons, and absorbed *in situ*. The interaction rate of

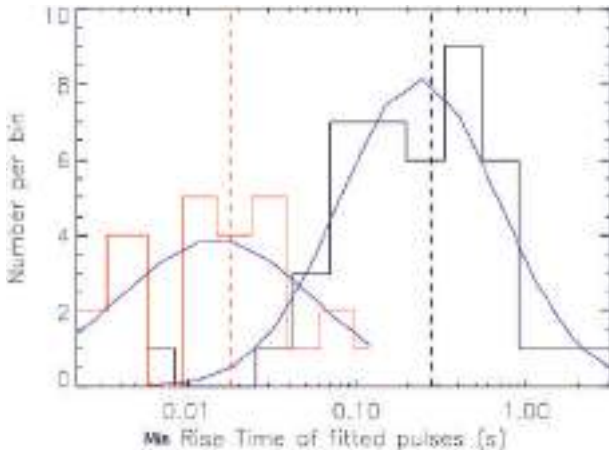
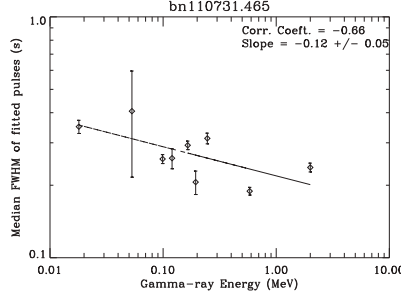


Fig. 3. A distribution of the minimum pulse rise time for long and short GRBs. The minimum variability time scale or the minimum fitted pulse rise time clearly shows a bimodal distribution showing that it can be a parameter to distinguish between long and short GRBs.

this process and corresponding opacity, $\tau_{\gamma\gamma}$, for the high-energy γ -rays depends on the target photon density and can be significant when both the high-energy and target photons are produced in the same physical region. Highly relativistic motion, with a bulk Lorentz factor $\Gamma \gg 1$, of such an emission region can reduce the $\gamma\gamma$ interaction rate and $\tau_{\gamma\gamma}$ greatly by allowing for a larger emitting radius and a smaller target photon density. Observation of a γ -ray spectrum up to an energy E_{max} thus can be used to put a lower limit on Γ (Lithwick & Sari 2001; Razzaque *et al.* 2004; Granot *et al.* 2008; Ackerman *et al.* 2010). Thus the evolution of the variability time scale leads to the study of the evolution of the bulk Lorentz factor which in turn is related to the evolution of the γ -ray opacity $\tau_{\gamma\gamma}$ during the prompt emission phase of a GRB. A delayed onset of the GeV photons, seen in several GRBs detected in the Fermi LAT, the emission is interpreted as due to the time evolution of the opacity in a GRB outflow (Hascoët *et al.* 2012). In addition, As pointed out by Granot *et al.* (2008), due to the temporal evolution of $\tau_{\gamma\gamma}$, the opacity cut-off in a time-integrated spectrum will be smoother than a sharp exponential decay: the cut-off transition will be close to a power-law steepening. This time evolution takes place within a given γ -ray pulse, and can be even stronger in a complex burst where the light curve is made up of many pulses (Aoi *et al.* 2010). Hence a study of the evolution of Γ_{min} would lead to a better understanding of the possible connection between the temporal structure of the light curve and the spectral evolution of the GRB. Figure 4a shows variation of the fitted pulse width (FWHM) as a function of γ -ray energy while Figure 4b shows a variation of the FWHM as a function of time since the GRB trigger time. It is well known that for lognormal pulse shapes the rise-time and FWHM

[An example of evolution of the pulse width (FWHM) as a function of energy as seen in GRB 1107311A.]



[Evolution of the pulse width (FWHM) as a function of time since trigger as seen in GRB 1107311A.]

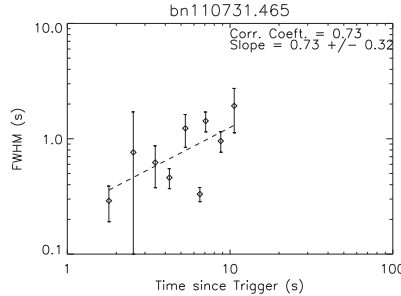


Fig. 4.

are strongly correlated (Bhat *et al.* 2012). Hence Figure 4a demonstrates that the variability time scale decreases with increasing γ -ray energy while Figure 4b shows that the variability time scale decreases since the trigger, indicating a trend like the hard-to-soft spectral evolution in GRBs. Figure 5 shows a typical example of the observed Γ_{min} evolution during a bright short Fermi GRB 090510 (Abdo *et al.* 2009). Here the Γ_{min} is estimated at two different epochs of the GRB (0.6 s–0.8 s, left panel and 0.8 s–0.9 s, right panel, post trigger) by assuming that the highest energy of the γ -ray (E_{max}) emitted in each interval originate from the same physical region as the observed low energy photons in the same time interval. The t_v were approximated conservatively to the FWHM of the fitted pulse during each interval. The data points with error bars correspond to the Γ_{min} calculated for the best-fit $t_v = \text{FWHM}$ and $\text{FWHM}/2$ in the respective time intervals.

4 Summary

A method is developed to estimate the optimum bin-width of the light curve to carry out pulse decomposition analysis of GRBs. The optimum bin-width is

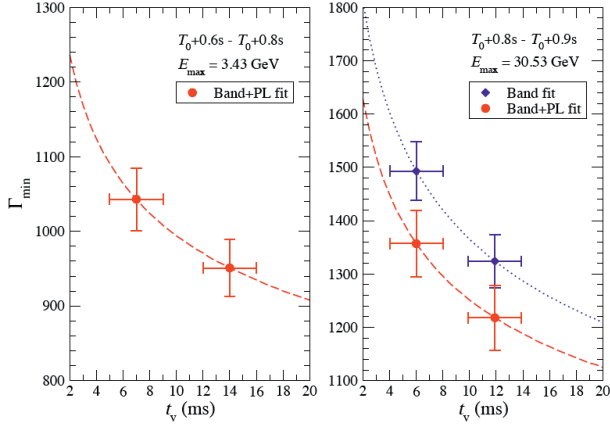


Fig. 5. The Γ_{\min} of the GRB 090510 prompt mission region as a function of the γ -ray variability time-scale t_v . The highest and low-energy (MeV) photons in each time-interval are assumed to originate from the same physical region. The data points correspond to the Γ_{\min} calculated for the best-fit $t_v = \text{FWHM}$ and $\text{FWHM}/2$ in the respective time intervals.

interpreted as the minimum variability time scale of the GRB because it is found to be statistically consistent with that estimated by an independent method which in turn is found to be consistent with the lowest of the rise-times of the fitted pulses to deconvolve the entire light curve of the GRB. The variability time scales were also estimated using the *fwhm* of the fitted pulses during the course of the burst and study the evolution of the bulk Lorentz factor. The variability time scales, t_b , were estimated at different γ -ray energies by the same pulse fitting technique using GRB light curves in different energy ranges. Using the estimated bulk Lorentz factor one can test the location of γ -ray emission regions in the internal shock scenario. The γ -ray emission radius is given by $R \sim 2\Gamma^2 ct_b/(1+z)$. Thus an energy dependent variation of t_b can be interpreted as collisions of shells at different radii producing γ -rays of different energies.

References

- Abdo, A.A., Ackerman, M., Ajello, M., *et al.*, 2009, Nature, 462, 331
- Ackerman, M., Asano, K., Atwood, W.B., *et al.*, 2010, ApJ, 716, 1178
- Aoi, J., Murase, K., Takahashi, K., Ioka, K., & Nagataki, S., 2010, ApJ, 722, 440
- Bhat, P.N., Briggs, M.S., Connaughton, V., *et al.*, 2012, ApJ, 744, 141
- Granot, J., Cohen-Tanugi, J., & do Couto e Silva, E., 2008, ApJ, 677, 92
- Hascoët, R., Daigne, F., Mochkovitch, R., *et al.*, 2012, MNRAS, 421, 525
- Kouveliotou, C., Meegan, C.A., Fishman, G.J., *et al.*, 1993, ApJ, 413, L101
- Lei, W.H., Wang, D.X., Gong, B.P., *et al.*, 2007, A&A, 468, 563
- Lithwick, Y., & Sari, R., 2001, ApJ, 555, 540

- Lu, Y., Huang, Y.F., & Zhang, S.N., 2008, ApJ, 684, 1330
MacLachlan, G.A., Shenoy, A., Sonbas, E., *et al.*, 2012, MNRAS, 425, L32
Norris, J.P., Bonnell, J.T., Kazanas, D., *et al.*, 2005, ApJ, 627, 324
Razzaque, S., Mészáros, P., & Zhang, B., 2004, ApJ, 613, 1072
Rees, M.J., & Mészáros, P., 1994, ApJ, 430, L93
Sari, R., & Piran, T., 1997, ApJ, 485, 270

PHOTOSPHERIC EMISSION FROM GAMMA-RAY BURSTS

M. Axelsson^{1,2}

Abstract. In spite of extensive research over the past decades, a complete physical picture of the origin of the prompt gamma-ray burst emission is still lacking. During recent years, evidence has been accumulating that the jet photosphere plays an important role. In this paper we summarize the lessons learned from *Fermi* observations regarding the behavior of the photosphere and discuss why photospheric emission does not necessarily appear as blackbody radiation. We concentrate on two strong and important bursts, GRB 090902B and GRB 110721A, which serve as examples of the standard appearance photospheric emission may have in gamma-ray burst spectra.

1 Introduction

Although the emission mechanisms active in the prompt phase of gamma-ray bursts (GRBs) are still under debate, there is much evidence that the photosphere of the relativistic outflow plays an important role in the formation of the observed spectrum (*e.g.* Lazzati & Begelman 2010; Ryde *et al.* 2010; Guiriec *et al.* 2011; Vurm *et al.* 2011; Giannios 2011; Zhang *et al.* 2011). A strong contribution from the photosphere was predicted on physical grounds already in early works by Goodman (1986) and Paczyński (1986). However, the observed spectra are in general nonthermal so this was not considered a viable model. Here, we summarize observations of GRBs made with the *Fermi Gamma-ray Space Telescope* which suggest that photospheric emission is indeed present in the spectra of many GRBs.

2 Early observations

The first observational hints of a photospheric component in GRBs came from *Compton Gamma-Ray Observatory/BATSE* data (20–2000 keV). Ryde (2004)

¹ Oskar Klein Center, Department of Physics, Stockholm University, 106 91 Stockholm, Sweden

² Department of Physics, KTH Royal Institute of Technology, 106 91 Stockholm, Sweden

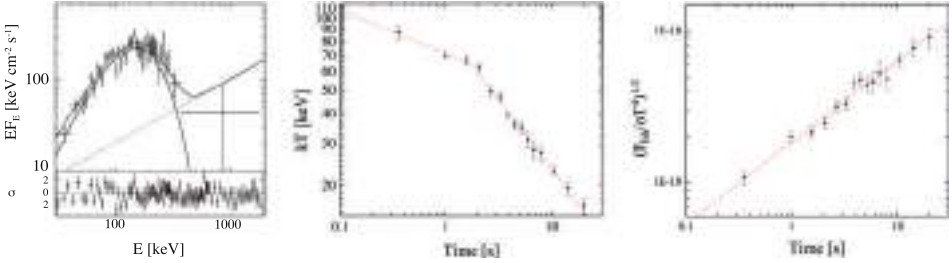


Fig. 1. Observational results from BATSE trigger 907. *Left:* spectrum showing a fit using a Planck function and power-law. *Middle:* evolution of the temperature of the Planck function during the burst. *Right:* ratio of observed flux to emergent flux.

found that in many individual emission pulses an equally good or better fit could be found by using a model comprising a Planck function and a power-law, as compared to the traditional Band function. Additionally, it was found that the evolution of the Planck function component during the prompt phase followed well defined and consistent characteristics. An example of such a BATSE observation is shown in Figure 1. The Planck component was interpreted as the photosphere of the GRB.

3 Results from Fermi

Since its launch in 2008, *Fermi* has seen over 1000 GRBs. The major advantage of *Fermi* over BATSE is that it has a much wider spectral coverage. Combining the two instruments – the Gamma-ray Burst Monitor (GBM; Meegan *et al.* 2009) and the Large Area Telescope (LAT; Atwood *et al.* 2009) – *Fermi* achieves continuous coverage from 8 keV to above 300 GeV. Although the majority of the GRBs detected by *Fermi* are seen only in the low-energy range, there have been 35 bursts with high-energy emission strong enough to be detected also by the LAT.

3.1 Multiple spectral components

Ryde (2004) showed that an alternative fit of a Planck function plus power-law could be used instead of a Band function in many cases, over the limited energy range provided by BATSE. With the wider energy coverage of *Fermi*, the picture has matured. In several GRBs, an additional spectral component is found below the peak of the Band function (the low-energy region of the Band function corresponds to the power-law seen in the BATSE range). Examples of such bursts are GRB 090820A (Burgess *et al.* 2011) and GRB 100924B (Guiriec *et al.* 2011). Adding a Planck function at lower energies, in addition to the Band function covering the majority of the emission, significantly improves the fit.

Recently, results from analysis of *Fermi* data from GRB 110721A were published (Axelsson *et al.* 2012). They show that also in this burst there is a need for

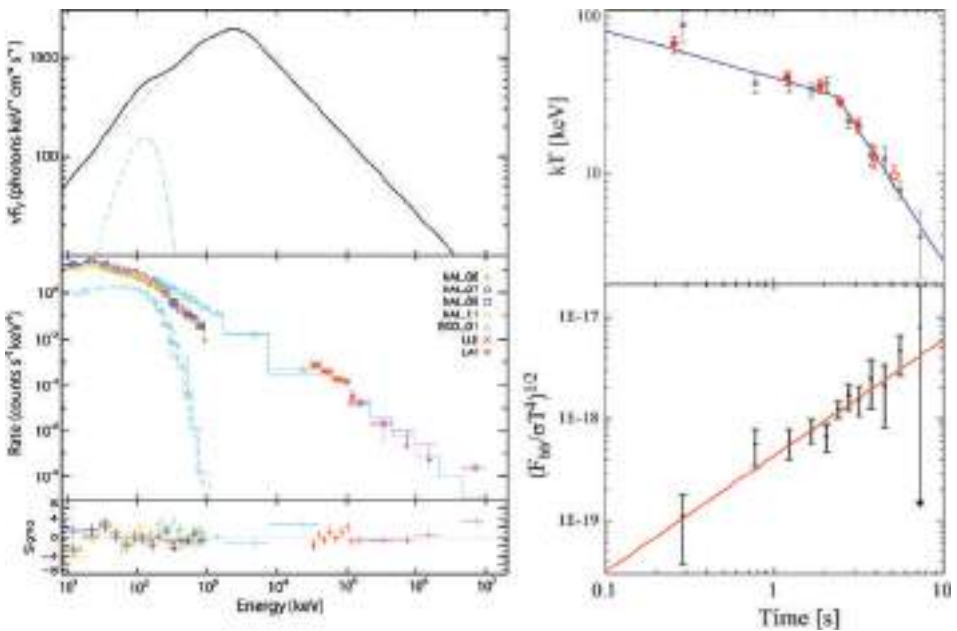


Fig. 2. *Left:* time-integrated spectrum of GRB 110721A fit with a model comprising a Band function combined with a Planck function. The upper panel shows the model spectrum in νF_ν representation, the middle panel the count spectrum and the lower panel the residuals of the fit. *Right:* evolution of the temperature (*top*) and ratio of observed to emergent flux (*bottom*) of the blackbody. In the *top panel*, filled circles indicate a $>5\sigma$ significance of the blackbody, filled circles a 3σ significance. The smaller points in both panels are from fits using a high time resolution, which lowers the significance of the component.

an extra component at low energies. During the first 3 seconds, this extra component (modeled with a Planck function) has a significance above 5σ . After this the significance drops to 3σ . The component is also required in the time-integrated spectrum, as shown in Figure 2.

In order to understand the nature of this extra component, we can study its evolution in time. Doing so, we find that it follows the same pattern as previously seen for the Planck function components in the BATSE observations (right panels in Figs. 1 and 2).

The fact that the components follow the same behavior strongly indicates that they are the result of the same physical process, and we connect them to the photosphere.

3.2 Dominating photospheric emission

Although the photospheric component is usually weak compared to the main emission peak fit by the Band function, in GRB 090902B the photospheric emission

dominates. At early times, the spectrum of this GRB shows a narrow peaked component, as well as a separate power-law component observed at energies both above and below the peak (Abdo *et al.* 2009).

During the first half of the GRB emission pulse, the peaked component is very narrow, with $\alpha \sim 0.3$ and $\beta \sim -4$, thus strongly violating the optically thin synchrotron limit. This led Ryde *et al.* (2010) to identify the component with photospheric emission, and it was shown that a multicolor blackbody provides a good fit to the data. A multicolor blackbody is expected on theoretical grounds, and while a standard blackbody provides an adequate approximation when the component is weak, it is not sufficient when the component dominates. This clear identification also led to a unique possibility to study the evolution of the photospheric emission. It was found that during the later half of the burst, the peaked component broadened significantly, to resemble more the typical Band function peak seen in the majority of bursts.

As we are clearly observing the same dominant component throughout the duration of GRB 090902B, the drastic change of appearance that is seen is strong evidence that photospheric emission need not appear as blackbody emission. At early stages the photospheric component was indeed close to a blackbody, allowing its identification. However, during the event physical conditions in the outflow changed, and this was mirrored in the shape of the photospheric component.

4 Non-Planckian photospheres

As shown by GRB 090902B, photospheric emission is not synonymous with blackbody radiation. The questions then arises on how the different spectral shapes can arise.

One possibility that is being explored is subphotospheric emission. In brief, in this scenario energy is dissipated below the photosphere, modifying the emergent spectrum. Different models propose different origins, such as magnetic reconnection (Giannios 2008), internal shocks (Ioka 2010) or collisional dissipation (Beloborodov 2010). By varying the amount of dissipation and parameters of the outflow, it is possible to produce a wide range of spectral shapes by such subphotospheric energy release (Pe'er *et al.* 2006; Nymark *et al.* 2011).

Recently, Lundman *et al.* (2012) showed that purely geometrical effects will also produce a broadening of the emergent spectrum. Considering relativistic limb darkening, they use a combination of analytical model and Monte Carlo simulation to study the emergent spectrum from a jet. They find that for a narrow jet, where the opening angle is of the order of the relativistic beaming angle, a broadening of the photospheric spectrum is expected for any viewing angle. For a broader jet, the broadening effect is strong only if the viewing angle lies along the edge of the outflow, *i.e.* is close to the jet angle.

5 Summary

The observations of GRBs with *Fermi* support previous claims of photospheric emission from *e.g.* BATSE. A growing number of GRBs show spectra with more

than one peaked component, and a Band function alone is not sufficient to model them. When adding a second component, the fit improves significantly. This second component follows well-defined characteristics, and we interpret it as due to photospheric emission. The bright GRB 090902B clearly shows that photospheric emission does not necessitate a Planck function in the spectrum, which is also supported by theoretical considerations. Several broadening mechanisms exist which will modify the emergent spectrum, *e.g.* subphotospheric dissipation and geometrical broadening. Including a photospheric component is thus a first step to understanding the physical origin of GRB prompt emission - something which the Band function cannot provide.

The *Fermi* LAT Collaboration acknowledges support from a number of agencies and institutes for both development and the operation of the LAT as well as scientific data analysis. These include NASA and DOE in the United States, CEA/Irfu and IN2P3/CNRS in France, ASI and INFN in Italy, MEXT, KEK, and JAXA in Japan, and the K.A. Wallenberg Foundation, the Swedish Research Council and the National Space Board in Sweden. Additional support from INAF in Italy and CNES in France for science analysis during the operations phase is also gratefully acknowledged.

References

- Abdo, A.A., Ackermann, M., Ajello, M., *et al.*, 2009, ApJ, 706, L138
- Atwood, W.B., Abdo, A.A., Ackermann, M., *et al.*, 2009, ApJ, 697, 1071
- Axelsson, M., Baldinid, L., Barbiellini, G., *et al.*, 2012, ApJ, 757, L31
- Beloborodov, A., 2010, MNRAS, 407, 1033
- Burgess, J.M., Preece, R.D., Baring, M.G., *et al.*, 2011, ApJ, 741, 24
- Giannios, D., 2011 [[arXiv:1111.4258](https://arxiv.org/abs/1111.4258)]
- Giannios, D., 2008, A&A, 480, 305
- Goodman, J., 1986, ApJ, 308, L47
- Guiriec, S., Connaughton, V., Briggs, M., *et al.*, 2011, ApJ, 727, L33
- Ioka, K., 2010, Progr. Theor. Phys., 124, 667
- Lazzati, D., & Begelman, M.C., 2010, ApJ, 725, 1137
- Lundman, C., Pe'er, A., & Ryde, F., 2012 [[arXiv:1208.2965](https://arxiv.org/abs/1208.2965)]
- Meegan, C., Lichti, G., Bhat, P.N., *et al.*, 2009, ApJ, 702, 791
- Nymark, T., Axelsson, M., Lundman, C., *et al.*, 2011 [[arXiv:1111.0308](https://arxiv.org/abs/1111.0308)]
- Paczynski, B., 1986, ApJ, 308, L43
- Pe'er, A., Mészáros, P., & Rees, M.J., 2006, ApJ, 642, 995
- Ryde, F., 2004, ApJ, 614, 827
- Ryde, F., Axelsson, M., Zhang, B.-B., *et al.*, 2010, ApJ, 709, L172
- Vurm, I., Beloborodov, A.M., & Poutanen, J., 2011, ApJ, 738, 77
- Zhang, B.-B., Zhang, B., Liang, E.-W., *et al.*, 2011, ApJ, 730, 141

GRBS OBSERVED BY MAXI

M. Serino¹, T. Sakamoto², A. Yoshida², N. Kawai³, M. Morii³,
M. Sugizaki¹, S. Nakahira⁴, H. Negoro⁵, T. Mihara¹, Y. Nishimura⁶,
Y. Ogawa⁶ and M. Matsuoka¹

Abstract. Monitor of All-sky X-ray Image (MAXI) on board International Space Station is capable of observing gamma-ray bursts (GRBs) and sending notices of GRBs or other transient events, using real time connection to the ground. MAXI observed 32 GRBs or short X-ray transients as of the end of September 2012. Among them, eleven events were simultaneously detected by other satellites. The observed rate of the MAXI GRBs is about one event per month. This rate is comparable to a past observation with larger effective area and larger field of view. The fact indicates that MAXI has better sensitivity to observe GRBs because of low background. The distribution of the spectral hardness of MAXI GRBs is similar to the results of a past instrument, which is sensitive to similar energy range.

1 Introduction

Monitor of All Sky Image (MAXI) is an X-ray instrument to monitor the X-ray sky. MAXI is one of the experiments on the Exposed Facility of Japanese Experiment Module (Matsuoka *et al.* 2009). MAXI consists of two types of cameras, which are Gas Slit Camera (GSC) and Solid-state Slit Camera (SSC). GSC has a relatively

¹ MAXI team, Institute of Physical and Chemical Research (RIKEN), 2-1 Hirosawa, Wako, Saitama 351-0198, Japan; e-mail: motoko@crab.riken.jp

² Department of Physics and Mathematics, Aoyama Gakuin University, 5-10-1 Fuchinobe, Chuo-ku, Sagamihara, Kanagawa 252-5258, Japan

³ Department of Physics, Tokyo Institute of Technology, 2-12-1 Ookayama, Meguro-ku, Tokyo 152-8551, Japan

⁴ ISS Science Project Office, Institute of Space and Astronautical Science (ISAS), Japan Aerospace Exploration Agency (JAXA), 2-1-1 Sengen, Tsukuba, Ibaraki 305-8505, Japan

⁵ Department of Physics, Nihon University, 1-8-14 Kanda-Surugadai, Chiyoda-ku, Tokyo 101-8308, Japan

⁶ Department of Applied Physics, University of Miyazaki, 1-1 Gakuen Kibanadai-nishi, Miyazaki, Miyazaki 889-2192, Japan

large effective area and field of view (FOV) than those of SSC. Therefore, GSC is suitable to detect GRBs.

MAXI/GSC has unique capability to observe below 10 keV photons of GRBs. Therefore MAXI/GSC can detect extremely soft GRBs such as X-ray flashes (XRFs; Heise *et al.* 2001). One of the most comprehensive study of GRBs in this energy range has been accomplished by Sakamoto *et al.* (2005). They utilized the data sets observed by the Wide-field X-ray Monitor (WXM) (Shirasaki *et al.* 2003) on the High Energy Transient Explorer 2 (HETE-2; Ricker *et al.* 2003). Because GSC has a similar energy range to WXM, the GRB samples of WXM/HETE-2 would be the most suitable samples to compare with our GSC samples.

In this paper, we introduce the performance of MAXI including the capability of alert system in Section 2. In Section 3, we show the global properties of the GRBs observed by MAXI using the GSC data. We discuss and summarize our results in Section 4.

2 Instruments and alert system of MAXI

2.1 Performance of MAXI/GSC

GSC consists of 12 proportional counters with slits and slat collimators (Mihara *et al.* 2011). Though the total detector area is 5350 cm^2 , the effective area to a point source is determined by the area of the slit, which is about 10 cm^2 . GSC looks toward horizontal and zenithal direction. The size of the FOV of MAXI/GSC is 160 degrees by 3 degrees for each direction, which covers 2% of the whole sky during a certain short period of time (~ 100 second exposures).

In Table 1 we summarized the performance of MAXI/GSC comparing with HETE-2/WXM. Both instruments utilize position-sensitive proportional counters at the focal plane, but the optic systems differ from each other. Coded mask systems enable instruments to have larger FOV and effective area. On the other hand, slit and collimator optics, which is utilized for GSC, can achieve a low background.

Table 1. Performance of MAXI GSC and HETE-2 WXM.

	MAXI GSC	HETE-2 WXM
FOV	$160^\circ \times 3^\circ$ (2 directions)	$80^\circ \times 80^\circ$
Sky coverage	2%	16%
Effective area	$\sim 10\text{ cm}^2$	53 cm^2
Energy range	2–20 keV	2–25 keV
Optics	slit and collimator	coded mask

2.2 MAXI transient notice

MAXI provides notices of GRBs and other transient events through MAXI mailing lists or via GCN.

There are two types of notices: the automatic notices and the manual notices. The automatic notices can be sent within 10 seconds to a few minutes of the burst time. The position accuracy of this type is about one degree. The manual notices are typically issued within few hours after the burst time. The position accuracy of this type is usually better than 30 arcmin.

3 Observation and results

3.1 Observed rate of MAXI GRBs

Table 2 shows the list of GRBs observed by MAXI/GSC. The total number of the GRBs is 32 as of the end of September 2012. Eleven GRBs (highlighted with asterisks in the table) are simultaneously detected by other satellites while the two thirds are only observed by MAXI.

Table 2. List of MAXI GRBs.

year (number)	GRB name
2009 (6)	GRB 090831*, GRB 090926B*, GRB 091012, GRB 091120*, GRB 091201, GRB 091230*
2010 (11)	XRF 100315A, 100327, GRB 100415A, GRB 100510A*, XRF 100616A, XRF 100701A, GRB 100823A*, 100911, 101030, XRF 101117A, 101210
2011 (5)	GRB 110213B*, 110402, GRB 110426A*, 110916, GRB 111024A
2012 (10)	GRB 121027A, GRB 120424A, GRB 120510A*, GRB 120528B, GRB 120528C, GRB 120614A, GRB 120622A, XRF 120626B, GRB 120711A*, GRB 120908A*

* Simultaneous detection with other satellites.

3.2 Flux and hardness of MAXI GRBs

Because the effective area of MAXI/GSC is relatively small comparing with the one of other instruments, most of the MAXI GRBs do not have enough statistics to carry out spectral analyses. Therefore we decided to study two parameters, the average flux and the hardness ratio. The average flux is determined as the total counts of the bursts in the 2–20 keV band divided by the total effective area multiply by the scan duration time around the burst. Here we define the hardness ratio as the flux in the 8–20 keV band divided by the flux in the 2–8 keV band.

We plotted MAXI GRBs in the flux–hardness space (Fig. 1). The bursts only observed by MAXI (triangles) tend to distribute at lower left part of the plot populated by soft and low-flux GRBs. On the other hand, most of the bright ($>1 \text{ counts cm}^{-2} \text{ s}^{-1}$) bursts, which are also observed by other instruments (circles), are relatively hard. From this figure, we conclude MAXI/GSC is sensitive to soft and dim bursts.

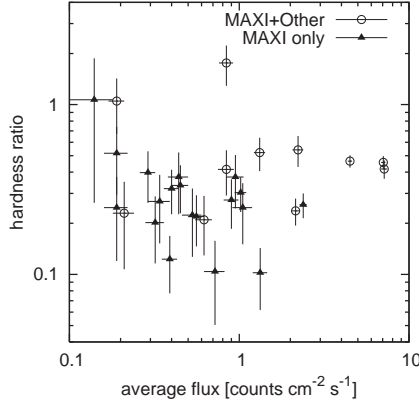


Fig. 1. Flux and hardness of MAXI GRBs. The bursts which are also observed by other instruments are plotted with circles. The bursts which are not observed by other instruments are plotted with triangles.

In order to compare the results with HETE-2/WXM, we plotted histograms of flux and hardness (Fig. 2). From the left panels, we can see that the average flux of the MAXI bursts are systematically lower than that of the WXM GRBs. This results confirm that the MAXI/GSC is more sensitive to weak GRBs than HETE-2/WXM. In the hardness distribution (right panels), there is no significant difference between the MAXI/GSC and the HETE-2/WXM samples. In Sakamoto *et al.* (2005), about one third of GRBs is classified into XRFs. Although it is difficult to classify GRBs solely from the MAXI data, we expect that roughly one third of the MAXI GRBs may be classified into XRFs.

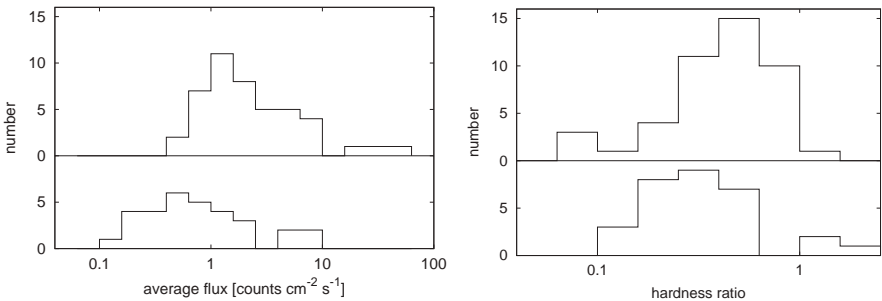


Fig. 2. Histograms of flux (*left*) and hardness (*right*) distribution of MAXI and HETE GRBs. The histograms of *top panels* are result of HETE-2/WXM (Sakamoto *et al.* 2005). The histograms of MAXI/GSC are plotted in the *bottom panels*.

4 Discussions and conclusion

MAXI observed 32 GRBs or short X-ray transients as of the end of September 2012. The observed rate is about once a month. The one third of the observed events are also detected by other instruments. Although MAXI/GSC has smaller sky coverage and smaller effective area, this rate is comparable to that of HETE-2/WXM. This fact suggests that MAXI/GSC is detecting dimmer bursts than HETE-2/WXM. Indeed the flux distribution of the MAXI/GSC bursts (Fig. 2) supports this hypothesis.

MAXI has unique capability to observe low-energy portion of GRBs below 10 keV. We showed that hardness distribution of MAXI GRBs is similar to that of HETE-2/WXM, which means about one third of them are expected to be XRFs.

Finally, we would like to emphasize that follow-up observations are needed to reveal the nature of XRFs. We strongly encourage follow-up observers to observe afterglows of MAXI XRFs.

References

- Heise, J., Zand, J.I., Kippen, R.M., *et al.*, 2001, in “Gamma-ray Bursts in the Afterglow Era”, ed. E. Costa, F. Frontera & J. Hjorth, p. 16
Matsuoka, M., Kawasaki, K., Ueno, S., *et al.*, 2009, PASJ, 61, 999
Mihara, T., Nakajima, M., Sugizaki, M., *et al.*, 2011, PASJ, 63, S623
Ricker, G.R., Atteia, J.-L., Crew, G.B., *et al.*, 2003, in “Gamma-Ray Burst and Afterglow Astronomy 2001: A Workshop Celebrating the First Year of the HETE Mission”, ed. G.R. Ricker & R.K. Vanderspek, p. 3
Sakamoto, T., Lamb, D.Q., Kawai, N., *et al.*, 2005, ApJ, 629, 311
Shirasaki, Y., Kawai, N., Yoshida, A., *et al.*, 2003, PASJ 55, 1033
Sugizaki, M., Mihara, T., Serino, M., *et al.*, 2011, PASJ, 63, S635

SEARCHING FOR GALACTIC SOURCES IN THE *SWIFT* GRB CATALOG

J.C. Tello¹, A.J. Castro-Tirado¹, J. Gorosabel^{1,2,3}, D. Pérez-Ramírez⁴,
S. Guziy⁵, R. Sánchez¹, M. Jelínek¹, P. Veres^{6,7} and Z. Bagoly⁶

Abstract. Since the early 90s Gamma Ray Bursts have been accepted to be of extra-galactic origin thanks to the isotropic distribution observed by BATSE and the redshifts observed in some of their optical or infrared counterparts. Nevertheless, there have been a few cases that upon further examination have turned out to be of galactic origin. Several of these galactic sources have presented a Fast Rise, Exponential Decay structure which leads us to believe that there could be an underlying correlation. In this work we do several statistical analyses to determine the degree of contamination by galactic sources that certain subsample of known FREDs have. And find that certain subsamples have a most probable contamination between 27% and 34%.

1 Introduction

Gamma Ray Bursts (GRB) afterglows fade within a few hours, and as a consequence, the redshift of most GRBs are unknown. In the past several studies have been carried out to indirectly determine the Galactic or extra-Galactic nature of the bursts by analyzing their spatial distribution in the sky Balazs *et al.* (1998), Mazets *et al.* (1981), Meegan *et al.* (1992), and historically it served as a strong argument against the Galactic origin of GRBs Paciesas *et al.* (1999). This technique has also been used to suggest a more local nature of long-lag bursts

¹ Instituto de Astrofísica de Andalucía (IAA-CSIC), Granada, Spain

² Unidad Asociada Grupo Ciencia Planetarias UPV/EHU-IAA/CSIC, Universidad del País Vasco UPV/EHU, Bilbao, Spain

³ Ikerbasque, Basque Foundation for Science, Bilbao, Spain

⁴ Universidad de Jaén, Campus Las Lagunillas, Jaén, Spain

⁵ Nikolaev National University, Nikolaev, Ukraine

⁶ Eötvös University, Budapest, Hungary

⁷ Bolyai Military University, Budapest, Hungary

Table 1. Dipolar and quadripolar moments as an indicator of the degree of isotropy in the samples.

Sample	$\langle \cos b \rangle$	$\langle \sin^2 b \rangle$
#1	0.7883	0.3397
#2	0.8221	0.2860
#3	0.8184	0.2909
#4	0.8344	0.2673
#5	0.8397	0.2622

by showing that they may be related to the super-Galactic structure Foley *et al.* (2008), Norris (2002). The observed light curve of each GRB varies from burst to burst, particularly during in the prompt phase when the gamma ray emission is emitted, where one or multiple peaks with a variety of shapes are observed. However, some of them present a fast rise and exponential decay (FRED hereafter) behavior. These have been correlated with other properties of the bursts Bhat *et al.* (1994), suggesting that they may be of a different nature than other GRBs.

There has been at least one reported GRB that upon closer examination has resulted to be a phenomenon from within the Milky Way Castro-Tirado *et al.* (2008), Stefanescu *et al.* (2008). This source displayed a FRED structure, which leads us to believe that there could be others like it. We aim to estimate the most probable degree of contamination by Galactic sources that certain samples of FREDs have.

2 Sample selection

To achieve a homogeneous distribution, only *Swift*-detected GRBs were taken into account. From the catalog of 596 GRBs detected by *Swift* before March 2011, 111 GRBs were selected because they had a FRED structure reported in a GCN. Using the information available in peer-reviewed papers⁸ and other GCN circulars related to the 111 FRED GRBs, the following subsamples were selected ⁹: **Sample 1:** All 111 FREDs detected by *Swift* until February 2011. **Sample 2:** 77 Bursts from Sample 1 discarding those that have a measured redshift. **Sample 3:** 71 FREDs from Sample 2, discarding those that have a stated high-redshift criteria in GCNs. **Sample 4:** 59 FREDs from Sample 2, discarding those with any type of indirect redshift indication. **Sample 5:** 49 FREDs from Sample 4 discarding those with multiple peaks. It is important to note that only sample 5 included solely those bursts that consisted of one pure FRED peak.

⁸Only two peer-reviewed papers were relevant for the sample selection Clemens *et al.* (2011), Perley *et al.* (2009).

⁹For a list of specific selected bursts see Tello *et al.* (2012).

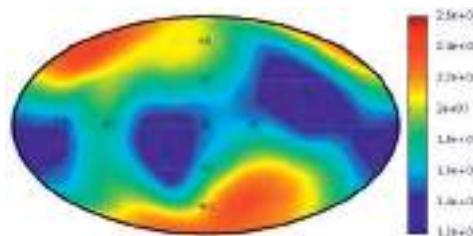


Fig. 1. Swift exposure map in Galactic coordinates derived for this study. Colors represent the exposure time (in seconds).

3 Anisotropy quantification

It has been proven Hartmann & Epstein (1989) that the mean dipolar and quadripolar moments of the Galactic coordinates ($\cos b$ and $\sin^2 b$, where b is the Galactic latitude) are good tools to quantify the isotropy with respect to the Galactic plane Castro Tirado (1994). The degree of isotropy of each sample was calculated using the coordinates available from the gamma-ray burst coordinate network (GCN) circulars for each burst. The results are shown in Table.

3.1 Exposure map

Owing to the nature of its instruments, orbit, and mission, *Swift*'s pointing toward the sky is not homogeneous. It is of particular relevance to note that there has been less integrated exposure time toward the Milky Way's disk than toward the Galactic poles. This fact would represent a bias for the nature of the study carried out for this publication if left unaccounted, therefore we created a map by integrating the exposure mask function for the BAT instrument, multiplied by the exposure times of all observations carried out between April 16, 2005 and February 1, 2011, taking into account the pointing and rotation of the BAT instrument¹⁰.

3.2 Monte Carlo simulations

Monte Carlo simulations were carried out to determine the probability mass function (PMF) of the average dipolar and quadripolar moments of random GRB distributions. Therefore random coordinates were generated, taking care that they had a homogeneous distribution on an spherical surface.

These random points were then used to determine if the observed samples' dipolar moments deviated from those of a completely isotropically generated sample. To do this we generated an equal number of random points to that of each sample, recording the value of the mean dipolar and quadripolar moment and iterating a

¹⁰The method used to derive the exposure map is the same as the one detailed in Veres *et al.* (2010).

statistically significant number of times ($\approx 10^6 - 10^9$ iterations). The histogram of the recorded values was then used to determine the values for standard deviations ($\sigma, 2\sigma, 3\sigma$).

3.3 Metropolis-Hastings algorithm

To account for the anisotropy of *Swift*'s exposure of the night sky, it was necessary to factor in the probability that a particular random source was detected by *Swift*. We used the Metropolis-Hastings algorithm for this, which will effectively generate random sources that are more likely to appear where the exposure is higher.

3.4 Contamination by Galactic sources

Considering that i) the density of matter of the Milky Way is roughly correlated with the amount of interstellar dust, and by consequence so is the amount of stellar sources, and ii) the transparency of gamma-rays to interstellar dust, we used maps of dust IR emission Schlegel *et al.* (1998) as a weighting mask for the Metropolis-Hastings algorithm to generate random Galactic sources.

The isotropically generated samples were contaminated by increasing the number of Galactically generated random sources (N) to observe how this affected the PMF of their dipolar and quadripolar moment. We considered all possible combinations for the number of GRBs in the different samples and took into account the *Swift* exposure map for each generated source.

4 Results

The Monte Carlo simulations of the isotropically generated random samples (weighted by the *Swift* exposure map) showed that the dipolar and quadripolar moments from the real samples consistently deviated from the average: with the exception of the first sample, all samples have dipolar and quadripolar moments located outside two standard deviations.

The probability distribution of samples that contained both isotropically and Galactically generated sources allowed us to compare how the contamination by Galactic sources affected the likelihood of obtaining certain momentum values. This technique is similar to the one used in the past for studying the degree of contamination by Galactic repeater gamma-ray sources present in two GRB catalogs Gorosabel *et al.* (1998).

By observing the probability of the observed values in each one of the curves that resulted from the simulations, we determined the relative probability that each one of those combinations of isotropically and Galactically generated sources would yield the observed momentums. Figure 2 shows the probability as a function of the amount of Galactic sources introduced in each sample.

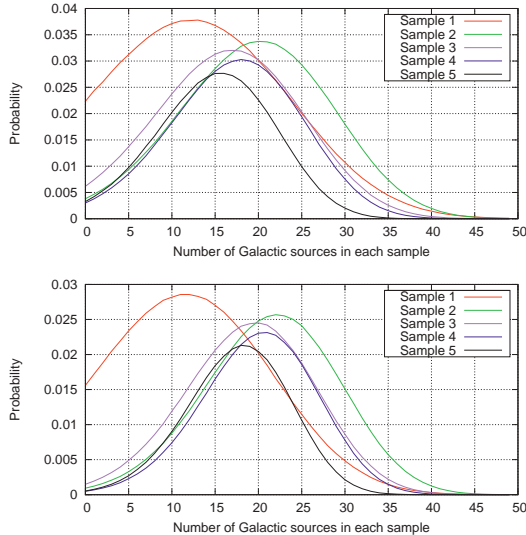


Fig. 2. Relative probability of obtaining the dipolar (*top*) and quadripolar (*bottom*) moments ± 0.002 measured in each samples for different amounts of simulated galactic sources.

5 Conclusions

With the exception of the first sample, all observed samples show dipolar and quadripolar moments outside two standard deviations from the mean of an isotropically generated distribution. Although this result is not conclusive, there is a high probability that the samples are not of a purely Extra-Galactic nature.

The amount of Galactic sources that are most probably contaminating the *Swift* GRB catalog is between 16 and 22. This value represents approximately 3% of the complete GRB *Swift* catalog. Sample 5 has been narrowed down so that it is likely that one out of every three is in fact a Galactic source.

The high Galactic extinction normally discourages optical ground-based spectroscopy of most low Galactic latitude GRBs. We showed that a large part of those abandoned follow-ups could reveal a missing population of Galactic events. So We encourage ground observers to follow-up those events, since it might lead to the discovery of unknown high-energy phenomena in our Galaxy.

We have made use of J. Greiner's GRB Table (<http://www.mpe.mpg.de/~jcg/grbgen.html>). This research has been partially supported by the Spanish Ministry of Economy and Competitiveness under the programmes AYA2011-24780/ESP, AYA2009-14000-C03-01/ESP, and AYA2012-39362-C02-02 and OTKA grant K077795. This study was carried out in the framework of the Unidad Asociada IAA-CSIC at the group of planetary science of ETSI-UPV/EHU. This work was supported by the Ikerbasque Foundation for Science.

References

- Balazs, L.G., Meszaros, A., & Horvath, I., 1998, A&A, 339, 1
- Bhat, P.N., Fishman, G.J., Meegan, C.A., *et al.*, 1994, ApJ, 426, 604
- Castro-Tirado, A.J., 1994, Copenhagen (Denmark: University of Copenhagen)
- Castro-Tirado, A.J., de Ugarte Postigo, A., Gorosabel, J., *et al.*, 2008, Nature, 455, 506
- Clemens, C., Greiner, J., Krühler, T., *et al.*, 2011, A&A, 529, A110
- Foley, S., McGlynn, S., Hanlon, L., McBreen, S., & McBreen, B., 2008, A&A, 484, 143
- Gorosabel, J., Castro-Tirado, A.J., Brandt, S., & Lund, N., 1998, A&A, 336, 57
- Hartmann, D., & Epstein, R.I., 1989, ApJ, 346, 960
- Mazets, E.P., Golenetskii, S.V., Ilinskii, V.N., *et al.*, 1981, Ap&SS, 80, 3
- Meegan, C.A., Fishman, G.J., Wilson, R.B., *et al.*, 1992, Nature, 355, 143
- Norris, J.P., 2002, ApJ, 579, 386
- Paciesas, W.S., Meegan, C.A., Pendleton, G.N., *et al.*, 1999, ApJS, 122, 465
- Perley, D.A., Cenko, S.B., Bloom, J.S., *et al.*, 2009, AJ, 138, 1690
- Schlegel, D.J., Finkbeiner, D.P., & Davis, M., 1998, ApJ, 500, 525
- Stefanescu, A., Kanbach, G., Słowińska, A., *et al.*, 2008, Nature, 455, 503
- Tello, J.C., Castro-Tirado, A.J., Gorosabel, J., *et al.*, 2012, A&A, 548, L7
- Veres, P., Bagoly, Z., Horváth, I., *et al.*, 2010, Am. Inst. Phys. Conf. Ser., 1279, 457

KONUS-WIND OBSERVATION OF THE ULTRA-LUMINOUS GRB 110918A

D. Frederiks¹, D. Svinkin^{1,2}, R. Aptekar^{1,2}, S. Golenetskii¹, E. Mazets¹,
P. Oleynik^{1,2}, V. Pal'shin^{1,2}, A. Tsvetkova¹, M. Ulanov^{1,2} and T. Cline³

Abstract. The exceptionally intense long GRB 110918A was discovered by several GRB observing missions: *INTEGRAL* (SPI-ACS), Konus-WIND, *Mars Odyssey* (HEND), and *MESSENGER* (GRNS) on September 18, 2011. This GRB was localized by the Interplanetary Network (IPN) and its bright X-ray counterpart was found in close vicinity of the IPN box in the *Swift*/XRT follow-up observations starting 1.2 days after the trigger. The optical afterglow was discovered by the Isaac Newton Telescope and its spectroscopic redshift $z = 0.982$ was measured with the GMOS spectrograph mounted on the Gemini-N telescope. GRB 110918A is the brightest burst detected by Konus-WIND for more than 17 years of its continuous observations. The instrument's light curves in three energy bands covering 22–1450 keV range show an extremely bright, short, hard pulse followed by three weaker, softer, partly overlapping pulses within next 25 seconds. A spectral lag between the light-curves is determined, showing a substantial increase in the course of the burst. The emission is detected up to 12 MeV. Modeling the time-integrated energy spectrum with the Band function yields a moderate value of $E_{peak} = 340$ keV, while the time-resolved spectral analysis reveals strong hardness-intensity correlation and a hard-to-soft evolution of the emission: E_{peak} falls from ~ 4 MeV at the onset of the huge initial pulse to ~ 50 keV at the final stage of the burst. The total 20 keV–10 MeV energy fluence amounts to $S = (7.8 \pm 0.4) \times 10^{-4}$ erg cm $^{-2}$ and a 64-ms peak flux $F_{max} = (9.2 \pm 0.4) \times 10^{-4}$ erg cm $^{-2}$ s $^{-1}$, which corresponds to a huge isotropic-equivalent energy release $E_{iso} = (2.1 \pm 0.1) \times 10^{54}$ erg and the record-breaking peak luminosity $L_{iso;max} = (4.7 \pm 0.2) \times 10^{54}$ erg s $^{-1}$.

¹ Ioffe Physico-Technical Institute, St. Petersburg 194021, Russia

² St. Petersburg State Technical University, St. Petersburg 195251, Russia

³ Emeritus: NASA's Goddard Space Flight Center, Greenbelt, MD 20771, USA

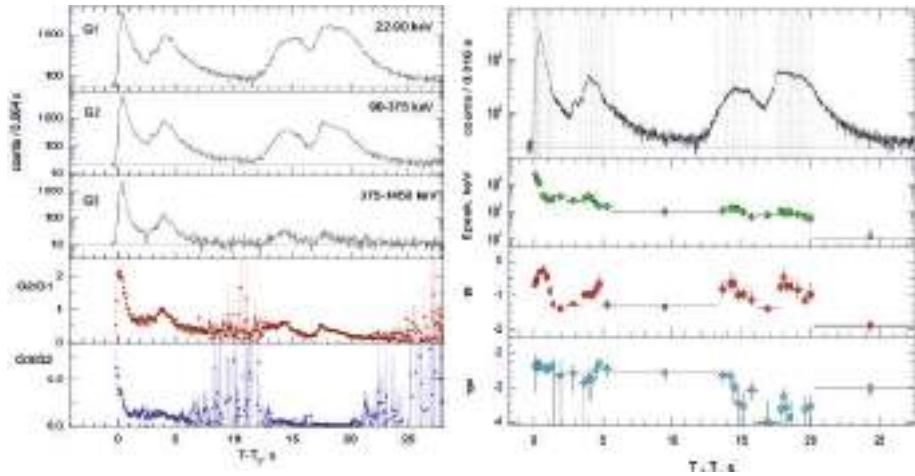


Fig. 1. *Left:* the light curves of GRB 110918A recorded by Konus-*WIND* in three energy bands (three upper panels) and their hardness ratios evolution (two lower panels). *Right:* the temporal behavior of the Band spectral model parameters (E_{peak} , α , β) obtained from the time-resolved fits. The light curve in the 22–1450 keV band is given for the reference in the upper panel.

1 Introduction

The exceptionally intense long GRB 110918A was discovered by several GRB observing missions: *INTEGRAL* (SPI-ACS), Konus-*WIND*, *Mars Odyssey* (HEND), and *MESSENGER* (GRNS) on Sep. 18, 2011. This burst source was localized by the Interplanetary Network (Hurley *et al.* 2011) and its bright X-ray counterpart was found in close vicinity of the IPN box in the Swift/XRT follow-up observations starting 1.2 days after the trigger (Mangano *et al.* 2011). The optical afterglow was discovered by the Isaac Newton Telescope (Tanvir *et al.* 2011) and its spectroscopic redshift $z = 0.982$ was measured with the GMOS spectrograph mounted on the Gemini-N telescope (Levan *et al.* 2011). A preliminary analysis of the Konus-*WIND* observation revealed that GRB 110918A is the most intense gamma-ray burst among ~ 2200 GRBs observed by the instrument since November, 1994 (Golenetskii *et al.* 2011). The high energy flux also suggests enormous isotropic-equivalent rest-frame energy (Frederiks & Pal'shin 2011). These preliminary estimates place GRB 110918A among the brightest GRBs ever observed in the era of cosmological GRBs and this burst deserves, without a doubt, a detailed consideration.

2 Time histories

GRB 110918A triggered the Konus-*WIND* γ -ray spectrometer (Aptekar *et al.* 1995) at $T_0 = 77222.856$ s UT (21:27:02.856) on September 18, 2011. In the triggered mode, count rates are recorded in three energy bands: G1(22–90 keV),

G2(90–375 keV), and G3(375–1450 keV) with an accumulation time varying from 2 to 256 ms. The burst light curve in the three energy bands (Fig. 1, left) is clearly divided into two groups of pulses ($T_0 - T_0 + 12$ s) and ($T_0 + 12$ s – $T_0 + 28$ s), each, in turn, having two pronounced peaks. As shown in the same Figure, the temporal evolution of the G2/G1 and G3/G2 hardness ratios indicates an apparent hardness-intensity correlation of the emission against a general tendency of spectral softening in the course of the event. In the G2+G3 energy band (90–1450 keV), the duration T_{90} is 19.6 ± 0.1 s and $T_{50} = 14.3 \pm 0.1$ s. The peak 64-ms count rate reached is $(1.46 \pm 0.02) \times 10^5$ counts/s in the bin starting at $T_0 + 0.368$ s. We examined the spectral lag using the cross-correlation function between the 16-ms G1, G2, and G3 light curves at different phases of the burst. The statistically significant positive lags of 40–400 ms are derived for both the first ($T_0 - T_0 + 12$ s) and the second ($T_0 + 12 - T_0 + 25$ s) groups of pulses. However, for the second group of pulses the observed lags are 2–4 times longer than for the initial phase of the event.

3 Spectral analysis and energetics in gamma-rays

During the main phase of GRB 110918A, 35 energy spectra were recorded in 128 quasi-log channels of two overlapping energy bands PHA1 (20–1450 keV) and PHA2 (375 keV–14 MeV). Their accumulation time is varied from 0.064 s to 8.192 s, depending on the current intensity of the burst, the emission is seen up to 12 MeV. The spectral analysis was performed with XSPEC, version 12.5. A good quality of the fit with the Band GRB function is achieved for the majority of the spectra, which enabled us to construct the temporal behavior of the model parameters α , β , E_{peak} (Fig. 1, right). The time-resolved spectral analysis confirms strong hardness-intensity correlation and a hard-to-soft evolution of the emission: the low-energy photon index α evolution is strongly correlated with the burst intensity, and E_{peak} falls from ~ 4 MeV at the onset of the huge initial pulse to ~ 50 keV at the final stage of the burst.

The spectrum at the culmination of the initial pulse is described by $\alpha = -0.33 \pm 0.09$ (90% conf.), $\beta = -2.3 \pm 0.1$, and $E_{peak} = 1080 \pm 150$ keV ($\chi^2 = 0.67$, 68 dof). We analyzed the time-averaged spectrum of the whole burst and its separate phases. It should be emphasized that, having $E_{peak} = 340 \pm 60$ keV, $\alpha = -1.65 \pm 0.05$, and $\beta = -2.25 \pm 0.09$ ($\chi^2 = 0.96$, 81 dof) the overall time-integrated spectrum is, indeed, an “average” one and doesn’t reflect the strong spectral evolution. As it is expected from the time-resolved spectral analysis, the average spectra of the first ($T_0 - T_0 + 13.312$ s) and the second ($T_0 + 13.312 - T_0 + 28.416$ s) groups of pulses are strongly different. With only the low-energy photon index being close ($\alpha \sim -1.2$), the values of E_{peak} differ almost by an order of magnitude (630 keV and 80 keV, respectively), and the high-energy photon index β is sufficiently harder for the first group of pulses (-2.3 vs. -3.3 for the second group).

Based on the results of our spectral and temporal analyses, we calculated the observed energetics of GRB 110918A in gamma-rays. The 20 keV–10 MeV energy

fluence S measured from T_0 to $T_0 + 28.416$ s amounts to $(7.8 \pm 0.5) \times 10^{-4}$ erg cm $^{-2}$. In the same energy range, the 64-ms peak energy flux $F_{max} = (9.2 \pm 0.4) \times 10^{-4}$ erg cm $^{-2}$ s $^{-1}$ in the interval beginning at $T_0 + 0.384$ s, at the culmination of the huge initial pulse.

Assuming the redshift $z = 0.982$ (Levan *et al.* 2011) and a standard cosmology with $H_0 = 71$ km/s/Mpc, $\Omega_M = 0.27$, and $\Omega_\lambda = 0.73$, we derive the following rest-frame parameters of the prompt gamma-ray emission: the isotropic-equivalent energy release $E_{iso} = (2.1 \pm 0.1) \times 10^{54}$ erg, the peak luminosity $L_{iso\ max} = (4.7 \pm 0.2) \times 10^{54}$ erg/s (both in the bolometric 1–10 000 keV energy range), and the intrinsic peak energy $E_{p,i} = 680 \pm 140$ keV. These estimations make GRB 110918A the most luminous gamma-ray burst ever observed in the cosmological era.

4 Summary

The detailed analysis of the ultra-luminous GRB 110918A observation by the Konus-*WIND* gamma-ray spectrometer reveals that the burst is the brightest among ~ 2200 GRBs recorded by the instrument since November, 1994. The record-breaking values of the peak count rate, peak energy flux, and the total energy fluence are obtained. Also, assuming the redshift $z = 0.982$, this burst is the most luminous GRB ever observed since the start of the era of cosmological GRB studies in 1997. The temporal behavior of the light curves hardness ratios, the obtained spectral lags, and the results of time-resolved spectral fits show an apparent hardness-intensity correlation of the observed emission and a general spectral softening in the course of the burst.

The detailed coverage of the Konus-*WIND* results on GRB 110918A as well as the refined IPN localization, the X-ray afterglow observations with *Swift*/XRT, and the optical monitoring with *Swift*/UVOT can be found in the forthcoming paper (Frederiks, Hurley *et al.*, in preparation).

This work was supported by a Russian Space Agency contract the Russian Foundation for Basic Research projects 11-02-12082-ofi-m-2011 and 12-02-00032-a, and the Ministry of Education and Science of Russian Federation contract #11.G34.31.0001 with SPbSPU and leading scientist G.G. Pavlov.

References

- Aptekar, R.L., Frederiks, D.D., Golenetskii, S.V., *et al.*, 1995, Space Sci. Rev., 71, 265
- Frederiks, D., & Pal'shin, V., 2011, GRB Coordinates Network, 12370, 1
- Golenetskii, S., Aptekar, R., Frederiks, D., *et al.*, 2011, GRB Coordinates Network, 12362, 1
- Hurley, K., Golenetskii, S., Aptekar, R., *et al.*, 2011, GRB Coordinates Network, 12357, 1
- Levan, A.J., Tanvir, N.R., Wiersema, K., *et al.*, 2011, GRB Coordinates Network, 12368, 1
- Mangano, V., Sbarufatti, B., Evans, P., & Krimm, H., 2011, GRB Coordinates Network, 12364, 1
- Tanvir, N.R., Wiersema, K., Levan, A.J., *et al.*, 2011, GRB Coordinates Network, 12365, 1

GAMMA-RAY BURSTS: THE DEPENDENCE OF THE SPECTRAL LAG ON THE ENERGY

P. Minaev¹, A. Pozanenko¹, S. Grebenev¹ and S. Molkov¹

Abstract. We investigated the dependence of a spectral lag against energy band based on 28 bright GRBs registered by SPI and IBIS/ISGRI of INTEGRAL observatory. It was found that for simple structure bursts or well separated pulses of multipulse bursts the spectral lag can be approximated by the relation of $\tau \sim A \lg(E)$, where A is a positive parameter, which correlates with pulse duration. We have not found any negative lag in simple structure bursts or in well separated pulses. While investigating the time profile of the whole burst negative lag may appear due to different spectral parameters of the pulses.

1 Introduction

Spectral evolution of gamma-ray bursts is one of the most interesting phenomenological properties. In most cases, we observe the evolution from the hard spectrum in the beginning, to soft, in the final phase of gamma-ray burst. Different dependencies between the spectral evolution and other properties of gamma-ray bursts have been found (Hakkila *et al.* 2011). One of the models describing spectral evolution of GRBs is based on curvature effect of the relativistic shocked shell (Ukwatta *et al.* 2012).

2 Data analysis and results

28 bright GRBs registered by SPI (Vedrenne *et al.* 2003) and IBIS/ISGRI (Ubertini *et al.* 2003) experiments of INTEGRAL observatory (Winkler *et al.* 2003) were investigated. Well separated pulses of multipulse events were investigated independently. So total number of analyzed events is 43. Method of investigation was based on cross-correlation analysis of light curves in two different energy bands. Details of cross-correlation analysis see in (Band 1997). In this analysis

¹ Space Research Institute of the Russian Academy of Sciences, Moscow, Russia;
e-mail: minaevp@mail.ru

cross-correlation function (CCF) of two light curves in different energy channels is formed. Position of the maximum in CCF curve determines the value of light curves time offset, which is called spectral lag. Spectral lag is positive when light curve in higher energy band is registered earlier than one in lower energy band.

Algorithm of our analysis consisted of next steps:

1. Building a GRB energy-time diagram (Fig. 1a) and visual analysis of GRB spectral and temporal properties (hardness of GRB spectrum, number of pulses, duration, etc.).
2. Building a light curves in narrow energy bands (up to 25 channels) and selection of time interval for analysis. Time resolution and energy channel width of light curves depend only on GRB properties.
3. Cross-correlation analysis of formed light curves to determine spectral lag between light curve in the first lowest energy channel and light curves in other channels.
4. Forming and approximation of spectral lag - energy relation (Fig. 1c) using two models (formulas 2.1–2.2), where parameter A (spectral lag index) characterizes spectral evolution. Energy value of each point of relation was defined as geometric mean of upper and lower energy limit of the energy channel in higher energy band.

$$\tau = A \log(E) + B. \quad (2.1)$$

$$\begin{aligned} \tau &= (A_1 \log(E) + B_1) \exp \left[\left[-\frac{\log(E)}{\log(E_{cut})} \right]^C \right] + \\ &\quad + (A_2 \log(E) + B_2) \left[1 - \exp \left[\left[-\frac{\log(E)}{\log(E_{cut})} \right]^C \right] \right]; \\ B_2 &= E_{cut}(A_1 - A_2) + B_1. \end{aligned} \quad (2.2)$$

In most cases lag - energy relation is well described by simple logarithmic model (2.1) (Fig. 1c, left). Positive slope of the relation means spectral evolution from hard spectrum to soft (positive value of spectral lag). But in 6 cases of 43 in the relation there is break (Fig. 1c, right). In this 6 cases two-logarithmic model with exponential break (2.2) was used to fit the relation.

Spectral lag - energy relation for separate pulses of GRBs or for GRBs with simple structure of light curves (Fig. 1b, left) shows no break (Fig. 1c, left) and no negative lag. Break in the relation and negative lag may appear due to different spectral parameters of the overlapping pulses and have no connection with physics of the GRB source.

For 9 well separated GRB pulses spectral lag index - duration relation was formed. The relation is well fitted by power law with power index equal to

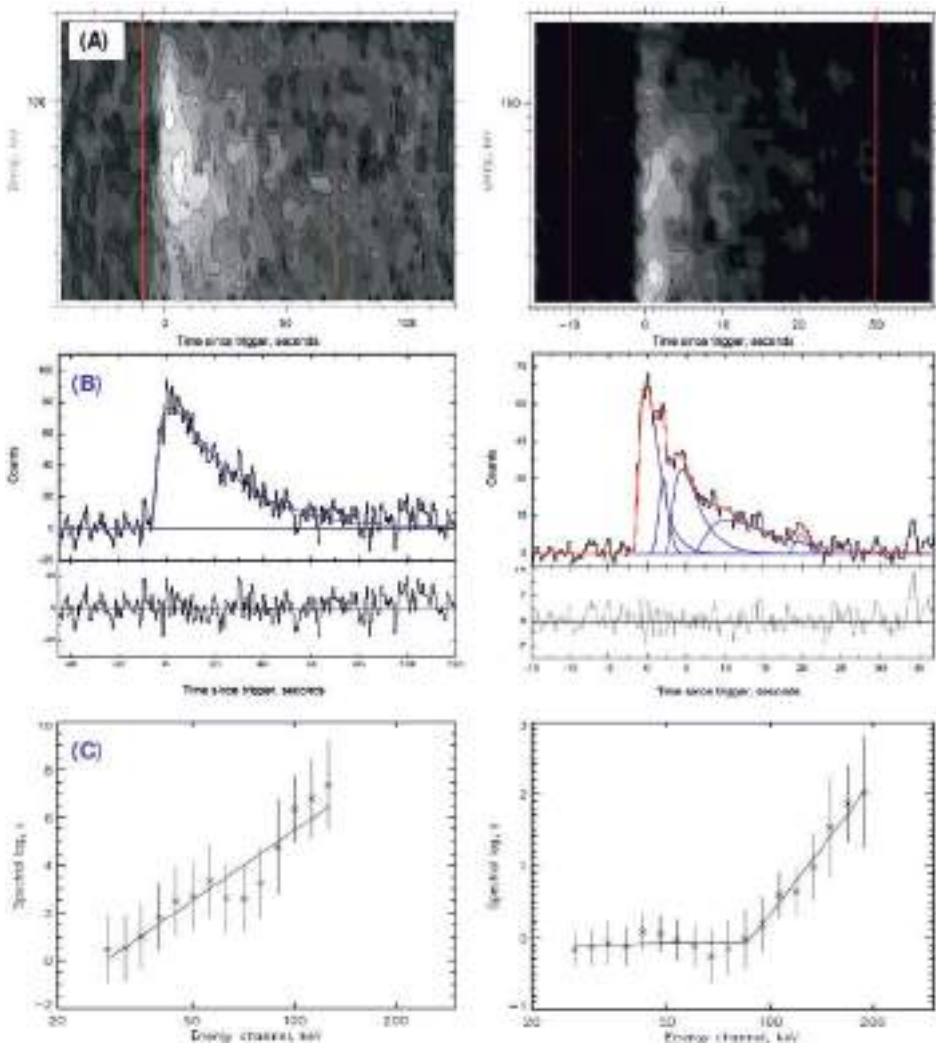


Fig. 1. Energy - time diagram (A), mask weighted light curve in [20–200] keV energy band (B) and spectral lag - energy relation (C) of GRB 050504 (*left*) and GRB 031203 (*right*).

1.14 ± 0.15 . There is one short GRB 081226 in the sample and it does not violate the correlation. So short GRBs may follow the same law as the long ones and it may be the evidence of the same emission mechanism in short and long GRBs. This correlation was also found in paper (Hakkila *et al.* 2011). But in that paper spectral lag between light curves in BATSE energy channels was used as spectral evolution parameter instead of spectral lag index.

3 Conclusions

Spectral evolution of 28 bright GRBs registered by SPI and IBIS/ISGRI of INTEGRAL observatory was investigated.

It was found that for simple structure bursts or well separated pulses of multpulse bursts the spectral lag can be approximated by the simple logarithmic law (2.1).

Parameter A (spectral lag index) is new alternative parameter characterizing spectral evolution of GRBs.

Spectral lag index correlates with pulse duration. The dependence of the spectral lag index on the duration of GRB pulses is presumably the same for long and for short GRBs.

Negative lag in simple structure bursts or in well separated pulses was not found.

The work was partially supported by RFBR grant 12-02-01336-a.

References

- Band, D., 1997, ApJ, 486, 928
- Hakkila, J., & Preece, R., 2011, ApJ, 740, 104
- Ubertini, P., Lebrun, F., Di Cocco, G., *et al.*, 2003, A&A, 411, L131
- Ukwatta, T., Dhuga, K., Stamatikos, M., *et al.*, 2012, MNRAS, 419, 614
- Vedrenne, G., Roques, J.-P., Schonfelder, V., *et al.*, 2003, A&A, 411, L63
- Winkler, C., Courvoisier, T., Di Cocco, G., *et al.*, 2003, A&A, 411, L1-L6

ON THE PROPERTIES OF SPECTRAL LAGS AND PEAK-COUNT RATES OF RHESSI GAMMA-RAY BURSTS

J. Řípa¹, A. Mészáros², P. Veres³ and I.H. Park¹

Abstract. A sample of 427 gamma-ray bursts (GRBs) was observed by the *RHESSI* satellite in Feb. 2002 - Apr. 2008. We calculated spectral lags and peak-count rates for the first time and constructed a new observational database. This database is statistically studied completing an earlier analysis of durations and hardness ratios. First, we discuss properties of short-, intermediate-, and long-duration GRBs in terms of peak-count rates and spectral lags. Second, we investigate the number of GRB groups using model-based clustering method together with Kolmogorov-Smirnov (K-S) and Anderson-Darling (A-D) tests. The results are: The inter. bursts have properties similar to short bursts. The groups of inter. and long bursts appear to be different. The inter. GRBs in the *RHESSI* and *Swift* databases seem to be different phenomena. This work is summary of Řípa *et al.* (2012).

1 Data sample and methods

Several classifications of GRBs have been done, *e.g.* by Horváth *et al.* (2006) or Minaev *et al.* (2010). In our work we fitted two and three lognormal functions to the distribution of durations and hardnesses of *RHESSI* sample of 427 GRBs and applied maximum likelihood (ML) ratio test. A group of intermediate-duration bursts has been found at significance level of 0.3% (Řípa *et al.* 2009, 2012).

The spectral lags, *i.e.* delay between low-energy (25–120 keV) and high-energy (400–1500 keV) counts in GRB light curves, and peak-count rates were calculated. The spectral lags were obtained by fitting the cross-correlation function (in a narrow interval around its peak) of background-subtracted count light curves at these two channels and derived at a time interval covering whole GRB. The properties

¹ Institute of Basic Science, Sungkyunkwan University, Suwon, South Korea;
e-mail: ripa.jakub@gmail.com

² Astronomical Institute of the Charles University, Prague, Czech Republic

³ Department of Astronomy and Astrophysics, Penn. State University, State College, USA

Table 1. *Left part:* results from the A-D tests of spectral lags. The null hypothesis is that two samples are drawn from the same distribution. P is the P-value of the test. *Right part:* the means, medians and standard deviations σ are listed.

Groups	A-D P (%)	Group	Mean L (ms)	Median L (ms)	σ (ms)
Inter.-Short	16.8	Short	4.9	1.9	16.7
Inter.-Long	4.2	Inter.	28.7	5.9	78.4
Short-Long	$<10^{-3}$	Long	178.0	50.8	874.9

of the three identified clusters of GRBs were studied by K-S and A-D tests (see Tables 1 and 2). Next a model-based clustering technique was applied on three variables: T_{90} durations, hardnesses H , and peak-count rates F . The Bayesian Information Criterion (BIC) was used (Table 3). The function which is maximized is: $BIC = 2 \ln l_{\max} - m \ln N$, where l_{\max} is the ML of the model, m is the number of free parameters, and N is the size of the sample. Surprisingly the group of long bursts is now separated into high- and low-peak flux clusters (see Fig. 1).

Table 2. *Left part:* results of the K-S test applied on the peak-count rates F . The K-S distance D and the K-S significance P are mentioned. *Right part:* the means, medians, and standard deviations of the peak-count rates are listed.

Groups	D	K-S P (%)	Group	Mean F (cnt/s)	Median F (cnt/s)	σ (cnt/s)
Inter.-Short	0.44	0.9	Short	9 490	5 160	20 420
Inter.-Long	0.55	3×10^{-5}	Inter.	4 410	2 550	5 590
Short-Long	0.69	$<10^{-6}$	Long	2 590	1 040	7 670

2 Conclusions

ML test in the duration-hardness plane of 427 *RHESSI* GRBs exhibits a third in duration intermediate group at significance level of 0.3%. The spectral lags and peak-count rates were calculated for GRBs observed by the *RHESSI* satellite for the first time and thus we constructed a new observational database. Then the three GRB clusters were analyzed with respect to the spectral lags and peak-count rates. The difference between short and long groups were confirmed. K-S and A-D tests applied on spectral lags and peak-count rates indicate that the inter. group in the *RHESSI* database might be a longer tail of the short group or at least has some common properties with this short group. Contrary to this, the inter. and the long groups seem to have different properties. We compared properties of *RHESSI* inter.-duration busts with those found by *Swift* (Veres *et al.* 2010; de Ugarte Postigo *et al.* 2011). The inter.-duration bursts found in these two databases seem to be represented by different phenomena.

Table 3. A summary of the results from the model-based clustering.

Model	k	BIC	ΔBIC	ΔBIC	ΔBIC	ΔBIC	Evidence
			$k = 1$	$k = 2$	$k = 3$	$k = 4$	
Two param.	EVI	2	-681.5	>10	\times	>10	Very strong
Three param.	EEE	3	-1156.6		>10	\times	>10
Four param.	VVV	2	-1768.4	>10	\times	>10	Very strong

Note. — The results for model-based clustering applied on two, three, and four parameters is presented. The values of BIC for the best fitted models with k components are listed, as well as the differences to the models with other number of components. $\Delta\text{BIC} > 10$ strongly supports the model with higher BIC. The volumes and shapes of all clusters may be equivalent (E) or may vary (V) and axes of all clusters may be restricted to parallel orientations with the coordinate axes (I).

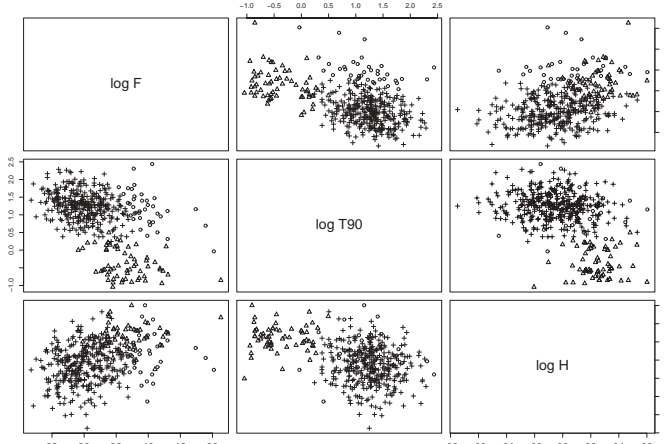


Fig. 1. GRBs with measured T_{90} , H , and F assigned to 3 groups by the best fit model (EEE). Triangles, circles, and crosses denote short-duration, long-duration high- and long-duration low-peak count rate GRBs, respectively.

This study was supported by the OTKA grant K77795, by the Grant Agency of the Czech Republic grant No. P209/10/0734, by the Research Program MSM00216-20860 of the Ministry of Education of the Czech Republic, and by Creative Research Initiatives (RCMST) of MEST/NRF.

References

- Horváth, I., Balázs, L.G., Bagoly, Z., et al., 2006, A&A, 447, 23
- Minaev, P.Yu., Pozanenko, A.S., Loznikov, V.M., et al., 2010, Astroph. Bull., 65, 326
- Řípa, J., Mészáros, A., Wigger, C., et al., 2009, A&A, 498, 399
- Řípa, J., Mészáros, A., Veres, P., et al., 2012, ApJ, 756, 44
- de Ugarte Postigo, A., Horváth, I., Veres, P., et al., 2011, A&A, 525, A109
- Veres, P., Bagoly, Z., Horváth, I., et al., 2010, ApJ, 725, 1955

FERMI/LAT OBSERVATIONS OF GRB 110625A

P.H.T. Tam¹, A.K.H. Kong¹ and Y.-Z. Fan²

Abstract. We report γ -ray afterglow observations of GRB 110625A using Fermi’s Large Area Telescope (LAT) above 100 MeV. Gamma-ray emission was clearly detected using data taken between 180 s and 580 s after the burst. The GeV light curve differs from a power-law decay, and probably consists of two emission periods. Simultaneous Swift/XRT observations did not show flaring behaviors, distinguishing its origin of the extended GeV emission from the case of GRB 100728A.

1 Introduction

Long-lived MeV–GeV emission of GRBs, first detected in the EGRET era, is now a common feature of LAT-detected GRBs (see, *e.g.*, Zhang *et al.* 2011). The nature of such temporally extended emission beyond the prompt GRB phase is not well understood, partly due to the rarity of GRBs whose GeV-emitting period is simultaneously observed in other wavelengths such as X-rays. By May 2011, the only two examples are: GRB 090510 and GRB 100728A. GRB 110731A is another LAT burst having *Swift*/XRT detection starting about 60 s after the burst (Bregeon *et al.* 2011; Littlejohns *et al.* 2011).

Here we report another such case: GRB 110625A, that was detected by Fermi/LAT and Swift/XRT simultaneously for several hundred seconds.

2 GRB 110625A

Fermi/GBM triggered on GRB 110625A at 21:08:18.24 UT (T_0) on 2011 June 25. The angle of the GRB position is 88° from the LAT boresight at T_0 . The autonomous rapid repoint maneuver repointed the LAT such that GRB 110625A was put in the field-of-view (FoV) of LAT from $\sim T_0 + 100$ to $T_0 + 600$. We analyzed the LAT data in this period as described in Tam *et al.* (2012).

¹ Institute of Astronomy and Department of Physics, National Tsing Hua University, Hsinchu 30013, Taiwan

² Purple Mountain Observatory, Chinese Academy of Sciences, Nanjing 210008, China

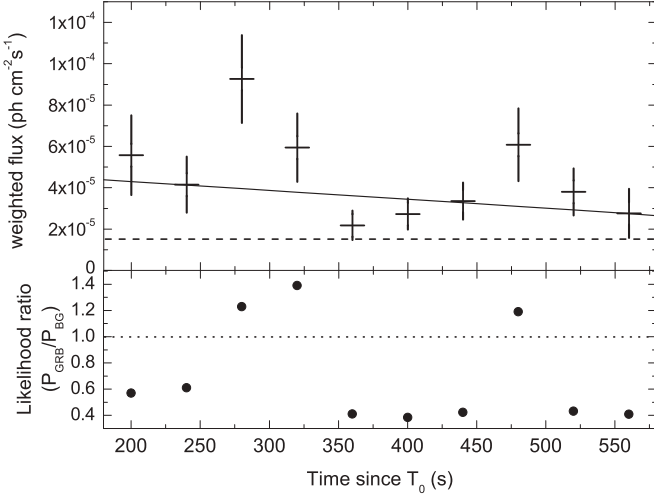


Fig. 1. *Top panel:* photon flux between 100 MeV and 20 GeV from GRB 110625A as observed using Fermi/LAT within a circular region of radius 10° , centered at the GRB position. The solid line represents the best-fit power law with $\chi^2/\text{d.o.f.} = 16.79/8$. The dashed line indicates the estimated number of background events averaged in the whole period. *Bottom panel:* ratio of the contribution from GRB 110625A over that from background based on a likelihood test. For details, see Tam *et al.* (2012).

Swift/XRT began data-taking of the burst at $T_0 \approx 150$ s and found the X-ray afterglow. No convincing candidate of optical/IR afterglow has been found.

3 The Fermi/LAT analysis results

Photon counts from a region-of-interest (ROI) of 10° -radius centered on the GRB position is weighted based on a maximum likelihood analysis and are plotted in Figure 1. It is apparent that the weighted light curve contains two peaks. We fit the weighted light curve with a simple power law, giving $\chi^2/\text{d.o.f.} = 16.79/8$. Thus the light curve deviates from a simple power law decay at the level of 96.77%.

Next we performed an unbinned maximum-likelihood analysis for photons arrived between $T_0 + 180$ s and $T_0 + 580$ s and yielded a spectral index of $\Gamma_\gamma = 2.7 \pm 0.3$ and a detection significance of $\sim 7\sigma$ of > 100 MeV γ -rays at the GRB 110625A position. We then divided the above period into three time bins and produced the background-subtracted light curve, as shown in Figure 2. The first and third data point represents the periods (I) $T_0 + 180$ s to $T_0 + 350$ s and (III) $T_0 + 420$ s to $T_0 + 580$ s, respectively. The period in-between (II) during which no emission was detected is plotted as a 90% confidence-level upper limit. We did not find significant spectral change between periods (I) and (III).

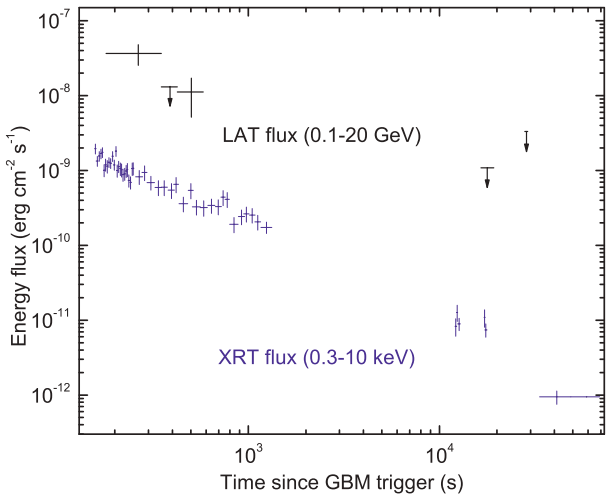


Fig. 2. The LAT and XRT energy flux from GRB 110625A (Evans *et al.* 2009). The X-ray light curve does not show any prominent X-ray flaring activity.

4 Conclusions

GRB 110625A is the third GRB detected by Fermi/LAT and Swift/XRT simultaneously. The GeV light curve differs from a simple power-law decay, and probably consists of two emission periods. The rapid decrease of GeV flux during both periods challenges the notion that the emission comes from the external forward shock. While in the case of GRB 100728A, late-time X-ray flares seem to accompany the GeV emission, no such flares are seen in the time frame during which GeV emission was detected. This suggests a different origin of the GeV emission between the two cases. We discuss the possibility that the GeV emission is the SSC radiation of an underlying ultraviolet (UV) flare (Tam *et al.* 2012). Multiwavelength coverage of the rare class of LAT GRBs during the GeV emitting period are crucial.

References

- Bregeon, J., McEnery, J., & Ohno, M., 2011, GCN Circ., 12218
- Evans, P.A., Beardmore, A.P., Page, K.L., *et al.*, 2009, MNRAS, 397, 1177
- Littlejohns, J., Evans, P.A., Beardmore, A.P., & Oates, S.R., 2011, GCN Circ., 12224
- Tam, P.H.T., Kong, A.K.H., & Fan, Y.-Z., 2012, ApJ, 754, 117
- Zhang, B.B., Zhang, B., Liang, E.-W., *et al.*, 2011, ApJ, 730, 141

INTRINSIC PROPERTIES OF *SWIFT* LONG GAMMA-RAY BURSTS

F.-W. Zhang¹

Abstract. We performed a statistical analysis of the intrinsic properties of long gamma-ray bursts (GRBs) observed by Swift. The intrinsic quantities are the rest-frame duration $T_{90,\text{rest}}$, the rest-frame peak energy $E_{\text{p},\text{rest}}$, the isotropic equivalent energy E_{iso} and the peak luminosity L_{iso} of the prompt emission. We find that the distributions of $T_{90,\text{rest}}$, $E_{\text{p},\text{rest}}$, E_{iso} and L_{iso} all span a wide range and the central values of these intrinsic quantities of long GRBs are $T_{90,\text{rest}} \sim 10$ s, $E_{\text{p},\text{rest}} \sim 520$ keV, $E_{\text{iso}} \sim 10^{53}$ erg and $L_{\text{iso}} \sim 4 \times 10^{52}$ erg/s. We also find both $E_{\text{p},\text{rest}}$ and L_{iso} are independent with T_{90} , but E_{iso} is correlated with T_{90} .

1 Introduction

Gamma-ray bursts (GRBs) are among the most distant objects observed in the Universe. Owing to numerous missions dedicated to detecting GRBs, significant advances of understanding the GRB phenomena have been made in recent decades. However, their nature is still a puzzle (see a review, Zhang 2011). One of the reasons is that their properties were basically studied in the observed frame instead of the rest frame. Thanks to the successful performance of Swift satellite (Gehrels *et al.* 2004), the growing sample of GRBs with known redshift allows us to further study their intrinsic properties.

2 Data analysis

The data selection criterion for our sample is based on the redshift and peak energy measurement. We first obtain a sample of 193 bursts with known redshift² detected by March, 2012. In order to obtain intrinsic duration $T_{90,\text{rest}}$ in a fixed energy band, at least two corrections (z -correction and k -correction) are needed due to cosmic expansion. The z -correction is straightforward and is achieved by

¹ College of Science, Guilin University of Technology, Guilin 541004, China

²<http://www.mpe.mpg.de/~jcg/grbgen.html>

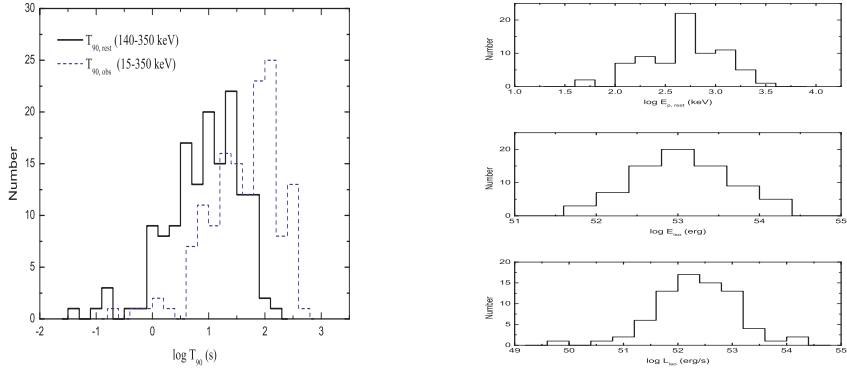


Fig. 1. *Left panel:* distributions of T_{90} for 147 BAT GRBs. The solid line and dashed line represent the T_{90} distribution in the rest-frame fixed energy bands (140–350 keV) and that in the observer frame (15–350 keV), respectively. *Right panel:* distributions of the $E_{p,\text{rest}}$, E_{iso} and L_{iso} .

multiplying the observed duration $T_{90,\text{obs}}$ by $(1+z)^{-1}$. And the k -correction is accomplished by choosing a energy band in the rest frame and then projecting that in the observer frame using the relation $E_{\text{obs}} = E_{\text{rest}}/(1+z)$. We choose 140–350 keV energy band in the rest frame in order to make the projecting energy bands lie in the Swift-BAT energy range 15–350 keV. The widely used Bayesian Block method (Scargle 1998) is adopted to extract burst duration in this work.

In our initial sample, some bursts are not bright enough to calculate the values of $T_{90,\text{rest}}$. Moreover, five super-long and peculiar GRBs (GRBs 060218, 100316D, 101225A, 110328A, 111209A) are not included in our sample. Therefore, we obtain a sample (S1) with 147 bursts (out of 193) that have the intrinsic duration $T_{90,\text{rest}}$. 75 long bursts from S1 have available the rest-frame peak energy $E_{p,\text{rest}}$, the isotropic equivalent energy E_{iso} and the peak luminosity L_{iso} establishing another sample (S2).

3 Distributions of T_{90} , $E_{p,\text{rest}}$, E_{iso} and L_{iso}

In the left panel of Figure 1, we present the duration distribution of 147 BAT GRBs both in the observer frame (15–350 keV; dashed line) and the rest frame (140–350 keV; solid line). Due to the rarity of short bursts, a bimodal distribution can not be recovered. The median value of $T_{90,\text{obs}}$ is 62 s, where 5 short bursts ($T_{90,\text{obs}} < 2$ s) are not calculated. The median value of $T_{90,\text{rest}}$ is 10 s, which is roughly consistent with previous results even though different energy ranges and different instruments are engaged (*e.g.* Pélangeon *et al.* 2008; Gruber *et al.* 2011).

The distributions of $E_{p,\text{rest}}$, E_{iso} and L_{iso} for sample S2 are shown in the right panel of Figure 1. From this figure we find that these three intrinsic quantities all span a wide range with the median values of 515 keV, 9.8×10^{52} erg and 3.6×10^{52} erg/s for $E_{p,\text{rest}}$, E_{iso} and L_{iso} , respectively. This result is also consistent with other observations (*e.g.* Pélangeon *et al.* 2008; Gruber *et al.* 2011).

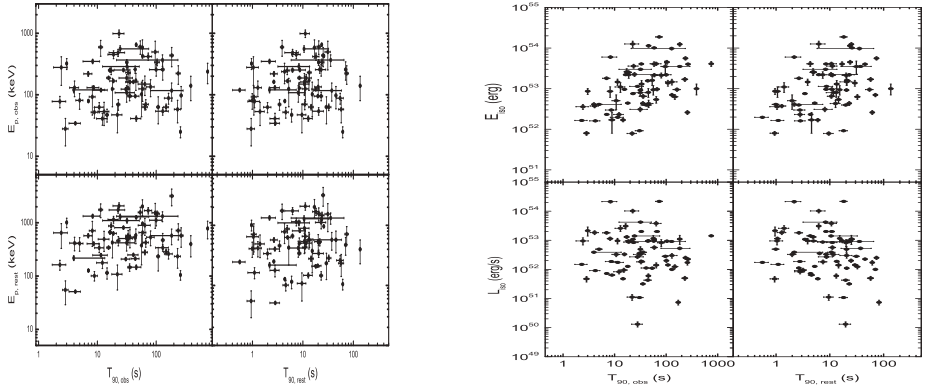


Fig. 2. *Left panel:* correlations between E_p and T_{90} . *Right panel:* correlations between E_{iso} , L_{iso} and T_{90} .

4 Correlations between E_p , E_{iso} , L_{iso} and T_{90}

The $E_{p,\text{rest}}-E_{\text{iso}}$ and $E_{p,\text{rest}}-L_{\text{iso}}$ correlations are extensively studied by many authors (*e.g.*, Amati *et al.* 2002; Yonetoku *et al.* 2004), but other correlations between these intrinsic quantities are not. Figure 2 (left panel) shows E_p vs. T_{90} both in the observer frame and in the rest frame. We find that they are not correlated in both frames. This result is consistent with our previous result for long GRBs without redshift measurement, which showed that the peak energy is not dependent with the duration for short and long classes separately (Zhang *et al.* 2012). The correlations between E_{iso} , L_{iso} and T_{90} are showed in Figure 2 (right panel). We find that E_{iso} is correlated with either the intrinsic duration $T_{90,\text{rest}}$ or the observed duration $T_{90,\text{obs}}$ ($E_{\text{iso}} \propto T_{90,\text{rest}}^{0.47 \pm 0.13}$ with the correlation coefficient $r = 0.49$ and $E_{\text{iso}} \propto T_{90,\text{obs}}^{0.50 \pm 0.11}$ with $r = 0.58$), but L_{iso} is not correlated with them.

This work was supported in part by the National Natural Science Foundation of China (11163003) and the Guangxi Natural Science Foundation (2010GXNSFB013050).

References

- Amati, L., Frontera, F., Tavani, M., *et al.*, 2002, A&A, 390, 81
- Gehrels, N., Chincarini, G., Giommi, P., *et al.*, 2004, ApJ, 611, 1005
- Gruber, D., Greiner, J., von Kienlin, A., *et al.*, 2011, A&A, 531, A20
- Pélangeon, A., Atteia, J.-L., Nakagawa, Y.E., *et al.*, 2008, A&A, 491, 157
- Scargle, J.D., 1998, ApJ, 504, 405
- Yonetoku, D., Murakami, T., Nakamura, T., *et al.*, 2004, ApJ, 609, 935
- Zhang, B., 2011, Comptes Rendus Physique, 12, 206
- Zhang, F.-W., Shao, L., Yan, J.-Z., & Wei, D.-M., 2012, ApJ, 750, 88

THE MULTI-BAND EMISSION PROFILE IN GRB

X.-H. Zhao^{1,2} and J.-M. Bai^{1,2}

Abstract. Gamma-ray burst (GRB) light curves generally are energy dependent, *i.e.*, the higher the photon energy, the narrower the pulse. In addition, the peak of the pulse at lower energies is usually delayed compared with that in higher energy. The phenomenon even exists in some X-ray flares and following optical flares. However, its origin is still unclear. Here we calculate the emission in different bands produced from different-thickness shocked shell due to radiative cooling, with the equal arrival time volume effect considered. We find the emission profile is energy dependent and that the light curves show spectral lag, which are consistent with the observations. This can be an explanation of the energy dependence of light curve and spectral lag in GRB, X-ray flare and following optical flare.

1 Introduction

Gamma-ray burst (GRB) light curves generally were found to be energy dependent in the BATSE/CGRO era, *i.e.*, the higher the photon energy, the narrower the pulse with a power-law slope of ~ -0.4 (Fenimore *et al.* 1995; Norris *et al.* 1996). And the pulse at lower energy is usually lagged compared with that in higher energy (Norris *et al.* 2000). There also exists spectral lag in some X-ray flares and simultaneous optical observation (*e.g.*, Kruhler *et al.* 2009; Rossi *et al.* 2011). Some explanations for the two phenomena have been proposed, including the radiative cooling and curvature effect. However, they both confront some severe problems in explaining the observations. The radiative cooling requires too low magnetic field, inconsistent with the current models (*e.g.*, Sari & Piran 1997; Piran 1999). The spectrum lag due to curvature effect is too small to fit the observation (*e.g.*, Shen *et al.* 2005). Here we considered the synchrotron cooling

¹ Key Laboratory for the Structure and Evolution of Celestial Objects, Chinese Academy of Sciences, Kunming 650011, China

² National Astronomical Observatories/Yunnan Observatory, Chinese Academy of Sciences, PO Box 110, Kunming 650011, China

will lead to different survival time for different energy of electrons behind internal shock so that the emission in different bands comes from shells with different width. Our motivation is explaining the two observations. We calculated the light curves with the equal arrival time volume effect considered in the second section. Discussion and conclusions are presented in the third section.

2 Shock hydrodynamics and light curves

GRB is usually considered to come from internal shocks, *i.e.*, the GRB central engine launches a lot of shells with different speeds and shocks will be produced when fast shells catch up with slow shells and collisions happen. The shocked electrons will give rise to the observed GRB by synchrotron or inverse Compton radiation. Suppose that a fast shell with speed of β_r catches up with a slow shell with speed of β_s and the two shells will undergo a full inelastic collision, where the width of both shells in the observed frame is $\Delta = R/\gamma_s^2$, $R = 2\gamma_s^2 c \delta t$ and γ_s being the radius of internal shock (δt is the variability time scale) and the Lorentz factor of slow shell, respectively. Two shocks, a reverse shock and a forward shock, will develop. For simplicity, here we only consider the reverse shock. The electrons after the shock will be accelerated. With the shock propagating in the fast shell, a “hot” region will form, in which the electrons have not yet had enough time to cool (safely neglecting the accelerating time of electrons). The width of the hot region is

$$\Delta_h = \gamma_m t'_{cool} c (\beta_m - \beta_{rs}), \quad (2.1)$$

where t'_{cool} is the comoving cooling Lorentz factor. For synchrotron emission, t'_{cool} is given by

$$\nu' = \frac{q_e B}{2\pi m_e c} \gamma_e^2, \quad P'_s = \frac{4}{3} \sigma_T c \frac{B^2}{8\pi} \gamma_e^2, \quad t'_{cool} = \frac{3}{\sigma_T} \left(\frac{2\pi m_e c q_e D}{B^3 \nu} \right)^{1/2}. \quad (2.2)$$

γ_m is the Lorentz factor of merged shell, which can be given $\gamma_m = \sqrt{\frac{\gamma_f m_f + \gamma_s m_s}{m_f/\gamma_f + m_s/\gamma_s}}$, where $\gamma_f(s)$ is the Lorentz factor of fast(slow) shells. B is the magnetic field behind the shock (in the comoving frame), given by $B = \sqrt{\frac{2L_{iso}\epsilon_B}{cR^2\gamma_m^2\epsilon_e}}$, where L_{iso} is the observed isotropic luminosity, ϵ_e and ϵ_B are the fractions of internal energy distributed to electrons and magnetic field. $D = 1/[\gamma(1 - \beta\mu)]$ is the Doppler factor. For an infinity thin shell and for a given time, the observed emission is from a surface symmetric around the line of sight, the equal arrival time surface, which is described by $R = \frac{\beta c T}{1 - \beta\mu}$. That means the emission is from an area. If the shell is not thin, for an observed time, T , the emission is from an equal time volume. The flux density is given by (Granot *et al.* 1999)

$$F_\nu(T) = 2\pi \frac{1+z}{d_L^2} \int_{\mu_0}^1 d\mu \int_{R_{in}(\mu, T)}^{R_{ex}(\mu, T)} r^2 dr D^2 j'_{\nu'}(\Omega', \nu\gamma(1 - \beta\mu), r, t) \quad (2.3)$$

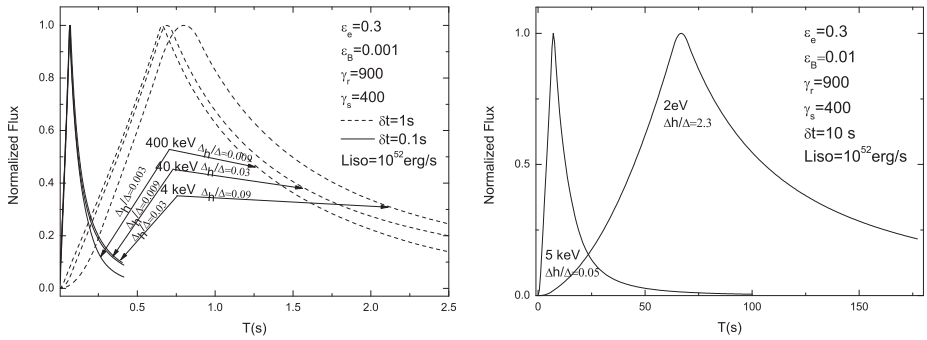


Fig. 1. The calculated Light curves in different bands.

R_{in} and R_{ex} are defined in Zhao *et al.* (2012), describing the emission is from an equal time *volume*. The comoving emissivity is given by $j'_{\nu'}(\Omega', \nu', r, t') = \frac{d[n'_e(r, t')P'(\nu')]}{d\Omega d\nu'} = \frac{n'_e(r, t')P'(\nu')}{4\pi}$. Here n'_e is the comoving electron number density, which is the function of r . The electron distribution is power law form with the slope of $p = 2.1$, and the corresponding synchrotron spectrum is broken power law with the low energy slope of $1/3$ and the high energy slope of $-(p - 1)/2$. The calculated light curves are shown in Figure 1. The spectrum lag and the pulse width extending in lower energy can be found. The spectrum lag is caused by a combination effect of shell geometry and synchrotron cooling. The softer the photon and thus the longer the cooling time of electrons, the wider the hot shell (Δ_h). The peak of a pulse for a wider hot shell will appears later, which will produce a lag. And a wider hot shell will also produce a wider pulse due to the equal arrival time volume effect.

3 Discuss and conclusions

The shocked shells with different thickness in different bands and equal arrival time volume may explain the observed energy dependence of light curve and spectral lag in GRB, X-ray flare and following optical flare.

References

- Fenimore, E., in't Zand, J., Norris, J., Bonnell, J., & Nemiroff, R., 1995, ApJ, 448, L101
- Kruhler, T., Greiner, J., McBreen, S., *et al.*, 2009, ApJ, 697, 758
- Granot, J., Piran, T., & Sari, R., 1999, ApJ, 513, 679
- Norris, J.P., Nemiroff, R.J., Bonnell, J.T., *et al.*, 1996, ApJ, 459, 393
- Norris, J.P., Marani, G.F., & Bonnell, J.T., 2000, ApJ, 534, 248
- Rossi, A., Schulze, S., Klose, S., *et al.*, 2011, A&A, 529, 142
- Sari, R., & Piran, T., 1997, MNRAS, 287, 110
- Shen, R.-F., Song, L.-M. & Li, Z., 2005, ApJ, 362, 59
- Zhao, X.-H., & Bai, J.-M., 2012, in preparation

ON THE PROMPT SIGNALS OF GAMMA RAY BURSTS

P. Chen¹, T. Tajima² and Y. Takahashi³

Abstract. We introduce a new model of gamma ray burst (GRB) that explains its observed prompt signals, namely, its primary quasi-thermal spectrum and high energy tail. This mechanism can be applied to either assumption of GRB progenitor: coalescence of compact objects or hypernova explosion. The key ingredients of our model are: (1) The initial stage of a GRB is in the form of a relativistic quark-gluon plasma lava; (2) The expansion and cooling of this lava results in a QCD phase transition that induces a sudden gravitational stoppage of the condensed non-relativistic baryons and form a hadrosphere; (3) Acoustic shocks and Alfvén waves (magnetoquakes) that erupt in episodes from the epicenter efficiently transport the thermal energy to the hadrospheric surface and induce a rapid detachment of leptons and photons from the hadrons; (4) The detached e^+e^- and γ form an opaque, relativistically hot leptosphere, which expands and cools to $T \sim mc^2$, or 0.5 MeV, where $e^+e^- \rightarrow 2\gamma$ and its reverse process becomes unbalanced, and the GRB photons are finally released; (5) The mode-conversion of Alfvén waves into electromagnetic waves in the leptosphere provides a snowplow acceleration and deceleration that gives rise to both the high energy spectrum of GRB and the erosion of its thermal spectrum down to a quasi-thermal distribution. According to this model, the observed GRB photons should have a redshifted peak frequency at $E_p \sim \Gamma(1 + \beta/2)mc^2/(1 + z)$, where $\Gamma \sim \mathcal{O}(1)$ is the Lorentz factor of the bulk flow of the lava, which may be determined from the existing GRB data.

Originally released as SLAC-PUB-8874 in 2001, this paper was never formally published.

¹ Department of Physics and Leung Center for Cosmology and Particle Astrophysics (LeCosPA), National Taiwan University, Taipei, Taiwan 10617 & KIPAC, SLAC, Stanford University, CA 94035, USA; e-mail: pisinchen@phys.ntu.edu.tw

² ZEST & Ludwig-Maximilians-Universitat Munchen, Fakultat f. Physik, am Coulombwall 1, 85748 Garching, Germany

³ Posthumous, Department of Physics, University of Alabama, Huntsville, AL 35899, USA

1 Introduction

The fireball model of GRB proposed in 1980 s (Paczynski 1986; Goodman 1986; Shemi & Piran 1990), which assumes a smooth expansion of the fireball, was later regarded as having difficulty to produce the high energy tail of the spectrum (Rees & Meszaros 1992; Meszaros & Rees 1993). This difficulty arises from the issue of baryon loading, where light particles (such as photons and electrons/positrons as well as neutrinos) cannot be easily detached from the opaque baryonic matter. It is generally believed that such a system would convert most of its energy into kinetic energy of the baryons rather than the luminosity. Indeed, Rees & Meszaros 1992, 1993 focused on this feature as the major issue of GRB and proposed an alternative fireball shock model. In this model the exploding e^+e^- plasma has a bulk Lorentz factor $\Gamma \sim 10^2 - 10^3$ at a radius of $\sim 10^5$ km. While this model addresses the issue of high energy tails, with a large Lorentz factor it remains a challenge to explain the spectral peak at several hundred keV.

The typical spectrum of a GRB consists of a relatively broad, thermal-like spectrum, with the peak energy E_p located at a few hundred keV, which contributes more than half of its total luminosity. In the illustrative case of GRB 990510, activities of low energy spectrum (< 62 keV) precede the main sudden onset of the high energy spectrum (> 30 keV) by a few 10 s of seconds. In addition to the spectrum around the peak, a substantial fraction of the total luminosity is contributed from the high energy tail, which can be characterized by a power-law with a (negative) index $\sim 2-2.5$. In terms of the time structure, GRBs can be classified into two types: the short bursts that last for $\sim 1-10$ sec and the long bursts that last for tens to hundreds of seconds. It is interesting to note that while the time duration and profile vary widely over several orders of magnitude, the GRB spectra described above are remarkably universal. Much attention has been devoted to analyzing GRB afterglow as a result of an expanding fireball, which leads to important correspondence between the observational data and phenomenological models. However, a comprehensive understanding of the underlying mechanisms that produces such a fireball and the prompt signals are still lacking.

We suggest that the key to the understanding of GRB lies in its prompt signals, in particular the thermal portion of the spectrum. In this article we propose a new GRB model which provides a unified picture on the early-stage evolution and thus the mechanism that produces the prompt signals of GRBs. The key ingredients of our model are:

1. In the final stage of either compact-object coalescence or hypernova explosion, large fragments of hadron matter are ejected, most likely non-isotropic. Heated by the release of a large fraction of the systems gravitational potential energy, the hadrons are melted into quarks and gluons with temperature ~ 200 MeV and density 10^{38} cm $^{-3}$, like a molten lava. The bulk flow of such a lava, or hadrosphere, however, is only mildly relativistic.
2. The expansion and cooling of this lava results in a QCD (quantum chromodynamics) phase transition at a temperature ~ 120 MeV and density

$\sim 2 \times 10^{37} \text{ cm}^3$ that condenses the relativistic quarks and gluons into non-relativistic baryons. These nonrelativistic baryons feel the strong gravity and stop their expansion. This results in the formation of a hardened hadrosphere boundary, analogous to the darkening of the lava surface.

3. Acoustic shocks and Alfvén waves (magnetoquakes) that erupt in episodes from the epicenter efficiently transport the thermal energy to the hadrospheric surface and induce a rapid detachment of leptons and photons from the hadrons.
4. The detached e^+e^- and γ form an opaque, relativistically hot leptosphere, which expands and cools to $T \sim mc^2$, or 0.5 MeV, below which $e^+e^- \rightarrow 2\gamma$ and its reverse process become unbalanced, and the GRB thermal photons are released. The observed peak of this portion of the GRB spectrum is $E_p \sim \Gamma(1 + \beta/2)mc^2/(1 + z)$, where $\Gamma \sim \mathcal{O}(1)$ is the Lorentz factor for the bulk flow of the lava, and z is the GRB redshift factor.
5. The existence of a nonlinear e^+e^- plasma-mediated mode-conversion effect that converts Alfvén waves into electromagnetic waves in the leptosphere. This process provides a novel snowplow acceleration and deceleration mechanism that produces both the high energy spectrum of GRB and the erosion of its thermal spectrum down to a quasi-thermal distribution.

Figure 1 is a schematic diagram that depicts our GRB model. In the following sections we elaborate these key points of our model in more details.

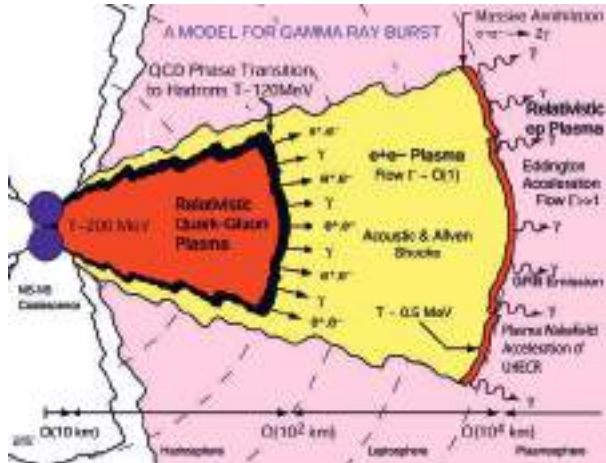


Fig. 1. A schematic diagram that depicts the various phases of the GRB dynamics in our model in the aftermath of the coalescence of a binary neutron star system.

2 Hadrosphere and QCD phase transition

We assume that in the final stage of either compact-object coalescence or hypernova explosion, the tremendous concentration of energy triggers the eruption of large fragments of baryon matter. The density of baryon matter under such circumstance is comparable to that of a neutron star, *i.e.*, $\sim 10^{38} \text{ cm}^3$. Heated by the system's released gravitational energy, which can be as large as $\sim 0.1 - 0.3$ of the total rest mass of the system, such baryon fragments can gain a thermal energy, or temperature, $\sim 200 \text{ MeV}$. Under high temperature and density, one expects from quantum chromodynamics (QCD) that the baryon matter turns into a deconfined quark-gluon plasma (Alford 1998). A quantitative description of such QCD phase transition has been a major challenge to nuclear physicists. The standard approach is to invoke grand canonical ensemble (in which the particle number is not fixed), and therefore the relation between the temperature and the chemical potential. Nevertheless, we believe that the phase transition happens at temperature $T \geq 120 \text{ MeV}$ for zero baryon and at density $\rho \geq 10^{39} \text{ cm}^3$ for much lower temperature (Liu 2001). Taking these conditions as our constraint and translating the chemical potential into an average particle density, we can parameterize the QCD phase boundary as

$$\left(\frac{\rho}{\rho_c}\right)^2 + \left(\frac{T}{T_c}\right)^2 = 1, \quad (2.1)$$

where $\rho_c \sim 10^{39} \text{ cm}^3$ and $T_c \sim 120 \text{ MeV}$. Clearly, the initial state of our system is in the quark-gluon phase.

Once quarks are deconfined at such energy-density, they are highly relativistic since their rest masses are as low as $m_u \sim 4 \text{ MeV}$ and $m_d \sim 7 \text{ MeV}$ for the up and down quarks, respectively. In this plasma there are about the same order of magnitude in the electron/positron (and neutrino) populations as well as thermal energies, since they are in (near) local thermal equilibrium with the relativistic quarks and gluons. Once this lava of quark-gluon plasma erupts, it adiabatically expands and cools. We call such a cluster the hadrosphere.

As the hadrosphere expands to the radius of $\sim 50 \text{ km}$, the quark-gluon plasma density reduces to $\rho_{q-g} \sim 2 \times 10^{37} \text{ cm}^3$. From thermodynamics the temperature and density are related by

$$\rho^{1-\gamma} T = \text{const.} \quad (2.2)$$

For relativistic particles, $\gamma = 4/3$, and we find $T \propto \rho^{1/3}$. Since $\rho \propto 1/V \propto 1/R^3$, we have $T \propto 1/R$. Thus the temperature drops to $T \sim 120 \text{ MeV}$ at this point. This is the temperature for QCD phase transition when the density is much lower than the critical one: $\rho \ll \rho_c$. Note, however, that in the case of NS-NS coalescence, the initial baryon density would be much higher than that of the nucleus, and therefore a much larger chemical potential. T_c , which is a function of both temperature and chemical potential, is thus much lower, at $\sim 10 - 20 \text{ MeV}$, and therefore the QCD phase transition is easier to reach. Once $T \sim T_c$, the quarks and gluons condensate into hadrons and turn nonrelativistic, which immediately feel the immense gravity

and are thus gravitationally trapped. This gravitational capture of baryonic matter marks the boundary of the hadrosphere.

Note that such a quark-gluon explosion needs not be spherically symmetric, and may be irregular or even in chunks. Under the extreme high densities, the hadrosphere is highly opaque and poor in convection. Thus the quark-gluon plasma near the boundary first condensate into baryons while its interior is still molten. This is analogous to the darkening of the lava surface after erupted from the volcano, where the interior of the lava is still red-hot.

3 Separation of photons and leptons from hadrosphere

As mentioned in the Introduction, one seeming difficulty in the fireball model is the lack of a mechanism to efficiently transport the tremendous luminous energy near instantly across the baryonic matter. Given the extremely high density and therefore short mean-free-path in the fireball, the transport of energy through individual particle kinematics, *i.e.*, thermal convection, would indeed be hard. This is the well-known problem of baryon loading. It may be overcome, however, by the transport of energy through collective plasma excitations.

In the final stage of compact-object coalescence or the collapse of supermassive star we expect the generation of strong acoustic waves (internal shocks) and Alfvén waves (we may call this magnetoquakes). These waves are efficient mass and energy carriers (Holcomb & Tajima 1991) in the interior of the hadrosphere as well as the leptosphere. For example, in the NS-NS or NS-BH coalescence, the violent perturbations of the strong magneticfield pressure of the host neutron stars ($B \sim 10^{12} - 10^{13}$ G) induces the excitation of magnetoquakes. As much as $\sim \mathcal{O}(10^{52})$ erg of energy may be carried by these waves. Due to the compactness of the progenitor, the period of these magnetoquakes is about $\sim \mathcal{O}(100)$ μsec during each episode. As these shocks approach the boundary of the hadrosphere, the torsional as well as the compressional Alfvén waves in the rapidly density-graded stellar magnetosphere are expected to exhibit interesting and important properties (Takahashi *et al.* 2000). One is precisely the possibility of transport of energies from the epicenter to the hadrosphere boundary during each episode of magnetoquake. Another is the possibility of mode-conversion in the leptosphere. The density of the leptospheric e^+e^- plasma decreases rapidly due to its expansion. In such an environment the torsional Alfvén waves can mode-convert themselves into the usual electromagnetic waves (Daniel & Tajima 1998).

At the surface of hadrosphere, where the non-relativistic baryons are suddenly slowed down by self-gravitation as a result of QCD phase transition, the still highly relativistic leptons are freely radiating through the surface and their chemical potentials are negligible. Thus in close analogy with the standard black-body emission process and according to the Stefan-Boltzmann law, $J = \alpha T^4$, where $\alpha = 5.67 \times 10^5 \text{ erg/sec/cm}^2/K^4$, the system can emit above 10^{52} ergs in 10^{-8} second with a temperature of 120 MeV and a radius of 50 km.

4 Mode-conversion in leptosphere

As mentioned earlier, the emitted e^+e^- and γ are so dense that they are not freely propagating outward. With tremendous near-instant supply of electrons and positrons, the radiated e^+e^- pairs (as well as photons and neutrinos) will likely create shocks. As mentioned in the previous section, the internal acoustic and Alfvénic shocks can provide efficient energy transport as well as snowplow acceleration within the dense hadrosphere. In addition, the Alfvén waves that continue to propagate across the leptosphere can induce a novel, linear and nonlinear phenomenon called mode-conversion. The density of the leptospheric e^+e^- plasma decreases rapidly due to its expansion. It has been observed in the particle-in-cell computer simulations that in such an environment the torsional Alfvén waves can mode-convert themselves into ordinary electromagnetic waves (Kippen 1999). Furthermore, it was observed that inside such an opaque plasma a self-induced transparency occurs. Namely, a large number of energetic particles are plowed and accelerated in front of the Alfvén wave, which are detached from the opaque, collisional bulk plasma.

When the mode-conversion occurs in the e^+e^- plasma, the converted EM waves proceed ahead of the Alfvén waves and the snowplowed particles, forming an integrated overall trinity structure. This structure is capable of converting a large fraction of the wave energy (magnetoquake energy) into kinetic energies of the accelerated particles, as well as the heating of the bulk plasma. In our scenario this mechanism provides the basis of the production of the nonthermal high energy spectrum of GRB. The mechanism of this transport is analogous to snowplowing: particles are pushed forward in front of the shock waves. We note that such process can also decelerate those particles that are on the “wrong side” of the slope between episodes of magnetoquakes (Chen *et al.* 2002). Such stochastic processes will dilute the pure thermal spectrum into a quasi-thermal one.

5 Quasi-thermal spectrum of GRB

By the time when the leptosphere expands to a radius $\sim 10,000$ km and cooled to below the two-photon pair production threshold, *i.e.*, $T \sim mc^2 \sim 0.5$ MeV, the two-photon pair production and its reversed pair annihilation processes,

$$e^+e^- \rightarrow 2\gamma \quad (5.1)$$

are out of balance, and the e^+e^- are largely annihilated into photons with a typical energy of $E_{p0} \sim 0.5$ MeV in the rest frame of the bulk flow. The observed peak energy of the GRB thermal spectrum should therefore be

$$E_p \sim \frac{\Gamma(1 + \beta/2)}{1 + z} E_{p0} \sim \frac{\Gamma(1 + \beta/2)}{1 + z} mc^2, \quad (5.2)$$

where z is the GRB redshift factor, $\beta^2 = 1 - 1/\Gamma^2$ and Γ is the Lorentz factor of the bulk flow of the lava. As explained above, such initially thermal spectrum

Table 1. Comparison of our model with observations based on the 7 GRB events from the BATSE catalog.

BurstName	E_p^{obs} [keV]	z	$mc^2/(1+z)$	Derived Γ
GRB 970508	481	0.84	278	1.3
GRB 970825	230	0.96	261	0.9
GRB 971214	156	3.41	116	1.1
GRB 980703	370	0.97	259	1.2
GRB 990123	550	1.60	197	1.9
GRB 990506	450	1.20	232	1.4
GRB 990510	174	1.62	195	0.9

will be eroded to a quasi-thermal one due to the stochastic nature of snowplow acceleration-deceleration interplay under random phases of magneto quakes or shock waves.

To compare our model with observations, we take long burst GRBs with redshift factors identified from Piran *et al.* (2000), based on the BATSE data. There are 8 events where both the redshift and the spectral peak, E_p , have been identified. Among these 8 events on, GRB 980425, is discarded because it is very local ($z \sim 0.01$) and its total luminosity fell sufficiently below the typical GRBs.

6 Conclusion

We have discussed the key features of our new model for GRB. Our scenario appears to be able to provide an explicit physical framework that can explain many of the GRB quasi-thermal spectrum characteristics. These include the release of $\sim 10^{52}$ erg of energy from a compact source, the promptness of such a release, and the origin of the GRB spectral peak as well as the high energy tail. Episodes of vibrations and eruptions of acoustic shocks and magnetoquakes, which should have a period of ~ 100 μ sec during each burst, induce a fine structure within the overall duration of the prompt GRB signals. We have not discussed the physics in the outer plasmosphere (which is formed beyond the boundary of the leptosphere where positrons are essentially all annihilated). The existence of the plasmosphere, however, is in our view essential to another very important astrophysical phenomenon, namely the production of ultra-high energy cosmic rays (UHECR) beyond 10^{20} eV.

This work was supported by US Department of Energy, contract DE-AC03-76SF00515 (PC), DE-FG03-96ER40954 (TT with UTA), W-7405-ENG-48 (TT with LLNL); and DE-FG-02-88ER41058 (YT); and by NASA, contract NAS898226 (YT).

References

- Alford, M., "New Possibilities for QCD at Finite Density", 1998, hep-lat/9809166
- Chen, P., Tajima, T., & Takahashi, Y., 2002, Phys. Rev. Lett., 89, 161101
- Daniel, J., & Tajima, T., 1998, ApJ, 498, 296
- Goodman, J., 1986, ApJ, 308, L47
- Holcomb, K.A., & Tajima, T., 1991, ApJ, 378, 682
- Kippen, R.M., 1999, GCN, 322
- Liu, K.-F., private communications, April 2001
- Meszaros, P., & Rees, M.J., 1993, ApJ, 405, 278
- Paczynski, B., 1986, ApJ, 308, L43
- Piran, T., Jimenez, R., & Band, D., 2000, The Energy Distribution of GRBs, in Gamma-Ray Bursts: 5th Huntsville Symposium, ed. R.M. Kippen *et al.*, AIP Porc. 1-56396-947
- Rees, M.J., & Meszaros, P., 1992, MNRAS 258, 41
- Shemi, A., & Piran, T., 1990, ApJ, 365, L55
- Takahashi, Y., Hillman, L.W., & Tajima, T., 2000 in High-Field Science, ed. T. Tajima, K. Mima, & H. Baldis (Kluwer Academic, NY), 171

Chapter III.
Prompt Emission-II Theory

RADIATIVE MECHANISMS IN GRB PROMPT EMISSION

A. Pe'er¹

Abstract. Motivated by the *Fermi gamma-ray space telescope* results, in recent years immense efforts were given to understanding the mechanism that leads to the prompt emission observed. The failure of the optically thin emission models (synchrotron and synchrotron self Compton) increased interest in alternative models. Optically thick models, while having several advantages, also face difficulty in capturing several key observables. Theoretical efforts are focused in two main directions: (1) mechanisms that act to broaden the Planck spectrum; and (2) combining the optically thin and optically thick models to a hybrid model that could explain the key observables.

1 Setting the stage: Understanding what we see

In the commonly accepted gamma-ray bursts (GRB) “fireball” model (Goodman 1986; Paczynski 1986; Rees & Meszaros 1992, 1994; Shemi & Piran 1990), the prompt emission is believed to arise from a prompt dissipation of a substantial fraction of the bulk kinetic energy of a relativistic outflow, originating from a central compact object. This model is found to be in good qualitative agreement with all observations to date; moreover, a great success of this model is the prediction of the afterglow emission, resulting from interaction of the propagating relativistic blast wave with the ambient interstellar matter (ISM) (Mészáros & Rees 1997; Sari *et al.* 1998).

In spite of these successes, this model is far from being complete. Many necessary details are missing: for example, the mechanism responsible for particle acceleration to high energies, required to explain the observed high-energy non-thermal emission is not explained. Similarly, the nature of the radiative processes that produce the observed signal are not specified. In addition, the dynamical part is not fully understood. While it was long thought that the conversion of explosion (gravitational) energy to kinetic energy (namely, acceleration to relativistic velocities) is mediated by photons (Paczynski 1986, 1990; Rees & Meszaros 1992),

¹ Physics Department, University College Cork, Cork, Ireland

in recent years there are accumulating evidence that magnetic field may play an important role in this process (Zhang & Pe'er 2009), resulting in a modified dynamics (Drenkhahn 2002; Drenkhahn & Spruit 2002). Moreover, nothing in the model predicts the radii in which energy is dissipated and radiation is produced.

The prompt GRB spectra is well modeled by a smoothly broken power law, known as the “Band” function (Band *et al.* 1993; Goldstein *et al.* 2012; Kaneko *et al.* 2006; Nava *et al.* 2011; Preece *et al.* 2000, 1998b). In spite of its great success in providing good fits to the observed data, this model has a crucial drawback: being mathematical in nature, by itself it does not provide any clue about the origin of the observed emission.

It was long thought that the observed radiation originates from synchrotron emission in the optically thin regime (Cohen *et al.* 1997; Mészáros *et al.* 1993, 1994; Tavani 1996). This idea was motivated by the fact that the observed radiation is non-thermal. Shock waves which are believed to exist in the plasma can accelerate particles to high energies via Fermi mechanism as well as generate strong magnetic fields, thereby providing the necessary ingredients for synchrotron emission (Blandford & Eichler 1987). These processes were recently realized in particle-in-cell (PIC) simulations (Haugbølle 2011; Sironi & Spitkovsky 2009, 2011; Spitkovsky 2008).

Although GRB spectra significantly vary from burst to burst and frequently within a single burst, there are several key observations which appear general. The synchrotron theory can therefore be confronted with these key results. These include:

1. Observed peak energy $E_{\text{peak}}^{\text{ob}} \sim 300 \text{ keV}$. While the synchrotron theory does not naturally provide this value, it is achievable under the assumption that both the electrons and magnetic field energies are close to equipartition with the post-shock thermal energy. For example, if the magnetic field is $B \approx 10^5 \text{ G}$, the characteristic electron’s Lorentz factor is $\gamma_{el} \sim 200$ and bulk Lorentz factor $\Gamma \sim 10^{2.5}$, similar values are obtained.
2. Narrow distribution of the peak energy: although the observed luminosity varies by several orders of magnitude, in most GRBs the observed peak energy is between $0.1 - 1 \text{ MeV}$. In the context of the synchrotron model, the observed peak energy is a function of B , γ_{el} and Γ . There is no natural reason to assume that the values of these free model parameters coincide in such a way as to produce the narrow clustering of $E_{\text{peak}}^{\text{ob}}$ observed.
3. The correlation seen between the peak energy and total energy ($E_{\text{peak}} - E_{\text{iso}}$ relation) (Amati *et al.* 2002; Ghirlanda *et al.* 2004; Golenetskii *et al.* 1983; Yonetoku *et al.* 2004): in the framework of the synchrotron model, it is possible to obtain the observed correlation only if additional assumptions are made, *e.g.*, about the dissipation radius.
4. A “universal” low energy spectral slope, $\alpha \approx -1$ (Goldstein *et al.* 2012; Kaneko *et al.* 2006; Nava *et al.* 2011): in the “Band” model fits, a narrow

clustering of the low energy spectral slope ($dN/dE \propto E^\alpha$) around $\alpha \approx -1$ is observed. The observed low energy hard spectral slope is in contradiction to the prediction of the synchrotron model theory. This is known as “synchrotron (model) line of death” (Ghirlanda *et al.* 2003; Preece *et al.* 2002, 1998a).

The failure of the synchrotron model has motivated the study of alternatives. A notable alternative is emission from the *optically thick* regions. While many of the details of the “fireball” model are uncertain, the existence of an optically thick region in the inner parts of the outflow is a robust prediction. Thus, photospheric emission is a natural outcome of the model, and, indeed was considered from the very early days (Goodman 1986; Paczynski 1986). However, as the observed spectrum *does not* resemble a Planck spectrum, this idea was abandoned for a long time.

2 Broadening mechanisms of Planck spectrum: Sub photospheric energy dissipation

The observed low energy spectrum is steeper than synchrotron model predictions, but is not as steep as to resemble a “Planck” spectrum. However, while there is no physical mechanism that can steepen the synchrotron spectra, one can think of several mechanisms that can broaden the Planck spectrum to produce the observed spectral slope.

Broadly speaking, there can be three ways in which the observed spectra can be achieved. First, the spectrum may contain two separate components: a “Planck” and optically thin synchrotron observed simultaneously. The observed spectrum is a combination of these two components. Following early analysis by Ryde (2004, 2005) and Ryde & Pe'er (2009), recently, with improved *Fermi* capabilities that enable *time-resolved* analysis, these components are ubiquitously observed (Axelsson *et al.* 2012; Guiriec *et al.* 2011, 2012; Larsson *et al.* 2011; Ryde *et al.* 2010; Starling *et al.* 2012; Zhang *et al.* 2011). The separation enables the study of the physical properties of both components (Pe'er *et al.* 2007, 2012; Zhao *et al.* 2011), and provides a natural explanation to the delay of the high energy emission seen (Abdo *et al.* 2009; Ackermann *et al.* 2010).

Second, sub-photospheric energy dissipation naturally leads to modification of the Planck spectrum (Beloborodov 2010; Giannios 2006, 2008, 2012; Ioka *et al.* 2007; Lazzati & Begelman 2010; Lazzati *et al.* 2009; Pe'er *et al.* 2005, 2006; Vurm *et al.* 2011). The basic idea is that kinetic energy dissipation, whether originating from internal shocks, magnetic reconnection or any other process, takes place at radii not much below the photospheric radius. By definition of the photospheric radius r_{ph} , the optical depth for scattering of a photon from r_{ph} to the observer (located at infinity) is equal to unity. The plasma contains many more photons than electrons: this can be seen by the fact that the average energy per photon (in the comoving frame) is much smaller than $m_e c^2$. Thus, while at r_{ph} the optical depth for *photon* scattering is unity, the optical depth for *electron* scattering is

much larger than unity. As a result, at r_{ph} , every electron undergoes many inverse Compton (IC) scatterings with the lower energy photons before decoupling. Each electron therefore loses its energy rapidly, on a time scale much shorter than the dynamical (expansion) time scale (see Pe'er *et al.* 2005 for details).

Assuming that the heating mechanism (of an unspecified nature) is continuously heating the electrons, or alternatively accelerating new electrons to high energies, the result is that the electron's distribution is in a quasi steady state, with temperature determined by balance between the external heating and the rapid IC cooling. This temperature is inevitably higher than the photon temperature, hence the plasma is characterized by **two temperatures**: $T_{el} > T_{ph}$.

If the dissipation, hence the electron heating occurs below, or even slightly above the photosphere, then the thermal photons IC scatter with the hotter electrons, producing a non-thermal spectrum. The emerging spectrum above the original thermal peak depends mainly on two free model parameters: (1) the optical depth τ in which the dissipation takes place: this determines the number of scattering for a single photon. On the one extreme, $\tau \rightarrow \infty$ (or $r_{dis} \ll r_{ph}$), the plasma have enough time to thermalize, and the energy given to the electrons is evenly distributed, resulting in a Planck spectrum. On the other extreme, $\tau \ll 1$, only very few photons are being up scattered, producing a high energy tail. In the intermediate regime, $\tau \approx \text{few - few tens}$, the spectrum significantly deviates from Planck. (2) The second free parameter is the ratio of the energy density in the electron and thermal photon components. If the dissipation considerably heats the electrons, deviation from a Planck spectrum is more pronounced.

Multiple IC scattering thus modifies the spectrum above the thermal peak. At lower frequencies, the spectrum is dominated by synchrotron emission from the energetic electrons. As these electrons are in a quasi steady state, the emerging spectrum does not expect to have a power law shape, as the electrons distribution cannot be described by a power law. Thus, overall, the expected spectra is expected to significantly deviate from the original Planck spectra, with significant synchrotron contribution at low energies, and high energy spectra dominated by multiple IC scatterings. Example of possible spectra under different conditions appear in Figure 1, taken from Pe'er *et al.* (2006). Recently, evidence for sub-photospheric energy dissipation was observed in analyzing the data of GRB 090902B (Ryde *et al.* 2011).

3 Theory of photospheric emission from collimated outflow

Even in the absence of sub-photospheric energy dissipation, the expected spectrum originating from the photosphere deviates from a pure "Planck" spectrum. This is due to the non-trivial shape of the photosphere. Consider first a spherical explosion: the mean free path of photons emitted from high angle to the line of sight, $\theta > 0$ and propagate towards the observer is larger than the mean free path of photons propagating at $\theta = 0$. This results in a strong angular dependence of the photospheric radius, $r_{ph} \propto \Gamma^{-2} + \theta^2/3$ (Pe'er 2008), where Γ is the bulk Lorentz factor.

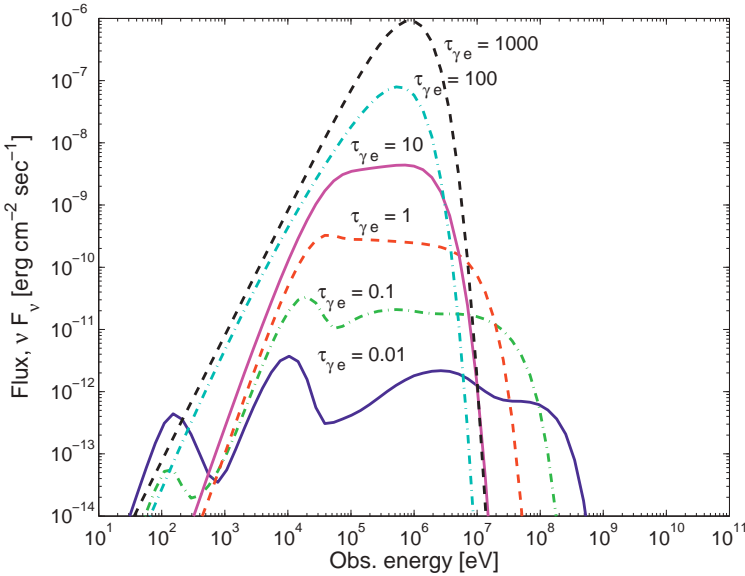


Fig. 1. Examples of time averaged spectra obtained for different values of the optical depth for photon scattering ($\tau = \tau_{\gamma e}$) at the dissipation radius, under the assumption that thermal component exists (from Pe'er *et al.* 2006). While for very high optical depth a “Planck” spectrum is obtained, for intermediate optical depth, multiple IC scattering results in nearly flat spectra above the thermal peak, while synchrotron emission modifies the spectrum at lower energies.

Moreover, by definition, the photospheric radius is the radius in which the optical depth for scattering $\tau = 1$. However, the last scattering process is not limited to this surface: photons have a finite probability of being scattered at any position in space in which scatterers (electrons) exist. An observer therefore sees simultaneously photons who’s last scattering location took place at a range of radii and angles to the line of sight; this leads to the concept of a “fuzzy photosphere”. As photons adiabatically cool below the photosphere, each of the observed photons has its own (comoving) energy, and has a unique Doppler boost. Thus, the observed spectrum differs than Planck spectrum, and is observed as a “gray body” spectrum (Beloborodov 2011; Pe’er 2008). If one considers a δ -function of emission at $t = 0$ (alternatively, if the inner engine is abruptly stopped), then at late times emission is dominated by photons emitted at high angles (off-axis). In this scenario, a very flat spectrum is obtained at late times, significantly different than a “Planck” (Pe’er & Ryde 2011).

While the original theory was developed for spherical outflows, in any realistic scenario the explosion is collimated. In the collapsar model, for example, as the jet drills its way through the collapsing stellar envelope it pushes material towards

the side, forming a hot cocoon. This material collimates the jet (Mizuta *et al.* 2011; Morsonyi *et al.* 2007; Zhang *et al.* 2003). Thus, when calculating emission from the photosphere one needs to consider the jet velocity profile, $\Gamma = \Gamma(\theta)$. Such a model therefore has 4 free parameters (as opposed to a single parameter, Γ in the spherical case): the maximum bulk Lorentz factor Γ_0 at the jet axis, the characteristic jet opening angle θ_j , viewing angle θ_v and a parameter p which determines the shape of the velocity profile decay ($\Gamma(\theta) \propto \theta^{-p}$).

Such a scenario was recently studied by Lundman *et al.* (2013). It leads to a few unexpected results. First, extended emission from higher angles is very pronounced. This can be understood as a phase space effect: the average scattering angle is $\approx \Gamma^{-1}$, and Γ varies with angle. Thus, more photons that originates from high angles (with lower Γ) are observed, compared to the spherical case. The obtained spectrum for narrow jet ($\theta_j \Gamma_0 \lesssim$ few) below the thermal peak is flat ($dN/dE \propto E^{-1}$), independent of viewing angle, and only weakly dependent on the Lorentz factor gradient (p). A similar result is obtained for wider jets, observed at $\theta_v \approx \theta_j$, which is the most likely scenario. The spectral slope calculated in this model is similar to the average low energy spectral slope observed. For wider jets ($\theta_j \Gamma_0 \gtrsim$ few), a multicolor black body is obtained. Second, the high energy spectral slope is modified by a similar mechanism: as the average scattering angle is $\approx \Gamma^{-1}$, photons are more likely to diffuse from region of low Γ to region of high Γ , where they are further boosted. This leads to a power law spectral slope at high energies, who's exact shape depends on the assumed jet profile. An example of the obtained spectra appears in Figure 2.

4 Summary

In spite of two decades of extensive research, the origin of GRB prompt emission remains elusive. A renewed interest in understanding this phenomena occurred with the superb data quality enabled by the *Fermi* satellite. Following the failure of the synchrotron model, significant efforts were given to understanding mechanisms that can act to broaden the Planck spectrum to fit into the observed “Band” spectrum.

Three ideas were suggested in recent years: (1) A combined optically thick and optically thin emission seen simultaneously; (2) sub-photospheric energy dissipation; and (3) geometrical broadening. While each of these ideas have its own success, as of today, none of these provide a full explanation to the observed spectrum. The success and weaknesses of any of these ideas are summarized in Table 1 below. In the table, (V) represents success, (X) represents failure, and (–) implies that currently the theory does not contradict the observation, but does not provide predictions either, or that additional assumptions are required.

Thus, as of today, no single model can fully explain all key observations, implying plenty of room for new ideas.

I would like to thank my collaborator and friend **Felix Ryde** for countless number of useful discussions.

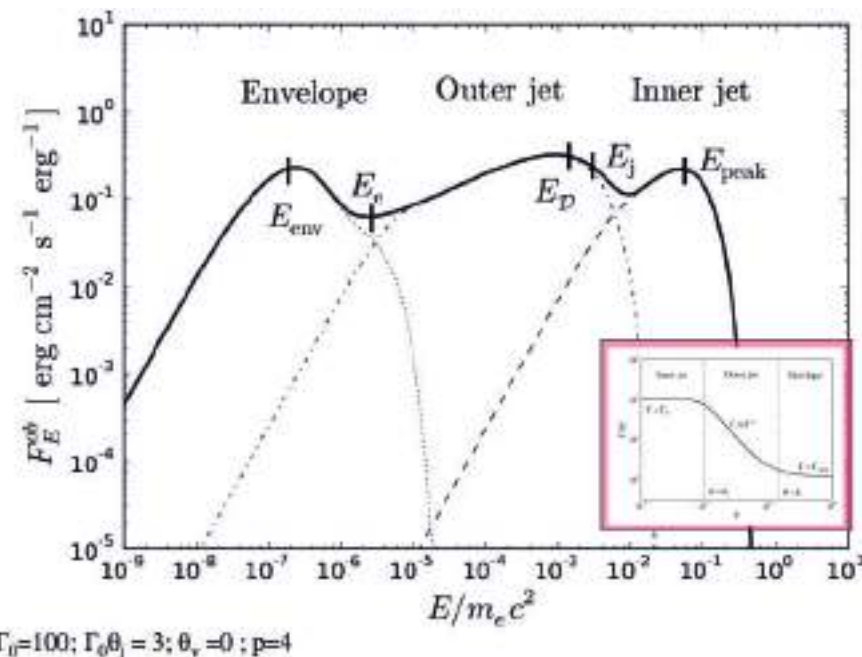


Fig. 2. Example of observed spectrum from a relativistic, optically thick outflow (taken from Lundman *et al.* 2013). A jet profile $\Gamma(\theta) \propto \Gamma_0 / (\theta/\theta_j)^{2p} + 1)^{1/2}$ was considered (inner onset). Separate contributions from the inner jet ($\Gamma \approx \text{const}$), outer jet ($\Gamma \propto \theta^{-p}$) and envelope ($\Gamma \gtrsim 1$) are marked. The combined effect is a very flat spectra, extended over many orders of magnitude. This result is found to be robust, very weakly dependent on the values of the free model parameters.

Table 1. Confronting current theoretical models with key observations.

Key observation	Optically thin synchrotron	Pure Planck + synch.	Sub phot. dissipation	energy dissipation	Geometrical broadening
$E_{\text{peak}}^{\text{ob}} \approx 300 \text{ keV}$	V	V	V	-V	
Narrow $E_{\text{peak}}^{\text{ob}}$ distribution	-	-	V	-	
$E_{\text{peak}} - E_{\text{iso}}$ correlation	-	X-	X-	X-	
Low energy spectral index $\langle \alpha \rangle \approx -1$	X	X	-	V	

References

- Abdo, A.A., Ackermann, M., Ajello, M., *et al.*, 2009, ApJ, 706, L138
 Ackermann, M., Asano, K., Atwood, *et al.*, 2010, ApJ, 716, 1178

- Amati, L., Frontera, F., Tavani, M., *et al.*, 2002, A&A, 390, 81
Axelsson, M., Baldini, L., Barbiellini, G., *et al.*, 2012, ApJ, 757, L31
Band, D., Matteson, J., Ford, L., *et al.*, 1993, ApJ, 413, 281
Beloborodov, A.M., 2010, MNRAS, 407, 1033
Beloborodov, A.M., 2011, ApJ, 737, 68
Blandford, R., & Eichler, D., 1987, Phys. Rep., 154, 1
Cohen, E., Katz, J.I., Piran, *et al.*, 1997, ApJ, 488, 330
Drenkhahn, G., 2002, A&A, 387, 714
Drenkhahn, G., & Spruit, H.C., 2002, A&A, 391, 1141
Ghirlanda, G., Celotti, A., & Ghisellini, G., 2003, A&A, 406, 879
Ghirlanda, G., Ghisellini, G., & Lazzati, D., 2004, ApJ, 616, 331
Giannios, D., 2006, A&A, 457, 763
Giannios, D., 2008, A&A, 480, 305
Giannios, D., 2012, MNRAS, 422, 3092
Goldstein, A., Burgess, J.M., Preece, R.D., *et al.*, 2012, ApJS, 199, 19
Golenetskii, S.V., Mazets, E.P., Aptekar, R.L., & Ilinskii, V.N., 1983, Nature, 306, 451
Goodman, J., 1986, ApJ, 308, L47
Guiriec, S., Connaughton, V., Briggs, M.S., *et al.*, 2011, ApJ, 727, L33
Guiriec, S., Daigne, F., Hascoët, R., *et al.*, 2012 [ArXiv e-prints 1210.7252]
Haugbølle, T., 2011, ApJ, 739, L42
Ioka, K., Murase, K., Toma, K., Nagataki, S., & Nakamura, T., 2007, ApJ, 670, L77
Kaneko, Y., Preece, R.D., Briggs, M.S., *et al.*, 2006, ApJS, 166, 298
Larsson, J., Ryde, F., Lundman, C., *et al.*, 2011, MNRAS, 414, 2642
Lazzati, D., & Begelman, M.C., 2010, ApJ, 725, 1137
Lazzati, D., Morsony, B.J., & Begelman, M.C., 2009, ApJ, 700, L47
Lundman, C., Pe'er, A., & Ryde, F., 2013, MNRAS, 428, 2430
Meszaros, P., Laguna, P., & Rees, M.J., 1993, ApJ, 415, 181
Meszaros, P., & Rees, M.J., 1997, ApJ, 476, 232
Mészáros, P., Rees, M.J., & Papathanassiou, H., 1994, ApJ, 432, 181
Mizuta, A., Nagataki, S., & Aoi, J., 2011, ApJ, 732, 26
Morsony, B.J., Lazzati, D., & Begelman, M.C., 2007, ApJ, 665, 569
Nava, L., Ghirlanda, G., Ghisellini, G., & Celotti, A., 2011, A&A, 530, A21
Paczynski, B., 1986, ApJ, 308, L43
Paczynski, B., 1990, ApJ, 363, 218
Pe'er, A., 2008, ApJ, 682, 463
Pe'er, A., Mészáros, P., & Rees, M.J., 2005, ApJ, 635, 476
Pe'er, A., Mészáros, P., & Rees, M.J., 2006, ApJ, 642, 995
Pe'er, A., & Ryde, F., 2011, ApJ, 732, 49
Pe'er, A., Ryde, F., Wijers, R.A.M.J., *et al.*, 2007, ApJ, 664, L1
Pe'er, A., Zhang, B.-B., Ryde, F., *et al.*, 2012, MNRAS, 420, 468
Preece, R.D., Briggs, M.S., Giblin, T.W., *et al.*, 2002, ApJ, 581, 1248
Preece, R.D., Briggs, M.S., Mallozzi, R.S., *et al.*, 1998a, ApJ, 506, L23

- Preece, R.D., Briggs, M., Mallozzi, R.S., *et al.*, 2000, ApJS, 126, 19
Preece, R.D., Pendleton, G.N., Briggs, M.S., *et al.*, 1998b, ApJ, 496, 849
Rees, M.J., & Meszaros, P., 1992, MNRAS, 258, 41P
Rees, M.J., & Meszaros, P., 1994, ApJ, 430, L93
Ryde, F., 2004, ApJ, 614, 827
Ryde, F., 2005, ApJ, 625, L95
Ryde, F., Axelsson, M., Zhang, B., *et al.*, 2010, ApJ, 709, L172
Ryde, F., & Pe'er, A., 2009, ApJ, 702, 1211
Ryde, F., Pe'er, A., Nymark, T., *et al.*, 2011, MNRAS, 415, 3693
Sari, R., Piran, T., & Narayan, R., 1998, ApJ, 497, L17
Shemi, A., & Piran, T., 1990, ApJ, 365, L55
Sironi, L., & Spitkovsky, A., 2009, ApJ, 707, L92
Sironi, L., & Spitkovsky, A., 2011, ApJ, 726, 75
Spitkovsky, A., 2008, ApJ, 682, L5
Starling, R.L.C., Page, K.L., Pe'er, A., Beardmore, A.P., & Osborne, J.P., 2012, MNRAS, 427, 2950
Tavani, M., 1996, ApJ, 466, 768
Vurm, I., Beloborodov, A.M., & Poutanen, J., 2011, ApJ, 738, 77
Yonetoku, D., Murakami, T., Nakamura, T., *et al.*, 2004, ApJ, 609, 935
Zhang, B., & Pe'er, A., 2009, ApJ, 700, L65
Zhang, B.-B., Zhang, B., Liang, E.-W., *et al.*, 2011, ApJ, 730, 141
Zhang, W., Woosley, S.E., & MacFadyen, A.I., 2003, ApJ, 586, 356
Zhao, X.-H., Li, Z., & Bai, J.-M., 2011, ApJ, 726, 89

WIDE-BAND SPECTRA OF PROMPT EMISSION

K. Asano¹

Abstract. The Fermi observatory has detected GeV photons from several GRBs. Some of them show an extra spectral component, which is a hint for emission mechanism of GRBs. Here we discuss the GeV emission mechanism according to several promising models. The difference between models will appear in temporal evolution of the photon spectrum. To verify this, instruments that can obtain high photon statistics like CTA are desired. We also discuss the photosphere model, which is recently supported by wide-band observations with Fermi.

1 Introduction

The typical spectrum of GRB prompt emission is described by the “Band function”, which has a peak at 0.1–1 MeV in the νF_ν -diagram. Below and above this peak energy ε_p , the spectrum is well fitted by power-law functions with photon indices α and β , respectively. This spectral shape implies that most of energy is emitted in 0.1–1 MeV range. In the standard internal shock model, shock-accelerated electrons are injected in a relativistically expanding region. The energy distribution of the accelerated electrons at the injection is a power-law shape with a minimum energy $\gamma_m mc^2$. Those electrons emit synchrotron photons, and the peak energy ε_p corresponds to the typical synchrotron-photon energy emitted from the minimum-energy electrons. However, the physical mechanism that determines γ_m is not revealed yet. It is also strange that the peak energies in a burst do not show intense variance in most cases. The peak energies seem stable and tend to distribute in a narrow energy range. Since the cooling timescale is much shorter than the dynamical timescale, cooled electrons will distribute below $\gamma_m m_e c^2$. As a result, this model predicts $\alpha = -1.5$, but the typical observed photon index is -1 .

An alternative model is the photosphere model. Relativistic outflows driven by radiation pressure become optically thin at a certain radius. Thermal photons

¹ Interactive Research Center of Science, Tokyo Institute of Technology, 2-12-1 Ookayama Meguro-ku, Tokyo 152-8550, Japan

from this photosphere are responsible for the spectral peak in this model. So ε_p , which corresponds to the photon temperature at the photosphere, becomes less sensitive to model parameters. This agrees with the observed stability of the peak energy. To reconcile this model with the observed spectra, extra photon production above and below ε_p is needed in addition to the Planck-like thermal spectrum.

The simple Band function does not bring us so rich information on the unknown emission mechanism of GRBs. Wider-band spectra, such as GeV gamma-rays or optical photons, may give us some clue for the emission mechanism. Historically, the first photon detection other than keV–MeV band during the prompt phase is the optical emission from GRB 990123 (Akerlof *et al.* 1999). This was interpreted as the reverse shock emission due to interaction between the outflow and interstellar medium. However, considering the discovery of the shallow decay phase of the afterglow in the “Swift era”, the reverse shock emission may be not ubiquitous. The optical emission in GRB 990123 could have the same origin as the prompt gamma-ray emission. This possibility has been reinforced by subsequent optical detections, such as GRB 041219 or GRB 080319B (Racusin *et al.* 2008), in which optical variations seem to correlate with the gamma-ray fluxes. In such famous examples, the optical fluxes exceed the extrapolation from the Band function in X-ray range. One possible interpretation is that the optical photons are emitted via synchrotron emission and the gamma-ray emission is due to SSC (synchrotron self-Compton). Another possibility is hadronic models. Asano *et al.* (2010) interpreted that the optical emission in GRB 080319B is synchrotron emission from secondary electron-positron pairs produced via hadronic cascade, which is initiated by photopion production from accelerated protons.

Interestingly, both the SSC and hadronic models in GRB 080319B predict GeV emission via second-order SSC and the hadronic cascade, respectively. The simultaneous observation from optical to GeV is desired to determine the model of the optical components, which may constrain the emission mechanisms for the main component as well. But, unfortunately, such an example is not appeared yet. In this paper, we discuss deviations from the simple Band function mainly based on observations with the Fermi observatory.

2 Fermi 2008-2009

The Fermi gamma-ray observatory was successfully launched 2008, and have detected several fantastic GRBs accompanying bright GeV emission. Some of them show an extra spectral component in GeV band. In the case of short GRB 090510 (Ackermann *et al.* 2010), a spectral excess around 10 keV is also reported. This soft excess is consistent with the power-law extrapolation from the GeV extra component. If the magnetic field is relatively low, a simple SSC model can make a GeV excess. But the low-energy excess seems difficult to be reproduced by SSC models. Nevertheless, time-dependent simulations with very low magnetic field show that remnant electrons emit 10 keV synchrotron photons after the electron injection ends (Asano & Mészáros 2011).

Another remarkable feature the Fermi found is delayed onset of GeV emission relative to MeV gamma-rays. In GRB 090510, the first intense MeV pulse of 0.1 sec timescale does not have significant signals in LAT, while the second MeV pulse synchronizes a LAT pulse. In a long GRB, 080916C, the LAT lightcurve shows a \sim 4 sec delay in its onset relative to the GBM lightcurve (Abdo *et al.* 2009). The delayed GeV onsets arouse possibility that the GeV emission is due to an early onsets of afterglow (Ghisellini *et al.* 2010; Kumar & Barniol Duran 2010) If the initial Lorentz factor is as large as 1000, the onset of the kinetic energy dissipation due to the external shock becomes early. So the afterglow emission can start before the prompt emission ends. In this scenario, the GeV extra component is explained by synchrotron emission from the external shock. This is consistent with the observed long-lived GeV emission. However, the LAT-lightcurve in GRB 090926A show an intense spike, which seems to coincide with a MeV spike (Ackermann *et al.* 2011). In addition, Maxham *et al.* 2011 claim that the energy-injection rate the GBM lightcurve suggests is not enough to explain the GeV flux in the prompt phase. Thus, the origin of the early GeV emission is likely internal rather than external.

Two zone models have been proposed to explain both the extra spectral component and delayed onset in GeV range (Toma *et al.* 2009, 2011; Zou *et al.* 2011). Emission originated from an inner radius, such as the photospheric emission, constitutes the main Band component. A cocoon surrounding the jet can emit soft photons as well. An energy dissipation of the outflow occurs and electrons are accelerated in this outer region. Those electrons up-scatter photons from the inside regions, which is responsible for the GeV emission. The geometrical configuration in the two models, namely the spatial separation between the source of the soft photons and the site of the dissipation region, can cause the delayed arrival of the up-scattered soft photons. In such two-zone models, the photons coming from behind tend to be scattered backward in the outer shell frame. This enhances the flux from the off-axis region. Asano & Mészáros (2011) show that the GeV lightcurve in such two-zone models tends to have a long tail, which is due to the contribution of the off-axis emission

However, as seen in GRB 090217A (Ackermann *et al.* 2010b), not all LAT-GRBs show delayed onset of GeV emission. So we may not need to persist in the afterglow models or two-zone models for the GeV emission. Another possible option is emission initiated by the hadronic cascade. Accelerated protons collide with photons and produce pions. The neutral pions decay into high-energy gamma-rays, while charged pions emit synchrotron photons before they decay into muons. Most of such high-energy photons are absorbed via $\gamma\gamma$ -pair production. Secondary electron-positron pairs emit photons via synchrotron or inverse Compton (IC) processes. If we adopt the hadronic model to GRB 090510, the required proton energy much exceeds the observed gamma-ray energy (Asano *et al.* 2009). In this case, the extra component has a hard spectrum with a photon index -1.6 so that IC emission should be prominent to model the extra component by the hadronic cascade. Therefore, the magnetic field becomes very weak, which lowers the efficiency of photopion production. As a result, the required proton

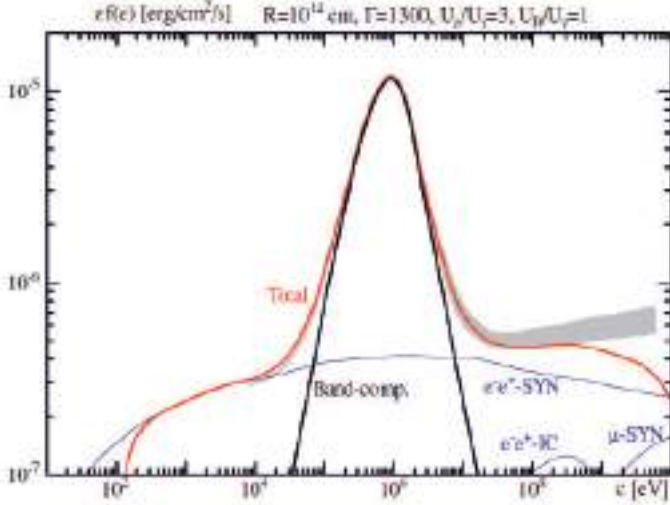


Fig. 1. Spectral fit by a hadronic model for GRB 090902B (Asano *et al.* 2010, ApJ, 725, L121).

luminosity is more than 100 times the gamma-ray luminosity. If the ultra-high energy cosmic rays (UHECR) above 10^{20} eV are mainly produced from GRBs, proton dominance in energy budget is required. The neutrino limit from GRBs with IceCube (Abbasi *et al.* 2012) seems severe for the UHECR-production scenario with GRBs, as claimed in Zhang and Kumar 2012. However, the neutrino flux largely depends on the model parameters such as Lorentz factor or emission radius (see *e.g.* Gao *et al.* 2012, and references therein). Considering the variety in parameters, the hadronic model seems still viable.

More plausible case for the hadronic model is GRB 090902B (Abdo *et al.* 2009b). In this case, the extra component has a flat spectrum, which dominates GeV and 10 keV regions. An IC component is not needed so that we can assume a strong magnetic field. Consequently, the required proton energy is comparable to the gamma-ray energy in MeV region (Asano *et al.* 2010, see Fig. 1).

Time-dependent simulations by Asano & Mészáros (2012) show that the hadronic GeV emission has a broader lightcurve than leptonic emission, and tends to delay relative to the MeV lightcurve (see Fig. 2). This tendency is due to the long acceleration timescale of protons and the continuous photopion production after the end of the particle injection.

In summary, each model has its own characteristic in the GeV lightcurve. The afterglow models predict smooth and featureless lightcurve, while GeV emission of internal origin may have a strong variability correlating with the MeV lightcurve. A long-tail in a GeV pulse may imply the two zone models with external Compton scattering. If we can statistically investigate the pulse onset

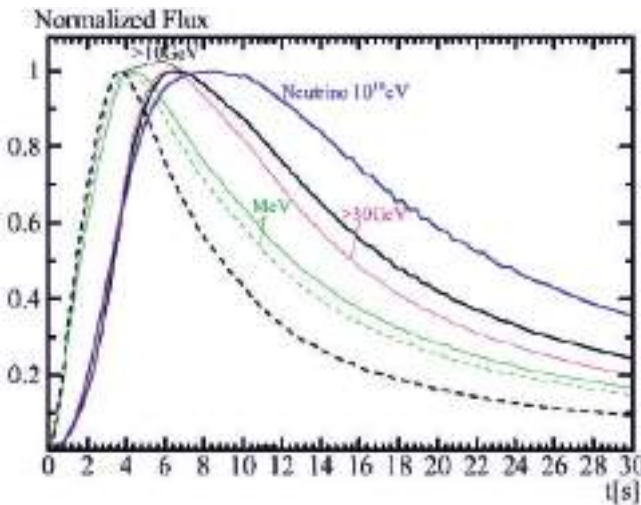


Fig. 2. Lightcurves for hadronic (solid) and leptonic (dashed) models (Asano & Mészáros 2012, ApJ, 757, 115).

and profile for GeV and MeV emissions, the difference in leptonic and hadronic models may be clarified.

Unfortunately, the effective area of the Fermi-LAT is not sufficient to distinguish the models. A future project of the air Cherenkov telescopes, CTA, will try to lower the energy threshold as low as ~ 30 GeV. The expected detection rate of GRBs with CTA is not so high. But if CTA detects a GRB, its high photon statistics bring us clue to determining the origin of the GeV emission (Inoue *et al.* 2012).

3 Fermi 2010-

Recently, the Fermi-LAT has not detected so intense GRBs. As the number of the GRB samples increases, the Fermi-LAT reveals that the extra-component in GeV range is not common for all GRBs (Ackermann 2012). The GRBs with extra components may belong to a particular group. However, by fitting the spectrum for a wide energy range, certain deviations from the Band function below ε_p have been found. Those spectra are said to be consistent with a superposition of the Band function and Planck spectrum.

Some authors claim that this implies the photospheric emission. For example, the time-resolved emission spectrum for GRB 110721A is well fitted by the Band function with an additional blackbody component (Axelsson *et al.* 2012). In this GRB, the initial peak energy $\varepsilon_p \sim 15$ MeV is the highest ever detected. The low-energy spectral index is about -1 , which is hard to be explained by the usual synchrotron model as we mentioned in Introduction. The dissipative photosphere models may explain this spectral shape. Some dissipation mechanism around the

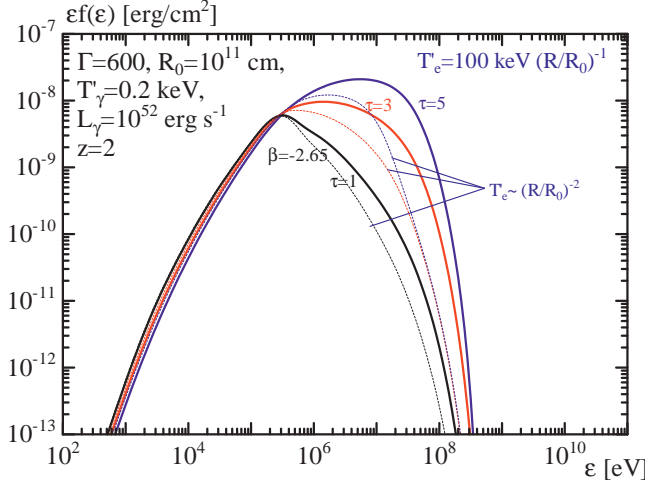


Fig. 3. Optical depth dependence in dissipative photosphere models. The electron temperature drops with proportional to R^{-1} (solid) and R^{-2} (dotted) (Asano & Mészáros in prep.).

photosphere heats electrons. Compton scattering by heated electrons may produce the Band-like spectrum with a 15 MeV peak.

However, the detected deviations from the Band function do not necessarily mean existence of the photospheric emission. Those spectra may be fitted with two Band functions. To begin with, it is not verified that the Band function is universal for the prompt emission. No model is assured to reproduce the Band spectrum so far. While the dissipative photosphere models are attractive, there is great uncertainty in the spectral shape. Beloborodov (2010) demonstrates the Band spectrum by a dissipation mechanism initiated by proton-neutron collisions. However, the spectral shape is sensitive to the model parameters. As shown in Figure 3, the parameter range that agrees with the Band function is very limited (Asano & Mészáros in prep.). In this calculation, the dissipation starts at $R = R_0$, and electron temperature is assumed to be evolved as $T = 100 \text{ keV} (R/R_0)^{-1}$ or $(R/R_0)^{-2}$. If the initial optical depth is larger than unity, photons are efficiently up-scattered above MeV. However, the resultant spectrum has a curved shape, which may be not consistent with the combination of the Band function and blackbody spectrum as claimed in GRB 110721A. On the other hand, a low initial optical depth results in poor efficiency to produce high-energy photons above ε_p . To verify the spectral curvature, we may need better photon statistics in 1–10 MeV energy range.

4 Hint on emission mechanism

As mentioned above, the most frequently discussed model to resolve the problem in the hard low-energy spectrum is the dissipative photosphere. The narrow Band

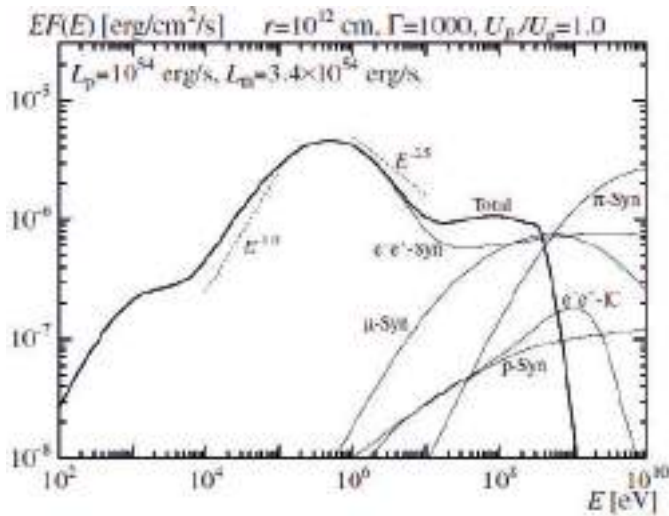


Fig. 4. Calculated spectrum for a turbulence heating/acceleration model with pp-induced hadronic cascade (Murase *et al.* 2012).

component in GRB 090902B (see Fig. 1) is an encouraging example for this model. However, the several detections of strong polarization (*e.g.* Yonetoku *et al.* 2012) are not advantageous for the photosphere model. The small radius and large Lorentz factor supposed in this model suggest a very short variability. But the typical variability timescale is ~ 0.1 sec. Therefore, the timescale of the engine activity should be so long that the outflow can be treated as a steady flow compared to the dynamical timescale at the photosphere.

Another model we recommend is continuous electron heating by turbulences. An internal shock due to a collision of two inhomogeneous shells can induce magnetohydrodynamical turbulence via the Richtmyer–Meshkov instability (Inoue *et al.* 2011). Such long-lived turbulences may heat/accelerate electrons via a similar process to the second-order Fermi acceleration. If this heating mechanism is effective, the balance between electron heating and cooling determines the typical energy of electrons. The synchrotron photon energy from the balanced electrons corresponds to the spectral peak energy. The resultant electron spectrum becomes hard, and the photon spectrum can be consistent with the low-energy spectral index (Asano & Terasawa 2009) Murase *et al.* (2012) demonstrate that a combination of this turbulent acceleration and high-energy electron injection due to pp-collision induced hadronic cascade at the photosphere can reproduce the Band function with low and high-energy extra components. In this model, the hadronic cascade can inject electrons in a high-energy region at which turbulence acceleration does not work because of synchrotron cooling. So the hard spectrum above ε_p and extra component are reproduced (see Fig. 4).

At present we do not have a convincing model to explain the Band spectrum yet. Each model has its advantages and disadvantages. In order to reveal the emission mechanism, future wide-band observations including temporal evolution will be indispensable.

I thank my collaborators, P. Mészáros, T. Terasawa, S. Inoue, K. Murase, S. Guiriec, T. Inoue, K. Ioka, and S. Gao. I am supported by Grants-in-Aid for Scientific Research No. 22740117 from the Ministry of Education, Culture, Sports, Science and Technology (MEXT) of Japan.

References

- Abdo, A.A., Ackermann, M., Arimoto, M., *et al.*, 2009, *Science*, 323, 1688
 Abdo, A.A., Ackermann, M., Ajello, M., *et al.*, 2009b, *ApJ*, 706, L138
 Abbasi, R., Abdou, Y., Abu-Zayyad, T., *et al.*, 2012, *Nature*, 484, 351
 Ackermann, M., Asano, K., Atwood, W.B., *et al.*, 2010, *ApJ*, 716, 1178
 Ackermann, M., Ajello, M., Baldini, L., *et al.*, 2010b, *ApJ*, 717, L127
 Ackermann, M., Ajello, M., Asano, K., *et al.*, 2011, *ApJ*, 729, 114
 Ackermann, M., Ajello, M., Baldini, L., *et al.*, 2012, *ApJ*, 754, 121
 Akerlof, C., Balsano, R., Barthelmy, S., *et al.*, 1999, *Nature*, 398, 400
 Asano, K., Guiriec, S., & Mészáros, P., 2009, *ApJ*, 705, L191
 Asano, K., Inoue, S., & Mészáros, P., 2010, *ApJ*, 725, L121
 Asano, K., & Mészáros, P., 2011, *ApJ*, 739, 103
 Asano, K., & Mészáros, P., 2012, *ApJ*, 757, 115
 Asano, K., & Mészáros, P., in preparation
 Asano, K., & Terasawa, T., 2009, *ApJ*, 705, 1714
 Axelsson, M., Baldini, L., Barbiellini, G., *et al.*, 2012, *ApJ*, 757, L31
 Beloborodov, A.M., 2010, *MNRAS*, 407, 1033
 Gao, S., Asano, K., & Mészáros, P., 2012, *JCAP*, 058
 Ghisellini, G., Ghirlanda, G., Nava, L., & Celotti, A., 2010, *MNRAS*, 403, 926
 Inoue, S., Granot, J., O'Brien, P.T., *et al.* (for the CTA Consortium), 2013, *Astrop. Phys.*, accepted
 Inoue, T., Asano, K., & Ioka, K., *ApJ*, 734, 77
 Kumar, P., & Barniol Duran, R., 2010, *MNRAS*, 409, 226
 Maxham, A., Zhang, B.B., & Zhang, B., 2011, *MNRAS*, 415, 77
 Murase, K., Asano, K., Terasawa, T., & Mészáros, P., 2012, *ApJ*, 746, 164
 Racusin, J.L., Karpov, S.V., Sokolowski, M., *et al.*, 2008, *Nature*, 455, 183
 Toma, K., Wu, X.-F., & Mészáros, P., 2009, *ApJ*, 707, 1404
 Toma, K., Wu, X.-F., & Mészáros, P., 2011, *MNRAS*, 415, 1663
 Yonetoku, D., Murakami, T., Gunji, S., *et al.*, 2012, *ApJ*, 758, L1
 Zhang, B., & Kumar, P., 2012 [[arXiv:1210.0647](https://arxiv.org/abs/1210.0647)]
 Zou, Y.-C., Fan, Y.-Z., & Piran, T., 2011, *ApJ*, 726, 2

GLOBAL PROPERTIES OF HIGH-ENERGY EMISSION FROM GAMMA-RAY BURSTS

N. Omodei¹, G. Vianello¹, F. Piron², V. Vasileiou², S. Razzaque³
and the Fermi Large Area Telescope collaboration

Abstract. In three years of observations the Large Area Telescope (LAT) on board the *Fermi* Gamma Ray Space Telescope has observed high-energy γ -ray emission from 35 gamma-ray bursts (GRBs). The first *Fermi*-LAT catalog of GRBs is in preparation within the *Fermi* LAT collaboration and will provide a systematic study of high-energy emission from GRBs. In this paper we present some of the main results, briefly discussing durations, energetics, time-resolved and time integrated LAT spectral analysis. We also discuss characteristics of LAT-detected emission such as its delayed onset and longer duration compared to emission detected by the GBM, and its power-law temporal decay at late times.

1 Introduction

The *Fermi* observatory was placed into orbit on 2008 June 11. It provides unprecedented breadth of energy coverage and sensitivity for advancing knowledge of GRB properties at high energies. It has two instruments: the Gamma-ray Burst Monitor (GBM; Meegan *et al.* 2009), comprised of twelve sodium iodide (NaI) and two bismuth germanate (BGO) detectors sensitive in the 8 keV–1 MeV and 150 keV–40 MeV respectively, and the Large Area Telescope (LAT; Atwood *et al.* 2009), a pair conversion telescope sensitive to γ rays in the energy range from \sim 20 MeV to \gtrsim 300 GeV. The wide field of view (\sim 2.4 sr at 1 GeV) of the LAT, its continuous observations in scanning mode, its broad energy range, its large effective area (\sim 6500 cm² on axis at usin $>$ 1 GeV), its low dead time per event (\sim 27 μ s), its efficient background rejection, and its good angular resolution

¹ Stanford University/KIPAC

² CNRS/IN2P3/LUPM

³ GMU/NRL

($\sim 0.8^\circ$ at 1 GeV) are vastly improved in comparison with those of EGRET. As a result, the LAT provides more GRB detections, higher statistics per detection, and more accurate localizations ($\lesssim 1^\circ$).

2 Properties of Gamma-Ray Burst emission at high energy

We have analyzed 3 years of *Fermi* LAT data using Pass 6 v3 Transient-event class above 100 MeV, significantly detecting 28 GRBs. We have also detected 7 additional GRBs using the “LAT Low Energy” (LLE) event class (Pelassa *et al.* 2010) which increases the effective area between ~ 20 MeV– ~ 1 GeV. While the rate of LAT GRBs is a small fraction of the rate of GRBs detected by the *Fermi*-GBM (Goldstein *et al.* 2012; Paciesas *et al.* 2012), there are unique features that emerge only at high energies. First we compute the onset time (T_{05}) and the duration (T_{90}) of the high-energy emission, and we compare our measurements with the durations reported in the GBM GRB catalog (Paciesas *et al.* 2012). In the left (right) panel of Figure 1 the >100 MeV LAT T_{05} (T_{90}) is compared to the GBM results (in the 50 keV–300 keV energy band).

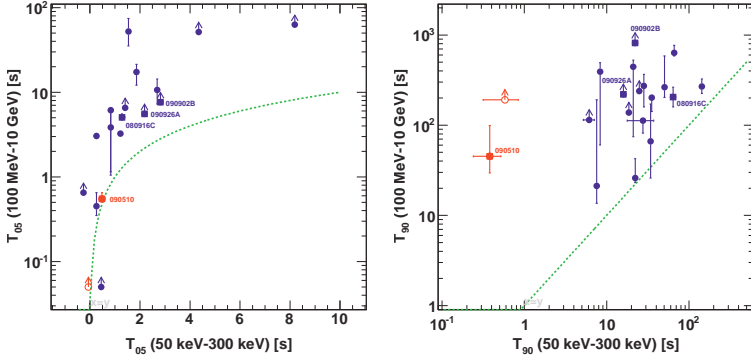


Fig. 1. *Left:* comparison between the >100 MeV T_{05} as measured using the LAT Transient class events and the 50 keV–300 keV T_{05} as measured by the GBM. *Right:* T_{90} . GBM data from Paciesas *et al.* (2012). Long (short) GRBs with filled blue (empty red) markers. Squares markers highlight the 4 brightest bursts (labeled).

We use the maximum likelihood technique implemented in the *Fermi* LAT ScienceTools to perform the spectral analysis from which we derive the fluences of the LAT GRBs. The left panel of Figure 2 shows the fluence measured by the LAT *versus* the fluence measured by the GBM. The bulk of the LAT GRB population, primarily composed of long GRBs, has a ratio of high- (100 MeV – 10 GeV) to low-energy (10 keV – 1 MeV) fluence $\lesssim 20\%$. It is interesting to note that short LAT-detected bursts (red markers) have a greater ratio of high- to low-energy fluence than the bulk of the long-GRB population (blue markers). In this figure,

we can see four hyper-fluent LAT bursts, GRBs 080916C, 090510, 090902B, and 090926A, having a more intense emission in the LAT energy range compared to the rest of the GRB population. It is worth examining whether the four brightest LAT bursts appear bright because they are systematically closer to us compared to the rest of the GRB population. To verify this, we calculate the E_{iso} in the 1 keV – 10 MeV rest frame energy range (shown as a function of the redshift in the right panel Fig. 2). The energy range matches that of previous works (Butler *et al.* 2007 for Swift bursts and Goldstein *et al.* 2012 for GBM bursts), allowing direct comparisons of E_{iso} . We find that the four brightest bursts also have the highest E_{iso} in their respective (long and short) categories.

Using LAT detections of GRBs, it has been discovered that extra power-law components are more common in GRBs compared to what was previously thought. More importantly, even if the high-energy emission can last longer than the usual keV-to-MeV emission, in some cases (GRBs 090510, 090902B, 090926A) it contributes significantly during the prompt phase. These two considerations suggest that the total energy budget at high energies can be an important fraction of the total energy reservoir.

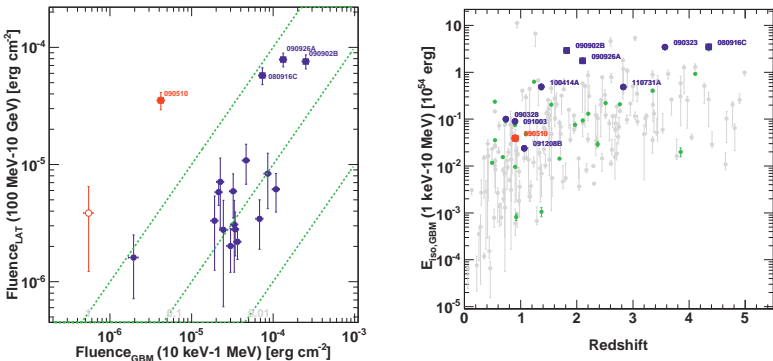


Fig. 2. *Left:* fluence measured by the LAT *versus* the fluence measured by the GBM. The three dashed lines denote the 100%, 10% and 1% fluence ratios. Colored symbols follow the convention of Figure 1. *Right:* isotropic energy in the 1 keV–10 MeV energy range of LAT-detected GRBs (blue/red symbols) compared with Swift GRBs (Butler *et al.* 2007) (grey dots) and GBM GRBs (Goldstein *et al.* 2012) (green).

To study the temporal decay of the extended emission detected by the LAT, we apply a time-resolved spectral analysis, and we compute the isotropic equivalent luminosity (as defined in Ghisellini *et al.* 2010) as a function of time, since the GBM trigger time. We then investigate the temporal decay by fitting the lightcurve with a simple power law or with a broken power law. Observations before the peak flux are excluded from the fit. In the left panel of Figure 3 we show all the detected long-lasting emissions, while in the right panel, we isolate the three GRBs (090510,

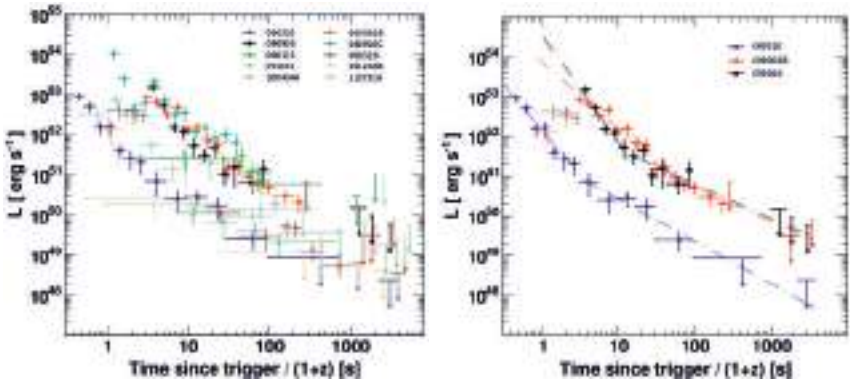


Fig. 3. *Left:* the decay of the luminosity L with time measured in the rest frame for all the GRBs with detected extended emission. *Right:* same quantity, but for 3 GRBs with a significant time break detected. Dashed-dotted lines are the best fits of the broken power law model to each GRB, while dashed crosses are the luminosities before the peak times.

090902B and 090926A) with a significant break detected in the lightcurve (chance probability smaller than 10^{-3}).

3 Discussion

In this study, we have presented some of the results that will be published in a LAT collaboration paper characterizing the high-energy emission of *Fermi*-LAT detected GRBs. Here we briefly discuss few important points.

The origin of the delayed onset of the LAT emission is poorly understood, but a possible interpretation is based on the early afterglow model for the temporally-extended LAT emission (De Pasquale *et al.* 2010; Ghisellini *et al.* 2010; Kumar & Barniol Duran 2009; Razzaque 2010). The bolometric flux from a coasting fireball increases as $\propto t^2$ (Sari 1997) before it decelerates and enters a self-similar phase (Blandford & McKee 1976; Rees & Meszaros 1994). The time required for the flux to increase and be detected by the LAT corresponds to the delay time in this scenario. The flux of LAT-detected emission at late times decays rather smoothly and can generally be fitted with a power law $F_\nu \propto t^{-\alpha_L}$. For three bright bursts (GRBs 090510, 090902B and 090926A), a broken power law fits the LAT data better than a single power law with the initial flux decay steeper than the later one, which is always close to $\alpha_L = 1$. In the context of the external shock, the bolometric flux decays as $\propto t^{-\alpha}$, with $\alpha = 1$ and $\alpha = 10/7$ for an adiabatic and a radiative fireball in a constant density environment (Ghisellini *et al.* 2010; Katz & Piran 1997; Sari 1997), respectively. A simple interpretation of $\alpha_L \approx 1$ flux decay-index for most LAT bursts suggests that the $\gtrsim 100$ MeV emission in

the long-lasting phase is more likely from an adiabatic fireball (De Pasquale *et al.* 2010; Kumar & Barniol Duran 2009; Razzaque 2010) rather than from a radiative fireball, as Ghisellini *et al.* (2010) had suggested. The observed break in the decay rate of the extended emission might be due to a transition from the prompt (internal shocks) to afterglow (external shock) emission.

Spectral analysis of bright bursts shows that the GRBs in which we detect with high significance a break in the lightcurves (GRBs 090510, 090902B and 090926A), also require an additional extra component (Abdo *et al.* 2009a,b; Ackermann *et al.* 2010, 2011; Giuliani *et al.* 2010). In these cases, the high-energy photon index of the Band function (β), is systematically softer (and more variable) than the photon index of the high energy extra component, indicating again a possible dichotomy between the prompt and the early afterglow.

Finally, the fluence of LAT GRBs (see Fig. 2) provides hints of two classes: a hyper-fluent class currently with four members (GRBs 080916C, 090510, 090902B, and 090926A); and a larger class with a lower typical fluence. The bolometric isotropic equivalent energy E_{iso} (see Fig. 2, right panel) is also higher for LAT bursts, suggesting that, in agreement with Cenko *et al.* (2011) and Racusin *et al.* (2011), LAT bursts possibly comprise the most energetic sub-sample of GRBs.

The *Fermi* LAT Collaboration acknowledges support from a number of agencies and institutes for both development and the operation of the LAT as well as scientific data analysis. These include NASA and DOE in the United States, CEA/Irfu and IN2P3/CNRS in France, ASI and INFN in Italy, MEXT, KEK, and JAXA in Japan, and the K.A. Wallenberg Foundation, the Swedish Research Council and the National Space Board in Sweden. Additional support from INAF in Italy and CNES in France for science analysis during the operations phase is also gratefully acknowledged.

References

- Abdo, A.A., Ackermann, M., Ajello, M., *et al.*, 2009a, ApJ 706, L138
- Abdo, A.A., Ackermann, M., Ajello, M., *et al.*, 2009b, Nature, 462, 331
- Ackermann, M., Ajello, M., Asano, K., *et al.*, 2011, ApJ, 729, 114
- Ackermann, M., Asano, K., Atwood, W.B., *et al.*, 2010, ApJ, 716, 1178
- Atwood, W.B., Abdo, A.A., Ackermann, M., *et al.*, 2009, ApJ, 697, 1071
- Blandford, R.D., & McKee, C.F., 1976, BAAS, Vol. 8, 539
- Butler, N.R., Kocevski, D., Bloom, J.S., & Curtis, J.L., 2007, ApJ, 671, 656
- Cenko, S.B., Frail, D.A., Harrison, F.A., *et al.*, 2011, ApJ, 732, 29
- De Pasquale, M., Schady, P., Kuin, N.P.M., *et al.*, 2010, ApJ, 709, L146
- Ghisellini, G., Ghirlanda, G., Nava, L., & Celotti, A., 2010, MNRAS, 403, 926
- Giuliani, A., Fuschino, F., Vianello, G., *et al.*, 2010, ApJ, 708, L84
- Goldstein, A., Burgess, J.M., Preece, R.D., *et al.*, 2012, ApJS, 199, 19
- Katz, J.I., & Piran, T., 1997, ApJ, 490, 772
- Kumar, P., & Barniol Duran, R., 2009, MNRAS, 400, L75

- Meegan, C., Lichti, G., Bhat, P.N., *et al.*, 2009, ApJ, 702, 791
Paciesas, W.S., Meegan, C.A., von Kienlin, A., *et al.*, 2012, ApJS, 199, 18
Pelassa, V., Preece, R., Piron, F., *et al.*, 2010 [[ArXiv e-prints](#)]
Racusin, J.L., Oates, S.R., Schady, P., *et al.*, 2011, ApJ, 738, 138
Razzaque, S., 2010, ApJ, 724, L109
Rees, M.J., & Meszaros, P., 1994, ApJ, 430, L93
Sari, R., 1997, ApJ, 489, L37

ON AMATI RELATION FOR GRB PROMPT EMISSION

L. Titarchuk¹ and R. Farinelli¹

Abstract. We propose a model for the spectral formation of Gamma Ray Burst (GRB) prompt emission, where the phenomenological Band function is usually applied to describe the GRB prompt emission. We suggest that the GRB prompt emission is mainly a result of the Comptonization of relatively soft photons of the star off electrons of a hot shell of plasma of temperature of the order of 10^9 K (or ~ 100 keV) that moves sub-relativistically with the bulk velocity substantially less than the speed of light. In this case, the Comptonization parameter is high and the interaction between a blackbody-like soft seed photon population and hot electrons leads to formation of a saturated Comptonization spectrum. We give an interpretation of the Amati relation between the intrinsic spectral peak photon energy and radiated energy or luminosity.

1 Introduction

Understanding the physical processes which give rise to the observed spectra of the prompt emission of Gamma Ray Bursts (GRB) is presently one of the most exciting issues studied by both the theoretical and observational community. The Band function (Band *et al.* 1993) up to now widely used to describe their prompt emission is a pure phenomenological model. It consists of two low-energy and high-energy power laws with photon index Γ_1 and Γ_2 , respectively, smoothly joined at some energy E_b . We offer a model to explain the GRB prompt spectral formation in the context of a photospheric scenario in which the main process is the Comptonization of the relatively soft photons of the star by a hot sub-relativistic outflow of velocity V_b within an area close to the photospheric radius (optical depth of 3–5) likely symmetric with respect to the rotational axis of the star (see Fig. 1 for illustration of our model). We use the theoretical and numerical results of the Comptonization problem reported in Titarchuk *et al.* (1997) and Farinelli *et al.* (2008) and finally in Titarchuk *et al.* (2012, hereafter TFFA12) for the case of

¹ Dipartimento di Fisica, Università di Ferrara, via Saragat 1, 44122 Ferrara, Italy

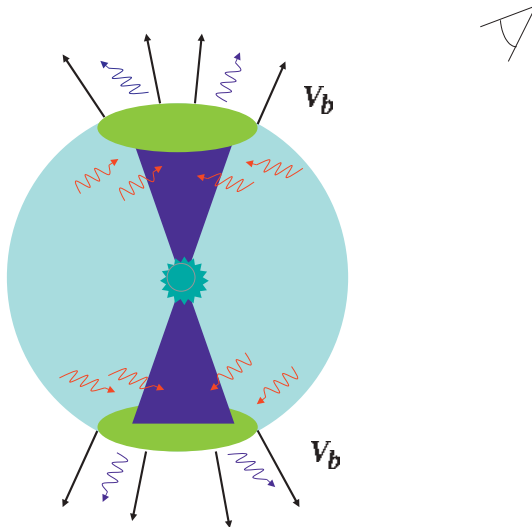


Fig. 1. X-ray spectral formation during explosion of a massive star (see also TFFA12).

an early subrelativistic bulk outflow phase produced during the supernova explosion. In Section 2 we demonstrate that our upscattering model of GRB radiation reproduces the Amati relation between the $EF(E)$ peak energy E_p and the GRB radiated energy E_{iso} or luminosity L_{grb} . In Section 3 we draw our conclusions.

2 The Amati relation and its interpretation

In spite of the still open discussion about the impact of possible selection effects on the correlation between the peak energy of $EF(E)$ diagram E_p and the GRB radiated energy or luminosity (Amati *et al.* 2002) it is a matter of fact that all GRBs with known redshifts, but one (GRB 980425), follow this relation (Amati *et al.* 2009). Thus it is crucial to understand the origin of this relation, namely which is the mechanism (at first glance universal) which gives rise to the relation $E_p \propto E_{iso}^{1/2}$ where E_p and E_{iso} are the peak energy of $EF(E)$ diagram and isotropic radiated energy (fluence) of GRB respectively during the prompt phase.

The main issue to be investigated is to check how the parameters of our model concur in determining the energy peak value E_p in the $EF(E)$ diagram and the total luminosity L_{grb} which integral over prompt emission time is E_{iso} . In Figure 2 we show the resulting Comptonization spectra which also include effect of the early sub-relativistic phase. The spectra becomes softer when the bulk parameter δ increases from 0.5 to 0.95 (see TFFA12 for details). We should emphasize that E_p is independent of values of the BB-like seed photon temperature kT_{bb} . Thus

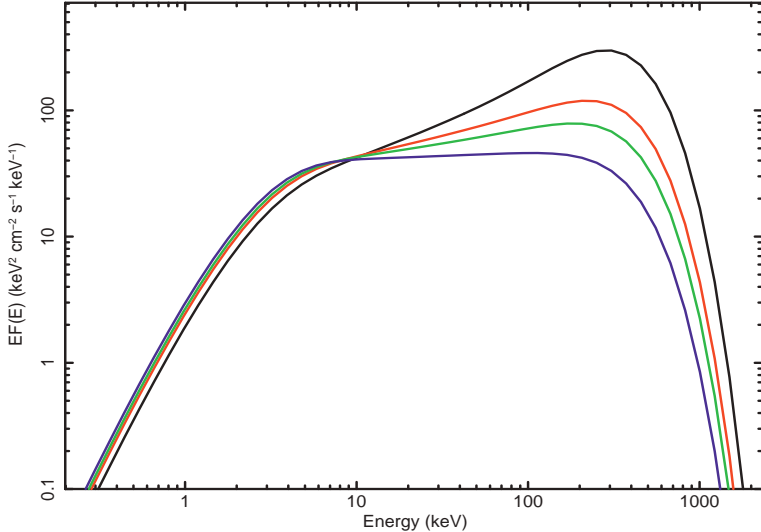


Fig. 2. Saturated Comptonization spectra modified by subrelativistic outflow (see TFFA12).

different values of kT_{bb} do not change E_p , but they determine the total (resulting) luminosity, as we discuss below.

The question that naturally arises is whether the observed dependence of E_p on E_{iso} (or on luminosity L_{grb}) and its intrinsic dispersion (Amati *et al.* 2008) is the fundamental effect of γ -ray emission.

As an example, in Figure 3 we report the results of the fit using our model (see TFFA12) of the time averaged prompt emission spectrum of GRB 990705 obtained with *BeppoSAX*.

The values of the best fit parameters of our model correspond to the case of the saturated Comptonization for which the resulting spectral index $\alpha \ll 1$ (see details in TFFA12). Sunyaev & Titarchuk 1980, 1985 derive the formula for the Comptonization enhancement factor η_{comp} which is a ratio of the resulting luminosity, that is in our case, the GRB luminosity L_{grb} to the injected luminosity of soft photons L_{soft} .

Namely

$$\eta_{\text{comp}} = \frac{L_{\text{grb}}}{L_{\text{soft}}} = q_{x_0}(\alpha) x_0^{\alpha-1} \quad (2.1)$$

where

$$q_{x_0}(\alpha) = \frac{\alpha(\alpha+3)\Gamma(\alpha+4)\Gamma(\alpha)\Gamma(1-\alpha)}{\Gamma(2\alpha+4)}(1-x_0^{1-\alpha}), \quad (2.2)$$

$x_0 = 2.7 kT_{\text{bb}}/kT_e$, kT_e is the electron temperature of the hot Compton spot (see Fig. 1) and $\Gamma(x)$ is the Gamma function. Thus when $\alpha \ll 1$

$$\eta_{\text{comp}} \propto kT_e. \quad (2.3)$$

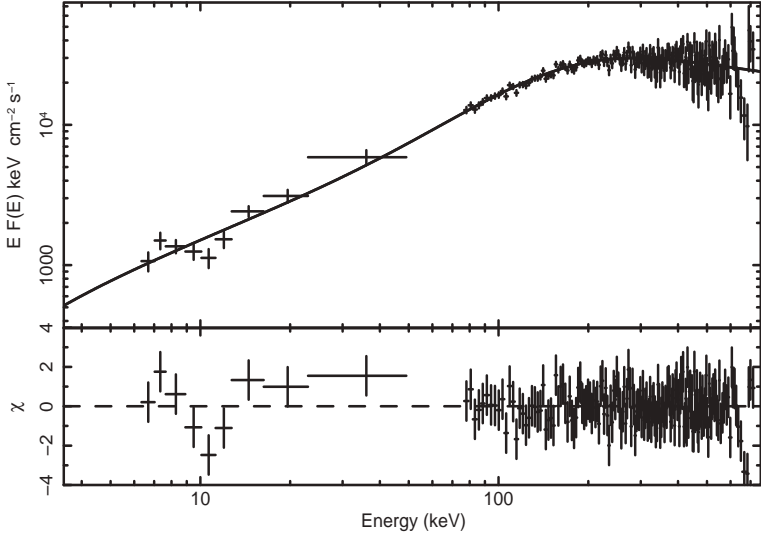


Fig. 3. The best-fit of $E F(E)$ BeppoSAX/WFC+GRBM diagram of GRB 990705 (see TFFA12).

But the flux of soft photons illuminating the hot spot (Compton cloud) L_{soft} is

$$L_{\text{soft}} = \pi B_{\text{soft}} S_{\text{hs}} \quad (2.4)$$

where B_{soft} is the intensity of the blackbody radiation of the star and S_{hs} is the surface area of Compton hot spot (see Fig. 1).

The thermal wave propagates in the hot spot with plasma velocity V_p whose value can change from one GRB to another.

As a consequence for each GRB $S_{\text{hs}} \propto (V_p t)^2$ (see Fig. 1) and then

$$S_{\text{hs}} \propto V_p^2 \propto kT_p = kT_e. \quad (2.5)$$

Thus the luminosity of the GRB hot spot L_{grb} should be

$$L_{\text{grb}} = \eta_{\text{comp}} L_{\text{soft}} \propto (kT_e)^2. \quad (2.6)$$

In order to calculate the GRB fluence $E_{\text{iso,grb}}$ one should integrate L_{grb} over the GRB prompt emission time T_{pr} , namely

$$E_{\text{iso}} = \int_0^{T_{pr}} L_{\text{grb}}(t) dt. \quad (2.7)$$

If the time-scale of the GRB prompt emission and its shape is more less the same for any burst then $E_p (\propto kT_e)$ is $E_{\text{iso}}^{1/2}$ which is precisely seen in the Amati relation (see Amati *et al.* 2002).

3 Discussion and conclusion

We have developed a spectral model aimed to describe the broadband prompt emission of GRBs. We propose that the spectral emission during the prompt phase, phenomenologically modeled by the Band function, is the result of an earlier phase where soft BB-like photons are Comptonized by an optically thick and hot electron shell ($T_e \sim 10^9$ K), something like a Compton cloud sub-relativistically moving outwards the star surface. On the other hand in the relativistic phase, these Comptonized photons are subjected to a second upscattering process which can be mathematically described by a broken powerlaw Green function whose spectral index models the high-energy slope of the Band function. An important prediction of our proposed model is that the peak energy in the EF(E) diagram originated in the early subrelativistic phase (see Fig. 1) is directly related to the plasma temperature of the hot plasma T_e . We demonstrate that *the resulting luminosity of X/ γ -rays luminosity of GRB L_{grb} is proportional to $(kT_e)^2$* (see Eq. (2.6)).

In fact, L_{grb} is a product of the Comptonization enhancement factor η_{comp} and luminosity of the soft blackbody photons $L_{bb,il}$ but in the case of the saturated Comptonization, when $\alpha \ll 1$, $\eta_{\text{comp}} \propto kT_e$ (see Eq. (2.1)) but $L_{bb,il}$ (or L_{soft}) is also proportional to kT_e because the surface area of Compton cloud illuminated by the soft photons is proportional to kT_e (see Eq. (2.5)). Thus we claim that the model dependence of $L_{\text{grb}} \propto (kT_e)^2$ on the hot plasma temperature T_e explains the observed Amati relation in which $E_{iso} = \int L_{\text{grb}}(t) dt \propto E_p^2$. It is worth noting that the peak energy E_{peak} of the emergent Wien spectrum should be equal to $3kT_e$ or $E_p = E E_{peak} = 4kT_e$ for $EF(E)$ -diagram.

An important prediction of our model is that the peak energy in the EF(E) diagram originates in the early sub-relativistic phase and is proportional to plasma temperature kT_e and the resulting luminosity L_{grb} is proportional to $(kT_e)^2$. This dependence is the same, after cosmological corrections, in the source and observer frame. In fact, no fine tuning related to some Lorentz Γ -factor of relativistic expansion is required. We claim that this result of our model *naturally* explains the physical origin of the Amati relation.

References

- Amati, L., Frontera, F., & Guidorzi, C., 2009, A&A, 508, 173
- Amati, L., Guidorzi, C., Frontera, F., et al., 2008, MNRAS, 391, 577
- Amati, L., Frontera, F., Tavani, M., et al., 2002, A&A, 390, 81
- Band, D., Matteson, J., Ford, L., et al., 1993, ApJ, 413, 281
- Farinelli, R., Titarchuk, L., Paizis, A., & Frontera, F., 2008, ApJ, 680, 602
- Sunyaev, R.A., & Titarchuk, L.G., 1980, A&A, 86, 121 (ST80)
- Sunyaev, R.A., & Titarchuk, L.G., 1985, A&A, 143, 374
- Titarchuk, L., Farinelli, R., Frontera, F., & Amati, L., 2012, ApJ, 752, 116 (TFFA12)
- Titarchuk, L., Mastichiadis, A., & Kylafis, N.D., 1997, ApJ, 487, 834

RELATIVISTIC FILAMENTATION INSTABILITY IN AN ARBITRARILY ORIENTED MAGNETIC FIELD

E. Pérez-Álvaro¹ and A. Bret¹

Abstract. Although high-energy cosmic rays (HECRs) and gamma-ray bursts (GRBs) are the most energetic phenomena occurring in the universe, their origin are important enigmas in the field of astrophysics. Today, the most studied scenario that attempts to explain them is known as the Fireball Model. This theory assumes that the particles are accelerated by a shock developing in the interior of a relativistic plasma from a supernova (SN). The filamentation (sometimes called “Weibel”) instability is believed to mediate collisionless shock formation from the collision of two plasma shells. It has been known for long that a flow aligned magnetic field can completely cancel this instability. In this work, we analyze the robustness of the filamentation instability which develops inside a plasma immersed in an arbitrarily oriented magnetic field.

1 Introduction

According to the Fireball Model, the GRBs generation mechanism is obtained when a central source releases a large amount of fluid consisting of electrons, positrons and in some cases contaminated by baryons (protons) in a very short time in a very small region (about 10^{12} cm). The plasma moving at relativistic speed is what is called Fireball. Inside the Fireball, shocks can develop in which the particles can be accelerated by means of electromagnetic interaction Narayan (1992). These shocks are generated when internal layers of the fireball come into contact. Particles accelerated by the shock begin to emit synchrotron radiation. In the Fireball, electromagnetic instabilities appear to be important for the development of electromagnetic shock. This phenomenon has been studied with numerical simulations Silva (2003) and it has been verified that the filamentation instability (which k is normal to the flow), is responsible for the shock development.

¹ ETSI Industriales, University of Castilla-La Mancha, Institute of Energetics Investigations and Industrial Applications, 13071 Ciudad Real, Spain

Within a magnetized medium, nearly all works consider a magnetic field \mathbf{B}_0 parallel to the movement, even though in real conditions, a magnetic field is not perfectly aligned. In the case of the collision of two plasmas in a magnetic field parallel to the direction of propagation, the filamentation instability is canceled from a critical value of the field Godfrey (1975). At this point, we want to investigate the development of the filamentation instability immersed in a magnetic field oriented arbitrarily in order to determine whether such suppression of this instability persists Bret & Perez Alvaro (2011).

2 Formalism and dispersion equation

We consider two identical electron-proton plasmas, with density n and traveling along the same direction of motion (z axis) but in opposite directions with same speed \mathbf{V}_0 and corresponding Lorentz factor $\gamma_0 = (1 - \mathbf{V}_0^2/c^2)^{-1/2}$. Being θ the angle between the magnetic field \mathbf{B}_0 and the flow, the magnetic field is defined as $\mathbf{B}_0 = B_0 \sin(\theta) \mathbf{u}_x + B_0 \cos(\theta) \mathbf{u}_z$. Since the mass of the proton is much greater than that of the electrons and the Lorentz factor is the same for both, we consider proton mass infinite.

We work in the cold fluid approximation and therefore the conservation and momentum equations for electrons are given by:

$$\frac{\partial n}{\partial t} + \nabla \cdot (n \mathbf{V}) = 0 \quad (2.1)$$

$$\frac{\partial \mathbf{p}}{\partial t} + (\mathbf{V} \cdot \nabla) \mathbf{p} = q \left[\mathbf{E} + \frac{\mathbf{V} \times (\mathbf{B} + \mathbf{B}_0)}{c} \right] \quad (2.2)$$

where $\mathbf{p} = \gamma m \mathbf{V}$, q and m are the momentum, charge and mass of the electron respectively. These equations were linearized thanks to a standard process Bret & Perez Alvaro (2011) and introduced in the expression for de current $\mathbf{J}_1 = q \sum_{j=1,2} (n_{j0} \mathbf{V}_{j1} + n_{j1} \mathbf{V}_{j0})$ where $j = 1, 2$ represents each plasma. In the same way the Maxwell-Faraday equation is linearized and introduced in the Maxwell-Ampere equation, to obtain:

$$\frac{c^2}{\omega_p^2} \mathbf{k} \times (\mathbf{k} \times \mathbf{E}_1) + \mathbf{E}_1 + \frac{4i\pi}{\omega} \mathbf{J}_1 = 0. \quad (2.3)$$

Equation (2.3) is tensorial of the form $T(\mathbf{E}_1) = 0$. The dispersion equation was obtained from $\det(T) = 0$ Bret & Perez Alvaro (2011). In addition, we used the dimensionless parameters $\mathbf{Z} = \frac{\mathbf{k} \mathbf{V}_0}{\omega_p}$, $x = \frac{\omega}{\omega_p}$, $\beta = \frac{V_0}{c}$ and $\Omega_B = \frac{\omega_p}{\omega_b}$ where $\omega_p^2 = \frac{4\pi n q^2}{m}$ is the electronic plasma frequency and $\omega_b = \frac{|q| B_0}{mc}$ the cyclotron frequency.

3 Results and analytical expressions

Filamentation instability grows exponentially like $e^{\delta t}$, where δ is the growth rate which is obtained by solving the dispersion equation $\det(T) = 0$, and taking the

imaginary part of the solution ω . To analyze the results, we observed the dependence of δ with the magnetic field parameter Ω_B and the reduced wave vector Z in different three-dimensional representations that were obtained for angles θ between $[0, \frac{\pi}{2}]$. Some examples for these 3D representations can be seen in Figure 1.

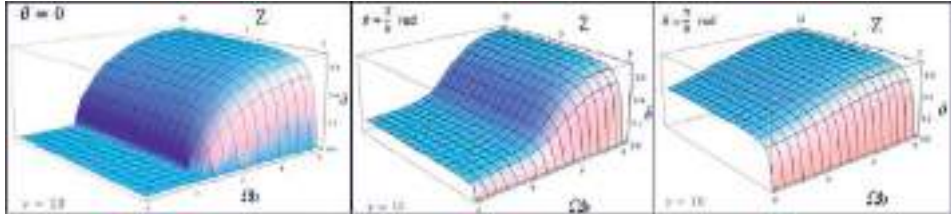


Fig. 1. Growth rate δ as a function for the magnetic field parameter Ω_B and reduced wave vector Z , with $\gamma = 10$. Left to right $\theta = 0$, $\theta = \frac{\pi}{6}$ and $\theta = \frac{\pi}{3}$.

Analyzing these representations, we notice the growth rate reaches a maximum for $Z \rightarrow \infty$, and compute the dispersion equation in this limit. This maximum growth rate can be evaluated analytically and reads δ^* :

$$\delta^* = \sqrt{\frac{2\beta^2 \sin^2(\theta)}{\gamma^3 \cos^2(\theta) + \gamma \sin^2(\theta)}}. \quad (3.1)$$

Using a Taylor expansion in the expression of the growth rate for weak magnetization, we obtain the value of the parameter of the critical field Ω_B^* beyond which the growth rate saturates:

$$\Omega_B^* = \frac{2\beta\sqrt{\gamma}}{\cos(\theta)}. \quad (3.2)$$

4 Conclusion

These results were obtained under various assumptions: cold plasmas, protons with infinite mass and identical plasmas. The Fireball model attempts to explain the origin of HECRs and GRBs assuming a shock develops within a relativistic plasma from a supernova can accelerate particles. Without the Filamentation instability the shock would not develop. We show in this paper that the filamentation instability can be canceled only if the motion of plasma and the magnetic field are fully aligned.

References

- Bret, A., & Pérez-Álvaro, E., 2011, Phys. Plasma, 18, 080706
- Godfrey, B.B., Shanahan, W.R., & Thode, L.E., 1975, Phys. Fluids, 18, 346
- Narayan, R., Paczynski, B., & Piran, T., 1992, ApJ, 395, L83
- Silva, L.O., Fonseca, R., Tonge, J.W., et al., 2003, ApJ, 596, L121

Chapter IV.
Jet Dynamics

GAMMA-RAY BURST JET DYNAMICS

J. Granot¹

Abstract. This is a brief review of some recent progress in our understanding of GRB jet dynamics, during the early acceleration phase and the later afterglow phase. In the acceleration phase I focus on the possible role of impulsive magnetic acceleration, and its ability to convert most of the initial magnetic energy into kinetic energy and naturally produce efficient internal shocks at mild magnetizations. For the afterglow phase I outline new generalized yet simple analytic models that finally agree with numerical simulations, and present recent simulation results for a jet propagating into a stratified external medium.

1 Introduction

GRB outflows are expected to be collimated into narrow bipolar jets, in analogy to other astrophysical relativistic outflow sources, such as active galactic nuclei (AGN) and micro-quasars (*e.g.*, Rhoade 1997). However, unlike some of these other sources GRB outflows are almost always unresolved, point sources, so there is only indirect evidence for jets in GRBs. Collimation into narrow jets can alleviate the “energy crisis” that arises from their very large energy outputs in γ -rays assuming isotropic emission, $E_{\gamma,\text{iso}}$ (the current record being $E_{\gamma,\text{iso}} \approx 4.9 M_{\odot} c^2$ for GRB 080916C; Abdo *et al.* 2009). If most of the γ -rays are emitted within a small fraction, $f_b \ll 1$, of the total solid angle (where $f_b \approx \theta_0^2/2$ for conical uniform narrow bipolar jets of initial half-opening angle θ_0), then the true energy output in γ -rays, E_{γ} , is much smaller than its isotropic equivalent value, $E_{\gamma} = f_b E_{\gamma,\text{iso}}$.

The angular structure of GRB outflows is important for inferring their true energy output and event rate, as well as properties of their central engine. Moreover, the jet structure and dynamics are crucial for correctly modeling and interpreting observations, and inferring from them important physical parameters such as the external density profile and the microphysical parameters of relativistic collisionless shocks. Nevertheless, the jet angular structure is still not very well constrained

¹ Department of Natural Sciences, The Open University of Israel, 1 University Road, PO Box 808, Raanana 43537, Israel

observationally, despite various efforts (*e.g.*, Granot 2005, 2007). Here I focus on the dynamics of a double-sided jet that is initially uniform with sharp edges and a half-opening angle $\theta_0 \ll 1$, which is the most widely studied jet angular structure.

The dynamics of GRB jets can be divided into several different parts or stages:

- **Launching:** the launching of the jet is likely magnetic, possibly due to the Blandford-Znajek mechanism operating in a newly formed, rapidly accreting stellar mass black hole, or an MHD pulsar-type wind for a millisecond magnetar central engine; neutrino - anti-neutrino annihilation may also play an important role. This first stage is still not very well understood.
- **Acceleration:** the two main candidates for the dominant acceleration mechanism are thermal acceleration (by the radiation pressure in an optically thick electron-positron, photon and baryon plasma – the fireball model) and magnetic acceleration (which is discussed in Sect. 2).
- **Propagation inside the progenitor star** (for GRBs of the long-soft class).
- **Collimation:** the jet collimation can be assisted by the interaction with the external medium, and in particular with the progenitor star for long GRBs, by the accretion disk wind, and by magnetic hoop stress.
- **Coasting** phase, which ends at the deceleration radius R_{dec} (expected for thermal acceleration, but does not always exist for magnetic acceleration).
- **Relativistic self-similar:** at $R > R_{\text{dec}}$ most of the energy is in the shocked external medium, the outflow composition and radial profile are essentially forgotten, but the angular profile persists. Locally, however, the flow approaches the Blandford & McKee (1976) spherical self-similar solution.
- **Sideways expansion:** once Γ drops below $1/\theta_0$, at radii $R > R_j$, significant jet lateral expansion is possible, but it is unclear to what extent it occurs in practice (this is discussed in detail in Sect. 3).
- **Newtonian self-similar:** eventually the flow becomes Newtonian and spherical, approaching the Sedov-Taylor self-similar solution.

Here the focus is on recent progress in our understanding of impulsive magnetic acceleration (in Sect. 2), and of the jet dynamics during the afterglow stage (in Sect. 3).

2 Magnetic acceleration: The role of strong time dependence

The two main competing acceleration mechanisms for GRB outflows are thermal and magnetic acceleration. Moreover, magnetic acceleration likely plays a key role also in other relativistic jet sources, such as AGN or micro-quasars. It was realized early on that the collimation and acceleration of initially very hot and high-pressure material near the source to highly super-sonic speeds (*e.g.* the

“twin exhaust” model for AGN jets; Blandford & Rees 1974) faces difficulties under realistic astrophysical conditions (it is subject to various instabilities; Smith *et al.* 1981). Hence, magnetic fields play an important role in many models for the launching, collimation and acceleration of relativistic jets. Most such models assume a steady flow, both as this may adequately describe outflows that vary slowly enough with time, and since it significantly simplifies the relevant dynamical equations and allows analytic self-similar solutions (*e.g.* Begelman & Li 1992; Vlahakis & Königl 2003). Strong magnetic fields near the source may also help avoid excessive mass loading and thus enable the jets to reach relativistic speeds.

A highly magnetized steady spherical flow accelerates only up to an asymptotic Lorentz factor $\Gamma_\infty \sim \sigma_0^{1/3}$ and magnetization $\sigma_\infty \sim \sigma_0^{2/3}$ (Goldreich & Julian 1970) where $\sigma_0 \gg 1$ is the initial value of the magnetization parameter σ (the ratio of electromagnetic to matter energy fluxes or enthalpy densities), *i.e.* most of the energy remains in electromagnetic form (a Poynting flux dominated flow). Collimation by an external pressure leading to an asymptotic jet half-opening angle θ_j can increase Γ_∞ and decrease σ_∞ by up to a factor of $\sim \theta_j^{-2/3}$, since lateral causal contact in the jet is maintained if θ_j does not exceed the Mach angle ($\theta_j \lesssim \theta_M \sim \sigma^{1/2}/\Gamma$, where energy conservation implies $\sigma\Gamma \sim \sigma_0$ as long as the flow remains highly magnetized, $\sigma \gg 1$). However, even under the most favorable conditions the asymptotic magnetization is $\sigma_\infty \geq 1$, which does not allow efficient energy dissipation in internal shocks within the outflow (Lyubarsky 2009, 2010a; Komissarov *et al.* 2009). A sudden drop in the external pressure, as may occur *e.g.* when a GRB jet exits its progenitor star, can result in a sudden additional acceleration (Komissarov *et al.* 2010; Tchekhovskoy *et al.* 2010) that can lead to $\Gamma_\infty \theta_j \gg 1$ as inferred in GRBs, but still with $\sigma_\infty \geq 1$.

These limitations of the “standard” steady, axi-symmetric and non-dissipative (or ideal MHD) magnetic acceleration have, on the one hand, led to the suggestion that the jets might remain Poynting flux dominated at large distances from the source and the observed emission is the result of magnetic reconnection events rather than internal shocks (Blandford 2002; Lyutikov 2006). On the other hand, other models suggested increasing the acceleration efficiency by relaxing one of the standard assumptions, such as axi-symmetry – leading to non-axi-symmetric instabilities that randomize the magnetic field orientation (Heinz & Begelman 2000). A highly tangled magnetic field effectively behaves like a relativistic fluid (with an adiabatic index of 4/3) and leads to efficient acceleration, similar to thermal acceleration of relativistic outflows. Moreover, both the kink instability mentioned above (Drenkhahn & Spruit 2002), as well as other instabilities (such as the Kruskal-Schwarzschild instability in a striped wind; Lyubarsky 2010b) can lead to magnetic reconnection, *i.e.* gradual magnetic dissipation, which in turn enhances the acceleration due to the conversion of magnetic to thermal energy, where the thermal pressure efficiently accelerates the outflow.

A natural alternative is replacing the usual steady-state assumption by strong time-dependence. This impulsive regime was sparsely studied, and mainly in the non-relativistic case (Contopoulos 1995). Recently, a new impulsive magnetic

acceleration mechanism was found that operates in the relativistic case (Granot *et al.* 2011), which can be much more efficient than magnetic acceleration in steady flows, and can lead to low magnetizations, $\sigma \ll 1$, thus enabling efficient dissipation in internal shocks. This qualitatively different behavior of impulsive outflows can be very relevant for GRBs, as well as for other relativistic jet sources such as tidal disruptions or flares in AGN or micro-quasars, or even giant flares in soft gamma repeaters (SGRs, thought to be magnetars – highly magnetized neutron stars). It also triggered renewed interest in this topic (*e.g.* Granot 2012a,b; Komissarov 2012; Levinson 2010; Lyutikov 2011).

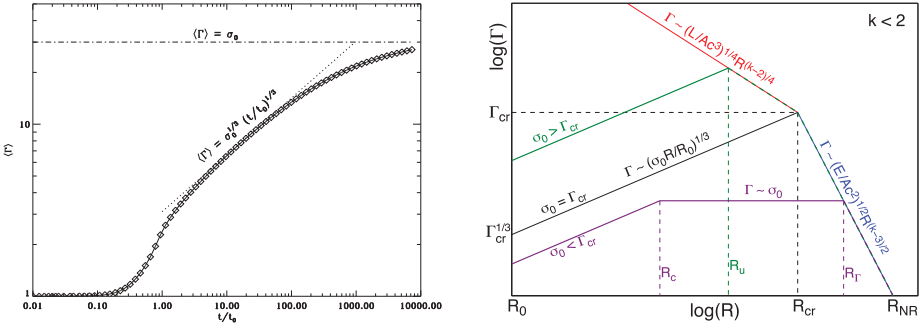


Fig. 1. *Left:* test case for impulsive magnetic acceleration: the energy-weighted mean Lorentz factor $\langle \Gamma \rangle$ of a finite cold shell of plasma initially uniform (with width l_0 , rest mass density ρ_0 and magnetic field B_0), highly magnetized ($\sigma_0 = B_0^2/4\pi\rho_0c^2 \gg 1$; $\sigma_0 = 30$ was used here) and at rest, whose back leans against a conducting “wall” while its front faces vacuum (from Granot *et al.* 2011), *versus* the time t in units of the shell’s initial fast magnetosonic crossing time $t_0 \approx l_0/c$. The analytic expectations (dotted and dashed-dotted lines) and the results of numerical simulations (diamond symbols joined by a solid line) are in very good agreement. *Right:* evolution of the typical (or energy-weighted average) Lorentz factor Γ with the distance $R \approx ct$ from the central source, for a finite shell similar to that described in the left panel, but for a spherical shell propagating into an external medium with a power-law density profile, $\rho_{ext} = AR^{-k}$ (from Granot 2012a).

The left panel of Figure 1 shows the results for our impulsive magnetic acceleration test case: a finite cold shell of plasma initially uniform (with width l_0 , rest mass density ρ_0 and magnetic field B_0), highly magnetized ($\sigma_0 = B_0^2/4\pi\rho_0c^2 \gg 1$) and at rest, whose back leans against a conducting “wall” while its front faces vacuum. A strong, self-similar rarefaction wave forms at the front of the shell (vacuum interface) and propagates towards its back, reaching the wall at $t = t_0 \approx l_0/c$. By this time the shell’s energy-weighted mean Lorentz factor and magnetization are $\langle \Gamma \rangle \sim \sigma_0^{1/3}$ and $\langle \sigma \rangle \sim \sigma_0^{2/3}$. At $t > t_0$ the shell detaches from the wall, keeps an almost constant width ($l \approx 2l_0$) and accelerates as $\langle \Gamma \rangle \sim \sigma_0/\langle \sigma \rangle \sim (\sigma_0 t/t_0)^{1/3}$ up to the coasting time $t_c = \sigma_0^2 t_0$. At $t > t_c$ the shell starts coasting at $\langle \Gamma \rangle \sim \sigma_0$ while its width grows ($l/2l_0 \sim t/t_c$) as its magnetization rapidly decreases ($\langle \sigma \rangle \sim t_0/t$),

resulting in complete conversion of magnetic to kinetic energy and allowing strong shocks to develop in the flow, which can lead to a large radiative efficiency.

The right panel of Figure 1 shows the evolution of a similar shell in spherical geometry that propagates into an external medium with a power-law density profile, $\rho_{\text{ext}} = AR^{-k}$. The initial shell magnetization σ_0 and density $\rho_0 \propto 1/\sigma_0$ are allowed to vary while keeping fixed the values of the initial time or length scale ($t_0 \approx R_0/c$ or R_0), energy ($E \sim Lt_0 \approx LR_0/c$ or power L), and external density ($k < 2$ in this figure, and A or $\rho_{\text{ext}}(R_0) = AR_0^{-k}$), which imply fixed $\Gamma_{\text{cr}} \sim (f_0\sigma_0)^{1/(8-2k)}$ where $f_0 = \rho_0/\rho_{\text{ext}}(R_0)$ and $R_{\text{cr}} \sim R_0\Gamma_{\text{cr}}^2$. Shown are the two dynamical regimes most relevant for GRBs. The purple line shows regime I ($1 < \sigma_0 < \Gamma_{\text{cr}}$ or a sufficiently low external density) where the shell initially expands as if into vacuum (as described in the left panel) and only after becoming kinetically dominated and expanding radially is it significantly decelerated by the external medium through a strong relativistic reverse shock, that can produce a bright emission that peaks on a timescale larger than the duration of the prompt GRB emission (the familiar low- σ “thin shell”; Sari & Piran 1995). Eventually, most of the energy is transferred to the shocked external medium and the flow approaches the Blandford-McKee (1976) self-similar solution.

The green line shows regime II ($1 < \Gamma_{\text{cr}} < \sigma_0 < \Gamma_{\text{cr}}^{3(4-k)/2}$) where the shell is significantly affected by the external medium while it is still Poynting dominated (at $R > R_u \sim R_0(f_0\sigma_0^{-1/3})^{3/(10-3k)}$), thus suppressing the reverse shock (which is either non-existent or very weak). The shell remains highly magnetized and gradually transfers its energy to the shocked external medium through $p dV$ work across the contact discontinuity up to R_{cr} , after which the flow approaches the Blandford-McKee solution. In this regime no significant reverse shock emission is expected, and the onset of the afterglow (*i.e.* the peak of the emission from the shocked external medium) is expected to be on a timescale comparable to the prompt GRB duration (*i.e.* a high- σ “thick shell”). In addition, there are other regimes not shown in this figure. In regime III ($1 < \Gamma_{\text{cr}}^{3(4-k)/2} < \sigma_0$) the external density is high enough that there is no impulsive acceleration stage where $\langle \Gamma \rangle \propto R^{1/3}$, and instead $\langle \Gamma \rangle \sim \sigma_0/\langle \sigma \rangle \propto R^{(k-2)/4}$ at $R_0 < R < R_{\text{cr}} \sim R_{\text{dec}}$, and then approaches the Blandford-McKee solution (its observational signatures are expected to be similar to regime II). In regime IV ($\Gamma_{\text{cr}} < 1$) the external density is so high that the flow remains Newtonian all along (as might happen while the GRB jet is propagating inside a massive star progenitor). There is also an exotic regime II* that exists only in a highly stratified external medium ($10/3 < k < 4$).

In practice, GRB variability times are typically large enough that the flow should first undergo quasi-steady collimation-induced acceleration that saturates, and only later the impulsive acceleration kicks in and operates until the flow becomes kinetically dominated. The effects of multiple sub-shells in the outflow can be important, and the collisions between them may provide efficient energy dissipation that can power the GRB emission (Granot 2012b; Komissarov 2012). They may also allow a low- σ “thick shell”, *i.e.* a strong relativistic reverse shock peaking on a timescale comparable to the prompt GRB emission, which is not possible for

a single shell. For a long-lived source (*e.g.* AGN) with initial sub-shell widths l_0 and separations l_{gap} each sub-shell can expand by a factor of $1 + l_{\text{gap}}/l_0$, and its magnetic energy decreases by the same factor (where $\sigma_\infty \sim l_0/l_{\text{gap}}$), and may be converted to kinetic or internal energy, or radiation. For a finite source activity, the merged shell can still expand further and convert more magnetic energy into other forms (even without interaction with an external medium). Important related points that warrant further study are the transition from impulsive to quasi-steady collimation induced acceleration, both in a single shell and in multiple sub-shells, as well as the dissipation in the interaction between sub-shells and its effect on the outflow acceleration and the resulting emission, such as a possible photospheric spectral component.

3 Jet dynamics during the afterglow stage

3.1 Reconciling between analytic models and numerical simulations

Here I summarize the main results of Granot & Piran (2012). Similar to most studies of GRB jet dynamics during the afterglow phase, we focused on an initially uniform jet with well defined, sharp edges. The jet dynamics have been studied mainly analytically (*e.g.* Rhoads 1999; Sari *et al.* 1999; Panaiteescu & Kumar 2001) and numerically using two dimensional special relativistic hydrodynamic simulations (*e.g.* Granot *et al.* 2001; Zhang & MacFadyen 2009), as well as with an intermediate “thin shell” approach (Kumar & Granot 2003) where the dynamical equations are integrated over the radial profile of the shocked fluid (thus reducing them to a set of 1D partial differential equations). Analytic models predict a rapid sideways expansion, with an exponential growth of the jet half-opening angle θ_j with radius R at $R > R_j$ where Γ drops below $1/\theta_0$. Numerical simulations, however, show a much more modest lateral expansion, with a quasi-logarithmic growth of $\theta_j(R > R_j)$, where most of the energy remains within the initial jet half-opening angle θ_0 until the flow becomes mildly relativistic, and only then does the flow start to gradually approach spherical symmetry. Such a behavior is obtained in analytic models under the crude approximation that the jet does not expand sideways significantly until it becomes non-relativistic (Granot *et al.* 2005).

Most simulations so far were for $\theta_0 = 0.2$, or even larger θ_0 . Recently, however, Wygoda *et al.* (2011) and later van Eerten & MacFadyen (2012) have performed simulations also for narrower initial jets, $\theta_0 = 0.05, 0.1, 0.2$. Wygoda *et al.* (2011) have found that significant lateral spreading starts when Γ drops below θ_0^{-1} , as predicted by analytic models, and tried to reconcile the apparent discrepancy with analytic models by attributing it to their small range of validity after significant lateral spreading starts ($1 \ll \Gamma < \theta_0^{-1}$) for the typical modest values of θ_0 used in the simulations. van Eerten & MacFadyen (2012) disagreed with this conclusion.

Granot & Piran (2012) have reconciled this debate by constructing generalized analytic models that remain valid when the jet becomes wide or sub-relativistic.

In particular, two different recipes were considered for the lateral expansion,

$$\frac{d\theta_j}{d \ln R} = \frac{\beta_\theta}{\beta_r} \approx \frac{1}{\Gamma^{1+a}\theta_j^a}, \quad a = \begin{cases} 1 & (\hat{\beta} = \hat{n}), \\ 0 & (u'_\theta \sim 1). \end{cases} \quad (3.1)$$

The first, old recipe ($a = 0$, which was used in most previous analytic works), corresponds to a mildly relativistic lateral expansion speed in the jet's comoving rest frame ($u'_\theta \sim 1$). The second, new recipe ($a = 1$), is based on the jump conditions for oblique shocks of arbitrary proper velocity ($u = \Gamma\beta$), which imply that the velocity of fluid just behind the shock front (in the downstream region) is in the direction of the local shock normal (*i.e.* perpendicular to the shock front at that location, $\hat{\beta} = \hat{n}$; Kumar & Granot 2003) in the upstream rest frame.

In addition, two different recipes were considered for sweeping-up the external medium, named after the shape of the swept-up region. In the “trumpet” model external medium is swept-up only at the front of the jet (part of a sphere within a double-sided cone), while in the “conical” model it is also swept-up along its sides, so that once the jet becomes spherical the swept-up mass equals that originally within a sphere of the same radius (while it is smaller in the trumpet model). These two recipes are the basis of two new analytic models, which remain valid for slow, wide jets. For comparison, results are also shown for the old “relativistic” model, which break down when the jet becomes mildly relativistic or wide (and sweeps-up mass similarly to the trumpet model).

The new analytic models fit the results of numerical simulations much better (see *left panel* of Fig. 2), mainly because they remain valid also in the mildly relativistic, quasi-spherical regime. They show that for modest initial jet half-opening angles, θ_0 , the outflow is not *sufficiently* ultra-relativistic when its Lorentz factor reaches $\Gamma = 1/\theta_0$ and therefore the sideways expansion is rather slow, showing no rapid, exponential phase. On the other hand, jets with an extremely narrow initial half-opening angle ($\theta_0 \ll 10^{-1.5}$ for $k = 0$ or $\theta_0 \ll 10^{-2}$ for $k = 2$; see *left panel* of Fig. 2), which are still sufficiently ultra-relativistic at $\Gamma = 1/\theta_0$, do show a phase of rapid, exponential lateral expansion. However, even such jets that expand sideways exponentially are still not spherical when they become sub-relativistic.

3.2 An afterglow jet propagating into a stratified medium

The clear association of long-soft GRBs with Type Ic supernovae, and thus with the death of a massive star, implies that the afterglow shock propagates into the pre-explosion stellar wind. This suggests a stratified external medium with a density profile $\rho_{\text{ext}} = AR^{-k}$. For a constant wind velocity v_w to mass-loss rate \dot{M}_w ratio, $k = 2$ and $A = \dot{M}_w/(4\pi v_w)$. However, as \dot{M}_w/v_w might vary before the explosion and is rather uncertain, it is worth to also consider other values of k .

Here I summarize the results of new 2D special relativistic hydrodynamic simulations by De Colle *et al.* (2012b), which are the first published simulation results for $k > 0$. We performed simulations of the GRB jet dynamics using the *Mezcal* code (De Colle *et al.* 2012a) and calculated the resulting afterglow emission, for

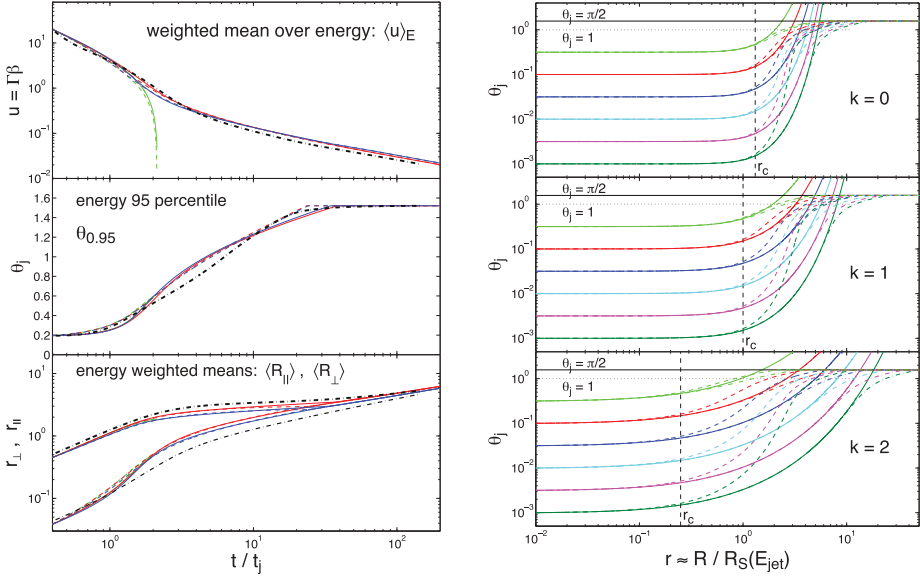


Fig. 2. *Left:* comparison, for $\theta_0 = 0.2$ and $k = 0$ (for an external density profile $\rho_{\text{ext}} \propto R^{-k}$), between the analytic models of Granot & Piran (2012) (thin lines) and the results of 2D special relativistic hydrodynamic simulations (from De Colle *et al.* 2012a,b) of a jet with initial conditions of a conical wedge of half-opening angle θ_0 taken out of the Blandford & McKee (1976) self-similar solution (thick dot-dashed black line), in terms of the jet proper velocity ($u = \Gamma\beta$), half-opening angle (θ_j) as well as normalized parallel (r_{\parallel}) and perpendicular (r_{\perp}) sizes. The green, red and blue lines are for the relativistic, trumpet, and conical models, respectively. Thin solid lines are for the new recipe for lateral expansion ($a = 1$) while thin dashed lines are for the old recipe ($a = 0$). *Right:* comparison between the relativistic (solid lines), trumpet (dot-dashed lines) and conical (dashed lines) models of GP12 in terms of the evolution of the jet half-opening angle θ_j with the normalized radius r , for $k = 0, 1, 2$ (*top to bottom panels*), where all models use our new recipe for the lateral spreading of the jet ($a = 1$). Results are shown for $\log_{10}(\theta_0) = -3, -2.5, \dots, -0.5$ (*using different colors*) while the values of $\theta_0 = 1, \pi/2$ and the critical radius $r_c = [(3 - k)/2]^{(3-a)/[(1+a)(3-k)]}$ where the lateral spreading is expected to become significant are shown for reference.

$k = 0, 1, 2$. The initial conditions were taken to be a conical wedge of half-opening angle $\theta_0 = 0.2$ taken from the spherical, self-similar Blandford-McKee solution.

The jet dynamics in stratified external media ($k = 1, 2$) are found to be broadly similar to those in a uniform external medium ($k = 0$), and the jet half-opening angle starts increasing logarithmically with time (or radius) once the Lorentz factor Γ drops below θ_0^{-1} (as θ_0 is modest; see Sect. 3.1). For larger k values, however, the lateral expansion speed is initially faster while $\Gamma > \theta_0^{-1}$ but slower at late times, since it increases as Γ decreases (*e.g.*, Eq. (3.1)), which in turn occurs more

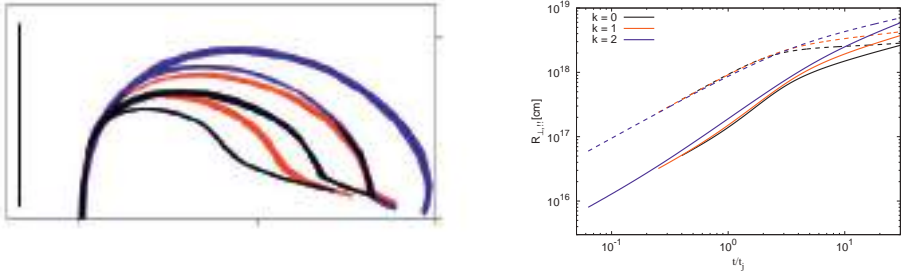


Fig. 3. *Left:* a comparison between the simulated bow shock structures for $k = 0$ (black), $k = 1$ (red) and $k = 2$ (blue), where $\rho_{\text{ext}} \propto R^{-k}$, at two times that have been selected so that the jet has the same Lorentz factor of 10 and 5 in all simulations. The evolutionary scale unit of $\frac{1}{2}ct$ is indicated with a black transverse bar (the simulations are normalized with respect to ct). The origin of the axis is located at the right bottom corner and the jet's main direction of propagation is to the left. *Right:* the transverse (R_{\perp}) and parallel (R_{\parallel}) size of the jet, averaged over the total energy excluding rest mass, as a function of the lab frame time in units of the jet break time (from De Colle *et al.* 2012a).

slowly for larger k (*e.g.*, in the spherical case $\Gamma \propto M^{-1/2} \propto R^{(k-3)/2}$), while $\Gamma(t_j) \approx \theta_0^{-1}$ for all k (such a behavior is also seen in analytic models, *e.g.*, Granot 2007; Granot & Piran 2012). Therefore, for larger k values the jet is initially wider at the same value of $\Gamma \geq \theta_0^{-1}$ (see *left panel* of Fig. 3), while later on at $\Gamma < \theta_0^{-1}$ it becomes Newtonian and approaches spherical symmetry more slowly as its parallel size R_{\parallel} keeps growing (while R_{\parallel} essentially stalls for $k = 0$ as the jet becomes sub-relativistic, until the flow approaches spherical symmetry; see *right panel* of Fig. 3; such a behavior also occurs in analytic or semi-analytic models: Granot *et al.* 2005; Granot & Piran 2012; see *lower panel* of Fig. 2).

The *left panel* of Figure 4 shows the shape of the jet break for $k = 0, 1, 2$. We find that contrary to analytic expectations (Kumar & Panaiteescu 2000), there is a reasonably sharp jet break in the lightcurve for $k = 2$. Moreover, the shape of the jet break is affected more by the viewing angle θ_{obs} (within the initial jet aperture, $\theta_{\text{obs}} \leq \theta_0$) than by the external density profile slope k (for $0 \leq k \leq 2$). Steeper density profiles (*i.e.* larger k values) are found to produce more gradual jet breaks while larger θ_{obs} cause smoother and later appearing jet breaks. For $\theta_{\text{obs}} = 0$ most of the steepening occurs within a factor of $\sim 2 - 4$ in time for $0 \leq k \leq 2$ while for $\theta_{\text{obs}} \sim (0.5 - 1)\theta_0$ it takes $\sim 1 - 2$ decades for $0 \leq k \leq 2$.

The *right panel* of Fig. 4 shows the radio lightcurves for the 2D simulations (*black lines*). The counter-jet becomes visible as it turns sub-relativistic, and for $k = 0$ this results in a clear bump-like feature in the light curve. However, for larger k values the jet decelerates and comes into view more gradually, causing only a mild flattening in the radio light curve that might be hard to discern when $k = 2$. This might, however, not help explain the lack of a clear flattening or rebrightening in the late radio afterglow of GRB 030329 (*e.g.*, Pihlström *et al.* 2007), since in

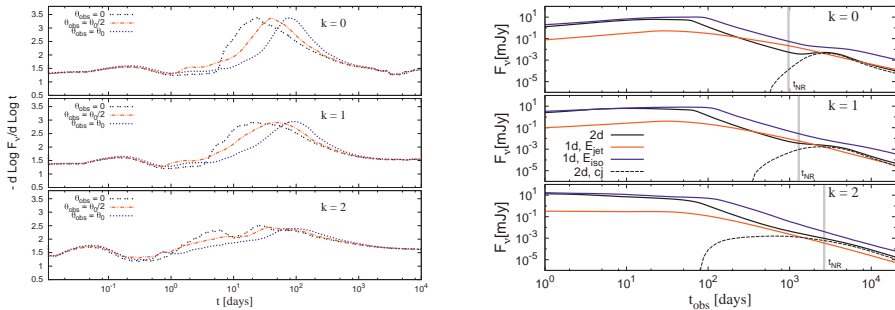


Fig. 4. *Left:* “jet break shape” – the temporal decay index $\alpha \equiv -d \log F_\nu / d \log t_{\text{obs}}$ as a function of the observed time t_{obs} (including electron cooling, at $\nu = 10^{17}$ Hz $> \nu_m$). *Right:* radio light curves (at $\nu = 1$ GHz) for $k = 0, 1, 2$ simulations in 2d, 1d with $E = E_{\text{jet}}$, and for a cone with half-opening angle θ_0 computed from spherical 1d simulations with $E = E_{\text{iso}}$. The contribution due to the counter-jet is included in the lightcurves, and explicitly shown (*dashed curves*) for the 2d simulations (from De Colle *et al.* 2012a).

that case detailed afterglow modeling (of the evolution of both the broad band flux densities and the afterglow image size) favors a uniform external density.

The *right panel* of Figure 4 also shows lightcurves for a spherical 1D simulation with the same true energy (*red lines*), and for a double-sided cone of half-opening angle θ_0 taken from a spherical 1D simulation (from De Colle *et al.* 2012a) with the same isotropic equivalent energy (*blue lines*). Late time radio calorimetry usually assumes a spherical flow near the non-relativistic transition time t_{NR} (*thick vertical gray lines*), and is thus likely to consistently over-estimate the true energy by up to a factor of a few for $k = 2$, but either over-predict or under-predict it by a smaller factor for $k = 0, 1$ (as can be seen by comparing the *red* and *black lines* in the figure).

4 Conclusions

Some recent progress in our understanding of GRB jet dynamics has been outlined. A strongly variable initially Poynting flux dominated outflow can convert most of the initial magnetic energy into kinetic and internal energy, thus allowing high radiative efficiencies from dissipation within the outflow – internal shock at a range of magnetizations. More generally, as our understanding of initially highly magnetized outflows improves, they are gradually becoming a more viable alternative to the traditional fireball model, making them worthy of further study.

The apparent discrepancy between the results of analytic models and numerical simulation for the degree of jet lateral expansion during the afterglow was finally reconciled. An early phase of exponential sideways expansion with radius occurs only for extremely narrow jets ($\theta_0 \ll 0.05$ for $k = 0$ or $\theta_0 \ll 0.01$ for $k = 2$) but is replaced by a slower, quasi-logarithmic sideways expansion for more modest

initial half-opening angles ($\theta_0 \gtrsim 0.05$ for $k = 0$ or $\theta_0 \gtrsim 0.01$ for $k = 2$). The jet first becomes sub-relativistic, and only then gradually approaches spherical symmetry.

Afterglow jets propagating into a stratified external medium ($k > 0$) expand sideways faster before the jet break and slower afterwards, compared to a uniform external medium ($k = 0$). Thus, they become spherical and sub-relativistic more slowly, which makes it hard to see a signature of their counter-jet in the lightcurve. Their jet break is generally smoother, but potentially detectable, and its sharpness depends more on the viewing angle (for $\theta_{\text{obs}} < \theta_0$) than on k (for $0 \leq k \leq 2$).

References

- Abdo, A.A., Ackermann, M., Arimoto, M., *et al.*, 2009, Science, 323, 1688
 Begelman, M.C., & Li, Z.-Y. 1992, ApJ, 397, 187
 Blandford, R.D., 2002, in Lighthouses of the Universe, ed. M. Gilfanov, *et al.* (Springer-Verlag, Berlin), 381
 Blandford, R.D., & McKee, C.F., 1976, Phys. Fluids, 19, 1130
 Blandford, R.D., & Rees, M.J., 1974, MNRAS, 169, 395
 Contopoulos, J., 1995, ApJ, 450, 616
 De Colle, F., Granot, J., Lopez-Camara, D., *et al.*, 2012a, ApJ, 746, 122
 De Colle, F., Ramirez-Ruiz, E., Granot, J., *et al.*, 2012b, ApJ, 751, 57
 Drenkhahn, G., & Spruit, H.C., 2002, A&A, 391, 1141
 Goldreich, P., & Julian, W.H., 1970, ApJ, 160, 971
 Granot, J., 2005, ApJ, 631, 1022
 Granot, J., 2007, Rev. Mex. A&A, 27, 140
 Granot, J., 2012a, MNRAS, 421, 2442
 Granot, J., 2012b, MNRAS, 421, 2467
 Granot, J., Komissarov, S.S., & Spitkovsky, A., 2011, MNRAS, 411, 1323
 Granot, J., Miller, M., Piran, T., *et al.*, 2001, in “GRBs in the Afterglow Era”, ed. E. Costa, F. Frontera & J. Hjorth (Berlin, Springer), 312
 Granot, J., & Piran, T., 2012, MNRAS, 421, 570
 Granot, J., Ramirez-Ruiz, E., & Loeb, A., 2005, ApJ, 618, 413
 Heinz, S., & Begelman, M.C., 2000, ApJ, 535, 104
 Komissarov, S.S., 2012, MNRAS, 422, 326
 Komissarov, S.S., Vlahakis, N., Königl, A., *et al.*, 2009, MNRAS, 394, 1182
 Komissarov, S.S., Vlahakis, N., & Königl, A., 2010, MNRAS, 407, 17
 Kumar, P., & Granot, J., 2003, ApJ, 591, 1075
 Kumar, P., & Panaiteescu, A., 2000, ApJ, 541, L9
 Levinson, A., 2010, ApJ, 720, 1490
 Lyubarsky, Y.E., 2009, ApJ, 698, 1570
 Lyubarsky, Y.E., 2010, MNRAS, 402, 353
 Lyubarsky, Y.E., 2010, ApJ, 725, L234
 Lyutikov, M., 2006, New J. Phys., 8, 119
 Lyutikov, M., 2011, MNRAS, 411, 422

- Panaitescu, A., & Kumar, P., 2001, ApJ, 554, 667
Pihlström, Y.M., Taylor, G.B., Granot, J., *et al.*, 2007, ApJ, 664, 411
Rhoads, J.E., 1997, ApJ, 487, L1
Rhoads, J.E., 1999, ApJ, 525, 737
Sari, R., Piran, T., & Halpern, J., 1999, ApJ, 519, L17
Sari, R., & Piran, T., 1995, ApJ, 455, L143
Smith, M.D., Norman, M.L., Wilson, J.R., *et al.*, 1981, Nature, 293, 277
Tchekhovskoy, A., Narayan, R., & McKinney, J.C., 2010, New Astron., 15, 749
van Eerten, H.J., & MacFadyen, A.I., 2012, ApJ, 751, 155
Vlahakis, N., & Königl A., 2003, ApJ, 596, 1080
Wygoda, N., Waxman, E., & Frail, D.A., 2011, ApJ, 738, L23
Zhang, W., & MacFadyen, A.I., 2009, ApJ, 698, 1261

COOLING-INDUCED STRUCTURES IN COLLAPSAR ACCRETION DISKS

A. Batta¹ and W.H. Lee¹

Abstract. The collapse of massive rotating stellar cores and the associated accretion is thought to power long Gamma ray bursts. The physical conditions make neutrino emission the main cooling agent in the flow. We have carried out an initial set of calculations of the collapse of rotating polytropic cores in three dimensions, making use of a pseudo-relativistic potential and a simplified cooling prescription. We focus on the effects of self gravity and cooling on the overall morphology and evolution of the flow for a given rotation rate in the context of the collapsar model. For the typical cooling times expected in such a scenario we observe the appearance of strong instabilities on a time scale t_{cool} following disk formation. Such instabilities and their gravitational interaction with the black hole produce significant variability in the obtained accretion rates, which would translate into luminosity variations when a more realistic neutrino cooling and luminosity scheme is implemented in future work.

1 Introduction

To date it is generally accepted that Gamma ray bursts (GRBs) are the result of cataclysmic events involving Neutron stars (NSs) or black holes (BHs). Moreover, long GRBs are generally associated with actively star forming galaxies and sometimes with a Supernova (SN) type Ib or Ic, taking place at the same time and place. A review by Woosley & Bloom (2006) shows the existing evidence at the time for the link of long GRB at low redshift with type Ic SNe.

In this work we will consider the *collapsar model* (Woosley 1993) to in which the formation of a GRB follows from the collapse of a pre-supernova (PreSN) star. In such a scenario, a BH is formed from the star's Fe core while the outer rotating layers collapse and form an accretion disk around the BH. With the high temperatures and densities expected in the disk ($T \geq 10^{10}$ K, $\rho \geq 10^9$ g cm⁻³), neutrino emission becomes the main cooling mechanism. These neutrinos provide the main

¹ Instituto de Astronomía, Universidad Nacional Autónoma de México, Apdo. postal 70-264, Ciudad Universitaria, D.F., México; e-mail: abatta@astro.unam.mx; wlee@astro.unam.mx

cooling mechanism, and may contribute, along with magnetically powered outflows, to power the GRB.

Besides the work by MacFadyen & Woosley (1999), (the first one to explore the collapsar scenario in a 2D hydrodynamic simulation) a body of work has been carried out in 2D with improved physics (realistic EOS, MHD (Proga *et al.* 2003), or improved neutrino cooling prescriptions (López-Cámara *et al.* 2009) but, they have not properly accounted for instabilities that may come from the combination of self gravity and cooling processes. For the 3D studies that have been carried out (Rockefeller *et al.* 2006; Taylor *et al.* 2011), we do not yet have a complete understanding of the importance of structure formation in the accretion flow and or heating/cooling mechanisms. Here we focus on the study of the effects of self gravity and cooling on 3D simulations of the collapse of a rotating polytropic envelope onto a BH in the context of the collapsar model.

2 Initial conditions and input physics

In the context of the collapsar model, we studied the collapse and accretion of $2.5 M_{\odot}$ rotating polytropic envelopes ($\gamma = 5/3$) onto a $2 M_{\odot}$ BH fixed at the center of the distribution. All numerical simulations were made using a modified version of GADGET-2 (Springel 2005).

The $2.5 M_{\odot}$ spherical polytropic envelope is located from $r_{int} = 844.69$ km to $R_s = 1715.7$ km, surrounding the $2 M_{\odot}$ BH at the center of the distribution. Such a polytropic envelope was given a solid body rotation just below breakup, which also guaranteed a circularization radius $r_c = 12.5 r_{acc}$ close to the accretion radius r_{acc} . We will consider a Paczynski-Wiita pseudo-potential (Paczynski & Wiita 1980) to account for the most important general relativistic effects determining the motion of matter near a non-rotating BH. The $2 M_{\odot}$ BH particle will be artificially fixed at the origin by canceling the forces acting on it. The Paczynski-Wiita potential will reproduce exactly, the location of the innermost stable circular orbit ($r_{isco} = 3r_g = 6GM_{BH}/c^2$) of a Schwarzschild BH, which will be considered as our accretion radius ($r_{acc} = 3r_g$).

We adopted a simplified cooling prescription based on a fixed cooling time t_{cool} dependent on the dynamical time scale of the accretion disk $t_{disk} \simeq 10^{-1}$ s, formed around the BH.

$$t_{cool} = \beta t_{disk}, \quad \frac{du}{dt} = -u/t_{cool}. \quad (2.1)$$

The efficiency parameter β determines how many times the gas must orbit the BH before it gets significantly cooled. To account for a cooling as efficient as neutrinos, we explored the case where t_{cool} is close to the neutrino cooling time scale t_{ν} . Therefore, we estimated the neutrino cooling time scale $t_{\nu} = u/q_{\nu}$ for the densities and temperatures expected near the BH. By considering an approximated EOS composed by relativistic non-degenerate electron-positron pairs and ionized H, as well as a neutrino cooling prescription q_{ν} accounting for pair annihilation and electron-positron capture (Narayan *et al.* 2001), the neutrino cooling time scale t_{ν} can be evaluated as a function of T and ρ from the internal energy and

cooling rate, respectively:

$$u = \frac{3}{2} \frac{kT\rho}{\mu m_p} + \frac{11}{4} a T^4, \quad q_\nu \simeq 5 \times 10^{33} T_{11}^9 + 9.0 \times 10^{23} \rho T_{11}^6 \text{ erg cm}^{-3} \text{ s}^{-1}. \quad (2.2)$$

This turns into a neutrino cooling time scale ranging from a few seconds to $\sim 10^{-4}$ s for $\rho = 10^{10}$ to 10^{12} g cm $^{-3}$ and $T = 10^{10}$ to 10^{11} K. Therefore, by using $t_{cool} = 1.23, 0.24, 0.12, 0.061, 0.012, 0.006$ s in our cooling scheme (2.1), we will explore the importance of the neutrino cooling efficiency in structure formation.

3 Results and discussion

By looking at the BH mass accretion rate $\dot{M} = dM/dt$, and the total energy loss rate $L_c = \int du/dt dV$ obtained for three different cooling schemes we will obtain information on the general changes in the behavior of the accretion flow with increasing cooling efficiency. Figure 1 shows the mass accretion rates (left panel) and the energy loss rates L_c (right panel) for models with $t_{cool} = 0.24, 0.061, 0.012$ s, (blue, black and orange lines respectively). Figure 1 shows that as the cooling efficiency increases, the variations in both \dot{M} and L_c become more intense. Moreover, intense increases in \dot{M} and L_c appear to coincide in time. This is possibly related to the fact that overdense regions become hotter and thus more intense emitters, and that the spiral structures they are associated with transport angular momentum more efficiently, raising the accretion rate. This clearly deserves quantification through further study.

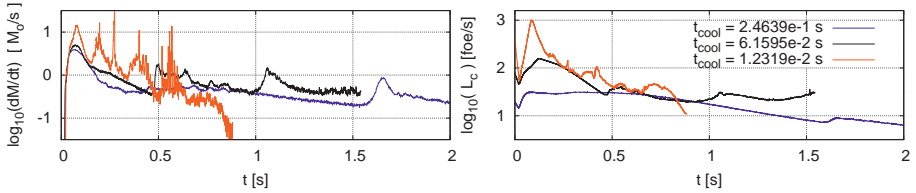


Fig. 1. Logarithm of the BH accretion mass rate \dot{M} in solar masses per second (*left panel*) and Logarithm of the energy loss rate L_c in foes per second (*right panel*), for models with $t_{cool} = 1.23, 0.24, 0.12, 0.061, 0.012, 0.006$ s, (red, blue, pink, black, orange and gray lines respectively). Intense variations in both L_c and \dot{M} coincide in time. $1\text{foe}=10^{51}$ erg.

In order to obtain information about the formation of non-axisymmetric instabilities at the disk, we performed a Fourier transform of the azimuthal distribution of mass $\Phi_M = \int [\int \rho(\phi, r, z) dz] r dr$ (Zurek & Benz 1986) defining the amplitude of the mode m by:

$$C_m = \frac{1}{2\pi} \int_0^{2\pi} e^{im\phi} \Phi_M d\phi. \quad (3.1)$$

The relative power $|c_m|^2 = |C_m|^2/|C_0|^2$ in the m -th mode indicates the intensity of m spiral arms compared to the disk integrated mass. If such spiral structures are present in the disk, they should be visible in density or internal energy maps. Moreover, they should be also visible as unstable regions by plotting the Toomre

parameter $Q_T = \kappa c_s / (\pi G \Sigma)$, determined by the surface density Σ , the local sound speed c_s and the local epicyclic frequency κ .

Figure 2 (left) shows the evolution of the relative power $|c_2|^2$ for the model with $t_{cool} = 0.25$ s. This mode has the most intense peak of all modes explored ($m = 1, 2, 3, 4$) whose increase begins around $t \simeq 1.5$ s, and is essentially the only one present. The peak shown at $t \simeq 1.6$ s coincides in time with the intense variations in Figure 1 of L_c and \dot{M} , and thus seem to originate from the changes in $|c_2|^2$. Consistently with the increase in relative power in $|c_2|^2$, in the right panel we can see the formation of only two spiral arms in the Toomre parameter map.

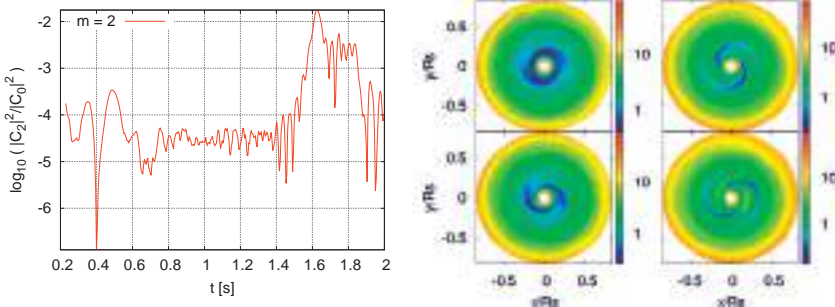


Fig. 2. Relative power $|c_2|^2$ for model with $t_{cool} = 0.24$ s (left panel) and evolution of the Toomre parameter Q at times $\simeq 1.6$ s where the azimuthal mode $m=2$ peaks.

In Figure 3 (left) we see the evolution of the relative power $|c_1|^2$ for the model with $t_{cool} = 0.061$ s, showing several peaks starting at $t \simeq 0.5$ s. The peak at around $t \simeq 0.6$ s in the $m = 1$ mode can be seen in the Toomre parameter maps shown in the right panel, where, unlike previously, higher modes are clearly present. We also notice the appearance of gas clumps due to the highly efficient cooling, whose disruption due to close encounters with the BH are able to induce intense variations in both \dot{M} and L_c . Such intense variations are noticeable only in the most efficiently cooled models.

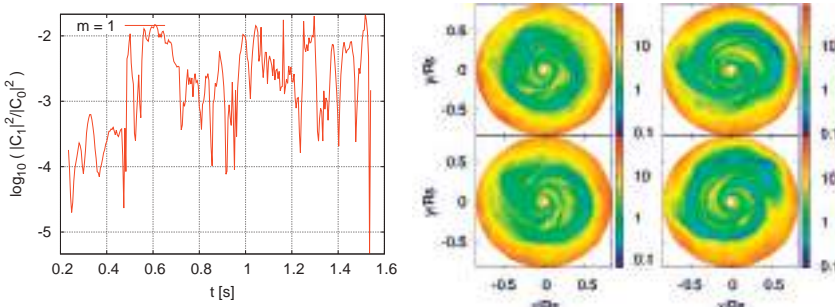


Fig. 3. Relative power $|c_1|^2$ for model with $t_{cool} = 0.061$ s (left panel) and evolution of the Toomre parameter Q at times $\simeq 0.6$ s, right after the first intense increase in all modes. Gas clumps appear due to the high cooling efficiency.

4 Summary

As we found in our simplified *collapsar* scenario, structure formation at the disk becomes more copious and intense with increasing cooling efficiency. The mass of spiral structures detected with the relative power $|c_m|^2$ becomes significantly higher when the cooling parameter β is smaller than ~ 0.6 . Spiral structures detected on the most efficiently cooled models have masses ranging between 0.01% – 0.1% of the disk's total mass. This, combined with the formation of massive gas clumps in the disk, indicates that relaxing the assumption that the BH remains fixed at the origin could lead to interesting behavior. Also, close encounters of gas clumps with the BH can produce significant increases in both the mass accretion and energy loss rates. Therefore, we expect that when more realistic initial conditions and more detailed neutrino cooling are implemented on future work, intense and copious structure may form, altering the neutrino emission itself, as well as the assumed BH-disk symmetric gravitational interaction. Future work will explore the scenario where the BH is able to move from its original position, as well as the implications of such structure formation events when producing a GRB.

Support from CONACyT (83254 and a graduate fellowship for AB) and the GRB 2012 Symposium LOC, as well as cpu-time at the IA-UNAM cluster Atocatl and at the ICN-UNAM cluster Diable is gratefully acknowledged.

References

- López-Cámara, D., Lee, W.H., & Ramirez-Ruiz, E., 2009, ApJ, 692, 804
- MacFadyen, A.I., & Woosley, S.E., 1999, ApJ, 524, 262
- Narayan, R., Piran, T., & Kumar, P., 2001, ApJ, 557, 949
- Paczynski, B., & Wiita, P.J., 1980, A&A, 88, 23
- Proga, D., MacFadyen, A.I., Armitage, P., & Begelman, M., 2003, ApJ, 599, L5
- Rockefeller, G., Fryer, C.L., & Li, H., 2006 [[arXiv:astro-ph/0608028](https://arxiv.org/abs/astro-ph/0608028)]
- Taylor, P.A., Miller, J.C., & Podsiadlowski, P., 2011, MNRAS, 410, 4, 2385
- Woosley, S.E., 1993, ApJ, 405, 273
- Woosley, S.E., & Bloom, J.S., 2006, ARA&A, 44
- Springel, V., 2005, MNRAS, 364, 1105
- Zurek, W.H., & Benz, W., 1986, ApJ, 308, 123

3D GRB JETS DRILLING THROUGH THE PROGENITOR

D. López-Cámara¹

Abstract. We present, for the first time, three dimensional (3D) adaptive mesh refinement simulations of a GRB jet crossing a pre-SN progenitor (with resolutions comparable to the resolutions of 2D simulations) (Lopez-Camara *et al.* 2012). The morphology, Lorentz factor, and symmetries, will be discussed in this presentation. Basically the evolution is divided into three main phases: the jet moving inside the progenitor; the jet just about break out of the progenitor; and the phase where the jet has broken out of the star and is now moving through the circumstellar medium. The resolution and 3D effects are also discussed. Still, as with all numerical work, the current investigation lacks in several aspects and needs improvement as well as further investigations.

1 Introduction

In most cases, the study of the jet-star interaction has been performed numerically, with analytic models used only for guidance (Bromberg *et al.* 2011; Matzner 2003; Morsanyi *et al.* 2007). Even so, studying the propagation of a relativistic outflow that is continuously shocked by a much denser environment is not trivial since the length-scale of features in the relativistic material is typically $\sim R/\Gamma$ and therefore a large dynamical range is involved. When possible, adaptive mesh refinement codes have been adopted (Lazzati *et al.* 2009, 2010, 2011a; Morsanyi *et al.* 2007, 2010; Nagakura *et al.* 2011), and the simulations have been limited to two dimensions (Aloy *et al.* 2000; Lazzati *et al.* 2009, 2010, 2011a; MacFadyen & Woosley 1999; MacFadyen *et al.* 2001; Mizuta & Aloy 2009; Mizuta *et al.* 2006; Morsanyi *et al.* 2007, 2010; Nagakura *et al.* 2011; Zhang *et al.* 2003). These studies have shown that even though the jet material is relativistic, the jet-head propagates sub-relativistically inside the star, thereby allowing causal contact between the bow shock at the head of the jet and the star. The shocked star material therefore

¹ Department of Physics, NC State University, 2401 Stinson Drive, Raleigh, NC 27695-8202, USA

drains at the sides of the jet producing a hot cocoon instead of being entrained in the jet.

Two dimensional simulations can provide important answers to the outstanding questions listed above. However, they are plagued by artifacts due to the presence of a symmetry axis in the center of the jet. While 3D simulations of GRB jets have been attempted in the past (Zhang *et al.* 2004), they were performed with a fixed grid code, casting doubt on the capability to resolve the required small scales. A 3D test case with AMR was presented by Wang *et al.* (2008), but since their jet-progenitor evolution did not converge as a function of the numerical resolution (unlike our study), not much could be inferred from their study. Thus, in this paper we present, for the first time, 3D adaptive mesh refinement (AMR) simulations of GRB jets crossing a pre-SN progenitor and then flowing through the circumstellar medium (CSM).

2 Initial setup

We consider the one-dimensional pre-supernova 16TI model from Woosley & Heger (2006) as our initial stellar configuration. The pre-SN progenitor was immersed in a CSM with constant density ($\rho_{CSM} = 10^{-10}$ g cm $^{-3}$). A relativistic jet (with half-opening angle of 10°, constant luminosity of 5.33×10^{50} erg s $^{-1}$, and an initial Lorentz Factor of 5, see Lopez-Camara *et al.* 2012 for further details), was imposed at all times as a boundary condition. In order to follow the temporal evolution of our initial setup, we solved the 3D gas-dynamic equations using the FLASH code (3D relativistic version in cartesian coordinates) (Fryxell *et al.* 2000). The simulation domain covered the top half of the pre-SN progenitor star as well as the CSM it is immersed in. The boundaries were set at $y_{min} = 10^9$ cm, $y_{max} = 2.4 \times 10^{11}$ cm, $x_{max} = -x_{min} = 6 \times 10^{10}$ cm, and $z_{max} = -z_{min} = 6 \times 10^{10}$ cm. Only the equatorial plane ($y = y_{min}$) was set with a reflective boundary condition, all other were set with transmission conditions. Even though it has been shown that close to the pre-SN's progenitor nucleus the neutrinos play an important role (López-Cámara *et al.* 2009), since the inner boundary was set so far away, $R_i \sim 10^9$ cm, equivalent to approximately 10^4 gravitational radii, from the region where neutrinos dominate (and where the compact object relativistic effects must be taken into consideration), the neutrino and general relativistic effects were safely ignored. Also, we ignored self gravity and the pre-SN's angular momentum. We justify this by pointing out that the dynamical timescale of the pre-SN is of order close to hours. Then, since the integration time in our numerical simulations is at most 20 s, we were safe to assume that the pre-SN progenitor remained practically static at all times.

3 Results and discussion

In Figure 1 (left panel) we show the density stratification maps for t=9.3 s. The morphology of our system is divided into two main phases: the jet moving inside

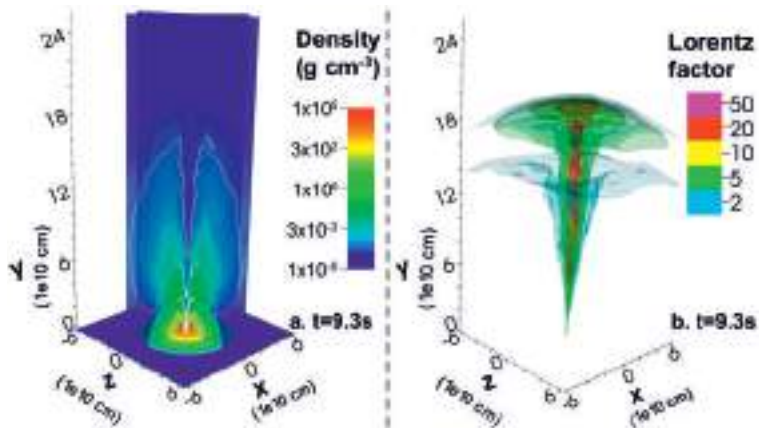


Fig. 1. Density stratification map (g cm^{-3}) (left panel), and Lorentz factor isocontour map (right panel) at $t = 9.3$ s.

the progenitor; and when the jet has broken out of the progenitor (and is now interacting with the CSM).

The “break out time” from our simulations ($t_{bo} = 4.2$ s) implies that the average propagation velocity of the jet inside the star is ~ 0.32 c. The jet, composed of low density material, has its initial opening angle reduced by relativistic hydrodynamic collimation effects. Before the break out time only a relativistic jet (with $\Gamma \sim 10$) is present. Once the jet breaks out of the stellar surface, the jet is accelerated and a cocoon forms. The high internal energy is able to accelerate material with Lorentz factors values of order $\Gamma \sim 10^2$ in some zones. To see the high Lorentz factor material in the jet, Figure 1 (right panel) we plot the Γ isocontours for $t = 9.3$ s. By this time certain regions in the polar axis reach Lorentz factor values as high as $\Gamma = 50$ (red isocontours).

In order to verify that the evolution of the jet from our results is not dependent on the numerical resolution, we ran a new model with the same setup and physics but with a maximum resolution two times finer than for the low resolution. In Figure 2 we show the density profiles for the three dimensional high resolution (3D HR), and low resolution (3D LR) case, as well as for the 2D HR model. Among the differences associated with the resolution, are a higher level of turbulence and a slower advance of the jet head in the HR model. The reason the 3D HD jet to move slower (than the 3D LR) is due to the fact that it has a wider jet. Since we are powering both jets equally, the narrow-LR jet will move faster. The reason for the 3D HR jet to show more less turbulence than its LR model is due to the fact that the 3D LR simulation has higher diffusion, and thus suppresses the small scale instabilities that are present in the HR model.

We also checked how the evolution of the jet through the stellar envelope and CSM differs in a 2D model. The basic morphology in the 2D case resembles that from the 3D model. In both cases we see a collimated jet that manages to drill

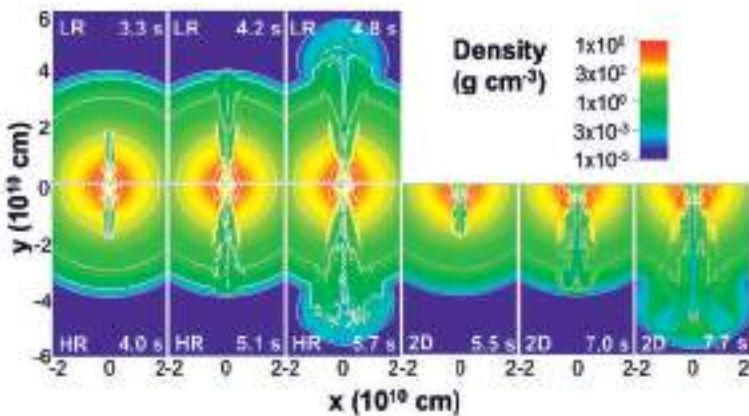


Fig. 2. Density stratification maps (g cm^{-3}) for the 3D LR model (*upper panels*), for the 3D HR resolution model (*lower left panels*), and the 2D model (*lower right panels*).

through the stellar envelope. Apart from the cylindrical symmetry imposed in the 2D model, there are many subtle differences between the 2D and 3D results: The jet moves slower in the 2D model than in the 3D one, and the 2D jet presents less turbulent-like morphology. The reason for the 3D jet to move faster is due to the fact that the jet in 3D simulations is narrower and can wobble around the jet axis finding the path of least resistance to proceed. In Figure 3 we show the internal energy map in the XZ plane for the 3D scenario. The XZ planes shown for each timeframe correspond to the position where the internal energy's (U) centroid of the forward shock front was located at. It is clear how the centroid of the U wobbles around the polar axis (contrary to the 2D case where it always moves through the polar axis).

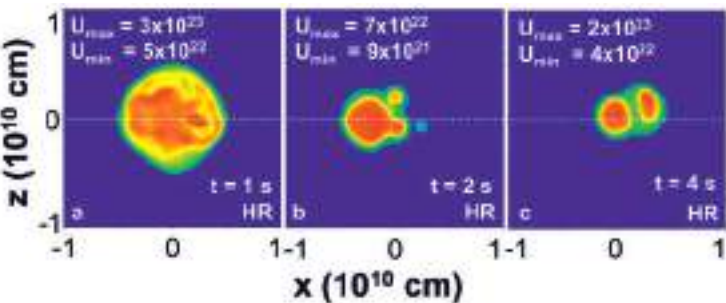


Fig. 3. Energy density (erg cm^{-3}) XZ stratification maps for the centroid of the head front of the jet-cocoon structure for different times.

4 Conclusions

We present, for the first time, 3D AMR simulations of GRB jets expanding inside a realistic pre-SN progenitor and then flowing through the CSM. Our numerical simulations, confirm that relativistic jets can propagate and break out of the progenitor star while remaining relativistic. The morphology is divided into two main phases: Pre- t_{bo} phase in which the jet moves at mildly relativistic velocities ($\sim c/2$) inside the progenitor's stellar envelope; and the post- t_{bo} phase in which the jet has broken out of the surface, it accelerates and reaches Lorentz factors of order $\Gamma \sim 50$. The resolution does not affect in great detail the flow and the morphology in each phase is well reproduced. Still, the amount of turbulence and variability observed in the simulations is higher for higher resolutions. Also, for finer numerical resolutions the jet moves slower. The propagation of the jet head inside the progenitor star is slightly faster in 3D simulations compared to 2D ones at the same resolution. This behavior is due to the fact that the jet in 3D simulations is narrower and can wobble around the jet axis finding the spot of least resistance to proceed.

References

- Aloy, M.A., Müller, E., Ibáñez, J.M., Martí, J.M., & MacFadyen, A., 2000, ApJ, 531, L119
- Bromberg, O., Nakar, E., Piran, T., & Sari, R., 2011, ApJ, 740, 100
- Fryxell, B., Olson, K., Ricker, P., *et al.*, 2000, ApJS, 131, 273
- Lazzati, D., Morsony, B.J., & Begelman, M.C., 2009, ApJ, 700, L47
- Lazzati, D., Morsony, B.J., & Begelman, M.C., 2010, ApJ, 717, 239
- Lazzati, D., Morsony, B.J., & Begelman, M.C., 2011, ApJ, 732, 34
- López-Cámara, D., Lee, W.H., & Ramirez-Ruiz, E., 2009, ApJ, 692, 804
- López-Cámara, D., Morsony, B.J., Begelman, M.C., & Lazzati, D., 2012
[arXiv:1212.0539]
- MacFadyen, A.I., & Woosley, S.E., 1999, ApJ, 524, 262
- MacFadyen, A.I., Woosley, S.E., & Heger, A., 2001, ApJ, 550, 410
- Matzner, C.D., 2003, MNRAS, 345, 575
- Mizuta, A., & Aloy, M.A., 2009, ApJ, 699, 1261
- Mizuta, A., Yamasaki, T., Nagataki, S., & Mineshige, S., 2006, ApJ, 651, 960
- Morsony, B.J., Lazzati, D., & Begelman, M.C., 2007, ApJ, 665, 569
- Morsony, B.J., Lazzati, D., & Begelman, M.C., 2010, ApJ, 723, 267
- Nagakura, H., Ito, H., Kiuchi, K., & Yamada, S., 2011, ApJ, 731, 80
- Wang, P., Abel, T., & Zhang, W., 2008, ApJS, 176, 467
- Woosley, S.E., & Heger, A., 2006, ApJ, 637, 914
- Zhang, W., Woosley, S.E., & Heger, A., 2004, ApJ, 608, 365
- Zhang, W., Woosley, S.E., & MacFadyen, A.I., 2003, ApJ, 586, 356

RADIO AFTERGLOW OF THE JETTED TIDAL DISRUPTION EVENT *SWIFT J1644+57*

B.D. Metzger¹, D. Giannios² and P. Mimica³

Abstract. The recent transient event Swift J1644+57 has been interpreted as resulting from a relativistic outflow, powered by the accretion of a tidally disrupted star onto a supermassive black hole. This discovery of a new class of relativistic transients opens new windows into the study of tidal disruption events (TDEs) and offers a unique probe of the physics of relativistic jet formation and the conditions in the centers of distant quiescent galaxies. Unlike the rapidly-varying γ /X-ray emission from Swift J1644+57, the radio emission varies more slowly and is well modeled as synchrotron radiation from the shock interaction between the jet and the gaseous circumnuclear medium (CNM). Early after the onset of the jet, a reverse shock propagates through and decelerates the ejecta released during the first few days of activity, while at much later times the outflow approaches the self-similar evolution of Blandford and McKee. The point at which the reverse shock entirely crosses the earliest ejecta is clearly observed as an achromatic break in the radio light curve at $t \approx 10$ days. I discuss the implications of Swift J1644+57 for the fraction of TDEs accompanied by relativistic jets; the physics of jet formation more broadly; and the prospects for detecting off-axis TDE radio emission, either via follow-up observations of TDE candidates discovered at other wavelengths or blindly with upcoming wide-field radio surveys.

1 Introduction

A rare glimpse into the properties of normally quiescent supermassive black holes (SMBHs) is afforded when a star passes sufficiently close that it is tidally disrupted. Numerical simulations of “tidal disruption events” (TDEs) show that a significant fraction of the shredded star remains gravitationally bound to the black hole (*e.g.*

¹ Department of Astrophysical Sciences, Princeton University, Princeton, NJ 08544, USA

² Department of Physics, Purdue University, West Lafayette, IN 47907, USA

³ Departamento de Astronomia y Astrofisica, University de Valencia, 46100 Burjassot, Spain

Ayal *et al.* 2000; Guillochon *et al.* 2009). Accretion of this stellar debris has long been predicted to power a thermal “flare” at optical, UV, and X-ray wavelengths that lasts for months to years after the merger (*e.g.* Lodato *et al.* 2009; Strubbe & Quataert 2009).

Giannios & Metzger (2011) explore the consequences if a modest fraction of the accretion power from a TDE is used to accelerate a collimated jet to ultra-relativistic speeds. Such a short-lived ejection cannot propagate far from the SMBH before beginning to interact and decelerate via its interaction with the surrounding circumnuclear medium (CNM). GM11 showed that the jet-CNM interaction is mediated by shocks, which powers synchrotron emission peaking on a timescale \sim months-years after the merger. An alternative model for radio emission from TDE jets was developed by Van Velzen *et al.* (2011), who instead focused on emission internal to the jet itself by making a phenomenological connection with the radio/X-ray correlations of stellar mass compact binaries.

The gamma-ray transient *Swift* J164449.3+573451 (hereafter Sw J1644+57) was detected by the *Swift*/BAT on March 25, 2011. Subsequent imaging at radio, optical, and X-ray wavelengths localized the event to within \lesssim 100 pc of the center of a compact galaxy at redshift $z \simeq 0.35$ (*e.g.* Berger *et al.* 2011). The coincidence of Sw J1644+57 with the galactic nucleus, combined with the lack of previously known GRBs with similar luminosity or duration (Levan *et al.* 2011), suggest that it most likely originated from a rapid onset of accretion onto a SMBH, as probably can only be explained by a TDE (Bloom *et al.* 2011). The SED of Sw J1644+57 showed two distinct components, suggesting different sources for the X-ray and radio emission. The high energy emission is rapidly variable, placing its origin at small radii close to the SMBH, likely from a location “internal” to the jet itself. Constraints on the brightness temperature instead place the radio emission at much larger radii, suggesting that it results from the shock interaction of the jet with the CNM, as originally predicted by GM11 just months prior to the discovery of Sw J1644+57.

2 Jet-CNM interaction

2.1 Evidence for the reverse shock crossing

Metzger *et al.* (2012; MGM12) model the radio emission from Sw J1644+57 in order to constrain the properties of the relativistic jet and the CNM surrounding the SMBH, using the observed X-ray luminosity as a proxy for the jet power. The X-ray light curve shows an initial period of several bright flares lasting for a duration $t_j \sim$ several days, before declining as a power-law in a manner roughly consistent with the expectations of fall-back accretion (Rees 1988) if the jet emission were to directly track the accretion rate.

Interaction between the matter in the relativistic jet and the CNM occurs in two stages: (1) Initially, at times $t \lesssim t_j$, the jet drives a forward shock (FS) into the CNM, while simultaneously a reverse shock (RS) propagates back through the ejecta. (2) At later times, once the RS has entirely crossed through the initial ejecta

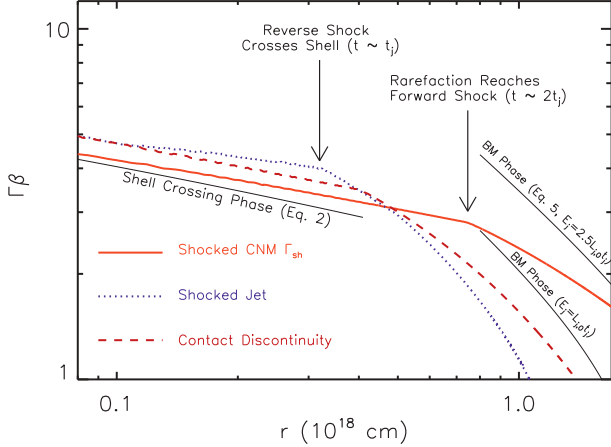


Fig. 1. Lorentz factor of the shocked circumnuclear medium (CNM) behind the forward shock (Γ_{sh} ; thick solid red line), of the contact discontinuity (dashed brown line) and of the shocked jet (dotted blue line), extracted directly from a one-dimensional hydrodynamic simulation. The calculation is performed assuming a jet duration $t_j = 3 \times 10^5$ s, initial jet luminosity $L_{j,0} = 10^{48}$ ergs s^{-1} and CNM radial density profile $n_{\text{cnm}} = 10(r/10^{18} \text{ cm})^{-1} \text{ cm}^{-3}$ ($k = 1$). Shown for comparison with black solid lines are the analytic approximations for Γ_{sh} during the early phase when the reverse shock is crossing through the shell of ejecta released during the initial period of constant jet luminosity ($t \lesssim t_j$), and at late times during the Blandford-McKee self-similar evolution ($t \gg 2t_j$) for different assumptions about the total energy of the blast wave $E_{j,\text{iso}}$. Note that a break occurs in the Lorentz factor of the shocked jet once the outflow reaches the radius $r = r_{\text{cross}} \approx 3 \times 10^{17} \text{ cm}$ (observer time $t \approx t_j$) at which the reverse shock has crossed entirely through the initial shell. The break in Γ_{sh} from this transition occurs at a somewhat larger radius $r \approx 7 \times 10^{17} \text{ cm}$ ($t \approx 2t_j$), once the rarefaction wave launched at $r \approx r_{\text{cross}}$ reaches the forward shock (from MGM12).

($t \gg t_j$), the blastwave approaches a self-similar expansion (*e.g.* of Blandford & McKee 1976; BM76).

The transition between stages (1) and (2) decreases the pressure of the shocked fluid, starting from behind the RS. The pressure drop is then communicated after a delay to the FS by a rarefaction that is launched from the back of the shocked shell. This signal propagates at the (relativistically hot) sound speed of the shocked fluid, reaching the FS at an observer time $t \sim 2t_j$, *i.e.* about twice the observed duration of peak jet activity. Figure 1 shows the evolution of the Lorentz factor Γ_{sh} of material at various locations within the shocked ejecta (measured in the lab frame), as calculated using a one-dimensional relativistic hydrodynamic simulation of a jet with a constant (isotropic) kinetic luminosity $L_{j,0} = 10^{48}$ erg s^{-1} , duration $t_j = 3 \times 10^5$ s, and initial Lorentz factor $\Gamma_j = 10$ (jet spreading is relatively minor as long as the jet is ultra-relativistic; *e.g.* Zhang & MacFadyen 2009). Note that

a break occurs once the RS has crossed the ejecta, first immediately behind the RS ($t \approx t_j$) and then later behind the FS ($t \sim 2t_j$). As we now discuss, this last break in the Lorentz factor produces an achromatic break in the resulting radio light curve since emission from the FS dominates that from the RS in the case of Swift J1644+57.

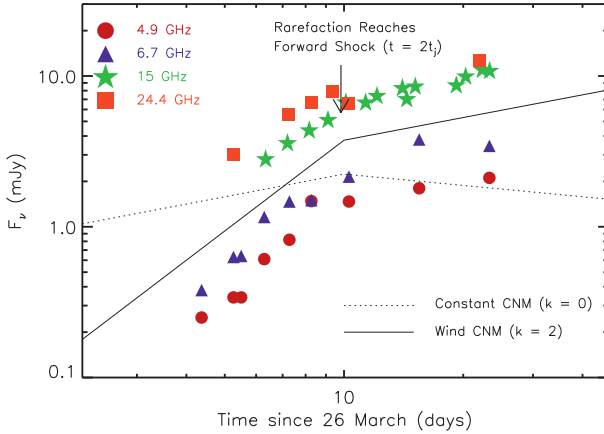


Fig. 2. Radio light curves of Swift J1644+57 from Zauderer *et al.* (2011) at several frequencies below the self-absorption break. The achromatic break observed at $t \sim 10$ days occurs when the rarefaction wave (produced once the reverse shock crosses the initial shell of ejecta) catches up to the forward shock. Shown for comparison are the predicted light curves (arbitrary normalization) if the CNM density has a constant (*dotted line*; $k = 0$) or a wind-type (*solid line*; $k=2$) radial profile (from MGM12).

Figure 2 shows the radio light curves of Sw J1644+57 from Zauderer *et al.* (2011) at several frequencies below the self-absorption frequency. The data are well fit by a power law $F_\nu \propto t^\alpha$ with $\alpha = 2$ at times $t \lesssim t_{\text{break}} = 10$ days, followed by a break to shallower rise $\alpha \approx 0.5$ at late times. As discussed above, this achromatic break is naturally explained as the rarefaction reaching the FS following the RS crossing the ejecta; the time of the break at $t_{\text{break}} \approx 2t_j \sim 10$ days is consistent with this picture (compare Figs. 1 and 2). Alternative explanations for the observed break (such as the “jet breaks” in normal GRB afterglows) are discussed by MGM12 and ruled out.

MGM12 show that for a CNM of density profile $n_{\text{cnm}} \propto r^{-k}$, the flux below the self-absorption frequency obeys $F_{\nu < \nu_{\text{sa}}} \propto t^{(k+2)/(4-k)} [\propto t^{(k-1)/(4-k)}]$ during and much after the RS crossing, respectively. The observed pre- and post-break slopes are that both broadly consistent with a wind-type CNM ($k = 2$), as was also found by Zauderer *et al.* (2011) based on independent arguments. Note that this is just the density profile sampled by the jet on the radial scales $0.01 \text{ pc} \lesssim r \lesssim 0.1 \text{ pc}$ probed by the first \sim week of observations.

2.2 Derived properties of the jet and CNM

If one assumes that by day 23 ($t \approx 6t_j$) the jet has approached the self-similar BM76 evolution and continues to propagate into a $n_{\text{cnm}} \propto 1/r^2$ medium, then the observed characteristic synchrotron frequency $\nu_m(t = 23 \text{ d}) \equiv \nu_{m,23} \approx 40 \text{ GHz}$, self-absorption frequency $\nu_{\text{sa}}(t = 23 \text{ d}) \equiv \nu_{\text{sa},23} \approx 10 \text{ GHz}$ and the 4.9 GHz flux $F_{\nu=4.9 \text{ GHz}}(t = 23 \text{ d}) \equiv F_{4.9,23} \approx 2 \text{ mJy}$ can be solved for the fraction ϵ_e of the shocked energy placed into ultra-relativistic electrons; the number density n_{18} at $r = 10^{18} \text{ cm}$; and the initial (unshocked) Lorentz factor of the jet Γ_j :

$$\epsilon_e = 0.12 \epsilon_{B,-2}^{-1/4} \left(\frac{\nu_{m,23}}{10 \text{ GHz}} \right)^{1/2} \left(\frac{\nu_{m,23}}{10 \text{ GHz}} \right)^{1/2} \quad (2.1)$$

$$n_{18} = 1.5 \text{ cm}^{-3} \epsilon_{B,-2}^{-3/8} \left(\frac{\nu_{m,23}}{40 \text{ GHz}} \right)^{5/12} \left(\frac{\nu_{\text{sa},23}}{10 \text{ GHz}} \right)^{5/6} \quad (2.2)$$

$$\Gamma_j = 17 \epsilon_{B,-2}^{5/32} \left(\frac{\nu_{m,23}}{40 \text{ GHz}} \right)^{-1/16} \left(\frac{\nu_{\text{sa},23}}{10 \text{ GHz}} \right)^{-5/8} \left(\frac{F_{4.9,23}}{2 \text{ mJy}} \right)^{-1/2}, \quad (2.3)$$

where ϵ_B is the fraction of the post-shock thermal energy in the magnetic field and we have assumed a jet with opening angle $\theta_j = 1/\Gamma_j$ (MGM12).

Equations (2.1)–(2.3) show that for $\epsilon_B \approx 10^{-3} - 0.1$ (as found in many GRB afterglows), one finds reasonable values for $\epsilon_e \approx 0.05 - 0.2$, $n_{18} \approx 0.3 - 10$, and $\Gamma_j \simeq 10 - 20$. The value of $\epsilon_e \approx 0.1$ is similar to those found in GRB afterglows, while n_{18} is somewhat lower than the gas density at a similar location in our own Galactic center near SgrA*. Since the jet Lorentz factor Γ_j is particularly robust, this constrains the beaming fraction of Sw J1644+57 to be $f_b \sim 1/2\Gamma_j^2 \approx 1 - 5 \times 10^{-3}$.

3 Discussion

3.1 Implications of jet beaming

The small beaming fraction $f_b \sim 3 \times 10^{-3}$ inferred for Swift J1644+57 has several implications. First, it implies that the true beaming-corrected peak luminosity of the prompt X-ray/ γ -ray emission may be as low as $\sim 10^{45} \text{ erg s}^{-1}$, similar to the Eddington luminosity of a $10^7 M_\odot$ SMBH. On the other hand, the beaming-corrected energy of the initial jet was $\sim 10^{51}$ ergs, which requires a jet efficiency of $\epsilon_j \approx 10^{-2}$ (fraction of accretion power placed into the jet) if Swift J1644+57 was indeed powered by the accretion of a solar-mass star. The beaming fraction we infer also appears to be larger than that required to reconcile the rate of J1644-like events with the TDE rate inferred by independent means (*e.g.* Van Velzen *et al.* 2011) by a factor of $\sim 10 - 30$ (Burrows *et al.* 2011). This hints that only a small fraction of TDE events are accompanied by [detectable] relativistic outflows.

The beaming-corrected luminosity of Sw J1644+57 also has implications for the physics of relativistic jet formation. AGN jets are generally thought to be

powered by a strong magnetic field which threads the black hole accretion disk or ergosphere. Since the magnetic flux through the initial star is $\sim B_\star R_\star^2$, then flux freezing results in a field near the BH horizon ($r \sim 2R_g$) of strength $B_{\text{BH}} \sim B_\star (R_\star/2R_g)^2 = 40B_{\star,3} M_6^{-2}$ G, where $R_\star \sim R_\odot$ and we have normalized the stellar field to an (optimistic) value of 1 kG. If the jet is dominated by Poynting flux near its base, then to order-of-magnitude the resulting jet power is

$$L_j \sim \pi (2R_g)^2 (B_{\text{BH}}^2 / 4\pi) c \sim 10^{36} B_{\star,3}^2 M_6^{-2} \text{ergs}^{-1}. \quad (3.1)$$

Comparing this expression to the (beaming-corrected) peak X-ray luminosity $L_X \sim 10^{45}$ erg s $^{-1}$ of Swift J1644+57 illustrates that the initial field of the disrupted star is by itself $\gtrsim 4$ orders of magnitude too low for any reasonable value of M_{BH} (Bloom *et al.* 2011).

A key unsolved theoretical issue in the physics of jet formation is whether the large scale magnetic field required to power the jet is advected from the outer boundary of the flow (*e.g.* Spruit & Uzdensky 2005), or whether it is generated locally in the disk by instabilities or dynamo action. Because the magnetic field strength of a solar-type star is insufficient to drive a jet as powerful as Swift J1644+57, this suggests that locally-generated fields may be responsible for the jet. Note that spontaneous large-scale poloidal field generation is *not* found in current MHD jet simulations, which instead find that a powerful jet of the magnitude required to explain Swift J1644+57 is not produced if the initial poloidal field is weak (*e.g.* De Veillers *et al.* 2005; Penna *et al.* 2010). If such a dynamo is indeed more efficient than found in current simulations and if observations show that only a fraction of (otherwise similar) tidal disruptions are accompanied by a jet would, this would suggest that a second parameter, such as the spin of the black hole, controls the jet strength.

3.2 Blind detection with future radio surveys

After the blast wave decelerates to mildly relativistic speeds, the jet begins to spread laterally (Zhang & MacFadyen 2009), eventually relaxing into a non-relativistic, spherical expansion (Sedov-Taylor phase) centered at the location of the deceleration of the blast. Radio emission becomes isotropic following this non-relativistic transition, in which case it could be visible even in cases where the initial high energy emission was missed because the jet was pointing in a different direction.

Radio astronomy is poised for a revolution in the study of time-domain (“transient”) phenomena over the coming decade, with new wide-field survey arrays coming online at both meter wavelengths (*e.g.* LOFAR, MWA, and LWA) as well as GHz frequencies (*e.g.* Apertif/WSRT, MeerKAT, and ASKAP). Frail *et al.* (2012) show that Swift J1644+57-like events viewed off-axis could in fact dominate the GHz transient sky, with 10–100 events potentially detectable per year by upcoming surveys (see also GM11). Future monitoring of Swift J1644+57 through the non-relativistic phase over the coming years will thus provide us with a better understanding of how similar events would appear to a viewer with a more typical

observing angle. If the emission remains bright at high frequencies, the radio lobes may become resolvable with VLBI on a similar timescale. With similar motivation, targeted searches have begun for late radio emission from TDE candidates detected previously at X-ray, UV, or optical wavelengths. Detections or upper limits from these studies will help constrain the diversity of relativistic outflows accompanying TDEs.

References

- Ayal, S., Livio, M., & Piran, T., 2000, ApJ, 545, 772
Berger, E., Levan, A., Tanvir, N.R., *et al.*, 2011, GRB Coordinates Network, 11854, 1
Berger, E., Zauderer, A., Pooley, G.G., *et al.*, 2012, ApJ, 748, 36
Blandford, R.D., & McKee, C.F., 1976, Phys. Fluids, 19, 1130
Bloom, J.S., Giannios, D., Metzger, B.D., *et al.*, 2011, Science, 333, 203
Burrows, D.N., Kennea, J.A., Ghisellini, G., *et al.*, 2011, Nature, 476, 421
De Villiers, J.-P., Hawley, J.F., Krolik, J.H., & Hirose, S., 2005, ApJ, 620, 878
Frail, D.A., Kulkarni, S.R., Ofek, E.O., Bower, G.C., & Nakar, E., 2012, ApJ, 747, 70
Giannios, D., & Metzger, B.D., 2011, MNRAS, 416, 2102
Guillochon, J., Ramirez-Ruiz, E., Rosswog, S., & Kasen, D., 2009, ApJ, 705, 844
Levan, A.J., Tanvir, N.R., Cenko, S.B., *et al.*, 2011, Science, 333, 199
Lodato, G., King, A.R., & Pringle, J.E., 2009, MNRAS, 392, 332
Lodato, G., & Rossi, E.M., 2011, MNRAS, 410, 359
Penna, R.F., McKinney, J.C., Narayan, R., *et al.*, 2010, MNRAS, 408, 752
Rees, M.J., 1988, Nature, 333, 523
Spruit, H.C., & Uzdensky, D.A., 2005, ApJ, 629, 960
Strubbe, L.E., & Quataert, E., 2009, MNRAS, 400, 2070
Ulmer, A., 1999, ApJ, 514, 180
van Velzen, S., Farrar, G.R., Gezari, S., *et al.*, 2011, ApJ, 741, 73
van Velzen, S., Körding, E., & Falcke, H., 2011, MNRAS, 417, L51
Zauderer, B.A., Berger, E., Soderberg, A.M., *et al.*, 2011, Nature, 476, 425
Zhang, W., & MacFadyen, A., 2009, ApJ, 698, 1261

MAGNETIC FIELD AMPLIFICATION AND SATURATION BY TURBULENCE IN A RELATIVISTIC SHOCK PROPAGATING THROUGH AN INHOMOGENEOUS MEDIUM

Y. Mizuno¹, M. Pohl², J. Niemiec³, B. Zhang⁴, K.-I. Nishikawa⁵
and P.E. Hardee⁶

Abstract. We perform two-dimensional relativistic magnetohydrodynamic simulations of a mildly relativistic shock propagating through an inhomogeneous medium. Simulation results show that the postshock region becomes turbulent owing to preshock density inhomogeneity, and the magnetic field is strongly amplified due to the stretching and folding of field lines in the turbulent velocity field. The amplified magnetic field evolves into a filamentary structure in two-dimensional simulations. The magnetic energy spectrum is flatter than the Kolmogorov spectrum and indicates that the so-called small-scale dynamo is occurring in the postshock region.

1 Introduction

In the standard GRB afterglow model, the radiation is produced in a relativistic blastwave shell propagating into a weakly magnetized plasma (*e.g.*, Piran 2005; Mészáros 2006). Although it is strongly model-dependent, detailed studies of GRB spectra and light curves have shown that the magnetic energy density in the emitting region is a fraction $\epsilon_B \sim 10^{-3} - 10^{-1}$ of the internal energy density (Panaitescu & Kumar 2002). However, simple compressional amplification of the weak pre-existing magnetic field of the circumburst medium (micro to sub-milli gauss) cannot make such high magnetization. The leading hypothesis for field amplification in GRB afterglows is the relativistic Weibel instability producing

¹ Institute of Astronomy, National Tsing-Hua University, Hsinchu, Taiwan R.O.C.

² Institute of Physics and Astronomy, Universitat Potsdam, Potsdam-Golm, Germany

³ Institute of Nuclear Physics PAN, Kraków, Poland

⁴ Department of Physics and Astronomy, University of Nevada, Las Vegas, NV, USA

⁵ CSPAR, University of Alabama in Huntsville, Huntsville, AL, USA

⁶ Department of Physics and Astronomy, University of Alabama, Tuscaloosa, AL, USA

filamentary currents aligned with the shock normal (Medvedev & Loeb 1999). However, it remains unclear whether magnetic fields generated on scales of tens of plasma skin depths will persist at sufficient strength in the entire emission region. Giacalone & Jokipii (2007) have performed non-relativistic magnetohydrodynamic (MHD) shock simulations including density fluctuations. They observed a strong magnetic-field amplification caused by turbulence in the postshock medium. Here we have investigated the magnetic-field amplification by turbulence in two-dimensional relativistic MHD simulations of a mildly relativistic shock wave propagating through an inhomogeneous medium.

2 Numerical setup and results

We use the 3D GRMHD code “RAISHIN” in 2D Cartesian geometry in special relativistic regime (Mizuno *et al.* 2006, 2011b). At the beginning of the simulations, an inhomogeneous cold plasma following a two-dimensional Kolmogorov-like power-law spectrum is established across the whole simulation region and uniformly flows in the positive x -direction with speed $v_0 = 0.5c$. The preshock plasma carries a weak constant parallel magnetic field ($B_x = 1.15 \times 10^{-2} (4\pi\rho_0 c^2)^{-1/2}$) with respect to the shock propagation directions. We set 4 times longer simulation box in the x -direction than that of Mizuno *et al.* (2011a). A detailed description of the initial set-up for the simulations can be found in Mizuno *et al.* (2011a).

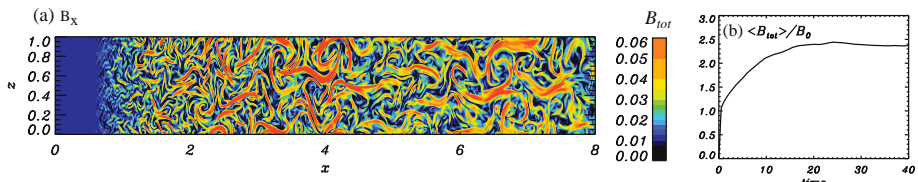


Fig. 1. a) Two-dimensional image of the total magnetic field strength at $t = 37.0L/c$. b) Time evolution of the volume-averaged total magnetic field strength in the postshock region normalized by the initial magnetic field strength.

Figure 1a shows a 2D image of the total magnetic field strength at $t = 37.0L/c$. When the preshock plasma with inhomogeneous density encounters the shock, the shock front is rippled, leading to significant, random transverse flow behind the shock. Since the preexisting magnetic field is much weaker than the postshock turbulence, the turbulent velocity field can easily stretch and deform the magnetic field lines. This creates regions with larger magnetic field intensity. In the region near the shock front, the vorticity scale size is small but in the region far away from the shock front, the vorticity scale size becomes larger and the magnetic field is strongly amplified. The amplified magnetic field evolves into a filamentary structure. The turbulent velocity is subsonic and super-Alfvénic in most of the postshock region.

Figure 1b shows the time evolution of magnetic field amplification indicated as a volume-averaged total magnetic field strength in the postshock region normalized by the initial magnetic field strength. The amplification of mean magnetic field is saturated around $t \sim 20L/c$. The saturation occurs when the magnetic energy is comparable to the turbulent kinetic energy. The local maximum magnetic field strength is much larger than the mean magnetic field, about 13 times larger than the initial magnetic field.

In order to understand the statistical properties of the turbulent fluctuations in the postshock region, it is helpful to observe their spectra. The kinetic-energy spectra almost follow a Kolmogorov spectrum in all cases, $E_{kin}(k) \propto k^{-8/3}$ in two-dimensional systems. The magnetic energy spectra are almost flat and strongly deviate from a Kolmogorov spectrum. Spectra flatter than a Kolmogorov spectrum are typical of the small-scale dynamo (*e.g.*, Brandenburg & Subramanian 2005; Inoue *et al.* 2011).

The present simulation suggests the likelihood of a scenario whereby preexisting large-scale preshock density inhomogeneity causes strong magnetic field amplification in the postshock region. This process will be important in GRBs and in AGN jets.

This work is supported by NSF awards AST-098010 and AST-098040, NASA awards NNX08AG83G and NNX12AH06G, Taiwan NSC award NSC 100-2112-M-007-022-MY3, and NCN as project DEC-2011/01/B/ST9/03183. The simulations were performed on the Columbia Supercomputer at NASA Ames Research Center and the Nautilus at the NICS in XSEDE project.

References

- Brandenburg, A., & Subramanian K., 2005, Phys. Rep., 417, 1
- Giacalone, J., & Jokipii, R., 2007, ApJ, 663, L41
- Inoue, T., Asano, K., & Ioka, K., 2011, ApJ, 734, 77
- Medvedev, M.V., & Loeb, A., 1999, ApJ, 526, 697
- Mészáros, P., 2006, Rep. Prog. Phys., 69, 2259
- Mizuno, Y., Nishikawa, K.-I., Koide, S., *et al.*, 2006, preprint [[arXiv:astro-ph/0609004](https://arxiv.org/abs/astro-ph/0609004)]
- Mizuno, Y., Pohl, M., Niemiec J., *et al.*, 2011a, ApJ, 726, 62
- Mizuno, Y., Nishikawa, K.-I., & Hardee, P.E., 2011b, ApJ, 734, 19
- Panaitescu, A., & Kumar, P., 2002, ApJ, 571, 779
- Piran, T., 2005, Rev. Mod. Phys., 76, 1143

RADIATION FROM ACCELERATED PARTICLES IN RELATIVISTIC JETS WITH SHOCKS, SHEAR-FLOW, AND RECONNECTION

K.-I. Nishikawa¹, B. Zhang², I. Dutan³, M. Medvedev⁴, P. Hardee⁵,
E.J. Choi⁶, K.W. Min⁶, J. Niemiec⁷, Y. Mizuno⁸, A. Nordlund⁹,
J.T. Frederiksen⁹, H. Sol¹⁰, M. Pohl¹¹ and D.H. Hartmann¹²

Abstract. We investigated particle acceleration and shock structure associated with an unmagnetized relativistic jet propagating into an unmagnetized plasma. Strong magnetic fields generated in the trailing shock contribute to the electrons transverse deflection and acceleration. We have calculated, self-consistently, the radiation from electrons accelerated in these turbulent magnetic fields. We found that the synthetic spectra depend on the bulk Lorentz factor of the jet, its temperature and strength of the generated magnetic fields. We have also investigated accelerated electrons in strong magnetic fields generated by kinetic shear (Kelvin-Helmholtz) instabilities. The calculated properties of the emerging radiation will guide our understanding of the complex time evolution and/or spectral structure in gamma-ray bursts, relativistic jets in general, and supernova remnants.

¹ Center for Space Plasma and Aeronomic Research, University of Alabama in Huntsville, 320 Sparkman Drive, ZP12, Huntsville, AL 35805, USA

² Department of Physics, University of Nevada, Las Vegas, NV 89154, USA

³ Institute of Space Science, Atomistilor 409, Bucharest-Magurele 077125, Romania

⁴ Department of Physics and Astronomy, University of Kansas, KS 66045, USA

⁵ Department of Physics and Astronomy, The University of Alabama, Tuscaloosa, AL 35487, USA

⁶ Korea Advanced Institute of Science and Technology, Daejeon 305-701, South Korea

⁷ Institute of Nuclear Physics PAN, ul. Radzikowskiego 152, 31-342 Kraków, Poland

⁸ Institute of Astronomy National Tsing-Hua University, Hsinchu, Taiwan 30013, R.O.C

⁹ Niels Bohr Institute, University of Copenhagen, Juliane Maries Vej 30, 2100 Copenhagen, Denmark

¹⁰ LUTH, Observatoire de Paris-Meudon, 5 place Jules Jansen, 92195 Meudon Cedex, France

¹¹ Institut of Physics and Astronomy, University of Potsdam, Karl-Liebknecht-Strasse 24/25, 14476 Potsdam-Golm, Germany

¹² Department of Physics and Astronomy, Clemson University, Clemson, SC 29634, USA

1 Simulation of kinetic Kelvin-Helmholz instability

Recent kinetic simulations have focused on magnetic field generation via electromagnetic plasma instabilities in unmagnetized flows without velocity shears. Three-dimensional (3D) particle-in-cell (PIC) simulations of Weibel turbulence (Nishikawa *et al.* 2009) have demonstrated subequipartition magnetic field generation. We have calculated, self-consistently, the radiation from electrons accelerated in the turbulent magnetic fields. We found that the synthetic spectra depend on the Lorentz factor of the jet, its thermal temperature and strength of the generated magnetic fields (Nishikawa *et al.* 2011, 2012). These works have neglected the role of velocity shear in the flow, which are an alternative mechanism to generate subequipartition magnetic fields in relativistic outflows (Alves *et al.* 2012). Furthermore, a shear flow upstream of a shock can lead to density inhomogeneities via the Kelvin-Helmholtz instability (KHI) which may constitute important scattering sites for particle acceleration.

We have performed simulations with a relativistic core jet surrounded by a sheared velocity layer with the stationary sheath plasmas as simulated in our RMHD simulations (Mizuno *et al.* 2007). In our initial simulations the initial conditions for the shear flow will have a core jet with $v_{core} = 0.9978c$ ($\gamma = 15$) pointing in the positive x direction in the middle of the simulation box as in Alves *et al.* (2012); the upper and lower quarter of the simulation box will contain a sheath also moving in the positive x direction with $v_{sheath} = 0$ (for this simulation). Overall, this structure is similar in spirit, although not in scale, to that proposed for active galactic nuclei (AGN) relativistic jet cores surrounded by a slower moving sheath, and is also relevant to gamma-ray burst (GRB) jets. In particular, we note that this structure is also relevant to the “jet-in-a-jet” or “needles” in a jet scenarios (Giannios *et al.* 2009, papers therein) which have been invoked to provide smaller scale high speed structures within a much larger more slowly moving AGN jet. Similar smaller scale structures within GRB jets are also conceivable.

This more realistic setup is different from the initial conditions used by the previous simulations with counter-steaming flow of Alves *et al.* (2012), and hence allows us to compute synthetic spectra in the observer frame far along the x -direction. As discussed by Alves *et al.* (2012), in our setup the growing kinetic KHI will propagate with the flow. For GRB jets, the relativistic jet core will have much higher density relative to the external medium. On the other hand, for an AGN the relativistic core is less dense than the surrounding sheath.

We have performed simulations using a system with $(L_x, L_y, L_z) = (1005\Delta, 205\Delta, 205\Delta)$ with the mass ratio of ion and electron, $m_i/m_e = 20$. Figure 1 shows the magnetic field structures generated by shearing relativistic electron-ion flows with $\gamma = 15$ with stationary sheath plasmas taken at time $t = 70\omega_{pe}^{-1}$. Figure 1a shows the magnetic field intensity of B_y plotted in the $y - z$ plane at the center of the box $x = 500\Delta$ (jet out of the plane) with the magnetic fields B_y (red), B_x (black), and B_z (blue) at $x = 500\Delta$ and $y = 100\Delta$. Figure 1c shows the x component of current. The relativistic jet is directed out of the plane and the positive current is generated at the jet side, whereas the negative current is

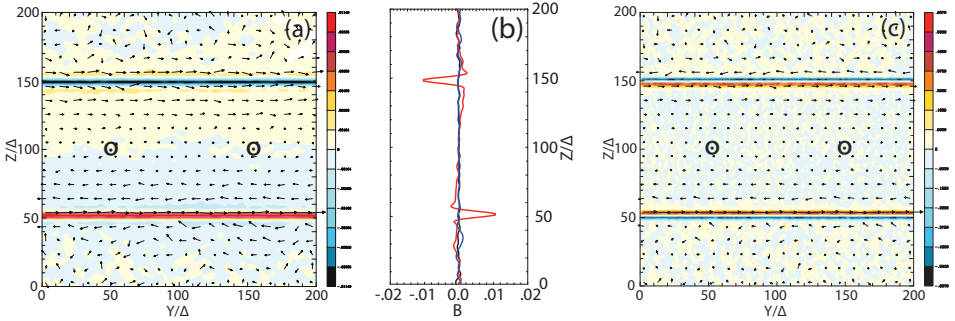


Fig. 1. Magnetic field structures generated by shearing relativistic electron-ion flows with $\gamma = 15$ with stationary sheath plasmas taken at time $t = 70 \omega_{pe}^{-1}$. Here ω_{pe} is the electron plasma frequency. The magnetic field intensity of B_y is plotted in the $y - z$ plane at the center of the box $x = 500\Delta$ (a) (jet out of the plane). Figure 1b shows the magnetic fields B_y (red), B_x (black), and B_z (blue) at $x = 500\Delta$ and $y = 100\Delta$. Figure 1c shows the x component of the current density. The relativistic jet is directed out of the plane and the positive current is generated at the core jet side and the negative current is generated in the sheath side. The positive currents are stronger than the negative ones, therefore the B_y components are generated as shown in Figure 1b.

generated in the sheath side. The positive currents are stronger than the negative currents, therefore the B_y components are generated as shown in Figures 1a and 1b. In a forthcoming study we will obtain synthetic spectra from accelerated particles in kinetic KHI as we did for shock simulations (Nishikawa *et al.* 2011, 2012).

This work is supported by NSF AST-0506666, AST-0506719, AST-0908010, and AST-0908040, NASA-NNG05GK73G, NNX07AJ88G, NNX08AG83G, NNX08 AL39G, NNX09AD16G, and NNX12AH06G. JN is supported by NCN through grant DEC-2011/01/B/ST9/03183. Simulations were performed at the Columbia facility at the NASA Advanced Supercomputing (NAS) and Kraken and Nautilus at The National Institute for Computational Sciences (NICS) which is supported by the NSF. This research was started during the program “Chirps, Mergers and Explosions: The Final Moments of Coalescing Compact Binaries” at the Kavli Institute for Theoretical Physics which is supported by the National Science Foundation under Grant No. PHY05-51164.

References

- Alves, E.P., Grismayer, T., Martines, S.F., *et al.*, 2012, ApJ, 746, L14
- Giannios, D., Uzdensky, D.A., & Begelman, M.C., 2009, MNRAS, 395, L29
- Mizuno, Y., Hardee, P., & Nishikawa, K.-I., 2007, ApJ, 662, 835
- Nishikawa, K.-I., Niemiec, J., Hardee, P.E., *et al.*, 2009, ApJ, 698, L10
- Nishikawa, K.-I., Niemiec, J., Medvedev, M., *et al.*, 2011, Adv. Space Res., 47, 1434
- Nishikawa, K.-I., Niemiec, J., Zhang, B., *et al.*, 2012, IJMP: Conf. Ser., 8, 259

ACCELERATION OF MAGNETIZED COLLAPSAR JETS AFTER BREAKOUT

K. Sapountzis¹ and N. Vlahakis¹

Abstract. In the collapsar model of long GRBs the jet is formed at the center of the progenitor star, propagates in its interior, and produces the observed gamma rays much after its breakout from the star. The loss of pressure support during breakout induces a strong rarefaction wave that propagates inside the jet and causes its bulk acceleration. This mechanism has been already studied using axisymmetric magnetohydrodynamic (MHD) simulations assuming a prescribed shape for the surface between the jet and its environment, as well as using simple rarefaction waves in planar geometry. Trying to improve over these works, we solve the steady-state, axisymmetric, relativistic MHD equations using the method of characteristics. In this way the jet boundary is found self-consistently and the rarefaction wave is studied in the axisymmetric geometry. In this poster we present our first results and a comparison with previous works.

1 Introduction

In our poster we studied the effects of rarefaction waves in an outflow as the one expected in GRB/Collapsar model focusing on the last acceleration phase, *i.e.* when the outflow emerges from the stellar envelope and beyond. According to the most accepted scenario the outflow originates from the core of the star and attains a first partial acceleration as it propagates inside the star. In its way out to the interstellar medium the pressure drops steeply posing discontinuous boundary conditions. The non-smooth boundary information propagates in the body of the outflow forming a weak discontinuity called rarefaction wave.

Except its unavoidable appearance at the time of the break out, rarefaction has implications that reveal new interesting features and solve some of the issues that the conventional MHD mechanism faces and especially in the interpretation

¹ Department of Astrophysics, Astronomy and Mechanics, Faculty of Physics, University of Athens, Greece

of the panchromatic breaks in the afterglow light curves. According to that mechanism the Lorentz factor achieved is closely associated with collimation ($\gamma\theta_j \sim 1$, where θ_j the jet opening) preventing the break. Moreover rarefaction is a very effective mechanism that besides its acceleration aspects it has the property of not affecting significantly the orientation and the collimation of the rarefied region (see Fig. 1 for the relevant geometry). Because of its importance in GRBs, rarefaction has been studied extensively in a number of sophisticated time dependent numerical simulations (Tchekhovskoy *et al.* 2010; Komissarov *et al.* 2010) and fewer analytical works (*e.g.* Sapountzis & Vlahakis 2012). Our present model is focused on the steady state case and due to the nature of the outflow we examine the ideal MHD equations in the relativistic limit. Two assumptions that define further our work is the axisymmetry and the cold outflow limit both of which are indicated by the physics of the problem but also from previous analytical works on the spatial scales and the hydrodynamical/thermal driven rarefaction (Sapountzis & Vlahakis 2012).

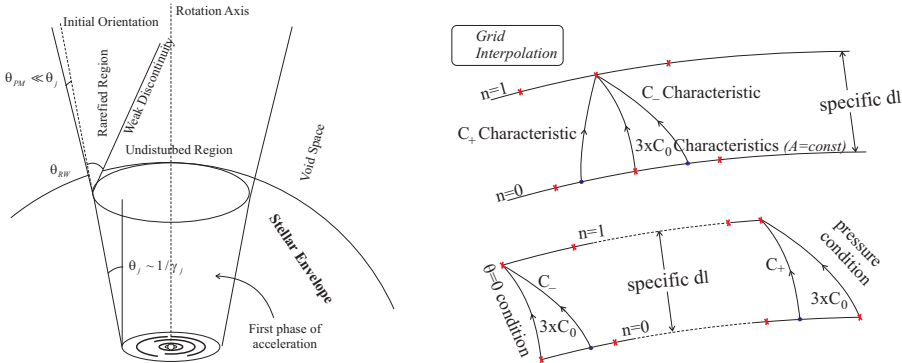


Fig. 1. *Left:* schematic representation of the geometry of the problem for the GRB/Collapsar model. Notice the negligible $\theta_{PM} \ll \theta_j$ angle allowing the appearance of the panchromatic break (see Discussion). *Right:* the algorithm we use based on the method of characteristics. The upper sketch deals with the intermediate points while the lower one the edging. Notice the consistent way that the boundary conditions are used in order to fill the missing characteristic.

2 Equations - algorithm

Under the assumptions mentioned above we project the MHD equations along and perpendicularly to the poloidal filed lines reaching to a system of the form

$$F(A, \ell) \frac{\partial U}{\partial \ell} + G(A, \ell) \frac{\partial U}{\partial A} = H(A, \ell) \quad U = [\omega \ z \ \theta \ S \ \Lambda]$$

where A the magnetic flux function which can be used to label the field lines, and ℓ the length along them, U the vector of the solution, F, G, H the matrixes defining the system and Λ, S introduced instead of $\partial\omega/\partial A, \partial z/\partial A$ to degrade equations.

cylindrical coordinates (ω, φ, z)	
$z = 10^4$ Initial Surface	$v_i = 0$ cylindrical flow
$\gamma_i = 100$ all over	$\zeta = 0.6$ model index
$B_{pi} = \frac{B_j}{[1 + (\omega/\omega_o)^2]^\zeta}$	$\omega_0 = 100$ constant
$B_{\varphi i} = -\frac{B_j \gamma_i}{(\omega/\omega_o)[1 + (\omega/\omega_o)^2]^\zeta} \cdot \sqrt{\frac{[1 + (\omega/\omega_o)^2]^{2\zeta} - 1 - 2\zeta(\omega/\omega_o)^2}{2\zeta - 1}}$	

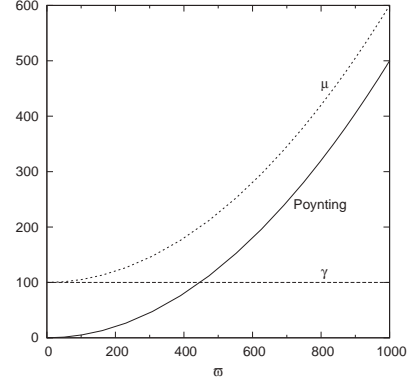


Fig. 2. *Left:* the initial quantities we used. *Right:* the energetics of the initial conditions.

The schema for the integration we used is based on the equation characteristics and among others has the advantage of not prescribing the shape of the last streamline, *i.e.* the boundary surface, as most numerical simulations require (Fig. 1). A first task was to find the conditions at the base of the flow satisfying the force balance and being consistent with the previous phase of acceleration (till the fast magnetosonic surface).

A flow like this might be split in two areas: (I) an inner core, that is weakly or no magnetized (hydrodynamic), where the energy is mostly the inertial of the plasma (cold flow), (II) a magnetic dominated area where most of the energy is in the Poynting flux. The initial parameters and a diagram on the initial energetics of the outflow are shown in Figure 2. Note that the total energy per mass μ determines also the maximum attainable Lorentz factor since at the end of the rarefaction and when Poynting energy vanishes, all the available energy becomes bulk kinetic ($\gamma \sim \mu$).

3 Results – discussion

The results of the integration are shown in Figure 3. We notice that rarefaction acceleration is a very efficient mechanism and most of the magnetic energy is converted to bulk kinetic, especially in the outer portion of the flow. This conclusion holds also in thermally driven flows. However as shown in Sapountzis & Vlahakis (2012) the hydrodynamic rarefaction tends to work in much larger distances, arguing in favor of the magnetic dominated scenario. Moreover the results in an axisymmetric flow seem not to be affected by the specific symmetry and remain the same as in the planar case. The acceleration efficiency, the bending of the flow (Prandtl-Meyer angle), the angle of the weak discontinuity are in agreement

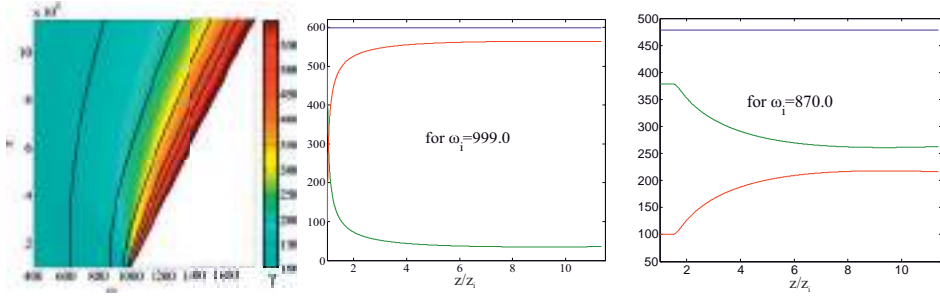


Fig. 3. *Left:* the physical shape of the flow and some field lines. The color refers to the spatial Lorentz factor distribution. Notice that the inner part has $\gamma_e \sim \mu$ and so no further acceleration is expected for this configuration. *Middle & Right:* the energetic evolution along two lines with initial cylindrical distance ω_i . Blue line represents the total energy μ , red the inertial one γ and green the Poynting flux.

with the analytical expressions given in Sapountzis & Vlahakis (2012). A further advantage of the rarefaction mechanism is the negligible Prandtl - Meyer angle ($\theta_{PM} \ll \theta_j$) resulting in high values of the $\gamma\theta$ product making it a plausible mechanism for the GRBs outflows. The main implication of axisymmetry is the reflection of the rarefaction wave on the rotation axis. The reflected wave ceases the acceleration, but this does not affect significantly the already high achieved efficiency. Among the advantages of our model is that the shape of the jet surface was obtained self consistently. Moreover our code is capable of analyzing in general superfast steady-state outflows supported by a given external pressure. Therefore it can improve existing jet models without the need of prescribing the boundary shape or it can be used to investigate the possible implications that a constant and negligible pressure might have in the rarefaction discussed above.

This research has been co-financed by the European Union (European Social Fund – ESF) and Greek national funds through the Operational Program “Education and Lifelong Learning” of the National Strategic Reference Framework (NSRF) - Research Funding Program: Heracleitus II. Investing in knowledge society through the European Social Fund.

References

- Komissarov, S.S., Vlahakis, N., & Königl, A., 2010, MNRAS, 407, 17
- Sapountzis, K., & Vlahakis, N., 2010, 25th Texas Symposium on Relativistic Astrophysics (Heidelberg-Germany) (<http://pos.sissa.it/cgi-bin/reader/conf.cgi?confid=123>)
- Sapountzis, K., & Vlahakis, N., 2012, MNRAS, submitted
- Tchekhovskoy, A., Narayan, R., & McKinney, J.C., 2010, NewA, 15, 749
- Vlahakis, N., & Königl, A., 2003, ApJ, 596, 1080

GRB PROMPT EMISSION AND THE PHYSICS OF ULTRA-RELATIVISTIC OUTFLOWS

F. Daigne¹

Abstract. Due to severe time constraints, the joint discussion for sessions I-IV has been extremely short considering the number of hot topics related to GRB prompt emission studies and the physics of GRB ultra-relativistic outflows. I attempt to briefly describe the main issues raised in the talks and posters presented during the conference.

1 Introduction

A series of excellent talks in Session I (historical remarks) has clearly shown the continuous effort made by the community of high-energy astrophysics since the discovery of GRBs to characterize their prompt emission with an always improving time resolution and spectral coverage. The most recent progress are mostly due to the *Swift* and *Fermi* satellites. Thanks to *Fermi*/GBM, a large sample of long and short GRBs with good quality spectra from 8 keV to 15 MeV is now available, and in a few cases, the LAT extends this spectral coverage up to several GeV. This allows to discuss the spectral shape, including the possible appearance of several spectral components, in a much more robust way than before, and to confirm and extend many known results on the spectral evolution of bursts.

Since the discovery of GRB afterglows in 1997 and the confirmation of their cosmological origin, the standard theoretical framework for the prompt emission is internal dissipation within an ultra-relativistic outflow. The former is needed to reproduce the high variability of the light curves and the latter is related to the well-known compactness problem: a large Lorentz factor is needed to avoid a strong $\gamma\gamma$ annihilation. This framework is well established and accepted. However, the community is far from agreeing on the “details” of this scenario: mechanism for the acceleration of the outflow (thermal *vs.* magnetic), composition and geometry of the outflow (magnetization? thermal content? neutron content?), nature of the internal dissipation (photosphere *vs.* internal shocks *vs* magnetic reconnection), nature of the radiative processes at work (comptonized thermal emission

¹ UPMC-CNRS, UMR 7095, Institut d’Astrophysique de Paris, 75014 Paris, France

vs. synchrotron *vs.* SSC *vs.* ...). Expectedly, most of the open issues debated during sessions I-IV of the conference are somehow related to these fundamental questions.

2 Agreeing on a list of key observations

Review talks on prompt emission models often start with a list of “key observations that any model should reproduce”. From the discussions during the conference, it clearly appears that a preliminary step is still needed: agreeing on this list.

- *Distribution of spectral parameters in GRB prompt spectra.* GRB spectral properties are at the heart of the debates on the origin of the prompt emission. However, the present status is not clear, at least for theorists. It is for instance often said that the distribution of peak energies is narrow, around a few 100 keV. This seems however in contradiction with most results presented during the conference which are based on the spectral analysis of *Fermi* bursts. The peak energy of the time-integrated spectrum varies a lot from a burst to another and peak energies well above 1 MeV can be observed, which complement the fact, known since *Beppo-SAX* and *HETE2*, that low-peak energy bursts well below 100 keV do exist. In addition, time-dependent spectral analysis become more and more available and usually show large variations, over more than one decade, of the peak energy within a single burst. Therefore, the old idea of a narrow distribution of the peak energy must probably be given up. It remains that the true distribution of the spectral parameters is of the greatest interest to understand the prompt emission. What are the minimum and maximum peak energies which are observed in time-dependent spectra? Photospheric models may have difficulties to explain the lowest and highest values. What is the distribution of the low-energy photon index? Synchrotron models are known to face severe difficulties to reproduce the largest values $\alpha > -1$. Recently, a deviation from the standard Band shape has been found in several bright GBM bursts, some being presented during this conference. This deviation may be attributed to an additional component with a quasi-thermal shape. When the spectral analysis is made with such two components, the spectral parameters of the main one (Band) are affected. Then the impact of this multi-component analysis on the distribution of the spectral parameters of the non-thermal emission will have to be investigated in the future and may change our general view on this issue.
- *Is there prompt GeV emission with an internal origin?* It seems natural to associate the long-lasting emission above 100 MeV detected by the LAT in a few bursts to the deceleration of the relativistic jet by its environment, as for the afterglow observed at lower frequencies. Going one step further, several authors proposed that the whole GeV emission (including the emission detected while the prompt emission in the GBM is still active) is due to the

external shock, whereas it is widely accepted that the prompt soft gamma-ray emission has an internal origin. This leads to an interesting open issue which was briefly discussed during the conference: is it possible to prove that there is GeV emission of internal origin, at least in some bursts? Possible tests may be related to the characterization of the variability of the GeV lightcurve. Some participants suggested that the short spike seen at all energies in GRB 090926A already tells us the answer. This issue is of great importance, not only to distinguish between the internal and external origin of the high-energy emission, but also because GeV emission of internal origin would put a severe constraint on the radius of the emission site.

- *Should we consider that the early steep decay seen by XRT is prompt high-latitude emission?* Another key observation to understand the origin of the prompt emission is due to *Swift*/XRT. A large majority of bursts show an early steep decay in X-rays, which starts at the end of the prompt emission in the BAT, and decays with a steep temporal index close to -3 . The most natural explanation is the high-latitude emission from the prompt phase, which was predicted in 2002. Several groups have made a detailed comparison between the model and XRT data and shown an excellent agreement. If this interpretation is correct, it puts strong constraints on the value of the radius at the end of the prompt phase, which must be large.

3 Observations

Many new observational results have been presented during the conference and raised some interesting issues.

- *Are the results of time-integrated/-dependent spectral analysis self-consistent?* As illustrated by several contributions, time-dependent spectra are now obtained for an increasing number of bursts and can be compared to the time-integrated spectrum which is always available. This leads to new issues, especially as most of the functionals used for the spectral analysis do not add up easily. The sum of two Band functions is not a Band function. The sum of several Band functions with a continuously evolving peak energy and intensity may also look like two smoothly connected power-laws, but the width of the transition around the break should increase when more Band functions are added, whereas this transition has a fixed width in the Band function. Therefore, the fact that the Band function is always used and seems to work well, both for the time-integrated and the time-dependent analysis with time bins of very different durations, is rather puzzling, especially as a strong spectral evolution is usually found within a given GRB. This issue is probably the most severe for the longest integration bins and one should question the information contained in the results of the time-integrated spectral analysis.
- *Hardness-intensity correlations: are they all self-consistent?* This issue is obviously related to the previous one. Several correlations have been found

between the hardness (measured by a hardness ratio, by the time-integrated peak energy or by the time-evolving peak energy) and the intensity (measured by the fluence or isotropic equivalent energy, by the peak flux or peak luminosity, or by the time-evolving flux or luminosity). For instance, a correlation between the time-dependent luminosity and the time-dependent peak energy has been recently found in a few *Fermi* burst and discussed during this conference. As the time-integration of such a correlation does not obviously give a new one between time-integrated quantities, the self-consistency between all these correlations should probably be studied, irrespective of the legitimate debate on possible selection biases.

- *Multi-component spectra: what is the spectral evolution of each component?* There is a growing interest for a multi-component spectral analysis of *Fermi* bursts, well illustrated during the conference: main non-thermal component (Band), possible additional quasi-thermal component at low energy, additional power-law-like component at high energy. Depending on the models, they may be associated to different radiation processes in the same region, or to different emission sites. The spectral evolution of each component may be the key to answer these questions and necessitates both an observational and theoretical effort, to characterize the observed evolution and to make predictions that can be compared to data.
- *The shape of the additional component at high energy and the associated low-energy excess.* The spectral analysis of a few *Fermi*/LAT bursts shows the need for an additional component, usually modeled by a single power-law, dominant at high energy (LAT range), and unexpectedly also at the lower end of the GBM spectral range (low-energy excess). Such a single power-law over \sim 6 decades is not easily reproduced by models, despite interesting attempts presented during the conference. However, a power-law is the simplest functional that can be used for spectral fits and it is probably only the quality of data that prevents better characterizing the spectral shape of this additional component. Any additional information of some possible curvature or cutoff, as in the only case GRB 090926A, would be valuable for the physical interpretation. A special interest should also be given to the associated low-energy excess: is it an X-ray component temporally correlated to the high-energy component or is it really a unique component over so many decades? It would be interesting to try to characterize this excess independently of LAT data, with the GBM or with an instrument having good X-ray capabilities, as MAXI whose results were presented during this conference.
- *Can we expect a *Swift*+*Fermi*/LAT burst?* As already mentioned, the physical origin of the GeV emission is even more puzzling than for the rest of the prompt emission, as both an internal and an external origin can be discussed. Part of the debate is related to the possibility of an early deceleration (before the end of the prompt phase). Unfortunately, early X-ray data are

not available for LAT bursts, which would put interesting constraints on this scenario. It would be especially interesting to detect the XRT early steep decay, as – as discussed above – it can provide a precise information on the end of the prompt phase. Therefore, a burst with a simultaneous trigger by the LAT and by *Swift* would be of the greatest interest.

- *Can we expect a Fermi/LAT burst with prompt optical data?* Prompt optical detections remain rare but can provide important constraints on the prompt emission sites, as discussed during the conference. There are several models proposed to explain the few cases where such observations are available. Some of them predict a bright GeV emission (as the SSC model proposed for the naked eye burst). Therefore, a *Fermi*/LAT burst with prompt optical data would have a real interest. However, due to two independent low detection rates, such an observation seems even more challenging than the one discussed in the previous item.

4 Models

A general discussion of the three main GRB prompt emission models is out of the scope of this short contribution. I briefly mention the main open issues associated with each of them, as well as a few additional questions more related to the central engine and jet physics.

- *Dissipative photospheres.* This model has the best understood physics. Detailed calculations are already available and some of them have been presented during the conference. However, most of them focus on a “typical” spectrum. As discussed above, spectral evolution is also a key feature of GRBs. Therefore, more realistic calculations with predictions for this evolution within a pulse or a more complex light curve would allow to go one step further in the comparison with data. One issue is to understand if this model is compatible with the recent results of a multi-component spectral analysis. Another issue which has also been debated during the conference is the prediction for the polarization of the prompt emission. However, as also discussed in another session of this conference, it is not clear to know if data to compare are already available on this side. More generally, it is interesting to note that photospheric emission is almost unavoidable in all GRB models. The real issue is to understand if it can alone explain the whole prompt emission. The answer is partially related to some items discussed before, such as the existence of GeV emission of internal origin or the interpretation of the XRT early-steep decay. If photospheric emission has to be complemented by additional processes above the photosphere, one should understand which component of the spectrum has a photospheric origin and, from the shape of this component, if sub-photospheric dissipation is mandatory.
- *Internal shocks.* The main uncertainty of this model is related to the microphysics, which is usually parametrized by simple parameters (ϵ_e , ϵ_B , ...)

which are kept constant within a burst and can not be related yet to the shock conditions by physical prescriptions. The recent progress in the theory of shock acceleration have been obtained in the ultra-relativistic regime and the mildly relativistic regime relevant for internal shocks has not really been explored yet. On the other hand, using this simple parametrization, it is possible to model light curves and spectra produced by internal shock, and this model is probably, among the three main possibilities, the one that has been compared the more in detail with data, with promising results. It would therefore be of the greatest interest to learn more about the relevance of the assumptions made for the microphysics. Another well known issue of the model is the energetics. However, if the efficiency of internal shocks is known, the constraints on the efficiency of the prompt phase are less clear. They are usually based on simple versions of the afterglow model, that fails to reproduce the complex phenomenology of the early afterglow. When more elaborated models are used, including for instance a late injection to reproduce X-ray plateaus, it usually leads to so high efficiencies that they become challenging not only for internal shocks but for all other models. Progress in afterglow studies is clearly needed to better characterize this issue.

- *Magnetic reconnection.* This model is motivated by observational and theoretical works favoring a magnetic acceleration for GRB jets. It should however be remembered that, as illustrated by several contributions in this conference, magnetic acceleration of the jet does not necessarily mean a high magnetization ($\sigma \geq 1$) at large distance where the prompt emission takes place. Magnetic reconnection can in principle solve many problems faced by the two previous models. On the other hand, the relevant physics is by far the least understood. Therefore, the main issue here is to know how to test the model and if detailed predictions for the temporal and spectral properties can be obtained for a comparison with data.
- *Central engine and relativistic ejection.* Several contributions have discussed the acceleration of the GRB outflow to relativistic speed and the early propagation of this jet, especially within the collapsing progenitor star in the case of long bursts. The relevant physics is very complex and in many cases, large simulations on super-computer are needed to address this problem in a realistic way. A clear difficulty is the lack of direct constraint, as the innermost region of the central engine is well below the photosphere and no light signal can be sent. If one focus on issues which are the most strongly connected to the prompt emission physics, one may list the two following questions: what is the final magnetization and thermal content at the end of the acceleration? What are the processes which govern the various timescales encountered in GRB light curves, from the shortest variability timescale to the duration of the prompt emission, including intermediate timescales such as pulse durations. We are probably still far from answering these two fundamental questions but the activity of the field has been beautifully illustrated during the conference with several convincing intermediate results.

- *Short vs. long bursts: where does the common physics start?* Finally, the existence of several classes of GRBs remain to be understood. Several contributions have discussed the differences between short and long bursts, or non-collapsar and collapsar bursts, based on the host galaxies, the properties of the prompt emission, the distribution of T_{90} , etc.. On the theoretical point of view, it is usually assumed that short and long bursts differ by their progenitors and environment but that the same physics is at work. However, different progenitors may lead to different central engine and/or ejection mechanism and/or composition and geometry of the jet and/or internal dissipation mechanism, ... With the recent progress in the observation of short GRBs, and especially the fact that some bright short GRBs can now be characterized with the same level of details than the long ones (temporal properties, spectral evolution), one may expect some progress in drawing the frontier between short and long bursts and understanding where the common physics start in these two classes of phenomena.

5 Conclusion

Forty five years after the discovery of GRBs, the understanding of the physical origin of the prompt emission remains a major challenge both on the observational and theoretical sides. As illustrated by the series of issues listed above, this is however a very active field of research with many stimulating discussions about various hot topics. Despite the difficulty, there is no doubt that new progress in the physics of the prompt emission and of GRB relativistic outflows will be achieved in the coming years.

Chapter V.

Afterglow Emission-I Long GRBs (Observations)

LINEAR AND CIRCULAR POLARIMETRY OBSERVATIONS OF GAMMA-RAY BURST AFTERGLOWS

K. Wiersema¹

Abstract. Follow-up observations of large numbers of gamma-ray burst (GRB) afterglows, facilitated by the Swift satellite, have produced a large sample of spectral energy distributions and light curves, from which the basic micro- and macrophysical parameters of afterglows may be derived. However, a number of phenomena have been observed that defy explanation by simple versions of the standard fireball model, leading to a variety of new models. Polarimetry has shown great promise as a diagnosis of afterglow physics, probing the magnetic field properties of the afterglow and geometrical effects (*e.g.* jet breaks). Unfortunately, high quality polarimetry of a significant sample of afterglows is difficult to acquire, requiring specialised instrumentation and observing modes. In this talk I will review the recent successes in afterglow polarimetry, also showing first results of new instruments and observing campaigns. I will particularly focus on jet breaks.

1 Introduction

Right after the first detection of optical afterglows of gamma-ray bursts (GRBs) and the diagnosis of GRB afterglow radiation as synchrotron emission, predictions have been made for the linear and circular polarisation of GRBs and their afterglows (see for a review Lazzati 2006 and references therein). While time resolved polarimetry of sources as faint and transient as GRB afterglows is technically complicated and requires specialised instrumentation on large telescopes, the rewards are high: from time resolved polarimetric light curves we can determine GRB parameters (*e.g.* the jet structure, magnetic field configuration, viewing angle, etc.) that can not easily be measured from light curves alone. The first detections of polarisation of afterglows in the pre-Swift era demonstrated technical feasibility, and shown that afterglows generally have low levels of polarisation ($\sim 1\%$) that vary as a function of time (see Lazzati 2006 for an overview of pre-Swift measurements).

The Swift era has provided further incentive to perform detailed polarimetry: the observed richness in afterglow light curve morphology (X-ray flares, plateaux,

¹ University of Leicester, University Road, Leicester LE1 7RH, UK

steep decays etc., see Evans *et al.* 2009 for statistics), has resulted in new models with various additional components to the standard fireball model, including for example the effects of high latitude emission, variable microphysics, energy injection mechanisms, etc.. Many of these new model ingredients can be explored via the large sample of well sampled Swift GRB afterglow light curves and spectral energy distributions (SEDs), but the large number of parameters and relatively low sensitivity of optical and X-ray light curves to some parameters (*e.g.* ϵ_B) make the addition of new independent constraints on the models, such as the linear or circular polarisation as a function of time, particularly useful.

2 Jet breaks

One of the primary focus points of polarimetry models of GRB afterglows has been the jet collimation and our viewing angle into the jet (the angle between our sightline and the jet axis): simple afterglow models show that small differences in viewing angles and internal jet structure lead to strong and in principle easily identifiable differences in the behaviour of the polarisation as a function of time, in contrast with the optical and X-ray light curves, in which the differences are small and difficult to detect (Rossi *et al.* 2004 and references therein). In the case of uniform, top-hat, jets with a unorderd magnetic field, a key prediction is the existence of two bumps in the polarisation light curve, with a 90 degree change in polarisation position angle around the time of the jet break. Confirmation of the existence of such a change in position angle would give a new, light curve independent way of estimating jet opening angles, internal jet structure and viewing angle, for assumed magnetic field configurations. However, as indicated by Lazzati *et al.* (2003), the presence of polarisation caused by scattering by dust particles in the host galaxy alters both the linear polarisation and polarisation angle light curves. This implies that to successfully use polarimetry as indicator of jet collimation, we require datasets that (*i*) span a wide time range, with data extending to far after the time of jet break; (*ii*) measure polarisation as a function of wavelength (*e.g.* through spectropolarimetry or multi-band imaging polarimetry), to separate the dust-induced polarisation from afterglow polarisation; (*iii*) have well sampled multi wavelength light curves so that the presence of a light curve break can be established.

Early attempts in the pre-Swift era did not detect a 90 degree angle change in polarisation light curves (see *e.g.* Covino *et al.* 2003; Greiner *et al.* 2003; Rol *et al.* 2003; Masetti *et al.* 2003; Gorosabel *et al.* 2004). The most important reason appears to be that in most cases the polarimetric light curves were too sparsely sampled (only half a dozen sources have 3 or more data points), and most of these have rather uncertain jet break times. The sources with best polarimetric coverage are 021004 and 030329, both of these have highly irregular optical light curves, characterised by rebrightenings and bumps. The case of 030329 in particular shows some correlated behaviour between the light curve bumps and polarisation behaviour (Greiner *et al.* 2003), which makes interpretation in terms of simple polarimetry models difficult (Granot & Königl 2003). Data of GRB 020813 may

also obey this correlation between light curve and polarisation variability: its polarisation curve is smooth (Fig. 1; Barth *et al.* 2003; Gorosabel *et al.* 2004; Lazzati *et al.* 2004) just like the optical light curve (Laursen & Stanek 2003).

Using the Very Large Telescope in Chile, we embarked on a campaign to obtain well-sampled polarimetry light curves of Swift bursts, selected solely by an initial on-board UVOT identification of an afterglow, thus avoiding an observational bias towards sources that have a long-lasting shallow afterglow decay. A first success of this campaign is the dataset presented in Figure 1 (for details see Wiersema *et al.* 2012). Presented in this figure are the linear polarisation data points of the afterglow of GRB 091018 as obtained with the FORS2 instrument (in R band, green symbols) and a datapoint obtained with the ISAAC instrument (in K_s band, open square), gathered over 3 nights after the burst. The optical and X-ray light curves of this afterglow show a break, with no change in the X-ray to optical spectral energy distribution, *i.e.* the break is achromatic. We interpret this break as a jet break: the horizontal axis of Figure 1 shows time since burst normalised by the jet break time. Immediately apparent is that data at $t/t_{\text{break}} < 2$ have a constant polarisation angle, data after that have a higher but variable angle. A weighted average angle of 6 degrees is found in the first interval, this is drawn as a dotted line in Figure 1. The dotted line at $t/t_{\text{break}} > 1.5$ is drawn at 96 degrees, and shows that the data is consistent with a 90 degree change in polarisation angle occurring slightly after $t/t_{\text{break}} = 1$. The uniform top hat jet model with random field predicts that two bumps should be visible in the polarisation curve, and each bump has a constant polarisation angle. The data at $t/t_{\text{break}} < 2$ is perfectly consistent with this prediction, if the viewing angle is slightly off-axis ($\sim 0.2 * \theta_{\text{jet}}$). The later data is not consistent with a simple broad bump with constant angle. Highlighted in an inset in Figure 1 is the behaviour of the polarisation angle around $t/t_{\text{break}} \sim 3$. The angle shows a rapid sweep of the source through the Stokes plane: angle and polarisation can jointly be explained if in addition to the expected smooth bump from the simple models there is a slowly variable, low polarisation component present with an angle nearly 90 degrees offset from the expected bump (96 degrees). The addition of these two components can largely reproduce the observed behaviour (Wiersema *et al.* in prep.). We therefore consider this case the first with a polarisation-based jet break identification.

There are further features of interest in the 091018 data. First of all, we acquired not only linear polarimetry, but also circular polarimetry in R , again using VLT FORS2, in between the first and second datapoint in Figure 1. These show a non-detection of circular polarisation, with a limit of $P_{\text{circ}} < 0.23\% (3\sigma)$ (Wiersema *et al.* 2012). There are no signs of reverse shock contribution to the afterglow of this burst, so we consider this a tight limit on the forward shock circular polarisation, and therefore on the presence of weak but ordered magnetic fields in the blast wave.

A second point of interest is the very low polarisation at early times. This, together with the angle behaviour described above, makes structured jet models very unlikely, but also sets a strong lower limit on the size and number of any coherent patches of emission on the blast wave (Gruzinov & Waxman 1999).

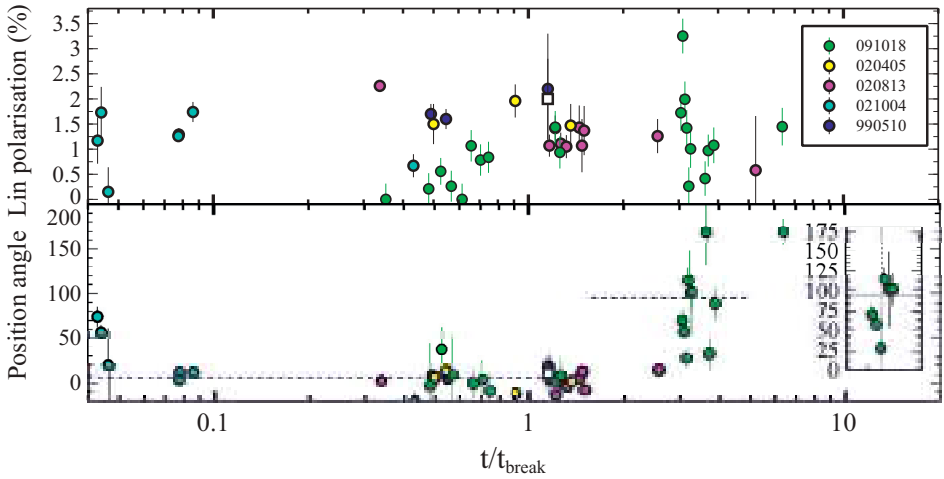


Fig. 1. This figure shows the linear polarisation data of a sample of pre-Swift bursts overlaid on the dataset of Swift GRB 091018 (Wiersema *et al.* 2012). For easier comparison, the polarisation angles of all datasets have been shifted so their average at t/t_{break} is the same as that of 091018 (angle θ), indicated by the horizontal dashed line for $t/t_{\text{break}} < 1.5$. The horizontal dashed line at $t/t_{\text{break}} > 1.5$ is drawn at an angle $\theta + 90^\circ$. The times of (candidate) jet breaks of the pre-Swift bursts are as found in Zeh *et al.* (2006).

Finally, if the fast variability behaviour at $t/t_{\text{break}} > 2$ is a common one, *i.e.* if it is something that may be seen in all afterglows rather than caused by something which is specific to this burst only, we may need a much larger emphasis on late-time polarimetry, in the sense that a 90 degree angle shift from early data can only be measured using several data points together. I would like to note that data taken after the conference of another GRB seem to imply that this behaviour is indeed a common one, though analysis is ongoing (Wiersema *et al.* in prep.).

On Figure 1 I also plot the pre-Swift GRBs which have 3 or more data points and an estimate of the jet break time from light curves (taken from Zeh *et al.* 2006), excluding GRB 030329 for reasons stated above. Polarisation angles are shifted so that their early time values fall on the GRB 091018 value, so that it is easier to see angle changes. This plot demonstrates that if all bursts behave like GRB 091018, there are not sufficient data points beyond $t/t_{\text{break}} > 2$ to diagnose a 90 degree angle change. One exception is GRB 020813, which has some data in this interval, but may have fallen victim to the same rapid variability behaviour as seen in GRB 091018.

3 Dust

As mentioned in the previous section, scattering of afterglow photons on dust particles in the host galaxy results in wavelength dependent linear polarisation. In

sight lines in our own Galaxy, the wavelength dependence is often described by the empirical Serkowski curve (Serkowski *et al.* 1975), the black dashed curve in Figure 1. The induced polarisation peaks with polarisation value P_{\max} at wavelength λ_{\max} . If we assume this curve, or a similar parametrisation, to also be valid for extragalactic sight lines, we can express the expected polarisation in different photometric bands (*e.g.* in R and K) in terms of dust parameter R_V (Klose *et al.* 2004). As can also be seen in Figure 1, the ratio of the detected polarisation in R and K does not show evidence for significant dust induced polarisation. This is also true for the other, pre-Swift, cases where wavelength dependent polarimetry exists (*e.g.* Barth *et al.* 2003), reflecting the low amount of dust seen in these sightlines, a low degree of dust grain alignment, or dust grain size distributions different from Galactic environments. Further study of dust induced polarisation in afterglows would be very useful, in particular because the high quality spectra and SEDs that can be obtained for these afterglows can be combined with polarimetry to better understand dust processing in GRB environments. Figure 2 shows that even at $z \sim 3$ the K band is red ward of the peak of the Serkowski curve, whereas the R band is blue ward for all but the very lowest redshift GRBs. To exploit this fact, we are performing a small survey of afterglows using the LIRIS instrument on the 4.2 m William Herschel Telescope, in imaging polarimetry mode, which has had some success already (Wiersema *et al.* 2012b).

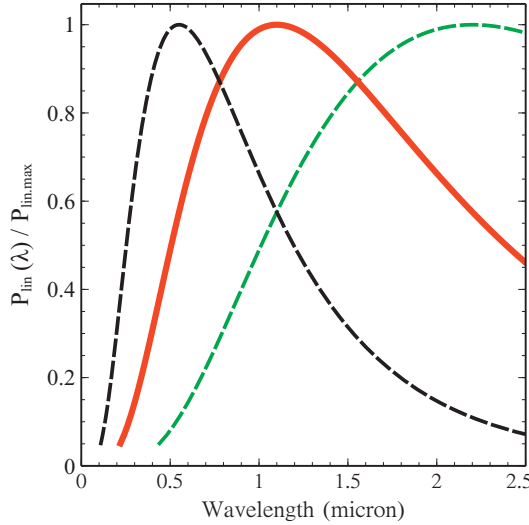


Fig. 2. The Serkowski curve, which gives an empirical description of the polarisation as a function of wavelength in the case of dust scattering in our own Galaxy, drawn at $z = 0, 1$ (red, the redshift of GRB 091018 is 0.97) and 3. The curve is characterised by a typical wavelength λ_{\max} at which maximum polarisation P_{\max} is present.

4 Reverse shocks and short time scales

In recent years, new, dedicated, instrumentation has succeeded in robustly measuring the polarisation of gamma-rays of the GRB prompt emission (Yonetoku *et al.* 2011). In all cases high values of polarisation were found, in contrast with the low values found in the late time forward shocks shown in Figure 1. The use of polarimetry instruments on robotic telescopes allows investigation of the transition of prompt to afterglow emission, and is able to probe the reverse shock (or its absence), and therefore investigate the magnetisation of the GRB ejecta. The case of GRB 090102 in particular showed a high polarisation likely associated with reverse shock (Steele *et al.* 2009). Early circular polarimetry of GRB afterglows can probe the ordered field component in reverse shock emission, and in some cases even fairly late observations may be sufficient for a detection (Wiersema *et al.* in prep.).

Resolving the decay of the reverse shock and rise of the forward shock will require the ability to acquire polarimetry at short timescales (exposure times), but short exposure polarimetry is also of some interest at late times: if the fast variability seen in GRB 091018 after the jet break is commonplace, we need short exposures to resolve its variability timescale. Secondly, the model where a large number of small patches of coherent magnetic field contribute to the received emission (Gruzinov & Waxman 1999) can be tested through short time scale variability tests. We use LIRIS at the WHT for this: the instrument utilises a double-Wollaston, and therefore records Q, U simultaneously in each exposure. We typically use 30 second exposure sets (3 sub exposures of 10 seconds), to get good sky subtraction in the Ks band. An analysis of field stars in a GRB field, shown in Figure 3, shows we can do linear polarimetry with polarisation errors of 1% in 30 second exposures for $Ks < 15.3$ (Vega magnitudes; Wiersema *et al.* in prep.).

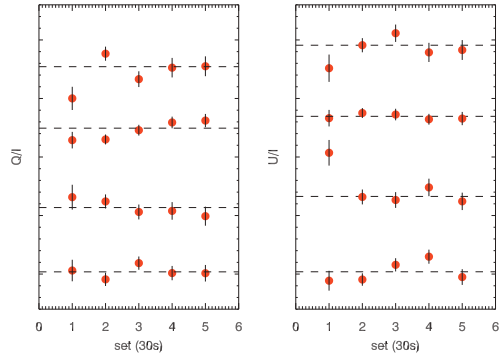


Fig. 3. Polarimetry of 4 field stars in a field associated with a GRB observation done in Ks band with LIRIS on the WHT. Measurements of Stokes Q, U are done on 30 second integrations. The values of the 4 stars are vertically displaced for clarity. The afterglow is too faint for meaningful polarimetry on these short time scales.

5 Conclusions

It is clear from the above that polarimetry of GRB afterglows is an important pursuit. The recent measurements of γ -ray polarisation of GRB prompt emission, the advent of polarimeters on robotic telescopes capable of probing the very early afterglow, and the increasing capabilities for polarimetry at longer wavelengths (*e.g.* ALMA, JVLA) highlight the importance of late-time, deep, and densely sampled polarisation curves. The recent results on GRB 091018 give some long sought-after confirmation of basic predictions of blast wave models, in particular a 90 degree change in polarisation angle after the jet break. Similar campaigns on other bursts are required to probe the relation of polarisation behaviour with other burst parameters, *e.g.* the bulk Lorentz factor, burst energetics, reverse shock properties and the viewing angle into the jet. Besides giving some support to jet break models, the dataset of GRB 091018 appears to show a new kind of unpredicted fast variability around or just after the jet break, illustrating that there is still plenty of discovery space left in afterglow polarisation studies.

References

- Barth, A.J., Sari, R., Cohen, M.H., *et al.*, 2003, ApJ, 584, 57
 Covino, S., Malesani, D., Ghisellini, G., *et al.*, 2003, A&A, 400, L9
 Evans, P.A., Beardmore, A.P., Page, K.L., *et al.*, 2009, MNRAS, 397, 1177
 Gorosabel, J., Rol, E., Covino, S., *et al.*, 2004, A&A, 422, 113
 Granot, J., & Königl, A., 2003, ApJ, 594, L83
 Granot, J., & Taylor, G.B., 2005, ApJ, 625, 263
 Greiner, J., Klose, S., Reinsch, K., *et al.*, 2003, Nature, 426, 157
 Gruzinov, A., & Waxman, E., 1999, ApJ, 511, 852
 Klose S., Palazzi, E., Masetti, N., *et al.*, 2004, A&A, 420, 89
 Laursen, L.T., & Stanek, K.Z., 2003, ApJ, 597, 107
 Lazzati, D., Covino, S., di Serego Alighieri, S., *et al.*, 2003, A&A, 410, 823
 Lazzati, D., 2006, NJPh, 8, 131
 Masetti, N., Palazzi, E., Pian, E., *et al.*, 2003, A&A, 404, 465
 Rol, E., Wijers, R.A.M.J., Fynbo, J.P.U., *et al.*, 2003, A&A, 405, 23
 Rossi, E.M., Lazzati, D., Salmonson, J.D., *et al.*, 2004, MNRAS, 354, 86
 Serkowski, K., Mathewson, D.L., & Ford, V.L., 1975, ApJ, 196, 261
 Steele, I.A., Mundell, C.G., Smith, R.J., *et al.*, 2009, Nature, 462, 767
 Wiersema, K., Curran, P.A., Krühler, T., *et al.*, 2012, MNRAS, 426, 2
 Wiersema, K., van der Horst, A.J., Levan, A.J., *et al.*, 2012b, MNRAS, 421, 1942
 Yonetoku, D., Murakami, T., Gunji, S., *et al.*, 2011, ApJ, 743, 30
 Zeh, A., Klose, S., & Kann, D.A., 2006, ApJ, 637, 889

IMPLICATIONS OF EARLY TIME OBSERVATIONS OF OPTICAL AFTERGLOWS OF GRBS

S.B. Pandey¹ and W. Zheng²

Abstract. Optical observations of afterglows at very times are very useful towards understanding the least known problem of GRB research field *i.e.* the transition from prompt emission to early afterglows. The comparison of a subset of well-monitored GRBs and their early time properties at optical are compared with that seen at XRT and BAT wavelengths. In most of the observed cases, the very early optical observations of GRBs do not trace the canonical decay nature seen at XRT wavelengths, suggesting different origins for the observed early emissions in the two bands. In some of the early optical light-curves, the decay followed by smooth rise features are consistent with the onset of the afterglow although such features are also expected if the emission is seen off-axis and/or the outflow is structured.

1 Introduction

Gamma Ray Bursts (GRBs) are short lived (10^{-3} to 10^3 seconds) extremely bright (Isotropic equivalent γ -ray energy $\sim 10^{52} - 10^{54}$ erg) cosmological γ -ray sources, emitting photons of energy ~ 10 keV–10 GeV. Followed by the GRB, ultra-relativistically ejected material interact with the surrounding medium through shocks and may produce afterglows, visible in all bands from X-ray to radio wavelengths. Afterglows being longer-lasting than GRB prompt emission, provide a multi-band platform to study these energetic cosmic explosions in detail (Zhang 2007; Gehrels *et al.* 2009).

Unlike to prompt gamma-ray emission, X-ray emission arises from the interaction of relativistic outflow with the ambient medium forming blast wave (Meszaros & Rees 1997; Sari *et al.* 1998). However, part of the early X-ray emission from GRBs (near contemporaneous) seems to be integral part of the prompt emission

¹ ARIES, Manora Peak, Nainital 263129, Uttarakhand, India

² Randall Laboratory of Physics, University of Michigan, 450 Church Street, Ann Arbor, MI 48109-1040, USA

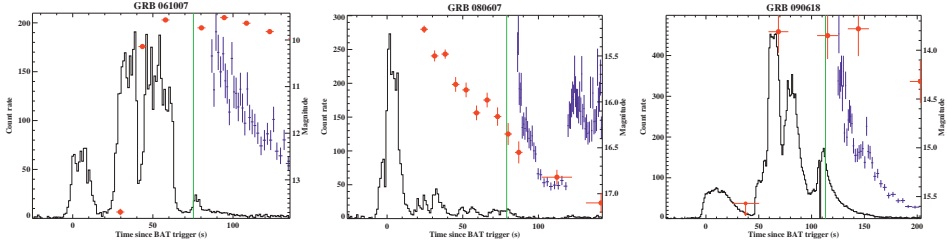


Fig. 1. This figure demonstrates examples of 3 GRBs (GRB 061007, GRB 080607 and GRB 090618) with near contemporaneous optical observations (red) along with the *Swift*-BAT (Black) and *Swift*-XRT (blue) observations. The green vertical line is the line at the duration of t_{90} in observer's frame. The optical light-curve in general does not trace the gamma-ray light-curves and follow a power-law rising/decaying behavior.

itself (Margutti *et al.* 2013). Also, the prompt emission gamma-ray spectrum seems broadly consistent with the Band's model (Band *et al.* 1993) showing deviations both at low and high energy ends (Abdo *et al.* 2009). So far, more than 3 dozen of GRBs have been observed at optical frequencies near contemporaneous to the prompt emission gamma-ray duration (Yost *et al.* 2007; Racusin *et al.* 2008). However, majority of the observed optical emissions does not seem like following the extrapolated Band's function, indicating a different origin for the emission at the two frequencies.

In the Swift era, $>10\%$ of the optical afterglows have been observed during the rising phase, peaking at time t_p and decaying as a power-law at later epochs. Such early rising optical afterglows are expected in a variety of models that describe the deceleration of the initial fireball (Sari & Piran 1999), off-axis emission (Panaitescu *et al.* 1998) and the outflow structure (Rossi *et al.* 2002). The peak time t_p and the brightness at the peak time of GRB optical afterglow light curves are distributed over several orders of magnitude (Oates *et al.* 2009; Panaitescu & Vestrand 2011; Rykoff *et al.* 2009).

2 Early time optical light curves of afterglows

Early optical observations of GRBs during the prompt emission or soon after, are clean tracers of the crucial properties of the fireball. Specifically, the early time monotonically rising light curves seen at optical frequencies can be used to understand the onset of the forward shock emission (Sari & Piran 1999) and reveal possible geometric effects associated with the structure of the jet (Panaitescu *et al.* 1998; Rossi *et al.* 2002).

In the case of thin shell approximation for fireball model (Sari & Piran 1999), *i.e.* $t_p > t_{90}$ (duration of the prompt emission), the light curve at optical frequencies should have a rising index of ~ 2 ($\nu_c <$ optical) or ~ 3 ($\nu_c >$ optical) in the case of *ISM* or 0.5 for a *WIND* density profile (Panaitescu & Vestrand 2011).

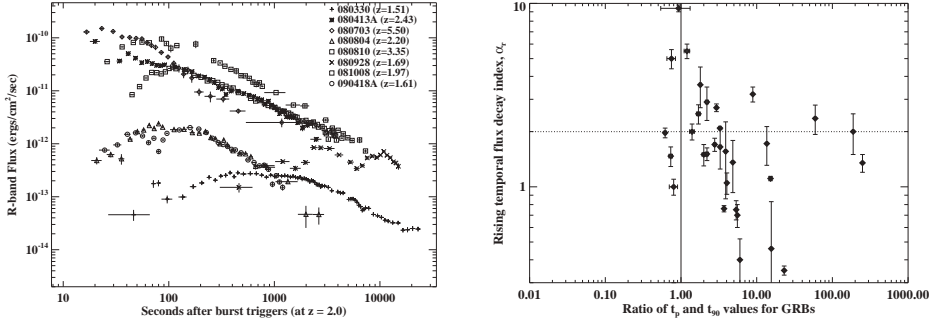


Fig. 2. In the *left panel*, ROTSE light curves of 8 afterglows observed at very early epochs showing the rising phase scaled to a common redshift of 2.0. The flux values of the GRBs have been corrected for the respective values of Galactic extinction and intergalactic absorptions. In the *right panel*, we plot α_r *vs.* ratio of t_p and T_{90} for 28 GRBs. Vertical solid line is line at $t_p = T_{90}$. Horizontal dotted line represents a line for $\alpha_r = 2.0$. A range of α_r values could be reproduced for different viewing angles if the emission is seen off-axis. These shallower rise indices might also indicate a possible contribution from early energy injection into the forward shock and/or the irregular structure of the early fireball.

2.1 A sub-sample of rising light-curves of afterglows

Analysis of very early observations of rising/decaying light-curves at optical frequencies for more than 40 GRBs (Rykoff *et al.* 2009; Melandri *et al.* 2010; Pandey *et al.* 2011) are discussed in the present analysis. The distribution of rising temporal indices are $0.1 < \alpha_r < 10$ and the values of α_r for a good fraction of the sample are flatter (see Fig. 2, right panel) than those predicted by various afterglow models (Sari & Piran 1999; Oates *et al.* 2009). The peak time of these light-curves were used to derive the fireball deceleration time t_p , which along with isotropic equivalent gamma-ray energy E_{iso} were used to estimate the bulk Lorentz factor Γ_0 using the formula described in (Molinari *et al.* 2007) for the deceleration of the fireball and the thin shell approximation (Sari & Piran 1999). The derived values of Γ_0 have a range of values varying from 100 to 1000 and seems like linearly correlated with respective values of E_{iso} (see Fig. 3, left panel) indicating that energetic GRBs have higher values of Γ_0 (Rykoff *et al.* 2009; Liang *et al.* 2012; Pandey *et al.* 2011).

A similar empirical correlation is also evident between Γ_0 and the rest-frame value of E_{peak} , the peak energy of the prompt emission spectrum of GRBs (Pandey *et al.* 2011). However, this correlation is poor due to underlying uncertainty in the determination of E_{peak} values for different GRBs. If the hint for the linear correlation between Γ_0 and E_{peak} is real (see Fig. 3, right panel), it could be useful to constrain models describing the geometry of the outflow, understanding the nature of XRFs in more detail (Dermer *et al.* 1999; Rossi *et al.* 2002; Yamazaki *et al.* 2007) and to understand the empirical relations (Amati and Ghirlanda) in

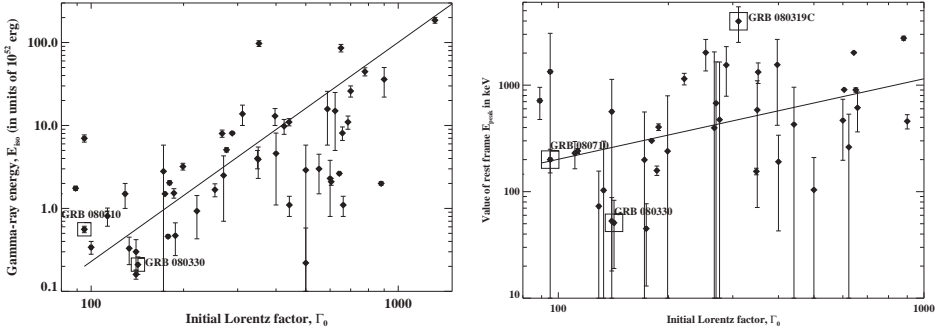


Fig. 3. In the *left panel*, we plot Isotropic equivalent gamma-ray energy E_{iso} vs. Γ_0 of 51 Swift GRBs, discussed in the present analysis. The line is a linear fit to the data assuming the limiting values of Γ_0 to be absolute and described as $\log \Gamma_0 = (0.41 \pm 0.05) \log E_{iso} + (2.16 \pm 0.23)$. In the *right panel*, we plot E_{peak} vs. Γ_0 for 40 GRBs and the fitted line is described as $\log \Gamma_0 = (0.82 \pm 0.29) \log E_{peak} + (0.45 \pm 0.70)$.

a more physical way. We hope to get more precise measurements of E_{peak} values of many more GRBs in near future from *Swift* and *Fermi*.

2.2 Constraints on reverse shock emission

The prompt optical emission were first detected for GRB 990123 (Akerlof *et al.* 1999) showing an optical flare that was interpreted as the signature of a reverse shock emission passing through the relativistic ejecta. In case of *Swift* GRBs, the early observations at optical-IR frequencies indicate that the reverse shock feature is not very common (Gomboc *et al.* 2009) in contrary to the predictions made earlier (Sari & Piran 1999). However, this feature has been clearly observed in handful of cases, for example GRB 060117 (Jelinek *et al.* 2006), GRB 061126 (Gomboc *et al.* 2008), GRB 090902B (Pandey *et al.* 2010) and GRB 110205 (Zheng *et al.* 2012). The detection/non-detection of reverse shock feature is very useful in constraining the outflow to be magnetized or baryon dominated. Early observations at much lower frequencies like radio and polarization observations in near future will help to know more about the nature of reverse shock emission for GRBs.

2.3 Dark GRBs

GRBs with no optical afterglows or having X-ray to optical spectral index $\beta_{OX} < 0.5$ are classified as dark GRBs (Jakobsson *et al.* 2004; van der Horst *et al.* 2009). During *Swift* era, rapid follow-up observations of afterglows at optical and near-NIR frequencies have enabled to collect a good sample of long duration GRBs (*e.g.* ROTSE, BOOTES, TORTORA, P60 and Faulkner telescopes), the underlying possible explanations and the fraction of the population in comparison to normal

GRBs with optical afterglows (Salvaterra *et al.* 2012; Nava *et al.* 2011; Greiner *et al.* 2011). The possible explanations for this population of bursts include, low-density environments, bursts occurring at higher redshifts with extinguished optical emission due to Lyman– α forest and that some of the bursts might occur in dusty environments. Recently, Melandri *et al.* (2012) analyzed a sub-sample of well-known dark GRBs with known redshifts and found that majority of dark GRBs have rather high X-ray flux and X-ray luminosity and at the same time lower observed optical flux. Also, these bursts have prompt properties similar to those normal bright events. This clearly indicates that most of the dark GRBs might belong to denser environments and their darkness might be related to circum-burst dust absorption.

3 Correlation between prompt optical/ γ -ray emission

Spectral energy distribution of the prompt emission of GRBs is one of the least-understood area. There are handful of known cases with optical emission detected contemporaneously with γ -rays for example GRB 990123 (Akerlof *et al.* 1999), GRB 041219A (Vestrand *et al.* 2005), GRB 050401 (Rykoff *et al.* 2005), GRB 050904 and GRB 051111 (Yost *et al.* 2007), GRB 080319B (Racusin *et al.* 2008) and GRB 080607 (Perley *et al.* 2011). However, in none of the cases there is any consistent correlation between prompt optical observations and the contemporaneous γ -rays. In Figure 4 (right panel), we plot 12 such examples of near contemporaneous observations, indicating that the emission at two frequencies have different physical origins. In a few cases, the optical and prompt γ -rays emissions seems to be correlated (GRB 051111, see Yost *et al.* 2007) and GRB 080319B (see Racusin *et al.* 2008) whereas in some of the cases the two emission components require a spectral break or some other possible origins. Broadly, the near contemporaneous observations at optical and γ -rays indicate that deceleration of the fireball occurs earlier than end of the high energy emission.

4 Early time optical and XRT light curves

In the *Swift* era, rapid follow-up observations at optical frequencies have collected a good number of GRBs with near-contemporaneous observations to those seen at XRT frequencies. The analysis of the temporal decay nature of these GRBs indicate that early time properties of GRBs have a diverse set of features, broadly consistent with the predictions made by the synchrotron fireball model for afterglows though outliers exist (Oates *et al.* 2009; Rykoff *et al.* 2009; Melandri *et al.* 2010). Specifically, the very early optical observations of most of GRBs do not trace the canonical decay nature seen at XRT frequencies and are broadly consistent with the “onset of the afterglow” or off-axis emission scenario for most of the observed features at early times. Also, at early epochs, spectral indices at XRT frequencies β_x are steeper than the combined spectral indices seen at XRT and optical frequencies *i.e.* β_{x-opt} (see Fig. 4, right panel). These observed features clearly

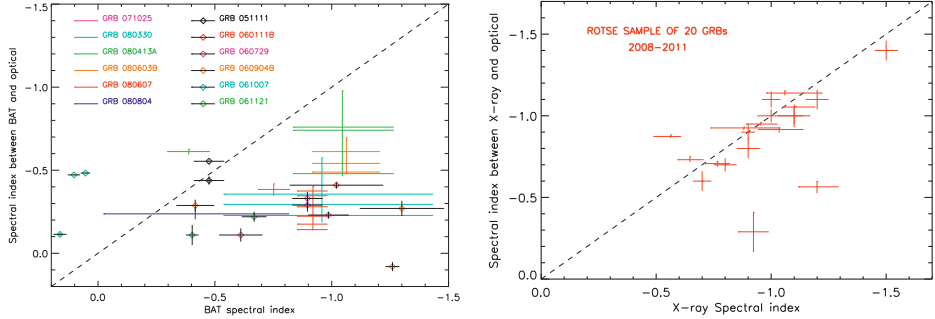


Fig. 4. In the *left panel*, we plot the *Swift*-BAT spectral index *vs.* spectral index between BAT and optical frequencies for 12 long-duration GRBs based on the preliminary analysis of our sample. The dashed line is the line of equality. In the *right panel*, we plot the *Swift*-XRT spectral index *vs.* spectral index between XRT and optical frequencies for 20 long-duration GRBs. The steeper XRT spectral indices in comparison to combined XRT-optical ones suggest for the *ISM* forward shock origin of the data.

indicate towards the forward shock model (Sari *et al.* 1998) for the observed date at optical and X-ray frequencies for the early afterglows of long duration GRBs.

So, early time optical data along with those observed at Gamma-ray and X-ray frequencies are very helpful in understanding the nature of these energetic cosmic explosions. With the help of many more upcoming robotic optical observatories, we hope to address some of the unsolved issues of this interesting research field.

This research has made use of the data obtained through the High Energy Astrophysics Science Archive Research Center On-line service, provided by the NASA/Goddard Space Flight Center. The authors thankfully acknowledge The ROTSE project to use some of the valuable data used for the present work.

References

- Abdo, A.A., Achermann, M., Ajello, M., *et al.*, 2009, ApJ, 706, L138
- Akerlof, C.W., Balsano, R., Barthelmy, S., *et al.*, 1999, Nature, 398, 400
- Band, D., Matteson, J., Ford, L., *et al.*, 1993, ApJ, 413, 281
- Dermer, C., Chiang, J., & Bottcher, M., 1999, ApJ, 513, 656
- Gehrels, N., Ramirez-Ruiz, E., & Fox, D.B., ARA&A, 2009, 47, 567
- Gomboc, A., Kobayashi, S., Guidorzi, C., *et al.*, 2008, ApJ, 687, 443
- Gomboc, A., Kobayashi, S., Mundel, C.G., *et al.*, 2009, AIP Conf. Proc., 1133, 145
- Greiner, J., Kruhler, T., Klose, S., *et al.*, 2011, A&A, 526, 30
- Jakobsson, P., Hjorth, J., Fynbo, J.P.U., *et al.*, 2004, ApJ, 617, L21
- Jelinek, M., Prouza, M., Kubanek, P., *et al.*, 2006, A&A, 454, L119
- Liang, E.W., Li, L., Gao, H., *et al.*, 2012, submitted to ApJ [arXiv:1210.5142]
- Margutti, R., Zaninoni, E., Bernardini, M.G., *et al.*, 2013, MNRAS 428, 729

- Melandri, A., Kobayashi, S., Mundell, C.G., *et al.*, 2010, ApJ, 723, 1331
Melandri, A., Sbarufatti, B., D'Avanzo, P., *et al.*, 2012, MNRAS, 421, 1265
Mészáros, P., & Rees, M., 1997, ApJ, 482, L29
Molinari, E., Vergani, S.D., Malesani, D., *et al.*, 2007, A&A, 469, 13
Nava, L., Salvaterra, R., Ghirlanda, G., *et al.*, 2011, accepted to MNRAS
[arXiv:1112.4470]
Oates, S.R., Page, M.J., Schady, P., *et al.*, 2009, MNRAS, 395, 490
Oates, S.R., Page, M.J., Schady, P., *et al.*, 2011, MNRAS, 412, 561
Panaiteescu A., Mészáros P., & Rees, M.J., 1998, ApJ, 503, 314
Panaiteescu, A., & Vestrand, W.T., 2011, MNRAS 414, 3537
Pandey, S.B., Castro-Tirado, A.J., Jelínek, M., *et al.*, 2009, A&A, 504, 45
Pandey, S.B., Swenson, C.A., Perley, D.A., *et al.*, 2010, ApJ, 714, 799
Pandey, S.B., Akerlof, C.W., Zheng, W., *et al.*, 2011, GRBs 2010-Annapolis, AIP Conf. Proc., 1358, 158
Perley, D., Morgan, A.N., Updike, A., *et al.*, 2011, AJ, 141, 36
Piran, T., 2005, Rev. Mod. Phys., 76, 1143
Racusin, J.L., Karpov, S.V., Sokolowski, M., *et al.*, 2008, Nature, 455, 183
Rossi, E., Lazzati, D., & Rees, M.J., 2002, MNRAS, 332, 945
Rossi, A., Schulze, S., Klose, S., *et al.*, 2011, A&A, 529, 142
Rykoff, E., Manganaro, V., Yost, S., *et al.*, 2005, ApJ, 631, L12
Rykoff, E.S., Aharonian, F., Akerlof, C.W., *et al.*, 2009, ApJ, 702, 489
Salvaterra, R., Campana, S., Vergani, S.D., *et al.*, 2012, ApJ 749, 68
Sari, R., & Piran, T., 1999, ApJ, 520, 641
Sari, R., Piran, T., & Narayan, R., 1998, ApJ, 497, L17
van der Horst, A.J., Kouveliotou, C., Gehrels, N., *et al.*, 2009, ApJ, 699, 1087
Vestrand, W.T., Wozniak, P.R., Wren, J.A., *et al.*, 2005, Nature, 435, 178
Yamazaki, R., Ioka, K., & Nakamura, T., 2004, ApJ, 607, L103
Yost, S.A., Aharonian, F., Akerlof, C.W., *et al.*, 2007, ApJ, 667, 1107
Zhang, Bing, 2007, ChJAA, 7, 1
Zhang, W., Shen, R.F., Sakamoto, T., *et al.*, 2012, ApJ, 751, 90

AN INTRINSIC CORRELATION BETWEEN GRB OPTICAL/UV AFTERGLOW BRIGHTNESS AND DECAY RATE

S.R. Oates¹, M.J. Page¹, M. De Pasquale², P. Schady³, A.A. Breeveld¹,
S.T. Holland⁴, N.P.M. Kuin¹ and F.E. Marshall⁵

Abstract. We examine 48 *Swift*/UVOT long Gamma-ray Burst light curves and find a correlation between the logarithmic luminosity at 200 s and average decay rate determined from 200 s onwards, with a Spearman rank coefficient of -0.58 at a significance of 99.998% (4.2σ). We determine the $\log L_{200\text{s}} - \alpha_{>200\text{s}}$ correlation to be intrinsic and discuss two possible causes: there is a property of the central engine, outflow or external medium that effects the rate of energy release so that the bright afterglows release their energy more quickly and decay faster than the fainter afterglows; alternatively, the observers viewing angle may produce the correlation, with observers at large viewing angles observing fainter and slower decaying light curves.

1 Introduction

In 2009, we analyzed a sample of 26 optical long Gamma-Ray Burst (LGRB) light curves (Oates *et al.* 2009), unearthing a correlation between the observed v -band magnitude at 400 s and the average UVOT light curve decay rate determined from 500 s. In order to have implications on our understanding of LGRBs this correlation must be observed in the rest frame, however due to the small sample size we could not confirm or exclude a correlation. Here we use a larger sample of

¹ Mullard Space Science Laboratory, University College London, Holmbury St. Mary, Dorking Surrey, RH5 6NT, UK; e-mail: sro@mssl.ucl.ac.uk

² University of Nevada, Las Vegas, Department of Physics & Astronomy, Box 454002, 4505 Maryland Parkway, Las Vegas, NV 89154-4002, USA

³ Max-Planck-Institut für Extraterrestrische Physik, Giessenbachstraße 1, 85748 Garching, Germany

⁴ Space Telescope Science Center, 3700 San Martin Dr., Baltimore, MD 21218, USA

⁵ Astrophysics Science Division, Code 660.1, NASA Goddard Space Flight Centre, 8800 Greenbelt Road, Greenbelt, Maryland 20771, USA

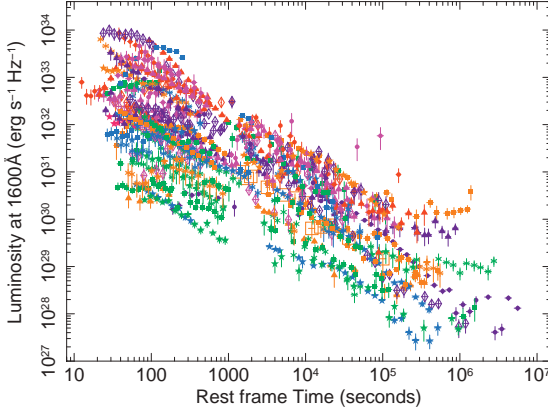


Fig. 1. Optical luminosity light curves of 56 LGRBs at restframe 1600 Å. For clarity, 3σ upper limits are not included.

48 high quality LGRB UVOT light curves to re-examine if there is a correlation between optical/UV afterglow intrinsic brightness and light curve decay rate.

2 Luminosity light curves

We selected 69 LGRBs from the second *Swift* UVOT GRB afterglow catalogue (Roming *et al.* 2013) using the criteria in Oates *et al.* (2009): the light curves must have a peak UVOT v -band magnitude brighter than 17.89, UVOT must observe from ≤ 400 to $\geq 10^5$ s after the BAT trigger and the colour of the afterglows must not evolve significantly with time, so that at no stage should the light curve from a single filter significantly deviate from any other filter light curve when normalized to the v filter. These ensure a high signal-to-noise light curve, covering both early and late times, can be constructed from the UVOT multi-filter observations using the method in Oates *et al.* (2009). The main steps were to normalize the multi-filter light curves to the v filter and then group them using a binsize of $\Delta t/t = 0.2$.

Of the 69 GRBs, luminosity light curves could be produced for the 56 that had redshifts and for which host E(B-V) values could be determined. For each of the 56 GRBs, the single filter count rate light curves were converted to luminosity at a common restframe wavelength of 1600 Å, and were corrected for both Galactic and host extinction.

3 Results

The luminosity light curves at 1600 Å, given in Figure 1 with units of $\text{erg s}^{-1} \text{Hz}^{-1}$, are clustered in a single group, with the largest range in luminosity at the earliest epochs, which becomes narrower as the light curves decay. This suggests that the most luminous GRBs decay the quickest, while the less luminous GRBs decay

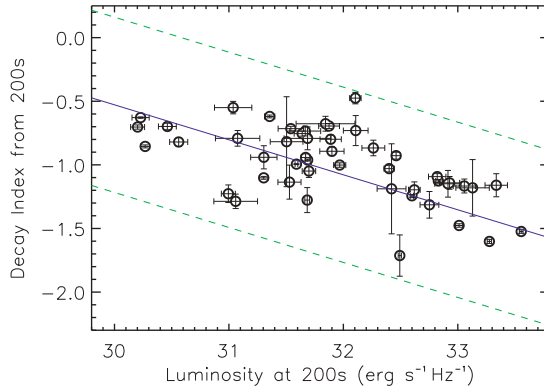


Fig. 2. Average decay index determined from the luminosity light curves after 200 s versus luminosity at 200 s. The blue solid line represents the best fit regression, $\log L_{200s} = (-3.636 \pm 0.004)\alpha + (28.08 \pm 0.13)$, and the green dashed lines represents the 3σ deviation.

more slowly. To verify this observation, we performed a Spearman Rank test on the logarithmic luminosity, $\log L_{200s}$, interpolated at 200 s using the data between 100 and 2000 s, and the average decay rate $\alpha_{>200s}$, determined by fitting a single power law to the light curves from 200 s onwards. We chose a restframe time of 200 s as all the light curves in the sample have observations by this time. For the 48 GRBs, for which we could determine $\log L_{200s}$ and $\alpha_{>200s}$ (see Fig. 2), a Spearman rank test gives a coefficient of -0.58 at a significance of 99.998% (4.2σ), confirming that luminous optical/UV afterglows decay quicker than less luminous ones.

To exclude the possibility that the correlation results from both parameters being related to redshift, we determined the partial Spearman rank correlation. This measures the degree of correlation between two parameters, excluding the effect of a third (see Kendall & Stuart 1979). This results in a coefficient of -0.50 with a confidence of 99.97% (3.5σ), and indicates that the L_{200s} – $\alpha_{>200s}$ correlation is not a result of the implicit correlation between these two parameters and redshift.

We also examined if the correlation was a result of the selection criteria or due to chance by performing a Monte Carlo simulation using 10^6 trials. For each trial, we simulated a random distribution of 48 pairs of $\log L_{200s}$ and $\alpha_{>200s}$. For each pair, we calculated the observed frame light curve, using the values of $\log L_{200s}$ and $\alpha_{>200s}$, and randomized parameters for redshift, extinction and k-correction. If the resulting observed frame light curve did not meet our selection criteria we discarded the $\log L_{200s}$ – $\alpha_{>200s}$ data point from the simulated distribution and drew a new pair of values until the selection criteria was met. Once 48 valid pairs had been verified, we ran a Spearman Rank correlation on the distribution.

Of the 10^6 trials, only 34 have a correlation coefficient equal to or indicating a stronger correlation than the real L_{200s} – $\alpha_{>200s}$ distribution. Therefore at 4.1σ

confidence, the $\log L_{200s} - \alpha_{>200s}$ correlation is not due to our selection criteria or by chance and implies that the $\log L_{200s} - \alpha_{>200s}$ correlation is intrinsic to LGRBs.

4 Discussion

We shall now examine 3 ways to produce a $\log L_{200s}$ and $\alpha_{>200s}$ correlation.

4.1 Basic GRB afterglow model

A correlation between $\log L_{200s}$ and $\alpha_{>200s}$ may be a natural result of the jet interacting with the external medium producing synchrotron emission, which results in a relationship $L \propto t^\alpha \nu^\beta$, where β is the spectral index, and, α and β are linearly related by the standard set of closure relations (*e.g.* Zhang *et al.* 2006). There are two scenarios that could produce the $\log L_{200s} - \alpha_{>200s}$ correlation. In the simplest scenario, the optical light curves, for all GRBs, are produced from the same spectral regime and therefore are produced from the same spectral segment and have the same density profile. A single closure relation would describe the relationship between α and β and we should expect a correlation between these two parameters and a correlation between $\log L_{200s}$ and β . However, we can exclude this scenario as we do not observe either of these correlations in Figure 3. In the second scenario, we consider the optical afterglows to be produced by multiple spectral regimes. In Figure 3 we display the closure relations for three most likely spectral regimes. In this more complex scenario, we should expect to see clustering of the luminosities around a given closure relation, but again we do not observe this in Figure 3. We thus exclude a basic standard afterglow model as the cause of the correlation.

4.2 Complex GRB afterglow model

There may be an additional mechanism or parameter in the standard model that regulates energy release in GRB afterglows, depending on the rate of decay, such that if the energy is released quickly the result is a bright-fast decaying afterglow, while if the energy is released more slowly a fainter-slower decaying afterglow is observed. One possibility could be continued energy injection. For instance, if the central engine does not release its energy all in one go, but releases it over a much longer duration, then we may expect faint - slowly decaying afterglow.

4.3 Off-axis and structured outflows

The $\log L_{200s} - \alpha_{>200s}$ correlation may instead be a geometric effect resulting from a range in viewing angle, θ_{obs} . The faint-slowly decaying optical afterglows would be those observed at the largest angles, while the bright-fast decaying light curves would be observed within the outflow (see Fig. 3 of Panaiteescu & Vestrand 2008). If the outflow is also structured, the result is similar, but the convergence time

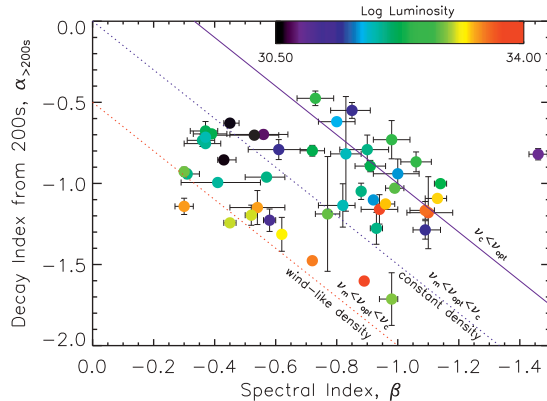


Fig. 3. Optical/UV temporal and spectral indices for the 48 GRBs. The lines represent 3 closure relations and a colour scale is used for the range in luminosity at 200 s, log L_{200s}.

and the range of light curve decays will vary, depending on the energy distribution within the jet.

5 Conclusions

We find an intrinsic correlation between optical/UV luminosity at 200 s and average decay rate determined from 200 s onwards with a significance of 99.998% (4.2 σ). We give two possible causes: an intrinsic mechanism or physical quantity that controls how quickly the energy is released, such that bright, fast-decaying afterglows release their energy more quickly than faint, slow-decaying afterglows; alternatively, the observers viewing angle may produce the correlation, with observers at large viewing angles observing fainter and slower decaying light curves.

This research has made use of data from the High Energy Astrophysics Science Archive Research Center (HEASARC) and the Leicester Database and Archive Service (LEDAS), provided by NASA's Goddard Space Flight Center and the Department of Physics and Astronomy, Leicester University, UK, respectively. SRO, AAB, NPMK, and MJP acknowledge the support of the UK Space Agency.

References

- Kendall, M., & Stuart, A., 1979, The advanced theory of statistics, Vol. 2, Inference and relationship
- Oates, S.R., Page, M.J., Schady, P., *et al.*, 2009, MNRAS, 395, 490
- Panaiteescu, A., & Vestrand, W.T., 2008, MNRAS, 387, 497
- Roming, P.W.A., Koch, T.S., Oates, S.R., *et al.*, 2013, in preparation
- Zhang, B., Fan, Y., Dyks, J., *et al.*, 2006, ApJ, 642, 354

PHYSICAL PROPERTIES OF RAPIDLY DECAYING AFTERGLOWS

M. De Pasquale¹, S. Schulze², D.A. Kann³, S. Oates⁴ and B. Zhang¹

Abstract. We analyze a sample of *Swift* X-ray and optical GRB afterglows which were chosen so as to reduce selection effects against the weakest events. We tentatively identify important differences in GRBs that show a fast decay with respect to the average GRB, in particular a tendency for the more energetic bursts to have a steeper afterglow decline. An explanation to this finding could be bursts in a wind environment are on average more energetic than bursts occurring in a constant density medium.

1 Introduction

The *Swift* mission (Gehrels *et al.* 2004) has ushered in an era of intense study of GRB afterglows. The high detection rate, ~ 100 GRBs/year, the prompt observations in X-ray and optical bands that begin ~ 100 s after the trigger, and the rapid dissemination of the coordinates to ground facilities have enabled observers to build large samples of multi-wavelength GRB afterglow light curves, that cover evolution from GRB onset to days or weeks later. We can therefore model the temporal and spectral behaviour in great detail and draw conclusions on the physical parameters of the bursts. In this work, we build on the analysis of Schulze *et al.* (2011), trying to understand whether there is any possible correlation between the decay slope of the afterglows and the energetics of the GRB.

2 Initial sample and its properties

Schulze *et al.* (2011) examined the complete dataset of *Swift* bursts occurring between launch and September 2009. They selected events that obeyed the following

¹ Department of Physics & Astronomy, University of Nevada, Las Vegas, USA

² Pontificia Universidad Católica de Chile, Chile

³ Thüringer Landessternwarte Tautenburg and Max-Planck-Institut für extraterrestrische Physik, Germany

⁴ Mullard Space Science Laboratory, University College London, UK

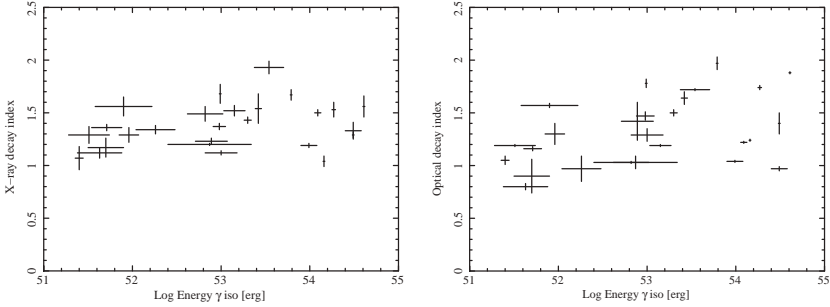


Fig. 1. *Left:* plot of X-ray decay slope α_X against the energy released in γ -rays at the prompt phase in the sample of Schulze *et al.* (2011). *Right:* same as left panel, but displaying α_{opt} rather than α_X .

criteria: i) known redshift (and thus known energetics); ii) X-ray and optical afterglows are not dominated by flares or bad data sampling iii) both the X-ray and optical afterglows satisfy the forward shock closure relations (Sari *et al.* 1998; Sari *et al.* 1999; Chevalier & Li 2000) in the adiabatic case, *i.e.*, the slow decline phase (Nousek *et al.* 2006) is not included in the study. For most events in Schulze *et al.* (2011), it is possible to distinguish between a circumburst medium with constant density profile (Interstellar medium like, ISM) and a stellar wind profile (wind). In the left and right panels of Figure 1, we show the decay slopes of the X-ray and optical bands, α_X and α_{opt} , *versus* the energy released in γ -rays during the prompt phase assuming isotropy, $E_{\gamma,iso}$, for this sample. The probability of a correlation, assessed given the value of Pearson correlation coefficient between α_X and $E_{\gamma,iso}$, is found to be less than 90%, thus it is not statistically significant. However, we find that a trend between α_{opt} and $E_{\gamma,iso}$ is more likely: the probability of a correlation, evaluated as above, is 97%.

3 Correlation tests

Motivated by these findings, we have used the same criteria as Schulze *et al.* (2011) to extend the previous sample to include bursts which occurred in 2010 and 2011. In the left and right panels of Figure 2, we show the decay indices against $E_{\gamma,iso}$ for this revised sample. The probability of a correlation between α_X and $E_{\gamma,iso}$ is now 99%, while between α_{opt} and $E_{\gamma,iso}$ it is 99.86%. By enlarging the sample, we find the probability for correlation has increased.

An immediate possibility to explain this correlation is that the most energetic bursts are already in the jet-break regime. Bursts with higher $E_{\gamma,iso}$ may have an earlier break, which is attributed to a collimated outflow. However, in the sample at hand, only $\sim 20\%$ of bursts have temporal indices consistent with a jet regime. If we remove such events, there is still a residual marginal trend, since the probability of a correlation between the decay slope and the energetics becomes 97.5%. While

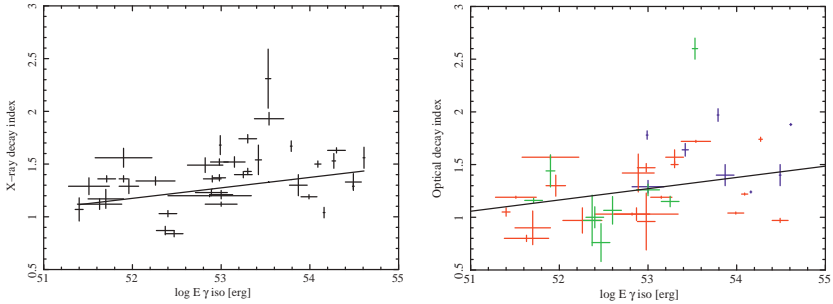


Fig. 2. *Left:* plot of the X-ray decay slope α_X against the energy released in γ -rays during the prompt phase in our updated sample. The line represents a linear fit of the data, in which only 1-D errors are taken into account. *Right:* same as left panel, but displaying α_{opt} rather than α_X . Blue, red and green points represent GRBs in wind environments, those in an ISM, and events for which the environment cannot be distinguished, respectively.

the statistical strength of this residual correlation is weak, we may speculate what could cause it, if it turns out to be real. The optical band is usually below the cooling frequency ν_c ; the forward-shock model predicts that the slope, under such a condition, is steeper in a wind than in an ISM environment, all other parameters being equal. Thus, bursts with steeper decaying optical slopes in our sample may be those in a wind environment, which combined with the correlation between α_{opt} and $E_{\gamma,iso}$ would imply that bursts in a wind medium are, on average, also more energetic. This scenario could also explain why the X-ray decay slope is not strongly correlated with $E_{\gamma,iso}$: contrary to the optical band, the X-ray band is usually above ν_c , and the decay slope, under such a condition, is not affected by the density profile of the medium. An examination of Table 3 in Schulze *et al.* (2011) may corroborate the scenario in which wind bursts are on average more energetic than those in an ISM. In this table, bursts in constant density medium span 4 decades in $E_{\gamma,iso}$, between $\sim 10^{51}$ to a few 10^{54} erg, while bursts in wind medium are all above 10^{53} erg. Looking at this in another way, this shows that 20% of burst in an ISM have $E_{\gamma,iso} > 10^{54}$ erg, while 50% of bursts in wind are above this threshold. In the left panel of Figure 3, we plot a histogram of $E_{\gamma,iso}$ of the bursts of our sample, distinguishing between those consistent with ISM and Wind medium. While these two sub-samples overlap, it seems that wind bursts are on average more energetic. A Kolmogorov-Smirnov test indicates that the two distributions may not be drawn from the same population ($P=1.8\%$). Finally, if we remove bursts in wind medium (blue points in right panel of Fig. 4), any hint of a correlation between optical decay slope and energetics basically disappears, since the probability decreases to $\sim 80\%$. All these hints point toward a scenario in which bursts in a wind medium are, on average, more energetic than those in an ISM, although they unquestionably do not prove it.

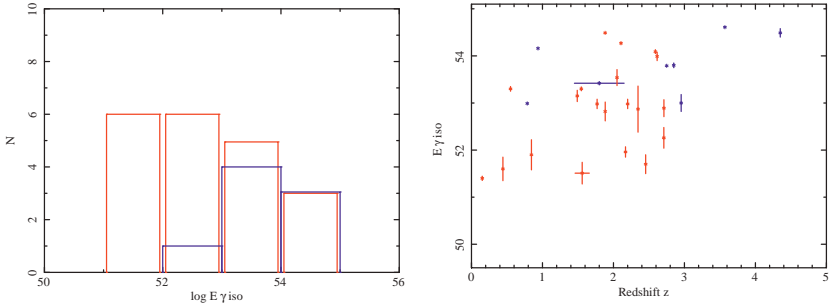


Fig. 3. *Left:* histogram with bursts found to be in a wind environment (blue) and an ISM (red). *Right:* the energy released in γ -rays versus redshift, bursts found to be in an ISM are red and wind are blue.

4 Possible bias

The speculations above, however, may be affected by the following bias. Due to the steeper decays, bursts in wind media generally need brighter afterglows to satisfy the criteria of the sample, and brighter afterglows generally imply higher $E_{\gamma,iso}$ as well. However, we find that this bias might not be pronounced. In the right panel of Figure 3 we plot $E_{\gamma,iso}$ vs. redshift. If the aforementioned bias was strong, one would expect to see a concentration of less energetic bursts at low redshift. However, this does not appear to be true.

We caution also that we are still within the regime of low-number statistics, for several bursts the density profile of the medium could not be ascertained, and we could only study those events for which data were published. One will need a larger and more complete sample to ascertain conclusively whether bursts in wind have larger $E_{\gamma,iso}$ than explosions in an ISM or not.

5 Conclusions

Within a sample of *Swift* bursts obeying the forward shock model, we find a strong indication for a correlation between $E_{\gamma,iso}$ and optical decay index. A correlation between $E_{\gamma,iso}$ and X-ray band decay index is less significant.

These correlations can be explained by the fact that a few energetic events are already in the post jet-break regime at early epoch. However, if we take these events out, we still have an indication for a correlation between α_{opt} and $E_{\gamma,iso}$. This correlation, if turns out to be real, may imply that bursts in stellar wind environment are on average more energetic than those in an ISM. The probability that distributions of $E_{\gamma,iso}$ of wind and ISM bursts are drawn from the same population is 1.8%. Observational biases which would favour brighter wind bursts need to be carefully taken into account, and we shall need a larger sample to

establish whether the progenitors of the most energetic bursts are also more likely to shape the environment around them with their stellar winds.

References

- Chevalier, R.A., & Li, Z.Y., 2000, ApJ, 536, 195
Gehrels, N., Chincarini, G., Giommi, P., *et al.*, ApJ, 611, 1005
Nousek, J.A., Kouveliotou, C., Grupe, D., *et al.*, ApJ, 642, 389
Sari, R., Piran, T., & Narayan, R., 1998, ApJ, 497, L17
Sari, R., Piran, T., & Halpern, J.P., 1999, ApJ, 519, L17
Schulze, S., Klose, S., Björnsson, G., *et al.*, 2011, A&A, 526, A23

TACKLING THE AFTERGLOW FORWARD-SHOCK MODEL WITH GROND

R. Filgas^{1,2}

Abstract. We present the scientific analysis of the GRB afterglow data obtained by the GROND, a seven-channel imager with four optical and three near-infrared detectors. Its unique capability to observe in all bands simultaneously, together with rapid triggering, precise photometry and high temporal resolution, give us the opportunity to study light curves and spectral energy distributions of GRB afterglows in unprecedented detail. This is demonstrated using the observations of three GRB afterglows that are used to put strong constraints on the standard GRB fireball scenario.

1 Introduction

Even though it is now almost half a century since the Gamma-Ray Bursts (GRBs) were discovered, the exact nature of their emission is still not clearly understood. The leading model for the radiation principle of GRBs is the fireball shock scenario (Mészáros 2002; Meszaros & Rees 1997; Piran 1999; Zhang & Mészáros 2004). In this model, the prompt gamma emission is produced by *internal shocks* when the faster fireball shell catches up with the shell with lower Lorentz factor. The fireball then propagates into the ambient medium, where it produces a blast wave. This *external shock* is responsible for the long-lived afterglow emission in all wavelengths below gamma-rays.

Most of the afterglow light curves observed before the launch of the *Swift* satellite (Gehrels *et al.* 2004) were consistent with this model (Halpern *et al.* 1999; Stanek *et al.* 1999). However, the more recent and detailed light curves of afterglows, obtained with the latest generation of GRB instruments capable of high sampling in both time and energy domains, showed features that needed various

¹ Institute of Experimental and Applied Physics, Czech Technical University in Prague, Horská 3a/22, 128 00 Prague 2, Czech Republic; e-mail: robert.filgas@utef.cvut.cz

² Max-Planck-Institut für extraterrestrische Physik, Giessenbachstraße 1, 85748 Garching, Germany

additions and modifications to the simplest fireball model. This work presents three such cases observed by the Gamma-Ray burst Optical Near-infrared Detector (GROND, Greiner *et al.* 2008). This instrument has provided high-quality, very well-sampled, simultaneous data in seven bands since 2007, when it was mounted at the 2.2 m MPI/ESO telescope at La Silla observatory in Chile. The high-precision data obtained by GROND allow for a detailed study of afterglow light curves (Nardini *et al.* 2011), jets of GRBs (Krühler *et al.* 2009), the dust in their host galaxies (Greiner *et al.* 2011; Krühler *et al.* 2011a; Schady *et al.* 2012), their redshifts (Greiner *et al.* 2009; Krühler *et al.* 2011b), their associations with SNe (Olivares E. *et al.* 2012), and provide tools to test the standard fireball scenario and its modifications.

Here we provide details of the GROND and *Swift*/XRT (in some individual cases together with *Swift*/UVOT, REM, BOOTES-3 and Stardome) observations of the afterglows of GRB 080413B, GRB 091127 and GRB 091029 and discuss their light curves and spectral energy distributions (SEDs) in the context of the fireball shock model thanks to the very good energy and time-domain coverage of our high-quality data. Throughout the work, we adopt the convention that the flux density of the GRB afterglow can be described as $F_\nu(t) \propto t^{-\alpha}\nu^{-\beta}$, where α is the temporal and β the spectral index. Unless stated otherwise in the text, all reported errors are at 1σ confidence level.

2 GRB 080413B

The first of the three presented cases is the afterglow of GRB 080413B (Filgas *et al.* 2011b), which in the optical/NIR domain shows an initial decay with a slope of $\alpha = 0.73 \pm 0.01$, interrupted at roughly 1 ks by a chromatic flattening (Fig. 1a). The decay is later resumed with a steeper temporal slope of $\alpha = 0.95 \pm 0.02$ until an achromatic jet break at roughly 330 ks. After the jet break the afterglow fades with a steep decay of $\alpha = 2.75 \pm 0.16$, which is flattened at the end ($> T_0 + 1$ Ms) by a possible faint host galaxy. The initial decay of the X-ray light curve has the same temporal slope as seen in the optical/NIR wavelengths but the plateau phase is completely missing. The significantly different evolution of the X-ray and optical/NIR light curve can be explained by a two-component jet (see Filgas *et al.* 2011b and references therein for details).

The initial shallow decay phase in all wavelengths could be the result of the emission of the decelerating narrow jet, which until its jet break dominates the afterglow emission. This jet break is hidden by the onset of the wide jet but from the model we can estimate its time to be at around 3.9 ks. From this value we can calculate the opening angle of the narrow jet to be $\theta_n \sim 1.7^\circ$. Assuming the time of the first R' band data point to be upper limit on the time of the emission peak, we calculate the initial Lorentz factor as $\Gamma_n > 190$. The wide-jet component is in this scenario responsible for the rebrightening of the optical/NIR light curve. The jet break at roughly 330 ks leads to an opening angle of the wide jet of $\theta_w \sim 9^\circ$ and the initial Lorentz factor, corresponding to the peak of the second jet, is then $\Gamma_w \sim 18.5$. The X-ray light curve has a much lower contribution from the second

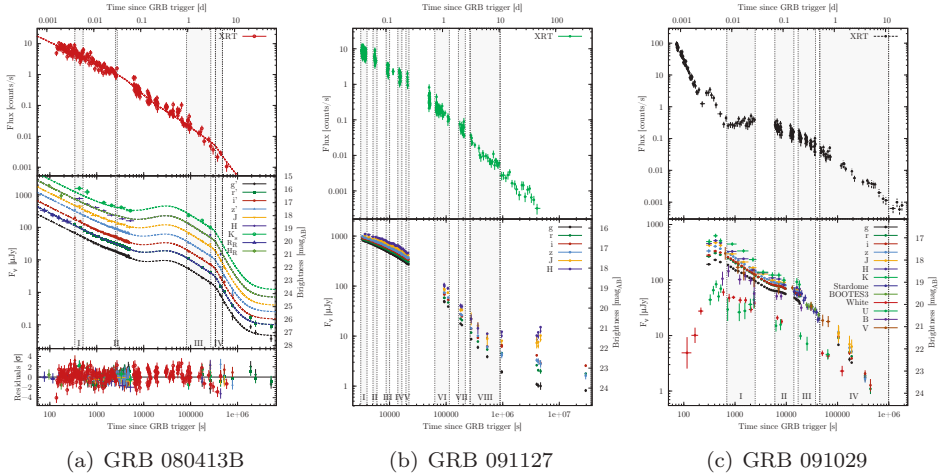


Fig. 1. Light curves of the X-ray (*top panels*) and optical/NIR (*middle panels*) afterglows. Upper limits are not shown for better clarity. Gray regions show the time intervals where the broad-band SEDs are reported.

component and therefore lacks the rebrightening. The case of the afterglow of GRB 080413B shows that we need a structured jet to explain all the features of its optical/NIR light curve and the difference between the X-ray and optical/NIR light curves. Moreover, it shows that GROND can provide observational data good enough to obtain parameters of both components of the jet from the light curve morphology.

3 GRB 091127

The case of the afterglow of GRB 091127 (Filgas *et al.* 2011a) proves that what looks like a typical afterglow, can hold the evidence of an extremely rarely observed phenomenon. The X-ray light curve (Fig. 1b) of this afterglow is best fitted using a smoothly broken power-law with an initial decay slope 1.02 ± 0.04 , a break at around 33 ks and a post-break temporal slope of 1.61 ± 0.04 . The optical/NIR light curve follows the same shape but with a much flatter initial temporal slope, which further flattens with the increasing wavelength of GROND filters. This suggests a strong color evolution, which is confirmed by measuring the spectral slope of each optical/NIR exposure thanks to simultaneous multi-band observing capabilities of GROND. From this we see that the optical/NIR spectral index rises from 0.23 ± 0.04 to 0.80 ± 0.08 between 3 and 300 ks. In addition, we constructed broad-band optical/NIR to X-ray SEDs at eight different time intervals, indicated in the light curve. Given that these broad-band SEDs proved to be inconsistent with a straight power-law, we used models that include a spectral break between the X-ray and optical/NIR data. This fit shows that the break evolves to larger

wavelengths in time, through and beyond the GROND bands. However, this fit with the sharp break requires the low-energy spectral index to be time-dependent, contrary to what the theory expects.

To keep the spectral indices constant, we fitted all eight broad-band SEDs simultaneously with two power-laws connected by a smooth break. The fit again shows the break moving towards the lower energies and allows us to obtain not only the speed of the break but also its shape. We identify the spectral break to be the cooling break, one of the frequencies typical for the synchrotron emission of GRB afterglows. The fit-derived smoothness of 2.2 ± 0.2 shows that the cooling break is very smooth, as predicted by Granot & Sari (2002). The calculated speed of the cooling break, which moves with the temporal power-law index of -1.23 ± 0.06 , is way faster than theoretical speed of $t^{-0.5}$ (Sari *et al.* 1998). We explain this by letting the fraction of energy in the magnetic field vary in time. To be consistent with our measurement of the cooling break speed, this microphysical parameter would have to rise in time as $\epsilon_B \propto t^{0.49}$.

4 GRB 091029

The last presented example is the afterglow of GRB 091029 (Filgas *et al.* 2012). It's light curve (Fig. 1c) is almost totally decoupled between the X-ray and optical/NIR domains. The X-ray light curve begins with a tail of the GRB emission, interrupted at ~ 200 s by an X-ray flare, followed by a shallow rise peaking around 7.4 ± 1.8 ks and a decay with temporal index of 1.20 ± 0.04 . On the other hand, the optical/NIR light curve shows a steep ($\alpha = -2.90 \pm 0.67$) initial rise from the start of the observations until the peak at around 400 s. The decay following the initial peak has a slope of $\alpha = 0.58 \pm 0.01$ until around 5 ks, when it starts to flatten. Fitting this shallow decay phase between 0.6 – 5 ks in each optical/NIR band separately shows a steepening of the temporal index with increasing wavelength of the GROND filters, suggesting that the afterglow gets bluer. This is confirmed by measuring the spectral slope β of the optical/NIR data as a function of time. This measurement shows that the optical/NIR spectral index decreases from 0.57 ± 0.04 to 0.26 ± 0.03 between 0.4 and 9 ks, and then slowly increases again to a value of 0.49 ± 0.12 at around 100 ks.

The almost total decoupling of the optical/NIR and the X-ray light curves of the afterglow of GRB 091029 suggests a double outflow origin. This is supported by our finding that the X-ray spectral hardness does not evolve synchronously with the optical spectral hardening at 0.3 – 10 ks. We conclude that the only scenario consistent with all the peculiarities of the observed light curve and spectra is the two-component jet setup, in which the outflows are at different stages of the synchrotron spectral evolution. The flattening of the broad-band SEDs in the optical/NIR region would be a result of the wide jet having both the cooling break ν_c and the injection frequency ν_m between the X-ray and optical/NIR wavelengths, while the narrow jet has only the cooling frequency ν_c between X-ray and optical/NIR bands. As the ratio between these two outflows changes, it would explain the spectral hardening in the optical/NIR bands, while being consistent

with the X-ray spectral slope staying constant thanks to equal p values in both outflows. The turnover in the spectral evolution at \sim 10 ks can be explained by the passage of the frequency ν_m through the GROND filters, after which the optical/NIR spectral index would be consistent with the spectral phase of the narrow jet. This scenario is difficult to confirm or disprove, though, by fitting the light curve and SEDs alone because this model has a large number of free parameters.

5 Conclusions

The growing number of well-sampled data sets from the latest generation of instruments like the GROND imager once again show that the standard fireball scenario is too simple to explain the observed data for some time now. The simplest fireball model has an increasingly difficult time to explain the complex light curves and spectral evolutions of numerous GRB afterglows. This is demonstrated in this work by three examples, the afterglow of GRB 080413B needed the two-component jet to explain its chromatic rebrightening, the afterglow of GRB 091127 needed the energy of the magnetic field to increase in time, and the afterglow of GRB 091029 is very difficult to explain in the fireball shock model framework at all, showing that some major modifications to the fireball scenario or even some alternate models might be needed to cope with our multi-wavelength data.

References

- Filgas, R., Greiner, J., Schady, P., *et al.*, 2012, A&A, 546, A101
- Filgas, R., Greiner, J., Schady, P., *et al.*, 2011a, A&A, 535, A57
- Filgas, R., Krühler, T., Greiner, J., *et al.*, 2011b, A&A, 526, A113
- Gehrels, N., Chincarini, G., Giommi, P., *et al.*, 2004, ApJ, 611, 1005
- Granot, J., & Sari, R., 2002, ApJ, 568, 820
- Greiner, J., Bornemann, W., Clemens, C., *et al.*, 2008, PASP, 120, 405
- Greiner, J., Krühler, T., Fynbo, J.P.U., *et al.*, 2009, ApJ, 693, 1610
- Greiner, J., Krühler, T., Klose, S., *et al.*, 2011, A&A, 526, A30
- Halpern, J.P., Kemp, J., Piran, T., *et al.*, 1999, ApJ, 517, L105
- Krühler, T., Greiner, J., Afonso, P., *et al.*, 2009, A&A, 508, 593
- Krühler, T., Greiner, J., Schady, P., *et al.*, 2011a, A&A, 534, A108
- Krühler, T., Schady, P., Greiner, J., *et al.*, 2011b, A&A, 526, A153
- Mészáros, P., 2002, ARA&A, 40, 137
- Meszaros, P., & Rees, M.J., 1997, ApJ, 476, 232
- Nardini, M., Greiner, J., Krühler, T., *et al.*, 2011, A&A, 531, A39
- Olivares, E.F., Greiner, J., Schady, P., *et al.*, 2012, A&A, 539, A76
- Piran, T., 1999, Phys. Rep., 314, 575
- Sari, R., Piran, T., & Narayan, R., 1998, ApJ, 497, L17
- Schady, P., Dwelly, T., Page, M.J., *et al.*, 2012, A&A, 537, A15
- Stanek, K.Z., Garnavich, P.M., Kaluzny, J., *et al.*, 1999, ApJ, 522, L39
- Zhang, B., & Mészáros, P., 2004, Int. J. Mod. Phys. A, 19, 2385

A COMPLETE SAMPLE OF LONG BRIGHT *SWIFT* GRBS

G. Tagliaferri¹, R. Salvaterra², S. Campana¹, S. Covino¹, P. D’Avanzo¹,
D. Fugazza¹, G. Ghirlanda¹, G. Ghisellini¹, A. Melandri¹, B. Sbarufatti¹,
S. Vergani¹ and L. Nava³

Abstract. Starting from the *Swift* sample we defined a complete subsample of 58 bright long Gamma Ray Bursts (GRB), 52 of them (90%) with a redshift determination, in order to characterize their properties. This complete sample of bright long- GRBs allowed us to investigate their evolution with cosmic time and properties. We focused in particular on the GRB luminosity function, on the spectral-energy correlations of their prompt emission, on the nature of dark bursts and on possible correlations between the prompt and the X-ray afterglow properties.

1 Introduction

Long Gamma Ray Bursts (GRB) are a powerful alternative possibility to study the star formation rate and probably the only one to directly study the stellar evolution up to the very young Universe, soon after the first massive stars have started to form and die. In fact, GRBs are associated to the death of very massive stars and, therefore, with star forming regions. Moreover, they are very bright objects that can be detected up to extremely high redshifts: so far we have a secure spectroscopic redshift of $z = 8.2$ and a photometric record holder of $z = 9.4$. At these redshift, the Universe was very young, less than 10% of its current age. Hence, although it is still not completely clear if GRBs provide an unbiased view, they can be used to study the history of the star formation and of the metallicity enrichment from the local Universe up to the epoch where the first stars are thought to form.

About one third of the bursts detected by *Swift* (Gehrels *et al.* 2004) has a measured redshift. While this represents an enormous improvement with respect to the pre-*Swift* situation, this is still too low to provide a complete sample in

¹ INAF-OABr, via Bianchi 46, 23807 Merate, Italy;

e-mail: gianpiero.tagliaferri@brera.inaf.it

² INAF-IASF Milano, via Bassini 15, 20133 Milano, Italy

³ APC Université Paris Diderot, 10 rue Domon et Duquet, 75205 Paris, France

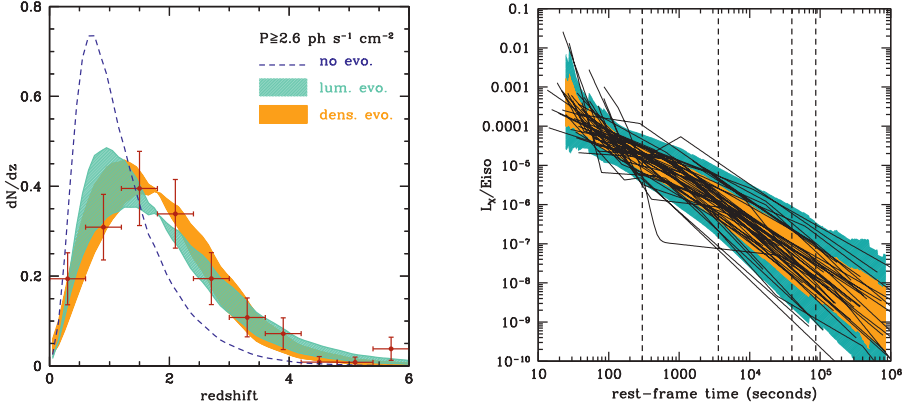


Fig. 1. *Left panel:* normalized redshift distribution of GRBs with $P \geq 2.6 \text{ ph s}^{-1} \text{ cm}^{-2}$ in the band 15–150 keV. Data points show the observed redshift distribution. The dashed line shows the expected distribution for the no-evolution case. Results of luminosity and density evolution models are also shown. *Right panel:* best fit of the X-ray luminosity light curves normalized to their E_{iso} . The rest frame times at which we computed the various correlations (see text) are marked with vertical dashed lines. The light (dark) shaded area represents the 1σ (2σ) scatter around the mean value of the L_{iso}/E_{iso} distribution (see D'Avanzo *et al.* 2012 for more details).

redshift. Moreover, this sample is very heterogeneous. Therefore we started from the criteria proposed by Jakobsson *et al.* (2004): i) the burst has been well localized by *Swift*/XRT and its coordinate quickly distributed; ii) the Galactic extinction in the burst direction is low ($A_V < 0.5$); iii) the GRB declination is $-70^\circ < \delta < 70^\circ$; iv) the Sun-to-field distance is $\theta_{\text{Sun}} > 55^\circ$; v) no nearby bright stars are present. This increases the completeness level in redshift to $\sim 50\%$. We then restricted our sample to GRBs that are relatively bright in the 15–150 keV *Swift*/BAT band, *i.e.* with a 1-s peak photon flux $P \geq 2.6 \text{ ph s}^{-1} \text{ cm}^{-2}$. This corresponds to an instrument that is ~ 6 times less sensitive than *Swift*, which give us a high level of confidence that all GRBs with a flux higher than our limit and that are inside the FOV of BAT when they explode will be detected. Therefore, our sample is complete with respect to our selection criteria and provide an unbiased view of the bright end of the GRB Log N - Log S. Clearly, we can not say what are the property of the burst at lower fluxes, to this end other samples are better suited. It also provide a sample that has more than 90% completeness in redshift. In fact, up to the end of May 2011, 58 GRBs match our selection criteria (see Salvaterra *et al.* 2012) and 52 of them have a measured redshift. Moreover, for 3 of the other 6 bursts the afterglow or the host galaxy has been detected in at least one optical filter, so that $\sim 95\%$ of the bursts in our sample have a constrained redshift. We note that, while our sample represents only $\sim 10\%$ of the full *Swift* sample, it contains more than 30% of long GRBs with known redshift.

2 Luminosity function, spectral-energy correlations, dark bursts

Our complete *Swift* sample is very powerful to test the evolution of the long GRB population with redshift. Still the number of burst is not large enough to derive the present day GRB rate density and obtain meaningful constrains to the GRB luminosity function (LF). In fact, with a sample of 58 burst it is not possible to discriminate between different evolution scenarios for the LF, the error bars are so large that even a no-evolution scenario could reproduce the data. Therefore, we derived the GRB luminosity function (LF) by jointly fitting the observed differential number counts in the 50–300 keV band of BATSE (Stern *et al.* 2002) and the observed redshift distribution of bursts in our sample. We note that the best-fit parameters derived in this way provide a good fit also of the *Swift* differential peak-flux number counts once the 15–150 keV band, the field of view of 1.4 sr and the observing lifetime of *Swift* are considered. We explored two general expressions for the GRB LF: a single power-law with an exponential cut-off at low luminosity and a broken power-law LF (Salvaterra *et al.* 2012).

As shown in Figure 1, left panel, if we assume that long GRBs trace the cosmic star formation and that their LF is constant in redshift, *i.e.* the no-evolution scenario, we can not reproduce the observed redshift distribution of our sample, confirming previous findings (Kistler *et al.* 2009; Virgili *et al.* 2011; Robertson & Ellis 2012; Jakobsson *et al.* 2012). We note that Elliott *et al.* (2012), using a different complete sample of GRBs observed by GROND of size (39 objects) similar to our sample, claim that there is no need of evolution in the GRB luminosity function. As said above, with a small number of sources the error bars in the data points are too big and even a non-evolving luminosity function is consistent with the data. We find the same results if we use only our sample of 58 sources, this is why we choose to fit also the BATSE sample. Therefore, to fit our data we considered two evolution scenarios: i) a luminosity evolution model in which the GRBs at higher redshift are typically brighter than the bursts at lower redshift and, ii) a density evolution model, in which the GRB formation rate increases with redshift. Both models can reproduce the observed redshift distribution; in particular we find that either the typical burst luminosity increases as $(1+z)^{2.3 \pm 0.6}$ or the GRB rate density as $(1+z)^{1.7 \pm 0.5}$ on top of the known cosmic evolution of the SFR (as computed by Li 2008). These result do not depend on the assumed expression of the GRB LF. We can also reproduce our data assuming no evolution of the GRB LF if we assume that GRBs form preferentially in low-metallicity environments. In this case we find that the metallicity threshold for GRB formation should be lower than $0.3 Z_{\odot}$ in order to account for the observations (Salvaterra *et al.* 2012).

One of the most debated issue in the GRB field is the existence or otherwise of the correlations between the GRBs spectral peak energy E_{peak} , the isotropic energetics E_{iso} and the isotropic luminosity L_{iso} . Having a complete sample of bright long GRBs, we can properly investigate about these correlations. As shown by Nava *et al.* (2012) a strong correlation is found between $E_{\text{peak}} - E_{\text{iso}}$ and $E_{\text{peak}} - L_{\text{iso}}$ for the bursts of this complete sample, with only one outlier, GRB 061021. Their slopes, normalizations and dispersions are consistent with those found with

the whole sample of bursts with measured redshift and E_{peak} . The biases present in the total sample commonly used to study these correlations do not affect their properties. We also find that there is no evolution with redshift of the $E_{\text{peak}} - E_{\text{iso}}$ and $E_{\text{peak}} - L_{\text{iso}}$ correlations. One of the argument used against these correlation is that they are due to the presence of flux limits in the existing samples of GRBs. By performing Monte Carlo simulations under different assumptions for their LF we studied the possible effects caused by the flux-limit selection in our complete sample on the $E_{\text{peak}} - L_{\text{iso}}$ correlation. If we assume that this correlation does not exist, we are unable to reproduce it as due to the flux limit threshold of our complete sample. The null hypothesis can be rejected at more than 2.7σ level of confidence (Ghirlanda *et al.* 2012a). We used this complete sample, together with other samples, also to study the distributions of the GRB jet opening angle θ_{jet} and the bulk Lorentz factor Γ_0 . We find that on average the “faster” bursts, *i.e.* those with larger values of Γ_0 , have smaller values of θ_{jet} (Ghirlanda *et al.* 2012b).

Beside studying the properties of the GRB prompt emission, our complete sample can be used to statistically study also their afterglow properties. It is well known that while thanks to its prompt reaction *Swift* almost always find a X-ray afterglow associated to a GRB, in the optical/NIR this is not the case. These GRBs are called “dark”-GRBs, for which there are various definitions based on the ratio between the optical and the X-ray fluxes (or their upper limits). With our complete sample of bright GRBs we have established the existence of a genuine dark population with $\sim 30\%$ of dark-burst (according to the definition of Jakobsson *et al.* 2004) expected for the whole class of long GRBs (Melandri *et al.* 2012). This population of dark-bursts has a redshift distribution and prompt properties very similar to those of the whole sample. At the same time their de-absorbed X-ray flux is slightly higher than the one of the non-dark events, while their optical flux is at the lower tail of the optical flux distribution. All these properties suggest that dark-bursts events generate in much denser environments with respect to normal bright events. In agreement with previous results, we can therefore exclude the high- z and the low-density scenarios as the cause of their darkness. The major cause of the optically dark events is the dust extinction (Melandri *et al.* 2012). We also find that there is a very tight correlation between the GRB darkness and their high X-ray column densities (Campana *et al.* 2012; Fynbo *et al.* 2009). Again, a strong indication that dark-GRBs are formed in a metal-rich environment where dust must be present. For the full sample of X-ray afterglows, using the *Swift* X-ray Telescope data, we find that the distribution of their intrinsic absorbing X-ray column densities has a mean value of $\log(N_H/\text{cm}^{-2}) = 21.7 \pm 0.5$, consistent with the one derived from the total sample of GRBs with redshift. The observed mild increase of the intrinsic column density with redshift is probably due to the contribution of intervening systems along the line of sight. (Campana *et al.* 2012).

To investigate whether there is a correlation between the X-ray afterglow luminosity and the prompt emission properties we computed the afterglow X-ray luminosities at four different rest frame times (5 min, 1 hr, 11 hr and 24 hr after trigger). Indeed, we find that E_{iso} , L_{iso} and the rest frame peak energy E_{peak} do correlate with the rest frame afterglow X-ray luminosity, but the significance

of each correlation decreases over time. This result can be explained by a GRB X-ray light curve due to a combination of different components whose relative contribution and weight change with time, with the prompt and afterglow emission dominating at early and late time, respectively. In particular, we found evidence that the plateau and the shallow decay phase often observed in GRB X-ray light curves are powered by activity from the central engine. The existence of the $L_X - E_{iso}$ correlation at late times (see Fig. 1, right panel) suggests a similar radiative efficiency among different bursts with on average about 6% of the total kinetic energy powering the prompt emission (D'Avanzo *et al.* 2012).

2.1 Conclusions

Using a well defined complete sample of bright GRBs with more than 90% of redshift determination, we characterized their luminosity function, properties of their prompt emissions and their correlation with the X-ray afterglow emissions. We find that strong luminosity or density evolution is required in order to reproduce the data. Alternatively, the GRB must preferentially form in low metallicity environment ($\leq 0.3 Z_\odot$). We confirm the existence of the $E_{peak} - E_{iso}$ and $E_{peak} - L_{iso}$ correlations, and showed that this can not be due to a bias introduced by the flux limited threshold of our sample. We also find that the cause of the dark nature of some GRBs ($\sim 30\%$ of the sample) is most likely due to dust extinction and find a strong correlation between the GRB darkness and their high X-ray column densities. Finally, the afterglow X-ray emissions do correlate with the prompt emissions even at later time (11 hours rest frame), with the X-ray light curve that is powered by activity from the central engine for long times.

References

- Campana, S., Salvaterra, R., Melandri, A., *et al.*, 2012, MNRAS, 421, 1697
- D'Avanzo, P., Salvaterra, R., Sbarufatti, B., *et al.*, 2012, MNRAS, 425, 506
- Elliott, J., Greiner, J., Khochfar, *et al.*, 2012, A&A, 539, 113
- Fynbo, J.P.U., Jakobsson, P., Prochaska, J.X., *et al.*, 2009, ApJS, 185, 526
- Gehrels, N., Chincarini, G., Giommi, P., *et al.*, 2004, ApJ, 611, 1005
- Ghirlanda, G., Ghisellini, G., Nava, L., *et al.*, 2012, MNRAS, 422, 2553
- Ghirlanda, G., Ghisellini, G., Salvaterra, R., *et al.*, 2012, MNRAS, 428, 1410
- Jakobsson, P., Hjorth, J., Fynbo, J.P., *et al.*, 2006, A&A, 617, L21
- Jakobsson, P., Hjorth, J., Malesani, D., *et al.*, 2012, ApJ, 752, 62
- Kistler, M.D., Yüksel, H., Beacon, J.F., *et al.*, 2009, ApJ, 705, L104
- Li, L.-X., 2008, MNRAS, 388, 1487
- Melandri, A., Sbarufatti, B., D'Avanzo, P., *et al.*, 2012, MNRAS, 421, 1265
- Nava, L., Salvaterra, R., Ghirlanda, G., *et al.*, 2012, MNRAS, 421, 1256
- Robertson, B.E., & Ellis, R.S., 2012, ApJ, 744, 95
- Salvaterra, R., Campana, S., Vergani, S.D., *et al.*, 2012, ApJ, 749, 68
- Stern, B.E., Atteia, J.-L., & Hurley, K., 2002, ApJ, 578, 304
- Virgili, F.J., Zhang, B., Nagamine, K., & Choi, J.-H., 2011, MNRAS, 417, 3025

OBSERVING GRB AFTERGLOWS, SNE AND THEIR HOST GALAXIES WITH THE 10.4 M GRAN TELESCOPIO CANARIAS (GTC)

J. Gorosabel^{1,2,3}, A.J. Castro-Tirado¹, A. de Ugarte Postigo^{1,4},
C.C. Thöne¹, R. Sánchez-Ramírez¹, D. Peréz-Ramírez⁵, J.C. Tello¹,
M. Jelínek¹ and S. Guziy^{1,6}

Abstract. We summarize the results of our programs started in 2009 with the 10.4 m Gran Telescopio Canarias (GTC) telescope. Since then its instruments have been subject of a continuous upgrade, making the GTC a competitive telescope for the GRB field. So far (Dec. 2012) the GTC have followed up 25 GRBs, measuring 10 redshifts, and discovering two SNe associated to GRBs. The new generation of instruments foreseen for the coming years will contribute substantially to enhance the knowledge of these puzzling explosions.

1 Introduction

With its 10.4 m segmented primary mirror the Gran Telescopio Canarias (GTC) is currently the largest optical telescope of the World. It is privilegedly located at the Observatory of Roque de los Muchachos (La Palma, Spain), several hours in advance with respect to other large aperture telescopes sited at the American continent.

Currently two instruments are mounted on the GTC, OSIRIS and CANARI-CAM, the second one still being in the commissioning phase. OSIRIS is an imager

¹ Instituto de Astrofísica de Andalucía (IAA-CSIC), Glorieta de la Astronomía s/n, 18008, Granada, Spain

² Unidad Asociada Grupo Ciencia Planetarias UPV/EHU-IAA/CSIC, Departamento de Física Aplicada I, E.T.S. Ingeniería, Universidad del País Vasco UPV/EHU, Alameda de Urquijo s/n, 48013 Bilbao, Spain

³ Ikerbasque, Basque Foundation for Science, Alameda de Urquijo 36-5, 48008 Bilbao, Spain

⁴ Dark Cosmology Centre, Niels Bohr Institute, Juliane Maries Vej 30, 2100, Copenhagen Ø, Denmark

⁵ Departamento de Física, Universidad de Jaén, Campus Las Lagunillas, 23071 Jaén, Spain

⁶ Astronomical Observatory, Nikolaev National University, Nikolaev, Ukraine

and spectrograph for the optical wavelength range ($0.365 - 1.05 \mu\text{m}$) located in a Nasmyth GTC focus. Its field of view is 7.8×8.5 arcmin (Cepa *et al.* 2003). Apart from the standard broad-band imaging and long-slit spectroscopic capability, it provides additional capabilities such as the narrow-band tunable filters (TFs) imaging. The OSIRIS TFs allow to construct filters as narrow as $\sim 10 \text{ \AA}$, so it is ideal to scan host galaxy fields tuned on the typical emission lines ([O II], [O III], H $_{\alpha}$, ...).

2 Main results of the GTC observations

25 GRBs have been followed up spectroscopically or photometrically since April 2009⁷. The reaction time of the spectroscopic Target of Opportunity (ToO) observations performed to date range from ~ 2 to ~ 24 hours. 12 spectroscopic triggers were executed, measuring 10 redshifts, implying a 83% success rate. Two new SNe were spectroscopically confirmed (GRB 120422A & GRB 111211A) and two new GRB host galaxies identified (the ones of GRB 101225A and GRB 101219A, both with $r'_{AB} > 26.5$). In addition, the host galaxy of the super-luminous SN 2006oz was also localized (Leloudas *et al.* 2012). Emission lines of two GRB host fields were detected with the TF (NGC 2770 and the host of GRB 111211A). Here we report a brief summary of the most relevant observations.

2.1 GRB 090709A

The observation by our group of this GRB represented the first scientific result of the GTC (Castro-Tirado *et al.* 2009). The GTC observations were carried out in the i' -band ~ 41 hours after the GRB. The non-detection of any source in the XRT error circle down to $i' \sim 25.5$ put constraining limits on the Galactic origin of the source (Cenko *et al.* 2010).

2.2 GRB 091127A

The GTC observed this GRB from 8 to 246 days after the burst in three epochs. The observations were carried in three broad-band filters ($r'i'z'$). The data were important to confirm the presence of a supernova (SN 2009nz) bump associated to the GRB. The GTC observations were also relevant to find evidence of a possible jet break in the afterglow lightcurve. The GTC data also provided precious

⁷GRB 090404, GRB 090709A (Castro-Tirado *et al.* 2009), GRB 091202 (de Ugarte Postigo *et al.* 2009), GRB 100316A, GRB 100418A, GRB 100614A (Guziy *et al.* 2010), GRB 100816A (Gorosabel *et al.* 2010a), GRB 101225A (Thöne *et al.* 2011a), GRB 110328A (Thöne *et al.* 2011b), GRB 110422A (de Ugarte Postigo *et al.* 2011a), GRB 110503A, GRB 110801A (Cabrera Lavers *et al.* 2011), GRB 110918A (de Ugarte Postigo *et al.* 2011b), GRB 111022B (Gorosabel *et al.* 2011a), GRB 111117A (Sakamoto *et al.* 2013), GRB 111211A (de Ugarte Postigo *et al.* 2012), GRB 111228A, GRB 120326A (Tello *et al.* 2012) GRB 120327A (Sánchez-Ramírez *et al.* 2012a), GRB 120422A (Sánchez-Ramírez *et al.* 2012b), GRB 120624B, GRB 120729A, GRB 120811C (Thöne *et al.* 2012), GRB 120907A (Sánchez-Ramírez *et al.* 2012c) and GRB 121226A (Castro-Tirado *et al.* 2012).

information on the host galaxy colours. See Vergani *et al.* (2011) for a detailed description.

2.3 GRB 100219A

This GRB was observed jointly with the VLT(+XS) and GTC. The VLT spectrum measured the metallicity from the afterglow spectrum, whereas the GTC detected a faint host galaxy at a magnitude level of $i' \sim 26.7$ (Thöne *et al.* 2013). These observations are (jointly with the ones of GRB 101225A, see below) one of the deepest observations we have carried out so far with the GTC.

2.4 GRB 101225A

GRB 101225A, also known as the Christmas Burst, has been one of the targets most extensively observed by our programs at GTC. The GTC data were crucial to detect the unusual thermal component of its optical emission, which was fitted by a cooling black body spectrum. The GTC also allowed to construct the spectral energy distribution (SED) of its likely supernova (Thöne *et al.* 2011c). The GTC observations (both spectroscopic and photometric) were carried out from ~ 2 to ~ 180 days after the gamma-ray emission. The GTC monitoring was based on 5 multi-colour and one spectroscopic visit (grism R300B). A deep late imaging revealed a faint object at $r'_{AB} = 26.90 \pm 0.14$ which we associate to its host galaxy.

2.5 GRB 110328A/Sw 1644+57

Sw 1644+57, initially named as GRB 110328A, seems not to be related to any stellar death as the previously discussed objects. The GTC data contributed to support the theory that this high-energy event was due to an outburst from a massive black hole in the nucleus of a galaxy.

Two photometric visits were performed in i' and z' bands 0.7 and 12.7 days after the burst, respectively. In addition 81 i' -band images of 20-seconds failed to detect rapid optical variability. GTC spectroscopy of Sw 1644+57 was obtained starting 15.7 hours after the burst. We used the R300B grism with a 1 arcsecond wide slit and a 2×2 binning, taking three exposures of 1200 seconds. The performance of the OSIRIS spectrograph with respect to Keck(+DEIMOS) and Gemini(+GMOS) was satisfactory, as displayed in Figure 2 of Levan *et al.* (2011).

2.6 NGC 2770

NGC 2770 at a distance of ~ 27 Mpc hosted two SNe simultaneously, the standard Ib-type SN 2007uy and the more studied SN 2008D, which was uniquely detected as an X-ray burst. In addition a third Supernova (SN 1999eh) occurred in the same galaxy a few years before. Thus, NGC 2770 represents a unique galaxy to compare the explosion sites of standard SNe and the one of a peculiar event like SN 2008D, which has been subject of an intensive debate due to its possible connection with Gamma-Ray Bursts. With this aim, we initiated in May 2010 a H_α imaging



Fig. 1. The image shows the H_α emitting regions (magenta) plotted on the broad-band image taken by VLT for NGC 2770. The narrow-band filter (FWHM $\sim 15 \text{ \AA}$) constructed with the TF produced a high contrast.

campaign using the TF with a width of 15 \AA (Gorosabel *et al.* 2011b). Then the H_α map was correlated with polarization data previously taken for SN 2007uy and SN 2008D with VLT, NOT and 2.2 m CAHA (Gorosabel *et al.* 2010b). We estimated the orientation of the interstellar polarization (ISP) at the position of SN 2007uy and, most interestingly, at the site of SN 2008D. The main result is that the electric vector of the ISP was aligned with H_α structures seen at the SN 2008D explosion site (see Gorosabel *et al.* 2011b for more details). Figure 1 shows the H_α image taken with the GTC over-imposed on the broad-band image taken with VLT.

3 The future of the GTC

A different set of instruments are expected to be progressively operative at GTC. In 2013-2014 CANARICAM will be operative. CANARICAM is a mid infrared ($7.5 - 25 \mu\text{m}$) imager with spectroscopic and polarimetric capabilities. CANARI-CAM is currently in the commissioning phase and we expect it will be suitable to observe at least nearby host galaxies.

In 2014 the CIRCE camera should arrive in the observatory. CIRCE is a near-IR ($1 - 2.5 \mu\text{m}$) imager with low-resolution spectroscopic and polarimetric capabilities. CIRCE will be our work-horse for high-redshift, dark GRBs and polarimetric studies. Further, a new generation of instruments is foreseen. Among them we remark MEGARA (an optical high-resolution IFU and MOS) and EMIR (a near-IR widefield medium-resolution multiobject spectrograph), which will be prepared to exploit the observation of bright afterglows, nearby host galaxies and their environments.

We think that all the above future instruments will contribute to make the GTC even a more efficient telescope for GRB science.

This study was carried out in the framework of the Unidad Asociada IAA-CSIC at the group of planetary science of ETSI-UPV/EHU. This work was supported by the Ikerbasque Foundation for Science.

References

- Cabrera Lavers, A., de Ugarte Postigo, A., Castro-Tirado, A.J., *et al.*, 2011, GCN 12234
 Castro-Tirado, A.J., de Ugarte Postigo, A., Gorosabel, J., *et al.*, 2009, GCN 9655
 Castro-Tirado, A.J., Jelinek, M., Sánchez-Ramírez, R., *et al.*, 2012, GCN 14114
 Cenko, S.B., Butler, N.R., Ofek, E.O., *et al.*, 2010, AJ, 140, 224
 Cepa, J., Aguiar-González, M., Bland-Hawthorn, J., *et al.*, 2003, SPIE 4841, 1739
 de Ugarte Postigo, A., Castro-Tirado, A.J., Gorosabel, J., *et al.*, 2009, GCN 10247
 de Ugarte Postigo, A., Castro-Tirado, A.J., Gorosabel, J., *et al.*, 2011a, GCN 11978
 de Ugarte Postigo, A., Gorosabel, J., Castro-Tirado, A.J., *et al.*, 2011b, GCN 12375
 de Ugarte Postigo, A., Thöne, C.C., Gorosabel, J., *et al.*, 2012, GCN 12802
 Gorosabel, J., Castro-Tirado, A.J., Tanvir, N.R., *et al.*, 2010a, GCN 11125
 Gorosabel, J., de Ugarte Postigo, A., Castro-Tirado, A.J., *et al.*, 2010b, A&A, 522, 14
 Gorosabel, J., Cabrera Lavers, A., Sánchez-Ramírez, R., *et al.*, 2011a, GCN 12494
 Gorosabel, J., de Ugarte Postigo, A., Castro-Tirado, A.J., *et al.*, 2011b, AdSpR, 47, 1421
 Guziy, S., Jelinek, M., Gorosabel, J., *et al.*, 2010, GCN 10967
 Leloudas, G., Chatzopoulos, E., Dilday, B., *et al.*, 2012, A&A, 541, L129
 Levan, A.J., Tanvir, N.R., Cenko, S.B., *et al.*, 2011, Science, 279, 1011
 Sakamoto, T., Troja, E., Aoki, K., *et al.*, 2013, ApJ, in press [[arXiv:1205.6774](https://arxiv.org/abs/1205.6774)]
 Sánchez-Ramírez, R., Gorosabel, J., Castro-Tirado, A.J., *et al.*, 2012a, GCN 13146
 Sánchez-Ramírez, R., Leloudas, G., de Ugarte Postigo, A., *et al.*, 2012b, GCN 13281
 Sánchez-Ramírez, R., Gorosabel, J., de Ugarte Postigo, A., *et al.*, 2012c, GCN 13723
 Tello, J.C., Sánchez-Ramírez, R., Gorosabel, *et al.*, 2012, GCN 13118
 Thöne, C.C., Guziy, S., Castro-Tirado, A.J., *et al.*, 2011a, GCN 11568
 Thöne, C.C., Gorosabel, J., de Ugarte Postigo, A., *et al.*, 2011b, GCN 11834
 Thöne, C.C., de Ugarte Postigo, A., Fryer, C.L., *et al.*, 2011c, Nature, 480, 72
 Thöne, C.C., de Ugarte Postigo, A., Gorosabel, J., *et al.*, 2012, GCN 13628
 Thöne, C.C., Fynbo, J.P.U., Goldoni, P., *et al.*, 2013, MNRAS, 428, 3590
 Vergani, S.D., Flores, H., Covino, S., *et al.*, 2011, A&A, 535, 127

STATISTICAL PROPERTIES OF GRB AFTERGLOW PARAMETERS AS EVIDENCE OF COSMOLOGICAL EVOLUTION OF HOST GALAXIES

G. Beskin¹, G. Oganesyan², G. Greco³ and S. Karpov¹

Abstract. The results of investigation of 43 peaked R-band light curves of optical transients of gamma-ray bursts with known redshifts are presented. The parameters of optical transients were calculated in the comoving frame, and then a search for pair correlations between them was conducted. As a result of the statistical analysis, a strong correlation between the peak luminosity and redshift was found for pure afterglows and the events with residual gamma activity, which can't be explained as an effect of observational selection. It suggests the cosmological evolution of the parameters of the local interstellar medium around the sources of gamma-ray burst. In the models of forward and reverse shock waves, a relation between the density of interstellar medium and redshift was built for gamma-ray burst afterglows. It was shown that for GRB host galaxies the star formation rate increases with redshift.

1 Introduction

Up to date, about 450 gamma-ray bursts (GRBs) with measured redshifts are known. The optical R-band light curves with distinct peaks were obtained for 43 cases only. These objects are the most interesting ones for a detailed analysis, as the presence of a peak allows us to identify the moment of the shock wave deceleration in the interstellar medium, which reflects the parameters of the interstellar medium. Among 43 such events, 11 are prompt optical peaks (P), coincident with gamma-ray activity (three events that may not be unambiguously classified as P were signed as P?), 22 are pure afterglows (A), and 10 more carry the signatures of an underlying gamma-activity (A(U)). Detailed results of investigation of correlations of different pairs of GRBs' parameters in these subsamples are given in Beskin *et al.* (2013). In this paper we present the analysis of connections between several optical characteristics of GRBs in source proper frame and their redshifts.

¹ Special Astrophysical Observatory of the Russian Academy of Sciences, Russia

² Southern Federal University, Russia

³ Astronomical Observatory of Bologna, INAF, Italy

2 Observational data

The results of R-band optical observations, as well as other parameters of GRBs, were taken from the dedicated publications on specific bursts, GCN-circulars (<http://gcn.gsfc.nasa.gov>), and from the GRBLog database (<http://grblogger.org/grblogger.php>). The initial observational parameters were as follows: the spectroscopic redshift z , the peak optical flux F_{opt} , the integral optical flux S_{opt} , the duration of optical emission t_{opt} , the time of the peak onset relative to the GRB trigger t_{peak} , the width of the optical peak t_{width} , the exponents of growth and decay of the optical light curve α_r and α_d , the GRB peak flux F_{iso} , the GRB integral flux S_{iso} , the GRB duration t_{90} and the photon index of the spectrum in the gamma-ray range α .

Considering the galactic extinction and host galaxy brightness, and using the k -correction for the average index of optical spectrum $\beta = 0.75$ in the standard cosmological model with $\Omega_M = 0.3$, $\Omega_\Lambda = 0.7$, $H_0 = 70 \text{ km s}^{-1} \text{ Mpc}^{-1}$, we obtained the following parameters in the proper frame of the source: the maximum optical luminosity L_{opt} , the isotropic equivalent of optical energy E_{opt} , the time parameters T_{opt} , T_{peak} , T_{width} and similarly in the gamma-ray range, L_{iso} , E_{iso} , T_{90} . For the bursts whose host galaxy extinction A_R are not available the mean value of A_R was utilised instead, using the A_V data collected in the “golden sample” presented by Kann *et al.* (2010). These data were divided into five redshift ranges and for each interval the corresponding mean value of A_V was obtained. Using these estimates along with the dependence of absorption on wavelength in SMC (Pei 1992), the A_R for each burst was computed.

The formulae for conversion from the observed frame to the proper one are taken from Beskin *et al.* (2013). Table 1 presents all pair correlations with unweighted Pearson correlation coefficients $R > 0.5$ and significance levels $SL < 1\%$, and the coefficients of corresponding linear regressions.

3 Results and discussion

To prove that the correlation between peak optical luminosity and the redshift is not caused by the selection effects, we plot in the right panel of Figure 1 the R-band apparent magnitudes of all bursts at the initial moment of optical detection (empty symbols) and at the moment of maximum (filled symbols) *versus* redshift. Note that the signatures of selection effects should be searched for in the set of initial brightness estimates at the first place. Let’s discuss whether they are present in our data.

1. Obviously, if the proper luminosities of sources do not increase with redshift (*i.e.* luminosity is the same on all z), then apparent brightness (flux measured by the observer) will decrease at least quadratically with $(1 + z)$. At the same time, right panel of Figure 1 demonstrates significant increase of the brightness at $z > 3$, both for the moments of detection and for the peaks.
2. For both large ($z > 3$) and small ($z < 1$) redshifts the objects are brighter than 18 mag, significantly brighter than the minimum value of 19–19.5 mag achieved by several objects at $1 < z < 3$. Therefore, neither small nor large z

Table 1. Pair correlations for different classes of GRB optical counterparts with the correlation coefficients greater than 0.5 and significances better than 1%. The four columns represent the linear regression ($a + bx$) coefficients, derived through the unweighted least squares fit. The stars mark the log-linear correlations, in contrast to the log-log correlations used otherwise.

Correlation	Type	a	b	Correlation	Type	a	b
$L_{\text{opt}} - L_{\text{iso}}$	Γ^*	4.58 \pm 7.98	0.98 \pm 0.11	$L_{\text{opt}} - L_{\text{iso}}$	A	2.19 \pm 12.82	0.99 \pm 0.26
	A	-0.63 \pm 0.79	0.63 \pm 0.13		$A+A(U)+P$	-24.96 \pm 16.83	1.54 \pm 0.36
	$A+A(U)+P?$	0.69 \pm 0.31	0.91 \pm 0.09		$A+A(U)+P$	2.94 \pm 8.51	0.91 \pm 0.18
	$A+A(U)$	-0.34 \pm 0.97	0.66 \pm 0.11		$A+A(U)$	-0.03 \pm 0.38	0.97 \pm 0.56
	$A+A(U)+P?$	0.29 \pm 1.23	0.96 \pm 0.09		$A+A(U)+P?$	2.68 \pm 3.21	0.91 \pm 0.28
$L_{\text{opt}} - L_{\text{peak}}$	Γ^*	4.44 \pm 0.22	0.19	$L_{\text{opt}} - L_{\text{peak}}$	Γ	-46.97 \pm 4.98	1.00 \pm 0.00
	A	-1.24 \pm 0.27	0.60 \pm 0.10		A	-1.20 \pm 3.44	1.00 \pm 0.42
	$A(U)$	10.62 \pm 0.47	0.46 \pm 0.14		$A+A(U)+P?$	-1.24 \pm 0.32	0.97 \pm 0.20
	$A+A(U)+P^*$	17.42 \pm 0.88	0.60 \pm 0.04		$A+A(U)$	-0.02 \pm 0.30	1.01 \pm 0.17
	$A+A(U)$	17.77 \pm 0.86	0.60 \pm 0.08		P	-0.05 \pm 0.21	1.01 \pm 0.11
$L_{\text{opt}} - L_{\text{initial}}$	P	0.97 \pm 0.07	0.93 \pm 0.19	$L_{\text{opt}} - L_{\text{initial}}$	A	-0.05 \pm 0.16	0.99 \pm 0.37
	$A+A(U)+P?$	17.26 \pm 0.82	0.70 \pm 0.08		$A+A(U)+P?$	-1.82 \pm 0.21	0.99 \pm 0.37
	A	-47.76 \pm 0.10	0.26 \pm 1.09		A	91.92 \pm 0.12	0.61 \pm 0.06
	$A+A(U)$	48.00 \pm 0.14	0.80 \pm 0.78		$A+A(U)+P$	48.82 \pm 0.13	0.60 \pm 0.12
	$A+A(U)+P?$	47.81 \pm 0.48	1.15 \pm 0.02		$A+A(U)$	32.82 \pm 0.39	0.31 \pm 0.26
$L_{\text{opt}} - (z+1)$	Γ	47.92 \pm 0.51	0.11 \pm 0.75	$L_{\text{opt}} - (z+1)$	A	0.82 \pm 0.15	0.92 \pm 0.29
	A	34.28 \pm 0.28	0.08 \pm 0.08		$A+A(U)+P$	31.24 \pm 0.18	0.81 \pm 0.27
	$A+A(U)+P^*$	24.7 \pm 0.30	2.17 \pm 0.01		$A+A(U)+P$	76.82 \pm 0.43	0.17 \pm 0.68
	$A+A(U)$	74.60 \pm 0.26	0.98 \pm 0.72		$A+A(U)$	50.94 \pm 0.59	0.40 \pm 0.54
	$A+A(U)+P?$	34.00 \pm 0.26	2.62 \pm 0.04		$A+A(U)+P?$	52.29 \pm 0.28	0.82 \pm 0.53
$L_{\text{opt}} - T_{\text{peak}}$	Γ^*	26.46 \pm 1.06	-0.64 \pm 1.04	$L_{\text{opt}} - T_{\text{peak}}$	Γ	55.74 \pm 0.04	-0.00 \pm 1.04
	P	31.26 \pm 1.05	-0.17 \pm 1.32		A		
$L_{\text{opt}} - T_{\text{initial}}$	Γ^*	-30.70 \pm 0.01	1.56 \pm 0.05	$L_{\text{opt}} - T_{\text{initial}}$	Γ	-27.00 \pm 1.97	1.37 \pm 0.20
	A	-22.31 \pm 1.22	1.30 \pm 0.25		$A+A(U)+P$	-29.09 \pm 1.03	1.19 \pm 0.19
	$A+A(U)+P?$	-0.00 \pm 0.10	1.66 \pm 0.03		$A+A(U)$	-17.20 \pm 0.99	1.00 \pm 0.19
	$A+A(U)$	-4.34 \pm 0.00	1.73 \pm 0.02		$A+A(U)+P?$	-30.00 \pm 0.03	1.37 \pm 0.10
	$A+A(U)+P?$	-41.46 \pm 0.13	1.69 \pm 0.21		A		
$T_{\text{peak}} - T_{\text{initial}}$	Γ	1.24 \pm 0.24	0.23 \pm 0.10	$T_{\text{peak}} - T_{\text{initial}}$	A	47.90 \pm 0.11	4.20 \pm 1.00
	$A+A(U)+P^*$	1.99 \pm 0.13	0.20 \pm 0.09		$A+A(U)$	49.94 \pm 0.11	3.89 \pm 0.79
	$A+A(U)$	1.22 \pm 0.16	0.26 \pm 0.09		$A+A(U)+P$	47.81 \pm 0.08	4.17 \pm 0.82
	$A+A(U)+P?$	1.15 \pm 0.14	0.29 \pm 0.09		$A+A(U)+P?$	47.82 \pm 0.49	4.11 \pm 0.75
$L_{\text{opt}} - \log(z)$	Γ	16.90 \pm 0.28	-0.03 \pm 0.02	$L_{\text{opt}} - \log(z)$	A	29.31 \pm 0.18	-0.00 \pm 0.28
	P				A		

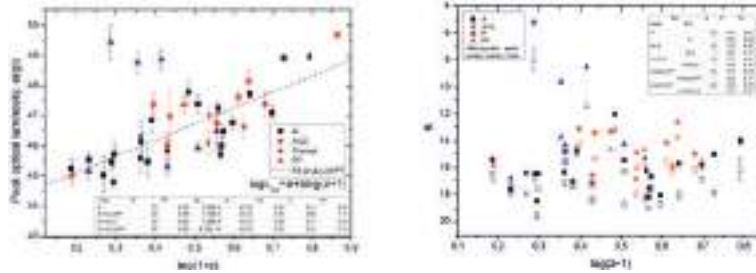


Fig. 1. *Left:* peak optical luminosity *vs.* redshift: coefficients of correlations, SL, parameters of linear regression. *Right:* peak and initial optical magnitudes *vs.* redshift: coefficients of correlations, SL.

display any signs of the bias due to crossing the detection limit line - both bright and faint sources are being detected on all redshifts.

- Finally, returning to $L_{\text{opt}} - (z+1)$ dependence (left panel of Fig. 1), we checked the correlation coefficients and linear regression parameters for $A+A(U)+P?$ subset in different redshift ranges. They are summarised in Table 2.

It is easy to see that even with exclusion of objects with $z < 1$ or with $z > 4$ or both, the luminosity still increases with redshift with good significance. Obviously, the correlation coefficient decreases a bit with decreasing of redshift range, but the

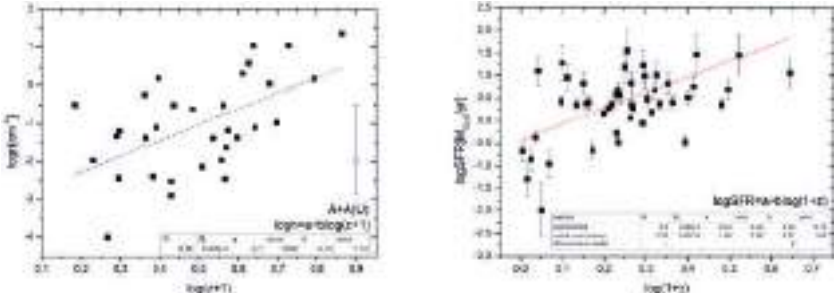


Fig. 2. *Left:* ISM density *vs.* redshift by model recalculation. *Right:* SFR *vs.* redshift correlation according to GRBHosts (<http://grbhosts.org>) database.

Table 2. Characteristics of the dependence of optical luminosity on redshift for A+A(U)+P? subset in different redshift ranges. Columns are the redshift range, number of sources in it, correlation coefficient, its significance level, and the linear regression parameters (a, b) with corresponding errors.

z	N	R	SL	a	err	b	err
all	35	0.83	9,39E-10	44,05	0,35	5,32	0,73
$z < 4$	32	0.73	1,73E-6	44,29	0,37	4,71	0,8
$z > 1$	31	0.78	1,91E-7	44,12	0,5	5,2	0,97
$1 < z < 4$	28	0,6	7,31E-4	44,55	0,55	4,22	1,11

regression parameters are nearly the same within the errors, and the power-law slope of the dependence is roughly 4–5.

Therefore, our analysis demonstrates that effects of observational selection which may cause the dependence of optical luminosity in peaks of light curves on redshift, are most probably absent in our data.

Therefore, we may consider the detected $L_{opt} - (z + 1)$ correlation (left panel of Fig. 1) as a real manifestation of evolution of optical luminosity of gamma-ray bursts.

There is no $L_{opt} - (z + 1)$ correlation for prompt optical sources in contrast to a strong correlation seen for afterglows. The prompt optical sources (P) are presumably produced as a result of collisions of internal shells in GRB sources, while the afterglows are formed as the shock wave enters the interstellar medium. Correspondingly, the $L_{opt} - (z + 1)$ correlation for the afterglows points to the dependence of the interstellar medium parameters on redshift. The simplest assumption is a dependence of the local interstellar medium density on redshift, which results in the observed $L_{opt} - (z + 1)$ dependence.

In the afterglow model with the front shock wave, the peak flux is a function of density, as we may assume that the frequency of optical emission lies between the characteristic frequency of radiation and the cooling frequency. Indeed, according to Panaitescu (2009), if the frequency of the afterglow spectral peak v_i is lower than the cooling frequency v_c , then the optical spectrum index is $\beta = \frac{p-1}{2}$, where p is a spectral index of emitting electrons, $p > 2$, $p = 2..3$ (Piran 2004), and $\beta = 0.5..1$.

If, on the other hand, the peak is in the $v > v_c$ region, then $\beta = \frac{E}{2} = 1..1.5$. At the same time, observations of optical spectra give $\beta < 1$ (Zafar 2011) with average value of $\beta = 0.75$, and therefore our assumption is correct. Then, according to Panaiteescu *et al.* (2011),

$$F \propto E n^{\beta+1/2} \Gamma_0^{4\beta},$$

where E is the total mechanical energy, n is the volume density of the surrounding gas, Γ_0 is the initial Lorentz factor of the ejecta, and β is the index of optical spectrum. Using $\Gamma_0 = 200$ with the dispersion of 100, the peak luminosity L_{opt} , $E_{\text{iso}} = \eta E$, ($\eta = 0.2$ – from Sari *et al.* 1999), and the deceleration radius $R_{\text{dec}} \propto t_{\text{dec}} \Gamma_0^2$ (Meszaros 2006), where $T_{\text{peak}} = t_{\text{dec}}$, $L_{\text{opt}} \propto R_{\text{dec}}^2 F$, $\eta \propto \frac{L_{\text{opt}}}{T_{\text{peak}}^2 E \Gamma^5}$, we obtain power-law $n - (z + 1)$ dependence with slope of 4.14 ± 1.13 (Fig. 2, left panel). With this dependence in hand, we may built a similar dependence for the star formation rate (SFR) in the GRBs vicinity using the Kennicutt-Schmidt law from Schaye *et al.* (2007): the star formation rate depends on the volume density of the interstellar medium as $\text{SFR} \propto n^{1.5}$. Finally, we acquired $\text{SFR} \propto (z+1)^{6.21 \pm 1.69}$.

Using the values of SFR taken from the GRBHosts (<http://grbhosts.org>) database, we have compared them to this relation. This is shown in Figure 2 (right panel), which also shows the model value of this dependence based on the ratios for the interstellar medium density from Ciardi *et al.* (2000) and the volume law of Kennicutt-Schmidt.

The obtained SFR – $(z+1)$ connection is consistent with the model dependence from Ciardi *et al.* (2000), but differs from the experimental correlation for the host galaxies from the GRBHosts (<http://grbhosts.org>) database. Presumably, this can be explained by the fact that our estimations of SFT are applied to small zones of GRB localisation, but not to the galaxies as a whole.

This work was supported by the RFBR No. 12-02-00743), and by the grant of the President of the Russian Federation for the support of young Russian scientists. S.K. has also been supported by a grant of the non-profit Dynasty foundation. G.B. thanks Landau Network-Centro Volta and Cariplio Foundation for fellowship and the Brera Observatory for hospitality.

References

- Beskin, G., Greco, G., Oganesyan, G., *et al.*, 2013, AP, 53, 5
- Ciardi, B., & Loeb, A., 2000, ApJ, 540, 687
- Kann, D.A., Klose, S., Zhang, B., *et al.*, 2010, ApJ, 720, 1513
- Meszaros, P., 2006, IOP, 69, I8, 2259
- Panaiteescu, A., 2009, Sixth Huntsville Symposium, AIP Conference Proceedings, 1133, 127
- Panaiteescu, A., & Vestrand, W.T., 2011, MNRAS, 414, I4, 3537
- Pei, Y.C., 1992, ApJ, 395, 130
- Piran, T., 2004, RvMP, 76, I4, 1143
- Sari, R., & Piran, T., 1999, ApJ, 520, 641
- Schaye, J., Dalla, V.C., 2008, MNRAS, 383, 1210
- Zafar, T., Watson, D., Fynbo, J.P.U., *et al.*, 2011, A&A, 532, id.A, 143

VLT/X-SHOOTER ABSORPTION SPECTROSCOPY OF THE GRB 120327A AFTERGLOW

V. D'Elia¹

Abstract. We analyze two X-shooter spectra of the GRB 120327A afterglow, acquired 2.1 and 30 hrs after the trigger. The ISM in the GRB host galaxy at $z = 2.8145$ is extremely rich in absorption features, with three components contributing to the line profiles. The hydrogen column density associated with GRB 120327A is $\log N_{HI}/\text{cm}^2 = 22.01 \pm 0.09$, and the metallicity of the host galaxy is in the range $[\text{X}/\text{H}] = -1.7$ to -1 with respect to the solar values, *i.e.*, a typical value for a GRB host galaxy. In addition to the ground state lines, we detect in the first observation several excited absorption features, which disappeared in the second observation. Using these features, we derive that component I is at $d_I = 200^{+100}_{-60}$ pc from the GRB, while component II is located closer, at $d_{II} = 100^{+40}_{-30}$ pc. These values are among the lowest found in GRBs. Comparing the abundances with star formation history models, we find that the GRB 120327A host galaxy abundances are compatible with a star formation efficiency of 10 Gyr^{-1} , typical of spheroids (elliptical or bulge).

1 Introduction

For a few hours after their onset, Gamma Ray Bursts (GRBs) are the brightest beacons in the far Universe, offering a superb opportunity to investigate both GRB physics and high redshift galaxies. Early time spectroscopy of GRB afterglows can give us precious information on the kinematics, geometry, ionization and metallicity of the interstellar matter of GRB host galaxies up to a redshift $z \sim 5$, and of intervening absorbers along the line of sight. Our dataset comprises two X-shooter spectra of GRB 120327A, acquired 2.1 and 30 hrs after the trigger. The resolution of our data is $R = 5000 - 9000$, corresponding to $20 - 35 \text{ km/s}$, the wavelength range is $3000 - 25\,000 \text{ \AA}$, and the signal-to-noise ratio of the first observation is $S/N = 15 - 30$.

¹ INAF-OAR & ASI ASDC, via Galileo Galilei Frascati (RM), Italy

2 Results

2.1 Detected lines

The host galaxy of GRB 120327A appears to be extremely rich in metals (Fig. 1). Metallic features are apparent from neutral (NI, OI, MgI, PI, ArI, CaI), low-ionization (CII, MgII, AlIII, AlIII, SiII, PII, SII, CaII, CrII, FeII, NiII, ZnII), and high-ionization (CIV, NV, OVI, SiIV, PV, SIV) species. All lines can be fitted with a three component Voigt model. Component II (*i.e.*, the central one) is taken as the reference redshift for the GRB host galaxy, since it is the most rich in excited features (see next sections). Component I is blue-shifted by 41 km/s, while component III is red-shifted by 35 km/s.

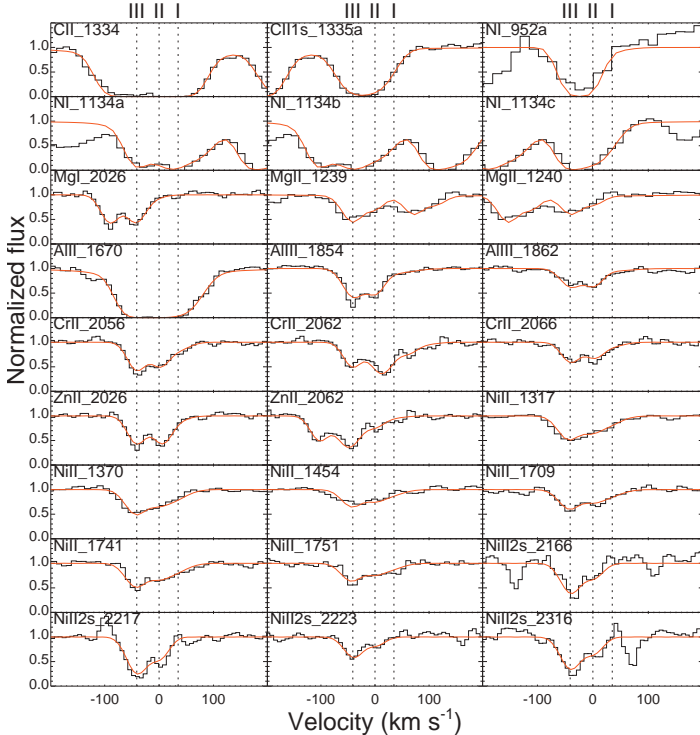


Fig. 1. A selection of lines detected in the GRB 120327A spectrum.

2.2 Abundances

We compute the abundances of the metallic column densities with respect to the Hydrogen one, and the GRB 120327A metal content with respect to solar values. CII, OI and AlIII are heavily saturated, thus the corresponding abundances are not reliable. The HI column has been estimated using Hydrogen features from the Ly α to the Ly δ . $\log N_{HI}/\text{cm}^2 = 22.01 \pm 0.09$, and the host metallicity is in the range $[X/H] = -1.7$ to -1 .

2.3 GRB/absorber distance

A plethora of excited levels, mainly from FeII, but also NiII, CII, OI, SiII (Fig. 1) are detected in the first epoch spectrum, while they are not present any longer in epoch 2. They are probably produced through indirect UV pumping by the GRB afterglow. Comparing the column densities of these levels with the predictions of time dependent, photo-excitation codes, it is possible to determine the GRB/absorber distance (Vreeswijk *et al.* 2007; D'Elia *et al.* 2009). This is $d_I = 200^{+100}_{-60}$ pc, and $d_{II} = 100^{+40}_{-30}$ pc for component I and II, respectively. Component III does not feature excited lines, so it should be located far away from the GRB.

2.4 Host galaxy characterization

Comparing the abundance ratios with star formation history models (Fan *et al.* 2010), information about the GRB host galaxy can be derived. In particular, the GRB 120327A host abundances are compatible with a star formation efficiency of 10 Gyr^{-1} , typical of spheroids (elliptical or bulge). Theoretical curves fail to reproduce O and C abundances because the corresponding absorption lines are heavily saturated. The models take into account dust evolution in the host galaxy.

3 Conclusions

We presented X-shooter spectroscopy of the GRB 120327A afterglow, at $z = 2.8145$. The ISM in the GRB host galaxy is extremely rich in absorption features, with three components contributing to the line profiles. The hydrogen column density associated with GRB 120327A is $\log N_{HI}/\text{cm}^2 = 22.01 \pm 0.09$, and the metallicity of the host is in the range $[\text{X}/\text{H}] = -1$ to -1.7 with respect to the solar values, *i.e.*, a typical value for a GRB host galaxy. In addition to a plethora of ground state lines, we detect in the first observation CII, OI, SiII, FeII, and NiII-excited absorption features, which disappeared in the second observation. We used these features to derive information on the distance between the host absorbing gas and the site of the GRB explosion. The distance of component I is found to be $d_I = 200^{+100}_{-60}$ pc, while component II is located closer to the GRB, at $d_{II} = 100^{+40}_{-30}$ pc. These values are among the lowest found in GRBs. Comparing the abundances with star formation history models, we find that the GRB 120327A host galaxy abundances are compatible with a star formation efficiency of 10 Gyr^{-1} , typical of spheroids (elliptical or bulge).

References

- D'Elia, V., Fiore, F., Perna, R., *et al.*, 2009, ApJ, 694, 332
- Fan, X.L., Yin, J., & Matteucci, F., 2010, A&A, 521, 73
- Vreeswijk, P.M., Ledoux, C., Smette, A., *et al.*, 2007, A&A, 468

GRBS FOLLOWED-UP BY THE BOOTES NETWORK

S. Guziy^{1,17}, A. Castro-Tirado¹, M. Jelínek¹, J. Gorosabel^{1,21,22},
P. Kubánek¹, R. Cunniffe¹, O. Lara-Gil¹, O. Rabaza-Castillo¹,
A. de Ugarte Postigo¹, R. Sánchez-Ramírez¹, J. Tello¹,
C. Pérez del Pulgar³, S. Castillo-Carrión⁴, J. Castro Cerón⁵,
T. de J. Mateo Sanguino⁶, R. Hudec⁷, S. Vitek⁸,
B. de la Morena Carretero⁹, J. Díaz Andreu⁹, R. Fernández-Muñoz¹⁰,
D. Pérez-Ramírez¹¹, P. Yock¹², W. Allen¹³, I. Bond¹⁴, I. Kheyfets¹⁷,
G. Christie¹⁵, L. Sabau-Graziati¹⁶, C. Cui¹⁸, Y. Fan¹⁹ and I.H. Park²⁰

¹ Instituto de Astrofísica de Andalucía, IAA-CSIC, PO Box 03004, 18080 Granada, Spain

² Image Processing Laboratory, Univ. de Valencia, Burjassot, Valencia, Spain

³ Departamento de Ingeniería de Sistemas y Automática, Univ. de Málaga, Spain

⁴ Servicio Central de Informática, Universidad de Málaga, Spain

⁵ European Space Astronomy Centre, ESAC, Villafranca del Castillo Madrid, Spain

⁶ Departamento de Ingeniería de Sistemas y Automática, Universidad de Huelva, E.P.S. de La Rábida, Huelva, Spain

⁷ Astronomical Institute, Academy of Sciences of the Czech Republic, 251 65 Ondřejov, Czech Republic

⁸ Czech Technical University, Faculty of Electronic Engineering, Dep. of Radioelectronics, Czech Republic

⁹ Estación de Sondeos Atmosféricos, ESAt de El Arenosillo, CEDEA-INTA, Mazagón, Huelva, Spain

¹⁰ Estación Experimental de La Mayora, EELM-CSIC, Algarrobo Costa, Málaga, Spain

¹¹ Universidad de Jaén, Campus Las Lagunillas, Jaén, Spain

¹² University of Auckland, New Zealand

¹³ Vintage Lane Observatory, Blenheim, New Zealand

¹⁴ Massey University, New Zealand

¹⁵ Stardome Observatory, Auckland, New Zealand

¹⁶ División de Ciencias del Espacio, INTA, Torrejón de Ardoz, Madrid, Spain

¹⁷ Astronomical Observatory, Nikolaev National University, Nikolaev, Ukraine

¹⁸ National Astronomical Observatory, Chinese Academy of Sciences, Beijing 100012, China

¹⁹ Yunnan Astronomical Observatory, CAS Kunming, 650011 Yunnan, China

²⁰ Ewha Womans University, Daehyundong 11-1, Seodaemungu, 120-750 Seoul, South Korea

²¹ Unidad Asociada Grupo Ciencia Planetarias UPV/EHU-IAA/CSIC, Departamento de Física Aplicada I, E.T.S. Ingeniería, Universidad del País Vasco UPV/EHU, Alameda de Urquijo s/n, 48013 Bilbao, Spain

²² Ikerbasque, Basque Foundation for Science, Alameda de Urquijo 36-5, 48008 Bilbao, Spain

Abstract. The Burst Observer and Optical Transient Exploring System (BOOTES), is a global robotic observatory network, which started in 1998 with Spanish leadership devoted to study optical emissions from gamma ray bursts (GRBs) that occur in the Universe. We present shot history and current status of BOOTES network. The Network philosophy, science and some details of 117 GRBs followed-up are discussed.

1 Introduction

The Burst Observer and Optical Transient Exploring System (BOOTES), started in 1998 as a Spanish-Czech collaboration devoted to study optical emissions from gamma ray bursts (GRBs).

The first BOOTES robotic astronomical station was located at INTA's Estación de Sondeos Atmosféricos in Centro de Experimentación de El Arenosillo, a dark-sky site near Mazagón (Huelva), center owned by the Instituto Nacional de Técnica Aeroespacial (INTA). The second observing station was opened in 2001 and it is located at the Estación Experimental de La Mayora (dubbed BOOTES-2), 240 km apart. The latter is run by the Consejo Superior de Investigaciones Científicas (CSIC). In 2009 BOOTES expanded abroad, with the third station (BOOTES-3) being installed in Blenheim (South Island, New Zealand). The fourth one (BOOTES-4) has been deployed in 2011 at the Lijiang Astronomical Observatory (unnan, China).

2 Location

Four BOOTES station are located in the three countries (Spain, New Zealand and China) that have different geographic coordinates. In our dreams and plans an installation of three new station in the other geographic locations (countries). A general view of BOOTES stations in the world is shown in Figure 1.

3 Science and goals

The observation of the GRB error box simultaneously to the GRB occurrence Although the first detected optical counterparts were not brighter than 19th mag few hours after the burst, there have been several GRBs for which optical transient emission has been detected simultaneously to the gamma-ray event, with magnitudes in the range 5–10. The faint transient emission that has been detected few hours after the event is a consequence of the expanding remnant that the GRB leaves behind it. This provides information about the surrounding medium, but not about the burster itself. The fast slewing 0.6 m BOOTES telescopes should produce important results in this field.

The detection of optical flashes (OTs) of cosmic origin that could be unrelated to GRBs and constitute a new type of different astrophysical phenomenon



Fig. 1. The telescopes locations in the world.

(perhaps associated to QSOs/AGNs). If some of them are related to GRBs, the most recent GRB models predict that there should be a large number of bursting sources in which only transient X-ray/optical emission should be observed, but no gamma-ray emission. The latter would be confined in a jet-like structure and pointing towards us only in a few cases.

The monitoring of high-energy targets in different optical, as ground-based support for the ESA's International Gamma-Ray Laboratory (**INTEGRAL**) in which Spain had, for the first time, the leadership in one of the instruments, the Optical Transient Camera (OMC). This included test of technologies, methods, data processing, ground-based observational network, etc.. **INTEGRAL** was launched in 2002.

The monitoring of several objects (bright AGNs/QSOs, old GRB positions, etc.) looking for recurrent optical transient optical emission arising from these sources. There are hints that sudden and rapid flares occurs, though of smaller amplitude. This will be achieved by means of the 0.6-m network of BOOTES telescopes.

4 GRBs with BOOTES network

GRBs are indeed one of the main scientific goals of BOOTES. We know that GRBs arise at cosmological distances (with mean redshift $z \sim 2.5$ and redshifts in the range ~ 0.01 to ~ 10), with huge isotropic equivalent radiated energy, and small timescales (in the range few ms to 10^2 s), thus implying a small emitting region. The spectrum is non-thermal and relativistic outflows ($\Gamma > 100$) are involved. A frequent assumption is that short and long GRBs (with the short ones representing 1/3 of the overall GRB population) are due to different progenitors leading to the same succession of events: formation of a compact object and ejection of

a relativistic outflow which produces the (long-lasting) afterglow at other wavelengths. Main program for BOOTES network system is observations optical counterparts for gamma ray burst: open and monitoring OT in different filters. The BOOTES network philosophy is: identical telescopes spaced around the Earth, identical filter sets: g'r'i'ZY, identical CCD cameras, impact on several scientific fields and public outreach, Castro-Tirado *et al.* (2012).

Some summary of GRB response at the BOOTES stations and examples of observations we are present below:

- **BOOTES-1/0.3 m.** Around 50 real-time follow-ups in 2004-2012, with 10 detections of the OA and 27 observations with upper limit, 12 publications (GCN circulars and other), Jelínek *et al.* (2010);
- **BOOTES-2/0.3 m.** 24 real-time follow-ups, with 9 upper limit of the OA and 5 publications;
- **BOOTES-2/0.6 m – TELMA.** 8 real-time follow-ups with 3 detections of the OA, 5 observations with upper limit, 7 publications;
- **BOOTES-3/0.6 m – YA.** 23 real-time follow-ups with 6 detections of the OA, 10 observations with upper limit, 18 publications;
- **BOOTES-4/0.6 m – MET.** 12 real-time follow-ups with 1 detection of the OA, 5 observations with upper limit, 2 publications (GCN circulars).

5 Discussion

We have shown the advances in establishing the worldwide network of BOOTES telescopes in different locations around the Earth. BOOTES has played a significant role in the gamma-ray burst field over the last decade. Multiwavelength observations (photometry, spectroscopy, polarimetry) are ideal to better understand the GRB diversity. As of Sep. 2012, the number of GRBs followed-up at the four BOOTES stations is 117, with 20 optical counterpart detections and 56 upper limits reported (the rest being too crowded fields or unusable due to dew, low airmass, unfocused images, ...), altogether leading to 44 publications.

Installing the remaining BOOTES stations will help in continuous monitoring for some celestial sources, building more precise light curve for the targets. BOOTES contributes significantly to the GLORIA Network (EU-FP7) too. More detailed information about the BOOTES network can be seen in <http://bootes.iaa.es>

We acknowledge the support of the Spanish Ministry Projects AYA 2009-14000-C03-01 and AYA 2012-39727-C03-01.

References

- Castro-Tirado, A.J., Jelínek, M., Gorosabel, J., *et al.*, 2012, BASI, in press
 Jelínek, M., Castro-Tirado, A.J., de Ugarte Postigo, A., *et al.*, 2010, AdAst, id. 432172

CATAclysmic variables and gamma-ray sources

E. Pavlenko¹, V. Malanushenko², S. Shugarov^{3,4} and D. Chochol⁴

Abstract. The cataclysmic variables are associated with high energy events and probably many of them could be potential gamma-ray sources. Up to now Fermi-LAT detected 3 gamma-ray transients, which belong to CVs and related objects: V407 Cyg, N Sco 2012 and N Mon 2012 = V959 Mon. We present the first multicolour observations of the slow classical nova V959 Mon.

1 Introduction

According to the modern X-ray observations, cataclysmic variables (CVs) represent a significant part of baryon matter of our galaxy (Revnivtsev *et al.* 2008; Pretorius & Knigge 2012). They are the close binary stars at the late stage of evolution, formed on a time scale 0.1 – 10 Gyrs (Townsley & Bildsten 2007). CVs are associated with high energy events. Many of CVs could be potential gamma-ray sources. It is worth to note that the classical Nova Cyg 1975 = V1500 Cyg explosion disrupted spin-orbital synchronism (Schmidt & Stockman 1991). A nova explosion probably caused also the asynchronous of the polar BY Cam, that currently is synchronizing with the same rate (Pavlenko *et al.* 2012) as V1500 Cyg (Schmidt & Stockman 1991; Pavlenko & Pelt 1991; Pavlenko & Malanushenko 1996; Pavlenko & Shugarov 2005). However only three gamma-ray transients that belong to CVs and related objects are known up to now: the symbiotic Mira V407 Cyg and classical novae N Sco 2012 and N Mon 2012, detected by Fermi-LAT.

2 Nova Mon 2012 = V959 Mon

Nova Monocerotis was discovered in the optical on August, 9 by S. Fujikawa (2012). It was found to be consistent with the gamma-ray transient Fermi J0639 discovered

¹ Crimean Astrophysical Observatory, Crimea, Ukraine

² Apache Point Observatory, New Mexico State University, USA

³ Sternberg Astronomical Institute, Lomonosov Moscow University, Russia

⁴ Astronomical Institute of the Slovak Academy of Sciences, Slovakia

in early June 2012 (Cheung *et al.* 2012a; Cheung *et al.* 2012b) and XRay/UV (Nelson *et al.* 2012). The observations at radio were also reported by Chomiuk *et al.* (2012). High resolution spectroscopy and *BVRI* photometry for August 16–20 was presented by Munari *et al.* (2012). The likely progenitor of Nova was found by Greimel *et al.* (2012).

We started our optical observations of V959 Mon 17 days after its optical discovery. The CCD multicolour $UBVR_JR_CI_C, H\alpha$ observations have been carried out and are currently ongoing with the Apache Point Observatory 0.5-m telescope which is owned and operated by the Astrophysical Research Consortium and with the 0.6-m telescope of the Astronomical Institute SAS at the Stará Lesná Observatory. Here we present the behaviour of this Nova during 18 nights between August 26 and October 20 in the $UBVR_JR_CI_C$ bands.

The measurements of the nova were done relatively to the comparison star 2 (designated by AAVSO). For this star we obtained $U = 12.13$, $B = 12.20$, $V = 11.72$, $R_J = 11.48$, $I_C = 11.18$, $R_C = 11.36$, $I_J = 11.04$.

As shown in Figure 1, the light curves of the nova V959 Mon in the $UBVR_JR_CI_C$ bands were different. The highest decline rate of 0.082 mag/day was detected in the R band up to JD 2456201.

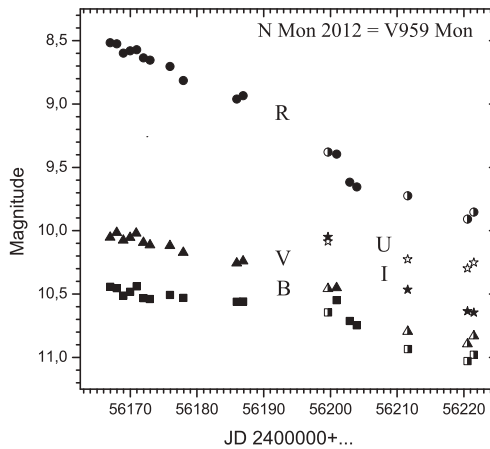


Fig. 1. The mean light curve of V959 Mon. The U data are marked by empty stars (Stará Lesná), the B data by filled squares (APO) and half-filled squares (Stará Lesná); the V data by filled triangles (APO) and half-filled triangles (Stará Lesná); the R_J data by filled circles (APO), the R_C data by half-filled circles (Stará Lesná) and the I_C data by filled stars (Stará Lesná).

As seen in two-colour diagrams presented in Figure 2, the nova V959 Mon became bluer during the decline. The $B - V$, $V - R_J$ diagram clearly show the existence of the red colour excess, probably caused by the existence of the circumstellar dust.

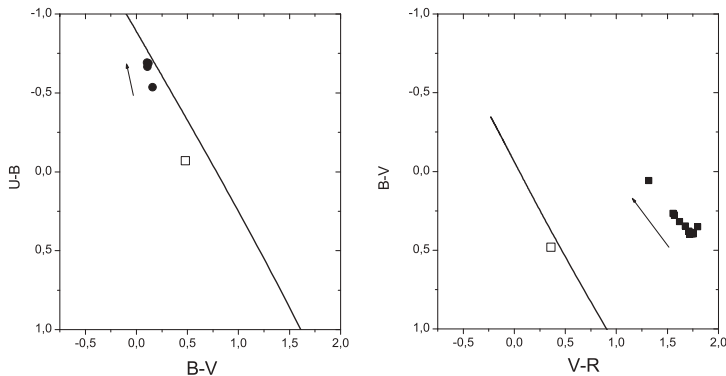


Fig. 2. The tracks of the V959 and position of the comparison star 2 (square) at the $U - B$, $B - V$ (for JD 2456199–2456221) and $B - V$, $V - R_J$ (for JD 2456166–2456200) diagrams. The black body in each diagram is drawn by the line. The arrow shows the change of colours of V959 Mon in chronological order.

The first observations of V959 Mon indicate that this is a very slow nova. The continuous multiwavelength observations of this unique object are strongly encouraged.

E. Pavlenko is grateful to SOC for the financial support for participation in the Symposium. This work was partially supported by the SAIA Scholarship, program “Kosmomikrofizika” of the Ukrainian Academy of Science and the Slovak Academy of Sciences grant VEGA No. 2/0002/13. This article was supported by the realization of the Project ITMS No. 26220120029, based on the supporting operational Research and development program financed from the European Regional Development Fund.

References

- Cheung, C.C., Hays, E., Venter, T., *et al.*, 2012, ATel, 4224
- Cheung, C.C., Shore, S.N., Gennaro, A., *et al.*, 2012, ATel, 4310
- Chomiuk, L., Cheung, T., Nelson, T., *et al.*, 2012, Atel, 4352
- Fujikawa, S., 2012, CBET, 3202
- Greimel, R., Drew, J., Steeghs, D., *et al.*, 2012, ATel, 4365
- Munari, U., Dallaporta, S., Valisa, P., 2012, Atel, 4320
- Nelson, T., Mukai, K., Chomiuk, L., *et al.*, 2012, Atel, 4321
- Pavlenko, E.P., Andreev, M., Babina, Yu., *et al.*, 2013, ASP Conf. Ser., in press
- Pavlenko, E.P., & Pelt, Ja., 1991, Ap, 34, 169
- Pavlenko, E.P., & Malanushenko, V.P., 1996, Afz, 39, 103
- Pavlenko, E.P., & Shugarov, S.Yu., 2005, ASP Conf. Ser., 330, 421
- Pretorius, M.L., & Knigge, C., 2012 [[ArXiv:1109.3162](https://arxiv.org/abs/1109.3162)]
- Revnivtsev, M., Churazov, E., Sazonov, S., *et al.*, 2008, A&A, 490, 37
- Schmidt, G.D., & Stockman, H.S., 1991, ApJ, 371, 749
- Townsley, D.W., & Bildsten, L., 2007, ASP Conf. Ser., 372, 557

GAMMA-RAY BURST OBSERVATIONS WITH ISON NETWORK

A. Pozanenko¹, L. Elenin², E. Litvinenko³, A. Volnova^{1,4}, A. Erofeeva⁵,
A. Matkin⁵, A. Ivanov⁶, V. Ivanov⁶, D. Varda⁷, E. Sinyakov⁷,
V. Nevski⁸, Yu. Krugly⁹, A. Erofeev⁵, N. Tungalag¹⁰, R. Inasaridze¹¹,
O. Kvaratskhelia¹¹, V. Kouprianov³ and I. Molotov²

Abstract. We present details of the ISON network for GRB follow-up and complete list of observations in 2010–2012.

1 The network description and results

The International Scientific Optical Network (ISON) comprises several worldwide (Fig. 1) small aperture automated telescopes (Table 1). The ISON project is originally devoted to space debris observations (Molotov *et al.* 2008). Since 2010 ISON started observations of GRB. The shortest time delay after GRB trigger (130 s) was achieved in robotic mode of ISON-NM. After two years of GRB follow-up (Table 2) one can conclude that the network of small aperture telescopes is an efficient tool for GRB detection and photometry. Totally we observed 33 GRBs, detected 15 optical transients, and in several cases we succeed to build a dense light

¹ Space Research Institute of the Russian Academy of Sciences, Moscow, Russia
e-mail: apozanen@iki.rssi.ru

² Institute for Applied Mathematics of the Russian Academy of Sciences, Moscow, Russia

³ Central Astronomical Observatory of the Russian Academy of Sciences, Pulkovo, Russia

⁴ Sternberg Astronomical Institute of Lomonosov Moscow State University, Moscow, Russia

⁵ Ussuriysk Astrophysical Observatory of the Russian Academy of Sciences, Far East Branch, Gornotayojnoye, Russia

⁶ Kuban State University, Krasnodar, Russia

⁷ Blagoveschensk Educational State University, Blagoveschensk, Russia

⁸ Astronomical Science Center “Proekt-Tekhnika”, Moscow, Russia

⁹ Institute of Astronomy of Kharkiv National University, Kharkiv, Ukraine

¹⁰ Research Center of Astronomy & Geophysics of the Mongolian Academy of Sciences, Ulaanbaatar, Mongolia

¹¹ Kharadze Abastumani Astrophysical Observatory of Ilia State University, Georgia

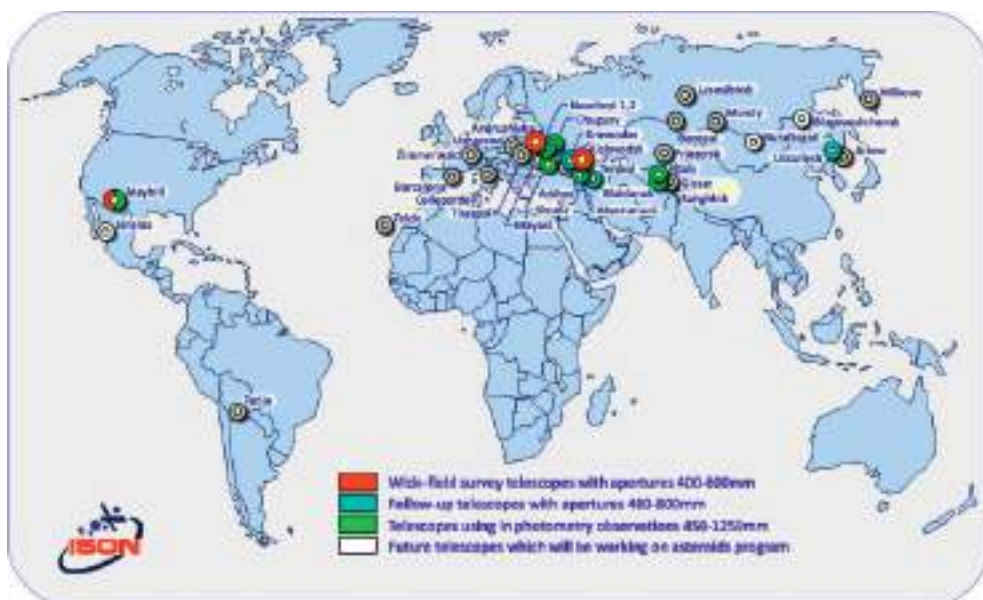


Fig. 1. Map of ISON observatories.

Table 1. ISON and cooperative telescopes used for GRB observations. * – taken from Kornilov *et al.* (2010), other data obtained from own monitoring.

Site	Telescope	Aperture, m	Num. of clear night hours/year
(M)ilkovo	ORI-22	0.22(f/2.45)	n/a
(U)ssuriysk	VT-50	0.5(f/2.3)	900
(B)lagoveshchensk	ORI-22	0.22(f/2.45)	1600
(H)ureltoget	ORI-40	0.4(f/2.3)	1400
(K)itab	ORI-40	0.4(f/2.3)	1650
(S)anglokh	VT-78a	0.19(f/1.54)	n/a
(A)bastumani	AS-32	0.7(f/3)	1200
K(I)slovodsk	SANTEL-400A	0.4(f/3)	1343*
K(R)asnadar	Astrosib RC-508	0.51(f/6.3)	1200
(N)ew Mexico	Centurion-18	0.45(f/2.8)	1800

curve of early optical afterglow (Fig. 2). Future development of GRB follow up within ISON includes robotization of the telescopes, elaboration of new wide-field telescopes for fast and deep follow up GBM/Fermi and synchronous observations of FOV of space borne observatories (*e.g.* Pozanenko *et al.* 2003), development of automatic pipelines for astrometry and photometry, and installation the telescopes in new observatories (Fig. 1).

Table 2. GRBs observed with ISON and cooperative observatories. In the column (2) the time delay between GRB trigger and start of observation is presented. In the (3) we provide brightness of the OT at the first detection (or 3σ UL). Most of observations are unfiltered. Brightness is estimated against USNO-B1.0 reference stars, R mag.

GRB	Delay	R _{mag} (obs.)	GCN num.	GRB	Delay	R _{mag} (obs.)	GCN num.
100728B	16.4 ^m	18.36(N)	11012, 11045	120402A	20.9 ^m	> 19.8(K)	13200
101804A	3.27 ^d	19.79(N)	11129, 11133	120404A	22.0 ^m	17.35(B)	13235
100901A	8 ^m	17.82(N)	11184, 11234	120802A	12.5 ^m	> 17.5(N)	13556, 13609, 13712
100906A	13.5 ^m	15.89(U)	11395	120803A	3.7 ^m	> 17.3(N)	13617
110719A	1.05 ^h	19.70(N)	12177	120811C	20.0 ^m	17.90(K)	13693, 13679
110820A	15.4 ^m	> 19.2(K)	12321	120816A	15 ^m	> 18.5(R)	n/a
111016A	3.82 ^h	> 19.2(K)	12486	120907A	12.9 ^m	18.55(I)	13761
111029A	3.61 ^m	> 18.3(N)	12500	120911A	2.45 ^m	> 18.4(N)	13759
111205A	2.90 ^d	> 19.8(N)	12736	120923A	6.43 ^m	> 19.7(N)	13820
111228A	0.84 ^d	19.27(N)	12832	121001A	7.1 ^m	19.0(R)	n/a
120106A	4.81 ^h	> 18.5(K)	12830	121011A	6.2 ^m	16.46(U)	13884
120116A	21.3 ^m	> 19.4(K)	12899	121108A	9.0 ^m	n/a(S)	n/a
120118B	45.0 ^m	> 19.5(K)	12900	121117A	1.75 ^h	> 18.9(B)	13978
120119A	1.26 ^h	18.97(N)	12871, 12881	121123A	5.2 ^h	19.01(A)	13988, 14200
120121A	2.78 ^h	> 19.7(N)	12887	121128A	0.43 ^d	20.24(A)	14201
120308A	3.3 ^m	17.30(N)	13019	121212A	2.3 ^m	20.7(S)	14071
120320A	12.6 ^m	> 16.7(B)	13198				

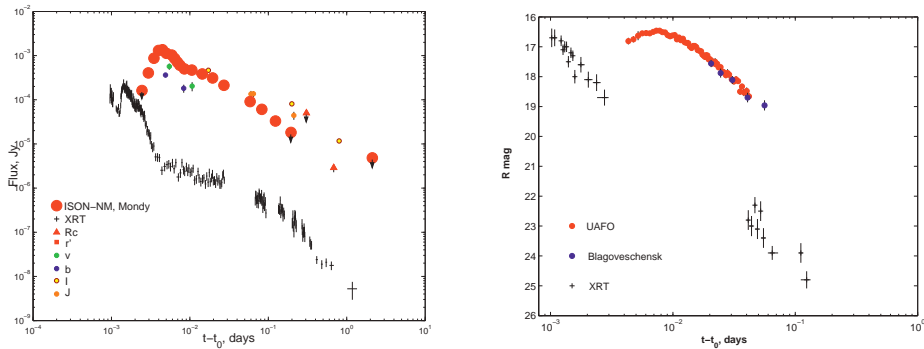


Fig. 2. *Left:* GRB 120308A: the ISON-MN began the observations of the optical transient 3.3 minutes after GRB trigger and continued it 5 hours. *Right:* GRB 121011A: the optical transient was recorded 6.2 minutes after the GRB trigger by Ussuriysk observatory.

The work was partially supported by RFBR grants 12-02-01336-a, 11-01-92202_Mong-a.

References

- Molotov, I., Agapov, V., Titienko, V., *et al.*, 2008, AdSpR, 41, 1022
- Kornilov, V., Shatsky, N., Vozniakova, O., *et al.*, 2010, MNRAS, 408, 1233
- Pozanenko, A., Chernenko, A., Beskin, G., *et al.*, 2003, ASPC, 295, 457

MANAGING GRB AFTERGLOWS OPTICAL/IR OBSERVATIONS IN THE WEB 2.0 ERA

D. Ricci¹ and L. Nicastro¹

Abstract. We present an overview of top internet technologies that can be used to build webtools and rich internet applications for astronomy. The aim is to simplify the data handling, reduction and access, in particular of optical/infrared images collected by traditional, automatic or robotic telescopes. These tools are particularly suitable for real-time management of GRB afterglow observations. Using these technologies we are developing a web-based images database management system. We present available features and discuss further improvements to the mentioned system.

1 Introduction

Modern web-based technologies are a unique opportunity for the astronomical community to simplify and modernize their work. A researcher is not simply a computer power user, but also, or “especially”, an experienced internet user. For that reason, tasks like 1. browsing a database to seek information about catalogues, astronomical objects, images, etc., 2. scheduling/launching remote observations, 3. performing simple statistics or data pre-reduction, 4. saving the analysis results for further purposes/analysis, all can be accomplished using nothing but an updated web browser.

We suggest to develop modern web-based tools as an alternative to old desktop-based instruments in particular to browse in a graphical and intuitive way data archives and analysis results (see *e.g.* Fig. 1). In fact, the management of a large amount of data produced every night by several ground- or space-based optical, infrared or other wavelength telescopes, is a primary problem in astronomy².

¹ INAF/Istituto di Astrofisica Spaziale e Fisica Cosmica, Bologna, via Gobetti 101, 40129 Bologna, Italy

²Virtual Observatories efforts (www.ivoa.net/) are targeted at putting together and making accessible the astronomical data, both with stand-alone and webtools, and most of all at promoting common protocols and exchange formats.

2 User layer technologies

A web page is an already accepted universal standard to interact with a computer. It hides to the end user all the low-level components that can evolve independently because of their modularity. Furthermore it is easily and generally available via any browser and is built on “generic” user’s experience. Finally the possibility of customization are almost infinite. We suggest to build astronomical webtools by adopting the following new web technologies: **html5** and **css3** to boost the contents (W3C Schools 2011). In particular the new revision of the **html** language provides: the **<canvas>** element for raster graphic applications, the **<svg>** tag for inline vector graphics, the **WebGL API** for rich 3D applications, **MathML** and **LATEX**-like tags to simplify the presentation of scientific results, local storage and application cache to build offline webtools; **d3.js**, **astro.js** to build **javascript** dynamic plots and charts into an **<svg>** element (Bostock 2012) and to implement specific astronomical tools, as for example a **fits** file explorer in a **<canvas>** element; **jquery** to perform easy **javascript** client-side and server-side asynchronous requests (jQuery Foundation 2009). This library is simple, modular, widely used and easily extensible with the possibility to write plugins for the community.

3 Management layer technologies

We suggest the so-called **LAMP** platform for the content management. The concept is generic enough to be portable to other operating systems without any particular effort. This layer consists in the set up of a **php** class to interact with the web page (via **jquery**) and another that uses **mysqli** to communicate with the **MySQL** database server, or even call custom **C++** APIs. The advantages of this approach consist in **portability**: by completely separating the server-side content, it is simpler to provide **html** templates that can be used to implement the same server functions in languages other than **php**; **team development**: the separation of the modules and the object-oriented approach are very convenient choices for the development of collaborative projects.

4 Current development and further improvements

We applied the concept mentioned in the previous sections to implement a webtool for the initialization, set-up and browsing of an images archive in a graphical and intuitive way. Currently our system is being developed within the **GLORIA** project. It supports the creation of a **MySQL** database for astronomical images management starting from user-selected images, *e.g.* collected by various telescopes. It allows to associate the **fits** header common keywords to a set of user-defined database fields by using custom metadata tables. A configurable **php** class provides the interaction with the database. After that, a **MCS** based **C++** program (Nicastro & Calderone 2007) is available to feed images into the DB (local or remote). We are extending the capabilities of this layer: association of user-chosen

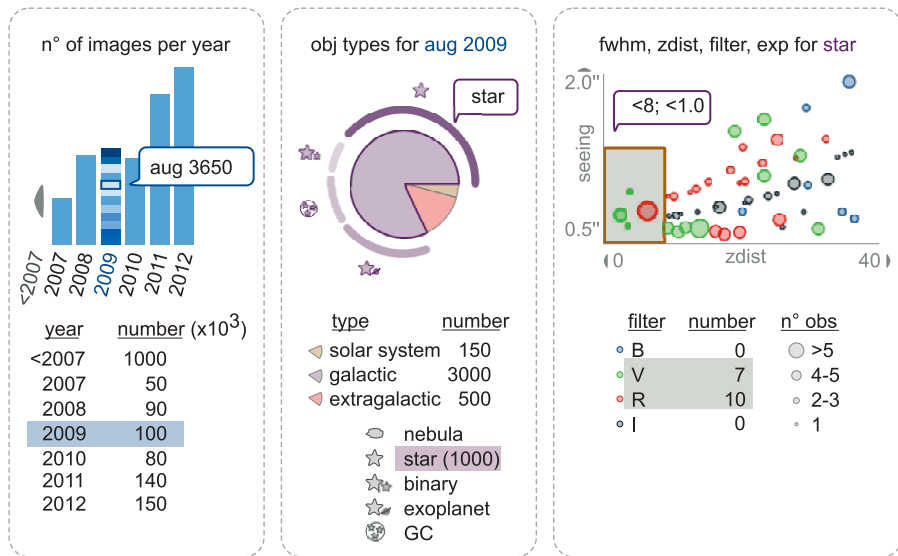


Fig. 1. Example of graphical browsing of a database of astronomical images.

keywords; definition of user accounts, access privileges and preferences (custom archive view). Our final goals are the following: **graphical browsing** of an image archive fed by an unlimited number of telescopes/cameras (see Fig. 1); **access and use** of object catalogs to perform visual and interactive analysis; **interactive tools** that mimic/extend `ds9-saoimage` (with dynamic cuts, statistics, etc.). The whole code will be released as free and open source software.

GLObal Robotic telescopes Intelligent Array for e-Science (GLORIA) is a project funded by the European Union Seventh Framework Programme (FP7/2007-2012) under grant agreement number 283783.

References

- Bostock, M., 2012, Data-Driven Documents, <http://d3js.org/>
- jQuery Foundation, 2009, Jquery official website, <http://jquery.com/>
- Nicastro, L., & Calderone, G., 2007, Astron. Soc. Pacific Conf. Ser., Vol. 376, Astronomical Data Analysis Software and Systems XVI, ed. R.A. Shaw, F. Hill & D.J. Bell, 323
- W3C Schools, 2011, HTML5, CSS3, PHP, jQuery web references, <http://www.w3schools.com/default.asp>

GRB 110715A: MULTIWAVELENGTH STUDY OF THE FIRST GAMMA-RAY BURST OBSERVED WITH ALMA

R. Sánchez-Ramírez¹, P. Hancock², T. Murphy², A. de Ugarte Postigo^{1,3}, J. Gorosabel^{1,4,5}, D.A. Kann^{6,7}, C.C. Thöne¹, A. Lundgren^{8,9}, A. Kamble¹⁰, S.R. Oates¹¹, J.P.U. Fynbo³, I. de Gregorio Monsalvo^{8,9}, D. Garcia-Appadoo^{8,9}, S. Martín⁸, N.P.M. Kuin¹¹, J. Greiner⁷ and A.J. Castro-Tirado¹

Abstract. GRB 110715A had a bright afterglow that was obscured in the optical by a high Galactic extinction. We discovered the submillimeter counterpart with APEX and followed it in radio with ATCA for over 2 months. Additional submm observations were performed with ALMA as a test of the ToO procedures during commissioning, becoming the first GRB afterglow to be detected by the observatory. UV, optical and NIR observations were performed with *Swift*/UVOT and 2.2 m/GROND in La Silla and X-ray data were obtained by *Swift*/XRT. The dataset is complemented with spectroscopic data from the VLT/X-shooter spectrograph. The absorption features present in the intermediate resolution optical/nIR spectra reveal a redshift of 0.8224 and a host galaxy environment with low ionization. We fit in the host galaxy absorption features two velocity components separated by 30 km/s, implying a host galaxy with low dynamical activity.

¹ Instituto de Astrofísica de Andalucía, IAA-CSIC, Glorieta de la Astronomía s/n, 18008, Spain

² Sydney Institute for Astronomy, School of Physics, The University of Sydney, NSW 2006, Australia

³ Dark Cosmology Centre, Niels Bohr Institute, Juliane Maries Vej 30, 2100 Copenhagen Ø, Denmark

⁴ Unidad Asociada Grupo Ciencia Planetarias UPV/EHU-IAA/CSIC, Departamento de Física Aplicada I, E.T.S. Ingeniería, Universidad del País Vasco UPV/EHU, Alameda de Urquijo s/n, 48013 Bilbao, Spain

⁵ Ikerbasque, Basque Foundation for Science, Alameda de Urquijo 36-5, 48008 Bilbao, Spain

⁶ Thüringer Landessternwarte Tautenburg, Sternwarte 5, 07778 Tautenburg, Germany

⁷ MPI für extraterrestrische Physik, 85740 Garching, Germany

⁸ European Southern Observatory, Vitacura Casilla 19001, Santiago de Chile 19, Chile

⁹ Joint ALMA Observatory, Alonso de Córdova 3107, Vitacura, Santiago, Chile

¹⁰ Harvard-Smithsonian Center for Astrophysics, 60 Garden St., Cambridge, MA 02138, USA

¹¹ Mullard Space Science Laboratory, University College London, Holmbury St. Mary, Dorking, Surrey RH5 6NT, UK

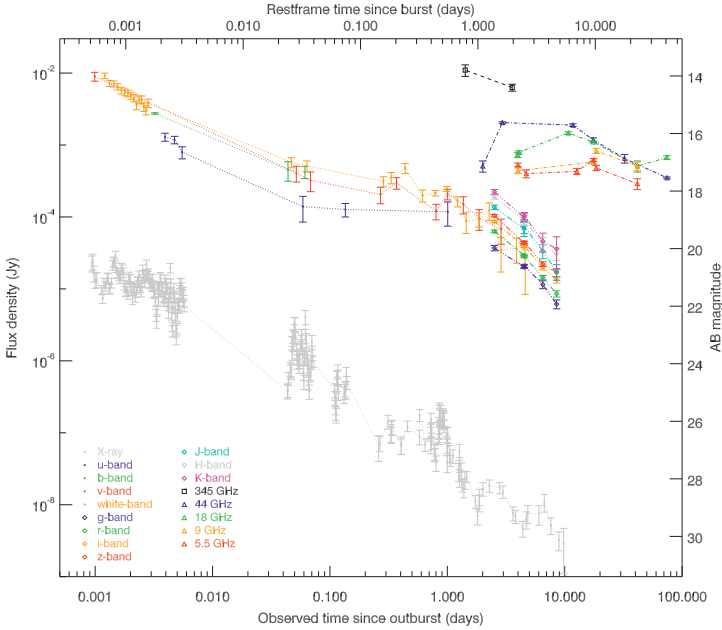


Fig. 1. Afterglow light curve in the 17 observed bands.

1 Observations

GRB 110715A (Sonbas *et al.* 2011) was an intense burst, discovered by the Burst Alert Telescope (BAT) onboard the *Swift* satellite. It was classified as a long burst, with a $T_{90} \sim 13$ s.

The burst happened at a galactic latitude of only 6 degrees, implying that it was optically obscured by dust from the Milky Way ($E_{(B-V)} = 0.59$), which complicated the optical follow-up. In spite of this, it was detected by the Ultra Violet/Optical Telescope (UVOT) on *Swift* just a few minutes after the gamma emission, providing us the unique optical dataset of the early times. This implied that the intrinsic luminosity of the event was high. In view of this, we triggered our target of opportunity programme at the 12 m Atacama Pathfinder EXperiment (APEX), using the LABOCA instrument to observe at $850\ \mu\text{m}$. Observations were performed 1.42 days after the GRB onset, and we discovered a bright submillimetre counterpart, with an intensity of $10.4 \pm 2.4\ \text{mJy}$ (de Ugarte Postigo *et al.* 2011), making it the fourth brightest GRB ever observed at these wavelengths (de Ugarte Postigo *et al.* 2012a).

As a test of the target of opportunity procedure, GRB 110715A was subsequently observed at Atacama Large Millimeter Array (ALMA), in what became the first observation of a GRB by this observatory.

Following the detection of the afterglow at submm wavelengths with APEX, radio observations were obtained with the Australia Telescope Compact Array

(ATCA) two and three days after the outburst. These observations resulted in further detections of the afterglow at 44 GHz (Hancock *et al.* 2011). Observations were obtained up to 75 days post burst at 44, 18, 9, and 5 GHz.

We obtained follow-up observations of the optical/NIR afterglow of GRB 110715A with the seven-channel imager GROND (Greiner *et al.* 2008) mounted on the 2.2 m MPI/ESO telescope stationed in La Silla, Chile. The afterglow is detected in all g, r, i, z, J, H and K filters between 2.5 and 8 days.

For the study of the X-ray emission, we made use of the *Swift*/XRT publicly available data (Evans *et al.* 2009). All the photometric observations are compiled in the form of a multi-band light curve in Figure 1.

The dataset is completed with a spectrum obtained with the X-shooter spectrograph at the Very Large Telescope, in Paranal Observatory (Chile), 12.7 hours after the GRB. The spectrum covers the complete range between 3000 and 24 800 Å, although the strong optical extinction only allows detection of the continuum above \sim 3600 Å.

2 Preliminary results

The ALMA Science Team reported a preliminary detection of this source of 4.9 ± 0.6 mJy at 850 μ m after only 25 mins on source with 7 antennas 3.6 days after the onset. In spite of this, it is the deepest observation of a GRB at this band up to date. The centroid of the ALMA position is found at equatorial coordinates (J2000), RA: 15:50:44.05, Dec: $-46:14:06.5$ with an uncertainty of $0''.3 \times 0''.1$ at a position angle of 76 degrees, which is the most precise localisation of the event. We detect absorption lines in the complete X-shooter spectrum that we identify as FeII*/FeII, MgI, MgII, CaI and CaII at a common redshift of 0.8224 ± 0.0002 . We have measured equivalent widths of these lines and limits for several others using a self-developed code. Following the prescription of de Ugarte Postigo *et al.* (2012b), we obtain a line strength parameter for GRB 110715A of $LSP = -0.42$, implying that this event is in the percentile 29 of line strengths, indicating a lower than average column density of material in the line of sight. This can point towards a small host galaxy. This is consistent with the fact that there are two velocity components in the absorption features spanning only 30 km s^{-1} , also lower than average.

References

- de Ugarte Postigo, A., Lundgren, A., Mac-Auliffe, F., *et al.*, 2011, GCN 12168
- de Ugarte Postigo, A., Lundgren, A., Martín, S., *et al.*, 2012, A&A, 538, A44
- de Ugarte Postigo, A., Fynbo, J.P.U., Thoene, C.C., *et al.*, 2012, A&A, 548, A11
- Evans, P.A., Beardmore, A.P., Page, K.L., *et al.*, 2009, MNRAS, 397, 1177
- Hancock, P.J., Murphy, T., & Schmidt, B.P., 2011, GCN 12171
- Sonbas, E., Barthelmy, S.D., Baumgartner, W.H., *et al.*, 2011, GCN 12158

COLOR INDICES OF OPTICAL AFTERGLOWS OF LONG GRBS IN THE *SWIFT* ERA

V. Šimon^{1,2}, G. Pizzichini³ and R. Hudec^{1,2}

Abstract. We show the power of the method of the color indices that uses the commonly available multiband photometry of optical afterglows (OAs) of long GRBs detected by *Swift*. Our study shows that for most OAs, in the observer frame, these colors, corrected for the Galactic reddening, display prominent clustering in the color-color diagrams. The color indices enable us to distinguish OAs from other types of objects even without available gamma-ray emission. The color-color diagrams can be used to assess the extinction inside the host galaxy. Our approach is also generally important for investigating the numerous faint OAs for which obtaining spectra with good S/N ratio is often impossible.

1 Introduction, data analysis, and results

Color indices of optical afterglows (OAs) of GRBs are a powerful and innovative approach to the study of such events. They help us to:

- (1) search for the common properties of the afterglows, especially in order to investigate the spectral energy distribution and its changes, even by using photometric filters with small or moderate telescopes,
- (2) constrain the properties of the interstellar medium in the host galaxy of GRB,
- (3) distinguish among the individual radiation mechanisms (*e.g.* synchrotron radiation *versus* supernova, which is important also for an investigation of the GRB-supernova relation),
- (4) find out whether an optical event is related to a GRB even if no gamma-ray monitor detected the GRB (*e.g.* if no gamma-ray monitor was observing at the time of the GRB),
- (5) search for orphan afterglows (GRBs with the jet not pointing directly towards the observer; gamma-ray emission is not detected, but the optical one may be

¹ Astronomical Institute, AS CR, 25165 Ondřejov, Czech Republic

² Czech Technical University in Prague, FEL, Prague, Czech Republic

³ INAF/IASF Bologna, via Gobetti 101, 40129 Bologna, Italy

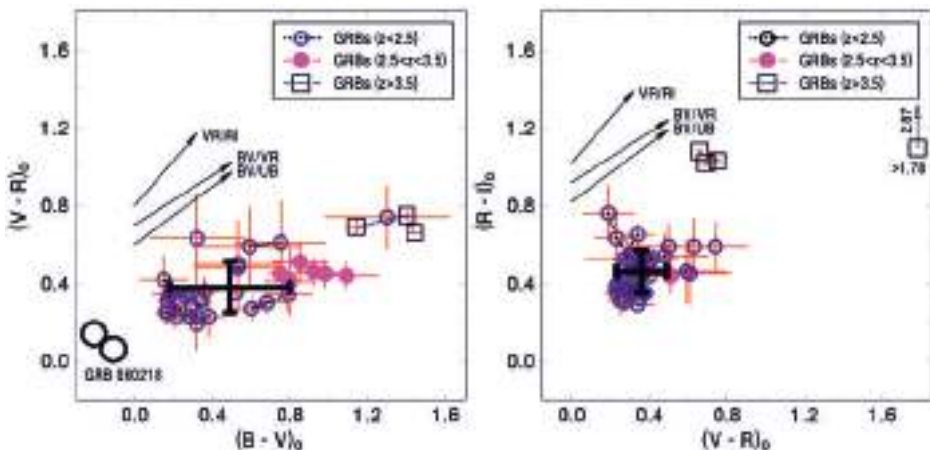


Fig. 1. Color-color diagrams of the OAs of *Swift* GRBs in the observer frame ($t - T_0 < 10$ d in the observer frame). The colors are corrected for the Galactic reddening using the maps of Schlegel *et al.* (1998). The large cross represents the mean colors (centroid) of the ensemble having $z < 3.5$. The OA of GRB 060218 is not included in calculating the centroid. The arrows denote the representative reddening outside our Galaxy: $E_{B-V} = 0.5$ mag.

observed; also gamma-ray emission too faint even when the jet is pointing towards the observer is possible). See Rhoads (1997) and Huang *et al.* (2002) for more.

Here, we compare the color indices of 21 *Swift* GRBs (from GRB 050128 to GRB 080810) with those used in our previous analysis (Šimon *et al.* 2001). Because of space limitations, the reader is referred to J. Greiner's Web page <http://www.mpe.mpg.de/~jcg/grbgen.html> for full references on each OA.

We show that a given color index of the ensemble of OAs with redshift $z < 3.5$ forms a very narrow belt with time. Namely, $(B - V)_0 = 0.46 \pm 0.28$ for $t - T_0$ from 0.0025 to 1.72 d; $(V - R)_0 = 0.38 \pm 0.13$ for $t - T_0$ from 0.0018 to 3.23 d; $(R - I)_0 = 0.46 \pm 0.11$ for $t - T_0$ from 0.0011 to 2.84 d. We note that OAs of the *Swift* GRBs are mapped in much earlier phases than before, which extends the belts to very small $t - T_0$. These belts in the time evolution of the color indices are valid even when the OA undergoes extreme changes of its brightness (the OA of GRB 080319B: a decrease by 7.9 mag during $t - T_0 < 4.6$ h). It is therefore possible to combine the data of the individual OAs obtained in different $t - T_0$.

The prominent concentration of colors of the OAs in Figure 1 is caused by the fact that most of the available measurements map part of the spectrum of the OAs with a very similar slope. This clustering enables us to identify the important properties of OAs at $t - T_0$ less than about 3.2 d. The spectral shape of OA is very smooth, with no bumps or strong lines, between the B to I bands in the observer frame. However, a real spectral break (not caused by the Lyman break) of some OAs is observed, as suggested by the tail in the $(B - V)_0$ vs. $(V - R)_0$ diagram (Fig. 1). These features display only negligible time evolution.

The color indices of the individual members of the ensemble were compared with the absolute magnitudes M_R corrected using our approach described in Šimon *et al.* (2001). These M_R , measured in the initial phase (the early decay), at the rest-frame $(t - T_0)_{\text{rest}} = 0.1$ d spanned over a very broad range between $M_R \approx -20$ and -27 . Spectra of most OAs in this spectral region are mutually quite similar while their luminosity in a given $t - T_0$ largely differs: the spectral shape in the fireball model (Sari *et al.* 1998) does not depend on the input energy, while the luminosity of the OA at a particular epoch depends on it.

The characterization of spectra of OAs by spectral index of the power-law function is valid only for a limited part of the real spectrum. The color indices are thus an important method for a study of the spectral properties of OAs, especially when a spectral break is present in some OAs.

The color indices of the OAs give us the possibility to separate the contributions of synchrotron radiation and supernova using the commonly available photometry (see Šimon *et al.* 2004, 2010). This is important mainly for analysis of faint OAs. Color indices are thus a much better tool to resolve the evolution of supernova in the profile of an OA than the light curves themselves.

Our present study confirms our previous findings that the color indices of the OAs are very specific. This also gives us hope to search whether an optical event is related to a GRB even without available gamma-ray detection.

As already stated in Section 1, the colors of OAs provide us with direct information about the environment of GRB. Several important consequences for the reddening inside the host can be made. The strong concentration of most colors of OAs suggests that the reddening inside their host galaxies must be quite similar and relatively small. *Swift* data show no variations of reddening even in the very early phase of the OA. Several possibilities exist: (a) GRBs with detected OAs are on the earth watching side of a star-forming region; (b) very low dust abundance in the host galaxy; (c) the density and dust abundance of the local interstellar medium (*e.g.* dust from the progenitor) is reduced by intense radiation of GRB (model by Waxman & Draine 2000).

Support by grant 102/09/0997 of the Grant Agency of the Czech Republic, CSIC-AV ČR collaborative project Investigation of Gamma Ray Bursts, and the project RVO:67985815 is acknowledged.

References

- Huang, Y.F., Dai, Z.G., & Lu, T., 2002, MNRAS, 332, 735
- Rhoads, J., 1997, ApJ, 487, L1
- Sari, R., Piran, T., & Narayan, R., 1998, ApJ, 497, L17
- Schlegel, D.J., Finkbeiner, D.P., & Davis, M., 1998, ApJ, 500, 525
- Šimon, V., Hudec, R., Pizzichini, G., & Masetti, N., 2001, A&A, 377, 450
- Šimon, V., Hudec, R., & Pizzichini, G., 2004, A&A, 427, 901
- Šimon, V., Pizzichini, G., & Hudec, R., 2010, A&A, 523, A56
- Waxman, E., & Draine, B.T., 2000, ApJ, 537, 796

A CASE STUDY OF DARK GRB 051008

A. Volnova^{1,2}, A. Pozanenko², J. Gorosabel^{3,4,5}, D. Perley⁶, D.A. Kann⁷,
D. Frederiks⁸, V. Rumyantsev⁹, A.J. Castro-Tirado³ and P. Minaev²

Abstract. We present multi-wavelength observations of the dark GRB 051008. The burst was not detected in the optical bands, however we discover the host galaxy and secured the redshift of the host with following campaign of multicolor observations of Shajn, NOT, Gemini North and Keck telescopes. We provide arguments that the galaxy could be in a complex of gravitationally bound galaxies. Our investigation of the GRB 051008 also confirms a tendency of host galaxies of dark bursts to be more dusty.

1 Observations and results

GRB 051008 was detected by the *Swift*/BAT at 16:33:21 UT on October 8, 2005 (Marshall *et al.* 2005). It was also detected in γ -ray domain by *Suzaku*/WAM (Ohno *et al.* 2005), Konus-*WIND*, and *INTRGRAL*/SPI-ACS. The *Swift*/XRT discovered an X-ray counterpart in \sim 50 minutes after the trigger because of the Earth constraint. 2.6-meter Shain telescope of Crimean observatory (ZTSh/CrAO)

¹ Sternberg Astronomical Institute of Lomonosov Moscow State University, Moscow, Russia

² Space Research Institute of the Russian Academy of Sciences, Moscow, Russia

³ Instituto de Astrofísica de Andalucía (IAA-CSIC), Glorieta de la Astronomía s/n, 18008, Granada, Spain

⁴ Unidad Asociada Grupo Ciencia Planetarias UPV/EHU-IAA/CSIC, Departamento de Física Aplicada I, E.T.S. Ingeniería, Universidad del País Vasco UPV/EHU, Alameda de Urquijo s/n, 48013 Bilbao, Spain

⁵ Ikerbasque, Basque Foundation for Science, Alameda de Urquijo 36-5, 48008 Bilbao, Spain

⁶ Department of Astronomy, California Institute of Technology, Pasadena, USA

⁷ Thüringer Landessternwarte Tautenburg, Tautenburg, Germany

⁸ Ioffe Physico-Technical Institute of the Russian Academy of Sciences, St. Petersburg, Russia

⁹ Scientific Research Institute Crimean Astrophysical Observatory, Nauchny, Ukraine

*e-mail: alinuss@gmail.com

did not detect any optical afterglow up to 23.3^m in ~ 30 minutes after the trigger (Rumyantsev *et al.* 2005). Together with XRT observations this allows to conclude that GRB 051008 is an optically dark burst with $\beta_{OX} < 0.18$. In Apr. 2006 the host galaxy of the source with R-band magnitude of 23.9^m was discovered by ZTSh/CrAO (Fig. 1, left). The probability for an accidental location of the Id3 galaxy inside the XRT error circle is estimated to be of about 1.96%. In 2005 – 2012 the observations of the host galaxy were carried out with Shain, Tautenburg, NOT, Gemini North, and Keck I telescopes in U , B , g' , V , R , i , I , Z and K' bands down to limiting magnitudes 25.4, 25.8, 27.2, 25.7, 26.1, 23.9, 25.2, 25.5, and 23.0 correspondingly. A long slit spectrum of the host galaxy was obtained in Jun. 2009 using the Low-Resolution Imaging Spectrometer (LRIS) on the Keck I telescope, no obvious line features are identified in the sky-subtracted 2D spectra.

The multiwavelength photometry was used to estimate the photometric redshift z_{phot} of the host galaxy and 4 nearby galaxies with *LePhare* package (Arnouts *et al.* 1999; Ilbert *et al.* 2006). We used the COSMOS population synthesis models library to obtain the best-fitted SED with emission lines and the redshift (Fig. 1, right). We used the PEGASE2 population synthesis models library with to obtain all the other required parameters. The host galaxy is best described by a template of a starburst galaxy with SMC reddening law at the redshift $z_{phot} = 2.85^{+0.03}_{-0.05}$ with the age of the dominant stellar population being about 0.025 Gyr and an intrinsic extinction of $A_V = 0.23^m$ and SFR about $80 - 100 M_\odot/\text{y}$. The redshift of the galaxy Id5 (see Fig. 1, left) is $z = 2.84^{+0.02}_{-0.03}$, it corroborates the hypothesis that the host galaxy is located in a gravitationally bound at least pair of galaxies with a distance of about 70 kpc.

GRB 051008 is a good example of a multi-peak event. Using SPI-ACS data we found at least 10 separated pulses which fit the light curve fairly well. Short duration peaks of the burst may be the cause of negligible spectral lag of -0.2 ± 0.3 defined from Konus-WIND data (between G1 and G3 channels).

We fitted the X-ray spectrum ~ 4 hours after the trigger with single power-law model absorbed by the Galactic N_H and $N_{H,host,z}$ of the host galaxy with fixed redshift. This model yields an X-ray photon index $\Gamma_X \sim 1.9$ and $N_{H,host,z} = 12.2 \times 10^{21} \text{ cm}^{-2}$ corresponding to the extinction along the line of sight $A_{V,GRB} = 5.5^m \pm 0.2^m$ (Güver & Özel 2009). This line-of-sight extinction can not be explained neither by the bulk absorption in the host galaxy nor by adding of a cooling break $\Delta\beta = 0.5$ in the energy range lower than the XRT band.

Swift/BAT, *INTEGRAL/SPI-ACS*, and *Swift/XRT* data were converted into 15 – 50 keV range in order to construct a joint X-ray light curve which was fitted by a broken power-law (Liang *et al.* 2007). The light curve of GRB 051008 X-ray afterglow belongs to a less frequent class of plateau-less XRT light curves and may represent only phases III and IV of the canonical X-ray afterglow (Racusin *et al.* 2009). The time of the light curve break t_b and z_{phot} allowed to estimate the isotropic equivalent energy for the burst $E_{iso} = (11.17 \pm 3.69) \times 10^{53} \text{ erg}$, the jet opening angle, and the total gamma radiation energy in case of constant ISM with the density of $n = 1 \text{ cm}^{-3}$ (Zhang *et al.* 2007) ($\theta_j = 1.7^\circ \pm 0.2^\circ$,

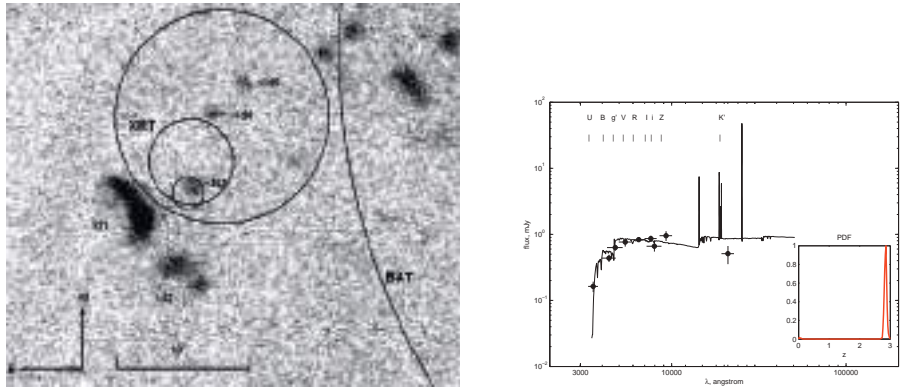


Fig. 1. *Left:* GRB 051008 and its immediate neighbourhood. The image was taken 255 days after the GRB in the R-filter, a 4800 s exposure, the NOT telescope. The burst error circles determined from the *Swift*/BAT and the *Swift*/XRT telescopes data are shown with solid lines. The smallest error box depicts the *Swift*/XRT refined error circle (Goad *et al.* 2007). The Id3 marker indicates the host galaxy of GRB 051008. *Right:* spectral Energy Distribution (SED) of the host galaxy in the observer frame. The best-fitted SED type obtained by LePhare (line) is the SED of starburst galaxy on $z = 2.85$. Observed flux in $UBg'VRiIZK'$ filters is shown by crosses. The associated Probability Distribution Functions is shown on the enclosed panel. The SED with emission lines is obtained using COSMOS SED library and SMC reddening law (Prévote *et al.* 1984).

$E_\gamma = (4.6 \pm 2.0) \times 10^{50}$ erg) and wind-like environment (Chevalier & Li 2000) ($\theta_j = 2.0^\circ \pm 0.2^\circ$, $E_\gamma = (6.8 \pm 4.4) \times 10^{50}$ erg).

GRB 051008 is dark neither due to high redshift nor due to bulk extinction in the host galaxy, which is moderate only. We suggest that the darkness of the burst is most probably due to a local extinction of the molecular cloud surrounding the progenitor of the burst. While the burst well fits Amati relation (Amati 2006), it is an outlier of Ghirlanda relation (Ghirlanda *et al.* 2004). Assuming that the break on the X-ray light curve is a real jet-break the latter can indicate a dense ($n = 10^3 - 10^6$ cm $^{-3}$) environment of the burst but it can also.

The work was partially supported by RFBR grants 12-02-01336-a, 11-01-92202-Mong-a.

References

- Amati, L., 2006, MNRAS, 372, 233
- Arnouts, S., Cristiani, S., Moscardini, L., *et al.*, 1999, MNRAS, 310, 540
- Chevalier, R.A., & Li, Z.-Y., 2000, ApJ 536, 195
- Ghirlanda, G., Ghisellini G., & Lazzati D., 2004, ApJ, 616, 331

- Goad, M.R., Tyler, L.G., Beardmore, A.P., *et al.*, 2007, A&A, 476, 1401
Güver, T., & Öznel, F., 2009, MNRAS, 400, 2050
Ilbert, O., Arnouts, S., McCracken, H.J., *et al.*, 2006, A&A, 457, 841
Liang, E.-W., Zhang, B.-B., & Zhang, B., 2007, ApJ, 670, 565
Marshall, F., Barthelmy, S., Cummings, J., *et al.*, 2005, GCN Circ. 4069
Ohno, M., Takahashi, T., Fukazawa, Y., *et al.*, 2005, GCN Circ. 4297
Prévet, M.L., Lequeux, J., Prévet, L., *et al.*, 1984, A&A, 132, 389
Racuzin, J., Liang, E.W., Burrows, D.N., *et al.*, 2009, ApJ, 698, 43
Rumyantsev, V., Biryukov, V., & Pozanenko, A., 2005, GCN Circ. 4081
Zhang, B., Liang, E., Page, K.L., *et al.*, 2007, ApJ, 655, 989

MILLIMETRE OBSERVATIONS OF GAMMA-RAY BURSTS AT IRAM

A.J. Castro-Tirado¹, M. Bremer², J.M. Winters², J.C. Tello¹,
S.B. Pandey³, A. de Ugarte Postigo^{1,4}, J. Gorosabel^{1,5,6}, S. Guziy⁷,
M. Jelinek¹, R. Sánchez-Ramírez¹, D. Pérez-Ramírez⁸
and J.M. Castro Cerón⁹

Abstract. Since 1997, and following our detection of the first mm afterglow, we have followed-up 70 GRBs, mainly with the IRAM’s Plateau de Bure Interferometer, what can be considered as the IRAM Legacy GRB Sample. 66 events were observed at 3 mm, with 19 of them being detected (with another 3 having marginal detections). 32 GRBs were followed up at 1 mm, with 6 of them being detected. Redshifts for the GRB afterglows lie in the range $z = 0.03\text{--}8.3$, with measured flux densities (at 3 mm) varying between 0.25 and 60 mJy (but usually < 1.5 mJy) with first observations taking place around 1–2 days after the GRB. Forward shock emission explains the observations with the exception of one particular case (GRB 090423 at $z = 8.2$) for which reverse shock emission is required.

1 Introduction

Since 1997, following our detection of the first millimeter (mm) afterglow (GRB 970508. Bremer *et al.* 1998) we are conducting pioneering mm observations

¹ Instituto de Astrofísica de Andalucía (IAA-CSIC), Glorieta de la Astronomía s/n, 18008 Granada, Spain

² Institute de Radioastronomie Milimetrique (IRAM), Saint Martin d’Hères, France

³ Aryabhatta Research Institute of Observational Sciences (ARIES), Nainital, India

⁴ Dark Cosmology Centre, Niels Bohr Institute, University of Copenhagen, 2100 Copenhagen, Denmark

⁵ Unidad Asociada CSIC-UPV/EHU, Departamento de Física Aplicada I, Escuela T. Superior de Ingeniería, Bilbao, Spain

⁶ Ikerbasque, Basque Foundation for Science, Alameda de Urquijo 36-5, 48008 Bilbao, Spain

⁷ Nikolaev Astronomical Observatory, University of Nikolaev, Ukraine

⁸ Universidad de Jaén, Spain

⁹ ESAC, Robledo de Chavela, Madrid, Spain

of GRBs with the IRAM's Plateau de Bure Interferometer (PdBI) in the French Alps.

Observations at these wavelengths are most essential due to the following reasons: i) Negligible absorption effects (like gamma-rays), *i.e.* dark or ultra- high- z bursts can be detected; ii) The peak of the GRB synchrotron spectrum peaks in the mm range; iii) No self-absorption effects (as seen at lower-frequencies); iv) Negligible interstellar scintillation effects (as seen at lower-frequencies); v) The peak of the GRB afterglow emission takes hours-days to cross the mm band; vi) PdBI is the only Northern Hemisphere observatory nowadays that has the sensitivity high enough to detect the mm afterglow emission for a considerable number of events (and perhaps even for detecting the forward emission too in some cases); vii) A logistics advantage: the flexibility of PdBI due to the fact that is a service observatory (with no observers present at the time of executing their programs) makes it easy to reschedule a target of opportunity (ToO) program.

This work enlarges the IRAM sample previously discussed (de Ugarte Postigo *et al.* 2012) as it does include additional datasets and the details can be seen in Castro-Tirado *et al.* (2013).

2 Observations and results

We have mainly used the PdBI (Guilloteau *et al.* 1992), located at 2550 m a.s.l. in the Haute Alpes (France). It is the most sensitive observatory in the Northern Hemisphere operating at millimetre wavelengths (0.8, 1.2, 2 and 3 mm). In 1996 is started observations with 5 antennae, increasing to 6 as of 2002. New generation receivers were installed in 2007. In fact, the wideband correlator WIDEX, installed in 2010, has significantly increased the number of detections due to its superb sensitivity. Additional observations were carried out on a very few cases with the 30 m IRAM antenna at Pico Veleta (2920 m a.s.l.) in Sierra Nevada (Spain).

Following our 16 yr study of GRB afterglows, the main results are the following ones:

1. The number of follow-ups amounted to 70, with 19 detections of mm afterglows achieved at 3 mm, 6 detections at 1 mm, with 4 of the events being simultaneously detected at 1 and 3 mm.
2. Redshifts for the GRB afterglows lie in the range $z = 0.03\text{--}8.3$, with measured flux densities (at 3 mm) varying between 0.25 and 60 mJy (but usually < 1.5 mJy) with first observations taking place around 1–2 days after the GRB. We have detected 2 (out of 3) GRBs at $z > 6$: GRB 050904 ($z = 6.3$) and 090423 ($z = 8.3$). On the lower redshift end, we have detected the low- z , faint GRB 090108 / SN 2008D ($z = 0.03$).
3. Amongst the long-duration class, we have detected four dark GRBs: GRB 051022 (associated with a $z = 0.809$ galaxy), GRB 090404 (whose galaxy is not properly identified), GRB 111215A (associated with a galaxy in the range $1.8 < z < 2.5$) and GRB 120624B.

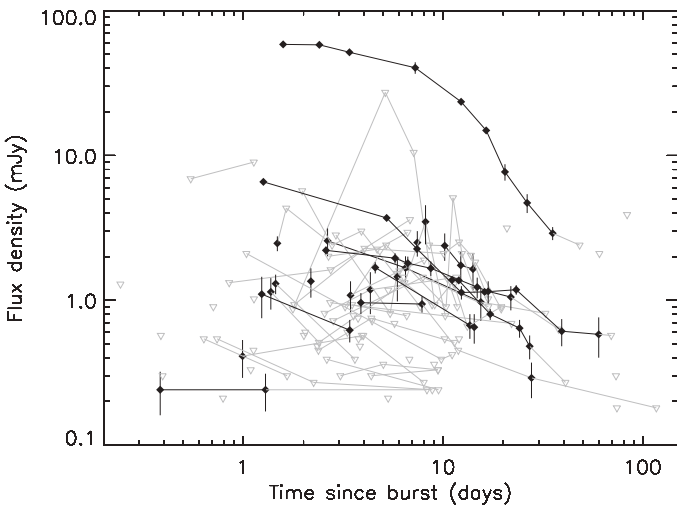


Fig. 1. The observed light curves and upper limits for 64 events observed at 3 mm as described in this work, with 18 of detected (black circles, filled) and 45 undetected (grey upside down triangles, empty). GRB 070610 and GRB 110328A are excluded as they have a different physical origin.

3 Conclusions

Millimetre observations are a powerful tool for gaining a better understanding of the GRB physics, especially the highly extinguished events and very high redshift bursts. The 23 GRBs detected imply a 32% success rate (for this non-blind sample). Millimetre observations are not affected by high-z or extinction and usually can lead to sample the synchrotron peak in the spectrum as well as detecting the tail of the prompt emission and the forward shock in one case (GRB 090423 at $z = 8.3$).

We acknowledge the support of the Spanish programs AYA2009-14000-C03-01 (MICINN) and AYA2012-39727-C03-01 (MINECO). Based on observations carried out with the IRAM Plateau de Bure Interferometer and with the 30 m Pico de Veleta antenna. IRAM is supported by INSU/CNRS (France), MPG (Germany) and IGN (Spain).

References

- Bremer, M., Krichbaum, T.P., Galama, T.J., *et al.*, 1998, A&A 332, L13
- Castro-Tirado, A.J., Bremer, M., Winters, J.-M., *et al.*, 2013, in press
- Guilloteau, S., Delannoy, J., Downes, D., *et al.*, 1992, A&A 262, 624
- de Ugarte Postigo, A., Lundgren, A., Martín, S., *et al.*, 2012, A&A, 538, A44

Chapter VI.
Afterglow Emission-II (Theory)

GRB AFTERGLOW

B. Zhang¹

Abstract. Recent observations of broad-band afterglow of gamma-ray bursts (GRBs) suggest that the standard external shock model cannot account for all the data. The observed “afterglow” of some GRBs includes the contributions from at least three emission components. Theoretically, there are naturally three emission sites. Besides the traditional external forward shock, the existence of X-ray flares demands late central engine activities of the GRB central engine, so that an “internal dissipation” region of the late wind is another emission site. After dissipation, this late wind would inevitably catch up with the blastwave, giving rise to a third emission site at a long-lasting reverse shock. Some recent efforts in understanding the broadband afterglow are reviewed.

1 Introduction

The sub-title of the “Fall 2012 Gamma-Ray Burst Symposium” is “15 years of Gamma-Ray Burst afterglow”. It is delightful to recall that afterglow was actually predicted before the discovery. Shortly after the publication of the seminal paper of Mészáros & Rees (1997), the first X-ray and optical afterglows were discovered for GRB 970228 (Costa *et al.* 1997; van Paradijs 1997), and the first radio afterglow was discovered for GRB 970508 (Frail *et al.* 1997). Since then, regular follow-up observations of GRBs have been carried out, and a large amount of broad-band afterglow data have been collected. The launch of the NASA’s dedicated GRB mission Swift (Gehrels *et al.* 2004) opened a new temporal window to study GRB afterglow in the early phase (starting from \sim 1 min after the γ -ray trigger). The launch of the high energy mission Fermi has led to the discovery of an extended GeV afterglow emission for some bright GRBs (*e.g.* Ghisellini *et al.* 2010; Zhang *et al.* 2011). The observed broad-band data present a perplexing picture, which calls for a rethinking of the origin of GRB afterglow.

¹ Department of Physics and Astronomy, University of Nevada, Las Vegas, USA

2 Observation overview

Before Swift, afterglow observations usually started several hours after the trigger. The optical afterglow at this stage typically displays a power law decay (*e.g.* Wijers *et al.* 1997; Harrison *et al.* 1999), with a steepening “jet” break in the day time scale (Frail *et al.* 2001). These are consistent with the predictions of the standard external forward shock afterglow models (*e.g.* Mészáros & Rees 1997; Sari *et al.* 1998, 1999; Dai & Lu 1998; Chevalier & Li 2000). Irregular wiggles and bumps were observed in some bright GRB optical afterglow lightcurves (*e.g.* Holland *et al.* 2003; Lipkin *et al.* 2004). Some early optical flashes were observed (*e.g.* Akerlof *et al.* 1999; Fox *et al.* 2003), which showed a steep decay slope early on (with a decay index ~ -2) before flattening to a more normal decay with a decay index -1 . This early component is consistent with being emission from the reverse shock (Mészáros & Rees 1997, 1999; Sari & Piran 1999a, 1999b; Kobayashi 2000; Zhang *et al.* 2003). The rapid slew of XRT and UVOT towards the GRB source allows detections of the GRB early afterglow within less than 100 s after the trigger. As a result, Swift has provided a rich trove of early afterglow data which revealed many, usually unexpected, interesting features (*e.g.* Nousek *et al.* 2006; O’Brien *et al.* 2006). Zhang *et al.* (2006) characterized the X-ray afterglow into 5 components: I. a steep decay phase that is smoothly connected with the tail of prompt emission; II. a shallow decay phase (or plateau); III. a “normal” decay phase with decay slope ~ -1 as expected in the standard model; IV. a late steepening phase that is consistent with the post-jet-break phase; and V. erratic X-ray flares that overlap on top of the broken power law segments.

It was soon realized that the steep decay phase (Tagliaferri *et al.* 2005; Zhang *et al.* 2007) is the tail of prompt emission (Barthelmy *et al.* 2005). It is likely the high latitude emission after the prompt emission ceases abruptly (Kumar & Panaitescu 2000; Zhang *et al.* 2006). This also suggests that the prompt emission region and the afterglow region are detached, establishing the internal origin of the GRB prompt emission (Zhang *et al.* 2006). The erratic X-ray flares (Burrows *et al.* 2005) have rapid rising and decaying slopes, which cannot be interpreted within the external shock model. This established the internal origin of the X-ray flares, which calls for delayed central engine activity (Burrows *et al.* 2005; Zhang *et al.* 2006; Fan & Wei 2005; Chincarini *et al.* 2007; Lazzati & Perna 2007; Maxham & Zhang 2009).

The broken power law segments (components II, III and IV defined in Zhang *et al.* 2006) can be interpreted within the framework of the external shock model, with the phase II interpreted as a refreshed forward shock due to continuous energy injection, phase III interpreted as the normal phase after energy injection is over, and phase IV interpreted as the post-jet-break phase (Zhang *et al.* 2006; Nousek *et al.* 2006; Panaitescu *et al.* 2006). Data analyses (Liang *et al.* 2007, 2008) suggest that there is essentially no spectral evolution across the two temporal breaks connecting the three segments, and the segment III usually satisfies the $\alpha - \beta$ “closure relations” predicted by the forward shock models (where α and β

are temporal decay index and spectral index of the X-ray afterglow, respectively, with the convention $F_\nu \propto t^{-\alpha} \nu^{-\beta}$.

Further confusions were introduced by two surprising observations. First, in some cases, an X-ray plateau is found to be followed by a very steep decay, a signature of internal origin of the emission (Troja *et al.* 2007; Liang *et al.* 2007; Lyons *et al.* 2010). This suggests that the late central engine activity of a GRB central engine not only can power erratic flare-like activities, but can also power a steady wind. This may point towards a spinning-down central engine such as a millisecond magnetar (Troja *et al.* 2007; Lyons *et al.* 2010). The second puzzling fact is that in some cases, the optical and X-ray lightcurves show a “chromatic” behavior, namely, there is no optical break at the X-ray break time, and *vice versa* (Panaitescu *et al.* 2006b; Liang *et al.* 2007, 2008). Since there is no spectral change across the X-ray break (Liang *et al.* 2007, 2008), this essentially rules out the possibility of interpreting both X-ray and optical data with one single jet component within the standard forward shock model. This drove a wave of modeling invoking emission not from the forward shock. One scenario interprets the entire X-ray and optical afterglow as emission from a long-lasting reverse shock (Uhm & Beloborodov 2007; Genet *et al.* 2007), which requires strong suppression of the forward shock emission that would otherwise outshines the reverse shock emission. The other proposal is that the entire X-ray afterglow is due to internal dissipation of a long-lasting central engine wind (Ghisellini *et al.* 2007; Kumar *et al.* 2008; Cannizzo & Gehrels 2009; Yu *et al.* 2010; Metzger *et al.* 2011).

To summarize, the X-ray and optical afterglow observations suggest that there might exist probably three emission components that shape the observed afterglow, one erratic X-ray flare component, two power law components - one gives a dominant contribution to the X-ray band and another to the optical band. There are cases that the X-ray and optical lightcurves are “achromatic”, so that they are dominated by the same emission component.

Lately, GeV afterglow was observed from several Fermi GRBs. They added more puzzles to the afterglow physics. While in the X-ray band, only a small fraction (say, 5%) of afterglow shows a single power law decay from the beginning (most others show the canonical lightcurve with the early steep decay and shallow decay components) (Evans *et al.* 2009; Liang *et al.* 2009), all the GeV afterglows show a single power law decay from the beginning (Abdo *et al.* 2009; Ghisellini *et al.* 2010; Zhang *et al.* 2011). Is this due to a selection effect, namely, only those X-ray afterglows with a single power law decay would have a bright enough GeV afterglow? One needs Fermi/LAT-Swift/BAT joint-triggered GRBs to test this idea (so that the early afterglow lightcurves in both X-ray and GeV bands are available). Currently there are two cases, *i.e.* GRB 090510 (De Pasquale *et al.* 2010) and GRB 110731A (Ackermann *et al.* 2013), both showing an achromatic single power law decay in both X-rays and GeV emission. This is consistent with the selection effect interpretation, but more cases are definitely needed to make a robust claim.

It is worth mentioning that even though multiple emission components exist in some GRBs that defy the simplest external shock model, there are indeed a good

fraction of afterglows that are “well-behaved”, namely, they seem to well follow the predictions of the simplest external forward shock model. A systematic analysis is needed to quantify the fraction of GRBs that abide by or defy the simplest models, and to study the possible differences of other observation properties of the two groups.

3 Standard model and new afterglow paradigm

The standard afterglow model invokes synchrotron emission from the external forward and (briefly) reverse shocks when the relativistic ejecta launched from the GRB engine interacts with the circumburst medium (Mészáros & Rees 1997; Sari *et al.* 1998, 1999; Dai & Lu 1998; Chevalier & Li 2000). The external shock theory is an elegant theory, since it invokes a limited number of model parameters, and has well predicted spectral and temporal properties. On the other hand, depending on many factors (*e.g.* energy injection, ambient density profile, collimation of the ejecta, forward *vs.* reverse shock dynamics, and synchrotron spectral regimes), there is a wide variety of the models. These models have distinct predictions on the afterglow decaying index, the spectral index, and the relation between them (the so-called “closure relation”), which have been widely used to interpret the rich multi-wavelength afterglow observations. Due to the page limit, we cannot discuss these models in detail. The closure relations of several widely used models during the deceleration phase have been collected in Table 1 of Zhang & Mészáros (2004), and Table 2 of Zhang *et al.* (2006). A complete thorough review of all the external shock models (including both forward and reverse shocks during the reverse shock crossing stage and self-similar deceleration stage) is being written (Gao *et al.* 2013).

The puzzling chromatic afterglow data discussed in Section 2 demands at least three emission components to account for the observations. It is encouraging to note that indeed there are three natural emission sites: 1. the traditional external forward shock; 2. an internal dissipation site in the late wind launched by the central engine; and 3. a long-lasting reverse shock due to the interaction between the late wind and the blastwave. One of the important discoveries by Swift is to realize that the GRB central engines “die hard”. The existence of late central engine activities inevitably introduces a messy system with at least these three emission sites. The challenge to understand GRB afterglow lies in identifying the contributions of various components from the data and investigating the relative importance of various emission components with the theoretical models.

4 Recent progress

So far there is no investigation that self-consistently solves this messy problem. In the following, I review several recent efforts in our group towards an understanding of the origin of broad-band afterglow.

4.1 Internal-external shock model to understand X-ray afterglow

Maxham & Zhang (2009) developed a shell model to investigate the interplay between internal shocks and the external shock. The code allows free injections of multiple mini-shells with certain distributions of energy and Lorentz factor. The shells can collide, merge, and emit photons from internal shocks. The leading shell would interact with the ambient medium and form a blast, while other shells can catch up with the blast to boost the total energy of the blast. Even though the details of the colliding processes (forward/reverse shock dynamics) are not introduced, this code can follow the general energy budget distribution in the internal shocks and in the blast, and therefore catches the essence of the internal-external shock model. By allowing multiple injection episodes, one can also reproduce X-ray flares. The general conclusion from such modeling is that X-ray flares demand late reactivation of the central engine. During the epoch with late central engine activity, the blastwave is continuously fed and therefore shows an extended shallow decay phase. One problem of this model is that given the standard forward shock parameters (ϵ_e and ϵ_B), the afterglow level is relatively bright as compared with prompt emission and X-ray flare emission. This is mostly due to the low energy dissipation efficiency of internal shocks. In order to reproduce the observed X-ray afterglow, one needs to either significantly increase the radiative efficiency of the prompt emission and X-ray flare emission (which demands a high-efficiency magnetic dissipation rather than the conventional internal shock dissipation, *e.g.* Zhang & Yan 2011), or to greatly suppress the forward shock emission (by lowering ϵ_e and ϵ_B , as is demanded by the reverse-shock dominated models (Uhm & Beloborodov 2007; Genet *et al.* 2007).

4.2 Long-lasting reverse shock model

In order to investigate the effect of a long-lasting reverse shock in more detail, Uhm *et al.* (2012) recently carried out a systematic analysis of the forward/reverse shock lightcurves within the framework of a long-lasting reverse shock model that invokes a distribution of Lorentz factor in the ejecta. By applying a Lagrangian description of the blastwave and accurately solving the blastwave dynamics, Uhm *et al.* (2012) calculated the forward and reverse shock lightcurves for a range of input ejecta stratification profiles. By comparing the light curves from the two shocks, we found that the reverse shock light curves are more sensitive to the input ejecta stratifications, and show richer features in the light curves, including steep declines, plateaus, bumps, re-brightenings, etc.. A collection of ejecta stratification profiles, blastwave dynamics, and the forward/reverse shock lightcurves are presented in Figure 1. In reality, the observed lightcurves should include contributions from the two shocks. The contribution from the reverse shock can show up if the reverse shock emission is enhanced (*e.g.* due to a higher ϵ_B from a more magnetized ejecta than the medium), or the forward shock emission is suppressed. Further modeling of the superposed light curves is needed in order to confront with the data. In any case, the results open a window to understand the puzzling afterglow data.

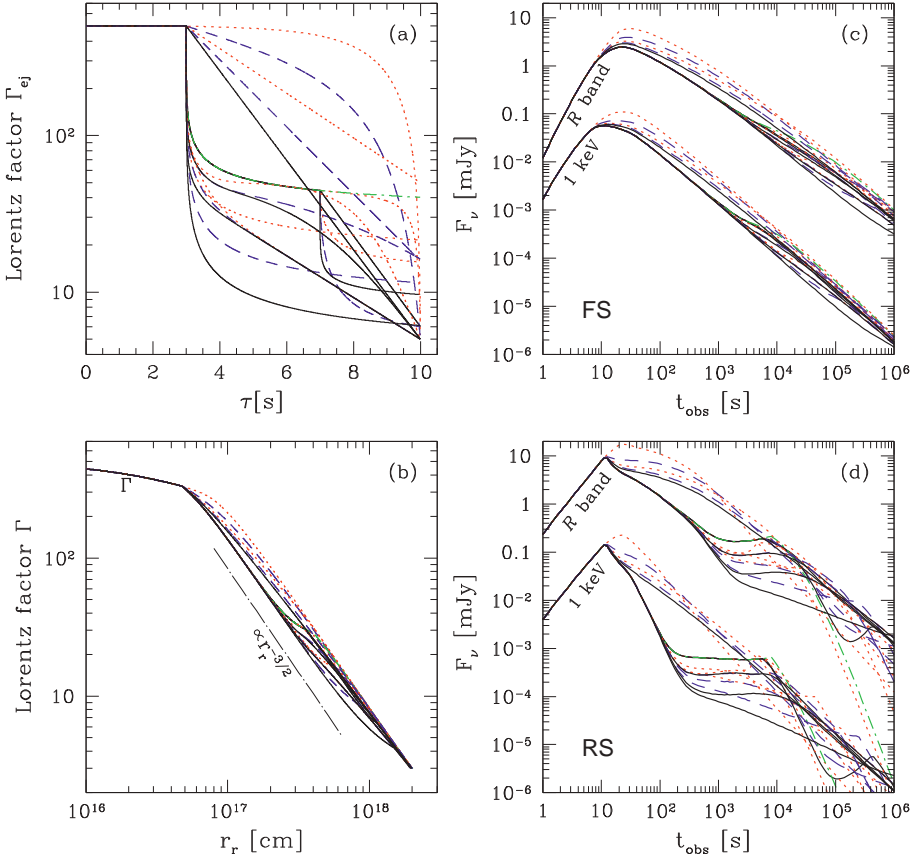


Fig. 1. Blastwave dynamics and forward/reverse shock lightcurves for 20 different models that invoke different ejecta stratification profiles. *Top left panel:* input ejecta stratification profiles; *Bottom left panel:* dynamical evolution of the blastwave; *Top right panel:* forward shock lightcurves in the X-ray and optical bands; *Bottom right panel:* reverse shock lightcurves in the X-ray and optical bands. From Uhm *et al.* (2012).

4.3 Cooling break

Applying the Lagrangian code developed by Lucas Uhm, one finds that the so-called cooling break is extremely smooth. In fact, it takes several decades in energy to approach the predicted $F_\nu \propto \nu^{-p/2}$ regime above the cooling break. Uhm & Zhang (2013) identified the key physical reason of this smooth transition, which stems from the different cooling histories of electrons accelerated at different epochs. Electrons accelerated earlier underwent a more rapid cooling early on when the magnetic field strength was much higher. This gives an additional spreading of the cooling breaks for different mini-shells. As a result, it is hard to define a global cooling break, so the slow-to-fast cooling transition takes a much longer time.

This explains the non-detection of any cooling break in 8 years of Swift data. In contrast, the injection frequency ν_m can be reasonably sharp. So whenever a sharp spectral break is observed, it should be related to particle injection rather than cooling. This result applies to a wide range of astrophysical systems involving synchrotron cooling.

4.4 Origin of GeV emission

The single-power-law decay of GeV flux of some GRBs led to the suggestion that the GeV emission is of the external forward shock origin (Kumar & Barniol Duran 2009, 2010; Ghisellini *et al.* 2010). Later studies suggest that during the prompt emission phase (when sub-MeV emission is going on), the main contribution to the GeV emission is from an internal dissipation region. Maxham *et al.* (2011) modeled the growth of blastwave during the prompt emission phase using the shell code developed earlier (Maxham & Zhang 2009), and found that the predicted external shock flux, when scaled to interpret the late GeV afterglow decay, cannot account for the flux during the prompt phase. A similar conclusion was reached independently by He *et al.* (2011) and Liu & Wang (2011) using a different approach to model individual GRBs. Observationally, the GeV peak is found to coincide with one of the spikes of the sub-MeV lightcurve, suggesting its internal origin (Zhang *et al.* 2011). The identification of the internal origin of GeV emission during the prompt emission phase is essential to constrain the emission radius through the two-photon pair production opacity constraint, which is found to be much larger than the photosphere radius (Zhang & Pe'er 2009). This disfavors the photosphere origin of the observed “Band function” spectrum of GRBs, and suggests that the composition of the ejecta is still magnetically dominated in the emission region (Zhang & Yan 2011).

5 Summary

The observations of GRB afterglow have entered a full multi-wavelength era. Even though the standard afterglow model works for some GRBs, a good fraction of GRBs show a chromatic behavior that cannot be interpreted within the standard model. The existence of X-ray flares demand late central engine activities, which inevitably introduces two more emission sites (the internal dissipation site and the reverse shock). This introduces a new paradigm of GRB afterglow, and greatly complicates GRB afterglow modeling.

I thank stimulative collaborations with Z. Lucas Uhm, He Gao, Amanda Maxham, Bin-Bin Zhang, and En-Wei Liang on the topics discussed in this review. This work is partially supported by NSF AST-0908362, NASA NNX10AD48G, and a Cheung Kong Scholar fellowship in Peking University, China.

References

- Abdo, A.A., Ackermann, M., Arimoto, M., *et al.*, 2009, Science, 323, 1688
- Ackermann, M., Ajello, M., Asano, K., *et al.*, 2013, ApJ, 763, 71

- Akerlof, C., Balsano, R., Barthelmy, S., *et al.*, 1999, *Nature*, 398, 400
- Barthelmy, S.D., Cannizzo, J.K., Gehrels, N., *et al.*, 2005, *ApJ*, 635, L133
- Burrows, D.N., Romano, P., Falcone, A., *et al.*, 2005, *Science*, 309, 1833
- Cannizzo, J.K., & Gehrels, N., 2009, *ApJ*, 700, 1047
- Chevalier, R.A., & Li, Z.-Y., 2000, *ApJ*, 536, 195
- Chincarini, G., Moretti, A., Romano, P., *et al.*, 2007, *ApJ*, 671, 1903
- Costa, E., Frontera, F., Heise, J., *et al.*, 1997, *Nature*, 387, 783
- Dai, Z.G., & Lu, T., 1998, *MNRAS*, 298, 87
- De Pasquale, M., Schady, P., Kuin, N.P.M., *et al.*, 2010, *ApJ*, 709, L146
- Evans, P.A., Beardmore, A.P., Page, K.L., *et al.*, 2009, *MNRAS*, 397, 1177
- Fan, Y.Z., & Wei, D.M., 2005, *MNRAS*, 364, L42
- Fox, D.W., Price, P.A., Soderberg, A.M., *et al.*, 2003, *ApJ*, 586, L5
- Frail, D.A., Kulkarni, S.R., Nicastro, L., Feroci, M., & Taylor, G.B., 1997, *Nature*, 389, 261
- Frail, D.A., Kulkarni, S.R., Sari, R., *et al.*, 2001, *ApJ*, 562, L55
- Gao, H., Lei, W.-H., Zou, Y.-C., Wu, X.-F., & Zhang, B., 2013, *New Astron. Rev.*, in preparation
- Gehrels, N., Chincarini, G., Giommi, P., *et al.*, 2004, *ApJ*, 611, 1005
- Genet, F., Daigne, F., & Mochkovitch, R., 2007, *MNRAS*, 381, 732
- Ghisellini, G., Ghirlanda, G., Nava, L., & Celotti, A., 2010, *MNRAS*, 403, 926
- Ghisellini, G., Ghirlanda, G., Nava, L., & Firmani, C., 2007, *ApJ*, 658, L75
- Harrison, F.A., Bloom, J.S., Frail, D.A., *et al.*, 1999, *ApJ*, 523, L121
- He, H.-N., Wu, X.-F., Toma, K., Wang, X.-Y., & Mészáros, P., 2011, *ApJ*, 733, 22
- Holland, S.T., Weidinger, M., Fynbo, J.P.U., *et al.*, 2003, *AJ*, 125, 2291
- Kobayashi, S., 2000, *ApJ*, 545, 807
- Kumar, P., & Barniol Duran, R., 2009, *MNRAS*, 400, L75
- Kumar, P., & Barniol Duran, R., 2010, *MNRAS*, 409, 226
- Kumar, P., Narayan, R., & Johnson, J.L., 2008, *MNRAS*, 750
- Kumar, P., & Panaiteescu, A., 2000, *ApJ*, 541, L51
- Lazzati, D., & Perna, R., 2007, *MNRAS*, 375, L46
- Liang, E.-W., Lü, H.-J., Hou, S.-J., Zhang, B.-B., & Zhang, B., 2009, *ApJ*, 707, 328
- Liang, E.-W., Racusin, J.L., Zhang, B., Zhang, B.-B., & Burrows, D.N., 2008, *ApJ*, 675, 528
- Liang, E.-W., Zhang, B.-B., & Zhang, B., 2007, *ApJ*, 670, 565
- Lipkin, Y.M., Ofek, E.O., Gal-Yam, A., *et al.*, 2004, *ApJ*, 606, 381
- Liu, R.-Y., & Wang, X.-Y., 2011, *ApJ*, 730, 1
- Lyons, N., O'Brien, P.T., Zhang, B., *et al.*, 2010, *MNRAS*, 402, 705
- Maxham, A., & Zhang, B., 2009, *ApJ*, 707, 1623
- Maxham, A., Zhang, B.-B., & Zhang, B., 2011, *MNRAS*, 415, 77
- Mészáros, P., & Rees, M.J., 1997, *ApJ*, 476, 232
- Mészáros, P., & Rees, M.J., 1999, *MNRAS*, 306, L39
- Metzger, B.D., Giannios, D., Thompson, T.A., Bucciantini, N., & Quataert, E., 2011, *MNRAS*, 413, 2031

- Nousek, J.A., Kouveliotou, C., Grupe, D., *et al.*, 2006, ApJ, 642, 389
O'Brien, P.T., Willingale, R., Osborne, J., *et al.*, 2006, ApJ, 647, 1213
Panaiteescu, A., Mészáros, P., Burrows, D., *et al.*, 2006a, MNRAS, 369, 2059
Panaiteescu, A., Mészáros, P., Gehrels, N., Burrows, D., & Nousek, J., 2006b, MNRAS, 366, 1357
Sari, R., & Piran, T., 1999a, ApJ, 517, L109
Sari, R., & Piran, T., 1999b, ApJ, 520, 641
Sari, R., Piran, T., & Halpern, J.P., 1999, ApJ, 519, L17
Sari, R., Piran, T., & Narayan, R., 1998, ApJ, 497, L17
Tagliaferri, G., Goad, M., Chincarini, G., *et al.*, 2005, Nature, 436, 985
Troja, E., Cusumano, G., O'Brien, P.T., *et al.*, 2007, ApJ, 665, 599
Uhm, Z.L., & Beloborodov, A.M., 2007, ApJ, 665, L93
Uhm, Z.L., Zhang, B., Hascoët, R., *et al.*, 2012, ApJ, 761, 147
Uhm, Z.L., & Zhang, B., 2013, ApJ, submitted [[arXiv:1301.0291](https://arxiv.org/abs/1301.0291)]
van Paradijs, J., Groot, P.J., Galama, T., *et al.*, 1997, Nature, 386, 686
Wijers, R.A.M.J., Rees, M.J., & Mészáros, P., 1997, MNRAS, 288, L51
Yu, Y.-W., Cheng, K.S., & Cao, X.-F., 2010, ApJ, 715, 477
Zhang, B., Fan, Y.Z., Dyks, J., *et al.*, 2006, ApJ, 642, 354
Zhang, B., Kobayashi, S., & Mészáros, P., 2003, ApJ, 595, 950
Zhang, B., & Mészáros, P., 2004, Int. J. Mod. Phys. A, 19, 2385
Zhang, B., & Pe'er, A., 2009, ApJ, 700, L65
Zhang, B., & Yan, H., 2011, ApJ, 726, 90
Zhang, B.-B., Liang, E.-W., & Zhang, B., 2007, ApJ, 666, 1002
Zhang, B.-B., Zhang, B., Liang, E.-W., *et al.*, 2011, ApJ, 730, 141

THEORETICAL ASPECTS OF THE FIREBALL SCENARIO

A. Bret¹, A. Stockem², E. Pérez-Álvaro¹, F. Fiúza², C. Ruyer³,
L. Gremillet⁵, R. Narayan⁴ and L.O. Silva²

Abstract. Collisionless shocks are a key ingredient of the Fireball scenario. Yet, their formation from the encounter of two collisionless plasma shells is not understood from first principles. When the shells interpenetrate, the overlapping region turns unstable, triggering the shock formation. As a first step towards a microscopic understanding of the process, we analyze here in details the initial instability phase. On the one hand, 2D relativistic PIC simulations are performed where two symmetric initially cold pair plasmas collide. On the other hand, the instabilities at work are analyzed, as well as the field at saturation and the seed field which gets amplified. For mildly relativistic motions and onward, Weibel modes with $\omega = 0 + i\delta$ govern the linear phase. We derive an expression for the duration of the linear phase in reasonable agreement with the simulations.

1 Introduction

The Fireball scenario for Gamma-Rays-Bursts (Nakar 2007) relies on shock particle acceleration (Blandford & Ostriker 1978), where the shock arises from the encounter of two ultra-relativistic plasma blobs ejected from a central engine.

The formation of a shock following the collision of two plasma shells is now numerically well documented (Spitkovsky 2008), and subsequent particle acceleration has been observed in simulations (Nishikawa *et al.* 2005). In addition, shock generation through counter-streaming plasmas has already been observed in laboratory (Joseph *et al.* 2011).

¹ ETSI Industriales, Universidad de Castilla-La Mancha, 13071 Ciudad Real, Spain

² GoLP/Instituto de Plasmas e Fusão Nuclear, Laboratório Associado, Instituto Superior Técnico, Lisboa, Portugal

³ CEA, DAM, DIF, 91297 Arpajon, France

⁴ Harvard-Smithsonian Center for Astrophysics, 60 Garden Street, MS-51 Cambridge, MA 02138, USA

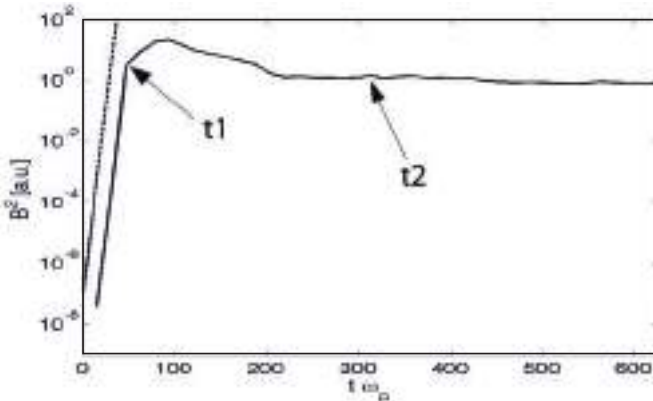


Fig. 1. Growth of the magnetic energy integrated over the transverse direction in the overlapping region. The dashed line is the theoretical growth-rate. The initial Lorentz factor was $\gamma_0 = 25$. All the field growth plots look qualitatively the same until $\gamma_0 = 10^4$. The saturation time τ_s is t_1 . By this time, the density in the overlapping region is still twice the shells density. The density jump ~ 3.3 times then builds up, and the shock is formed around $t = t_2$. The field at saturation is $B(\tau_s)$.

Although the full shock formation process has been now repeatedly observed, a first principle understanding of the very birth of the shock is still lacking. Such an understanding could provide an accurate timing of the shock formation time, and constraints the conditions required to form it in the first place. Whether they are in the lab, in a computer or in the vicinity of a supernova, it should be possible to separate the scenario leading to the shock into two phases. In the first phase, plasma shells make contact, then overlap, and the overlapping region turns unstable. An instability grows and saturates. At this junction, the total density in the overlapping region is roughly the sum of each plasma density. A second phase is therefore needed during which nonlinear processes pick-up the system from the end of the linear phase, and build-up the Rankine-Hugoniot expected density jump near the borders of the interpenetrating shells.

The present paper is concerned with the first of these two phases. The collision of two identical cold relativistic pair plasmas has been simulated in 2D with the PIC Code OSIRIS. This setup has been chosen for its simplicity, allowing for a neat comparison with theory as the only free parameter is the initial Lorentz factor of the shells γ_0 . Periodic boundary conditions are applied in the transverse direction. The evolution of the magnetic field in the overlapping region is displayed on Figure 1 for $\gamma_0 = 25$. The saturation time τ_s (t_1 on the figure) is defined as the end of the exponential growth of the field energy integrated over the overlapping region. The field at saturation is simply $B(\tau_s)$.

As it amplifies a seed field from its initial fluctuation value to saturation, the instability governs this first phase of the shock formation for a time τ_s that we labeled “saturation time”. A theoretical determination of this time which

represents a lower bound to the shock formation time, is the main result of this paper.

2 Instability analysis

We here deal with the first phase of the shock formation, namely the instability of the overlapping region. Indeed, if counter streaming collisionless plasmas were not unstable, they would simply go through each other without anything happening.

The full unstable \mathbf{k} spectrum has been analyzed long ago in the cold regime, where a shell is much denser than the other (Watson *et al.* 1960). These early results were recently generalized to the hot symmetric case (Bret & Deutsch 2005; Bret *et al.* 2010). For wave-vectors aligned with the flow, we find two-stream unstable modes. Then, for wave-vectors normal to the flow, we find the filamentation, or Weibel, instability. Finally, modes propagating at arbitrary angle with the flow are also unstable (Bret *et al.* 2004). As the two plasmas penetrate each other, all the modes are excited. But the fastest growing one quickly overcomes the other, and shapes the linear phase. For the case we consider, a calculation of the growth-rate for every possible \mathbf{k} 's shows that only oblique and filamentation instabilities can dominate. The transition from oblique to filamentation occurs for $\gamma_0 = \sqrt{3/2}$ (Bret *et al.* 2012). Beyond this threshold, filamentation governs the interaction with a growth rate,

$$\frac{\delta}{\omega_p} = \frac{v_0}{c} \sqrt{\frac{2}{\gamma_0}} \sim \sqrt{\frac{2}{\gamma_0}}. \quad (2.1)$$

Comparing this value with the growth of the field observed in the overlapping region results in a very satisfactory agreement, as evidenced in Figure 1. We also verified that the Weibel/Oblique transition does occur around $\gamma_0 = \sqrt{3/2}$.

Noteworthily, it has been known for long that a flow aligned magnetic field can cancel the Weibel instability. But recent works performed in the cold regime proved the instability can never be canceled this way, providing the field is not perfectly aligned (Bret & Pérez-Álvaro 2011).

3 Saturation time

Knowing the growth-rate (2.1) should allow for an accurate timing of the linear phase. Assuming that the instability amplifies a seed field of amplitude B_i up to a saturation level B_s , we can write for the saturation time τ_s ,

$$B_f = B_i e^{\delta \tau_s} \Rightarrow \tau_s = \frac{1}{2\delta} \ln \left(\frac{B_f^2}{B_i^2} \right), \quad (3.1)$$

where, for convenience, we consider the field energy B^2 ratio, instead of the field itself. Determining the saturation time amounts then to determine the initial and final fields.

One way to derive the value of the saturation field $B_f = B(\tau_s)$, consists in stating that the field grows exponentially as long as it is small enough for the system to fit the linear approximation. Since a field B_f affects particles on a time scale given by the cyclotron frequency, this implies Medvedev & Loeb (1999),

$$\frac{qB_f}{\gamma_0 mc} = \delta \Rightarrow B_f = \frac{\gamma_0 m}{q} \delta c. \quad (3.2)$$

Accounting in addition for the growth-rate expression (2.1) gives,

$$B_f^2 = 2\gamma_0 \left(\frac{mc\omega_p}{q} \right)^2, \quad (3.3)$$

which fits very well the values observed in the simulations.

Regarding the initial field amplitude, the idea is that the instability mechanism picks up a seed field from the spontaneous fluctuations of the system, and amplifies it. Various authors have been dealing with plasma fluctuations (Sitenko 1967), and the ability of PIC simulations to correctly render them has been checked by (Dieckmann *et al.* 2004) in the non-relativistic electrostatic case. Inserting the resulting B_i in Equation (3.1) for the saturation time,

$$\tau\omega_p = \frac{\sqrt{\gamma_0}}{2\sqrt{2}} \ln \left[\frac{n(c/\omega_p)^3}{\sqrt{2}\pi} \frac{\mu\gamma_0^{3/2}}{\frac{15}{4\gamma_0} + \mu \ln \left[\frac{1+4\gamma_0/\mu}{1+\gamma_0/4\mu} \right]} \right], \quad \mu = \frac{mc^2}{k_B T}, \quad (3.4)$$

where n is the plasma density.

Simulations have been run with nearly cold colliding plasma shells, with thermal velocity $\mu = 10^6$. The time to reach saturation observed from the simulations is compared on Figure 2 with Equation (3.4). Clearly, the scaling is correct while a factor 1.7 is consistently lacking.

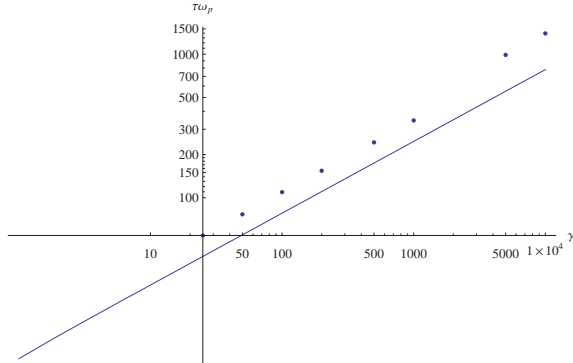


Fig. 2. Saturation time in ω_p units measured from simulations, circles, vs. Equation (3.4).

4 Conclusion

This work represents a first step towards a first principles understanding of a collisionless shock formation. The equation derived already represents a lower bound to the shock formation time. Multiplied by c , it just tells how large the colliding plasma shells must be, if a shock is to be formed.

Future works focused on the second phase of the shock formation, namely the building-up of the density jump, should provide a theory of the full process hopefully able to constraint progenitors parameters in GRB's physics.

References

- Nakar, E., 2007, Phys. Rep., 442, 166
Blandford, R., & Ostriker, J., 1978, ApJ, 221, L29
Spitkovsky, A., 2008, ApJ, 682, L5
Nishikawa, K.-I., Hardee, P., Richardson, G., *et al.*, 2005, ApJ, 622, 927
Joseph, J.A., Thomas, J.E., Kulkarni, M., *et al.*, 2011, Phys. Rev. Lett., 106, 150401
Faïnberg, Y.B., Shapiro, V.D., & Shevchenko, V., 1970, Soviet Phys. JETP, 30, 528
Watson, K.M., Bludman, S.A., & Rosenbluth, M.N., 1960, Phys. Fluids, 3, 741
Bret, A., & Deutsch, C., 2005, Phys. Plasmas, 12, 082704
Bret, A., Gremillet L., & Dieckmann, M.E., 2010, Phys. Plasmas, 17, 120501
Bret, A., Firpo M.-C., & Deutsch, C., 2004, Phys. Rev. E, 70, 046401
Bret, A., Stockem A., Fiuza F., *et al.*, 2012, Submitted to Phys. Plasmas
Bret, A., & Pérez-Álvaro, E., 2011, Phys. Plasmas, 18, 080706
Medvedev, M.V., & Loeb, A.A., 1999, ApJ, 526, 697
Sitenko, A.G., 1967, Electromagnetic Fluctuations in Plasma (Academic Press, New York)
Dieckmann, M.E., Ynnerman, A., Chapman, S.C., *et al.*, 2004, Phys. Scripta, 69, 456

SIMILARITIES: GRB 940217, GBR 090926A AND GRB 980923

J.R. Sacahui¹, M.M. González¹, N. Fraija¹, J.L. Ramirez¹ and W.H. Lee¹

Abstract. Few GRBs clearly present distinct High-Energy (HE) component that evolve independent of the usual Band function that describes the prompt keV-emission. This component can be long or short lasting compared to the burst duration. However, most of models only explain the long duration HE component. We have developed a leptonic model on the external shock framework to describe the HE components. We propose that the short HE component that falls in the MeV regime in coincidence with the prompt phase and, the second long lasting GeV-emission could be understood as synchrotron self-Compton (SSC) emission from the reverse and forward shock respectively. This model requires a magnetized jet and a reverse shock in the thick shell case. This model already has been proven in GRB 980923 and GRB 090926A, the former with a short duration MeV-component and the latter with both long GeV- and short MeV- HE components. All fluxes, energies and durations are consistent with the observed values. Here, we apply this model to GRB 940217 that presented similarities with GRB 090926A and GRB 980923.

1 Introduction

Photons with energies ≥ 100 MeV have been detected in some long and short gamma-ray bursts (GRBs). In some bursts, these photons arrived within the prompt emission as in GRB 941017 (Hurley *et al.* 1994; Winkler *et al.* 1995), but they can also be delayed as in GRB 090926A (Ackerman *et al.* 2011) or last even much shorter than the prompt emission as in GRB 980923 (González *et al.* 2012).

General hadronic (Asano *et al.* 2009; Dermer & Razzaque 2010) and leptonic (Papathanassiou & Meszaros 1996; Sari *et al.* 1996) interpretations have been discussed to explain these photons. Within the hadronic models, the two most investigated scenarios are synchrotron radiation from high-energy (HE) protons accelerated in the relativistic jet and photo-pion decay from $p\gamma$ interactions where

¹ Instituto de Astronomía, UNAM, 04510, México; e-mail: jsacahui@astro.unam.mx;
magda@astro.unam.mx; nfraija@astro.unam.mx; joselo@ciencias.unam.mx;
wlee@astro.unam.mx

protons are accelerated at the shocks and photons come from the prompt emission or an external radiation field. On leptonic models the HE emission is proposed to be IC, SSC and synchrotron emission of accelerated electrons in internal (Panaitescu & Meszaros 2000; Papathanassiou & Meszaros 1996) or external (Sari *et al.* 2001; Wang *et al.* 2001a) shocks.

GRB 980923 (González *et al.* 2012) and GRB 090926A (Ackerman *et al.* 2011) presented a short MeV-peak and a keV-tail with longer duration than the prompt emission. The MeV-peak have not been reported in other bursts. GRB 090926A showed a long lasting GeV-component. We have pointed (Fraija *et al.* 2013) some similarities and differences between these bursts and developed a model (Fraija *et al.* 2012a,b; Sacahui *et al.* 2012) to described the HE components apparent in both bursts.

Fraija *et al.* (2012) and Sacahui *et al.* (2012) described for GRB 980923 and GRB 090926A respectively, the short MeV-peak in both bursts and the long-lasting GeV high-component in GRB 090926A as SSC emission from external shocks. Furthermore, they explored synchrotron emission in a unified way to explain the observed tail at lower energies. In both GRBs, different equipartition parameters were considered for the reverse and forward shocks ($\epsilon_{B,r} \neq \epsilon_{B,f}$ and $\epsilon_{e,r} \neq \epsilon_{e,f}$), leading to a highly magnetized ejecta.

On the other hand, GRB 940217 was one of the longest and also the most energetic burst seen by the Compton Telescope (COMPTEL) (Winkler *et al.* 1995). It was also detected, the Energetic Gamma-Ray Experiment Telescope (EGRET) (Winkler *et al.* 1995) and Interplanetary Network (Ulysses/Burst and Transient Source Experiment, BATSE) (Hurley *et al.* 1994). The duration of the bursts given by T90 was 162 sec as reported by Winkler *et al.* (1995). The total fluence above 20 keV was $(6.6 \pm 2.7) \times 10^{-4}$ erg cm $^{-2}$, as observed by BATSE large area detectors (Hurley *et al.* 1994). The EGRET spark-chamber recorded 10 photons while the main emission was in progress. Following this, an additional 18 photons were recorded for \sim 5400 s, including an 18-GeV photon \sim 4500 s after the main emission had ended. The COMPTEL Telescope observed Winkler *et al.* (1995) GRB 940217 in the energy range of 0.3–30 MeV. Five episodes were identified in the reported light curve. In particular, a fifth episode or peak at UT = 83088.75s (burst trigger at UT = 82962 s) with a duration of 18 s is observed only at energies higher than 30 MeV. This short peak was described as a simple power law with a spectral index of $1.78^{+0.52}_{-0.38}$ (Winkler *et al.* 1995).

In this work we apply the model presented by Fraija *et al.* (2012) and Sacahui *et al.* (2012) on GRB 940217 to describe its high-energy components. We introduce standard values for the input parameters and obtain break energies, fluxes, duration, etc. in agreement with the observed values.

2 External shock leptonic emission

We use the model described by Fraija *et al.* (2012) and Sacahui *et al.* (2012). Here, we present a brief summary of the model. For a detailed description of the model see (Fraija *et al.* 2012a; Sacahui *et al.* 2012).

In the external shock model, GRB emission is produced when an expanding relativistic shell interacts with the circumburst medium producing forward and reverse shocks. In addition to the dynamics of the forward shock, a reverse shock propagating back into the shell is expected, which would decelerate or not the shell depending on the evolution of the reverse shock: thick or thin shell respectively. For the forward shock, we assume that electrons are accelerated to a power-law distribution of Lorentz factors γ_e with a minimum Lorentz factor γ_m : $N(\gamma_e) d\gamma_e \propto \gamma_e^{-p} d\gamma_e$ where $\gamma_e \geq \gamma_m$ and $\epsilon_{e,f}$ and $\epsilon_{B,f}$ are the constant fractions of the shock energy that is transferred into the electrons and the magnetic field, respectively. These equipartition parameters are given by: $\epsilon_{e,f} = U_e / (4\gamma_f^2 \eta_f m_p)$ and $\epsilon_{B,f} = B_f^2 / (32\pi \gamma_f^2 \eta_f m_p)$ where γ_f is the bulk Lorentz factor and η_f is the density of the surrounding medium.

Given the cooling electron Lorentz factor $\gamma_{e,c} = 3m_e(1+z)/(16\epsilon_{B,f}\sigma_T m_p t_{d,f} \Gamma_f^3 \eta_f)$ and the deceleration time $t_{d,f} = (1+z)(3E/32\pi m_p \eta_f \Gamma_f^8)^{1/3}$, the highest break energy and maximum flux of the synchrotron photons radiated by electrons at a distance D from the source in natural units are given by,

$$\begin{aligned} E_{m,f} &\sim \frac{2^{5/2} \pi^{1/2} q_e m_p^{5/2} (p-2)^2}{m_e^3 (p-1)^2} (1+z)^{-1} \epsilon_{e,f}^2 \epsilon_{B,f}^{1/2} n_f^{1/2} \gamma_f^4 \\ F_{max,f} &\sim \frac{m_e \sigma_T}{36 \pi m_p^{1/2} q_e} (1+z) \epsilon_{B,f}^{1/2} n_f^{1/2} D^{-2} E \end{aligned}$$

where E is the isotropic energy. Now, electrons in the forward shock region can upscatter the synchrotron photons in accordance to the following equations: $E_{m,f}^{(SSC)} \sim \gamma_m^2, E_{m,f}$. Then the SSC break energy is given by,

$$E_{m,f}^{(SSC)} \sim \frac{6 q_e m_p^{15/4}}{2^{5/4} (3\pi)^{1/4} m_e^5} (1+z)^{5/4} \epsilon_{e,f}^4 \epsilon_{B,f}^{1/2} n_f^{-1/4} E^{3/4} t_f^{-9/4}.$$

When the reverse shock crosses the shell it heats up and accelerates electrons. In the thick shell case the reverse shock becomes relativistic during the propagation and the shell is significantly decelerated. The crossing time of the reverse shock might be much smaller as long as the σ magnetization parameter increases, thus for $\sigma \sim 1$, the time for the short MeV-peak would be $t_d \sim T_{90}/6$, which could be in agreement for bright GRBs according to Lamb *et al.* (2005).

For the reverse shock the maximum flux, break energy of synchrotron and SSC break energy are given by,

$$\begin{aligned} E_{m,r} &\sim \frac{4 \pi^{1/2} q_e m_p^{5/2} (p-2)^2}{m_e^3 (p-1)^2} (1+z)^{-1} \epsilon_{e,r}^2 \epsilon_{B,r}^{1/2} \Gamma_r^2 n_r^{1/2} \\ F_{max,r} &\sim \frac{m_e \sigma_T}{2^{3/4} 36 \pi m_p^{1/2} q_e} (1+z)^{7/4} \epsilon_{B,r}^{1/2} n_r^{1/4} D^{-2} E^{5/4} \Gamma_r^{-1} T_{90}^{-3/4} \\ E_{m,r}^{(SSC)} &\sim \frac{2^{21/4} \pi^{3/4} m_p^{13/4} (p-2)^4}{3^{1/4} m_e^5 (p-1)^4} (1+z)^{-7/4} \epsilon_{e,r}^4 \epsilon_{B,r}^{1/2} \Gamma_r^4 n_r^{3/4} E^{-1/4} T_{90}^{3/4}, \end{aligned}$$

we have used the equations given above to calculate the duration of the HE components, their break energies and the energy fluxes associated to the break energies. The parameters used for forward and reversed shocks are given in Table 1. A search in the parameter space to look for possible solutions was performed. The calculated values are given in Table 2, for comparison the observed maximum energies, the associated energy fluxes and the durations of the components are also given. We also show the solutions for GRB 090926A and GRB 980923 as reported by Fraija *et al.* (2012) and Sacahui *et al.* (2012) for comparison.

Table 1. Parameters used.

GRBs	940217	980923	090926A
Forward shock			
$\epsilon_{B,f}$	10^{-4}	10^{-5}	$10^{-4.3}$
$\epsilon_{e,f}$	0.35	0.95	0.1
n_f (cm $^{-3}$)	10	1	10
γ_f	600	600	600
Reverse shock			
$\epsilon_{B,r}$	0.125	0.125	0.125
$\epsilon_{e,r}$	0.35	0.6	0.65
n_r (cm $^{-3}$)	10	10	10
γ_r	1000	1000	1000

Table 2. Calculated quantities using the model described in the text. When available, the observed values are given.

GRBs	940217	980923	090926A
Quantities	calculated (observed)	calculated (observed)	calculated (observed)
Forward shock			
$E_{m,f}$ (keV)	175.5 (–)	78.9 (128.5)	10.13 (~50)
$E_{m,f}^{(SSC)}$ (GeV)	10.9 (~18)	– (–)	18.4 (~10)
Duration of	1000 (~5600)	– (–)	100 (~100)
the component (s)			
$(\nu F_{\nu \text{max}})^{SSC}$ (erg cm $^{-2}$ s $^{-1}$)	2.52×10^{-6} (~ 10^{-6})	1.2×10^{-7} (~ 10^{-6})	1.09×10^{-6} (~ 10^{-6})
Reverse shock			
$E_{m,r}$ (eV)	47.9 (–)	0.14 (–)	0.17 (–)
$E_{m,r}^{(IC)}$ (MeV)	34.8 (≥ 30)	427.2 (≥ 150)	414.3 (400)
Duration of	27 (~7)	6 (~2)	6 (~1)
the component (s)			
$(\nu F_{\nu \text{max}})^{SSC}$ (erg cm $^{-2}$ s $^{-1}$)	3.34×10^{-7} ($\leq \times 10^{-6}$)	2.2×10^{-6} (~ 10^{-6})	8.2×10^{-6} (~ 10^{-6})

3 Results and discussion

The parameters used to describe these components are similar to the ones found for both GRB 980923 (Fraija *et al.* 2012a,b) and GRB 090926A (Fraija *et al.* 2012c; Sacahui *et al.* 2012), as expected because of the similarities in the observables (spectral index, energy ranges, etc.). Our model is very dependent on the value of $\epsilon_{B,r} = 0.125$ implying a value of the magnetization parameter of $\sigma \sim 1$ and therefore a presence of a highly magnetized jet. This high degree of magnetization gives rise to a shorter duration (as compared with the burst duration) of the emission at the reverse shock in the thick shell case. The parameters used (see Table 1) to describe the observations are typical for GRBs. The current model accounts for many characteristics of the bursts: energies, spectral indices, fluxes, durations of the components in a unified manner.

In summary, we have presented a leptonic model based on external shocks to describe the short MeV- peak and longer lasting GeV emission in a unified manner for GRB 940217 as done before for GRB 980923 and GRB 090926A. These bursts seem to form a subset of bursts with a same dynamic at the jet and a magnetized ejecta.

This work is partially supported by DGAPA-UNAM (Mexico) Project No. IN105211, IN110212 and Conacyt Project No. 103520.

References

- Ackerman, M., Ajello, M., Asano, K., *et al.*, 2009, ApJ, 729, 114
- Asano, K., Guiriec, S., & Meszaros P., 2009, ApJ, 705, L191
- Dermer, C.D., & Razzaque, S., 2010, ApJ, 724, 1366
- Fraija, N., Gonzalez, M.M., & Lee, W.H., 2012, ApJ, 751, 33
- Fraija, N., Gonzalez, M.M., & Lee, W.H., 2012 [[arXiv:1110.6421](https://arxiv.org/abs/1110.6421)]
- Fraija, N., Gonzalez, M.M., Sacahui, J.R., & W.H. Lee, 2012, PoS GRB 2012, 27
- Fraija, N., Gonzalez, M.M., Sacahui, J.R., *et al.*, 2013, in preparation
- González, M.M., Sacahui, J.R., Ramirez, J.R., *et al.*, 2012, ApJ, 755, 140
- Hurley, K., Dingus, B.L., Mukherjee, R., *et al.*, 1994, Nature, 372, 652
- Lamb, D.Q., Donaghy, T.Q., & Graziani, C., 2005, ApJ, 620, 355
- Panaitescu, A., & Meszaros, P., 2000, ApJ, 544, L17
- Papathanassiou, H., & Meszaros, P., 1996, ApJ, 471, L91
- Sacahui, J.R., Fraija, N., Gonzalez, M.M., *et al.*, 2012, ApJ, 755, 127
- Sari, R., Narayan, R., & Piran, T., 1996, ApJ, 473, 204
- Sari, R., & Esin, A.A., 2001, ApJ, 548, 787
- Wang, X.Y., Dai, Z.G., & Lu, T., 2001, ApJ, 546, L33
- Winkler, C., Bennett, K., Hanlon, L.O., *et al.*, 1994, Ap&SS, 231, 153

Chapter VII.

Short GRBs

MULTI-WAVELENGTH OBSERVATIONS OF SHORT-DURATION GAMMA-RAY BURSTS: RECENT RESULTS

D.A. Kann^{1,2,3}

Abstract. The number of detections as well as significantly deep non-detections of optical/NIR afterglows of Type I (compact-object-merger population) Gamma-Ray Bursts (GRBs) has become large enough that statistically meaningful samples can now be constructed. I present within some recent results on the luminosity distribution of Type I GRB afterglows in comparison to those of Type II GRBs (collapsar population), the issue of the existence of jet breaks in Type I GRB afterglows, and the discovery of *dark* Type I GRBs.

1 Introduction

Similar to 1997 for Type II (long-duration, collapsar population) GRBs⁴, the advent of the *Swift* satellite (Gehrels *et al.* 2004) in the year 2005 saw the discovery of Type I GRB afterglows and their placement within the cosmological context (Gehrels *et al.* 2005; Hjorth *et al.* 2005; Fox *et al.* 2005; Berger *et al.* 2005). In the following seven years, over 50 Type I GRBs have been precisely localized by *Swift* BAT and XRT, and many of these have either detected optical afterglows⁵, or at least significantly deep limits thereon. Host-galaxy follow-up has also yielded a significant number of redshifts for these events.

¹ Max-Planck-Institut für extraterrestrische Physik, Giessenbachstraße, 85748 Garching, Germany; e-mail: kann@tls-tautenburg.de

² Universe Cluster, Technische Universität München, Boltzmannstraße 2, 85748 Garching, Germany; e-mail: kann@tls-tautenburg.de

³ Thüringer Landessternwarte Tautenburg, Sternwarte 5, 07778 Tautenburg, Germany; e-mail: kann@tls-tautenburg.de

⁴In this work, we follow the classification scheme detailed in Zhang *et al.* (2009), which labels GRBs associated with the core-collapse of massive stars “Type II” and those which are not (but are likely associated with the mergers of compact objects) “Type I”. This classification is independent of duration.

⁵A few Type I GRBs have also been detected at radio wavelengths (Berger *et al.* 2005; Soderberg *et al.* 2006) and in very high-energy gamma-rays during and shortly after the prompt emission (Abdo *et al.* 2010; Ackermann *et al.* 2010).

In the last years, a multitude of results on Type I GRB afterglows have been published. In these proceedings, we wish to focus on three issues: The luminosity of Type I GRB afterglows, the existence and detectability of jet breaks, and *dark* Type I GRBs.

2 The luminosity of Type I GRB afterglows vs. those of Type II GRBs

In two papers (Kann *et al.* 2006, 2010), we studied large samples of Type II GRB afterglows, with one aspect we focused on being the luminosity of the afterglows. Knowledge of the redshift, the rest-frame dust extinction and the intrinsic spectral slope allows a shift of the afterglow light curve to any redshift, we choose $z = 1$ as a reference system to compare the afterglows. In Kann *et al.* (2011), we followed up with a study of all Type I GRB afterglows with detections or significantly deep upper limits up to the beginning of 2010, and compared these afterglows with our Type II GRB sample⁶ (adding three more Type II GRBs in this paper to the sample). Since the publication of Kann *et al.* (2011), we have undertaken additional studies using GROND (Greiner *et al.* 2008), focusing on the post-break evolution of the short-duration Type II GRB 090426 (Nicuesa Guelbenzu *et al.* 2011), the extremely luminous Type I GRB 090510 (Nicuesa Guelbenzu *et al.* 2012a) and a large sample of Type I GRBs with GROND afterglow follow-up (Nicuesa Guelbenzu *et al.* 2012b).

In Figures 1 and 2, we plot our afterglow light curve samples. Hereby, the Type II GRB afterglows form a gray “background” which we will not discuss further. We divide our Type I GRB sample into four different subsamples, depending on whether an optical afterglow has been discovered or not, and whether we consider the redshift of the GRB secure, or if it is insecure or just estimated (see Kann *et al.* 2011 for more details).

Already from Figure 1, it is clear that Type I GRB afterglows are generally fainter than those of Type II GRBs. In the figure, we highlight two events, GRB 090426 and GRB 090927 (Nicuesa Guelbenzu *et al.* 2011, 2012b) which had short durations, under or on the classic 2 s dividing line (Kouveliotou *et al.* 1993), but which are considered to be Type II GRBs (see also Levesque *et al.* 2010; Xin *et al.* 2010 and Thöne *et al.* 2011 concerning GRB 090426).

In Figure 2, all afterglows have been transformed to a common redshift of $z = 1$, using the method of Kann *et al.* (2006), and can be directly compared. Again, we separate the Type I GRB afterglow sample into the four subsamples delineated above. Panaitescu *et al.* (2001) already predicted that Type I GRB afterglows should be significantly fainter, working on the hypothesis that these GRBs have compact-object-merger progenitors, which are likely to occur in a significantly less dense interstellar medium than their collapsar counterparts, and such large offsets have indeed been found (*e.g.*, Fong *et al.* 2010; Berger 2010; Kann *et al.* 2011). We fully confirm this result in our samples (and note that the distribution of

⁶See also Gehrels *et al.* (2008) and Nysewander *et al.* (2009) for similar studies of this specific issue.

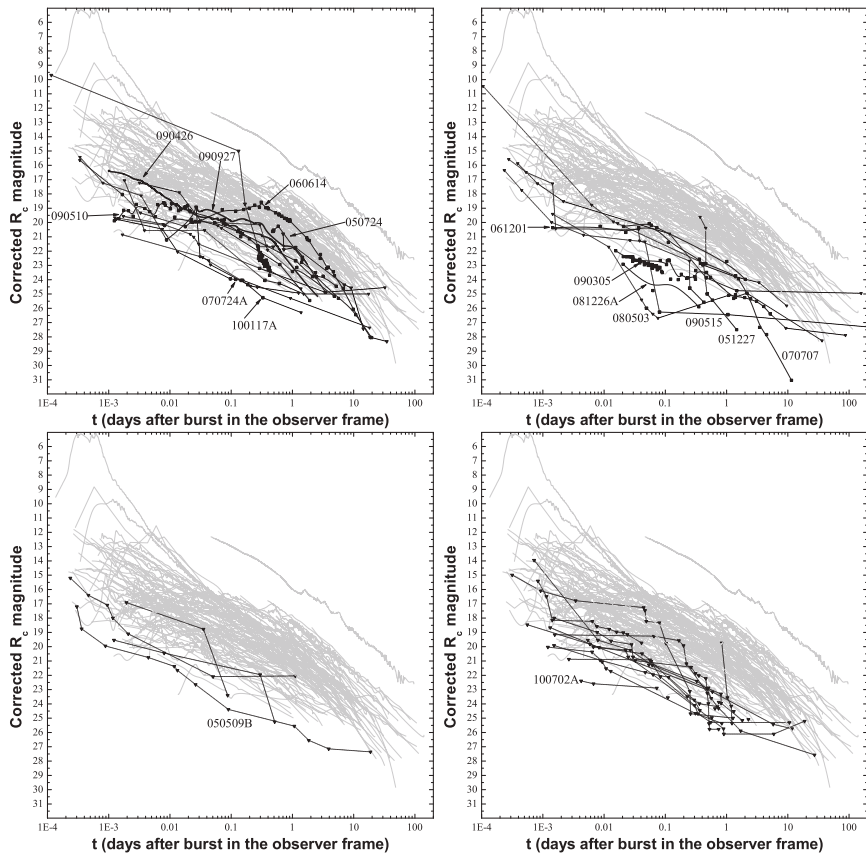


Fig. 1. Observed afterglows of Type I and Type II GRBs (corrected for Galactic extinction). The Type II GRB afterglow sample forms the gray “background”. *Top left:* Type I GRB afterglows with detections (as well as additional upper limits for the same GRBs) and redshifts we consider secure. We additionally highlight, with thick black lines, two Type II GRB afterglows whose GRBs had very short durations, under the classical temporal dividing line. *Top right:* as top left, but with insecure redshifts (or simple estimates). *Bottom left:* Type I GRBs with upper limits only, but secure redshifts. *Bottom right:* as bottom left, but with insecure redshifts. Outstanding GRBs are named. From these plots, it is already clear that Type I GRB afterglows are, in the whole, fainter than those of Type II GRBs, with many having no afterglow detected to upper limits much deeper than all Type II GRB afterglow detections in our sample.

luminosities for those samples with uncertain redshifts does not differ significantly from the samples with secure redshifts). We find that in the mean, the sample with detections and secure redshifts is 5.8 ± 0.5 mag fainter than the mean magnitude of the Type II GRB afterglow Golden Sample (see Kann *et al.* 2010 for definitions of the different Type II GRB afterglow samples), this makes it $\approx 210_{-80}^{+120}$ times less

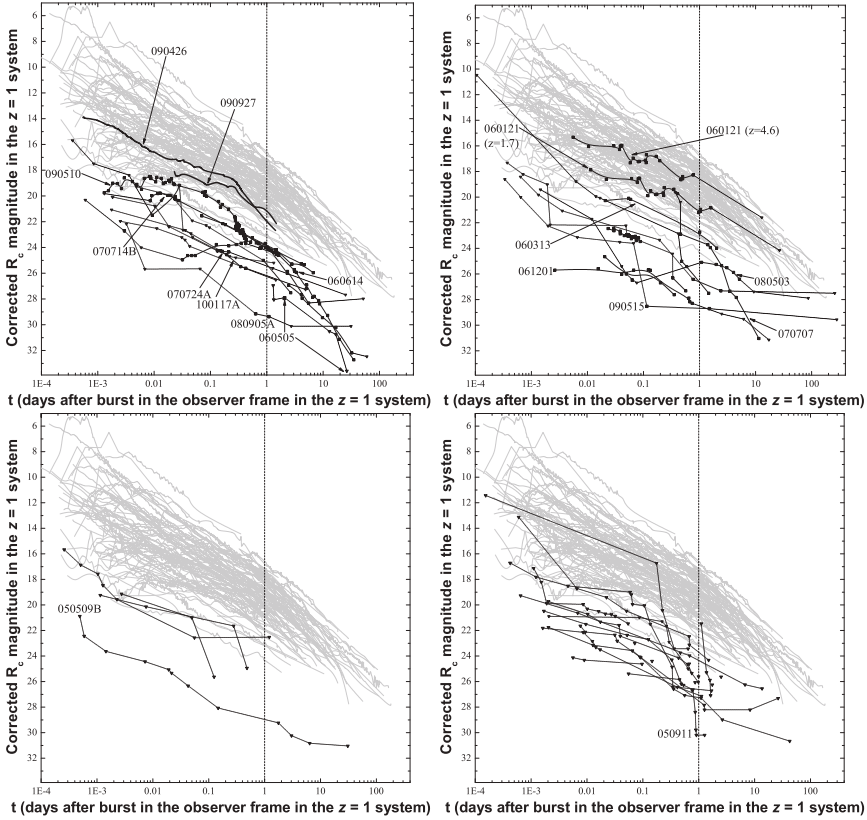


Fig. 2. Afterglows of Type I and Type II GRBs after correcting for rest-frame extinction (where applicable) and shifting to a common redshift of $z = 1$. Sample distribution is as in Figure 1. The two Type II GRB afterglows in the *top left*, while among the fainter ones in their class, are clearly more luminous than those of Type I GRBs, which are almost all significantly fainter than those of Type II GRBs. The only exception is GRB 060121, *top right*, which we propose to be a short-duration Type II GRB.

luminous. This is roughly a factor of 5 – 20 less luminous than Panaitescu *et al.* (2001) had initially predicted. A comparison with their assumption shows that Panaitescu *et al.* (2001) overestimated both the typical isotropic energy release of Type I GRBs, and also likely the typical external medium density. We note that the additional Type I GRBs added from Nicuesa Guelbenzu *et al.* (2012b) are in full agreement with the luminosity distribution found so far, but for the most part do not have secure redshifts, and therefore do not contribute to the most meaningful comparison sample.

Figure 2 also clearly shows that while the afterglows of GRB 090426 and GRB 090927 are among the fainter Type II afterglows, they are more luminous than any of the Type I GRB afterglows, and therefore these GRBs likely belong

to the collapsar population (for additional arguments, see links above as well as Grupe *et al.* 2009) despite their very short duration, possibly making them similar to the case of GRB 060121 (de Ugarte Postigo *et al.* 2006; Levan *et al.* 2006; Kann *et al.* 2011). Similar to cases of possible Type I GRBs which are “too long”, these examples show that likely Type II GRBs exist which are “too short” (see also Virgili *et al.* 2011), and therefore extended criteria beyond the simple (detector-dependent) duration are needed, as have been discussed by Zhang *et al.* (2009).

3 The issue of jet breaks in Type I GRB afterglows

The existence of a so-called “jet break” due to the collimation of the GRB emission was proposed early in the afterglow era (Rhoads 1997), and has been studied extensively in the optical (*e.g.*, Zeh *et al.* 2006) and the X-rays (*e.g.*, Racusin *et al.* 2009) for Type II GRB afterglows. The question of the existence of such breaks for Type I GRB afterglows is at the same time a question of the degree of collimation such GRBs exhibit, considering the preferred model of compact-object mergers does not provide an extended envelope for the jet to propagate through which might aid in the collimation of the jet. Recent numerical studies (*e.g.*, Rezzolla *et al.* 2011) indicate that collimation will indeed be achieved, but what of the observational situation?

The first optical Type I GRB afterglow, that of GRB 050709, was observed to very faint magnitudes (Hjorth *et al.* 2005; Fox *et al.* 2005), but no jet break was found in these observations (Watson *et al.* 2006). As we detailed above, Type I GRBs exhibit very faint afterglows in the optical, and often, detections at late times are additionally hampered by the influence of the host galaxy (though some GRBs are offset so strongly that they do not lie on the host galaxy light, of course). Therefore, the best strategy to pursue the issue of Type I GRB collimation is to obtain late-time X-ray follow-up. While also less luminous than those of Type II GRBs in the X-rays, the corresponding reduction in X-ray-afterglow brightness is typically less extreme, and there are no issues of source confusion. Still, such observations are generally beyond the capabilities of the *Swift* satellite and therefore have to be performed by *Chandra* or *XMM-Newton*.

Two Type I GRBs with bright X-ray afterglows in 2005 were followed up at late times in such a way. GRB 050724 did not exhibit any break in its X-ray light curve until at least 2 Ms after the GRB, and Grupe *et al.* (2006) derived an opening angle of $\gtrsim 25^\circ$ from the observations, implying the afterglow was essentially uncollimated. On the other hand, Burrows *et al.* (2006) report on the detection of a clear break in the light curve of the energetic Type I GRB 051221A, implying a jet opening angle of $\Theta_{\text{jet}} \approx 4 - 8^\circ$.

The single case of significant detection of steep late-time decay in the optical is the extremely luminous GRB 090510, first reported by McBreen *et al.* (2010), and confirmed by the more thorough analysis of Nicuesa Guelbenzu *et al.* (2012a). This decay has been interpreted to be post-break, but the theoretical interpretation of the complicated multi-wavelength afterglow yields inconclusive results

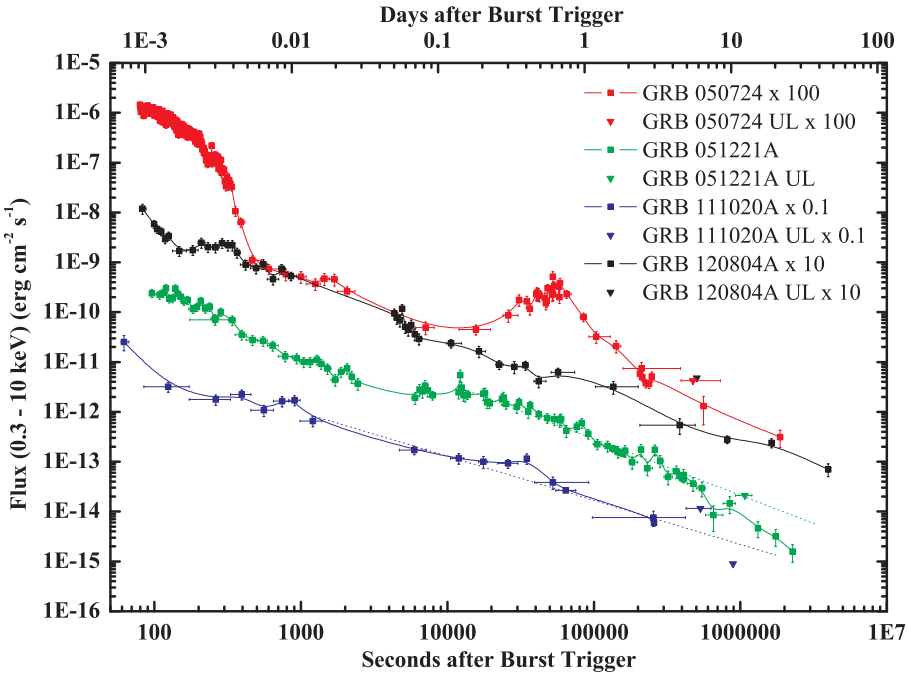


Fig. 3. The X-ray afterglows, as measured by *Swift*, *Chandra* and *XMM-Newton*, of four Type I GRBs with late-time observations ($\gtrsim 1$ Ms). For clarity, the fluxes have been shifted up or down relative to the measured values by the factors given in the legend. GRBs 050724 and 120804A show unbroken decays up to several weeks after the GRB, whereas GRBs 051221A and 111020A show breaks in their light curves, which may be due to jet breaks (for GRB 111020A, the break is only found via a *Chandra* upper limit which is significantly deeper than the light-curve extrapolation). We highlight these breaks by extrapolating the earlier decay to late times (dotted lines).

(Kumar & Barniol Duran 2010; De Pasquale *et al.* 2010). If due to an actual jet break, an extreme collimation of $\approx 1^\circ$ is implied.

Recently, further late-time observations of X-ray afterglows have been reported. Fong *et al.* (2012) studied the afterglow of GRB 111020A, deriving the existence of a break from a late, deep *Chandra* non-detection, and computing an opening angle similar to that of GRB 051221A. Another counterexample was found in GRB 120804A (Berger *et al.* 2012; Troja *et al.*, in preparation), which shows a non-breaking afterglow to out beyond 4 Ms. We show the light curves of all four GRB afterglows in Figure 3.

Nicuesa Guelbenzu *et al.* (2012b) compared the jet-opening-angle distribution of Type II and Type I GRBs and concluded that while there is an indication for a wider distribution for Type I GRBs, the issue is still hampered by the unknown distribution of the circumburst medium density, the lack of redshifts, etc.. More

precise values could be derived with the help of radio observations, but Type I GRBs are almost never detected in the radio, as very deep limits on two above-mentioned GRBs show (Fong *et al.* 2012; Berger *et al.* 2012).

4 The existence of dark Type I GRB afterglows

An afterglow is called “dark” when the optical luminosity is suppressed with respect to a conservative (usually $\beta_X = 0.5$) extrapolation of the X-ray luminosity into the optical range (Jakobsson *et al.* 2004; Role *et al.* 2005; van der Horst *et al.* 2009), under the assumption that the external (forward) shock is responsible for the afterglow emission (*e.g.*, Sari *et al.* 1998). This is often congruent with an optical non-detection despite deep and fast follow-up, but even optically bright afterglows can be dark according to the given definition, an example is the highly extinguished but ultra-luminous afterglow of GRB 080607 (Perley *et al.* 2011). In the case of Type II GRBs, extensive studies have revealed most dark GRBs are due to rest-frame extinction in the GRB host galaxy, either local and patchy, or globally in highly reddened galaxies (*e.g.*, Perley *et al.* 2009; Greiner *et al.* 2011; Krühler *et al.* 2011; Rossi *et al.* 2012), only a small number occur at very high redshifts and are dark due to Lyman absorption being redshifted into the optical.

One would naively expect darkness not to be an issue for Type I GRB afterglows; after all, they should usually occur far from the birthplaces of the massive stars that created the compact objects which represent the progenitor system of the GRBs. One of the assumptions Kann *et al.* (2011) made in the cases where afterglow data did not allow the rest-frame extinction to be constrained (*i.e.*, almost all cases) was that $A_V = 0$ mag. But this need not always to be the case, and evidence is mounting that some Type I GRB afterglows are reddened, or even truly dark.

One of the first indications was found by Ferrero *et al.* (2007) when studying the SED of GRB 050709, it exhibited a steep spectral slope in the optical and a strong curvature when combined with an NIR detection⁷, implying a large rest-frame extinction $A_V \approx 0.7$ mag, and this despite the large offset from its host galaxy (Fox *et al.* 2005). The first clear evidence for a Type I GRB afterglow affected by host-galaxy dust extinction was the very red afterglow of GRB 070724A, discovered by Berger *et al.* (2009), which exhibits $A_V \approx 0.9 - 1.3$ mag. Kann *et al.* (2011) also find evidence for even higher extinction ($A_V \approx 1.5$ mag) in the case of GRB 070809. Such a value is large even compared to most Type II GRB afterglows with definite extinction measurements (*e.g.*, Kann *et al.* 2010; Krühler *et al.* 2011).

More recently, several Type I GRBs with deep observations all exhibit evidence for significant rest-frame extinction. Both GRB 111020A (Fong *et al.* 2012) and

⁷While this detection was of low significance, it was significantly deeper than expected if the optical slope were just extrapolated into the NIR assuming a significantly lower extinction value. Since no SED including the X-rays was constructable, the result is to be taken with caution, though.

GRB 120804A (Berger *et al.* 2012) have already been mentioned in the context of the jet-break question. GRB 111020A shows evidence for a very high neutral-hydrogen column density from X-ray observations, though a direct link to the optical extinction cannot be made, as the dust-to-gas ratio in the host galaxy is unknown. In the case of GRB 120804A, an optical afterglow is discovered, and is found to be strongly suppressed *vs.* the X-ray afterglow, making the GRB classically dark, the required extinction is very high, $A_V \approx 2.5$ mag. Additionally, this GRB is extraordinary as it is the first GRB that has been detected in an Ultra-Luminous InfraRed Galaxy⁸. A third recent example is GRB 111117A (Margutti *et al.* 2012; Sakamoto *et al.* 2013), which also exhibits evidence for a high neutral-hydrogen column density from X-ray observations, and $A_V \gtrsim 0.5$ mag is implied. In all these cases, the evidence for a dense sightline clashes with the host-galaxy offset derived from the subarcsecond optical or *Chandra* X-ray positions⁹. Deeper observations will be needed to elucidate why the afterglows of Type I GRBs are resembling those of Type II GRBs more and more.

I wish to express thanks to all my colleagues who worked diligently with me on my *Swift*-era afterglow papers, and the GROND team for further cooperation. Furthermore, I extend thanks to Alberto Castro-Tirado and the rest of the conference team for inviting me to Spain, as well as to the anonymous referee for a very constructive report.

References

- Abdo, A.A., Ackermann, M., Ajello, M., *et al.*, 2010, ApJ, 712, 558
 Ackermann, M., Asano, K., Atwood, W.B., *et al.*, 2010, ApJ, 716, 1178
 Berger, E., Price, P.A., Cenko, S.B., *et al.*, 2005, Nature, 438, 988
 Berger, E., Cenko, S.B., Fox, D.B., *et al.*, 2009, ApJ, 704, 877
 Berger, E., 2010, ApJ, 722, 1946
 Berger, E., Zauderer, B.A., Levan, A., *et al.*, 2012, ApJ, submitted [[arXiv:1209.5423](https://arxiv.org/abs/1209.5423)]
 Burrows, D.N., Grupe, D., Capalbi, M., *et al.*, 2006, ApJ, 653, 468
 De Pasquale, M., Schady, P., Kuin, N.M.P., *et al.*, 2010, ApJ, 709, L146
 de Ugarte Postigo, A., Castro-Tirado, A.J., Guziy, S., *et al.*, 2006, ApJ, 648, L83
 Ferrero, P., Sanchez, S.F., Kann, D.A., *et al.*, 2007, AJ, 134, 2118
 Fong, W., Berger, E., & Fox, D.B., 2010, ApJ, 708, 9
 Fong, W., Berger, E., Margutti, R., *et al.*, 2012, ApJ, 756, 189
 Fox, D.B., Frail, D.A., Price, P.A., *et al.*, 2005b, Nature, 437, 845
 Gehrels, N., Chincarini, G., Giommi, P., *et al.*, 2004, ApJ, 611, 1005

⁸The Type I GRB 100206A had already been found in a less-Luminous InfraRed Galaxy (Perley *et al.* 2011).

⁹We note that it could be possible that these GRBs originate in very faint background galaxies, wherein they are more deeply embedded. In that case, though, the redshift is very likely to be even higher, increasing the derived neutral hydrogen column density as well as the optical extinction. Furthermore, it seems unlikely that such a projection effect would affect all the cases mentioned above.

- Gehrels, N., Sarazin, C.L., O'Brien, P.T., *et al.*, 2005, *Nature*, 437, 851
Gehrels, N., Barthelmy, S.D., Burrows, D.N., *et al.*, 2008, *ApJ*, 689, 1161
Greiner, J., Bornemann, W., Clemens, C., *et al.*, 2008, *PASP*, 120, 405
Greiner, J., Krühler, T., Klose, S., *et al.*, 2011, *A&A*, 526, A30
Grupe, D., Burrows, D.N., Patel, S.K., *et al.*, 2006, *ApJ*, 653, 462
Grupe, D., Kuin, N.M.P., Cummings, J.R., *et al.*, 2009, GCN Report 252.1
Hjorth, J., Watson, D., Fynbo, J.P.U., *et al.*, 2005b, *Nature*, 437, 859
Jakobsson, P., Hjorth, J., Fynbo, J.P.U., *et al.*, 2004, *ApJ*, 617, L21
Kann, D.A., Klose, S., & Zeh, A., 2006, *ApJ*, 641, 993
Kann, D.A., Klose, S., Zhang, B., *et al.*, 2010, *ApJ*, 720, 1513
Kann, D.A., Klose, S., Zhang, B., *et al.*, 2011, *ApJ*, 734, 96
Krühler, T., Greiner, J., Schady, P., *et al.*, 2011, *A&A*, 534, A108
Kouveliotou, C., Meegan, C.A., Fishman, G.J., *et al.*, 1993, *ApJ*, 413, L101
Kumar, P., & Barniol Duran, R., 2010, *MNRAS*, 409, 226
Levesque, E.M., Bloom, J.S., Butler, N.R., *et al.*, 2010, *MNRAS*, 401, 963
Levan, A.J., Tanvir, N.R., Fruchter, A.S., *et al.*, 2006, *ApJ*, 648, L9
Margutti, R., Berger, E., Fong, W., *et al.*, 2012, *ApJ*, 756, 63
McBreen, S., Krühler, T., Rau, A., *et al.*, 2010, *A&A*, 516, A71
Nicuesa Guelbenzu, A., Klose, S., Rossi, A., *et al.*, 2011, *A&A*, 531, L6
Nicuesa Guelbenzu, A., Klose, S., Krühler, T., *et al.*, 2012a, *A&A*, 538, L7
Nicuesa Guelbenzu, A., Klose, S., Greiner, J., *et al.*, 2012b, *A&A*, 548, A101
Nysewander, M., Fruchter, A.S., & Peer, A., 2009, *ApJ*, 701, 824
Panaiteescu, A., Kumar, P., & Narayan, R., 2001, *ApJ*, 561, L171
Perley, D.A., Cenko, S.B., Bloom, J.S., *et al.*, 2009, *AJ*, 138, 1690
Perley, D.A., Morgan, A.N., Updike, A., *et al.*, 2011, *AJ*, 141, 36
Perley, D.A., Modjaz, M., Morgan, A.N., *et al.*, 2012, *ApJ*, 758, 122
Racusin, J.L., Karpov, S.V., Sokolowski, M., *et al.*, 2009, *ApJ*, 698, 43
Rezzolla, L., Giacomazzo, B., Baiotti, L., *et al.*, 2011, *ApJ*, 732, L6
Rhoads, J.E., 1997, *ApJ*, 487, L1
Rol, E., Wijers, R.A.M.J., Kouveliotou, C., *et al.*, 2005, *ApJ*, 624, 868
Rossi, A., Klose, S., Ferrero, P., *et al.*, 2012, *A&A*, 545, A77
Sakamoto, T., Troja, E., Aoki, K., *et al.*, 2013, *ApJ*, in press [[arXiv:1205.6774v2](https://arxiv.org/abs/1205.6774v2)]
Sari, R., Piran, T., & Narayan, R., 1998, *ApJ*, 497, L17
Soderberg, A.M., Berger, E., Kasliwal, M., *et al.*, 2006, *ApJ*, 650, 261
Thöne, C.C., Campana, S., Lazzati, D., *et al.*, 2011, *MNRAS*, 414, 479
van der Horst, A.J., Kouveliotou, C., Gehrels, N., *et al.*, 2009, *ApJ*, 699, 1087
Virgili, F.J., Zhang, B., OBrien, P.T., *et al.*, 2011, *ApJ*, 727, 109
Watson, D., Hjorth, J., Jakobsson, P., *et al.*, 2006, *A&A*, 454, 123
Xin, L.-P., Liang, E.-W., Wei, J.-Y., *et al.*, 2010, *MNRAS*, 410, 27
Zeh, A., Klose, S., & Kann, D.A., 2006, *ApJ*, 637, 889
Zhang, B., Zhang, B.-B., Virgili, F.J., *et al.*, 2009, *ApJ*, 703, 1696

SHORT DURATION GAMMA-RAY BURST WITH EXTENDED EMISSION

A. Pozanenko¹ and M. Barkov^{1,2}

Abstract. Assuming that the extended emission (EE) with broad dynamic range is a common property of short duration bursts, we propose a two-jet model which can describe both short main episode of hard spectra emission, specific for short bursts, and softer spectra EE by the different off axis position of the observer. The model involves a short-duration jet, which is powered by heating due to $\nu\bar{\nu}$ annihilation, and a long-lived Blandford–Znajek (BZ) jet with a significantly narrow opening angle. We also discuss observational tests of two-jet model.

1 Introduction

Prompt gamma-ray emission of SGRB consists of a short main episode, sometimes resolved into substructure of short pulses, which we call the Initial Pulse Complex (IPC). The duration, T_{90} , of the IPC of the short bursts is usually less than ~ 2 s. However, in the sum of light curves of many short bursts, aligned relative to the main peak of the IPC, significant extended emission (EE) has been observed up to ~ 100 s in different experiments and energy bands (*e.g.* Fig. 1, left).

Extended emission has actually been observed in individual light curves of some SGRB, confirmed with KONUS, BAT/Swift, BATSE, SPI-ACS/INTEGRAL. Despite the T_{90} of some bursts being less than 2 seconds, those the EE are significantly detected. Otherwise some long bursts ($T_{90} > 2$ s) could be classified as short bursts with EE. Finally, the ultimate example of an apparently long burst (Fig. 1, right) with all signatures of short bursts is Swift GRB 060614 (Gehrels *et al.* 2006).

Usually the EE has a peak flux much smaller than the analog parameters of the IPC. The ratio of the fluences of the EE and IPC can vary in a wide range. While the spectrum of EE is softer than in IPC, the EE poses the absence of spectral lag (when it can be measured due to statistical reason) which is compatible with the lag

¹ Space Research Institute of the Russian Academy of Sciences, Moscow, Russia
e-mail: apozanen@iki.rssi.ru

² Max-Planck-Institut für Kernphysik, Saupfercheckweg 1, 69117 Heidelberg, Germany

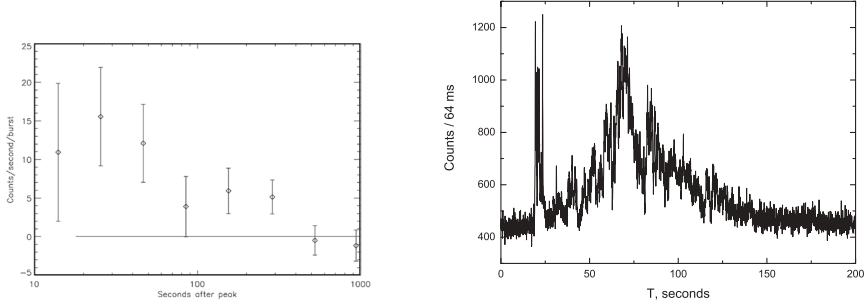


Fig. 1. *Left:* light curve in 50 – 300 keV energy band for 100 short (< 1 s), summed, background subtracted, BATSE bursts after peak alignment, with peak time suppressed. Adapted from Connaughton 2002. *Right:* light curve of GRB 060614 in 15 – 150 keV energy band as recorded with BAT/Swift, time bin is 64 ms.

properties of IPC. Additionally, variability of the EE is not negligible. Certainly the EE can be a manifestation of prolonged activity of the central engine.

Thus one could suggest that short duration bursts have a distinctive feature, such as extended emission with very broad dynamic range of flux and fluence of the EE. We propose that EE is an inherent property of short bursts, and an observable property of the EE can be explained by the different angular position of the observer with respect to the axis of the coaxial jets (Fig. 2).

2 The model

In our model (Barkov & Pozanenko 2011), we assume the merging of two NSs or a NS+BH system which can lead to the formation of a fast-rotating black-hole ($a = J/M_{BH}^2$, where a is the dimensionless BH spin parameter). Simulations of the merging of a BH+BH or BH+NS give final values of a in the range $0.3 \leq a \leq 0.65$ (Baker *et al.* 2008), and in our calculations, we will assume $a = 0.5$, the formation of a relatively massive $M_d \sim 0.001 - 0.2 M_\odot$ and compact $R_d \sim 10^7$ cm, accretion disk.

To explain the EE of SGRBs, we suggest a two-component model with neutrino heating and an electromagnetic Blandford-Znajek (BZ) mechanism. A short main episode (IPC) of SGRB is the result of a fast accretion period, which launches a neutrino-powered jet. After a few seconds, neutrino heating becomes ineffective, however, the lower accretion rate can keep the central engine active for a longer time due to the BZ mechanism. The duration of the BZ-powered jet will depend on the mass in the accretion disk.

The accretion time of the main mass of the compact disk with radius $R_d \sim 10^7$ cm is short 0.1 – 1 s. Following Metzger *et al.* (2008), the accretion rate can be estimated as

$$\dot{M}_d \approx f M_d / t_{visc}, \quad (2.1)$$

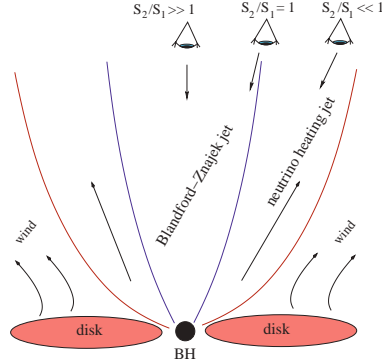


Fig. 2. An observer will register different flux of IPC (S_1) and EE (S_2) depending on the angle of view against the axis of the jets.

where $t_{visc} = R_d^2/\nu$ is the viscosity time scale and ν is the viscosity, and the factor $f \approx 1.6$. For the viscosity we have used an α -prescription, $\nu = \alpha c_s H$, where $c_s = (P/\rho)^{1/2}$ is the isothermal sound speed and H is the half-thickness of the disc. The initial viscosity time scale is

$$t_{visc,0} \approx 0.02\alpha_{-1}^{-1} M_{0.5}^{-1/2} R_{d,7}^{3/2} \left(\frac{H}{R_d} \right)^{-2} \text{ s}, \quad (2.2)$$

where $M_{0.5} = M/10^{0.5} M_\odot$ is the mass of the BH, $\alpha_{-1} = \alpha/0.1$ is the standard dimensionless viscosity, $R_{d,7} = R_d/10^7$ cm is the radius of the accretion disk.

We assume that only a fraction $\sim (R/R_d)^p$ of the available material is accreted onto the BH (Blandford & Begelman 1999). The rest of the mass will be lost to an outflow, and the parameter “p”, can vary from 0 (no wind) up to 1 (powerful wind). The mass accretion rate will depend on the time as $\dot{M} \sim t^{-4/3}$ and $\dot{M} \sim t^{-8/3}$ for $p = 0$, and $p = 1$, respectively. Consequently, a luminosity is linearly dependent on the accretion rate and will be influenced by magnetic flux evolution.

For the accretion of a thick disk, the maximum luminosity due to BZ mechanism can be estimated following Komissarov & Barkov (2010). The pressure of the magnetic field can be a fraction, $\beta = 8\pi P_g/B^2$, of the gas pressure in the disk at MSO, from MSO magnetic field accretes to the BH horizon. In such a way, the luminosity of the BZ mechanism becomes a weak function of the BH spin parameter, a (if $0.5 \leq a \leq 1$) and can be estimated as

$$L_{BZ} \approx \frac{0.05}{\alpha_{-1}\beta_1} \dot{M}_{in} c^2 \approx 10^{48} \alpha_{-1}^{-1} \beta_1^{-1} \dot{M}_{in,-5} \text{ erg s}^{-1}, \quad (2.3)$$

where $\beta_1 = \beta/10$.

The main source of the neutrino heating is the neutrino annihilation reaction $\nu\tilde{\nu} \rightarrow e^+e^-$. The heating rate can be described by Zalamea & Beloborodov (2010)

$$L_{\nu\tilde{\nu}} \approx 3 \times 10^{50} X^{-4.7} M_{BH,0.5}^{-3/2} \dot{M}_{in,0}^{9/4} \text{ ergs s}^{-1}, \quad (2.4)$$

where $X \equiv R_{mso}/4R_g$. This formula is valid when the accretion rate is higher than $\sim 0.05\alpha_{-1}^{5/3} M_\odot \text{ s}^{-1}$, this critical value of the accretion rate is a function of a . As the accretion rate becomes lower, the efficiency of neutrino heating drops dramatically and becomes negligible.

In our model, the distribution of SGRBs in the intensity of the EE is a selection effect due to different angular positions of the observer (Fig. 2) with respect to the axis of coaxial jets and a dispersion of opening angles of the $\nu\bar{\nu}$ and BZ jets. The $\nu\bar{\nu}$ -powered jet has the opening angle $\theta_{\nu\bar{\nu}} \sim 0.1$ and can be significantly wider than the opening angle of the jet powered by the BZ mechanism, $\theta_{BZ} \sim 1/\Gamma$.

3 Observational tests

There are other models of the EE (MacFadyen *et al.* 2005; Metzger *et al.* 2008; Lazatti *et al.* 2010). However we can suggest some tests to discern between models and find possible parameter of the two-jet model.

In our model the opening angle $\theta_{\nu\bar{\nu}}$ is wider than the opening angle θ_{BZ} . Actually, the ratio of $\theta_{BZ}/\theta_{\nu\bar{\nu}}$ calculated from the fluence ratio of the EE and IPC, is always less than 1 (Bostancı *et al.* 2013). Indeed, the ratio $\theta_{BZ}/\theta_{\nu\bar{\nu}}$ was calculated with a-priori suggestions about the jet luminosity.

Another test of the BZ-jet properties is a type of functional dependency of the EE with time. Luminosity is linearly dependent on the accretion rate which is described by a power law. There is a signature that the EE decay part may be described by the power law (Minaev *et al.* 2010). Indeed, the decay part of observed EE might be investigated to restrict the wind parameter p .

A further possible test might be the absence/presence of a jet break in an afterglow light curve. Jet-breaks could be observed if $1/\Gamma$ (where Γ is bulk motion Lorentz factor) less than the opening angle of the jet cone. Meanwhile, the opening angle of the jet powered by the BZ mechanism is $\theta_{BZ} \sim 1/\Gamma$. Would the nature of the GRB afterglow be only BZ-jet interacting with the ISM, we could not observe any jet break. One can suggest that if the fluence of the EE is greater than the fluence of the IPC the jet break will not occur. Other consequence of the two-jet model might be re-brightening (or second peak) in an afterglow light curve.

Since in our model $\theta_{BZ} < \theta_{\nu\bar{\nu}}$ a number density of burst with less pronounced EE is more than with EE comparable with the IPC. It is really true if we take the fluence ratio of the EE and IPC of BATSE bursts with the EE (Fig. 3). The best parameter for number density estimation is the ratio of the peak flux of EE and peak flux of IPC since peak flux is directly related with the luminosity in Equations (2.3) and (2.4).

Finally, there is a problem of dichotomy of short bursts with EE. In our model each short burst has to be accompanied by EE. However, the more off-axis the observer is placed, the less will be the intensity of EE and hence the less will be the ratio of peak fluxes of EE and IPC. The ratio tends to zero continuously. In statistical analysis of SPI-ACS/INTEGRAL short bursts without individual EE in each particular event, the EE was found in the averaged light curve (Minaev *et al.* 2010). Contrary, Norris *et al.* (2010) investigating BAT/Swift short burst

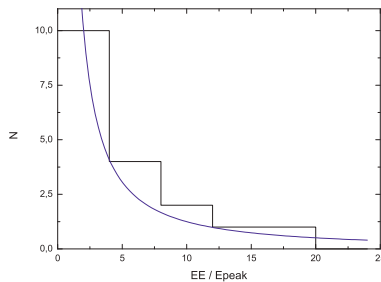


Fig. 3. Number of SGRBs *vs.* fluence ratio of EE and IPC (Bostancı *et al.* 2013).

found no EE on average in an ensemble of 39 GRBs without EE in each individual event.

Finally, the occurrence of the BZ-jet depends on the initial parameters of the accretion disc (mass, radius, spin parameter; see Barkov & Pozanenko 2011). So it is not fully prohibited that in some combinations of initial parameters the BZ-jet could not be started and hence there will be no prolonged activity of the central engine. In this case the EE would be fully suppressed.

The work was supported by RFBR grant 12-02-01336-a.

References

- Baker, J.G., Boggs, W.D., Centrella, J., *et al.*, 2008, Phys. Rev. D, 78, 4, id. 044046
 Barkov, M.V., & Pozanenko, A.S., 2011, MNRAS, 401, 2161
 Blandford, R.D., & Begelman, M.C., 1999, MNRAS, 303, L1
 Bostancı, Z.F., Kaneko, Y., & Göğüş, E., 2013, MNRAS 428, 1623
 Connaughton, V., 2002, ApJ, 567, 1028
 Gehrels, N., Norris, J.P., Barthelmy, S.D., *et al.*, 2006, Nature, 444, 1044
 Komissarov, S.S., & Barkov, M.V., 2010, MNRAS, 402, L25
 Lazzati, D., Morsony, B.J., & Begelman, M.C., 2010, ApJ, 717, 239
 MacFadyen, A.I., Ramirez-Ruiz, E., & Zhang, W., 2005 [[ArXiv:astro-ph/0510192](https://arxiv.org/abs/astro-ph/0510192)]
 Metzger, B.D., Piro, A.L., & Quataert, E., 2008, MNRAS, 390, 781
 Metzger, B.D., Quataert, E., & Thompson, T.A., 2008, MNRAS, 385, 1455
 Minaev, P.Y., Pozanenko, A.S., & Loznikov, V.M., 2010, Astron. Lett., 36, 707
 Norris, J.P., Gehrels, N., & Scargle, J.D., 2010, ApJ, 717, 411
 Zalamea, I., & Beloborodov, A.M., 2010 [[ArXiv:1003.0710](https://arxiv.org/abs/1003.0710)]

SHORT GRB AFTERGLOWS OBSERVED WITH GROND

A. Nicuesa Guelbenzu¹, S. Klose¹, A. Rossi¹, S. Schmidl¹, J. Greiner²,
D.A. Kann², J. Elliott², F. Olivares E.², A. Rau², P. Schady²,
V. Sudilovsky², T. Krühler³, P. Ferrero⁴, S. Schulze⁵, P.M.J. Afonso⁶,
R. Filgas⁷ and M. Nardini⁸

Abstract. We report on follow-up observations of 20 short-duration gamma-ray bursts ($T_{90} < 2$ s) performed in $g'r'i'z'JHK_s$ with the Gamma-Ray Burst Optical Near-Infrared Detector (GROND) between mid-2007 and the end of 2010. This is the most homogeneous and comprehensive data set on GRB afterglow observations of short bursts. In three cases, GROND was on target within less than 10 min after the trigger, leading to the discovery of the afterglow of GRB 081226A and its faint underlying host galaxy. In addition, GROND was able to image the optical afterglow and follow the light curve evolution in five further cases: GRBs 090305, 090426, 090510, 090927, and 100117A. Three of the aforementioned six bursts with optical light curves show a break: GRBs 090426 and 090510 as well as GRB 090305. For GRB 090927, no break is seen in the optical/X-ray light curve until about 150 ks/600 ks after the burst. A decay slope of the optical afterglow of GRB 100117A could be measured. Using these data supplemented by about ten events taken from the literature, we compare the jet half-opening angles of long and short bursts. We find a tentative evidence that short bursts have wider opening angles than long bursts. However, the statistics are still very poor and follow-up observations of these events are therefore very important to gain as much observational data as possible.

¹ Thüringer Landessternwarte Tautenburg, Germany

² Max-Planck-Institut für Extraterrestrische Physik, Germany

³ Dark Cosmology Centre, Niels Bohr Institute, University of Copenhagen, Denmark

⁴ Instituto de Astrofísica de Canarias (IAC), Spain

⁵ Centre for Astrophysics and Cosmology, Science Institute, University of Iceland, Iceland

⁶ American River College, Department of Physics and Astronomy, CA, USA

⁷ Institute of Experimental and Applied Physics, Czech Technical University in Prague, Czech Republic

⁸ Università degli studi di Milano-Bicocca, Italy

1 Introduction

Until 2005 no afterglow of a short burst had ever been detected, while many important discoveries had already been made for the long-burst sample (redshifts, supernova light, collimated explosions). There are two main reasons for this situation. Firstly, there is a substantially smaller detection rate of short bursts compared to long bursts. Secondly, short-burst afterglows are rarely brighter than $R = 20$, even minutes after a trigger (*e.g.*, Kann *et al.* 2010; Kann *et al.* 2011). This general faintness makes their discovery and detailed follow-up very challenging. Observations of jet breaks in short-burst afterglow light curves are rather sparse, in the optical as well as in the X-ray band. In this work, for those six GRBs with an optical afterglow we estimated the corresponding jet half-opening angle.

2 Results

Observations with GROND (Greiner *et al.* 2008) mounted at the 2.2-m ESO/MPG telescope on La Silla (Chile) provide a complete sample of events observed with the same instrument at the same telescope. The capability of GROND to observe in seven bands simultaneously, from g' to K_s , provides a unique opportunity to follow the color evolution of an afterglow and to stack several bands in order to reach higher detection thresholds. Between July 2007 and December 2010, a total of 220 GRBs were observed. In this work, we have selected all those bursts with a duration of $T_{90} \leq 2$ s (within 1σ) and an error circle smaller than 3 arcmin in radius resulting in a sample of 20 targets. For six of the 20 events an optical afterglow was imaged by GROND. Here, we center in those six cases. Complete information about all targets can be found in Nicuesa Guelbenzu *et al.* (2012b).

- **GRB 081226A: Discovery of the optical afterglow.** The afterglow of GRB 081226 was located in the southern part of a very faint host galaxy. It was detected in all optical bands and best-sampled in the r' band. Fitting the light curve with a power-law plus host galaxy component gives a decay slope of $\alpha = 1.3 \pm 0.2$, which is in agreement with the X-ray data (Evans *et al.* 2010). This points to an afterglow in the pre-jet break evolutionary phase. The Gemini r' -band data is in agreement with the GROND light curve (Fig. 1).
- **GRB 090305: Discovery of a jet break.** Gemini-S/GMOS observed and discovered the optical afterglow (Cenko *et al.* 2009) but no light curve was published so far. Figure 1 shows the result of the simultaneous fit of all data (GROND and Gemini) using a broken power-law. The fit finds a break in the light curve at $t_b = 6.6 \pm 0.4$ ks, a pre-break decay slope of $\alpha_1 = 0.56 \pm 0.04$, and a post-break decay slope of $\alpha_2 = 2.29 \pm 0.60$. The pre-break decay slope is rather shallow but not unusual (*e.g.*, Zeh *et al.* 2006). There is no X-ray light curve available for this afterglow.

- **GRB 090426: Discovery of a jet break.** The duration ($T_{90} = 1.28$ s) of GRB 090426 places it firmly among the short burst population, while its high redshift ($z = 2.609$), host galaxy properties, and prompt emission are more similar to those of long-duration GRBs (*e.g.*, Thöne *et al.* 2011).

We present additional multi-color photometry of the optical/ NIR afterglow of GRB 090426 from 0.3 to 2.5 days. Our data show that a light curve break exists at 0.4 days, which is followed by a steep decay. This light curve decay is achromatic in the optical/NIR bands, and interpreted as a post-jet break phase (Fig. 2). The half-opening angle of the jet as well as the luminosity of the optical afterglow provide additional evidence that GRB 090426 is probably linked to the death of a massive star rather than to the merger of two compact objects. This event is in detail discussed in Nicuesa Guelbenzu *et al.* (2011).

- **GRB 090510: Discovery of a second break in the light curve.** The *Swift* discovery of the short GRB 090510 has raised considerable attention mainly because of two reasons: it had a bright optical afterglow, and it is among the most energetic events detected so far. As noted by several authors, the post-break decay slope seen in the UVOT data is much shallower than the steep decay in the X-ray band, pointing to a (theoretically hard to understand) excess of optical flux at late times (De Pasquale *et al.* 2010).

Based on the GROND data, we confirm that the optical afterglow of GRB 090510 did indeed enter a steep decay phase starting around 22 ks after the burst and did follow a post-jet break evolution at late times. The break seen in the optical light curve around 22 ks in combination with its missing counterpart in the X-ray band could be due to the passage of the injection frequency across the optical bands, as already theoretically proposed in the literature (Kumar & Barniol Duran 2010). Our results imply that there is no more evidence for an excess of flux in the optical bands at late times (Nicuesa Guelbenzu *et al.* 2012a).

- **GRB 090927: Constraints on a jet break.** The GROND r' -band light curve of GRB 090927 can be fitted with a single power-law that has a slope of $\alpha = 1.32 \pm 0.14$ ($\chi^2/\text{d.o.f.} = 0.39$; Fig. 2). The data suggest that the optical flux was nearly constant between two and four hours after the burst. At the same time, the X-ray light curve shows strong fluctuations but seems to be in a plateau phase.

Assuming a single power-law decay for the X-ray light curve, we obtain $\alpha_X = 1.30 \pm 0.07$ for $t > 20$ ks. However, the light curve decay after the break is then too shallow for a post-jet break decay slope. We thus conclude that also the X-ray afterglow is best described by pre-jet break evolution up to the end of the XRT observations at about 600 ks after the burst. A decay slope of 1.3 is in agreement with the ensemble statistics of pre-jet break decay slopes for long-burst afterglows (*e.g.*, Zeh *et al.* 2006).

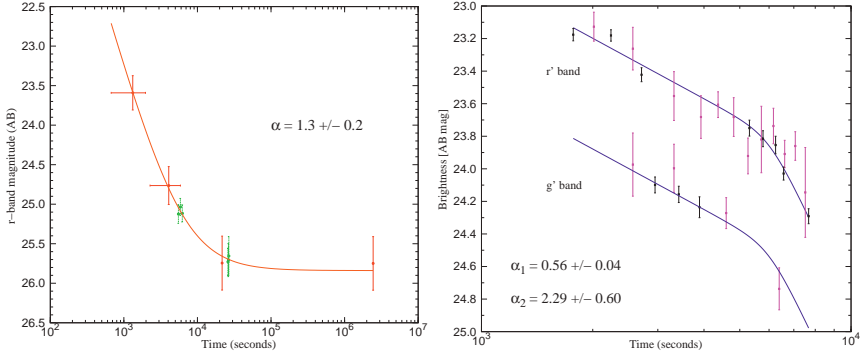


Fig. 1. *Left:* light curve of the afterglow of GRB 081226. Shown are GROND (in red) and Gemini (in green) r' -band data. *Right:* light curves of the afterglow of GRB 090305 in g' and r' as seen by GROND (violet) and Gemini (dark blue).

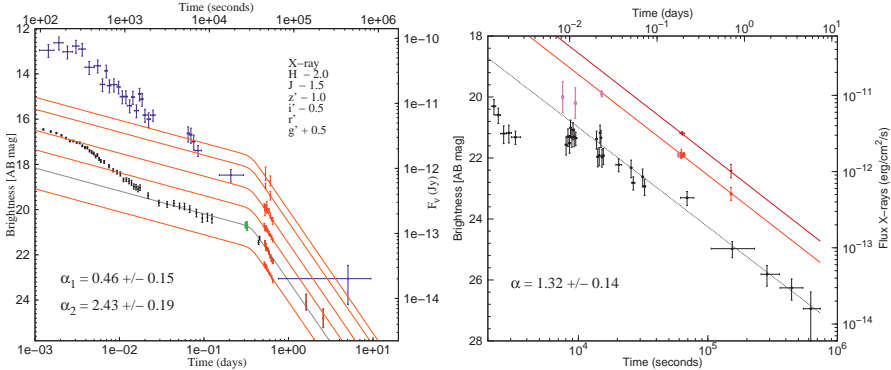


Fig. 2. *Left:* multi-color light curve of the afterglow of GRB 090426 (public r' band data in black, GROND data in red, TLS data in green, *Swift*/XRT X-ray data in blue). *Right:* light curves of the afterglow of GRB 090927 (r' band data in red, shifted i' band data in brown, public additional r' band data in violet, *Swift*/XRT X-ray data in black).

- **GRB 100117A: Constraints on a jet break.** The optical afterglow on top of its host galaxy was discovered by Fong *et al.* (2011) and also seen by GROND. Combining the data from Fong *et al.* with the data obtained by GROND gives $\alpha \sim 1.3$, with no evidence for a break until at least 8.3 hr after the burst (see Fig. 10 in Nicuesa Guelbenzu *et al.* 2012b).

3 Jet half-opening angles

Figure 3 shows the observed distribution of jet half-opening angles of long-bursts taken from Lu *et al.* (2012) compared to the short-burst sample. At first view,

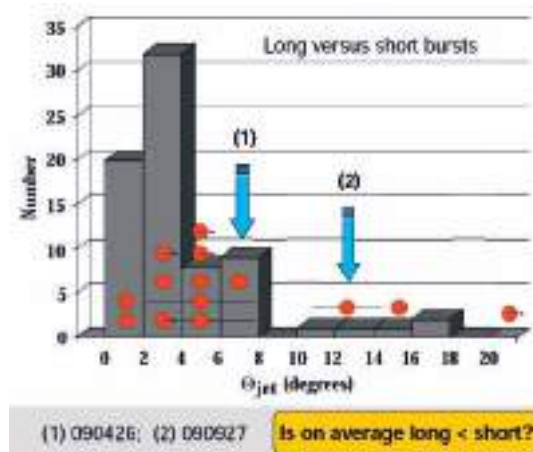


Fig. 3. Observed distribution of jet half-opening angles of 74 long bursts compared to the short-burst sample. Since the latter has much less data, we do not plot a histogram but only points. An arrow indicates a lower limit on Θ_{jet} .

this figure shows tentative evidence that short bursts have wider jet-opening angles than long bursts. However, some caution is necessary. First of all, when calculating the jet half-opening angles, Lu *et al.* assumed $n = 0.1 \text{ cm}^{-3}$ and $\eta_\gamma = 0.2$ throughout. Even though Θ_{jet} is only modestly sensitive to changes in both parameters, gas densities derived for bursts based on multi-wavelength data show a spread from burst to burst by several orders of magnitude. Second, error bars in Θ_{jet} are not taken into account in the histogram. Similarly, our standard assumption of $n = 0.01 \text{ cm}^{-3}$ for short bursts is also a simplification. For individual bursts it can be wrong by a factor of up to 100 in both directions. Finally, our plot contains only long bursts with measured jet break times. A more detailed study should also contain those long bursts for which only a lower limit on Θ_{jet} can be given.

References

- Cenko, S.B., Cobb, B.E., Perley, D.A., *et al.*, 2009, GCN, 8933
- De Pasquale, M., Schady, P., Kuin, N.P.M., *et al.*, 2010, ApJ, 709, L146
- Evans, P.A., Willingale, R., Osborne J.P., *et al.*, 2010, A&A, 519, A102
- Fong, W., Berger, E., Chornock, R., *et al.*, 2011, ApJ, 730, 26
- Gehrels, N., Ramirez-Ruiz, E., Fox, D.B., *et al.*, 2009, A&A, 543, A10
- Greiner, J., Bornemann, W., Clemens, C., *et al.*, 2008, PASP, 120, 450
- Kann, D.A., Klose, S., Zhang, B., *et al.*, 2010, ApJ, 720, 1513
- Kann, D.A., Klose, S., Zhang, B., *et al.*, 2011, ApJ, 734, 96
- Kumar, P., & Barniol Duran, R., 2010, MNRAS 409, 226

- Lu, R.-J., Qin, S.-F., Liang, E.W., *et al.*, 2012, ApJ, 745, 168
Nicuesa Guelbenzu, A., Klose, S., Rossi, A., *et al.*, 2011, A&A, 531, L6
Nicuesa Guelbenzu, A., Klose, S., Krühler, T., *et al.*, 2012, A&A 538, L7
Nicuesa Guelbenzu, A., Klose, S., Greiner, J., *et al.*, 2012, A&A 548, A101
Thöne, C.C., Campana, S., Lazzati, D., *et al.*, 2011, MNRAS, 414, 479
Zeh, A., Klose, S., Kann, D.A., *et al.*, 2006, ApJ, 637, 889

GRB EMISSION IN NEUTRON STAR TRANSITIONS

M.A. Pérez-García¹, F. Daigne² and J. Silk³

Abstract. In this contribution we briefly introduce a mechanism for short gamma ray burst emission different from the usually assumed compact objects binary merger progenitor model. It is based on the energy release in the central regions of neutron stars. This energy injection may be due to internal self-annihilation of dark matter gravitationally accreted from the galactic halo. We explain how this effect may trigger its full or partial conversion into a quark star and, in such a case, induce a gamma ray burst with isotropic equivalent energies in agreement with those measured experimentally. Additionally, we show how the ejection of the outer crust in such events may be accelerated enough to produce Lorentz factors over those required for gamma ray emission.

1 Introduction

Short gamma ray bursts (SGRBs) are highly energetic phenomena in the Universe that according to its time duration (Kouveliotou *et al.* 1993) can be considered to be $\Delta t < 2$ s. Energetically, they can emit isotropic equivalent energies in the range $E_{\text{iso}} \approx 10^{48} - 10^{52}$ erg, and some with beamed emission. The beaming factor accounts for the milder emission at the source, E_{iso}/f_b , due to the geometrical finite solid angle, defined as $f_b = (\frac{\Omega}{4\pi})^{-1}$. Typically, there is a large spread in f_b but it can be $\sim 10 - 100$. To date, although highly uncertain, such a rapid release of huge energies is thought to correspond to the merger of two compact objects, each of them possibly being either a neutron star (NS) or a black hole (BH). NSs are compact-sized objects with a typical mass $M \sim 1.5 M_\odot$ and radius $R \sim 12$ km born in a supernova event. The interior of these objects is largely unknown and periodically revisited (Glendenning 2000) but the large densities supposedly

¹ Departament of Fundamental Physics and IUFFyM, University of Salamanca, Plaza de la Merced s/n 37008 Salamanca, Spain

² UPMC-CNRS, UMR 7095, Institut d’Astrophysique de Paris, 75014 Paris, France

³ Oxford Physics, University of Oxford, Keble Road OX1 3RH, Oxford, UK

attained in the core of these objects of about $\rho \sim 4 \cdot 10^{14}$ g/cm³ well overpass the nuclear saturation density of regular finite nuclei. In this context, matter is well described by a degenerate system of nucleons where temperature effects are negligible as compared to the Fermi energies of the nuclear species population, $k_B T/E_F << 1$. It is expected that the *core*, most of the NS, is formed by a dense soup of nucleons or even heavier baryons bearing strangeness. The equation of state (EoS) describing the interior is largely uncertain but mainly concerns weak and strong interactions and can be treated using a variety of methods. We will consider in this contribution a relativistic field model with two parameterizations, the TM1 (Sugahara *et al.* 1994) and TMA (Toki *et al.* 1995) EoSs.

These objects have a strong gravitational potential as probed, for example, in the absorption lines in the spectra of 28 bursts of the low-mass X-ray binary EXO 0748–676 (Cottam *et al.* 2002). The mass-to-radius ratio was probed in this way, since $z = (1 - R_S/R)^{-1/2} - 1$ with $R_S = 2GM/c^2$ the Schwarzschild radius, and it was possible to determine that $z = 0.35$ for this object, a huge value as compared to cluster masses of $\sim 10^{14} M_\odot$, where it is estimated to be $z \sim 10^{-5}$ or the sun $z \sim 10^{-6}$ (Lopresto *et al.* 1991). This provided the first observational direct evidence that NSs are indeed made of tightly packed matter and confirms that could be considered very effective accretors from a companion or from matter distributed in the galactic halo.

In this light the sun has been considered of interest for the indirect detection of dark matter (DM). This so-far undetected component of our Universe is thought to amount $\sim 23\%$, for a review see (Bertone 2010). There is a number of DM particle candidates in current theoretical models so called *beyond* the Standard model where they naturally arise, the most popular being the lightest supersymmetric particle, the neutralino. As it seems there are some indications that either from accelerator, direct or indirect searches the discovery may be not too far. Particle DM candidates with masses $m_\chi \sim 4 - 12$ GeV/c² in the direct and $m_\chi \sim 130$ GeV/c² in the indirect search are currently under debate. In this sense the fact that DM could be a self-annihilating Majorana fermion could lead to dramatic consequences from the astrophysical point of view as we will explain in what follows.

2 SGRB engine model in brief

It has been claimed that NSs could accrete DM from the galactic halo and due to a density enhancement at the core of the NS, spark seeding based on DM self annihilation may be possible (Pérez-García *et al.* 2010). This sort of *Trojan mechanism* would allow, in principle, the release of energies comparable to binding of quarks in baryons and, therefore, the deconfinement of the quark content. Once quark lumps are formed they are energetically very stable and they could grow or coalescence helped by the pressure softening of this type of matter. It has been studied (Bhattacharyya *et al.* 2006) that a macroscopic conversion burning front may indeed be possible (partially) fully converting the NS into a (hybrid) quark star (QS) (Pérez-García & Silk 2012). Typically, the object converting has an

energy reservoir that is a factor of order unity the gravitational binding energy, and if such a transition takes place the mass of the resultant QS is close to the initial NS ($M_{QS} \approx M_{NS}$). When it is converted a fraction of the two object binding energies $f_{QS/NS} \approx \left| \left(\frac{M_{QS}}{M_{NS}} \right)^2 \left(\frac{R_{NS}}{R_{QS}} \right) - 1 \right|$ is released. In order to see if this type of single non-repeating catastrophic events have an occurrence rate compatible with current limits on those of SGRBs we compare them to those of Supernova type II formation and we see (Pérez-García *et al.* 2012) that even considering the large uncertainty in the values of beaming factors, indeed there must be a non-trivial time delay probability distribution and only in rare cases such events must take place since $\frac{\mathcal{R}_{\text{SGRB}}}{\mathcal{R}_{\text{NS} \rightarrow \text{QS}, \text{max}}^{\text{(SNII)}}} \simeq (8 \times 10^{-4} \rightarrow 3 \times 10^{-3}) \left(\frac{\langle f_b \rangle}{50} \right)$.

Regarding the properties in the host galaxy there is no definite place for the SGRBs, being allowed in all regions in either type of galaxy. There is however less correlation than with respect to long GRBs that show a correspondence with central regions of star forming galaxies. In this model the progenitors (*i.e.* NSs) show a natural mechanism to un-correlate due to a natal kick velocity of the order $v \sim 10^3$ km/s providing off-sets of the order $d \sim v\tau$ where τ is the delay to the conversion. In this model it is highly uncertain since it depends on the drift history of the NS and the inhomogeneous cluster of the DM environment traversed over time scales of $\tau \sim 10^3 - 10^7$ yr according to the details of the DM steady accretion and deduced ages of *regular* NSs.

As for the energetics, the amount of kinetic energy of the expelled outer crust is a fraction of the gravitational energy $E_{\text{kin}} \simeq f_{\text{ej}} \Delta E_{\text{grav}}$ if acceleration is complete. As explained, the isotropic equivalent energy that could be radiated as gamma-rays by such an ejecta can be estimated by

$$E_{\gamma, \text{iso}} \simeq 3.5 \times 10^{51} \left(\frac{f_b}{100} \right) \left(\frac{f_\gamma}{0.1} \right) \left(\frac{f_{\text{ej}}}{10^{-3}} \right) \left(\frac{R_{NS}}{12 \text{ km}} \right)^{-1} \left(\frac{M}{1.5 M_\odot} \right)^2 \text{ erg}, \quad (2.1)$$

where f_γ is the efficiency of gamma-ray energy extraction from the ejecta and could range from $\sim 0.01 - 0.1$. This estimate of $E_{\gamma, \text{iso}}$ is in reasonable agreement with observations of SGRBs: the NS \rightarrow QS conversion scenario investigated here can reproduce measured energies in SGRBs for $f_b f_\gamma f_{\text{ej}} \simeq 3 \times 10^{-4} - 0.3$.

In Figure 1 we show the isotropic equivalent energy (logarithmic scale) as a function of the progenitor NS mass, obtained with the TM1 (squares) and TMA (circles) EoS. From top to bottom a value of the product of three efficiency fractions, $f_b f_\gamma f_{\text{ej}} \simeq 0.3, 0.01, 3 \times 10^{-4}$ has been assumed. We can see that the major dependence is due to the microphysics efficiency of the model and ejection but the interior EoS mainly affects the possibility of more massive progenitors. This is quite natural consequence of the fact that the mass-radius relationships for both EoS are similar in shape but they attain different maximum masses. Due to the fact that typical energies are in the range $E_{\gamma, \text{iso}} \approx 10^{48} - 10^{52}$ erg, it leads to consider that smaller efficiency fractions are even able to produce SGRBs in light of this mechanism. However further details and modeling is needed.

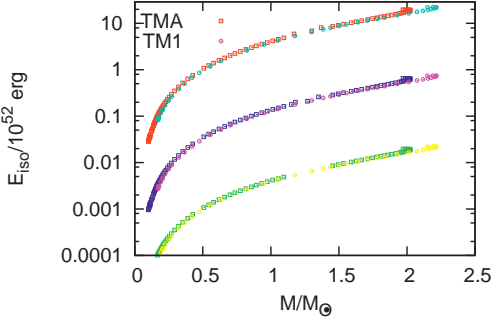


Fig. 1. Isotropic equivalent energy as a function of the progenitor NS mass (in M_{\odot} units) as obtained with the TM1 (squares) and TMA (circles) EoS. From *top* to *bottom* a value of $f_b f_{\gamma} f_{ej} = 0.3, 0.01, 3 \times 10^{-4}$ has been assumed.

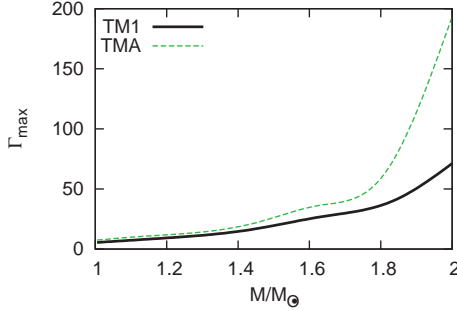


Fig. 2. Maximum Lorentz factor as a function of the mass (in M_{\odot} units) of the progenitor NS as computed with the TM1 (solid line) and TMA (dashed line) EoS. An ejection fraction of $f_{ej} = 10^{-2}$ has been assumed.

As for Lorentz factors they can be estimated from the ejected mass, M_{ej} , and E_{kin} as,

$$\Gamma_{max} = \frac{E_{kin}}{M_{ej}c^2} \simeq 19 \left(\frac{f_{ej}}{10^{-3}} \right) \left(\frac{R_{NS}}{12 \text{ km}} \right)^{-1} \left(\frac{M}{1.5 M_{\odot}} \right)^2 \left(\frac{M_{ej}}{10^{-5} M_{\odot}} \right)^{-1}. \quad (2.2)$$

As the fraction of the energy injected in the outer crust is not too small ($f_{ej} \geq 10^{-3}$) $\Gamma_{max} > 15$, in agreement with the observational constraints and even ultra-high relativistic ejecta with $\Gamma_{max} > 100$ are allowed if only the *outer* crust is expelled. The mass in the outer crust can be computed from the integration of the structure equations (Oppenheimer & Volkoff 1939) (for the non-rotating case) from the neutron drip, $\rho_{ND} \approx 4 \times 10^{11} \text{ g/cm}^3$, out to the very external radius in the NS.

In Figure 2 we show the maximum Lorentz factor Γ_{max} as a function of the NS mass (in M_{\odot} units) for the TM1 (solid line) and TMA (dashed line) EoSs. For each value of the progenitor mass, the outer crust value is obtained as the mass from the radial value where the baryonic density falls below the neutron

drip density. An ejection fraction of $f_{\text{ej}} = 10^{-2}$ has been assumed as an average typical value. We can see that for masses above $M \simeq 1.4 M_{\odot}$ gamma ray emission is allowed, and typical NS measured masses confirm this range. In particular, the value of $1.97 \pm 0.04 M_{\odot}$ for the mass of PSR J1614–223048 measured using Shapiro time delay (Demorest *et al.* 2010) can be reached in this context using the TMA EoS description. In addition to the gamma ray emission it is expected a multi-messenger correlated signal emitted in gravitational waves and neutrinos. In this sense advanced versions of LIGO/VIRGO and KM3 net detectors could detect this in the coming future.

3 Conclusions

In the present contribution we discuss whether a non-repeating cataclysmic event of the type NS→QS transition driven by DM could produce SGRBs and what would be typical values of isotropic energies and maximum Lorentz factors. We compare the energy released by SGRBs with the energetics of the progenitor model that we propose for two popular NS EoS. We discuss the short GRB event rate in light of this scenario as compared to observed rates, as well as the natural delay time between the regular NS phase and the QS formation and the properties of the host galaxies of short GRBs. We analyze crust masses for the same EoSs that could be expelled due to the NS→QS conversion and we obtain that Lorentz factors could be ultra-relativistic for large enough progenitors.

We thank the MICINN (Spain) MULTIDARK, FIS-2009-07238 and FIS2011-14759-E, FIS2012-30926 projects and the ESF-funded COMPSTAR project for partial financial support. MAPG acknowledges IAP for its kind hospitality while this work was completed.

References

- Bhattacharyya, A., Ghosh, S.K., Joarder P.S., Mallick, R., & Raha, S., 2006, Phys. Rev. C, 74, 065804
- Bertone, G., 2010, ed., Particle Dark Matter: Observations, Models and Searches (Cambridge University Press), ISBN 978-0-521-76368-4
- Cottam, J., Paerels, F., & Mendez, M., 2002, Nature, 420, 51
- Demorest, P.B., Pennucci, T., Ransom, S.M., *et al.*, 2010, Nature, 467, 1081
- Glendenning, N.K., 2000, Compact stars (Springer-Verlag, New York)
- Kouveliotou, C., Meegan, C.A., Fishman, G.J., *et al.*, 1993, ApJ, 413, L101
- Lopresto, J.C., Schrader, C., & Pierce, A.K., 1991, ApJ, 376, 757
- Oppenheimer, J.R., & Volkoff, G.M., 1939, Phys. Rev., 55, 374
- Pérez-García, M.A., Silk, J., & Stone, J.R., 2010, Phys. Rev. Lett., 105, 141101
- Pérez-García, M.A., & Silk, J., 2012, Phys. Lett. B, 711, 6
- Pérez-García, M.A., Daigne, F., & Silk, J., 2012, submitted
- Sugahara, Y., & Toki, H., 1994, Nucl. Phys. A, 579, 557
- Toki, H., Hirata, D., Sugahara Y., *et al.*, 1995, Nucl. Phys. A, 588, 357

SPECTRAL EVOLUTION OF SHORT GRBS ON SUB-MILLISECOND TIME SCALE

A. Cherenenko¹

Abstract. There has been growing consensus that short and long GRBs are associated with two different populations of astrophysical sources: mergers and SN explosions, respectively. While temporal properties of short and long GRBs could be considered with similar depth and accuracy, patterns of spectral variability of the 2 classes of GRBs are much harder to compare. This is due to the fact, that short GRBs exhibit variability on time scales shorter than 1 ms and count rate, measured at such short time scales, is not sufficient for reliable spectroscopy even for the brightest events.

In this situation, any new possibility to look at spectral evolution of short GRBs on sub-millisecond time scales in terms of spectral parameters, may provide more solid background for theoretical analysis. In this paper we present analysis of spectral evolution of short GRBs in terms of Band spectral function parameters, using the earlier developed Global Fit approach (GFA).

1 Introduction

Doing spectroscopy of transient or variable gamma-ray sources an observer normally finds himself dealing, even with modern large area detectors, with low count rate data that considerably limits the time resolution. This is because spectral functions used for spectroscopy of gamma-ray emission are normally non-linear in any parameter space and the number of approximated spectral parameters $n \gg 1$. Any nonlinear approximation procedure for such a function becomes unstable even for moderately noisy data.

Fortunately, for a fine time resolution spectroscopy, there have been numerous indications that spectral parameters of GRB spectra manifested a high degree of correlation along a given GRB (*e.g.* Ford 1995). If one assumes that some of the spectral parameters are not independent ones but rather are functions of the other

¹ Space Research Institute, Moscow

parameters, then the dimension of the optimization procedure could be reduced and one could sample the emission to smaller S/N ratios, which means either better time resolution or fainter sources. The improvement may be estimated having in mind that $\Delta t_{min} = \frac{S/N^2}{R}$, where R is count rate. For example, reducing the number of adjustable parameters from typical value of 3 to 1, one could improve time resolution by an order of magnitude. As a result, spectral evolution and variations of the integrated flux could be investigated with a comparable a time resolution.

2 Sub-millisecond spectroscopy with global fit analysis

Mathematical formulation and statistical justification of the hypothesis of functional interrelation between spectral shape parameters, which we use for time resolved spectroscopy of GRBs is described in details in (Chernenko 2002).

In short, we assume that 1) instantaneous spectra of GRBs in keV–MeV domain are of the Band shape (Band *et al.* 1993) and 2) the parameters of this spectral shape are functionally depended as follows:

$$\left| \begin{array}{l} \alpha = \alpha_0 + \alpha_R \cdot \lg(R) + \alpha_E \cdot \lg(E_0) \\ \beta = \beta_0 + \beta_R \cdot \lg(R) + \beta_E \cdot \lg(E_0). \end{array} \right. \quad (1)$$

The method of Global Fit Analysis (GFA) being allows one to estimate, for the entire duration of a GRB, the time history of E_0 and the set of global parameter of Equation (1). An example GFA application is presented in Figure 1.

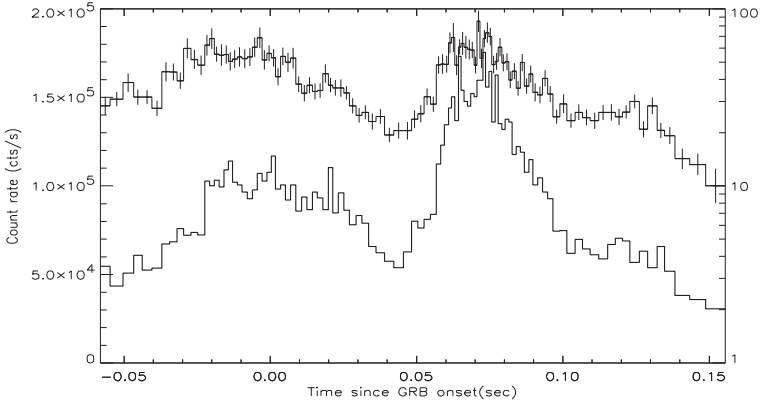


Fig. 1. Time history of count rate R is presented for BATSE GB 930905 by thick line. Overplotted by thin lines with error bars is time history of E_0 derived from GFA. The data had been re-binned with the threshold $S/N = 15$ per time interval in the range $25 \sim \text{keV} - 2 \sim \text{MeV}$, which allowed us to sample spectral evolution with time resolution down to $450 \mu\text{s}$.

3 Patterns of spectral evolution in short GRBs

As it was shown in Cherenko (2002), the GFA can be universally used for spectral analysis of GRBs in keV–Mev range. GFA allows one to reduce spectral variability to 2 independent parameters, $\mathbf{R}(t)$ and $\mathbf{E}_0(t)$. Therefore, scatter plots of $\mathbf{E}_0(t)$ vs. $\mathbf{R}(t)$ become natural tool for analysing and comparing spectral evolution across different GRBs. Figure 2 presents such a **GFA scatter plot** for BATSE GB 930905, the burst also presented in Figure 1.

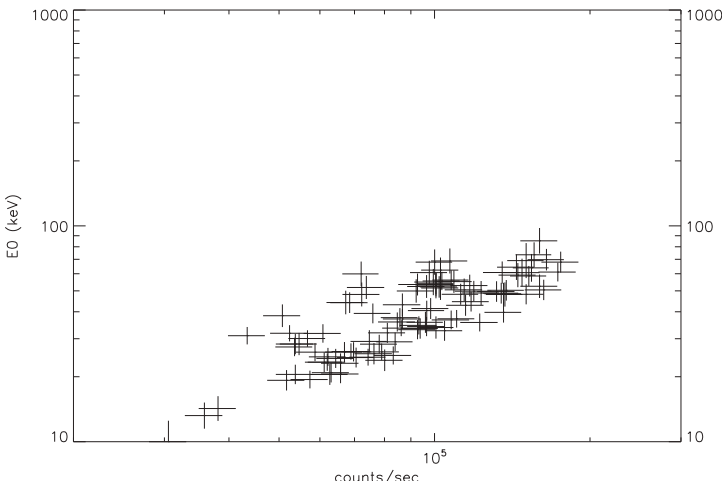


Fig. 2. Scatter plot of E_0 vs. count rate \mathbf{R} is presented for BATSE GB 930905. The data points correspond to Figure 1. Most of the points lay along a line which is characteristic to hardness-intensity correlation, while some points form clouds above this line that are typical for hard-to-soft evolution across individual peaks.

Detailed analysis of short GRB, using GFA scatter plots is beyond the scope of this paper. However, even from this example one may conclude that, despite being a classical short GRB, GB 930905 manifests, in terms of $\mathbf{E}_0(t)$ vs. $\mathbf{R}(t)$ both patterns of spectral evolution, typical for long GRBs: hardness intensity correlation, and hard-to-soft evolution. And it manifests this on sub-millisecond time scale.

4 Conclusions

While analysis of GRB hosts and their afterglows give us hints to the astronomical nature of their progenitors, it is investigation of prompt gamma-ray emission that brings us closer to understanding physical processes of GRB generation. The similarity of patterns of spectral evolution of prompt gamma-ray emission in short and long GRBs indicate that while progenitors of short and long GRBs are different, physical conditions at the engines may be similar.

The work was supported, in part, by RFBR grant 12-02-01336-a.

References

- Ford, L.A., Band, D.L., Matteson, J.L., *et al.*, 1995, ApJ, 439, 307
Band, D., Matteson, J., Ford, L., *et al.*, 1993, ApJ, 413, 281
Chernenko, A., 2002, in the Proceedings of the IAU 8th Asian-Pacific Regional meeting,
v.2, ed. S. Ikeuchi, J. Hearnshaw & T. Hanawa, 321

NUCLEOSYNTHESIS FROM LGRB-TYPE ACCRETION DISKS

T. Liu^{1,2}, L. Xue^{1,3}, W.-M. Gu¹ and J.-F. Lu¹

Abstract. We investigate the vertical structure and element distribution of neutrino-dominated accretion flows around black holes in spherical coordinates with reasonable nuclear statistical equilibrium. According to our calculations, heavy nuclei tend to be produced in a thin region near the disk surface. In this thin region, we find that ^{56}Ni is dominant in the flow with low accretion rate (*e.g.*, $0.05 M_{\odot} \text{ s}^{-1}$). The solutions indicate that ^{56}Ni comes from the central engine, whose decay may drive the bumps in the light curve of core-collapse supernova.

1 Introduction

The popular model of the central engine in gamma-ray bursts (GRBs) is named neutrino-dominated accretion flows (NDAFs, see, *e.g.*, Gu *et al.* 2006, Liu *et al.* 2007, 2008, 2010a, 2012a, 2013; Sun *et al.* 2012). The NDAF involves a hyperaccreting spinning stellar black hole with mass accretion rates in the range of $0.01 \sim 10 M_{\odot} \text{ s}^{-1}$. The extreme state is a hotbed to produce heavy nuclei, and the central region of GRBs is an ideal location to supply an extremely hot and dense state. Actually, nucleosynthesis should also be involved in the NDAFs model. The purpose of this paper is to investigate the element distribution in the vertical direction of NDAFs for long GRBs (LGRBs) with detailed neutrino physics and precise nuclear statistical equilibrium (Seitenzahl *et al.* 2008). The detailed equations is in Liu *et al.* (2013).

¹ Department of Astronomy and Institute of Theoretical Physics and Astrophysics, Xiamen University, Xiamen, Fujian 361005, China

² State Key Laboratory of Theoretical Physics, Institute of Theoretical Physics, Chinese Academy of Science, Beijing 100190, China

³ Nicolaus Copernicus Astronomical Center, Bartycka 18, 00-716 Warszawa, Poland

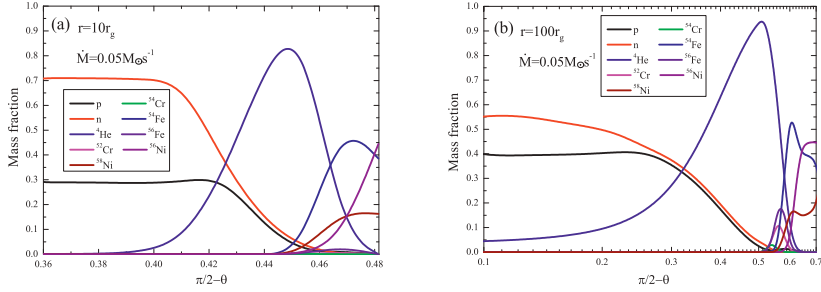


Fig. 1. Variations of the mass fraction of the main elements with θ at $r = 10r_g$ and $100r_g$ for $\dot{M} = 0.05 M_\odot s^{-1}$.

2 The distribution of heavy nuclei

Figure 1 shows the variations of the mass fraction (also approximately equals the number density) of free neutron and proton, and the other major nuclei with opening angle of the disk θ at $r = 10r_g$ and $100r_g$ for $\dot{M} = 0.05 M_\odot s^{-1}$ corresponding to (a) and (b). ^{56}Ni dominates at the disk surface, and the other heavy nuclei also appear in these cases. The solutions show that the proportion of the nuclear matter increases with radius for a certain accretion rate. The mass fraction of ^{56}Ni near the surface increases with radius. In the middle region, ^4He is dominant for any accretion rate. The free neutrons and protons are dominant near the equatorial plane of the disk in the hot and dense state. Most of the free protons are transformed into the free neutrons due to the Urca process, which causes the dominant free neutrons and the decrease of electron fraction.

3 Discussion

When a massive star collapses to a black hole, a powerful supernova occurs. The newborn hyperaccreting black hole may power a GRB. Conjecturally, the optical light curve bumps of the supernovae accompanied with LGRBs is driven by the decay of ^{56}Ni in the outflows coming from the central engine. We have described self-consistently how to produce ^{56}Ni and other elements in the central region of LGRBs with the NDAF model. Only for the low accretion rate corresponding to the central engine of LGRBs, ^{56}Ni dominates near the disk surface. More daringly, if the outflow occurs from the disk surface, which consists of ^{56}Ni and the other heavy nuclei, the bumps in supernova light curve can be naturally generated due to ^{56}Ni decay in the outflow from NDAFs. Actually, Liu *et al.* (2012a) revisited the vertical structure of NDAFs and showed that the possible outflow may appear in the outer region of the disk according to the calculations of the vertical distribution of the Bernoulli parameter. We also noticed that the basic equations of NDAF are similar to that of slim disk. The high-speed outflow may be generated near the disk surface in the two-dimensional simulations of supercritical disk (*e.g.*,

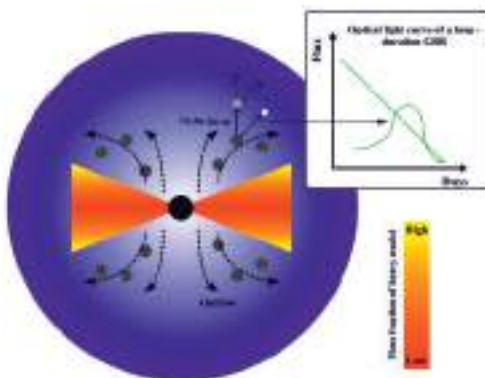


Fig. 2. Schematic picture of a Nickel factory in the collapsar.

Ohsuga & Mineshige 2011). All these suggest that an outflow near the disk surface may appear in NDAF model. Nickel existing in the outflows from the surface of NDAF with the low mass accretion rate may be the most important source of LGRB ^{56}Ni production (see Fig. 2).

This work was supported by the National Basic Research Program (973 Program) of China under grant 2009CB824800, and the National Natural Science Foundation of China under grants 11003016, 11073015, 11103015, 11222328, and 11233006.

References

- Gu, W.-M., Liu, T., & Lu, J.-F., 2006, ApJ, 643, L87
- Liu, T., Gu, W.-M., Dai, Z.-G., *et al.*, 2010a, ApJ, 709, 851
- Liu, T., Gu, W.-M., Xue, L., *et al.*, 2007, ApJ, 661, 1025
- Liu, T., Gu, W.-M., Xue, L., *et al.*, 2012a, Ap&SS, 337, 711
- Liu, T., Gu, W.-M., Xue, L., *et al.*, 2008, ApJ, 676, 545
- Liu, T., Liang, E.-W., Gu, W.-M., *et al.*, 2010b, A&A, 516, A16
- Liu, T., Liang, E.-W., Gu, W.-M., *et al.*, 2012b, ApJ, 760, 63
- Liu, T., Xue, L., Gu, W.-M., *et al.*, 2013, ApJ, 762, 102
- Ohsuga, K., & Mineshige, S., 2011, ApJ, 736, 2
- Seitenzahl, I.R., Timmes, F.X., Marin-Laflèche, A., *et al.*, 2008, ApJ, 685, L129
- Sun, M.-Y., Liu, T., Gu, W.-M., *et al.*, 2012, ApJ, 752, 31

A GTC STUDY OF THE AFTERGLOW AND HOST GALAXY OF THE SHORT-DURATION GRB 100816A

D. Pérez-Ramírez¹, J.P. Norris², J. Gorosabel^{3,4,5}, A.J. Castro-Tirado³,
L. Hernández-García³, A. de Ugarte Postigo³, S. Guziy⁶, J.C. Tello³,
R. Sánchez-Ramírez³ and P. Ferrero⁷

Abstract. We present the results from an optical monitoring campaign aimed at studying the afterglow properties of the short GRB 100816A. We implemented a new way of processing the *Swift*-BAT data, and based on it we reclassified this burst as short, discarding the initial classification as long. Observations were carried out mainly with the GTC Telescope within the four following days after the burst to investigate the optical photometry of its afterglow, and a year later to localize the host. We completed the optical imaging with the 1.23 m and 3.5 m CAHA Telescopes. We built and fitted the nIR-optical SED for the characterization of the host. The best fit of the SED ($\chi^2/\text{d.o.f.} = 1.656$) obtained for assumed values of a solar metallicity, and an extinction of $A_V = 0.2$ mag is obtained for a starburst galaxy with a dominant stellar population aging about 360 Myr.

1 *Swift* detection of GRB 100816A

GRB 100816A was detected by *Swift*-BAT (Oates *et al.* 2010) on the 16th August 2010. The initial estimated T_{90} duration (15–350 keV) was 2.9 ± 0.6 s. A preliminary classification for this GRB based on this parameter and spectral lag analysis although inconclusive pointed out to a long burst (Kouveliotou *et al.* 1993).

¹ Universidad de Jaén, Campus Las Lagunillas, s/n, Jaén, Spain

² Physics Department, Boise State University, Boise, ID 83725, USA

³ IAA-CSIC, Glorieta de la Astronomía s/n, 18008 Granada, Spain

⁴ Unidad Asociada CSIC-UPV/EHU, Dpto de Física Aplicada I, ETSI, 48013 Bilbao, Spain

⁵ Ikerbasque, Basque Foundation for Science, Alameda de Urquijo 36-5, 48008 Bilbao, Spain

⁶ Nikolaev National University, Nikolaev, Ukraine

⁷ Instituto de Astrofísica de Canarias, C/ vía Láctea, s/n, Tenerife, Spain

Assuming a redshift of $z = 0.8049$ (Tanvir *et al.* 2010) and a standard cosmology model, the isotropic energy release was estimated to be $E_{iso} = (5.8 \pm 0.7) \times 10^{51}$ erg, and the peak luminosity $(L_{iso})_{max} = (7.3 \pm 1.3) \times 10^{51}$ erg s $^{-1}$ (Golenetskii *et al.* 2010).

2 The *Swift*-BAT data analysis reveals a short burst

We implemented a new approach in the processing of the *Swift*-BAT data following Norris *et al.* (2010, 2011) procedures. We utilized the raw event data with better statistics (with about 3 times more count rate with non-tagged data than the mask-tagged data) and fitted locally the background at two time intervals. We found a duration over the same energy range $T_{90} = 1.99 \pm 0.02$ (1σ error). Figure 1 illustrates the *Swift*-BAT time profile summed over the canonical energy range 15–350 keV and binned to 8 ms resolution. The use of a finer binning did not reveal any additional significant feature. The burst basically consists of one episode of continuous, mostly smooth emission accompanied with several overlapping substructures with widths as narrow as ~ 100 ms. We also included in the analysis the spectral lag considerations that together with duration makes GRB 100816A a candidate to short burst. More details on the procedure and *Swift*-BAT data analysis in Pérez-Ramírez *et al.* (2013).

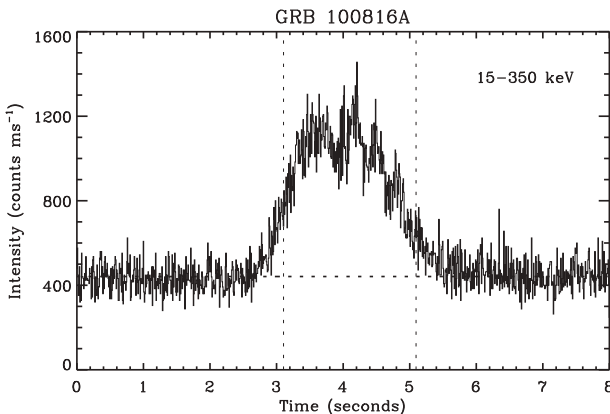


Fig. 1. The *Swift*-BAT time profile of GRB 100816A summed over the canonical energy range 15–350 keV and binned to 8 ms resolution.

3 Optical lightcurve for the GRB 100816A afterglow using the GTC and CAHA Telescopes

Once the *Swift*-UVOT detected the presence of an optical afterglow (OA), we started a monitoring campaign in two fronts: in the immediate timescale, *i.e.*

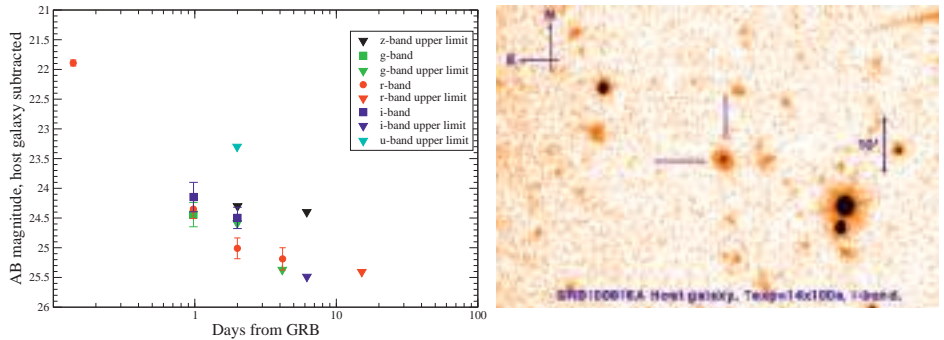


Fig. 2. a) The GTC optical light curve once the host galaxy contribution has been subtracted. **b)** *i*-band GTC deep image showing the host for GRB 100816A obtained the 8th July 2011.

minutes after the burst when we were able to activate the modest but remotely available 1.23 m CAHA Telescope, obtaining early observations of the OA (0.14 hours after the burst, Terrón *et al.* 2010). Later on, we carried out *ugriz* observations with the 10.4 m GTC equipped with OSIRIS. We observed the complete data set in the *BVRI* filters at 1.23 m CAHA Telescope. For a series of four nights, we observed the OA with the 10.4 m GTC and were able to obtain the complete lightcurve shown in Figure 2a. The OA appears in the *r* band about 22 mag hours after the burst, decreasing up to 25.5 within the following four days.

4 The nIR-optical SED for the GRB 100816A host galaxy

The host galaxy for GRB 100816A was detected a year later in a deep *i*-band image with the 10.4 m GTC (Fig. 2b). We built the Spectral Energy Distribution (SED) for the GRB 100816A based on the photometric *ugriz* points obtained with the 10.4 m GTC plus an additional nIR point, in the *H*-band, observed with the 3.5 m CAHA Telescope. The fit of the SED provides information on the stellar population age, the stellar mass, and on the host galaxy absolute luminosity. We based our SED fitting analysis on templates constructed adopting the metallicity derived from spectroscopic study ($Z = Z_{\odot}$). We mainly utilized synthetic templates, but checks have also been performed using observational templates (Kinney *et al.* 1996). The synthetic SED analysis is based on the code HyperZ (Bolzonella *et al.* 2000). The construction of the HyperZ templates was performed using the GALAXEV public code (Bruzual & Charlot 2003). Figure 3 shows our photometric points and the best fit obtained for assumed values of a solar metallicity, and an extinction of $A_V = 0.2$ mag. The best fit ($\chi^2/\text{d.o.f.} = 1.656$) is obtained for a starburst galaxy with a dominant stellar population aging about ~ 0.36 Gyr. More details on the host in Pérez-Ramírez *et al.* (2013).

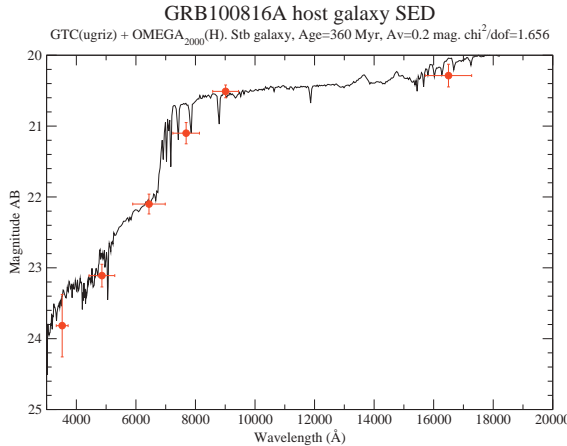


Fig. 3. The nIR-optical SED for the GRB 100816A host galaxy.

5 Conclusions

We present the results from an optical monitoring campaign with the 1.23 m and 3.5 m CAHA Telescopes, and the 10.4 m GTC Telescope aimed at studying the afterglow properties of the short-hard GRB 100816A. The GTC campaign was carried out within the four following days after the burst to investigate the optical photometry of the afterglow, and a year later, to localize the host. We built and fitted the nIR-optical SED for the characterization of the host, obtaining the best fit for a starburst galaxy with a dominant stellar population aging about 360 Myr, assuming values of a solar metallicity, and an extinction of $A_V = 0.2$ mag. We implemented on this work a new approach for the *Swift*-BAT data processing and conclude that GRB 100816A is a candidate to short burst. However, the galaxy specification and galaxy type together with inconclusive result on lag, and soft spectrum do not point out to the short nature of GRB 100816A. Comprehensive investigations are being carried out on the morphological nature of the event.

DPR acknowledges support by the Universidad de Jaén and the Spanish program AYA2012-39727-C03-01 (MINECO). JGU acknowledges support by the Unidad Asociada UPV/EHU-IAA/CSIC and the Ikerbasque Foundation for Science.

References

- Bolzonella, M., Miralles, J.-M., & Pelló, R., 2000, A&A, 363, 476
- Bruzual, G., & Charlot, S., 2003, MNRAS, 344, 1000
- Golenetskii, S., Aptekar,R., Frederiks, D., *et al.*, 2010, GCN Circ 11127
- Kinney, A.L., Calzetti, D., Bohlin, R.C., *et al.*, 1996, ApJ, 467, 38

- Kouveliotou, C., Meegan, C.A., Fishman, G.J., *et al.*, 1993, ApJ, 413, L101
Norris, J.P., Gehrels, N., & Scargle, J.D., 2010, ApJ, 717, 411
Norris, J.P., Gehrels, N., & Scargle, J.D., 2011, ApJ, 735, 23
Oates, S., Barthelmy, S.D., Beardmore, A.P., *et al.*, 2010, GCN Circ 11102
Pérez-Ramírez, D., Gorosabel, J., Castro-Tirado, A.J., *et al.*, 2013, in preparation
Tanvir, N.R., Vergani, S., Hjorth, J., *et al.*, 2010, GCN Circ 11123
Terrón, V., Fernández, M., Castro-Tirado, A.J., *et al.*, 2010, GCN Circ 11112

HIGH-ENERGY EMISSION IN SHORT GRBS AND THE ROLE OF MAGNETAR CENTRAL ENGINES

A. Rowlinson¹ and P.T. O'Brien²

Abstract. A significant number of long Gamma-ray Bursts (GRBs) detected by the *Swift* Satellite have a plateau phase signifying ongoing energy injection. Using BAT and XRT observations, we find that many short GRBs show similar behavior which challenges the typical short GRB progenitor model. We suggest the remnant of neutron star - neutron star mergers may not collapse immediately to a black hole (or even collapse at all) forming instead a magnetar. This model predicts that there would be a plateau phase in the X-ray lightcurve followed by a shallow decay phase, if it is a stable magnetar, or a steep decay if the magnetar collapses to a black hole within a few hundred seconds. By fitting this model to all short GRB BAT-XRT lightcurves, we show that a magnetar could power the observed energy injection. This model can be tested using the next generation gravitational wave observatories.

1 Introduction

The standard progenitor theory for Short Gamma-Ray Bursts (SGRBs) is the merger of two neutron stars (NSs) or a NS and a black hole (BH) which then collapse to form a BH (*e.g.* Lattimer & Schramm 1976; Eichler *et al.* 1989) and the majority of the material in the accretion disk will be accreted in ~ 2 s (Rezzolla *et al.* 2011). This model can be used to explain flares in the X-ray lightcurve via the late time accretion of material on highly eccentric orbits (*e.g.* Rosswog 2007), but is not able to explain any prolonged energy injection.

However, there are some SGRBs that show evidence of significant energy injection which cannot be explained by the BH central engine model. For example GRB 090515, a SGRB with a bright X-ray plateau (Rowlinson *et al.* 2010). An

¹ Astronomical Institute “Anton Pannekoek”, University of Amsterdam, Postbus 94249, 1090 GE Amsterdam, The Netherlands

² Department of Physics & Astronomy, University of Leicester, University Road, Leicester LE1 7RH, UK

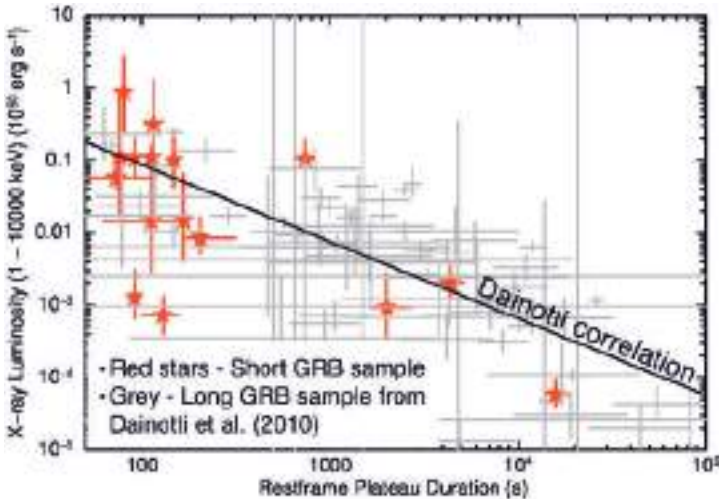


Fig. 1. The sample of SGRBs lie on the correlation between plateau luminosities and durations identified for Long GRBs by Dainotti *et al.* (2010).

alternative model, which can explain X-ray plateaus in SGRBs, is that the merger of two NSs forms a magnetar (millisecond pulsar) with sufficient rotational energy to prevent immediate gravitational collapse (*e.g.* Dai & Lu 1998; Dai *et al.* 2006). The magnetar will be rotating with initial spin periods of a few milliseconds and will spin down rapidly via the emission of gravitational waves and dipole radiation (Zhang & Mészáros 2001). The mass of the central engine will determine its evolution. If the mass is $>1.5 M_{max}$, where M_{max} is the maximum possible mass of a NS, then the central engine will immediately collapse to a BH (the typical SGRB progenitor model). Alternatively if the mass is $<1.5 M_{max}$, the merger will form a magnetar which is supported by its own rapid rotation. If the mass of the magnetar is $>M_{max}$, as it spins down it will reach a critical point at which it is no longer able to support itself and the magnetar will collapse to a BH.

In this conference proceeding, we summarise the search conducted for evidence of prolonged energy injection in SGRB lightcurves and show that a magnetar central engine could explain many of the observed features (the full analysis is described in Rowlinson *et al.* 2013).

2 Short GRBs show signs of energy injection

We created combined BAT-XRT, 0.3–10 keV, lightcurves for all SGRBs in the *Swift* sample with $T_{90} \leq 2$ s detected by the Burst Alert Telescope (BAT) until March 2012 and which were promptly observed by the X-ray Telescope (XRT), giving a sample of 43 SGRBs. We fitted them using a simple broken powerlaw model (utilising the method in Evans *et al.* 2009). Using the SGRB redshift (known for

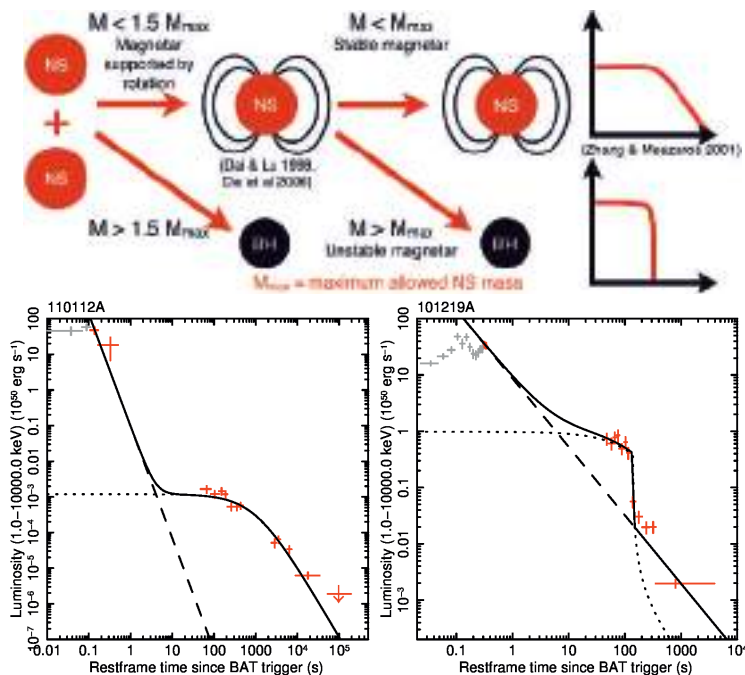


Fig. 2. *Top:* a cartoon illustrating the possible outcomes of the merger of two NSs, depending on the mass of the central object, and a sketch of the expected lightcurves for stable and unstable magnetars. *Bottom left:* GRB 110112A fitted with the stable magnetar model. *Bottom right:* GRB 101219A fitted with the unstable magnetar model.

10 SGRBs in the sample), or the average redshift for SGRBs when the redshift is unknown, the BAT-XRT lightcurves were converted to restframe lightcurves using a k-correction (Bloom *et al.* 2001).

Some of the SGRB sample ($\sim 50\%$) show evidence of a shallow decay phase or plateau, consistent with prolonged energy injection. In Figure 1, we plot the X-ray luminosity of the plateau phase against the restframe duration of the plateau for the sample of SGRBs. These SGRBs are consistent with a correlation identified by Dainotti *et al.* (2010) for a sample of long GRBs. This energy injection cannot be explained by the typical progenitor model.

3 A magnetar central engine can explain energy injection

In the magnetar model, each possible outcome of the merger of two NSs give a characteristic lightcurve as shown in Figure 2. Assuming constant radiative efficiency, the dipole radiation from a magnetar predicts a plateau phase with a shallow decay phase (for stable magnetars) or a steep decay phase (when an unstable magnetar collapses to a BH).

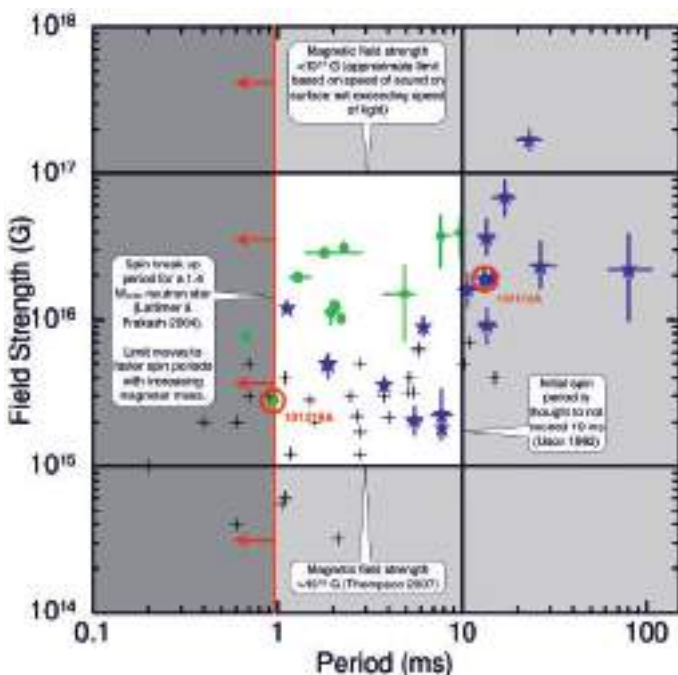


Fig. 3. The magnetic field strengths and initial spin periods of the magnetar fits for the sample of SGRBs. Blue stars - stable magnetar candidates, green circles - unstable magnetar candidates and black crosses - LGRB magnetar candidates (Lyons *et al.* 2010; Dall’Osso *et al.* 2011; Bernardini *et al.* 2012). Circled in red are the two SGRBs plotted in Figure 2. Dark grey regions are forbidden regions, light grey regions are those which are loose constraints on the initial magnetar properties from different theoretical arguments (given in figure) and the white region is the expected region for newly born magnetars.

We fit the magnetar model (as described in Zhang & Mészáros 2001) to 28 rest frame SGRB lightcurves (those with sufficient X-ray data), with an additional powerlaw component whose decay rate is governed by the curvature effect (Kumar & Panaiteescu 2000). The emission is assumed to be 100% efficient and isotropic. Additionally, the model neglects enhanced angular momentum losses at early times due to neutrino-driven mass loss (Metzger *et al.* 2011).

All the SGRBs fitted can be explained using a magnetar central engine, with 18 firm candidates and the remaining are possible candidates depending on various assumptions within the model. Two example fits are shown in Figure 2. The magnetar model outputs the initial spin period and magnetic field strength of the fitted magnetar. These values are plotted in Figure 3 along with theoretical constraints on the magnetic fields and spin periods of newly formed magnetars. Many of the candidates lie within the expected region for a newly formed magnetar.

4 Conclusions

We have shown that SGRBs show evidence of prolonged energy injection that can be explained by the magnetar central engine model. This model may be testable using the next generation gravitational wave detectors as each phase of the model (inspiral, magnetar and collapse to BH) has an associated gravitational wave signal. Using predicted sensitivities, Advanced LIGO may be able to detect all 3 phases for sources within 100 Mpc (Abadie *et al.* 2010), although the rates are expected to be very low, whilst the Einstein Telescope would have a much higher chance of detection (Hild *et al.* 2011).

References

- Abadie, J., Abbott, B.P., Abbott, R., *et al.*, 2010, CQGra, 27, 173001
 Bernardini, M.G., Margutti, R., Mao, J., Zaninoni, E., & Chincarini, G., 2012, A&A, 539, A3
 Bloom, J.S., Frail, D.A., & Sari, R., 2001, AJ, 121, 2879
 Dai, Z.G., & Lu, T., 1998, A&A, 333, L87
 Dai, Z.G., Wang, X.Y., Wu, X.F., & Zhang, B., 2006, Science, 311, 1127
 Dainotti, M.G., Willingale, R., Capozziello, S., Fabrizio, Cardone V., & Ostrowski, M., 2010, ApJ, 722, L215
 Dall'Osso, S., Stratta, G., Guetta, D., Covino, S., de Cesare, G., & Stella, L., 2011, A&A, 526, A121
 Eichler, D., Livio, M., Piran, T., & Schramm, D.N., 1989, Nature, 340, 126
 Evans, P.A., Beardmore, A.P., Page, K.L., *et al.*, 2009, MNRAS, 397, 1177
 Hild, S., Abernathy, M., Acernese, F., *et al.*, 2011, CQGra, 28, 094013
 Kumar, P., & Panaiteescu, A., 2000, ApJ, 541, L51
 Lattimer, J.M., & Prakash, M., 2004, Science, 304, 536
 Lattimer, J.M., & Schramm, D.N., 1976, ApJ, 210, 549
 Lyons, N., O'Brien, P.T., Zhang, B., *et al.*, 2010, MNRAS, 402, 705
 Metzger, B.D., Giannios, D., Thompson, T.A., Bucciantini, N., & Quataert, E., 2011, MNRAS, 413, 2031
 Rezzolla, L., Giacomazzo, B., Baiotti, L., *et al.*, 2011, ApJ, 732, L6
 Rosswog, S., 2007, MNRAS, 376, L48
 Rowlinson, A., O'Brien, P.T., Tanvir, N.R., *et al.*, 2010, MNRAS, 409, 531
 Rowlinson, A., O'Brien, P.T., Metzger, B.D., Tanvir, N.R., & Levan, A.J., 2013, MNRAS, 608
 Thompson, T.A., 2007, RMxAC, 27, 80
 Usov, V.V., 1992, Nature, 357, 472
 Zhang, B., & Mészáros, P., 2001, ApJ, 552, L35

Chapter VIII.
Progenitors and Environments

DISSECTING THE GRB ENVIRONMENT WITH OPTICAL AND X-RAY OBSERVATIONS

S. Campana¹

Abstract. GRB's environment can be studied through the imprint (*i.e.* absorption) it leaves on the afterglow emission. Fast optical observations allowed us to observe line variability and to derive the distance and composition of the absorbing medium. However, given the huge GRB ionizing flux, this medium starts showing up in the optical spectra only at relatively large distances ($\gtrsim 100$ pc). A complementary view comes from the X-ray band, where the overall contribution of all metals bends the power law X-ray afterglow spectrum. We will review and compare optical and X-ray studies of the circumburst medium.

1 Introduction

Long duration Gamma-ray Bursts (GRBs) are associated with the death of massive stars. This evidence comes principally from the association of close-by GRBs ($z \lesssim 0.5$) to type Ic Supernovae (Woosley & Bloom 2006). In addition, GRBs occur in the most luminous part of their host galaxies (Svensson *et al.* 2010). These observational facts clearly point to a close relationship between star formation and GRBs, suggesting that the ambient medium in which GRBs explode is denser than the interstellar medium and typical of star forming regions. In this contribution we will focus on the properties of the ambient medium that can be envisaged through optical and X-ray studies.

2 Dark GRBs

Since the discovery of GRB afterglows it has become clear that a number of GRBs lack an optical afterglow (Fynbo *et al.* 2001). Given the different observing conditions, a more rigorous definition is needed besides the “no optical afterglow” statement. Based on the predictions of the fireball model (Mészáros & Rees 1997)

¹ INAF - Osservatorio astronomico di Brera, via Bianchi 46, 23807 Merate (LC), Italy;
e-mail: sergio.campana@brera.inaf.it

one can require that the optical to X-ray spectral index β_{OX} (*i.e.* the slope between the fluxes in the R -band and at 1 keV) should be lower than 0.5 (Jakobsson *et al.* 2004). This will characterize optically sub-luminous bursts, *i.e.* fainter than expected from the fireball model. With the advent of the *Swift* satellite, X-ray spectral slopes were available and a somewhat different definition was put forward by van der Horst *et al.* (2009) for which β_{OX} is shallower than $\beta_X - 0.5$.

Earlier studies suggested that 20 – 50% range of GRBs are dark, and dust absorption, high redshift or intrinsically dim afterglows are possible causes. With the advent of complete samples of GRBs this matter can be settled on more solid grounds. The flux limited Swift-BAT6 sample (Salvaterra *et al.* 2012) and the GROND sample (Greiner *et al.* 2011) both provide a fraction of 25 – 40% of dark GRBs (Melandri *et al.* 2012) and likely indicate dust absorption (possibly helped in some cases by a relatively large redshift) as their likely cause. At variance with earlier studies also the distribution of optical absorptions, A_V , in complete samples of GRBs is not negligible, showing a continuum of values from zero to a few (Covino *et al.* 2013; Greiner *et al.* 2011, see Fig. 1a).

A clearer picture arises from X-ray studies where a connection between the intrinsic (*in situ*) absorbing column density and the GRB darkness was found. Comparing the intrinsic column density distribution of dark and non-dark GRBs of the Swift-BAT6 sample, a Kolmogorov-Smirnov test returns a probability of 2×10^{-6} (corresponding to 4.8σ) for Jakobssons darkness definition and 1×10^{-5} (4.4σ) for van der Horsts definition. These results indicate that the intrinsic absorption as evaluated in the X-ray band is highly correlated with the darkness of a GRB (Campana *et al.* 2012, see Fig. 1b).

3 Optical spectroscopy

Optical absorption (A_V) and X-ray column density (N_H) provide a cumulative (integral) measure of the matter along the line of sight. Deeper insight comes from (high resolution) spectroscopic studies. These studies reveal that the absorption lines relative to the GRB site is made up by several components and trace the distribution of matter along the line of sight within the host galaxy (in addition to lines coming from intervening systems). The strongest lines are CII, CIV, OI, SiII, SiIV, MgI and FeII and are characterized by blue as well as red-shifts, spanning up to $\pm 150 \text{ km s}^{-1}$. These lines are interesting and provide a clue on the number of absorbing systems as well as on the metallicity of the host galaxy, but we can have only an indirect idea of their distances from the GRB site. Indirect modeling based on ionization potential and burst flux can lead to estimate a minimal distance from the GRB of $>50 - 100 \text{ pc}$, for *e.g.* the MgI line in GRB 051111 (Prochaska *et al.* 2005).

The key element to assess the absorption systems' distances is line variability. The first line variation was observed in GRB 020813, comparing a Keck/LRIS spectrum obtained ~ 5 hr after the GRB event with a VLT/UVES spectrum acquired ~ 16 hr after the first one: a FeII fine-structure transition ($J = 7/2$) was clearly detected to vary (Dessauges-Zavadsky *et al.* 2006). The line variability

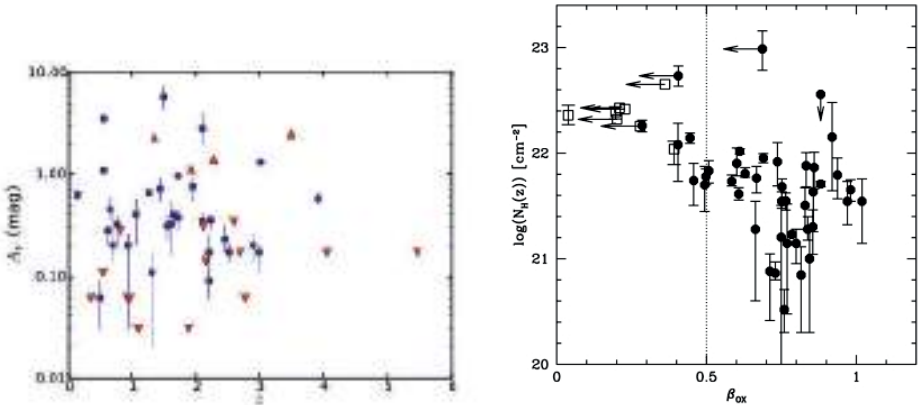


Fig. 1. *Left panel:* redshift dependence of A_V in the complete Swift-BAT6 sample (from Covino *et al.* 2013). The A_V have been estimated through Spectral Energy Distribution fitting. *Right panel:* column density (N_H) as a function of the spectral index β_{OX} for the Swift-BAT6 GRBs computed in Melandri *et al.* (2012). The dashed line for $\beta_{OX} = 0.5$ divides dark and non-dark GRBs according to Jakobsson *et al.* (2004). The open squares (filled circles) indicate dark (non-dark) GRBs according to van der Horst *et al.* (2009, from Campana *et al.* 2012).

technique was first exploited with GRB 060418. For this burst the VLT Rapid Response Mode (RRM) was activated producing spectra at 13, 15, 20, 30 and 90 min after the burst onset. Fine structure variability in six FeII lines were clearly detected (together with Ni II; Vreeswijk *et al.* 2007, Fig. 2a). Modeling of these line variations led us to exclude collisional excitation and IR excitation as viable mechanisms. On the contrary, UV pumping (powered by the GRB UV flux) was found to be the dominant mechanism and led to estimate the absorbing region distance to be 0.5 ± 0.1 kpc. The best example is provided by the naked-eye burst GRB 080319B observed with VLT/UVES in RRM (see Fig. 2b). Six different absorption systems were identified within the host galaxy, spanning a distance range of 0.6–1.7 kpc (D'Elia *et al.* 2009). In addition to fine structure variability, in only one case a variability (decrease) in the Lyman α line intensity was detected. The optical spectra of GRB 090426 taken at 1 and 12 hr after the burst, show a 3.8σ decrease in the line Equivalent Width. This is the first compelling evidence for photoionization of the material from the star-forming region of the progenitor itself. Based on a tailored photoionization code the distance of the absorber has been estimated in ~ 80 pc (Thöne *et al.* 2011, Fig. 3a).

A summary of all the absorption systems distances in GRB afterglow spectra is shown in Figure 3b. These are all derived from fine structure line variations apart from GRB 090426. Distances range from 80 pc to a few kpc. This scale is comparable to the expected size of the shock among the progenitor's wind and the Interstellar Medium (ISM). All the material within ~ 100 pc is heavily affected by the GRB photo-ionizing flux.

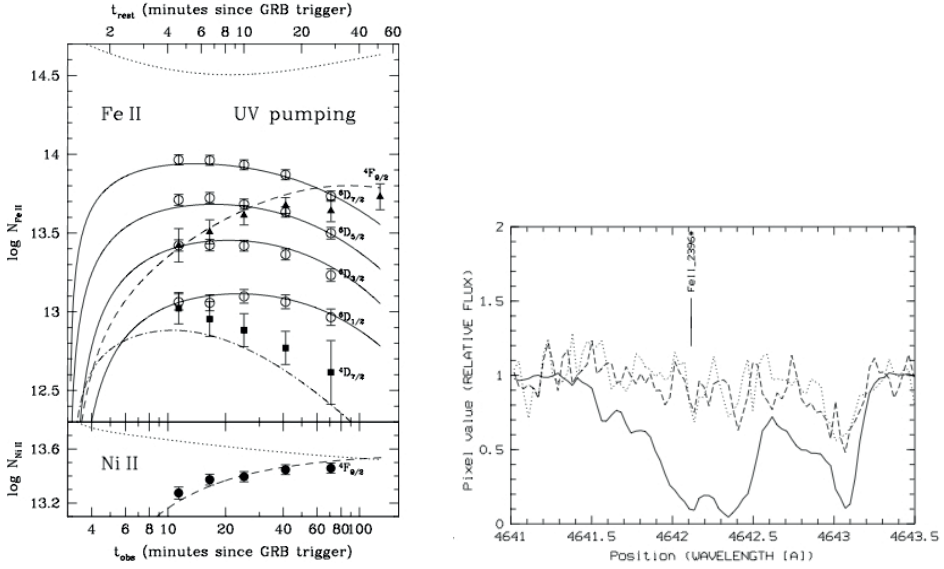


Fig. 2. *Left panel:* Fe II and Ni II column density variations observed in GRB 060418 with several VLT/UVES observations. Line variations are very well described by the UV pumping model (from Vreeswijk *et al.* 2007). *Right panel:* UVES spectra of GRB 080319B around the fine-structure FeII $\lambda 2396^*$ line. The solid line refers to the 1st epoch spectrum (8.5 min after the trigger), the dashed line refers to the 2nd spectrum (1.9 hr), and the dotted line to the 3rd spectrum (2.9 hr; from D'Elia *et al.* 2009).

4 X-ray observations

At optical wavelengths the GRB flux is too strong and no line variations are observed to arise within ~ 100 pc. To probe the medium closer to the progenitor, one can look at higher ionization lines, like S⁺⁴, N⁺⁵, and O⁺⁶. These lines are observed (sometimes) in GRB optical spectra but, up to now, no variations were revealed. As a matter of fact at optical wavelengths we are unable to dissect the closest medium to the GRB. This is due to the high GRB photoionization flux. Ideally we can try to study the medium at even shorter wavelengths, hoping that the GRB ionizing flux effects are reduced. Given the spectral resolution and effective area of current X-ray facilities it is difficult to reveal line or absorption edge variations in the X-ray spectra of GRBs (unless possibly with the Reflection Grating Spectrometers on board XMM-Newton). Along these lines one can try to study (X-ray) column density variations, *i.e.* the integrated absorption caused by metals surrounding the GRB site.

A study of the intrinsic absorbing column density in the complete sample of Swift-BAT6 bursts shows that these events are heavily absorbed with a mean absorption of $\log(N_H/\text{cm}^{-2}) = 21.7 \pm 0.5$ (Campana *et al.* 2012). In addition, the distribution is consistent with the expected distribution obtained by putting

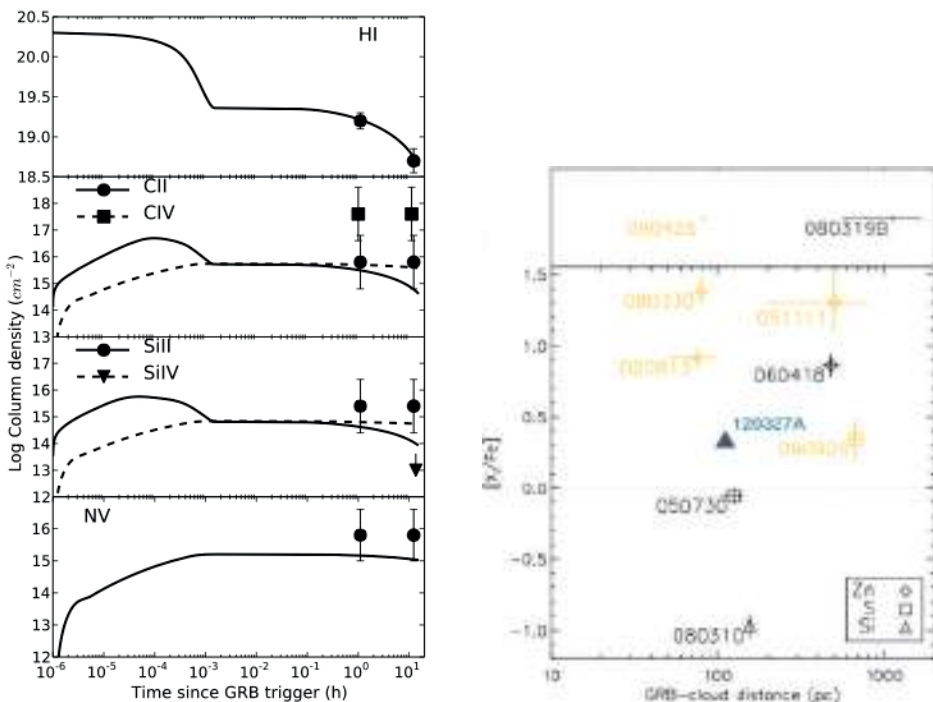


Fig. 3. *Left panel:* temporal evolution of the absorbing columns of H, C, Si and N ions. The best-fitting evolution of the absorbing columns as derived from our photoionization model is overlaid (from Thöne *et al.* 2011). *Right panel:* summary of absorbing system distances in GRB afterglow optical spectra (from Vreeswijk *et al.* 2012).

GRBs randomly within Giant Molecular Clouds similar to the ones observed in our Galaxy (Campana *et al.* 2010, 2006). This testifies once more that GRBs occur in dense regions. A comparison between optical and X-ray column densities shows interesting results. After correcting for metallicities, X-ray absorbing columns are always larger than optical columns (N_{HI}) by a factor of ~ 10 (but in some cases much more, see Fig. 4a). This is can be interpreted as a manifestation of GRB photoionization (Campana *et al.* 2010; Watson *et al.* 2007).

Column density variations are needed to assess the absorber distance. These are difficult to detect due to the spectral changes associated to the afterglow evolution. In the high-redshift GRB 050904 a column density variation has been detected by several groups (Watson *et al.* 2006; Boér *et al.* 2006; Gendre *et al.* 2006; Campana *et al.* 2007). This has been modeled with a photoionization code leading to the characterization of the absorbing medium (Fig. 4b). The absorbing region is estimated to lie very close to the GRB site, some 5–10 pc away (Campana *et al.* 2007). In addition, the optical transient was observed at $t_{\text{obs}} \sim 200$ s (*i.e.* 27 s rest frame) in white light, indicating very little absorption. The little extinction implied by the early optical observation can be explained by a dust component

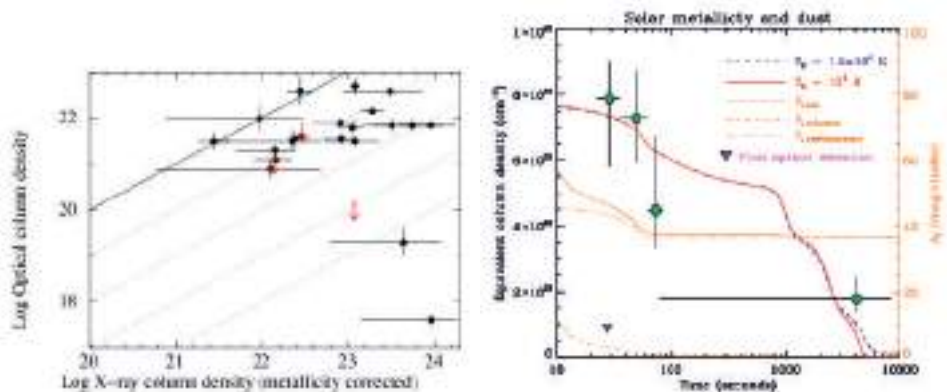


Fig. 4. *Left panel:* X-ray (metallicity corrected) versus optical column densities for GRBs. The continuous line refers to equal optical to X-ray values, the dotted lines to n -th orders of magnitude difference (from Campana *et al.* 2010). *Right panel:* evolution of the column density measured in the X-ray afterglow of GRB 050904 (circles with error bars at 1σ). Time is in the rest frame ($z = 6.4$). The thick solid and the thick dashed lines show the best-fit models for different initial temperatures. The photoionization code has in input the observed light curve of GRB 050904 (Cusumano *et al.* 2006). The drop in absorption at $t \sim 1000$ s (rest frame) corresponds to a group of bright X-ray flares. The thin solid line (and right y-axis) shows the amount of absorption that would be observed in the J band (rest frame 7 eV) if the X-ray absorbing medium were polluted with Galactic-like dust. Thin dashed and dot-dashed lines show the absorption due to silicates only and to carbonaceous grains only (from Campana *et al.* 2007).

rich in silicates and depleted in carbonaceous grains. This could be the result of an ISM enriched by pair-instability supernovae. The involved mass is very large but it is in line with the medium density of ~ 700 cm $^{-3}$, estimated through radio studies (Frail *et al.* 2006).

5 Conclusions

The ambient medium surrounding GRBs is complex but it holds the potential to unveil the progenitor's latest stages and nature. There is strong evidence to connect (long) GRBs to star formation and their formation site to dense ambient media. Optical high-resolution spectroscopic studies can dissect the GRB environment in exquisite detail, sampling however regions larger than ~ 100 pc. To probe the ambient medium closer to the progenitor, we need to trace higher energy transitions, thus reducing the influence of the huge GRB photoionization flux. This cannot be done with current facilities, lacking a fast-slewing, high spectral resolution X-ray telescope. An integral description of the X-ray absorption (N_H) can be in any case gathered thanks to the Swift/XRT instrument and in a few cases N_H variations enable us to probe the absorbing medium in the proximity of the GRB progenitor.

This work has been supported by ASI grant I/004/11/0. The number of people I have to thank is very large so I will put just initials: MGB, SC, GC, PDA, VDE, MDV, GG1, GG2, DL, DM, AM1, AM2, LN, NP, PR, RS, BS, GT, CT, SDV.

References

- Boér, M., Atteia, J.L., Damerdji, Y., *et al.*, 2006, ApJ, 638, L71
Campana, S., Mangano, V., Blustin, A.J., *et al.*, 2006, A&A, 454, 113
Campana, S., Lazzati, D., Ripamonti, E., *et al.*, 2007, ApJ, 654, L17
Campana, S., Thöne, C.C., de Ugarte Postigo, A., *et al.*, 2010, MNRAS, 402, 2429
Campana, S., Salvaterra, R., Melandri, A., *et al.*, 2012, MNRAS, 421, 1697
Covino, S., Melandri, A., Salvaterra, R., *et al.*, 2013, MNRAS, submitted
Cusumano, G., Mangano, V., Chincarini, G., *et al.*, 2006, Nature, 440, 164
D'Elia, V., Fiore, F., Perna, R., *et al.*, 2009, ApJ, 694, 332
Dessauges-Zavadsky, M., Chen, H.-W., Prochaska, J.X., *et al.*, 2006, ApJ, 648, L89
Frail, D., Cameron, P.B., Kasliwal, M., *et al.*, 2006, ApJ, 646, L99
Fynbo, J.P.U., Gorosabel, J., Dall, T.H., *et al.*, 2001, A&A, 373, 796
Gendre, B., Galli, A., Corsi, A., *et al.*, 2007, A&A, 462, 565
Greiner, J., Krühler, T., Klose, S., *et al.*, 2011, A&A, 526, A30
Jakobsson, P., Hjorth, J., Fynbo, J.P.U., *et al.*, 2004, A&A, 427, 785
Melandri, A., Sbarufatti, B., D'Avanzo, P., *et al.*, 2012, MNRAS, 421, 1265
Mészáros, P., & Rees, M.J., 1997, MNRAS, 288, L51
Prochaska, J.X., Chen, H.-W., & Bloom, J.S., 2005, ApJ, 648, 95
Salvaterra, R., Campana, S., Vergani, S.D., *et al.*, 2012, ApJ, 749, 68
Svensson, K.M., Levan, A.J., Tanvir, N.R., *et al.*, 2010, MNRAS, 405, 57
Thöne, C.C., Campana, S., Lazzati, D., *et al.*, 2011, MNRAS, 414, 479
van der Horst, A.J., Kouveliotou, C., Gehrels, N., *et al.*, 2009, ApJ, 699, 1087
Vreeswijk, P.M., Ledoux, C., Smette, A., *et al.*, 2007, A&A, 468, 83
Vreeswijk, P.M., Ledoux, C., De Cia, A., & Smette, A., 2012, MSAIS, 21, 14
Watson, D., Reeves, J.N., Hjorth, J., *et al.*, 2006, ApJ, 637, L69
Watson, D., Hjorth, J., Fynbo, J.P.U., *et al.*, 2007, ApJ, 660, L101
Woosley, S.E., & Bloom, J.S., 2006, ARA&A, 44, 507

EARLY UV/OPTICAL EMISSION OF THE TYPE IB SN 2008D

M.C. Bersten¹

Abstract. We propose an alternative explanation for the post-breakout emission of SN 2008D that cannot be reproduced by the explosion of a normal Wolf-Rayet star. We explored several physical scenarios and proposed that the early emission was enhanced by the presence of ^{56}Ni in the outermost layers of the ejecta in addition to the usual internal distribution. This kind of double-peaked ^{56}Ni distribution could be explained by the formation of jets during the explosion.

1 Introduction

The type Ib supernova (SN) 2008D attracted a good deal of attention because of some unusual observational features such as the detection of an X-ray transient (XRT) and an early optical light-curve peak. So far only Type Ic SNe have been associated with gamma-ray bursts (GRB) but given the detection of a weak XRT and the large explosion energy and mass derived for SN 2008D by Mazzali *et al.* (2008) and Tanaka *et al.* (2009) (T09), it has been suggested that this SN may be a transitional object between the highly energetic SNe Ic and normal core-collapse SNe. The nature of the XRT is controversial. Some authors are in favor of the supernova shock-breakout origin while others consider that the transient was caused by a mildly relativistic jet penetrating through the envelope of the progenitor star. Irrespective of the origin of the XRT, here we focus on the analysis of the early UV/optical emission using radiation-hydrodynamical calculations.

2 A High-Velocity blob of ^{56}Ni

To analyze the early emission of SN 2008D we use a hydrodynamical code that self-consistently calculates the shock wave propagation, the breakout and the later SN evolution (Bersten *et al.* 2011). We adopt a pre-SN model with He core of $8 M_{\odot}$, $R = 1.4 R_{\odot}$, $E = 8.4 \times 10^{51} \text{ erg s}^{-1}$, and $M_{\text{Ni}} = 0.07 M_{\odot}$ (from here

¹ Kavli Institute for the Physics and Mathematics of the Universe, Todai Institutes for Advanced Study, University of Tokyo, 5-1-5 Kashiwanoha, Kashiwa, Chiba 277-8583, Japan

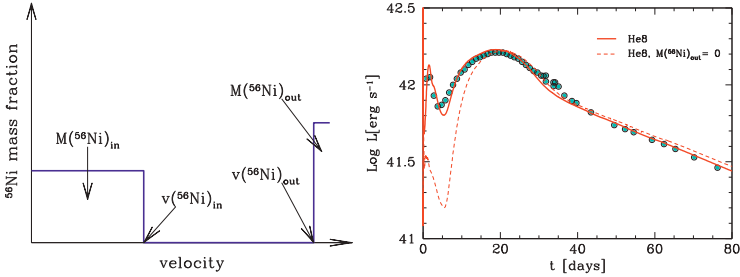


Fig. 1. *Left:* schematic doubly-peaked ^{56}Ni distribution. *Right:* bolometric LC for model He8 with (solid line) and without (dashed line) external ^{56}Ni compared with the observations of SN 2008D.

on He8). The election of our initial model was based on the very good overall agreement obtained in T09 using this model. Figure 1 shows the resulting light curve (LC) for He8 model (dashed line) as compared with the observations (Maund *et al.* 2009). Clearly, this model cannot explain the early emission shown by the observations. The difference in luminosity between the hydrodynamical model and the observations at early times is >0.5 dex. To avoid this problem, we artificially placed some ^{56}Ni in the outermost layers of the ejecta in addition to the usual internal distribution, as schematically shown in the left panel of Figure 1. A model based on He8 but with an external ^{56}Ni of $\approx 0.01 M_\odot$ at $v > 20,000 \text{ km s}^{-1}$, is shown with a solid line Figure 1. The agreement between this model and the observations is now excellent.

2.1 Alternative approaches

Figure 2 shows the prediction of analytic models for the cooling of the outer envelope proposed by Chevalier & Fransson (2008) (CF08) and Rabinak & Waxman (2011) (RW11) to explain the early emission of SN 2008D. These models assume 1) pre-explosion density $\rho \propto (1 - r/R)^n$ valid while the mass above of the photosphere is $< 0.1 M_\odot$ and (2) constant opacity. The models show have the same parameters as model He8 (solid lines), and $E = 2 \times 10^{51} \text{ erg s}^{-1}$, $M = 5 M_\odot$ and $R = 9 R_\odot$ (dashed lines). Three different hydrodynamical calculations are also shown: model He8 with (red solid line) and without (red dashed line) external ^{56}Ni and a model assuming an opacity of $\kappa_{e-} = 0.2 \text{ g cm}^{-2}$ for electron-scattering for pure helium. From this comparison we find that (a) the analytic models are valid only until 1.5 days after the explosion where only two data points are available. And (b) larger initial radius improves the agreement with the observations. To test the effect of radius we artificially modified our pre-SN model in two ways (a) attaching mass-less envelopes ($< 0.01 M_\odot$) or different radii to He8 model, and (b) attaching massive envelopes with $9 R_\odot$ at different points inside the He8 model. The LCs for these two types of models are shown in Figure 2 (right panel) with thick and thin lines, respectively. While the low-mass envelopes cannot

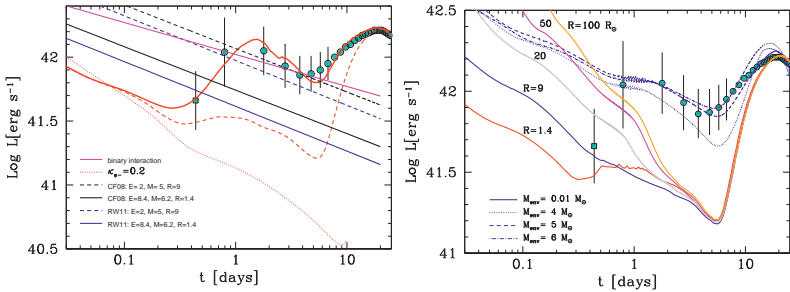


Fig. 2. *Left:* comparison between the bolometric luminosity of the analytic models of CF08 (black lines), RW11 (blue lines) and K10 (magenta line) and hydrodynamical models (red lines). *Right:* bolometric LC for models with mass-less (thick lines) and massive (thin lines) envelopes attached to the He8 model.

satisfactorily reproduce the early LC, the massive ones give reasonably good fits, excluding the earliest data point. However, the massive-envelope models give a much poorer fit to the LC around the main peak, and they pose the additional problem of finding a physical explanation to such an unusual density profile. Finally, we tested the possibility that the early emission was due to interaction of the ejecta with a binary companion using the analytic predictions by Kasen (2010; K10) (magenta line in left panel of Fig. 2). However, the binary separation required to fit the early emission should be $< 3 R_{\odot}$, which is too small for a system containing two massive stars.

3 Conclusion

The early post-breakout emission of SN 2008D cannot be explained as the cooling of the outer layers after the explosion of a normal Wolf-Rayet star. Alternatively, we found an excellent agreement with the observed bolometric LC of SN 2008D by assuming $0.01 M_{\odot}$ of ^{56}Ni mixed out to high velocity ($v > 20,000 \text{ km s}^{-1}$). This type of ^{56}Ni distribution may indicate the presence of jets (Maund *et al.* 2009).

References

- Bersten, M.C., Benvenuto, O., & Hamuy, M., 2011, ApJ, 729, 61
- Chevalier, R.A., & Fransson, C., 2008, ApJ, 683, L135
- Kasen, D., 2010, ApJ, 708, 1025
- Mazzali, P.A., Valenti, S., Della Valle, M., *et al.*, 2008, Science, 321, 1185
- Modjaz, M., Li, W., Butler, N., *et al.*, 2009, ApJ, 702, 226
- Rabinak, I., & Waxman, E., 2011, ApJ, 728, 63
- Tanaka, M., Tominaga, N., Nomoto, K., *et al.*, 2009, ApJ, 692, 1131
- Maund, J.R., Wheeler, J.C., Baade, D., *et al.*, 2009, ApJ, 705, 1139

THE CIRCUMSTELLAR MEDIUM SURROUNDING ROTATING MASSIVE STARS AS GRB PRECURSORS

B. Pérez-Rendón¹, J. Higuera², G. García-Segura³, A. Santillán⁴
and L. Hernández-Cervantes⁵

Abstract. Long duration Gamma Ray Bursts (LGRB) are thought to originate from massive rotating stars and the interaction of their expanding jet will be affected by the structure of their circumburst medium. In this work we use rotating stellar models of massive stars to determine the state of circumburst material in various types of progenitor scenarios and we describe how this external matter can appear in GRB observations.

1 Introduction

Massive stars ($M > 8 M_{\odot}$) lose a considerable amount of mass in form of stellar wind before the end of their life and the stellar mass loss affects the stellar evolution itself. The stellar wind parameters change in each evolutionary stage, shaping a wide variety of structures in the surrounding gas. If the collapsar conditions are fulfilled by the star, the structure of its circumstellar medium could be revealed in the signal of the long Gamma Ray Burst (LGRB) which can occur at the end of the life of these massive stars. According to Yoon *et al.* (2006) the collapsar model for a LGRB requires three essential ingredients: the removal of the hydrogen envelope, a massive core and enough angular moment in it, and these conditions are achieved by rotating massive stars with low metallicities that become a Wolf-Rayet star (WR) at the end of their life. In this work we use numerical simulations to describe the circumstellar medium around massive stars that fulfill these conditions in order to study the origin of the blue-shifted absorption features observed in LGRB

¹ Depto. de Investigación en Física, Universidad de Sonora, Hermosillo, Sonora, México

² Departamento de Física, Universidad de Sonora, Hermosillo, Sonora, México

³ Instituto de Astronomía, UNAM, Ensenada, Baja California, México

⁴ Dirección General de Cómputo y de Tecnologías de Información y Comunicación, DGCTIC, UNAM, México City, México

⁵ Instituto de Astronomía, UNAM, Ciudad Universitaria, México City, México

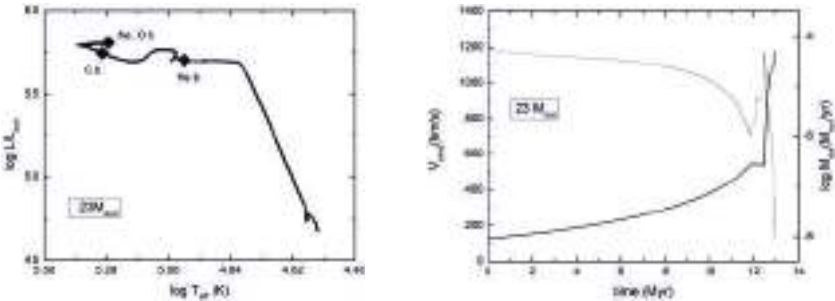


Fig. 1. *Left panel:* evolutionary track of a $23 M_{\odot}$ rotating star. The onset of each burning phase is indicated in the figure. *Right panel:* mass loss rate (thick line) and terminal velocity (broken line) of the stellar wind as function of time.

afterglows (Prochaska *et al.* 2008) or to explore the influence of circumstellar gas in the evolution of the LGRB itself (Ramírez-Ruiz *et al.* 2005). In this work we built a stellar evolution model representing a star with $M_{\text{ZAMS}} = 23 M_{\odot}$ and we calculate their circumstellar gas evolution.

2 Numerical simulations

We study the case of a fast rotating $23 M_{\odot}$ star with low metallicity ($Z = Z_{\odot}/10$). The initial angular velocity is set to $\Omega_0 = 0.5 \Omega_{\text{crit}}$ where Ω_{crit} is the critical angular velocity. With this rotation rate the chemically homogeneous evolving stellar model fulfills the conditions of a stellar LGRB progenitor (as in van Marle *et al.* 2008). Additional to these parameters, the input physics were implemented as described in Pérez-Rendón *et al.* (2009). The evolutionary track in Hertzsprung-Russell diagram (HRD) is shown in Figure 1. Due to the fast rotation this model avoids redward evolution in HRD and evolves directly to helium main sequence. We have obtained the stellar mass loss rate, wind velocity and rotation velocity as a function of time and we use it as inner boundary conditions in an explicit hydrodynamical code (ZEUS-3D, Stone & Norman 1992) to simulate the hydrodynamical evolution of circumstellar medium, using a bidimensional grid (400×180 cells, the longest one covering 25 pc in the radial direction) during the entire life of the star.

3 Results and discussion

The medium around massive stars is continually shaped during the progenitor lifetime due to the mass loss and the velocity of their winds. During main sequence (MS) the stellar wind carves a circumstellar wind blown cavity surrounding the star, bordered by a thin, dense and cold shell (Weaver *et al.* 1977) with a radius greater than 20 pc. At 5×10^5 years before the core collapse the star reaches critical rotation and the mass loss rate increases from $\log \dot{M} (M_{\odot} \text{ yr}^{-1}) = -6.5$ to -4.3

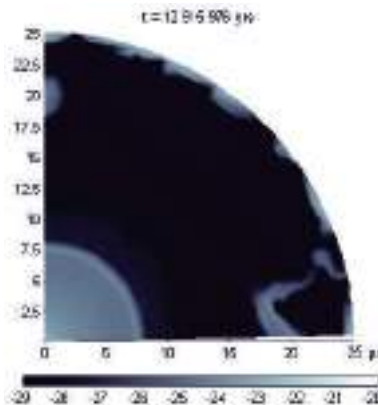


Fig. 2. Density around our $23 M_{\odot}$ rotating model at the end of its life. We show the logarithm of gas density in g cm^{-3} .

while the average wind velocity drops from $\approx 10^3 \text{ km s}^{-1}$ to small velocities about 100 km s^{-1} . This wind is characterized by a large mass loss rate and a small wind velocity (high density wind). A shell of shocked wind starts to build up closer to the star and is unstable due to Vishniac and/or Rayleigh-Taylor instabilities while it propagates outwards.

The temporary shells in CSM created during the stellar evolution have disappeared by the time the star reaches the end of its life leaving a highly turbulent wind bubble. The last phase of slow and high density wind builds a turbulent thin shell close to the star. The explosion of the central star will then occur in this non-isotropic medium with different densities that may influence the emission of the GRB signal.

This work has been supported by CONACyT project 104651.

References

- Pérez-Rendón, B., García-Segura, G., & Langer, N., 2009, A&A, 506, 1249
 Prochaska, J.X., Dessauges-Zavadsky, M., & Ramírez-Ruiz, E., *et al.*, 2008, ApJ, 685, 344
 Ramírez-Ruiz, E., García-Segura, G., & Salmonson, J.D., *et al.*, 2005, ApJ, 631, 435
 Stone, J.M., & Norman, M.L., 1992, ApJS, 80, 753
 van Marle, A.J., Langer, N., Yoon, S.-C., *et al.*, 2008, A&A, 478, 769
 Weaver, T.A., McCray, R., Castor, J., *et al.*, 1977, ApJ, 218, 377
 Yoon, S.-C., Langer, N., & Norman, C.A., 2006, A&A, 460, 199

GRB AFTERGLOWS: A STORY YET TO BE WRITTEN

S. Covino¹

Abstract. This is brief summary of the joint discussion about GRB afterglows held in Marbella during the Gamma-Ray Burst Symposium 2012. It is based on hints proposed by many authors in their talks and offers a (personally biased) view of some of the open issues in the field. No attempts have actually been applied to really cover all the discussed subjects, and consequently only a few topics are chosen as representatives of the activities going on in the field, admittedly with some emphasis for observational results.

1 The external shock scenario

There are no doubts that the availability of a new generation of optical imagers as GROND² (Greiner *et al.* 2008) are providing amazing datasets able to better set several questions affecting the discussions about afterglow modeling (*e.g.* Greiner *et al.* 2011). GROND data essentially allow a subset of the optical afterglows to be studied with a richness of spectral information often comparable to that provided by the XRT aboard *Swift*³. It is not therefore a surprise to discover well sampled and with high quality data events (*e.g.* Filgas *et al.* 2012) during the afterglow evolution not easily classifiable within the standard external shock scenario (Piran 2004; Zhang & Mészáros 2004) in the optical/NIR range. This might partly question a common belief requiring that the optical afterglow is often a “bona fide” external shock emission while in the soft X-rays energy range there are contributions of multiple processes.

2 Prompt/afterglow data correlations

A proper coverage of the optical/NIR afterglow evolution seems mandatory for any improvements of our knowledge of the phenomenology. And it is intriguing

¹ INAF / Brera Astronomical Observatory, via E. Bianchi 46, 23807, Merate (LC), Italy

²<http://www.mpe.mpg.de/~jcg/GROND/>

³<https://heasarc.gsfc.nasa.gov/docs/swift/swiftsc.html>

to see that as soon as samples of events with adequate follow-up data are built new possible correlations are proposed and discussed (Oates *et al.* 2012) reheating a field already providing results still waiting for a proper interpretation. It was stressed that some of the observed correlations, both between afterglow parameters or between prompt and afterglow data, can more easily be interpreted in alternative scenarios as the “cannonball” model (Dado & Dar 2012, 2013). A different approach to a statistical study of afterglow (and prompt) data is based on the selection of GRB samples highly complete in redshift (Salvaterra *et al.* 2012), likely allowing to derive a more reliable statistical description of GRB parameters for the events satisfying the selection criteria. In particular, the well known and highly debated “Amati/Ghirlanda/Yonetoku” correlations (Nava *et al.* 2012) hold for a subset of bright, at high energies, *Swift* GRBs.

3 Afterglow polarization

After the successful polarimetric campaigns carried out mainly with the ESO-VLT (Covino 2009) showing that late-time afterglows are polarized at a few per cent level, and the exciting detection of high polarization during the early afterglow (Steele *et al.* 2009; Uehara *et al.* 2012) the field is now offering new results based on intensive campaigns devoted to single events observable under favorable conditions. In particular very stringent upper limits on the circular polarization of late-time optical afterglows have been derived (Wiersema *et al.* 2012), allowing the possibility to put meaningful constrains on any ordered magnetic field components in the optical afterglow emitting region.

4 Short GRBs

Short GRBs are still attracting a considerable interest in the community in spite of their elusive nature compared to the longer durations GRBs (Kann *et al.* 2011; Kann 2013). Again GROND is providing a wealth of data of unprecedented quality (Nicuesa Guelbenzu *et al.* 2012; Rossi *et al.* 2012). The observationally-driven classification threshold between short and long duration GRBs at about 2 s has been questioned (Bromberg *et al.* 2013), suggesting that a fair fraction of *Swift* GRBs classified as short can actually be long as due to an instrument spectral sensitivity bias for the detection of generic short duration events, coupled with the intrinsic duration distribution of the two GRB classes.

5 GRB environment

The study of the environment of GRBs has been commonly carried out by low- and high-resolution spectroscopy (*e.g.* D’Elia *et al.* 2011; Piranomonte *et al.* 2011; Vergani *et al.* 2011) as by means of host galaxy studies (Graham & Fruchter 2013; Perley *et al.* 2012; Savaglio 2013; Savaglio *et al.* 2012; Tanvir *et al.* 2012). Alternatively, information about the GRB line of sights have been derived by

analysis of large samples of X-ray and optical/NIR observations (Campana *et al.* 2010, 2012).

References

- Bromberg, O., Nakar, E., Piran, T., & Sari, R., 2013 [[arXiv:1210.0068](#)]
- Campana, S., Thöne, C.C., de Ugarte Postigo, A., *et al.*, 2010, MNRAS, 402, 2429
- Campana, S., Salvaterra, R., Melandri, A., *et al.*, 2012, MNRAS, 421, 1697
- Covino, S., 2009 [[arXiv:0906.5440](#)]
- Dado, S., & Dar, A., 2012, ApJ, 749, 100
- Dado, S., & Dar, A., 2013 [[arXiv:1207.3630](#)]
- D'Elia, V., Campana, S., Covino, S., *et al.*, 2011, MNRAS, 418, 680
- Filgas, R., Greiner, J., Schady, P., *et al.*, 2012, A&A, 546, 101
- Graham, J.F., & Fruchter, A.S., 2013 [[arXiv:1211.7068](#)]
- Greiner, J., Bornemann, W., Clemens, C., *et al.*, 2008, PASP, 120, 405
- Greiner, J., Krüler, T., Klose, S., *et al.*, 2011, A&A, 526, 30
- Kann, D.A., Klose, S., Zhang, B., *et al.*, 2011, ApJ, 734, 96
- Kann, D.A., 2013 [[arXiv:1212.0040](#)]
- Nava, L., Salvaterra, R., Ghirlanda, G., *et al.*, 2012, MNRAS, 421, 1256
- Nicuesa Guelbenzu, A., Klose, S., Greiner, J., *et al.*, 2012, A&A, 548, 101
- Oates, S.R., Page, M.J., De Pasquale, M., *et al.*, 2012, MNRAS, 426, 86
- Perley, D., Modjaz, M., Morgan, A.N., *et al.*, 2012, ApJ, 758, 122
- Piran, T., 2004, RvMP, 76, 1143
- Piranomonte, S., Vergani, S.D., Onori, F., *et al.*, 2011, AN, 332, 283
- Rossi, A., Klose, S., Ferrero, P., *et al.*, 2012, A&A, 545, 77
- Salvaterra, R., Campana, S., Vergani, S.D., *et al.*, 2012, ApJ, 749, 68
- Savaglio, S., 2013 [[arXiv:1212.0144](#)]
- Savaglio, S., Rau, A., Greiner, J., *et al.*, 2012, MNRAS, 420, 627
- Steele, I.A., Mundell, C.G., Smith, R.J., *et al.*, 2009, Nature, 462, 767
- Tanvir, N.R., Levan, A.J., Fruchter, A.S., *et al.*, 2012, ApJ, 754, 46
- Uehara, T., Toma, K., Kawabata, K.S., *et al.*, 2012, ApJ, 752, 6
- Vergani, S.D., Flores, H., Covino, S., *et al.*, 2011, A&A, 535, 127
- Wiersema, K., Curran, P.A., Krüler, T., *et al.*, 2012, MNRAS, 426, 2
- Zhang, B., & Mészáros, P., 2004, IJMPA, 19, 2385

Chapter IX.
Host Galaxies

THE COSMIC EVOLUTION OF GAMMA-RAY BURST HOST GALAXIES

S. Savaglio¹

Abstract. Due to their extreme luminosities, gamma-ray bursts (GRBs) can be detected in hostile regions of galaxies, nearby and at very high redshift, making them important cosmological probes. The investigation of galaxies hosting long-duration GRBs (whose progenitor is a massive star) demonstrated their connection to star formation. Still, the link to the total galaxy population is controversial, mainly because of the small-number statistics: ~ 1 , 100 are the GRBs detected so far, ~ 280 those with measured redshift, and ~ 70 the hosts studied in detail. These are typically low-redshift ($z < 1.5$), low luminosity, metal poor, and star-forming galaxies. On the other hand, at $1.5 < z < 4$, massive, metal rich and dusty, interacting galaxies are not uncommon. The most distant population ($z > 4$) is poorly explored, but the deep limits reached point towards very small and star-forming objects, similar to the low- z population. This “back to the future” behavior is a natural consequence of the connection of long GRBs to star formation in young regions of the universe.

1 Introduction

Long duration gamma-ray bursts (GRBs), the majority of known GRBs, are associated with the core collapse of massive stars ($M > 40 M_{\odot}$; Heger *et al.* 2003), preferentially located in regions experiencing immediate star formation (Fruchter *et al.* 2006). They are so luminous in the γ -ray that they can shine through highly absorbed galaxies, normally difficult to see using conventional techniques. It is often claimed that GRB hosts are special galaxies, characterized by low chemical enrichment (*e.g.*, Levesque *et al.* 2010). However, high metallicities have been measured in several hosts at $z > 2$ (Savaglio 2012; and references therein) suggesting that intense star formation might be the dominant factor producing a GRB (Fynbo *et al.* 2008; Pontzen *et al.* 2010), rather than metallicity.

¹ MPI f. Extraterrestrial Physics, Garching bei München, Germany

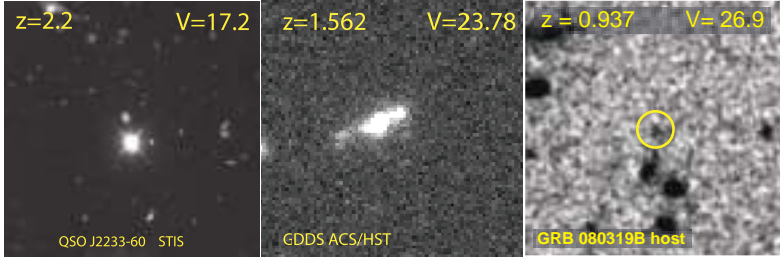


Fig. 1. The ISM in the distant universe is investigated by observing different targets. *From left to right:* a bright ($m_V = 17.2$) QSO, a faint ($m_V = 23.8$) field galaxy and a very faint ($m_V = 26.9$) GRB host galaxy. The GRB host is ~ 8000 times fainter than the QSO.

In the past, the heavy element enrichment of the universe has been measured from the interstellar medium (ISM) of substantially different galaxy populations (Fig. 1). For a long time, absorption lines in the cold ISM (damped Lyman- α systems, DLAs) in bright QSO spectra were easily accessible to the highest redshift. More recently, 8-m class telescopes allowed the detection of emission lines in the hot ISM of star-forming galaxies up to $z \sim 3$ (Maiolino *et al.* 2008). Now, GRBs can probe both components of the ISM simultaneously, almost regardless of galaxy brightness. An extreme case is the host of GRB 080319B ($z = 0.937$, Fig. 1) characterized by a stellar mass $M_* \sim 5.5 \times 10^7 M_\odot$, metallicity $\log Z/Z_\odot \sim 0.7$, star formation rate $SFR = 0.1 M_\odot \text{ yr}^{-1}$, and specific star formation rate $sSFR = 1.8 \text{ Gyr}^{-1}$ (Tanvir *et al.* 2010). For comparison, the median values of a sample of 46 GRB hosts are: $z = 0.75$, $M_* = 2 \times 10^9 M_\odot$, $SFR = 2.5 M_\odot \text{ yr}^{-1}$, and $sSFR = 1.25 \text{ Gyr}^{-1}$ (Savaglio *et al.* 2009).

2 The properties of GRB host galaxies

Not all GRB hosts are metal poor (Fig. 2). At $z < 2$, a few exceptions were found (Levesque *et al.* 2010; Perley *et al.* 2012; Krühler *et al.* 2012; Niino *et al.* 2012). At $z > 2$, GRB-DLAs display a large dispersion, between the $\sim 1/100$ solar value in GRB 090926A at $z = 2.1062$ (Rau *et al.* 2010), and the gas-rich pair (separation $\sim 700 \text{ km s}^{-1}$) in GRB 090323 at $z = 3.57$ (Savaglio *et al.* 2012).

Figure 3 displays an instructive composite of ~ 25 GRB-afterglow spectra in the interval $\lambda\lambda = 2200-2900 \text{ \AA}$, mainly in the redshift interval $z = 0.9-1.5$, at red and blue ends, respectively (Christensen *et al.* 2011). The metallicity is not measured in the sample, but cold-ISM absorption lines are strong, especially in optically dark bursts (having an optical to X-ray spectral index $\beta_{\text{OX}} < 0.5$). Moreover, the comparison in the same figure to the composite spectra of representative galaxy populations suggests that those GRB hosts cannot be metal poor and/or small. The average spectrum of 13 massive galaxies at $z \sim 1.6$ (median $M_* = 2.4 \times 10^{10} M_\odot$, $SFR = 30 M_\odot \text{ yr}^{-1}$, $sSFR = 1.2 \text{ Gyr}^{-1}$; Savaglio *et al.* 2004) is very

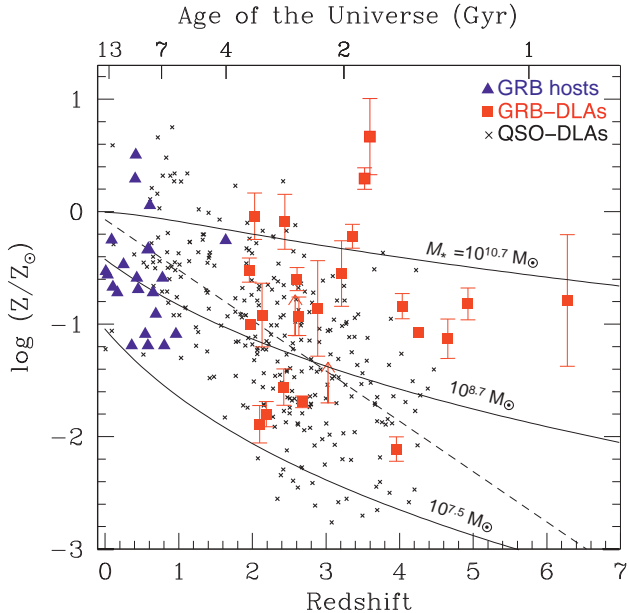


Fig. 2. Metallicities of GRB-DLAs at $z > 2$ (red squares; Savaglio *et al.* 2012; and references therein) and GRB hosts at $z < 2$ (blue triangles; Savaglio *et al.* 2009; Levesque *et al.* 2010; Perley *et al.* 2012; Krühler *et al.* 2012; Niino *et al.* 2012). With the exception of the metal-rich host of the short GRB 100206 at $z = 0.407$ (Perley *et al.* 2012), these are all long GRBs. QSO-DLAs are black crosses (dashed line: linear correlation). Solid curves are expected metallicities of star-forming galaxies with different stellar masses, derived from the empirical mass-metallicity relation and its redshift evolution (Savaglio *et al.* 2005).

similar to the GRB composite. The one of a complete sample of UV-bright $z \sim 1$ galaxies has much weaker absorption lines, but sizable emission lines (from the hot gas), with the tendency of stronger absorbers to be more common in brighter galaxies (Martin *et al.* 2012). These galaxies have $\text{SFR} = 1 - 100 M_{\odot} \text{ yr}^{-1}$ and $M_* = 10^{9.5} - 10^{11.3} M_{\odot} \text{ yr}^{-1}$ ($s\text{SFR} = 0.07 - 6 \text{ Gyr}^{-1}$). A similar composite is the one of 28 local ($z < 0.05$) starburst and star-forming galaxies, with median metallicity $\log Z/Z_{\odot} = -0.5$, UV luminosity and K -band absolute magnitude $L_{1500} = 5 \times 10^{39} \text{ erg s}^{-1} \text{ \AA}^{-1}$ and $M_K = -21.35$ ($-25.1 < M_K < -15.4$; Leitherer *et al.* 2011). Using the empirical relations in Savaglio *et al.* (2009), we derive $M_* \sim 6 \times 10^9 M_{\odot}$, $\text{SFR}_{1500} \sim 1 M_{\odot} \text{ yr}^{-1}$, and (assuming an optical extinction $A_V \sim 1$) an uncertain $s\text{SFR}$ of a few Gyr^{-1} . Surprisingly enough, these values are not very dissimilar from those of the $z \sim 0.75$ GRB host sample (Savaglio *et al.* 2009), despite the apparent difference with the GRB composite. We notice that the median redshift of the GRB host sample is lower than the redshift interval covered by the GRB composite ($z = 0.9 - 1.5$), indicating again a redshift evolution of the galaxy population hosting GRBs.

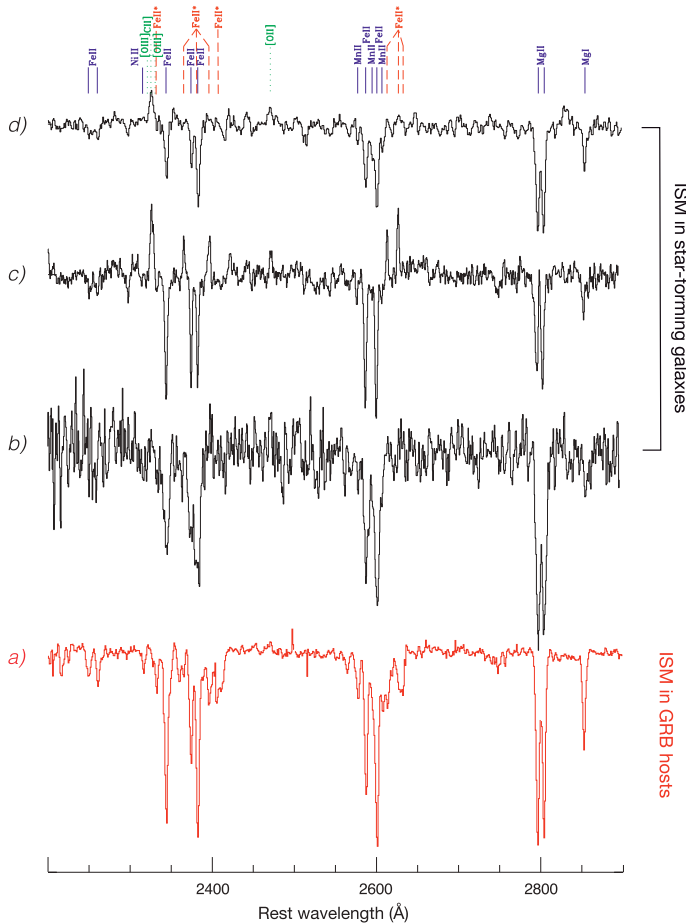


Fig. 3. Composite UV spectra probing the ISM of galaxy populations, normalized and arbitrarily shifted on the y -axis for clarity. *From bottom to top:* a) $z = 0.9 - 1.5$ GRB afterglow composite (Christensen *et al.* 2011); b) $z \sim 1.6$ massive galaxies (Savaglio *et al.* 2004); c) $z \sim 1$ UV bright galaxies (Martin *et al.* 2012); d) local starburst and star-forming galaxies (Leitherer *et al.* 2011). Spectra are in scale and shifted for clarity. Vertical marks indicate resonance (solid blue), fluorescent (dashed red), and nebular (dotted green) lines.

3 More massive GRB hosts at $z > 1.5$

At $z > 1.5$, some GRB hosts are metal rich, massive (Fig. 4), dusty (dark GRBs), or highly star forming (Hunt *et al.* 2011; Krühler *et al.* 2011; Rossi *et al.* 2012). This kind of galaxies can be very bright in the sub-millimeter. However, latest study of a large sample at $z < 1$ show not significant radio emission (Michalowski *et al.* 2012). One possible explanation is that the SFR in the low- z universe does

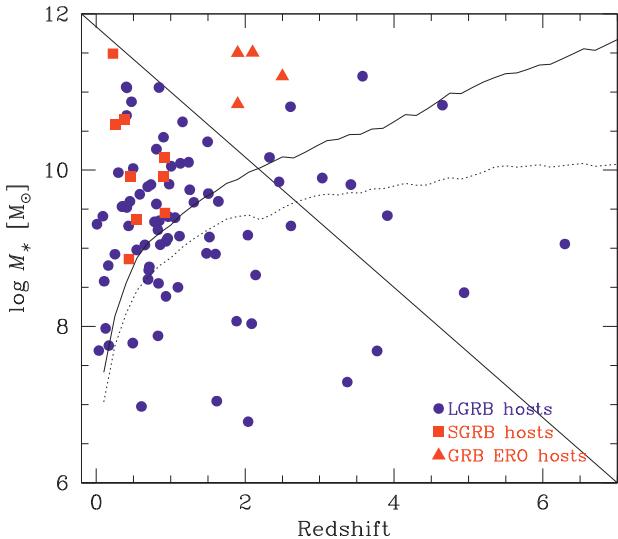


Fig. 4. Stellar mass of GRB hosts as a function of redshift. Circles and squares are hosts associated with long and short GRBs, respectively (Savaglio *et al.*, in prep.). Triangles are extremely red object (EROs) associated with optically dark GRBs (see Hunt *et al.* 2011 for details; Rossi *et al.* 2012). Solid and dashed lines represent the stellar mass of a galaxy with observed AB K -band magnitude $m_K = 24.3$, and old stellar population or constant SFR, respectively.

not occur mainly in sub-mm galaxies (SMGs), which can only account for at most 20% of the cosmic SFR density (Michalowski *et al.* 2010). The steep redshift evolution indicates that future surveys can bridge the gap at $2 < z < 4$, and a sizable fraction of high- z GRB hosts be SMGs.

The fraction of pair absorbers in $z > 1.5$ GRB afterglow spectra has been found to be almost three times higher than in QSO-DLAs (which probe random galaxies), suggesting that galaxy interactions may play a role in the formation of massive stars at high redshift (Savaglio *et al.* 2012; and references therein). Another indication is the large fraction (at least 40%) of known GRB hosts at $z > 1.5$ showing interaction, disturbed morphologies, or galaxy pairs (Chen 2012; Krühler *et al.* 2012; Thöne *et al.* 2011; Vergani *et al.* 2011). A few examples with a typical separation 10 – 15 kpc is shown in Figure 5. The interaction hypothesis is not surprising if one considers the higher fraction of galaxy mergers seen in the past of the universe with respect to today (Bluck *et al.* 2012).

4 Ultra luminous supernovae at high redshift and the link to GRBs

Galaxy mergers trigger instantaneous episodes of star formation or bursts. Thus, they are favorable sites of GRBs, and also ultra luminous supernovae (ULSNe). The latter are so bright that one day (when Extremely Large Telescopes will be

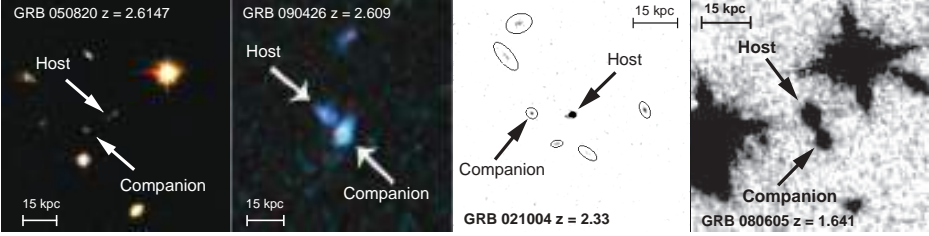


Fig. 5. From left to right: the field of GRB 050820 (Chen 2012), GRB 090426 (Thöne et al. 2011), GRB 021004 (Fynbo et al. 2005) and GRB 080605 (Krühler et al. 2012). All have a companion galaxy at the same redshift and separation ≤ 15 kpc.

operational) they will be used to explore the ISM at $z > 1.5$, in territories difficult to achieve today with QSOs or GRBs.

There are more than one connection between GRBs and ULSNe. High- z ULSNe, similar to type IIn and super-luminous supernovae (SLSNe, $M_g < -21.0$), are associated with very massive ($\sim 40 - 250 M_\odot$) and rare progenitors (Cooke et al. 2009; Gal-Yam 2012). ULSNe typically occur in faint, low mass and low metallicity galaxies (Neill et al. 2011) and have been detected from $z = 0.1$ to 1.6. The spectrum of one beautiful example, PS1-11bam at $z = 1.566$, is in Figure 6 (Berger et al. 2012). ULSNe are also unique in other ways. Unlike normal SN II or Ia, they are UV bright ($M_{\text{UV}} \sim -20$ to -23) and, unlike GRBs, are bright for several months. They can be identified and followed up in the optical for $z > 1.5$ (Cooke et al. 2012), which has the advantage that they do not need a γ -ray or X-ray satellite, for fast identification and precise localization. GRBs can lose 3–4 magnitudes in one day, and, at the moment, their discoveries are possible mainly thanks to the dedicated satellite *Swift*, which will be supported until 2014.

Cooke et al. (2012) suggested that star forming episodes in interacting galaxies at $z > 2$ increase the chance of observing the deaths of very a massive star. Moreover, Cooke et al. (2010) have shown that the number of close, interacting Lyman-break galaxy (LBG) pairs is higher than that expected from normal galaxy clustering, and that Ly α emission (a tracer of star formation) is anticorrelated with the separation of LBG pairs. These facts together suggest that LBG pairs are good sites of ULSNe, and hence GRBs.

5 Back to the future: GRB hosts at $z > 5$

The investigation of GRB hosts at $z > 4$ has been so far particularly difficult, which resulted only in rest-frame UV (*e.g.*, star formation) detections. At $z > 5$, only 5 GRB host fields have been observed (Basa et al. 2012; Tanvir et al. 2012), and no detection. If no dust correction is applied (dust is not expected to be abundant in a < 1 Gyr-old universe), the UV-luminosity limit L_{1500} can be translated into $\text{SFR}_{1500} < 2.5 M_\odot \text{ yr}^{-1}$ (Savaglio et al. 2009). Remarkable are the deep NIR observations with HST of the host of GRB 090423 ($z = 8.23$), which lead to $m_{\text{AB}} > 30.29$ (Tanvir et al. 2012), or $L_{1500} < 3.7 \times 10^{38} \text{ erg s}^{-1}$ and $\text{SFR} < 0.06 M_\odot \text{ yr}^{-1}$.

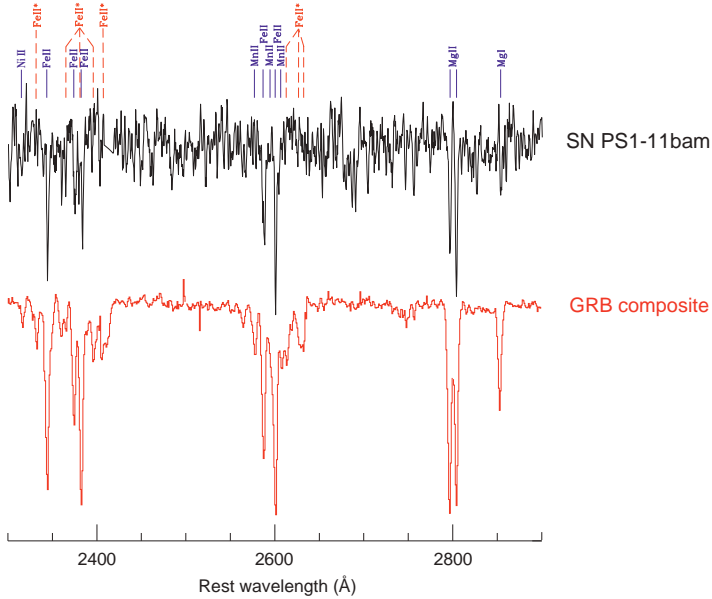


Fig. 6. Lower spectrum: the GRB afterglow composite of Figure 3. Upper spectrum: ultra luminous supernova PS1-11bam at $z = 1.566$ (Berger *et al.* 2012). Its host has $\text{SFR} \sim 10 M_{\odot} \text{ yr}^{-1}$, stellar mass $M_* \sim 2 \times 10^9 M_{\odot}$ and $s\text{SFR} \sim 5 \text{ Gyr}^{-1}$.

We can compare these low SFR limits to the stellar mass expected from numerical simulations. About 70% of the hosts at $z > 6$ predicted by Salvaterra *et al.* (2013) have stellar mass in the range $M_* = 10^6 - 10^8 M_{\odot}$ (Fig. 7), while star formation and metallicity are in the intervals $\text{SFR} = 0.03 - 0.3 M_{\odot} \text{ yr}^{-1}$ and $\log Z/Z_{\odot} = 0.01 - 0.1$. The comparison with a new observed sample at low redshift (81 GRB hosts, 70% at $z < 2$; Savaglio *et al.*, in prep.) shows that in the past GRB hosts must have been really small. The SFR limit of the host of GRB 090423 indicates that a very low stellar mass, $M_* \sim 10^6 M_{\odot}$, is possible if $s\text{SFR} < 60 \text{ Gyr}^{-1}$. *Vice versa*, if we assume $s\text{SFR} \sim 10 \text{ Gyr}^{-1}$, the limit $\text{SFR} < 0.06 M_{\odot} \text{ yr}^{-1}$ would give $M_* < 6 \times 10^6 M_{\odot}$.

In summary, intrinsically faint GRB hosts are observed at $z < 1.5$, whereas an important fraction are massive galaxies at intermediate redshift. Finally, in the primordial universe they are again likely small, star-forming, with no or little dust content.

6 Conclusions

The impact of GRB host galaxies on the understanding of galaxy formation and evolution is still affected by small number statistics. Their knowledge is mainly limited to the $z < 1.5$ regime, where ~ 60 galaxies studied in detail point to

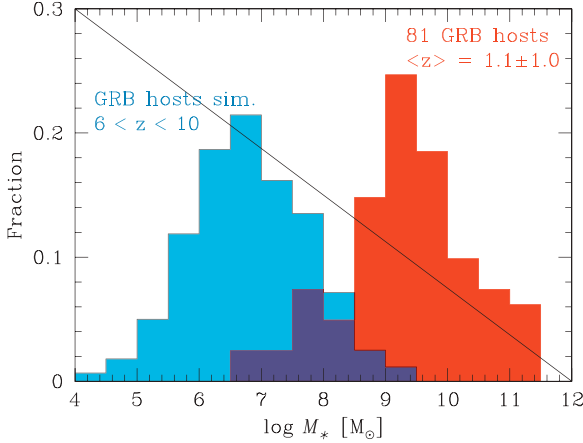


Fig. 7. Fraction of GRB hosts with different stellar masses. *Left histogram:* $z > 6$ hosts of numerical simulations (Salvaterra *et al.* 2013); 70% are the interval $M_* = 10^6 - 10^8 M_\odot$. *Right histogram:* 81 hosts at low redshift; 70% are at $z < 2$ (Savaglio *et al.*, in prep.).

a generally small, star forming and metal poor object. However, at $z > 1.5$, metallicity, mass and dust extinction show a large spread, suggesting a different population. Additionally, about a half shows disturbed morphologies, interactions with nearby galaxies and mergers. All this is nicely connected to the idea that local massive ellipticals today were bursty in the past, with some of them experiencing close encounters with other galaxies, which likely triggered intense episodes of star formation. The recent discovery of ultra luminous supernovae at $z > 1.5$, which have in common with GRBs a very massive progenitor, will certainly help understanding the nature of galaxies hosting these energetic events in the distant universe. At very high redshift, $z > 5$, the situation might have changed again, because massive galaxies must have been very rare. At these distances, deep searches failed to detect any GRB host, and relatively low SFRs were inferred. Unless dust content was very high back then (unlikely), low SFRs means low galaxy mass. Therefore, GRB hosts in the past could have been more similar to the local counterparts.

I thank Lise Christensen and Christy Tremonti for their help with composite spectra, and the workshop organizers for the kind invitation.

References

- Basa, S., Cuby, J.G., Savaglio, S., *et al.*, 2012, A&A, 542, A103
- Berger, E., Chornock, R., Lunnan, R., *et al.*, 2012, ApJ, 755, L29
- Bluck, A.F.L., Conselice, C.J., Buitrago, F., *et al.*, 2012, ApJS, 747, 34
- Chen, H.-W., 2012, MNRAS, 419, 3039

- Christensen, L., Fynbo, J.P.U., Prochaska, J.X., *et al.*, 2011, ApJ, 727, 73
Cooke, J., Sullivan, M., Barton, E.J., *et al.*, 2009, Nature, 460, 237
Cooke, J., Berrier, J.C., Barton, E.J., *et al.*, 2010, MNRAS, 403, 1020
Cooke, J., Sullivan, M., Gal-Yam, A., *et al.*, 2012, Nature, 491, 228
Fruchter, A., Levan, A.J., Strolger, L., *et al.*, 2006, Nature, 441, 463
Fynbo, J.P.U., Gorosabel, J., Smette, A., *et al.*, 2005, ApJ, 633, 317
Fynbo, J.P.U., Prochaska, J.X., Sommer-Larsen, J., *et al.*, 2008, ApJ, 683, 321
Gal-Yam, A., 2012, Science, 337, 927
Heger, A., Fryer, C.L., Woosley, S.E., *et al.*, 2003, ApJ, 591, 288
Hunt, L., Palazzi, E., Rossi, A., *et al.*, 2011, ApJ, 736, L36
Krühler, T., Greiner, J., Schady, P., *et al.*, 2011, A&A, 534, A108
Krühler, T., Fynbo, J.P.U., Geier, S., *et al.*, 2012, A&A, 546, A8
Leitherer, C., Tremonti, C.A., Heckman, T.M., *et al.*, 2011, AJ, 141, 37
Levesque, E., Kewley, L.J., Berger, E., *et al.*, 2010, AJ, 140, 1557
Levesque, E.M., Kewley, L.J., Graham, *et al.*, 2010, ApJ, 712, L26
Maiolino, R., Nagao, T., Grazian, A., *et al.*, 2008, A&A, 488, 463
Martin, C.L., Shapley, A.E., Coil, A.L., *et al.*, 2012, ApJ, 760, 127
Michałowski, M., Hjorth, J., & Watson, D., 2010, A&A, 514, A67
Michałowski, M.J., Kamble, A., Hjorth, J., *et al.*, 2012, ApJ, 755, 85
Neill, J.D., Sullivan, M., Gal-Yam, A., *et al.*, 2011, ApJ, 727, 15
Niino, Y., Hashimoto, T., Aoki, K., *et al.*, 2012, PASJ, 64, 115
Perley, D.A., Modjaz, M., Morgan, A.N., *et al.*, 2012, ApJ, 758, 122
Pontzen, A., Deason, A., Governato, F., *et al.*, 2010, MNRAS, 402, 1523
Rau, A., Savaglio, S., Krühler, T., *et al.*, 2010, ApJ, 720, 862
Rossi, A., Klose, S., Ferrero, P., *et al.*, 2012, A&A, 545, A77
Salvaterra, R., Maio, U., Ciardi, B., *et al.*, 2013, MNRAS, in press
Savaglio, S., 2012, IAU Symposium, 279, 212
Savaglio, S., Glazebrook, K., Abraham, R.G., *et al.*, 2004, ApJ, 602, 51
Savaglio, S., Glazebrook, K., Le Borgne, D., *et al.*, 2005, ApJ, 635, 260
Savaglio, S., Glazebrook, K., & Le Borgne, D., 2009, ApJ, 691, 182
Savaglio, S., Rau, A., Greiner, J., *et al.*, 2012, MNRAS, 420, 627
Tanvir, N.R., Rol, E., Levan, A.J., *et al.*, 2010, ApJ, 725, 625
Tanvir, N.R., Levan, A.J., Fruchter, A.S., *et al.*, 2012, ApJ, 754, 46
Thöne, C., Campana, S., Lazzati, D., *et al.*, 2011, MNRAS, 414, 479
Vergani, S.D., Piranomonte, S., Petitjean, P., *et al.*, 2011, Astron. Nach., 332, 292

KECK OBSERVATIONS OF 160 GAMMA-RAY BURST HOST GALAXIES

D.A. Perley¹, J.S. Bloom² and J.X. Prochaska³

Abstract. We present a preliminary data release from our multi-year campaign at Keck Observatory to study the host galaxies of a large sample of Swift-era gamma-ray bursts via multi-color ground-based optical imaging and spectroscopy. With over 160 targets observed to date (and almost 100 host detections, most of which have not previously been reported in the literature) our effort represents the broadest GRB host survey to date. While targeting was heterogeneous, our observations span the known diversity of GRBs including short bursts, long bursts, spectrally soft GRBs (XRFs), ultra-energetic GRBs, X-ray faint GRBs, dark GRBs, SN-GRBs, and other sub-classes. We also present a preview of our database (currently available online via a convenient web interface) including a catalog of multi-color photometry, redshifts and line ID's. Final photometry and reduced imaging and spectra will be available in the near future.

1 Introduction

Studies of the host galaxies of cosmic gamma-ray bursts have been slow to catch up with the revolution in the field sparked by the 2004 launch of the *Swift* satellite (Gehrels *et al.* 2004). While the large numbers of GRBs detected by *Swift* have enabled rapid strides in the understanding of the early behavior and multiwave-length evolution of GRB afterglows (as well as setting records for the brightest and most distant such events; see Gehrels *et al.* (2009) for a review of *Swift* GRB results), host-galaxy follow-up remains a quite observationally-intensive endeavor, accessible only to large ground-based telescopes or major space observatories. The typical *Swift* long-duration GRB is at a redshift of $z > 2$ (Jakobsson *et al.* 2006);

¹ Department of Astronomy, California Institute of Technology, MC 249-17,
1200 East California Boulevard, Pasadena CA 91125, USA

² Department of Astronomy, University of California, Berkeley, CA 94720, USA

³ Department of Astronomy and Astrophysics, UCO/Lick Observatory,
University of California, Santa Cruz, CA 95064, USA

the typical host is $R = 25$ mag and often fainter (Hjorth *et al.* 2012). So while most pre-*Swift* GRBs with afterglow localizations also have known host galaxies, the number of published hosts in the *Swift* era remains quite limited in comparison to the number of GRBs that have occurred since the *Swift* launch (over 700). Host spectroscopy is even more challenging to acquire.

Nevertheless, host galaxy observations provide a wealth of information that cannot be gleaned by other means—the integrated properties of the galaxy (mass, luminosity, age, physical size, and so on) are essential to a proper understanding of the gamma-ray burst progenitor and its cosmological context. In fact, for a significant fraction of bursts, host galaxy observations provide the *only* way to understand the burst environment in any detail or to measure redshifts. In particular, an absorption redshift has never been derived from a short burst afterglow, and “dark” gamma-ray bursts lack (by definition) a bright afterglow. Indeed, about 75% of all Swift GRBs have no afterglow redshift.

Starting in 2005 (shortly after the launch of *Swift*), we have been continuously conducting deep observations of gamma-ray burst positions to produce a legacy sample of gamma-ray burst host galaxies that is both *large* enough to expand on pre-*Swift* results in a meaningful way and *diverse* enough to incorporate not just “ordinary” bright long-duration bursts but also to enable the detailed study of interesting GRB subclasses that were hardly constrained by pre-*Swift* studies at all. In this summary, we present a brief outline of our host discovery program and a preview of early science results.

2 Program summary and observations

Our observations do not constitute a single homogeneously-defined survey, but rather represent a combination of smaller projects. Most observations were conducted between 2005–2010 under a series of proposals (PI J. Bloom) focusing on *host discovery* and basic characterization (via the observed-frame optical color), and placing *redshift constraints*, in particular to rule out a large high- z fraction that was suggested in some early works (*e.g.*, Bromm & Loeb 2002). These observations are supplemented by observations from a number of other researchers (PIs Kulkarni, Ofek, Prochaska) on individual observations of interest plus a few target-of-opportunity observations which were not afterglow-dominated. Observations continue today, mostly focused on supplementing multi-color photometry and determining photometric redshifts. Multiple instruments were employed but the large majority of observations were conducted with the Low Resolution Imaging Spectrograph (LRIS; Oke *et al.* 1995).

Nights were scheduled classically, and therefore were subject to a variety of observing conditions (seeing, transmission, lunation, etc.). For observations on nonphotometric nights on imaging fields without Sloan Digital Sky Survey calibration data, we separately observed with the 1-meter Nickel Telescope at Lick Observatory and the 60-inch Telescope at Palomar Observatory to obtain calibrations of these fields.

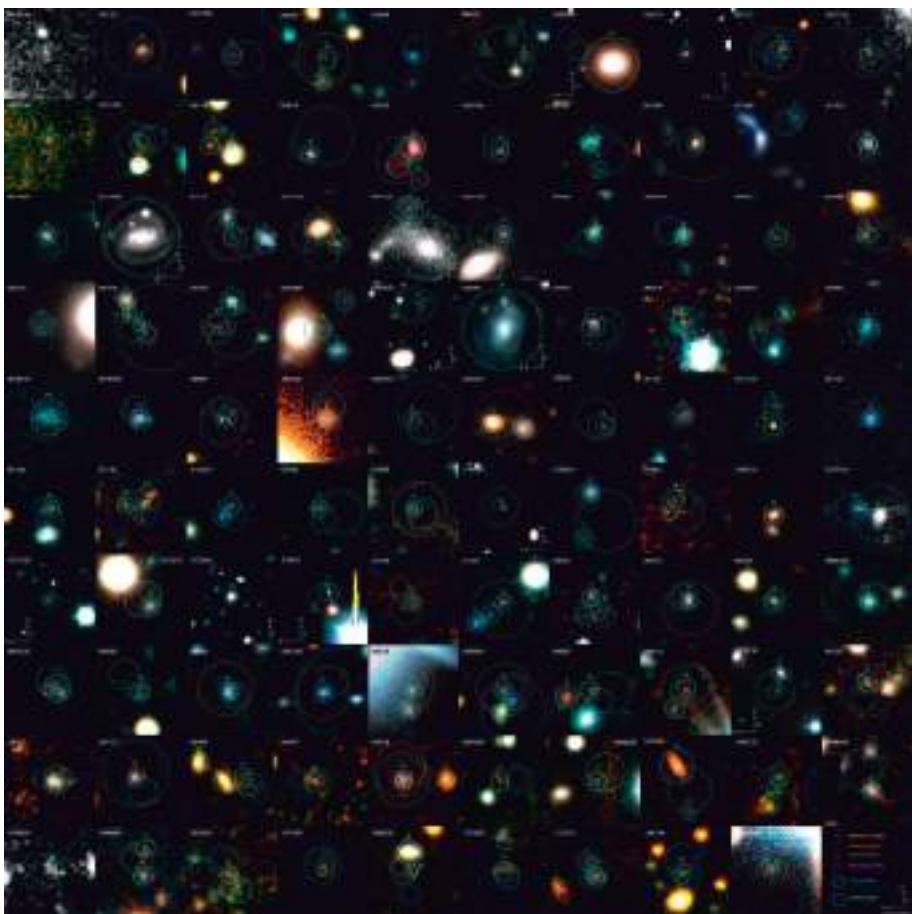


Fig. 1. Mosaic of 99 (out of 105) probable host galaxies detected in the survey. Host galaxies are identified with an H; afterglow positions and other objects of interest are also marked (see legend at bottom right). Images are $10'' \times 10''$ unless labeled otherwise by a scalebar.

As of December 2012, we have imaged a total of 159 unique GRB fields (excluding observations during heavy clouds, fields with severe contamination at the host position by nearby stars, or observations shortly after the GRB which were afterglow-dominated). Host galaxies or likely host candidates have been detected in 105 of these cases (Fig. 1). We have acquired spectroscopy (typically relatively shallow integrations of 30–90 minutes per target) for 48 targets leading to 21 redshift measurements, 14 of which were new at the time of observation.

Nearly all hosts were observed in at least two optical filters (usually *g* plus either *R* or *I*), although usually not in the NIR. This means that while we are sensitive exclusively to the young stellar population in all but the closest ($z < 1.0$) hosts

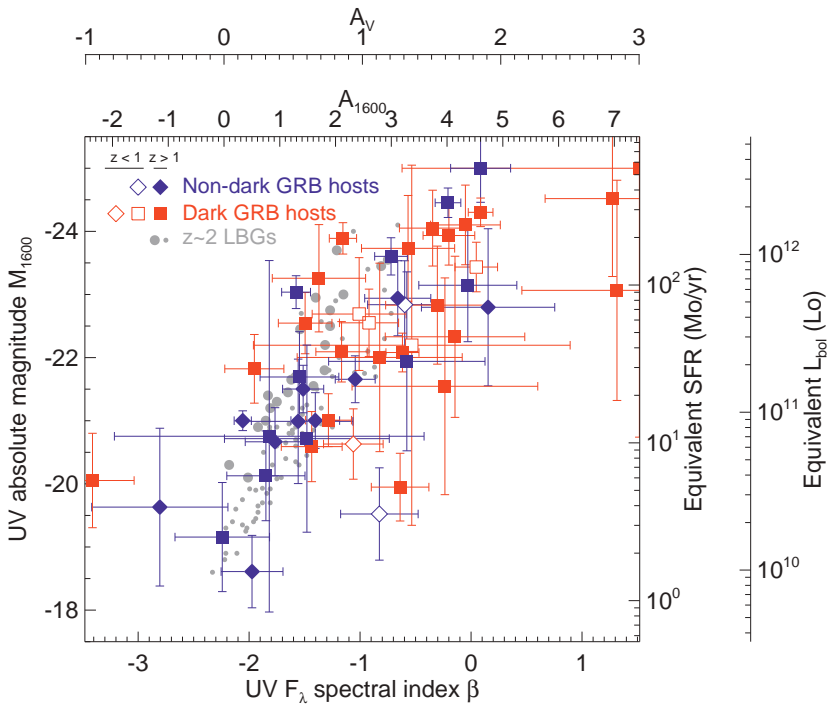


Fig. 2. Dust-corrected UV luminosity *versus* the UV spectral index β (determined from a power-law fit to all filters above the Balmer break) for GRB host galaxies in the sample, plus a sample of pre-Swift hosts with photometry taken from Savaglio *et al.* (2009) and grbhosts.org. Among $z > 1$ GRBs very luminous host galaxies are actually quite common once dust attenuation is corrected for. A significant fraction, although not all, of these most luminous hosts correspond to optically-dark or otherwise dust-obscured GRBs. Also plotted are a sample of field-selected $z \sim 2$ galaxies from Meurer *et al.* (1999).

and therefore cannot usefully constrain the ages or stellar masses of our sample, we can constrain the average dust reddening of using the empirical UV-slope method (*e.g.*, Meurer *et al.* 1999).

3 Preview of results

While GRB host galaxies are canonically thought of as very blue and nearly dust-free (*e.g.*, Le Floc'h *et al.* 2002), most of the hosts we detect show evidence for significant reddening: $A_V = 1.0 - 2.5$ mag is typical for the sample. A large fraction of the reddest hosts are “dark” bursts (Fig. 2), consistent with the interpretation of these events as dust-extinguished, but even optically bright bursts often have fairly red slopes. Of course, this measurement is naturally biased to the most luminous hosts in the sample, which are expected to have higher mean dust

attenuations than the more “canonical” ultra-faint hosts (*e.g.* the host of GRBs 030329; Gorosabel *et al.* 2005), which we cannot detect at $z \sim 2$. Nevertheless, it is clear that very (bolometrically) luminous hosts are relatively common at $z \sim 2$.

Many short GRBs we have observed show no evidence for a host within the XRT error circle at all, which is curious given that the known short GRB redshift distribution is heavily concentrated at $z < 1$ and includes several quite luminous galaxies (Prochaska *et al.* 2006). This population of apparently “hostless” events suggests a progenitor that has been ejected far from its original host in some cases (see also Berger 2010).

The hardness of the prompt emission does not appear to correlate in any significant way with the properties of its host. In particular, spectrally-soft *Swift* X-ray flashes (E_{peak}) generally have blue, star-forming hosts similar to those of harder long-duration GRBs.

4 Data access

We have placed online at <http://www.astro.caltech.edu/grbhosts/> an index containing imaging thumbnails of all hosts observed during the project and (for most detected hosts) photometry from the R and I filters as well as a list of measured redshifts and line identifications. As we complete final calibration checks in the coming year, we plan to augment this website with photometry on the remaining objects and filters. Reduced and calibrated images and extracted spectra will all be placed online for community use. Users interested in data on particular events of interest before then are encouraged to contact us for more information.

References

- Berger, E., 2010, ApJ, 722, 1946
- Bromm, V., & Loeb, A., 2002, ApJ, 575, 111
- Gehrels, N., Chincarini, G., Giommi, P., *et al.*, 2004, ApJ, 611, 1005
- Gehrels, N., Ramirez-Ruiz, E., & Fox, D.B., 2009, ARA&A, 47, 567
- Gorosabel, J., Pérez-Ramírez, D., Sollerman, J., *et al.*, 2005, A&A, 444, 711
- Hjorth, J., Malesani, D., Jakobsson, P., *et al.*, 2012, ApJ, 756, 187
- Jakobsson, P., Levan, A., Fynbo, J.P.U., *et al.*, 2006, 447, 897
- Le Floc'h, E., Duc, P.-A., Mirabel, I.F., *et al.*, 2003, A&A, 400, 499
- Meurer, G.R., Heckman, T., & Calzetti, D., 1999, ApJ, 521, 640
- Oke, J.B., Cohen, J.G., Carr, M., *et al.*, 1995, PASP, 107, 375
- Prochaska, J.X., Bloom, J.S., Chen, H.-W., *et al.*, 2006, ApJ, 642, 989
- Savaglio, S., Glazebrook, K., & Le Borgne, D., 2009, ApJ, 691, 182

THE REDSHIFT DISTRIBUTION OF THE TOUGH SURVEY

P. Jakobsson¹, J. Hjorth², D. Malesani², J.P.U. Fynbo², N.R. Tanvir³,
B. Milvang-Jensen² and T. Krühler²

Abstract. We present the redshift results from a Very Large Telescope (VLT) program aimed at optimizing the legacy value of the *Swift* mission: to characterize a homogeneous, X-ray selected, sample of 69 GRB host galaxies. Fifteen new redshifts have been secured, resulting in a 77% (53/69) redshift completion, making the survey the most comprehensive in terms of redshift completeness of any sample to the full *Swift* depth, available to date. We present the cumulative redshift distribution and derive a conservative, yet small, associated uncertainty. We constrain the fraction of *Swift* GRBs at high redshift to a maximum of 14% (5%) for $z > 6$ ($z > 7$). The mean redshift of the host sample is assessed to be $\langle z \rangle \gtrsim 2.2$. Using this more complete sample, we confirm previous findings that the GRB rate at high redshift ($z \gtrsim 3$) appears to be in excess of predictions based on assumptions that it should follow conventional determinations of the star formation history of the universe, combined with an estimate of its likely metallicity dependence. This suggests that either star formation at high redshifts has been significantly underestimated, for example due to a dominant contribution from faint, undetected galaxies, or that GRB production is enhanced in the conditions of early star formation, beyond those usually ascribed to lower metallicity.

1 Introduction

We have secured GRB host galaxy information for a homogeneous sample of 69 *Swift* GRBs with a large program at the VLT (Hjorth *et al.* 2012). The sample

¹ Centre for Astrophysics and Cosmology, Science Institute, University of Iceland, Dunhagi 5, 107 Reykjavík, Iceland

² Dark Cosmology Centre, Niels Bohr Institute, University of Copenhagen, Juliane Maries Vej 30, 2100 Copenhagen Ø, Denmark

³ Department of Physics and Astronomy, University of Leicester, University Road, Leicester LE1 7RH, UK

has been carefully selected and obeys strict and well-defined criteria. To optimize the survey, we focused on systems with the best observability, which also have the best available information. The main results of The Optically Unbiased GRB Host (TOUGH) survey is presented in Malesani *et al.* (2013), Jakobsson *et al.* (2012), Milvang-Jensen *et al.* (2012) and Krühler *et al.* (2012), including fundamental properties of the hosts, Ly α emission and new redshifts.

Here we present the TOUGH campaign for missing redshifts via VLT/FORS (Jakobsson *et al.* 2012) and VLT/X-shooter (Krühler *et al.* 2012). We attempted spectroscopic observations of most TOUGH host candidates with $R \lesssim 25.5$ mag that did not have a reported reliable redshift.

2 Redshift measurements and constraints

We have obtained 15 new host redshifts; Figure 1 shows the cumulative redshift distribution of the 53 TOUGH bursts with a measured redshift. Also plotted is a conservative systematic error band (hatched region) containing information for all the 69 TOUGH bursts. The shaded region represents the likely statistical (1σ standard error of the sample) uncertainty of the measured redshift distribution under the assumption that it is a true random sample of the overall population. The sampling error and the conservative systematic error region are shown separately to clearly illustrate that incompleteness dominates the sample, and more is gained by reducing the systematics rather than increasing the sample size. Using both error regions we can set a conservative limit on the maximum number of *Swift* bursts at $z > 6$ ($z > 7$): 14% (5%).

The average (median) redshift of the 53 TOUGH bursts is $\langle z \rangle = 2.23$ ($\tilde{z} = 2.14$), significantly lower than the early *Swift* results indicated (Jakobsson *et al.* 2006). This difference may simply reflect the comparatively small samples analyzed in that paper, but could also be due to an increased success in measuring redshifts $z < 2$ using weaker absorption lines in afterglow spectra, and via host galaxies. Indeed, the average of the 15 new redshifts is $\langle z \rangle = 1.78$. The mean redshift of the whole TOUGH sample could be as low as $\langle z \rangle \sim 1.7$ (upper boundary of the hatched region) although it is unlikely that the majority of bursts with unknown redshifts would be located at very small distances. In fact, it is more probable that $\langle z \rangle \gtrsim 2.2$ since we have only targeted the brightest galaxies in the sample ($R \lesssim 25.5$ mag) for spectroscopic follow-up.

3 Modelling

Illustrative model fits are presented in Jakobsson *et al.* (2012) and described in detail there. We assume that the GRB rate follows the star-formation rate (SFR) history, and consider two different SFR history parameterizations which we label as follows. *SFR1* is an update (Li 2008) of the SFR history models of Hopkins & Beacom (2006) to include data from Bouwens *et al.* (2008) and Reddy *et al.* (2008), combined with a low-metallicity modification following the prescription of Langer & Norman (2006). *SFR2* is model A from Schmidt (2009) which represents

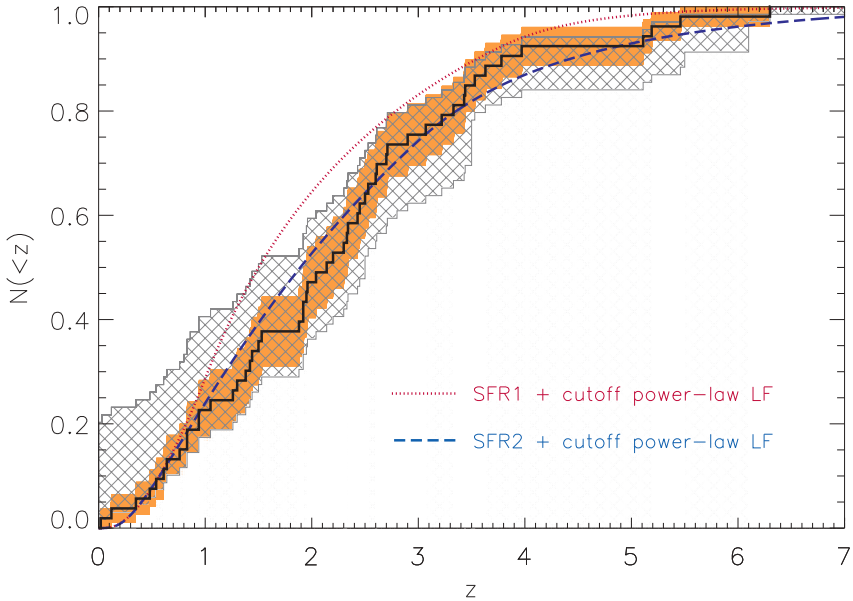


Fig. 1. **Thick solid curve:** the cumulative fraction of GRBs as a function of redshift for the 53 *Swift* bursts in the TOUGH sample with a measured redshift ($\langle z \rangle = 2.23$). **Hatched region:** this is a conservative error region showing the systematic error on the thick solid curve. **Shaded region:** statistical region showing the 1σ sampling error band around the thick solid curve. **Dotted curve:** the expected redshift distribution for *Swift* observable long GRBs using the *SFR1* history parameterization, *i.e.* the canonical SFR history discussed in Hopkins & Beacom (2006) (see the main text). **Dashed curve:** the same redshift distribution for the *SFR2* history parameterization, *i.e.* a model where the SFR history remains constant beyond $z \sim 3$ (Schmidt 2009) (see the main text). From Jakobsson *et al.* (2012).

a SFR history which remains constant beyond $z \sim 3$. It may, for example, be considered a more extreme low-metallicity correction to the cosmic SFR. Or it may represent a correction (Kistler *et al.* 2009; Virgili *et al.* 2011) to the high-redshift SFR as estimated from flux-limited surveys by the integration of galaxy luminosity functions (LFs) thus obtained. This would be due to a large amount of hidden star formation in faint, low-mass, and high specific SFR galaxies of the type that GRBs tend to be associated with at lower redshift.

Modeling is performed in the standard manner (Guetta & Piran 2007) to produce log N -log L number count distributions for various parameters of the LF, which are then fit by χ^2 minimization to the observed log N -log L distribution of all *Swift* bursts with peak photon flux $> 1 \text{ cm}^{-2} \text{ s}^{-1}$. We emphasize that the redshift distribution is not part of this fitting procedure, but is always purely a result. In Figure 1, we plot the redshift distributions from our best fitting models in comparison to the TOUGH redshift data.

At face value, these results seem to imply that GRBs follow a cosmic SFR history that is significantly enhanced at high redshift compared to estimates from flux-limited surveys. Given what is known about GRB hosts, it is entirely feasible that GRBs trace star formation at high redshift that would be undetectable by other means. It is of course also possible that the simple low-metallicity enhanced SFR parameterization used in the *SFR1* model is inadequate, or that the LF could have a more complex form and/or evolve with redshift. It should also be noted that Elliott *et al.* (2012) find that there is no strong preference for a metallicity cut.

4 Discussion

It is possible that star formation at high redshifts has been significantly underestimated. Even at $z \sim 2$ it appears that the galaxy LF has a substantially steeper faint-end slope than locally (Reddy & Steidel 2009), while recent LF studies in the Hubble Ultra-Deep Field have concluded that at $z \gtrsim 7$ so-far undetected galaxies are likely to completely dominate the total star formation activity (Bouwens *et al.* 2012; Tanvir *et al.* 2012). Alternatively, it could be that GRB production is substantially enhanced in the conditions of early star formation, beyond the metallicity-dependent rate correction already applied. In the long run, large complete samples of GRB redshifts should shed light on whether the GRB rate is proportional to SFR or whether other effects play an important role.

We have now reached a point in GRB research where a single burst rarely elucidates and illuminates our general understanding of the field. It is important to focus on well-defined samples and population studies, where systematics and biases can be minimized. *Swift* has made it possible to build such a sample and thanks to new available instrumentation, such as the VLT/X-shooter (Vernet *et al.* 2011), we can continue to follow this track into the future.

References

- Hjorth, J., Malesani, D., Jakobsson, P., *et al.*, 2012, ApJ, 756, 187
- Malesani, D., Hjorth, J., Fynbo, J.P.U., *et al.*, 2013, ApJ, in preparation
- Jakobsson, P., Hjorth, J., Malesani, D., *et al.*, 2012, ApJ, 752, 62
- Milvang-Jensen, B., Fynbo, J.P.U., Malesani, D., *et al.*, 2012, ApJ, 756, 25
- Krühler, T., Malesani, D., Milvang-Jensen, B., *et al.*, 2012, ApJ, 758, 46
- Jakobsson, P., Levan, A.J., Fynbo, J.P.U., *et al.*, 2006, A&A, 447, 897
- Li, L.-X., 2008, MNRAS, 388, 1487
- Hopkins, A.M., & Beacom, J.F., 2006, ApJ, 651, 142
- Bouwens, R.J., Illingworth, G.D., Franx, M., *et al.*, 2008, ApJ, 686, 230
- Reddy, N.A., Steidel, C.C., Pettini, M., *et al.*, 2008, ApJS, 175, 48
- Langer, N., & Norman, C.A., 2006, ApJ, 638, L63
- Schmidt, M., 2009, ApJ, 700, 633
- Kistler, M.D., Yüksel, H., Beacom, J.F., *et al.*, 2009, ApJ, 705, L104

- Virgili, F.J., Zhang, B., Nagamine, K., *et al.*, 2011, MNRAS, 417, 3025
Guetta, D., & Piran, T., 2007, JCAP, 7, 3
Reddy, N.A., & Steidel, C.C., 2009, ApJ, 692, 778
Elliott, J., Greiner, J., Khochfar, S., *et al.*, 2012, A&A, 539, 113
Bouwens, R.J., Illingworth, G.D., Oesch, P.A., *et al.*, 2012, ApJ, 752, L5
Tanvir, N.R., Levan, A.J., Fruchter, A.S., *et al.*, 2012, ApJ, 754, 46
Vernet, J., Dekker, H., D'Odorico, S., *et al.*, 2011, A&A, 536, 105

GRB–SN CONNECTION IN SAO RAS OBSERVATIONS

A.S. Moskvitin¹, V.V. Sokolov¹, V.N. Komarova *et al.*¹

Abstract. We present the results of SAO RAS 6-m BTA spectral observations of GRBs and XRFs with the signs of SNe: GRB/XRF 060218 (SN 2006aj) and XRF 080109 (SN 2008D). The properties of these events are similar to those of usual core-collapse SNe without GRBs. Some spectral features in the cases of SN 2006aj and SN 2008D may be interpreted as hydrogen and helium traces. This supports an idea of presence of a relic envelope around the progenitor star and the shock break-out effects observed in X-rays, UV and optics.

1 GRB–SN

Work on the search of optical candidates of GRBs started in SAO RAS in 1993. The main aim of this program was to find objects associated with old (archive) bursts with small boxes of localization ($\sim 1 \text{ arcmin}^2$). Because of fast decay of the afterglow brightness and the presence of numerous objects in the error areas the first optical identification with the starforming galaxies was made only in 1997. The next year the GRB follow-up team in cooperation with the Spain team started observing GRB afterglows and their host galaxies (Sokolov 2011).

During recent few years an idea about connection between long-duration GRBs and core-collapse SNe (types Ib and Ic) was supported by numerous observations of such events (Hjorth & Bloom 2011). However, spectroscopically such an association was carried out only for nearby objects. Apparently, in the visible range this can be reliably done for events at redshifts up to $z \sim 0.5$, when the brightness of an SN (especially at maximum) will still dominate in the overall radiation. It would be interesting to compare properties of SNe with and without GRBs. Here the researchers are facing a problem: why some nearby GRBs are not associated with SNe (Della Valle *et al.* 2006)?

In SAO RAS we study the evolution of SNe associated with GRBs (and the XRFs), and also usual core-collapse SNe and usual long-duration GRBs without such a link.

¹ SAO RAS, Russia; e-mail: mosk@sao.ru; sokolov@sao.ru; vkom@sao.ru

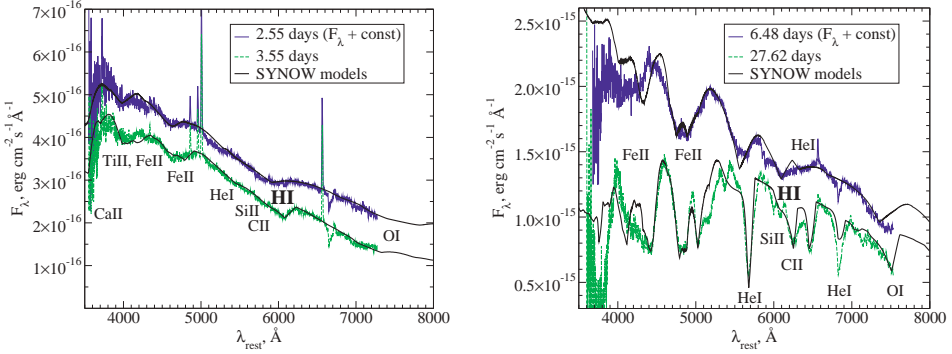


Fig. 1. Left pannel: the spectra of GRB/XRF 060218 (SN 2006aj) obtained with the BTA since 2.55 ($V_{ph} = V_{HI} = V_{HeI} = 33\,000 \text{ km/s}$) and 3.55 ($V_{ph} = 18\,000 \text{ km/s}; V_{HI} = V_{HeI} = 24\,000 \text{ km/s}$) days after the trigger. Right pannel: the spectra of XRF 080109 (SN 2008D) obtained with the BTA since 6.48 ($V_{ph} = V_{HeI} = 17\,000 \text{ km/s}; V_{HI} = 23\,000 \text{ km/s}$) and 27.62 ($V_{ph} = 8500 \text{ km/s}; V_{HeI} = 10\,500 \text{ km/s}; V_{HI} = 15\,000 \text{ km/s}$) days after the trigger.

International photometrical and spectral monitoring of GRBs and SNe (in collaboration with India, USA, Turkey, Spain, etc.) is ongoing in SAO for many years. Follow-up of early phases of SNe and GRBs, explosion asymmetry, wide luminosity range, hosts, and very distant objects are the most interesting tasks for this programs (Moskvitin *et al.* 2010b). In the nearest future we plan to make polarimetrical observations too with the BTA/MANIA.

2 GRB 060218/SN 2006aj and XRF 080109/SN 2008D

One of the most interesting object was the burst GRB/XRF 060218 ($z = 0.1683$) with strong X-ray and UV components (dominating in the first hours) and supernova signs (SN 2006aj). These effects can be explained by interaction between SN shock and a stellar-wind envelope around a massive progenitor star (the “shock breakout” which is also visible at early stages of some SNe).

The object was observed with the BTA 2.55 and 3.55 days after the trigger. The spectra were modelled in the Sobolev approximation with the SYNOW code (Branch *et al.* 2003; Elmhamdi *et al.* 2006). The detected detail near 6200 \AA were interpreted as hydrogen line with high velocities: 33 000 km/s for the first epoch, and 24 000 km/s for the second one (left pannel of Fig. 1, and Sonbaş *et al.* 2008). This may be a sign of stellar-wind envelope around a massive progenitor star.

Another significant event observed at SAO RAS with the BTA was the X-ray flash XRF 080109 associated with SN 2008D. This object was also observed spectroscopically with the BTA. The spectra were modelled with the help of SYNOW code to interpret broad features, especially near 6200 \AA , and to measure expansion velocities. It was shown that Si II can not fit this absorption because of limitation

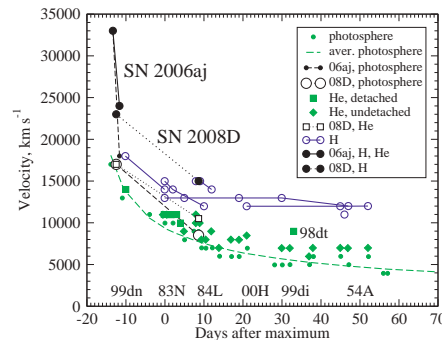


Fig. 2. Comparison of properties of usual Ib SNe (Branch *et al.* 2002), SN 2006aj and SN 2008D: expansion velocities of pseudo-photosphere, Helium and Hydrogen.

by the heavier elements such as Fe II. However C II remains a candidate for interpretation of this line (right pannel of Fig. 1, and Moskvitin *et al.* 2010a).

The assumption about the presence of envelopes around progenitor stars is confirmed by agreement between velocities of lines interpreted as hydrogen and helium, and the empiric power-law velocity drop with time for envelopes of classic core-collapse supernovae (Fig. 2, and Branch *et al.* 2002). Detection of a P Cyg profile of the H β line in the spectra of optical afterglows of GRBs can be a conclusive argument in favor of this hypothesis (Moskvitin *et al.* 2010a).

The authors are grateful to T.N. Sokolova and A.A. Volnova. This work was supported by the RFBR grant 11-02-12696-IND-a; the program No. 17 “Active processes in galactic and extra-galactic objects” of the Department of Physical Sciences of the Russian Academy of Sciences; and grants No. 14.B37.21.0251 and No. 14.A18.21.1179 from FTP of the RF Ministry of Education and Science.

References

- Branch, D., Benetti, S., Kasen, D., *et al.*, 2002, ApJ, 566, 1005
- Branch, D., Baron, E.A., & Jeffery, D. J., 2003, chapter in “Supernovae and Gamma-Ray Bursters”, ed. Kurt W. Weiler, Lect. Notes Phys. 598, 47 [[astro-ph/0111573](#)]
- Della Valle, M., Chincarini, G., Panagia, N., *et al.*, 2006, Nature, 444, 1050
- Elmhamdi, A., Danziger, I.J., Branch, D., *et al.*, 2006, A&A, 450, 305
- Hjorth, J., & Bloom, J.S., 2011, Chapter 9 in “Gamma-Ray Bursts”, Cambridge Astrophysics Series 51, ed. C. Kouveliotou, R.A.M.J. Wijers & S. Woosley (Cambridge University Press), p. 169 [[arXiv:1104.2274](#)]
- Moskvitin, A.S., Sonbaş, E., Sokolov, V.V., *et al.*, 2010, Astrophys. Bull., 65, 132 [[arXiv:1004.2633](#)]
- Moskvitin, A.S., Fatkhullin, T.A., Sokolov, V.V., *et al.*, 2010, Astrophys. Bull., 65, 230 [[arXiv:1008.0773](#)]
- Sokolov, V.V., 2011, submitted to BASI [[arXiv:1111.1406](#)]
- Sonbaş, E., Moskvitin, A.S., Fatkhullin, T.A., *et al.*, 2008, Astrophys. Bull., 63, 228 [[arXiv:0805.2657](#)]

X-SHOOTER SLIT OBSERVATIONS OF GRB HOST GALAXIES

S.D. Vergani^{1,2}

Abstract. The Italian-French X-shooter GRB host program started at the end of 2009 and allowed us to collect the spectra of about 30 host galaxies in the 300–2400 nm range from a redshift of about $z = 0.1$ to $z = 2.7$. We are using these spectra to retrieve information on the host metallicities, star formation rates and extinctions. An accurate slit positioning allowed us to discover in some cases close-by galaxies at the same redshift than the GRB host. Thanks to the comparison of the afterglow and host spectra, it is possible to assess for possible interactions of these systems. We also looked for the counterparts of the foreground absorbers present in the afterglow spectra, but we obtained very few identifications.

1 Introduction

The X-shooter spectrograph is the first of the ESO/VLT second generation instruments (D’Odorico *et al.* 2004; Vernet *et al.* 2011) and has the unique capability to produce spectra covering simultaneously a spectral range from ~ 3000 to $24\,000 \text{ \AA}$. The consortium that built the instrument had access to GTO (Guaranteed Observation Time) extended over 3 years (2009–2012). Within the GTO we developed our Italian-French program dedicated to the study of the host galaxies of long gamma-ray bursts (LGRB). Thanks to the unique spectral range coverage and sensitivity of the X-shooter spectrograph we can now extend LGRB host studies to high redshift (previously mainly limited to $z < 1$) and determine the properties (star formation rate, metallicity, extinction...) of a larger sample of these objects. Our program is divided into two sub-programs: one dedicated to slit observations of LGRB hosts at $z > 0.8$ and the other devoted to IFU (Integral Field Unit) observations of 10 GRB hosts at $z < 0.5$. This is the first IFU survey of LGRB hosts.

The following sections are dedicated to the slit program only.

¹ INAF, Osservatorio Astronomico di Brera, via E. Bianchi 46, 23807 Merate, Italy

² GEPI, Observatoire de Paris, CNRS, Univ. Paris Diderot, 5 place Jules Janssen, 92195 Meudon, France

2 The slit spectra of the Italian-French X-shooter LGRB host program

To date we collected 24 slit spectra: 9 for LGRB hosts at $0.8 < z < 1.5$ and 15 at $z > 1.5$. The data reduction of the sample is completed and the data analysis is ongoing. Some highlights of this ongoing study will be presented in the following sections. Emission lines of the hosts are detected in 15/24 cases (see Fig. 1). Considering the sensitivity of X-shooter and supposing that the hosts are star forming, the non-detections imply that also at high redshift many LGRB hosts are faint dwarf galaxies. Nonetheless the detected lines can be also very strong, indicating that the host galaxy population covers a variety of types of star forming galaxies.

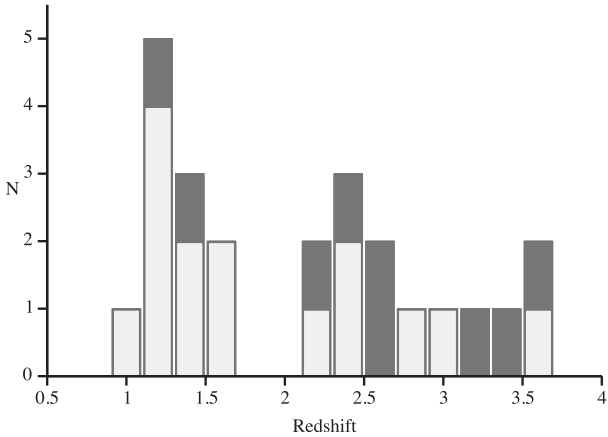


Fig. 1. Redshift distribution of the host galaxies observed in our GTO program (black). The superposed white bars represent the galaxies for which emission lines have been detected.

3 Mass-metallicity relation

The study of GRB hosts can bring useful information to galaxy evolution studies (see Savaglio 2012a and Savaglio 2013, these proceedings). LGRB hosts form a sample of galaxies not selected by luminosity, that can be complementary to those of current surveys of galaxies. It has been shown that at $z < 1$ their mass-metallicity relation follows a trend with a significant offset from the relation found from the surveys of emission line galaxies (Han *et al.* 2010; Levesque *et al.* 2010). In order to explain this behavior and to build a complete picture of galaxy evolution, it is important to increase the LGRB host sample to confirm this result and to determine if and how it evolves at higher redshift. The preliminary mass and metallicity values for three hosts of our sample at $z > 1.5$ are in agreement with the mass metallicity relation found by Erb *et al.* (2006) for star forming galaxies at $z \sim 2$ (Fig. 2). With the whole set of data we should be able to assess if the agreement is confirmed.

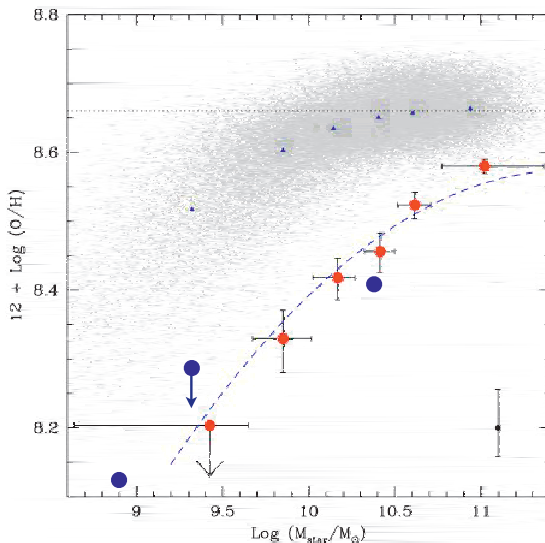


Fig. 2. Mass-metallicity plot for SDSS field star forming galaxies (grey small dots, upper part of the plot) and star forming galaxies at $z \sim 2$ (red dots). The error bar in the lower right corner shows the calibration uncertainty. From Erb *et al.* (2006). Blue dots represent the preliminary values for three LGRB hosts at $z > 1.5$ of our X-shooter sample.

4 The host galaxies of dark GRBs

To date the sample of LGRB hosts is biased against dark GRBs. Within our program we are observing also some dark GRB host galaxies, such as the one of GRB 070306 at $z \simeq 1.5$. The afterglow of this GRB showed an extinction corresponding to $A_V = 5.5 \pm 0.5$ (Jaunsen *et al.* 2008). The X-shooter spectrum of the host shows many emission lines, from the [OII] doublet to the [SII] one (see Fig. 3). Our preliminary results indicate that the host galaxy has a star formation rate $SFR \simeq 100 M_{\odot} \text{ yr}^{-1}$, a metallicity of $12 + \log(O/H) \sim 8.4$ and an $A_V = 1.3 \pm 0.2$ (considering a SMC extinction curve; similar values are obtained using MW or LMC curves), much less than the amount found for the afterglow extinction, and more than the value retrieved from the host spectral energy distribution (Krühler *et al.* 2011). These results, added to those reported by other groups (see also Krühler *et al.* 2011), suggest that dark GRB hosts extend the host population towards more massive galaxies with higher SFR.

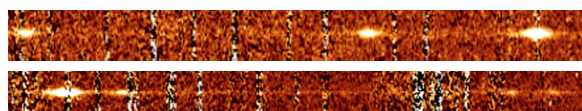


Fig. 3. 2D spectrum (NIR X-shooter arm) of the host of GRB 070306. The emission lines of $H\beta$, [OIII]5007 doublet (*top panel*), $H\alpha$, [NII] and [SII] doublet (*bottom panel*) are shown.

5 Looking for foreground absorber counterparts

The surveys of strong MgII intervening absorbers along GRB lines of sight gave the surprising result of an excess of these systems compared to QSO lines of sight (*e.g.*: Prochter *et al.* 2006; Vergani *et al.* 2009). To study the origin of the gas traced by the MgII absorbers, it is of great interest to enlarge the sample of the galaxies responsible for the MgII absorptions towards GRBs and compare their properties with the sample detected for QSO absorbers. Hence, when possible, we placed the slit in order to cover other galaxies present in the GRB field, close-by to the host galaxy. We identified two counterparts only. The strong MgII absorbers are thought to be associated with star forming galaxies (*e.g.*: Zibetti *et al.* 2007) and their impact parameters should be smaller for stronger systems (see Schulze *et al.* 2012 and references therein). The non-detection of the counterparts in our search can be at odds with these assumptions, but a deeper analysis is needed.

6 Joining emission and absorption studies: Hosts interaction with other galaxies

Some of the galaxies targeted in our foreground absorber counterpart search turned out to be galaxies at the same redshift of the GRB (*e.g.*: Fig. 4). For 40% of the $z > 1.3$ galaxies in our sample, we found evidences for interactions with another galaxy in the field, at distances up to ~ 40 kpc (see also Savaglio *et al.* 2012b). The combination of the study of the absorption features present in the afterglow spectra and the emission lines of the host galaxy spectra, makes possible to build a more complete picture of the properties of the host and potentially also to retrieve some spatial information on the host gas distribution and on the interaction (see Chen 2012). We can use our data to carry out this kind of studies. An example is the ongoing work on the field of the GRB 021004 (see Vergani *et al.* 2011).



Fig. 4. Section of the NIR 2D spectrum of the GRB 021004 host, showing the [OIII] $\lambda 5007\text{\AA}$ lines of the GRB host and the close-by galaxy A at ~ 15 kpc. This detection together with the profile shape and spatial extension of the host Ly α emission line (see Vergani *et al.* 2011) suggests a possible interaction between these two galaxies. The high velocity blue-shifted absorption features present in the afterglow spectra could be then due to some outflowing gas connected with this interaction.

On behalf of the Italian-French X-shooter GRB host collaboration. Based on observations made with ESO Telescopes at Paranal Observatory under programmes ID 084.A-0631, 085.A-0795, 086.A-0874, 087.A.0451 and 089.A-0843 (PIs: S. Piranomonte and H. Flores).

References

- Chen, H.-W., 2012, MNRAS, 419, 3039
D'Odorico, S., Andersen, M.I., Conconi, P., *et al.*, 2004, Soc. Photo-Opt. Instrum. Eng. (SPIE) Conf. Ser., ed. A.F.M. Moorwood & M. Iye, Vol. 5492, 220
Erb, D.K., Shapley, A.E., Pettini, M., *et al.*, 2006, ApJ, 644, 813
Han, X.H., Hammer, F., Liang, Y.C., *et al.*, 2010, A&A, 514, A24
Jaunsen, A.O., Rol, E., Watson, D.J., *et al.*, 2008, ApJ, 681, 453
Krühler, T., Greiner, J., Schady, P., *et al.*, 2011, A&A, 534, A108
Levesque, E.M., Kewley, L.J., Berger, E., & Jabran Zahid, H., 2010, AJ, 140, 1557
Prochter, G.E., Prochaska, J.X., Chen, H.-W., *et al.*, 2006, ApJ, 648, L93
Savaglio, S., 2012, Astron. Nachr., 333, 480
Savaglio, S., Rau, A., Greiner, J., *et al.*, 2012, MNRAS, 420, 627
Schulze, S., Fynbo, J.P.U., Milvang-Jensen, B., *et al.*, 2012, A&A, 546, A20
Vergani, S.D., Petitjean, P., Ledoux, C., *et al.*, 2009, A&A, 503, 771
Vergani, S.D., Piranomonte, S., Petitjean, P., *et al.*, 2011, Astron. Nachr., 332, 292
Vernet, J., Dekker, H., D'Odorico, S., *et al.*, 2011, A&A, 536, A105
Zibetti, S., Ménard, B., Nestor, D.B., *et al.*, 2007, ApJ, 658, 161

ON THE METAL AVVERSION OF LGRBS

J.F. Graham^{1,2} and A.S. Fruchter¹

Abstract. Recently, it has been suggested that the metallicity aversion of long-duration gamma-ray bursts (LGRBs) is not intrinsic to their formation, but rather a consequence of the anti-correlation between star-formation and metallicity seen in the general galaxy population. To investigate this proposal, we compare the metallicity of the hosts of LGRBs, broad-lined Type Ic (Ic-bl) supernovae (SNe), and Type II SNe to each other and to the metallicity distribution of star-forming galaxies using the SDSS to represent galaxies in the local universe and the TKRS for galaxies at intermediate redshifts.

The differing metallicity distributions of the LGRB hosts and the star-formation in local galaxies forces us to conclude that the low-metallicity preference of LGRBs is not primarily driven by the anti-correlation between star-formation and metallicity, but rather must be overwhelmingly due to the astrophysics of the LGRBs themselves. Three quarters of our LGRB sample are found at metallicities below $12+\log(\text{O/H}) < 8.6$, while less than a tenth of local star-formation is at similarly low metallicities. However, our SN samples are statistically consistent with the metallicity distribution of the general galaxy population. Using the TKRS population of galaxies, we are able to exclude the possibility that the LGRB host metallicity aversion is caused by the decrease in galaxy metallicity with redshift. The presence of the strong metallicity difference between LGRBs and Ic-bl SNe largely eliminates the possibility that the observed LGRB metallicity bias is a byproduct of a difference in the initial mass functions of the galaxy populations. Rather, metallicity below half-solar must be a fundamental component of the evolutionary process that separates LGRBs from the vast majority of Ic-bl SNe and from the bulk of local star-formation.

¹ Space Telescope Science Institute, 3700 San Martin Drive, Baltimore, MD 21218, USA

² Department of Physics and Astronomy, Johns Hopkins University, Baltimore, MD 21218, USA

1 Introduction

We compare the metallicity distribution of the hosts of Long-duration Gamma Ray Bursts (LGRB) with that of several other related populations: Type II supernovae (SNe) (which can serve as markers of star-formation), broad-lined Type Ic (Ic-bl) SNe (the specific type of SNe found coincident with LGRB events), and the general star-forming galaxy population. We perform this comparison across these different populations not primarily by number of galaxies but rather by weighting by their star-formation rates (SFRs). Our results show that, not only are the hosts of LGRBs at lower metallicities than either SNe hosts or general star-forming galaxies, but also that while Type Ic-bl and Type II SNe track star-formation (within our statistical ability to measure), more than three-quarters of our LGRBs are clustered in the lowest metallicity tenth of the star-formation.

To this end, we have compiled all spectra for LGRB and Type Ic-bl SNe hosts with host emission spectroscopy sufficient to allow metallicity measurement. To relate these events to the general star-forming galaxy population we have extracted the (approximately 137,000) galaxies from the Sloan Digital Sky Survey (SDSS) with line measurements suitable for metallicity measurement. This has also allowed us to compile a sample of the more common Type II SNe hosts simply by selecting the galaxies within our existing volume-limited SDSS sample which are known to have hosted such Type II SNe events with all the expected advantages of inter-sample consistency. Additionally, in order to better match the redshift range of our LGRB population, we extend our general star-forming galaxy population out to a redshift range of approximately unity via the addition of the higher redshift Team Keck Redshift Survey (TKRS) galaxy population.

Our analyses are based on four physical properties redshift, metallicity, rest frame B-band absolute magnitude, and (for most of our galaxies) the SFR. To maximize inter-sample consistency we have calculated independent metallicities using a common metallicity diagnostic, scale, and code via the R_{23} method implementation of Kobulnicky & Kewley (2004). R_{23} uses the ratio of oxygen to hydrogen line strengths (and the ratio of two oxygen lines to characterize the degree of ionization) to estimate the oxygen abundance in HII regions as a proxy of the total galaxy metallicity. This method however has a metallicity degeneracy issue where metal line emission cools the electron temperature causing the oxygen line strength, that was originally increasing with metallicity, to subsequently decrease yielding undifferentiable oxygen line strengths for both a high and low metallicity value. To resolve this degeneracy we have used observations of the $[N\text{ II}]/\text{H}\alpha$ line ratio, itself a crude metallicity indicator, to select between the upper and lower metallicity branch. For a few Type Ic-bl SNe we are forced to rely on this $[N\text{ II}]/\text{H}\alpha$ diagnostic exclusively with a corresponding increase in error. When comparing galaxies we use the B-band galaxy luminosity rather than galaxy mass as reliable host mass estimates were not available for a substantial fraction of the objects in our samples. We determine the SFRs from the galaxy's $\text{H}\alpha$ emission via the Kennicutt (1998) metric. The primary difficulty with this is adjusting the $\text{H}\alpha$ line flux for slit and fiber losses.

2 Results

As shown in Modjaz *et al.* (2008) the low metallicity bias of LGRBs is visually apparent in a simple scatterplot of host metallicity *versus* absolute magnitude, when compared to that of the hosts of Type Ic-bl SNe and the general star-forming galaxy population, represented by the SDSS. This result becomes even more impressive with the approximate three fold increase the the number of LGRBs and a 50% increase in number of Type Ic-bl SNe presented in Figure 1. In this figure, we also add a second general star-forming galaxy population, the TKRS, to better reflect the higher redshift distribution of the LGRBs. In our first presentation of the scatter plot, we present the metallicity measured at the location of the LGRBs and SNe within their hosts to show the actual metallicity of the environment responsible for their creation. In later plots, however, we switch to plotting the host galaxy central metallicities in order to better compare with the general galaxy population. To obtain a fair sample of the galaxy population, we use a subset of the SDSS star-forming population restricted to a volume-limited sample. Even this population, however, does not represent the way we expect SNe or LGRBs to choose their hosts. Their probability of going off in a particular galaxy should be proportional to the rate of star-formation in that galaxy (all other things being equal). To better emulate the expected occurrence of LGRBs and SNe, we then further select among these galaxies via random selection weighted by the underlying star-formation of each galaxy. These volume-limited and star-formation weighted samples are plotted along with the similarly volume-limited Type II SNe in Figure 2.

As can be seen in Figure 2, the distribution of the star-formation weighted sample is significantly different from the distribution of galaxies by number with a large bias towards brighter galaxies having a greater fraction of star-formation. As the LGRBs in our sample extend to a redshift of about one, far beyond the reach of the SDSS, let alone our smaller volume-limited survey, we must consider the evolution of metallicity with redshift as a complicating factor. However the effect of abundance evolution over the redshift range of our sample is nowhere near as dramatic as the metal aversion of the LGRB population as a whole. While there are three LGRB hosts in the high metallicity range of our sample (LGRBs 051022, 020819B, & 050826), is it clearly apparent in all three metallicity *vs.* luminosity scatterplots (Figs. 1 & 2) that while the SNe are distributed with the general star-forming galaxy population the LGRBs are on whole at the bottom of the metallicity distribution. It is notable that the three high metallicity (out of 14 total) LGRBs do appear consistent with the general star-forming galaxy population of comparable brightness and redshift. This is intrinsically surprising as were the metal aversion to remain in effect for these objects we would expect their occurrence, if still in the high metallicity range, to be far lower than the typical metallicity for the population at that luminosity and redshift (*i.e.* either an outlier of said population or among the lowest galaxies available within it).

While the metallicity *vs.* luminosity scatterplots show quite conclusively that the hosts of LGRBs are at lower metallicites than either SNe hosts or general

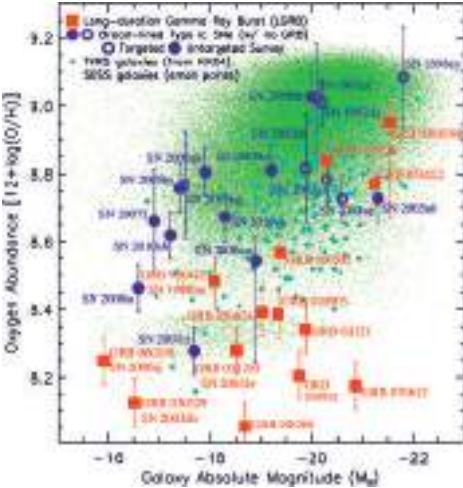


Fig. 1. Site Metallicity *vs.* absolute B-band galaxy luminosity of LGRB (squares) and broad-lined Type Ic SNe hosts (circles). Filled circles represent SNe selected in an untargeted manner whereas open circles are from galaxy targeted SNe surveys (and thus may be biased in galaxy properties by target selection). Star-forming galaxies from the SDSS (small dots) and TKRS (diamonds) are plotted in the background to provide a low and high redshift comparison sample respectively. Note the profound difference between the LGRB metallicity values and those of the Type Ic-bl SNe.

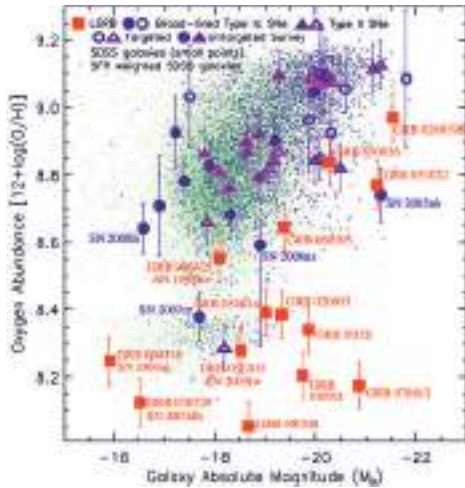


Fig. 2. Central Metallicity *vs.* B-band absolute galaxy luminosity. The Type II SNe hosts (purple triangles), SDSS galaxies (small green points) and the star-formation weighted random SDSS galaxies synthetic population (small blue points) shown here are limited to the sample redshift range of $0.02 < z < 0.04$. In order to get reasonable comparison samples, no redshift cut has been applied to the Type Ic-bl host population or the LGRB population. Note that the star-formation weighted random SDSS galaxy population tracks the SNe quite well in luminosity-metallicity space.

star-forming galaxies, they do not directly address whether this metallicity bias could be caused by the anti-correlation between SFR and metallicity of Mannucci *et al.* (2010) as claimed in Mannucci *et al.* (2011). To confront this issue, we plot in Figure 3 the integrated star-formation of the SDSS sample as a function of metallicity in comparison with the cumulative distributions of LGRBs and SNe. A similar plot, with a much smaller LGRB sample and no comparison of SNe, was first shown by Stanek *et al.* (2006). Both the non-LGRB Type Ic-bl SNe and Type II SNe track the distribution of star-forming SDSS galaxies quite well. The LGRBs however display a profound preference for lower metallicities. Thus the CCSNe track star-formation independent of its metallicity, while LGRBs do not.

However, this result could still be consistent with the Mannucci *et al.* (2010) relation, if the SFRs of the LGRB host were wildly discrepant from the other populations. To exclude this possibility, in Figure 4 we directly compare the SFRs of the LGRB and SNe hosts to the general star-forming SDSS galaxy population.

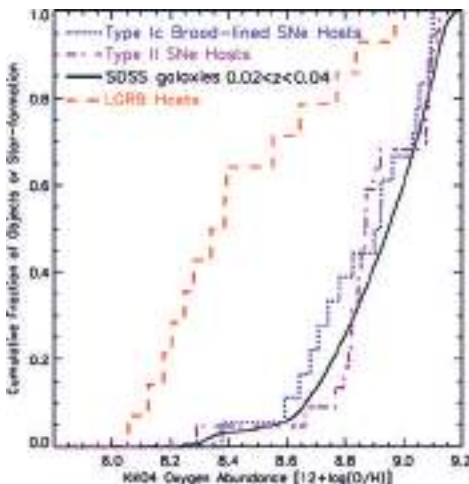


Fig. 3. Cumulative fraction of population (LGRBs and SNe) or total star-formation (redshift-cut SDSS star-forming sample) *vs.* galaxy central metallicity. Only the SDSS galaxies, and the Type II SNe hosts (which are all included in the SDSSS sample), are limited to the redshift-cut range. The LGRB hosts have metallicities considerably lower than would be obtained simply by following star-formation while both types of supernovae are consistent with the star-formation distribution. Thus the metallicity distribution of LGRBs cannot be explained only by association with star-forming galaxies.

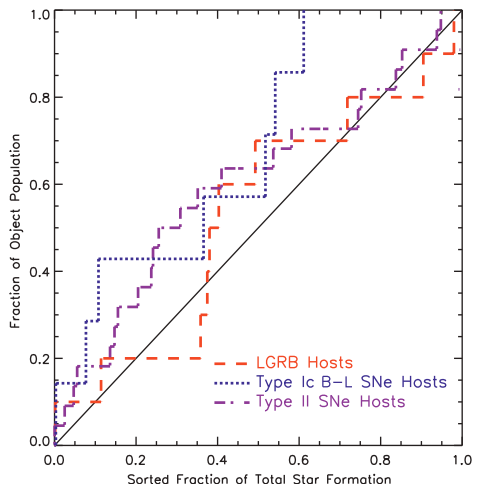


Fig. 4. Normalized cumulative distribution of star-formation fractional values for the SNe and LGRBs. For each object we determine the fraction of star-formation contained in SDSS galaxies of equal or lesser SFR than the object's host. All populations are reasonably consistent with the diagonal line indicating a reasonably consistent SFR distribution. Thus while LGRB hosts do have higher than average SFRs, as noted by Mannucci *et al.* (2011), their SFRs agree with what one would expect of a population that tracks star-formation. Thus metallicity, not SFR, must be the source of the discordant results shown in Figure 3.

This comparison is performed by taking the SFR of each LGRB and SNe host and determining the fraction of the total star-formation in the general SDSS galaxy population that occurs in galaxies with less star-formation than the host. These fractional values are then sorted and plotted as a normalized cumulative histogram. Should the distribution of star-formation for a given object type follow the general star-forming SDSS galaxy population then this histogram would track a diagonal line on the plot. For the SNe, the SDSS comparison sample is volume-limited. However, for the LGRBs, which are intrinsically a magnitude-limited sample, we use the entire SDSS, as a comparison magnitude-limited sample. Both the LGRBs and targeted Type II SNe population track the diagonal well, indicating a good correspondence between the SFRs of the two populations and the general SDSS galaxy population, and suggesting that SFR is correlated with LGRB and SNe formation.

3 Conclusions

We have shown quite conclusively in various scatterplots that the hosts of LGRBs are at lower metallicities than either SNe hosts or general star-forming galaxies. However, in order to directly address the question posed by Mannucci *et al.* (2011), of whether SFR can explain metallicity, we plot as a function of metallicity the integrated star-formation of the SDSS sample in comparison with the cumulative distributions of LGRBs and SNe. There we find that three quarters of our LGRBs are found in the bottom low-metallicity tenth of the star-formation, with the remaining quarter (like our SNe populations) appearing to track star-formation independent of metallicity. Assuming, all else being equal, that LGRBs (and SNe) occur proportionally to the allowable star-formation this bias indicates that LGRBs clearly prefer much lower metallicity host environments (as first suggested in Stanek *et al.* 2006 and shown with a much larger sample here). We also consider the SFR distribution of the LGRB and SNe populations and find that they are consistent with the SFR distribution of the SDSS sample and especially consistent if this comparison is limited only to SDSS objects of similar metallicity. Interestingly we find that the SFR distribution of the low-metallicity SDSS galaxies is reasonably similar to that of the entire SDSS population and cannot determine which the LGRB population best tracks.

In contrast to LGRBs, both our Type II and Type Ic-bl SNe populations appear to track the metallicity of the integrated SDSS star-formation. This is what one would expect if star-formation alone is sufficient to explain the metallicity distribution of both SNe types. Nonetheless, any metallicity bias, even one much more minor than that seen with LGRBs, has significant implications for a unified standard formation model for Type Ic SNe, Type Ic-bl SNe, and LGRBs. Kelly & Kirshner (2012) and Sanders *et al.* (2012) have looked at the metallicity distribution of different SNe types *vs.* each other (without relation to the SDSS or LGRBs) and highlight a bias towards Type Ic-bl SNe preferentially occurring in slightly lower metallicities than the other SNe populations (including the non-bl Type Ic SNe). Due to our strict volume limits, imposed to allow comparison with the SDSS, our Type II SNe sample is far smaller than that used in these other works. And we have made a decision to only look at two SNe types – Type II SNe as a hopefully truly unbiased indicator of star-formation, and Type Ic-bl SNe, due to their close association with LGRBs. Thus, while our work is well suited for its primary purpose of determining whether the metallicity distribution of LGRB hosts differs from other star-forming galaxies, it is much less powerful for distinguishing relative metallicity preferences of SNe. However, the metallicity differences between Type Ic-bl and other SNe, hinted at in our sample and perhaps seen more clearly in these other works, is dwarfed by the strong metallicity bias seen in LGRBs.

The presence of a metallicity bias between LGRBs and Type Ic-bl SNe poses a problem for explanations of the LGRB metallicity bias being the incidental result of an IMF difference in their host galaxies. In nearly all cases where one would have expected to detect a Type Ic underlying a LGRB to have been detected,

one has been found, and where good spectroscopy is available, the Type Ic is broad-lined (see Cano 2012 for a good discussion of this point). Thus, many and perhaps all Type Ic-bl SNe share a common progenitor type with LGRBs. One would therefore expect the masses of Type Ic-bl SNe progenitors to be similar to those of LGRBs. Thus while IMF differences between galaxies could play some role in determining where one finds LGRBs, the IMF is almost certainly far less important than galaxy metallicity.

These observations do not agree with the suggestion of Mannucci *et al.* (2011) “that the difference with the mass-metallicity relation is due to higher than average SFRs [of LGRB hosts] and that LGRBs with optical afterglows do not preferentially select low-metallicity hosts among the star-forming galaxies.” While the average SFR of LGRB hosts is indeed higher than that of typical SDSS galaxies, this is because LGRBs do not choose galaxies based on number but rather based on SFR (as well as metallicity). The star-formation distribution of the LGRB host population tracks that of similar metallicity SDSS galaxies. Indeed, due to the fact that the star-formation distribution of galaxies in the SDSS is largely independent of metallicity, they track the star-formation distribution of the entire SDSS as best as can be determined with only the 11 LGRBs for which we have good SFRs. The LGRB hosts population is explicitly concentrated in the low metallicity end of the available star-formation. While the LGRB hosts themselves may remain consistent with the mass, metallicity, and SFR relation of Mannucci *et al.* (2010), this relationship is not sufficient to explain the observed concentration of LGRBs in low metallicity star-formation.

Nonetheless, the preference of LGRBs for low-metallicity hosts is not absolute. Three cases of LGRBs in roughly solar metallicity hosts (LGRBs 051022, 020819B, & 050826) demonstrate that LGRBs can occur at high metallicity. However, such events are quite rare. These high-metallicity objects are all at substantial redshifts (99% of the galaxies in the SDSS sample lie closer than the closest of these LGRBs), and thus the search volume needed to find them was large. As a result, our sample overemphasizes high-metallicity LGRBs compared to the distribution likely to be found in a volume-limited survey. The presence of these objects does not substantially detract from our main conclusion, that on the whole, LGRBs have a strong intrinsic preference for low metallicity environments.

References

- Cano, Z., 2012 [[arXiv:1208.0307](https://arxiv.org/abs/1208.0307)]
- Kelly, P.L., & Kirshner, R.P., 2012, ApJ, 759, 107
- Kennicutt, R.C., Jr., 1998, ARA&A, 36, 189
- Kobulnicky, H.A., & Kewley, L.J., 2004, ApJ, 617, 240
- Mannucci, F., Cresci, G., Maiolino, R., *et al.*, 2010, MSRAS, 408, 2115
- Mannucci, F., Salvaterra, R., & Campisi, M.A., 2011, MSRAS, 414, 1263
- Modjaz, M., Kewley, L., Kirshner, R.P., *et al.*, 2008, AJ, 135, 1136
- Sanders, N.E., Soderberg, A.M., Levesque, E.M., *et al.*, 2012, ApJ, 758, 132
- Stanek, K.Z., Gnedin, O.Y., Beacom, J.F., *et al.*, 2006, Acta Astronomica, 56, 333

PROBING GALAXY EVOLUTION WITH GAMMA-RAY BURSTS

N.R. Tanvir¹

Abstract. The brightest gamma-ray bursts (GRBs) would be detectable at very high redshifts and so offer a probe of star-formation and galaxy evolution into the reionization era and even beyond. Localisation of their bright afterglows pinpoints their host galaxies, however faint, and can give not only redshifts but also metallicity estimates, information on the presence of dust and molecules, and HI column densities. Statistical samples of well-observed GRBs at high redshift may therefore reveal the evolution of the global star formation rate, chemical enrichment, far-ultraviolet escape fraction and the faint-end of the galaxy luminosity function; all of which are very difficult to establish via conventional galaxy searches. To date, only a handful of $z > 6$ GRBs have been identified, but their presence at $z > 8$ begins to realise their potential as searchlights to illuminate the early Universe.

1 Introduction

Gamma-ray bursts and their afterglows are incredibly bright and are found over a huge range in redshift (*e.g.*, Jakobsson *et al.* 2012). Since they are associated with the deaths of short-lived, massive stars (*e.g.*, Hjorth *et al.* 2003), they pinpoint the amount and location of star-formation through cosmic time (*e.g.*, Tanvir & Jakobsson 2007). The power-law spectra of the afterglows provide ideal backlights for studies of abundance patterns and dust, thus offering the chance to map cosmic chemical evolution (*e.g.*, Fynbo *et al.* 2006), and HI column in both the host (*e.g.*, Jakobsson *et al.* 2006) and intergalactic medium (IGM). As I describe below, these probes are highly complementary to other routes to investigating early star and galaxy populations, and reionization.

¹ University of Leicester, Department of Physics and Astronomy, University Road, Leicester LE1 7RH, UK

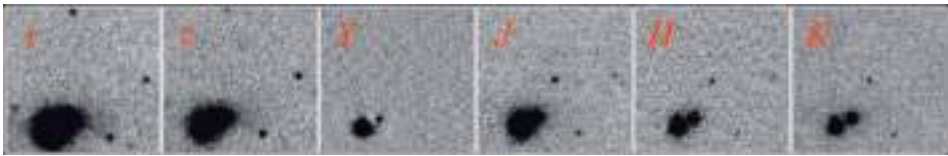


Fig. 1. Optical (GMOS-N) and infrared (NIRI) imaging of the afterglow of GRB 120923A (centred in each panel) from Gemini-North showing it to be a Y -band drop-out, and hence likely at $z > 8$.

2 The search for high redshift gamma-ray bursts

Although the brightest GRBs should be detectable by *Swift*/BAT at very high redshifts (*e.g.*, $z \sim 20$; Racusin *et al.* 2008; Bloom *et al.* 2009), the rate of bursts at $z > 7$ is expected to be low, and finding them requires deep and rapid optical and infra-red afterglow follow-up to search for optical drop-outs and obtain redshifts. The first example to be found was GRB 090423 (Tanvir *et al.* 2009; Salvaterra *et al.* 2009), which, indeed, at $z = 8.2$ was the highest spectroscopic redshift measured for any source. Remarkably, within a few days another very high redshift source was identified, although unfortunately in the case of GRB 090429B no spectroscopy was possible and we must rely on the photometric redshift of $z \sim 9.4$ (Cucchiara *et al.* 2011).

Since then, the rate of discoveries has remained low, and it has become clear that the majority of faint, red afterglows are in dusty systems rather than at high- z (*e.g.*, Tanvir *et al.* 2008; Perley *et al.* 2009; Greiner *et al.* 2011). Very recently GRB 120923A was identified as another $z > 8$ candidate based on optical and infrared photometry (Levan *et al.* 2012; see also Fig. 1); refined analysis of these data, and also spectroscopic data acquired with VLT and *HST*, are in progress at the time of writing. The faintness of this afterglow (AB magnitude ~ 22.5 at discovery) confirms that follow-up with large aperture telescopes is required if we are not to miss some of these rare events.

3 The host galaxies of high redshift GRBs

If GRBs trace massive star formation – certainly a plausible hypothesis in the early universe – then an unbiased sample of their host galaxies should reflect the star-formation weighted galaxy luminosity function. If in turn the star-formation rate is proportional to the ultraviolet (UV) luminosity, again plausible in for low-dust, low-metallicity early stellar populations, then the GRB hosts should follow the luminosity-weighted galaxy luminosity function. This argument has been applied to a sample of the hosts of six GRBs in the range $5 < z < 9.5$ by Tanvir *et al.* (2012). Even in relatively modest *HST* integrations, prior knowledge of the exact location of the burst (and indeed the redshift) allows us to search to very deep levels. None of the hosts was significantly detected to typical AB magnitudes limits

of ~ 28 , suggesting that a large proportion of high- z star formation is occurring in very faint galaxies. Specifically, the conclusion was that this result is consistent with a rapidly steepening galaxy luminosity function at $z > 6$, as advocated, for instance, by Bouwens *et al.* (2011), but marginally inconsistent with a non-evolving LF.

Interestingly, studies of the redshift distribution of GRBs (*e.g.*, Jakobsson *et al.* 2012 and Robertson & Ellis 2012 for recent discussions) also seem to require an enhanced star-formation rate at $z > 3$, consistent with an increasing proportion being missed in traditional flux-limited surveys.

4 Future developments

The sample of high redshift GRBs identified by *Swift* will provide important targets for the next generation of near-infrared telescopes, including *JWST* and the planned 30 m class ground-based telescopes. Furthermore, providing there are satellites able to provide triggers in that era, spectroscopic observations of $z > 7$ afterglows are likely to provide stringent constraints on the IGM neutral fraction at the position of the burst along with the HI column density and metallicity in the host (see Fig. 2). If this can be done for a sample of several tens of such events, it will allow us to map the time-line of reionization and to assess the early chemical evolution of the universe (including looking for signatures of population III nucleosynthetic yields; *cf.*, Cooke *et al.* 2012). Crucially, since only cases with very low host HI column density could possibly allow significant amounts of ionising UV radiation to escape from the stellar population giving rise to the GRB, the distribution of host column densities will set tight constraints on the average escape fractions for light from massive stars (*e.g.*, see Chen *et al.* 2007; Fynbo *et al.* 2009). Unless this is considerably higher than that usually measured at lower redshifts, it is unlikely that this radiation was sufficient reionized the universe.

5 Conclusions

I have argued that GRBs provide a powerful complement to traditional studies of galaxy evolution, offering a route to abundances, dust properties etc. for star-forming galaxies over all redshifts. Despite the sample of *Swift* bursts at $z > 5$ to date being relatively modest in size (although new results are pending final analysis), already the searches for their hosts, and the implications their number as a function of redshift has for the global star-formation rate density, are providing important indications that the majority of high redshift star formation is occurring in galaxies below the detection limits of the deepest surveys for Lyman-break galaxies.

In the future, observations of GRBs and their hosts with next generation facilities, particularly *JWST* and 30 m class telescopes, promise to establish the properties of star-forming galaxies in the era of reionization in unprecedented detail. *Swift* is unlikely to remain operational into this era, thus there is very strong

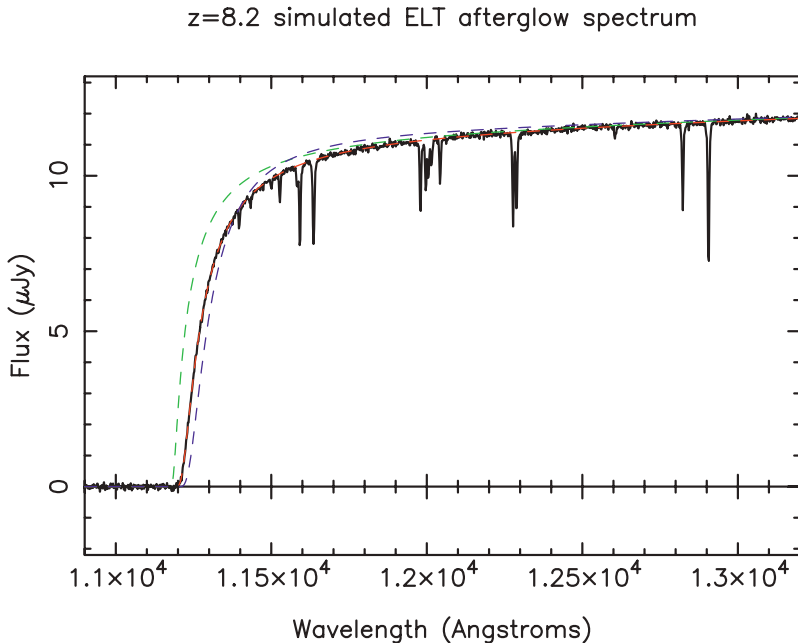


Fig. 2. Simulated spectrum (black solid line) around the Ly α break showing the quality of data which would be obtained with a ~ 40 m telescope such as the proposed E-ELT for an afterglow with magnitude approximately the same as that obtained for GRB 090423 observed by the VLT (Tanvir *et al.* 2009). The host galaxy in this case was chosen to have an HI column density of 10^{21} cm $^{-2}$, and a metallicity of $Z \approx Z_{\odot}/10$, and the IGM was taken to be 100% neutral. The green dashed line shows a model with just a neutral IGM (with redshift fixed at that given by the metal lines), and the blue dashed line shows an attempt to fit a model with an ionised IGM and only absorption in the host. Neither component alone is a credible fit, illustrating that high S/N data of this sort can be used to decompose IGM and host galaxy contributions (red dashed line).

motivation for development of a powerful successor mission, ideally one even better able to discover and identify very high redshift GRBs.

References

- Bloom, J.S., Perley, D.A., Li, W., *et al.*, 2009, ApJ, 691, 723
- Bouwens, R.J., Illingworth, G.D., Oesch, P.A., *et al.*, 2011, ApJ, 737, 90
- Chen, H.-W., Prochaska, J.X., & Gnedin, N.Y., 2007, ApJ, 667, L125
- Cooke, R., Pettini, M., & Murphrey, M.T., 2012, MNRAS, 425, 347
- Cucchiara, A., Levan, A.J., Fox, D.B., *et al.*, 2011, ApJ, 736, 7
- Fynbo, J.P.U., Starling, R.L.C., Ledoux, C., *et al.*, 2006, A&A, 451, L47
- Fynbo, J.P.U., Jakobsson, P., Prochaska, J.X., *et al.*, 2009, ApJS, 185, 526

- Greiner, J., Krühler, T., Klose, S., *et al.*, 2011, A&A, 526, 30
Hjorth, J., Sollerman, J., Møller, P., *et al.*, 2003, Nature, 423, 847
Jakobsson, P., Fynbo, J.P.U., Ledoux, C., *et al.*, 2006, A&A, 460, L13
Jakobsson, P., Hjorth, J., Malesani, D., *et al.*, 2012, ApJ, 752, 62
Levan, A.J., Perley, D.A., Tanvir, N.R., *et al.*, 2012, GCN 13802
Perley, D.A., Cenko, S.B., Bloom, J.S., *et al.*, 2009, AJ, 138, 1690
Racusin, J.L., Karpov, S.V., Sokolowski, M., *et al.*, 2008, Nature, 455, 183
Robertson, B.E., & Ellis, R.S., 2012, ApJ, 744, 95
Salvaterra, R., Della Valle, M., Campana, S., *et al.*, 2009, Nature, 461, 1258
Tanvir, N.R., & Jakobsson, P., 2007, RSPTA, 365, 1377
Tanvir, N.R., Levan, A.J., Rol, E., *et al.*, 2008, MNRAS, 388, 1743
Tanvir, N.R., Fox, D.B., Levan, A.J., *et al.*, 2009, Nature, 461, 1254
Tanvir, N.R., Levan, A.J., Fruchter, A.S., *et al.*, 2012, ApJ, 754, 46

THE MASS-SFR-METALLICITY RELATION OF STAR FORMING GALAXIES AND ITS EVOLUTION: IMPLICATIONS FOR GRB/SN HOST GALAXIES

Y. Niino¹

Abstract. Observed properties of gamma-ray burst (GRB) host galaxies are important clues to understand the nature of GRB progenitors. However, the properties of the host galaxies don't directly tell us the nature of the GRB progenitors, and the decipherment of the clue relies on our understanding of general galaxies. The relation between stellar mass, star formation rate (SFR), and metallicity of star forming galaxies (so called the fundamental metallicity relation) has recently attracted attention regarding its possible impact upon our understanding on the properties of the long GRB host galaxies. In this study, I show the possibility of redshift evolution of the mass–SFR–metallicity relation which has been claimed to be independent of redshift, and discuss implications of the evolving relation for the properties of GRB/SN host galaxies.

1 Introduction

The stellar mass–metallicity (M_{\star} – Z) relation of the long gamma-ray burst (GRB) host galaxies is shifted toward low-metallicity compared to that of the field star forming galaxies (Levesque *et al.* 2010). High SFR galaxies have lower Z than low SFR galaxies with similar mass (Mannucci *et al.* 2010), and hence the shift of the M_{\star} – Z relation of the long GRB host galaxies may be a result of the SFR– Z correlation (Kocevski & West 2011; Mannucci *et al.* 2011). Galaxies at wide range of redshifts ($0.1 \lesssim z \lesssim 3$) agree with a single M_{\star} –SFR– Z relation, and hence the relation is claimed to be independent of redshift.

If the shift of the M_{\star} – Z relation of the long GRB host galaxies is a result of the SFR– Z correlation, host galaxies of other SFR tracing transients are expected to have similar shift of the M_{\star} – Z relation. However the M_{\star} – Z relation of Type II supernova (SN) host galaxies is not shifted (Stoll *et al.* 2012).

¹ Division of Optical and Near-Infrared Astronomy, National Astronomical Observatory of Japan, 2-21-1 Osawa, Mitaka, Tokyo, Japan

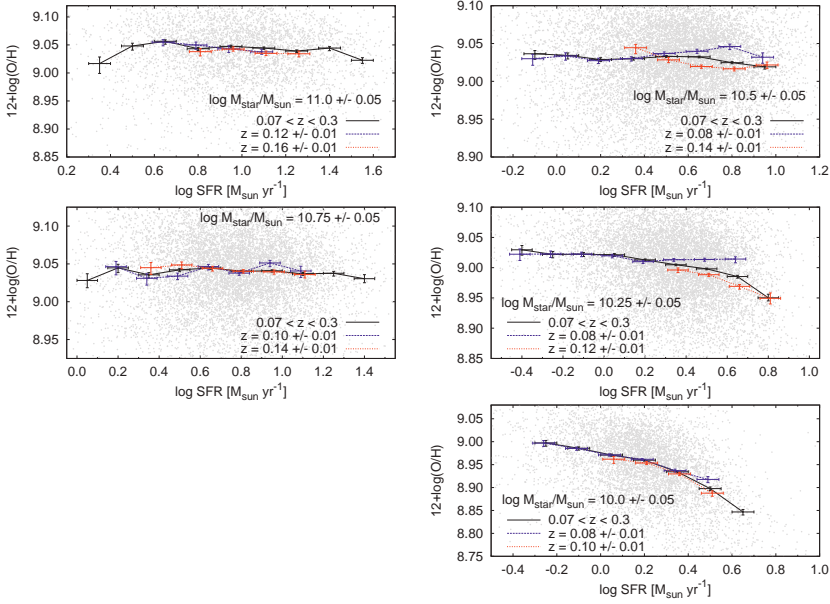


Fig. 1. The SFR–Z relations at various M_{\star} . The systematic redshift dependence is found in the mass ranges $M_{\star} < 10^{10.5} M_{\odot}$.

2 Evolution of the M_{\star} –SFR–Z Relation

The M_{\star} –SFR–Z relation is originally defined by galaxies in the Sloan Digital Sky Survey (SDSS) spectroscopic sample at $z \sim 0.1$. Within the redshift range of the SDSS galaxies ($0.07 \leq z \leq 0.3$), galaxies with larger M_{\star} and SFR reside at higher redshifts. The galaxies at $z > 0.3$ which are confirmed to be consistent with the relation also have higher SFR at higher redshifts. Hence in the previous studies of the M_{\star} –SFR–Z relation, SFR and redshift of galaxies are degenerate. Thus it is not clear whether the metallicity is dependent on SFR or redshift.

If the M_{\star} –SFR–Z relation actually evolves with redshift, the evolution may explain the difference between the M_{\star} –Z relations of the long GRB host galaxies and the type II SN host galaxies. Type II SNe are typically at lower redshifts than the low redshift sample of long GRBs. Separating the SDSS galaxies into narrow redshift bins, we find difference of the M_{\star} –SFR–Z relation between different redshifts in the mass ranges $M_{\star} < 10^{10.5} M_{\odot}$ (Fig. 1, see Niino 2012 for detail).

3 Testing artificial effects

In this section, we test artificial effects that may produce seeming evolution of the M_{\star} –SFR–Z relation using the SDSS galaxies with $M_{\star} = 10^{10.5 \pm 0.05} M_{\odot}$ and $\text{SFR} = 10^{0.8 \pm 0.05} [M_{\odot}/\text{yr}]$ (see the top-right panel of Fig. 1).

3.1 The fiber aperture effect

The spectroscopic fiber covers larger area of a galaxy at higher redshifts, and metallicity of a galaxy is often lower in the outskirts than at the center. Thus the difference of fiber covering fraction may cause seeming difference of metallicity.

We investigate the correlation between the fiber covering fraction and the metallicity of galaxies. Unlike expected from the metallicity gradient, galaxies with larger fiber covering fraction have higher metallicity. We note that galaxies with larger radius have smaller metallicity (Ellison *et al.* 2008). The positive correlation between the fiber covering fraction and the metallicity suggests that the fiber covering fraction is determined by the intrinsic radius of galaxies rather than their redshift. We also note that it is difficult to explain why we find the evolution only in the low mass range, by the fiber aperture effect.

3.2 Sampling bias due to the limiting magnitude

The galaxies in the SDSS sample are brighter at higher redshifts, due to the limiting magnitude of the spectroscopic target selection. The difference of metallicity may results from the difference of luminosity.

We separate the low redshift galaxies ($z \sim 0.8$) into bright and faint subsamples (at $M_r = -21.5$). The bright and faint subsamples have consistent metallicity distributions to each other, while the metallicity distributions of the bright subsample and the high redshift ($z \sim 1.4$) sample are inconsistent to each other. Note that the low redshift bright sample galaxies have similar M_r to those of the high redshift sample galaxies.

4 Conclusions

The M_{\star} -SFR-Z relation is different between $z < 0.1$ and > 0.1 . This redshift evolution is hardly explained by the observational effects. This evolution of the M_{\star} -SFR-Z relation could explain the difference of the M_{\star} -Z relations between the host galaxies of the Type II SNe and long GRBs.

References

- Ellison, S.L., Patton, D.R., Simard, L., & McConnachie, A.W., 2008, ApJ, 672, L107
- Kocevski, D., & West, A.A., 2011, ApJ, 735, L8
- Levesque, E.M., Kewley, L.J., Berger, E., & Zahid, H.J., 2010, AJ, 140, 1557
- Mannucci, F., Cresci, G., Maiolino, R., *et al.*, 2010, MNRAS, 408, 2115
- Mannucci, F., Salvaterra, R., & Campisi, M.A., 2011, MNRAS, 414, 1263
- Niino, Y., 2012, ApJ, 761, 126
- Stoll, R., Prieto, J.L., Stanek, K.Z., & Pogge, R.W., 2012 [[arXiv:1205.2338](https://arxiv.org/abs/1205.2338)]

A DEEP SEARCH FOR THE HOST GALAXIES OF GRBS WITH NO DETECTED OPTICAL AFTERGLOW

A. Rossi¹, S. Klose¹, P. Ferrero², J. Greiner³, A. Updike⁴, D.A. Kann^{1,3},
T. Krühler⁵ and A. Nicuesa Guelbenzu¹

Abstract. Long gamma-ray bursts (GRBs) pinpoint star-forming galaxies as they are linked to the deaths of massive stars. In most cases, these galaxies have been found to be blue, sub-luminous and of low-metallicity. However, our recent survey have demonstrated that a sizeable fraction of GRBs reside in massive, dusty and star-forming extremely red objects (EROs, $(R - K)_{AB} > 3.5$). The most remarkable case is the host of GRB 080207, one of the reddest galaxies ever associated with a GRB. This discovery suggests that at least a fraction of GRB afterglows trace a subpopulation of massive starburst galaxies, which are markedly different from the most studied blue, sub-luminous and compact GRB host galaxies.

1 Introduction

Gamma ray bursts (GRBs) are the most luminous phenomena in the Universe, coming from remote galaxies up to redshift $z \sim 8$ (*e.g.*, Salvaterra *et al.* 2009; Tanvir *et al.* 2009). Among all the detected GRBs, about 90% are long GRBs lasting more than two seconds and signal the death of a very massive star. GRB hosts (GRBHs) are better known in the low- z regime (up to $z \lesssim 1.5$), where they have been found to be sub-luminous, blue, with low metallicity and moderate star formation (*e.g.*, Savaglio *et al.* 2009). However, recent surveys showed that this is just a fraction of the host population (Hjorth *et al.* 2012; Rossi *et al.* 2012).

Up to 30% of long bursts are classified as dark GRBs. A GRB is considered as a dark burst if the optical flux is lower than expected when extrapolating the X-ray flux to the optical bands (*e.g.*, Jakobsson *et al.* 2004). In Greiner *et al.* (2011) we

¹ Thüringer Landessternwarte Tautenburg, Sternwarte 5, 07778 Tautenburg, Germany

² Instituto de Astrofísica de Canarias (IAC), 38200 La Laguna, Tenerife, Spain

³ Max-Planck-Institut für Extraterrestrische Physik, Giessenbachstraße, 85748 Garching, Germany

⁴ Department of Physics and Astronomy, Dickinson College, Carlisle, PA 17013, USA

⁵ Dark Cosmology Centre, Niels Bohr Institute, Univ. of Copenhagen, Juliane Maries Vej 30, 2100 København, Denmark

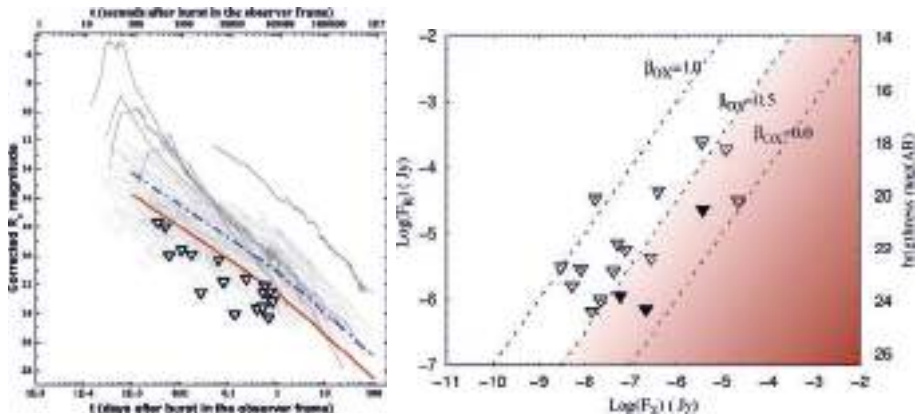


Fig. 1. *Left:* the R_C -band light curves of all (long) afterglows in the sample of Kann *et al.* (2010, 2011). All data have been corrected for Galactic extinction. Triangles indicate equivalent R_C -band upper limits of the afterglows in our sample. The blue dashed/dotted line approximately indicates the mean of the afterglow brightness distribution. The brown solid line indicates the border line of all targets. *Right:* observed upper limits in the R_c band compared to the measured flux density at 1.73 keV (the logarithmic mean of the Swift/XRT window, 0.3–10 keV) for the 17 bursts in our sample. The bursts falling in the gray area are dark according to Jakobsson *et al.* (2004).

show that extinction by dust in combination with a modest redshift is the main cause of the optical dimness of dark GRBs. However, their host galaxies, especially those of the most extinguished ones, are poorly studied, because observations are mainly limited to the optical bands.

Here, we focus on the search for the host galaxies of a sample of 17 long GRBs with arcsec-sized *Swift*/XRT error circles but no detected optical/NIR afterglow in spite of deep and rapid follow-up observations. Our study is based on deep R_C and K_s -band observations performed at the ESO/VLT, partly supported by observations with the seven-channel imager GROND (Greiner *et al.* 2008) at the 2.2-m telescope on La Silla and other facilities. Firstly, we verify whether the bursts can be classified as dark GRBs. Afterwards, we identify the host-galaxy candidates and study their color properties to check if these can be different from the hosts of optically bright GRBs.

2 Results

Six events, namely GRBs 050717, 050922B, 070429A, 080207, 080218B, and 080602, are dark according to Jakobsson *et al.* (2004) (Fig. 1, right).

For 15 of the 17 bursts we find at least one galaxy inside the doubled XRT error circle, in two cases only a deep upper limit in R_C and K_s can be provided. In seven cases we discover extremely red objects (EROs; Elston *et al.* 1988) in the error circles, at least four of them might be dust-enshrouded galaxies. The



Fig. 2. The figures show the VLT/ISAAC *K*-band images of the ERO host galaxies of three dark GRBs in the sample.

most remarkable case is the host of the dark GRB 080207 which has a colour of $(R_C - K_s)_{AB} \sim 4.7$ mag, therefore it is the reddest galaxy ever associated with a GRB. Thanks to our results we doubled the known number of EROs hosting GRBs. On average these galaxies differ from the blue, sub-luminous, low-metallicity host galaxies that are normally associated with optically bright GRBs (*e.g.*, Savaglio *et al.* 2009). Instead, their color recall those of ultra-luminous infrared galaxies or even sub-millimeter galaxies (*e.g.*, Pope *et al.* 2005).

3 Conclusions

Optically dim afterglows result from cosmological Lyman drop out and dust extinction, but the former process is only required for a minority of cases ($\lesssim 1/3$). Extinction by dust in the host galaxies might explain all other events. Thereby, a seemingly non-negligible fraction of these hosts are globally dust-enshrouded, extremely red galaxies. This suggests that bursts with optically dim afterglows trace a subpopulation of massive star-burst galaxies, which are markedly different from the main body of the GRB host galaxy population, namely the blue, sub-luminous, compact galaxies.

References

- Elston, R., Rieke, G.H., & Rieke, M.J., 1988, ApJ, 331, L77
- Hjorth, J., Malesani, D., Jakobsson, P., *et al.*, 2012, ApJ, 756, 187
- Greiner, J., Krühler, T., Klose, S., *et al.*, 2011, A&A, 526, A30
- Greiner, J., Bornemann, W., Clemens, C., *et al.*, 2008, PASP, 120, 405
- Jakobsson, P., Hjorth, J., Fynbo, J.P.U., *et al.*, 2004, ApJ, 617, L21
- Kann, D.A., Klose, S., Zhang, B., *et al.*, 2010, ApJ, 720, 1513
- Kann, D.A., Klose, S., Zhang, B., *et al.*, 2011, ApJ, 734, 96
- Pope, A., Borys, C., Scott, D., *et al.*, 2005, MNRAS, 358, 149
- Rossi, A., Klose, S., Ferrero, P., *et al.*, 2012, A&A, 545, A77
- Salvaterra, R., Della Valle, M., Campana, S., *et al.*, 2009, Nature, 461, 1258
- Savaglio, S., Glazebrook, K., & Le Borgne, D., 2009, ApJ, 691, 182
- Tanvir, N.R., Fox, D.B., Levan, A.J., *et al.*, 2009, Nature, 461, 1254

STUDY OF BTA, HUBBLE, AND SPITZER GRB 021004 DEEP FIELDS

I.V. Sokolov¹, O.J.A. Bravo Calle² and Yu.V. Baryshev²

Abstract. The photometric redshifts were derived, based on photometry data in visual and infrared. Deep fields were observed during gamma-ray bursts investigation with the SAO RAS 6-meter telescope (BTA), Spitzer and Hubble Space Telescope. BTA BVRI images were used, as well as F475W, F606W, F814W of ACS at the Hubble Space Telescope and Spitzer IRAC ch1 3.6 μm , ch3 5.7 μm . Each BTA BVRI exposure was about one-hour long, reaching objects up to the \sim 27th stellar magnitude. The GRB 021004 field was investigated. A catalog of 874 discovered objects is being made as well as color diagrams and Hubble diagram for these objects.

1 The GRB deep fields

Deep multi-wavelength surveys are an important tool in studying the formation and evolution of galaxies. Infrared data is particularly useful in these surveys. Several deep fields were observed with the BTA during GRB follow-up campaign. These fields are: GRB 970508 (BVRI), GRB 980703 (BVRI), GRB 990123 (BVRI), GRB 991208 (BVRI), GRB 000926 (BVRI), GRB 021004 (BVRI). The exposures were about 1 hour long. Typical field sizes are \sim 4' \times 4'.

2 The extraction of objects in GRB 021004 deep fields

We used visual and IR bands to cover the GRB deep fields. The GRB 021004 field images are presented in Figure 1. These are visual BTA BVRI, Hubble ACS F435W, F606W, F814W, and SPITZER IRAC infrared images. Photometric redshifts of galaxies detected in the field based on BTA/BVRI were measured (Baryshev *et al.* 2010) using the HyperZ (Bolzonella *et al.* 2000) software package.

¹ Institute of Astronomy RAS, Russia; e-mail: ilia333@land.ru

² Saint Petersburg State University, Russia

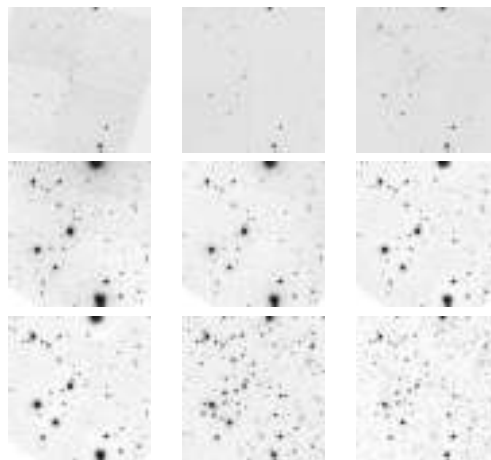


Fig. 1. GRB 021004 field: three upper images are taken with HST, the next four are taken with BTA (the *middle row* and *bottom left*), and the last two are taken with the Spitzer Space Telescope. Field sizes are $4' \times 4'$.

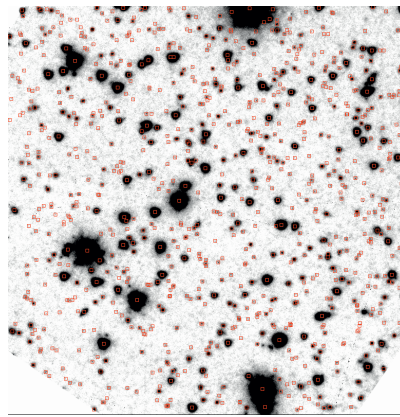


Fig. 2. The stack of all bands, which was used for detection of objects. 874 objects were extracted. The objects are marked with red boxes.

We used the software package SExtractor (Bertin *et al.* 1996) for the search and photometry of a large number of objects in the field. We used the dual-image mode, where the stack of all images is used for detection and the photometry is performed on the single images. Used this way, the SExtractor measures the flux in the exact same apertures in all bands. The “STAR CLASS” parameter of the SExtractor package served as a criterion for separating the star-shaped and extended objects. An object is considered star-shaped if its “STAR CLASS” parameter is greater than 0.7. The 3σ excess of intensity over the background was selected as a detection limit, where σ stands for the background fluctuations.

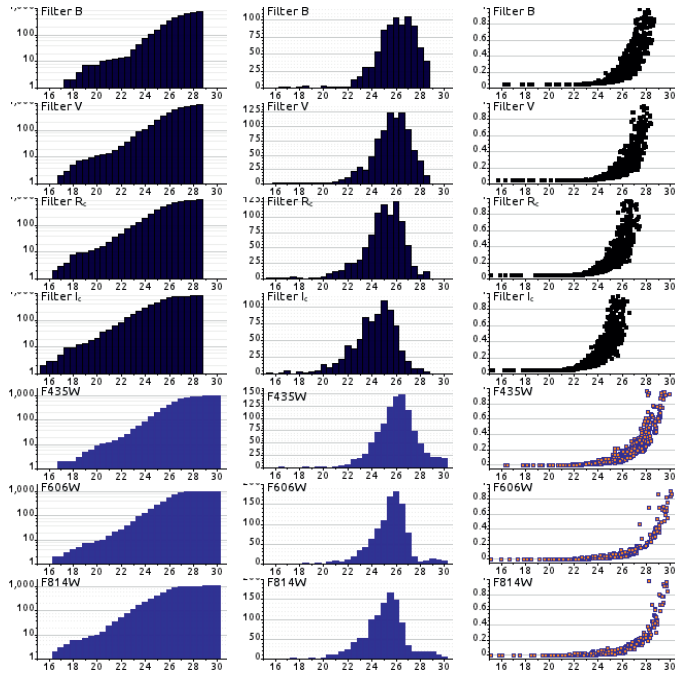


Fig. 3. Magnitude-count, differential magnitude-count and magnitude-error diagrams for 874 objects. *Top* four rows are for BTA/BVRI, *bottom* three rows for HST F435W, F606W, F814W. The x-axis is magnitude. The y-axis in first two columns is the number of objects, in the third column - the magnitude error. The diagrams show the depth of the images.

A detected candidate is considered a real object if it occupies at least four adjacent elements of the CCD chip.

3 Conclusion

The catalog of 874 detected objects will be available online. It includes the photometry data in each of the nine used bands for each of the detected object. Other GRB deep fields are going to be processed in the similar way.

BTA/BVRI/GRB 021004 redshift estimates (Baryshev *et al.* 2010) can be considered only as a first approximation. It is supposed to measure photometrical redshifts more precisely with these HST and SPITZER observations (Fig. 1).

References

- Baryshev, Yu.V., Sokolov, I.V., Moskvitin, A.S., *et al.*, 2010, Study of faint galaxies in the field of GRB 021004, *Astrophys. Bull.*, 65, 327
- Bertin, E., & Arnouts, S., 1996, *A&AS*, 117, 393
- Bolzonella, M., Miralles, J.-M., & Pelló, R., 2000, *A&A*, 363, 476

THE MULTI-BAND STUDY OF THE ENVIRONMENT OF THE RC J0311+0507 RADIO GALAXY: A STEP FORWARD TO UNDERSTAND MASSIVE STELLAR SYSTEM FORMATION AT $Z > 4$

Yu.N. Parijskij¹, O.P. Zhelenkova², P. Thomasson^{3,4}, A.I. Kopylov²,
A.V. Temirova¹, I.V. Sokolov⁵, V.N. Komarova² and O.J.A. Bravo Calle⁶

Abstract. The radio galaxy RC J0311+0507 was investigated in the “Big Trio” project, which aims to search for distant radio galaxies. Optical spectroscopy performed at the 6-m telescope measured its redshift as 4.514. The source is one of the most luminous objects in the high redshift Universe having $L \approx 3 \times 10^{29} \text{ W Hz}^{-1}$ at 500 MHz, that suggests the presence of a super massive black hole with a mass of about $10^{10} M_{\odot}$ inside the parent galaxy. Mechanisms of the formation of galaxies with black holes of such masses in the early stage of the Universe is not yet clear. Based on a collection of deep images taken in 10 optical and infrared bands we started a photometric study of the environment of this radio galaxy to detect possible neighborhood.

1 Discovery of the distant powerful radio galaxy

RC J0311+0507 was recognized as having an Ultra Steep Spectrum (USS) in the frequency range 365–4850 MHz ($\alpha = -1.31$, $S \propto \nu^{\alpha}$) in the early stages of the “Big Trio” survey project (Goss *et al.* 1992; Parijskij *et al.* 1996; Parijskij *et al.* 2000). The project, aimed at searching and studying very distant radio galaxies, is composed by: the RATAN-600 radio telescope as the survey instrument, the VLA radio telescope as the imaging instrument, and the 6-m optical telescope of the Special

¹ Saint-Petersburg Branch of SAO RAS, Russia; e-mail: unipar@rambler.ru

² Special Astrophysical Observatory of RAS, Russia; e-mail: zhe@sao.ru

³ Jodrell Bank Centre for Astrophysics, UK; e-mail: pt@jb.man.ac.uk

⁴ Institute for Radio Astronomy and Space Research, New Zealand

⁵ Institute of Astronomy RAS, Russia; e-mail: ilia333@land.ru

⁶ Saint Petersburg State University, Russia

Astrophysical Observatory of the Russian Academy of Sciences (SAO RAS) for spectroscopy. The only known object close to the position of was the radio galaxy 4C + 04.11, and VLA images of it suggested an asymmetric double structure. Optical photometric and spectroscopic observations with the 6-m telescope allowed the identification of its host galaxy ($R = 22.8$) and the measure of its redshift. Indeed, its spectrum showed the presence of a strong emission line at 6703 Å which was interpreted as $Ly\alpha$ at a redshift of $z = 4.514$ (Kopylov *et al.* 2006).

New MERLIN and EVN maps of this object, at 1658 MHz and 4999 MHz respectively, with an order of magnitude better resolution than those of the VLA have shown the multi-component structure and overall curved structure of the radio source (Parijskij *et al.* 2010). The extent of RC J0311 + 0507 ($\sim 2.8''$) appears to be approximately the same as that of the optically visible galaxy. A multi-component structure for a radio galaxy is not a very rare phenomenon, although in the case of RC J0311 + 0507, the radio luminosity of each components appears to be greater than $10^{28} \text{ W Hz}^{-1}$ at 500 MHz, which is comparable with the luminosities of the main lobes of the most powerful FRII radio galaxies. The precise nature of the components is not clear, but it is possible that nuclear source activity has been stimulated by multi-merging effects and/or that the jet is propagating through and interacting with a denser environment.

An estimation of the black hole (BH) mass in RC J0311 + 0507 can be made from the correlation between the BH mass and the total and core radio luminosities (Franceschini *et al.* 1998). The derived value seems to indicate that RC J0311 + 0507 is an object with a supermassive black hole (SMBH) with a mass $\approx 10^{10} M_\odot$.

2 Photometric study of the RC J0311+0507 environment

We started the photometric study of the RC J0311 + 0507 environment using the available optical and infrared data. Deep photometric images include: the 6-m SAO RAS telescope observations in the B, V, R, I bands and in the SED607, SED665 and SED707 intermediate-band filters (20–30 min exposures at 1.2–2''); the 3.8-m UKIRT telescope K band observations (100 min exposure and 0.7–1.1'' seeing); the 8-m SUBARU telescope observations from the SMOKA archive in B, R, V bands and NL671 narrow-band filter (30, 60, 48 and 160 min, respectively, with 0.3–0.4'' seeing); images in 3.6 and 4.5 μk bands (30 and 45 min exposures respectively) from the Spitzer Heritage Archive.

All the available data were partially processed or reprocessed in a uniform manner using the ESO-MIDAS astronomical data reduction system and the Subaru Data Reduction and Analysis (SuperCam) package for the reduction of the data acquired at that telescope. Figures 1 and 2 resulting reprocessed V, R, I, SED607 and SED655 band images taken at the 6-m SAO RAS telescope and the processed NL671 narrow-band image taken with SUBARU.

The estimation, obtained by the sum of frames, shows a slight increase in the surface density of objects around the radio source. This may indicate the presence

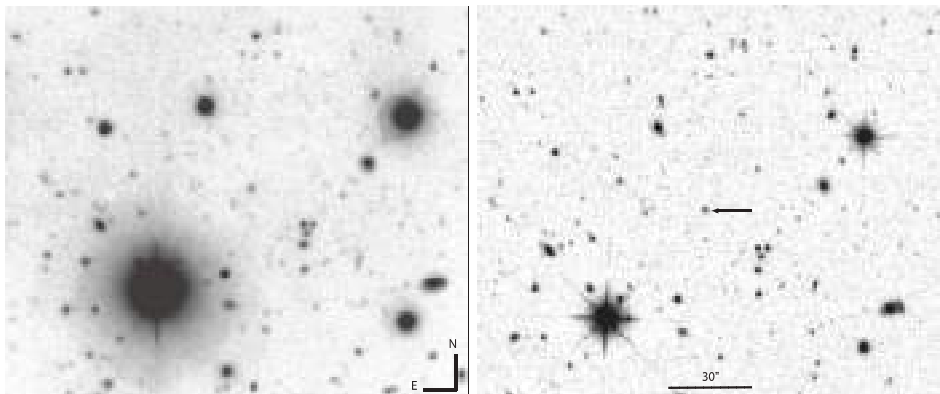


Fig. 1. *Left:* the sum of the R, I, SED665, SED707 images obtained with the 6-m SAO RAS telescope; *right:* the UKIRT K-band image. An arrow marks the host galaxy location.

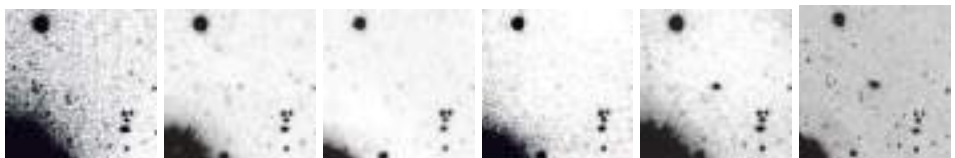


Fig. 2. The 6-m SAO RAS telescope images, obtained with the SCORPIO reducer, *left to right* V, R, I, SED607 and SED655 bands. The last image to the right is the NL671 narrow-band image taken at the 8-m SUBARU telescope. The host galaxy of the RC J0311 + 0507 locates in the center of images.

of closely located to RC J0311 + 0507 objects. The SED665 and NL671 narrow-band images show an extended $\text{Ly}\alpha$ -envelope (see the last two images in Fig. 2).

3 Conclusion

RC J0311 + 0507 appears to be a remarkable object, its study and of other similar systems with SMBH of about $10^{10} M_\odot$ at redshifts greater than 4 could help to better understand their formation. We here reported on the first results of our multi wavelength photometric approach to study the environment of the radio galaxy RC J0311 + 0507. We plan a further study using known models of evolution of galaxies such as PEGASE (Fioc M. & Rocca-Volmerange B. 1999), LePHARE (Arnouts S. *et al.* 1999) and GALEV (Kotulla R. *et al.* 2009) in order to estimate photometric redshifts of near located and all field objects.

References

- Arnouts, S., Cristiani, S., Moscardini, L., *et al.*, 1999, MNRAS, 310, 540
Fioc, M., & Rocca-Volmerange, B., 1997, A&A, 326, 950
Franceschini, A., Vercellone, S., & Fabian, A.C., 1998, MNRAS, 297, 817
Goss, W.M., Parijskij, Yu.N., Soboleva, N.S., *et al.*, 1992, AstRep, 69, 673
Kopylov, A.I., Goss W.M., Parijskij, Yu.N., *et al.*, 2006, AstL, 32, 433
Kotulla, R., Fritze, U., Weilbacher, P., *et al.*, 2009, MNRAS, 396, 463
Parijskij, Yu.N., Zhelenkova, O.P., Kopylov, A.I., *et al.*, 2010, PoS 10th EVN Symposium, id. 31
Parijskij, Yu.N., Goss, W.M., Kopylov, A.I., *et al.*, 1996, Bull. SAO, 40, 5
Parijskij, Yu.N., Goss, W.M., Kopylov, A.I., *et al.*, 2000, A&A Trans., 19, 297

GRB HOST GALAXIES: A FASCINATING RESEARCH FIELD

S. Klose¹

Abstract. Because of time constraints, there was no discussion on GRB host galaxies. Nevertheless, it is worth to extract the main points from the talks and posters presented during the conference.

1 Substantial activity in the field

The overwhelming majority of observational data concerns the hosts of long bursts (*e.g.*, Savaglio *et al.* 2009; see also the www page of the GHostS project²), and meanwhile even redshift trends of host galaxy properties can be discussed (Savaglio, these proceedings). There is a lively discussion ongoing in the community whether or not long GRB hosts trace and quantify the evolution of the cosmic star-formation rate (SFR) and what the relations between mass, metallicity, and SFR tell us here (Graham *et al.*; Niino *et al.*; Savaglio *et al.*, these proceedings; Mannucci *et al.* 2011). More and more spectroscopic data of GRB hosts are published, either based on afterglow follow-up observations (*e.g.*, Christensen *et al.* 2011) or based on host galaxy studies. At least in the latter case it is obvious that this mainly remains a job for 8-m class optical telescopes. Observations with VLT/X-Shooter are particularly fascinating here (Vergani *et al.*, these proceedings; Vergani *et al.* 2011).

Increasing interest develops towards a study of those hosts that harbor dark bursts, and the MIR/FIR/submm band is particularly intriguing here (Palazzi *et al.*, these proceedings). This holds in particular after it has been discovered that a substantial population of dark bursts might be hosted by extremely red, globally dust-enshrouded objects (Rossi *et al.* 2012), and that the hosts of the dustiest GRBs point to a population of luminous, massive, and chemically evolved galaxies (Krühler *et al.* 2011), which are very different from the majority of GRB hosts. Obviously, there is a lot to investigate here.

On the far site, the hosts of high- z events remain fascinating (Basa *et al.* 2012), in particular since basically all of them remain undetected even for HST

¹ Thüringer Landessternwarte Tautenburg, 07778 Tautenburg, Germany

²<http://www.grbhosts.org/>

(Tanvir *et al.*, these proceedings; Tanvir *et al.* 2012). It seems we have to await here the next generation of ground and space-based optical telescopes in order to learn more about these galaxies (or these galaxy building blocks). Given that GRBs are the potential messengers of the first stars in the universe, chances are not small that these hosts will be among the first targets for these future telescopes.

On the near site, we might divide between the hosts of near-by GRB-SNe and the hosts of short bursts. The host of SN 1998bw still represents the nearest GRB host galaxy; it promises the best achievable data quality with respect to angular resolution. Substantial work has already been done here (*e.g.*, Christensen *et al.* 2008; Fynbo *et al.* 2000; Michałowski *et al.* 2009), and also in the case of other $z < 0.1$ GRBs the observational data can be of remarkable scientific quality (*e.g.*, Thöne *et al.* 2008). On the contrary, after some early enthusiasm in the years 2005/06 (*e.g.*, Fox *et al.* 2005; Gehrels *et al.* 2005), the following years have not given us so many nearby short burst host galaxies (the most remarkable exception is GRB 080905A at $z = 0.122$; Rowlinson *et al.* 2010). Most of these hosts are at cosmological distance (*e.g.*, Berger 2009). Hopefully, more high-resolution data will be obtained with HST soon.

2 Looking forward

The GRB field is rapidly developing and host galaxies are becoming an important observational target.

A better understanding of the nature of the long and short burst progenitors requires a deeper look into their birth places, deep in angular resolution in particular. For long bursts this mainly concerns the metallicity issue and the decision between the single and the binary star scenario. For this task, the host of SN 1998bw remains the best target in our days. More such near-by events are needed, but given the GRB redshift distribution, we might have to wait for another ten years, or so, to get this picture right. For short bursts, distance is the main challenge, too. Some open questions are: What are the characteristic ages of the short burst progenitors, are they representing a young or an old stellar population? Well possible that just a single nearby event in the coming years will bring us a big step forward in our understanding of the progenitor properties.

Following the very successful TOUGH survey with the ESO/VLT (Jakobsson *et al.*, these proceedings) also large amounts of Keck data become public now (Perley *et al.*, these proceedings), while HST remains the work horse for unprecedented deep and high-resolution host galaxy data (Fruchter *et al.*, these proceedings). ALMA and the *Herschel* satellite, following *Spitzer*, have opened the window into the MIR/FIR/submm regime (Sokolov *et al.*, these proceedings). Together with VLA, ATCA, WSRT, and GMRT this offers the possibility of a detailed characterization of the SED of host galaxies from radio to UV wavelengths, with the goal to derive the SFR and other galaxy parameters (*e.g.*, Hunt *et al.* 2011; Michałowski *et al.* 2012; Svensson *et al.* 2012). We can expect a fascinating progress on GRB host galaxy studies in the coming years.

References

- Basa, S., Cuby, J.G., Savaglio, S., *et al.*, 2012, A&A, 542, 103
Berger, E., 2009, ApJ, 690, 231
Christensen, L., Vreeswijk, P.M., Sollerman, J., *et al.*, 2008, A&A, 490, 45
Christensen, L., Fynbo, J.P.U., Prochaska, J.X., *et al.*, 2011, ApJ, 727, 73
Fox, D., Frail, D.A., Price, P.A., *et al.*, 2005, Nature, 437, 845
Fynbo, J.P.U., Holland, S., Andersen, M.I., *et al.*, 2000, ApJ, 542, 89
Gehrels, N., Sarazin, C.L., O'Brien, P.T., *et al.*, 2005, Nature, 437, 851
Hunt, L., Palazzi, E., Rossi, A., *et al.*, 2011, ApJ, 736, 36
Krühler, T., Greiner, J., Schady, P., *et al.*, 2011, A&A, 534, 108
Mannucci, F., Salvaterra, R., & Campisi, A., 2011, MNRAS, 414, 1263
Michałowski, M.J., Hjorth, J., Malesani, D., *et al.*, 2009, ApJ, 693, 347
Michałowski, M.J., Kamble, A., Hjorth, J., *et al.*, 2012, ApJ, 755, 85
Rossi, A., Klose, S., Ferrero, P., *et al.*, 2012, A&A, 545, 77
Rowlinson, A., Wiersema, K., Levan, A.J., *et al.*, 2010, MNRAS, 408, 383
Savaglio, S., Glazebrook, K., & Le Borgne, D., 2009, ApJ, 691, 182
Svensson, K.M., Levan, A.J., Tanvir N.R., *et al.*, 2012, MNRAS, 421, 25
Tanvir, N.R., Levan, A.J., Fruchter, A.S., *et al.*, 2012, ApJ, 754, 46
Thöne, C.C., Fynbo, J.P.U., Östlin, G., *et al.*, 2008, ApJ, 676, 1151
Vergani, S.D., Flores, H., Covino, S., *et al.*, 2011, A&A, 535, 127

Chapter X.

Instrumentation and Techniques-I (Ongoing Projects)

RECENT PROGRESS ON GRBS WITH *SWIFT*

N. Gehrels¹ and J.K. Cannizzo²

Abstract. We are in an exciting period of discovery for gamma-ray bursts (GRBs). The *Swift* observatory is detecting ~ 90 GRBs yr^{-1} , providing arcsecond localizations and sensitive observations of the prompt and afterglow emission. In addition, rapid-response telescopes on the ground are providing new capabilities to study optical and radio emissions. The combined data set is enabling great advances in our understanding of GRBs including afterglow physics, short burst origin, and the GRB-supernova connection.

1 Introduction

GRBs are the most luminous explosions in the universe and are thought to be the birth cries of black holes. They are a product of the space age, discovered (Klebesadel *et al.* 1973) by *Vela* and observed by satellites for 40 years. Despite impressive advances over the past three decades, the study of bursts remains highly dependent on the capabilities of the observatories which carried out the measurements. The era of the *Compton Gamma Ray Observatory* (*CGRO*) led to the discovery of more than 2600 bursts in just 9 yr. Analyses of these data produced the key result that GRBs are isotropic on the sky and occur at a frequency of roughly two per day all sky (Meegan *et al.* 1991). The hint from earlier instruments was confirmed that GRBs come in two distinct classes of short and long bursts, with distributions crossing at ~ 2 s duration (Kouveliotou *et al.* 1993). The *BeppoSAX* mission made the critical discovery of X-ray afterglows of long bursts (Costa *et al.* 1997). With the accompanying discoveries by ground-based telescopes of optical (van Paradijs *et al.* 1997) and radio (Frail *et al.* 1997) afterglows, long GRBs were found to emanate from star forming regions in host galaxies at a typical distance of $z = 1$. *BeppoSAX* and the later *HETE-2* mission also found evidence of associations of GRBs with Type Ic SNe. This supported

¹ Astroparticle Physics Division, NASA/Goddard Space Flight Center, Greenbelt, MD 20771, USA

² CRESST/Joint Center for Astrophysics, Univ. of Maryland, Baltimore County, Baltimore, MD 21250, USA

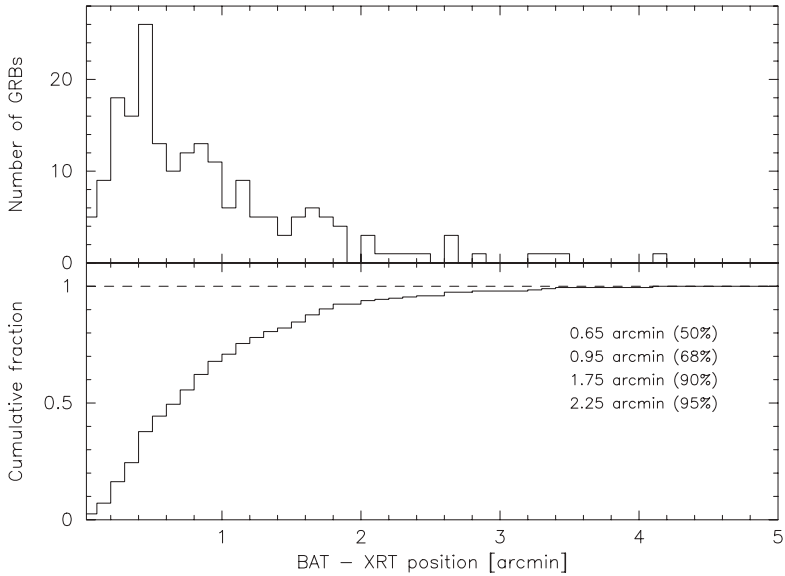


Fig. 1. Histogram (*top*) and the cumulative fraction (*bottom*) of the angular difference between the BAT ground position and the XRT position; 68% and 90% of BAT ground positions are within 0.95 and 1.75 arcmin from the XRT position, respectively (Sakamoto *et al.* 2008).

the growing evidence that long GRBs are caused by “collapsars” where the central core of a massive star collapses to a black hole (MacFadyen & Woosley 1999).

2 Swift GRBs

Swift (Gehrels *et al.* 2004) is a dedicated GRB observatory that is now measuring many properties of the prompt and afterglow radiation. It carries a wide-field Burst Alert Telescope (BAT) (Barthelmy *et al.* 2005a) that detects GRBs and positions them to arcmin accuracy, and the narrow-field X-Ray Telescope (XRT) (Burrows *et al.* 2005) and UV-Optical Telescope (UVOT) (Roming *et al.* 2005) that observe their afterglows and determine positions to arcsec accuracy, all within \sim 100 s. The BAT detects the bursts in the 15 – 150 keV band and determines a position accurate to within \sim 2 arcminutes (Fig. 1) on-board within 12 s. The position is provided to the spacecraft which is then repointed to the burst location in less than 2 minutes to allow XRT (Fig. 2) and UVOT observations of the afterglow. Alert data from all three instruments is sent to the ground via NASA’s TDRSS relay satellite. The full data set is stored and dumped to the Italian Space Agency’s equatorial Malindi Ground Station.

The *Swift* mission was built by an international team from the US, UK, and Italy, with contributions also from Germany and Japan. After five years of

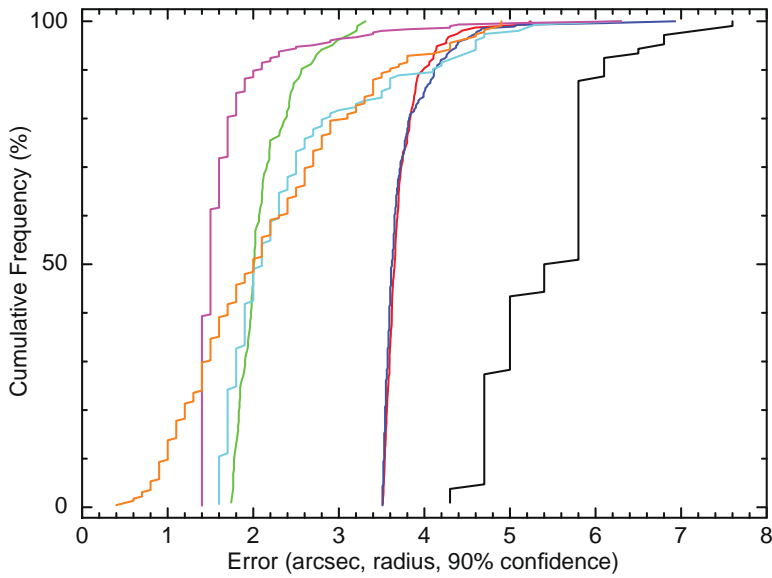


Fig. 2. The cumulative frequency of the 90% confidence error radius for XRT GRB positions determined using different techniques (Evans *et al.* 2009). We highlight two curves, the green curve which gives the on-board corrected positions, and the black curve which gives the on-board raw positions.

development it was launched from Kennedy Space Center on 20 November 2004. Full normal operations commenced on 5 April 2005.

BAT has detected ~ 720 GRBs in 8 yr, a rate of $\lambda = 90 \text{ yr}^{-1}$. The cumulative distribution of time intervals between successive GRBs follows $e^{-\lambda t}$ (Fig. 3). Approximately 90% of the BAT-detected GRBs have repointings within 5 minutes (the remaining 10% have spacecraft constraints that prevent rapid slewing). Of those, virtually all bursts observed promptly have detected X-ray afterglow. Already, 80% of the known X-ray afterglows are from *Swift*. The fraction of rapid-pointing GRBs that have UVOT detection is $\sim 30\%$. Combined with ground-based optical observations, about 60% of *Swift* GRBs have optical afterglow detection. To date there are a total of 273 redshift determinations, of which 41 are pre-*Swift* bursts (Fig. 4). There are 225 redshifts for *Swift* GRBs.

GRBs are incredibly bright. A typical galaxy at a redshift of only $z = 3$ is fainter than $m \simeq 27$ in the optical, whereas GRBs can be in the range $m \simeq 15 - 20$. The brightest was a naked eye object. Table 1 presents optical data for the highest redshift GRBs observed to date, where the look-back time t_{LB} is given in column 2. Multiwavelength observations of the current record holder, GRB 090429B (at $z \simeq 9.4$), are providing information about the universe at a time when it was only about 4% of its current age, and shed light on the process of reionization in the early universe (Cucchiara *et al.* 2011).

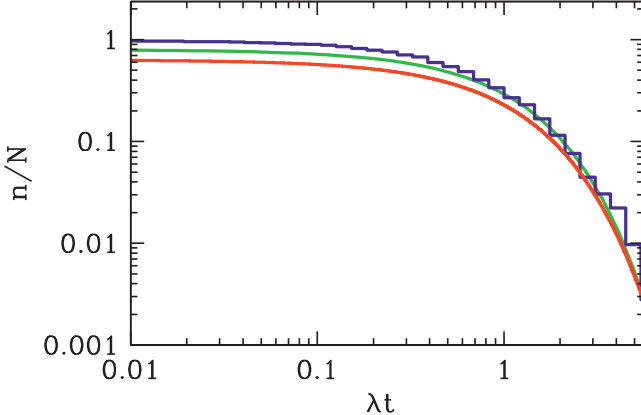


Fig. 3. The cumulative frequency distribution function for the intervals of time between all 720 *Swift* GRBs observed to date (counting from the largest values downward), shown in blue. For comparison the green curve shows $e^{-\lambda t}$, where $\lambda = 90 \text{ yr}^{-1}$, and the red curve shows the results from a Monte Carlo simulation with $N = 10^6$. For ease of viewing the green and red curves have been shifted downward 0.1 and 0.2 dex, respectively. The value $\lambda t = 1$ along the x -axis corresponds to the mean interval between *Swift* GRBs of 4.06 d.

Table 1. High z GRBs.

z	$t_{LB}(\text{Gyr})$	GRB	Brightness			
9.4	13.1	090429B	$K = 19$	@	3 hr	
8.2	13.0	090423	$K = 20$	@	20 min	
~8	13.0	120923				
6.7	12.8	080813	$K = 19$	@	10 min	
6.3	12.8	050904	$J = 18$	@	3 hr	
5.6	12.6	060927	$I = 16$	@	2 min	
5.3	12.6	050814	$K = 18$	@	23 hr	
5.11	12.5	060522	$R = 21$	@	1.5 hr	

2.1 Short GRBs

At *Swift*'s launch, the greatest mystery in GRB astronomy was the nature of short-duration, hard-spectrum bursts (Fig. 5). Although more than 50 long GRBs had afterglow detections, no afterglow had been found for any short burst. In May 2005 (GRB 050509B), *Swift* provided the first short GRB X-ray afterglow localization (Gehrels *et al.* 2005). This burst plus the *HETE-2* GRB 050709 and *Swift* GRB 050724 led to a breakthrough in our understanding of short bursts (Gehrels *et al.* 2005; Bloom *et al.* 2006; Fox *et al.* 2005; Villasenor *et al.* 2005; Hjorth *et al.* 2005; Barthelmy *et al.* 2005b; Berger *et al.* 2005). There are now 68 localizations

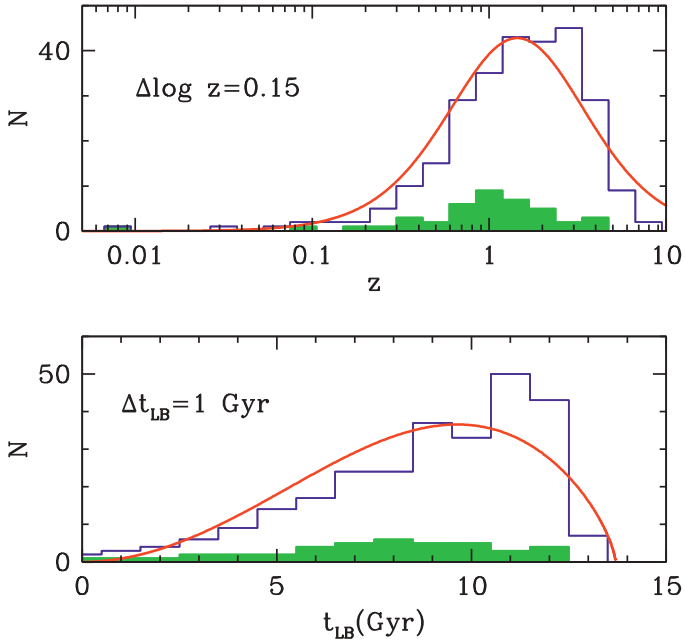


Fig. 4. The distribution of redshifts for all GRBs to date ($N = 273$, shown in blue). The green distribution indicates the pre-*Swift* values ($N = 41$), the red line indicates the evolution of a comoving volume element, $(dV/dz)(1+z)^{-1}$, and the lower panel shows the distribution plotted in look-back time t_{LB} . The normalizations on the red lines are calculated so as to minimize the sum of the squares of the differences with the histogram values in each bin. The factor $(1+z)^{-1}$ multiplying the comoving volume element is necessary to account for cosmological time dilation, given that the GRB rate has units $\text{volume}^{-1} \text{ time}^{-1}$.

for short GRBs, mainly from *Swift*. Most of these have XRT detections, and about one third have host identifications or redshifts.

In stark contrast to long bursts, the evidence starting from the first accurately localized short bursts is that they can originate from regions with low star formation rate. GRB 050509B and 050724 were from elliptical galaxies with low current star formation rates, while GRB 050709 occurred in a region of a star forming galaxy with no nebulosity or evidence of recent star formation activity in that location. Recent *HST* observations of locations of short GRBs in their hosts reveal that short bursts trace the light distribution of their hosts while long bursts are concentrated in the brightest regions (Fong *et al.* 2010). Short GRBs are also different from long GRBs in that accompanying supernovae are not detected for nearby events (Bloom *et al.* 2006; Fox *et al.* 2005; Hjorth *et al.* 2005). Taken together, these results support the interpretation that short bursts are associated with an old stellar population, and may arise from mergers of compact binaries [*i.e.*, double neutron star or neutron star - black hole (NS-BH) binaries].

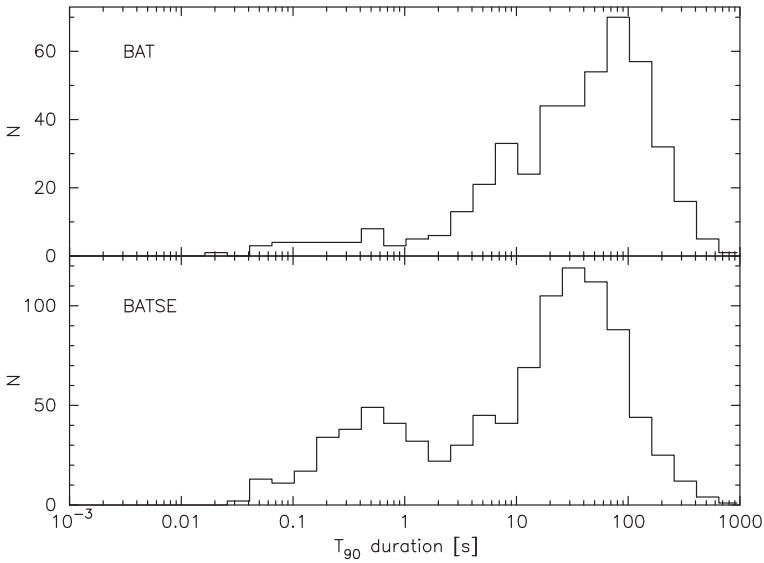


Fig. 5. T_{90} distribution of BAT GRBs from the mask-weighted light curves in the 15 – 350 keV band and the corresponding distribution for *CGRO/BATSE* GRBs from the light curves in the 50 – 350 keV band (Sakamoto *et al.* 2011). Short GRBs constitute about 9% of the total number for BAT GRBs, and about 25% of the total number for BATSE GRBs. This difference is due to the narrower BAT energy band.

2.2 Interesting case of the hostless GRB 070125

There was not an obvious host galaxy for GRB 070125. Deep ground-based imaging reveals no host to $R > 25.4$ mag. Cenko *et al.* (2008) present an analysis of spectroscopic data which reveals only weak Mg II lines indicative of halo gas. In the field are two blue galaxies offset by $\gtrsim 27$ kpc at $z = 1.55$. If there is an association with one of them, it would imply a velocity $\sim 10^4$ km s $^{-1}$ over a ~ 20 Myr lifetime of the massive progenitor. The only known way of achieving this would have been a prior close interaction with a massive BH. However, this interpretation was muddied by Chandra *et al.* (2008), who inferred a dense environment, based on bright, self-absorbed radio afterglow. They proposed a scenario in which the high density material lies close to the explosion site, and the lower density material further away. They note GRB 070125 was one of the brightest GRBs ever detected, with an isotropic release of 10^{54} erg (by comparison, $M_\odot c^2 \simeq 2 \times 10^{54}$ erg). The prompt emission from GRB 070125 was also seen by *Suzaku/WAM* (Onda *et al.* 2010).

2.3 GRBs and supernovae

On 18 February 2006 *Swift* detected the remarkable burst GRB 060218 that provided considerable new information on the connection between SNe and GRBs.

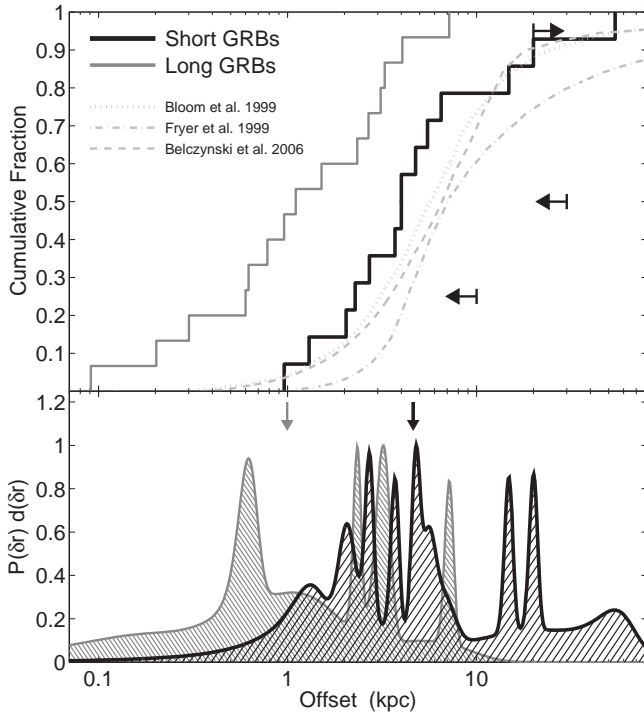


Fig. 6. Projected physical offsets within their host galaxies based on *HST* observations for short GRBs (black) and long GRBs (gray), from Fong *et al.* (2010). Data from long GRBs taken from (Bloom *et al.* 2002). *Top panel* shows the cumulative distributions; *bottom panel* shows the differential distributions. Arrows in the *bottom panel* mark the median value for each distribution. The median value for short GRBs, ≈ 5 kpc, is about 5 times larger than for long GRBs. Arrows in the *top panel* exhibit the strongest constraints on the offset distribution. Also shown in the *top panel* are predicted offset distributions for NS-NS binary mergers in Milky Way type galaxies based on population synthesis models (Bloom *et al.* 1999; Fryer *et al.* 1999; Belczynski *et al.* 2006).

It lasted longer than and was softer than any previous burst, and was associated with SN 2006aj at only $z = 0.033$. The BAT trigger enabled XRT and UVOT observations during the prompt phase of the GRB and initiated multiwavelength observations of the supernova from the time of the initial core collapse. The spectral peak in prompt emission at ~ 5 keV places GRB 060218 in the X-ray flash category of GRBs (Campana *et al.* 2006), the first such association for a GRB-SN event. Combined BAT-XRT-UVOT observations provided the first direct observation of shock-breakout in a SN (Campana *et al.* 2006). This is inferred from the evolution of a soft thermal component in the X-ray and UV spectra, and early time luminosity variations. Concerning the supernova, SN 2006aj was dimmer by a factor ~ 2 than the previous SNe associated with GRBs, but still $\sim 2 - 3$ times brighter than

normal SN Ic not associated with GRBs (Pian *et al.* 2006; Mazzali *et al.* 2006). GRB 060218 was an underluminous burst, as were two of the other three previous cases. Because of the low luminosity, these events are only detected when nearby and are therefore rare occurrences. However, they are actually $\sim 5 - 10$ times more common in the universe than normal GRBs (Soderberg *et al.* 2006).

3 Conclusions

The future is bright for GRB astronomy. *Swift* will be in orbit for > 10 more years and should be operating for at least 5 more years. To date, *Swift* has already detected more than 700 GRBs, and new things are constantly popping up. *Swift* has found that short GRBs reside in demonstrably different environments than long GRBs do, and are not accompanied by SNe. The spatial distributions over their host galaxies are much more spread out than for long GRBs (Fig. 6 – taken from Fong *et al.* 2010). The weight of the evidence lends credence to the NS-NS merger model. Distant GRBs are elucidating the properties of the high z universe and probing into the era of re-ionization. In spite of the rich progress in the field, several open questions remain: What are the detailed properties of short GRBs? Do GRBs accompany the demise of the earliest stars? Is there direct evidence for beaming, as was once thought from panchromatic observations? How prominent a role do off-axis GRBs play?

References

- Barthelmy, S.D., Barbier, L.M., Cummings, J.R., *et al.*, 2005a, Space Sci. Rev., 120, 143
- Barthelmy, S.D., Chincarini, G., Burrows, D.N., *et al.*, 2005b, Nature, 438, 994
- Belczynski, K., Perna, R., Bulik, T., *et al.*, 2006, ApJ, 648, 1110
- Berger, E., Price, P.A., Cenko, S.B., *et al.*, 2005, Nature, 438, 988
- Bloom, J.S., Prochaska, J.X., Pooley, D., *et al.*, 2006, ApJ, 638, 354
- Bloom, J.S., Sigurdsson, S., & Pols, O.R., 1999, MNRAS, 305, 763
- Burrows, D.N., Hill, J.E., Nousek, J.A., *et al.*, 2005, Space Sci. Rev., 120, 165
- Campana, S., Mangano, V., Blustin, A.J., *et al.*, 2006, Nature, 442, 1008
- Cenko, S.B., Fox, D.B., Penprase, B.E., *et al.*, 2008, ApJ, 677, 441
- Chandra, P., Cenko, S.B., Frail, D.A., *et al.*, 2008, ApJ, 683, 924
- Costa, E., Frontera, F., Heise, J., *et al.*, 1997, Nature, 387, 783
- Cucchiara, A., Levan, A.J., Fox, D.B., *et al.*, 2011, ApJ, 736, 7
- Evans, P.A., Beardmore, A.P., Page, K.L., *et al.*, 2009, MNRAS, 397, 1177
- Fong, W., Berger, E., & Fox, D.B., 2010, ApJ, 708, 9
- Fox, D.B., Frail, D.A., Price, P.A., *et al.*, 2005, Nature, 437, 845
- Frail, D.A., Kulkarni, S.R., Nicastro, L., *et al.*, 1997, Nature, 389, 261
- Fryer, C.L., Woosley, S.E., & Hartmann, D.H., 1999, ApJ, 526, 152
- Gehrels, N., Chincarini, G., Giommi, P., *et al.*, 2004, ApJ, 611, 1005
- Gehrels, N., Sarazin, C.L., O'Brien, P.T., *et al.*, 2005, Nature, 437, 851

- Hjorth, J., Watson, D., Fynbo, J.P.U., *et al.*, 2005, *Nature*, 437, 859
Klebesadel, R.W., Strong, I.B., & Olson, R.A., 1973, *ApJ*, 182, L85
Kouveliotou, C., Meegan, C.A., Fishman, G.J., *et al.*, 1993, *ApJ*, 413, L101
MacFadyen, A.I., & Woosley, S.E., 1999, *ApJ*, 524, 262
Mazzali, P.A., Deng, J., Nomoto, K., *et al.*, 2006, *Nature*, 442, 1018
Meegan, C.A., Fishman, G.J., Wilson, R.B., *et al.*, 1991, *Nature*, 355, 143
Onda, K., Tashiro, M.S., Nakagawa, Y.E., *et al.*, 2010, *PASJ*, 62, 547
Pian, E., Mazzali, P.A., Masetti, N., *et al.*, 2006, *Nature*, 442, 1011
Roming, P.W.A., Kennedy, T.E., Mason, K.O., *et al.*, 2005, *Space Sci. Rev.*, 120, 95
Sakamoto, T., Barthelmy, S.D., Barbier, L., *et al.*, 2008, *ApJS*, 175, 179
Sakamoto, T., Barthelmy, S., Baumgartner, W., *et al.*, 2011, in *Gamma Ray Bursts 2010*,
ed. J.E. McEnery, J.L. Racusin & N. Gehrels (AIP: New York), 1358, 51
Soderberg, A.M., Kulkarni, S.R., Nakar, E., *et al.*, 2006, *Nature*, 442, 1014
van Paradijs, J., Groot, P.J., Galama, T., *et al.*, 1997, *Nature*, 386, 686
Villasenor, J.S., Lamb, D.Q., Ricker, G.R., *et al.*, 2005, *Nature*, 437, 855

THE INTERPLANETARY NETWORK

K. Hurley¹, I.G. Mitrofanov², D. Golovin², M.L. Litvak², A.B. Sanin²,
W. Boynton³, C. Fellows³, K. Harshman³, R. Starr³, S. Golenetskii⁴,
R. Aptekar⁴, E. Mazets⁴, V. Pal'shin⁴, D. Frederiks⁴, D. Svinkin⁴,
D.M. Smith⁵, W. Hajdas⁶, A. von Kienlin⁷, X. Zhang⁷, A. Rau⁷, K. Yamaoka⁸,
T. Takahashi⁸, M. Ohno⁹, Y. Hanabata⁹, Y. Fukazawa⁹, M. Tashiro¹⁰,
Y. Terada¹⁰, T. Murakami¹¹, K. Makishima^{12,13}, T. Cline^{14,15}, S. Barthelmy¹⁴,
J. Cummings^{24,16}, N. Gehrels¹⁴, H. Krimm^{25,17}, D. Palmer¹⁸, J. Goldsten¹⁹,
E. Del Monte²⁰, M. Feroci²⁰, M. Marisaldi²¹, V. Connaughton²², M.S. Briggs²²
and C. Meegan²³

¹ U.C. Berkeley Space Sciences Laboratory, 7 Gauss Way, Berkeley, CA 94720-7450, USA

² Institute for Space Research, Profsojuznaja 84/32, Moscow 117997, Russian Federation

³ University of Arizona, Lunar and Planetary Laboratory, Tucson, AZ 85721, USA

⁴ Ioffe Physico-Technical Institute of the Russian Academy of Sciences, St. Petersburg 194021, Russian Federation

⁵ Department of Physics and Santa Cruz Institute for Particle Physics, U.C. Santa Cruz, CA 95064, USA

⁶ Paul Scherrer Institute, 5232 Villigen PSI, Switzerland

⁷ Max-Planck-Institut für extraterrestrische Physik, Giessenbachstrasse, Garching, 85748 Germany

⁸ Institute of Space and Astronautical Science, 3-1-1 Yoshinodai, Sagamihara, Kanagawa 229-8510, Japan

⁹ Department of Physics, Hiroshima University, 1-3-1 Kagamiyama, Higashi-Hiroshima, Hiroshima 739-8526, Japan

¹⁰ Department of Physics, Saitama University, 255 Shimo-Okubo, Sakura-ku, Saitama-shi, Saitama 338-8570, Japan

¹¹ Department of Physics, Kanazawa University, Kadoma-cho, Kanazawa, Ishikawa 920-1192, Japan

¹² Department of Physics, University of Tokyo, 7-3-1 Hongo, Bunkyo-ku, Tokyo 113-0033, Japan

¹³ Makishima Cosmic Radiation Laboratory, The Institute of Physical and Chemical Research (RIKEN), 2-1 Hirosawa, Wako, Saitama 351-0198, Japan

¹⁴ NASA Goddard Space Flight Center, Code 661, Greenbelt, MD 20771, USA

¹⁵ Emeritus

¹⁶ Joint Center for Astrophysics, University of Maryland, Baltimore County, 1000 Hilltop Circle, Baltimore, MD 21250, USA

¹⁷ Universities Space Research Association, 10211 Wincopin Circle, Suite 500, Columbia, MD 21044, USA

¹⁸ Los Alamos National Laboratory, PO Box 1663, Los Alamos, NM 87545, USA

¹⁹ Applied Physics Laboratory, Johns Hopkins University, Laurel, MD 20723, USA

²⁰ INAF/IASF-Roma, via Fosso del Cavaliere 100, 00133 Roma, Italy

²¹ INAF/IASF-Bologna, via Gobetti 101, 40129 Bologna, Italy

²² University of Alabama in Huntsville, NSSTC, 320 Sparkman Drive, Huntsville, AL 35805, USA

²³ Universities Space Research Association, NSSTC, 320 Sparkman Drive, Huntsville, AL 35805, USA

²⁴ UMBC/CRESST/NASA Goddard Space Flight Center, Code 661, Greenbelt, MD 20771, USA

²⁵ CRESST/NASA Goddard Space Flight Center, Code 661, Greenbelt, MD 20771, USA

Abstract. We describe the current, 9-spacecraft Interplanetary Network (IPN). The IPN detects about 325 gamma-ray bursts per year, of which about 100 are not localized by any other missions. We give some examples of how the data, which are public, can be utilized.

1 Introduction

The current IPN consists of one or more experiments on nine missions: AGILE, *Fermi*, RHESSI, *Suzaku*, and *Swift*, in low-Earth orbit; INTEGRAL, in a high apogee Earth orbit; Konus-*Wind*, at L₁, \sim 5.5 light-seconds from Earth; and MESSENGER and *Odyssey*, in orbit around Mercury and Mars, respectively. This configuration is an ideal one in many respects. The 5 low-Earth orbit missions assure that virtually every burst is detected by at least one Earth-orbiting mission, providing an important vertex for triangulation. The two planetary missions give long baselines which make precise localizations possible. And INTEGRAL and Konus assure redundancy and overdetermination of the localizations in many cases. Indeed, even without the planetary missions, the mini-network of 5 low-Earth orbiters, plus INTEGRAL and Konus, often make it possible to obtain relatively small error boxes for many bursts. Figure 1 shows the configuration of the IPN, which is an all-sky, full-time monitor not only of GRBs, but also of magnetar bursts, and other high-energy phenomena.

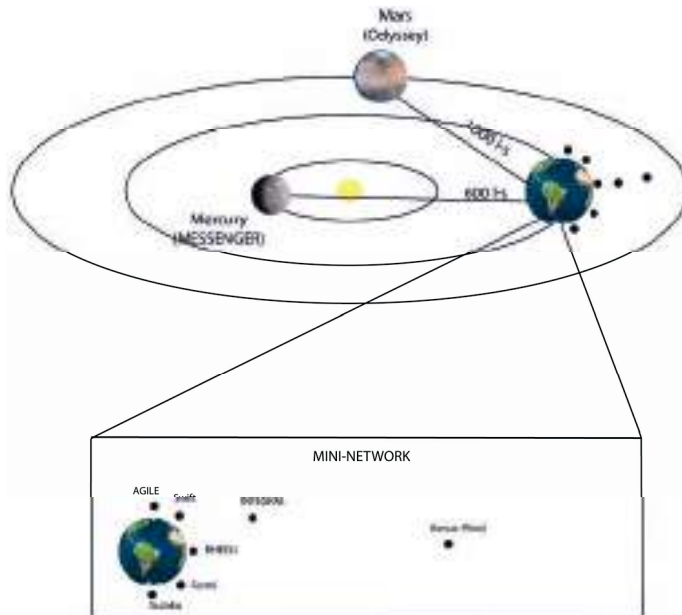


Fig. 1. The 9-spacecraft IPN. The near-Earth mini-network often produces small error boxes in the absence of detections by distant spacecraft.

Fig. 2. A Venn diagram showing the relation between the number of bursts per year detected by the IPN, *Swift*, and *Fermi*. *Swift* observes an average of 162 bursts per year, counting those both inside (~ 100) and outside (~ 62) the coded field of view. *Fermi* observes a total of 245, and the IPN observes a total of 325. Of the 325 IPN bursts, 190 are also detected by *Fermi*, and 125 are also detected by *Swift* (of which ~ 77 are inside the coded field of view). 73 bursts per year are detected by the IPN, *Swift*, and *Fermi*. 100 IPN bursts per year are not detected by either *Swift* or *Fermi*.

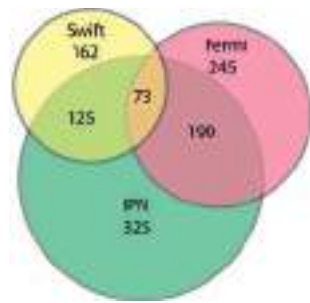


Figure 2 shows the relation between bursts detected by the IPN and bursts detected by *Swift* and *Fermi*. Roughly 100 IPN GRBs/year are not detected by those missions. Moreover, about 70 of the 190 GRBs/year which are detected by the IPN and *Fermi* can be localized by the IPN to error box areas which are several orders of magnitude smaller than those of *Fermi* alone.

Finally, Figure 3 shows the sensitivity of the IPN as a function of GRB peak flux. Another measure of sensitivity is to consider the redshifts of IPN bursts, which range from 0.7 to 4.5.

2 Some uses of IPN data

2.1 Refining *Fermi* GBM and LAT localizations

IPN error boxes are typically orders of magnitude smaller than *Fermi* GBM error circles. Indeed, they are comparable in size to, or often smaller than, LAT error circles. Figure 4 shows one example. Refining these error circles helps the GBM team understand their systematic uncertainties, and aids the LAT team in identifying bursts with high-energy emission.

2.2 GRBs from optically detected energetic supernovae

The optical signatures of energetic Type Ib/c supernovae are frequently found in GRB afterglow lightcurves. But can GRBs be identified by searching at the times and positions of optically-discovered energetic supernovae? IPN searches have now been conducted for 23 supernovae, from SN1997dq to SN2012ap (Hurley & Pian 2008; Sanders *et al.* 2012; Corsi *et al.* 2011; Soderberg *et al.* 2012; Margutti *et al.* 2012; Walker *et al.* 2013). The advantage of the IPN in these searches is its all-sky, full-time coverage. The negative results to date constrain the beaming and energetics of these SNe; the search is continuing.

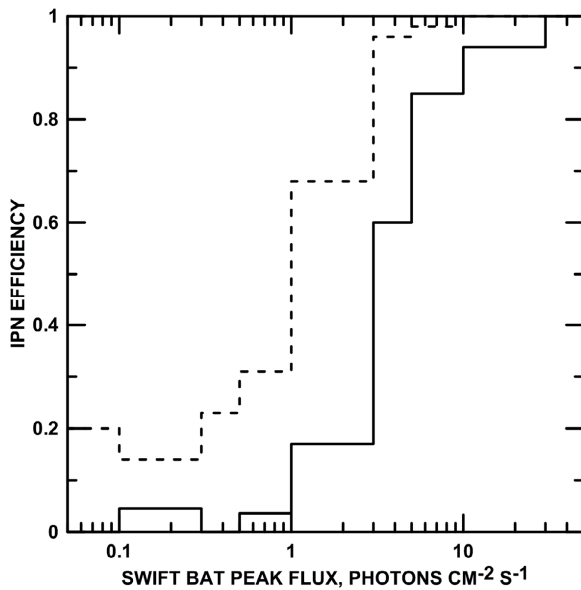


Fig. 3. The IPN sensitivity to GRBs as a function of their peak flux. The peak flux is measured by the *Swift* BAT in the 15 – 150 keV energy range over 1 second. The dashed line shows the probability that any two or more IPN spacecraft will detect the burst. The solid line shows the probability that any two or more widely separated IPN spacecraft will detect it; the latter bursts can be localized to some extent.

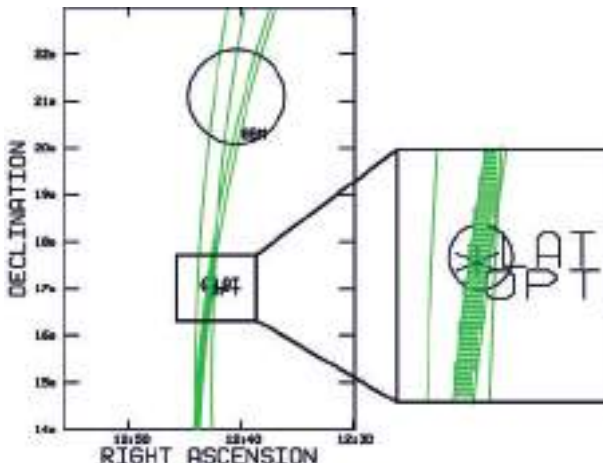


Fig. 4. *Fermi* GBM, LAT, and IPN localizations of GRB 090323. The two IPN annuli intersect to form the error box shaded in green. A zoom of this region shows the LAT error circle and the location of the optical afterglow (asterisk) in more detail (Hurley *et al.* 2009; Ohno *et al.* 2009; Updike *et al.* 2009).

2.3 Non-electromagnetic emission from GRBs

The IPN provided a large number of GRBs to the AMANDA project for searches for neutrino emission (Achterberg *et al.* 2008), and continues to collaborate with the IceCube project, where a search involving over 100 bursts is in progress. The LIGO and Virgo collaborations are looking at ~ 380 IPN bursts which occurred during Science Run 5 (2005–2007), and ~ 525 IPN bursts which occurred during Science Run 6 (2009–2010, preliminary results in Abadie *et al.* 2012). These are the most extensive searches for GRB-related gravitational radiation to date. The unique aspect of the IPN data is that there are ~ 100 events/year that are not observed by *Swift* or *Fermi*, and, in addition, that the bursts tend to be the more nearby and/or energetic ones.

2.4 Some other projects

IPN localizations are being used to search for polarization using the GAP polarimeter on the Japanese IKAROS mission, and to derive the energy spectra of bursts observed by the *Suzaku* HXD WAM. By refining *Fermi* GBM localizations, the IPN is useful to the MAGIC and HAWC projects, which are searching for very high energy gamma-ray emission from bursts. IPN observations are also useful for determining the nature of candidate orphan afterglows.

3 Short bursts

Since its inception, the IPN has had a high detection rate of short-duration GRBs. The first precise localization (~ 800 sq. arcsec.) of a short GRB was published in Laros *et al.* (1981), and deep searches (magnitude 23.5) by Chevalier *et al.* (1981) revealed objects that were “probably distant galaxies unrelated to the burst source”. Today, the detection rate is about 20/year (Pal’shin *et al.* 2013). Although it is not possible to localize these bursts with the speed that *Swift* achieves, they nevertheless play an important role in many projects, particularly the LIGO/Virgo searches.

4 The IPN database

IPN data are public. The IPN database (www.ssl.berkeley.edu/ipn3/index.html) contains, among other things:

1. An 11,000 publication GRB bibliography (1972–2012),
2. A list of 25,000 events (mainly cosmic, SGR, and solar), giving the dates and times of bursts, and a list of which spacecraft detected them (1990–2012), and
3. 7000 GRB localizations (1990–2012).

These lists are growing constantly. Some parts of the database are updated on a roughly daily basis, while others are updated less frequently. Work is underway to provide a user interface to search the localizations, which consist of annuli, more efficiently. Potential users are urged to contact khurley@ssl.berkeley.edu to make sure that the database is fully populated for their projects. This applies particularly to the localizations, where the database is incomplete simply due to a lack of manpower.

5 The future

The missions which are currently part of the IPN are expected to continue operating at least through 2013, and many of them will probably operate for much longer, with lifetimes limited mainly by funding. New missions which can be incorporated into the network include, but are not limited to, the Japanese *Astro-H* (2013 launch) and ESA's *Bepi-Colombo* (2015).

Support for the IPN has been provided in the US by NASA grants NNX09AU03G (*Fermi*), NNX08AX95G (INTEGRAL), NNX09AO97G (*Swift*), NNX09AV61G (*Suzaku*), NNX07AR71G (MESSENGER), and by JPL Contract Y503559 (*Odyssey*). The Konus-*Wind* experiment is supported by a Russian Space Agency Contract and by RFBR grant 11-02-12082-ofi-m.

References

- Abadie, J., Abbott, B., Abbott, R., *et al.*, 2012, ApJ, 760, 12
- Achterberg, A., Ackermann, M., Adams, J., *et al.*, 2008, ApJ, 674, 357
- Chevalier, C., Ilovaisky, S., Motch, C., *et al.*, 1981, A&A, 100, L1
- Corsi, A., Ofek, E., Frail, D., *et al.*, 2011, ApJ, 741, 76
- Hurley, K., & Pian, E., 2008, AIP, 937, 488
- Hurley, K., Goldsten, J., von Kienlin, A., *et al.*, 2009, GCN, 9023
- Laros, J., Evans, W., Fenimore, E., *et al.*, 1981, ApJ, 245, L63
- Margutti, R., Soderberg, A., Chomiuk, L., *et al.*, 2012, ApJ, 751, 134
- Ohno, M., Cutini, S., McEnery, J., *et al.*, 2009, GCN, 9021
- Pal'shin, V., Hurley, K., Svinkin, D., *et al.*, 2013 [[arXiv:1301.3740](https://arxiv.org/abs/1301.3740)]
- Sanders, N., Soderberg, S., Valenti, R., *et al.*, 2012, ApJ, 756 184
- Soderberg, A., Margutti, R., Zauderer, B., *et al.*, 2012, ApJ, 752, 78
- Updike, A., Filgas, R., Kruehler, T., *et al.*, 2009, GCN, 9026
- Walker, E., *et al.*, 2013, in preparation

STATUS AND PERSPECTIVES OF MINI-MEGATORTORA WIDE-FIELD MONITORING SYSTEM WITH HIGH TEMPORAL RESOLUTION

S. Karpov¹, G. Beskin¹, S. Bondar², A. Perkov², E. Ivanov²,
A. Guarnieri³, C. Bartolini³, G. Greco⁴, A. Shearer⁵ and V. Sasyuk⁶

Abstract. Here we briefly summarize our long period experience of constructing and operating wide-field monitoring cameras with sub-second temporal resolution to look for optical components of GRBs, fast-moving satellites and meteors. General requirements for hardware for such systems are discussed along with algorithms of real-time detection and classification of various kinds of short optical transients. We also give a status report on the next generation, multi-objective and transforming monitoring system, the MegaTORTORA, whose 6-channel (Mini-MegaTORTORA-Spain) and 9-channel prototypes (Mini-MegaTORTORA-Kazan) we are building now at SAO RAS. This system combines a wide field of view with subsecond temporal resolution in monitoring regime, and is able to reconfigure itself, in a fractions of second, to follow-up mode which has better sensitivity and provides us with multi-color and polarimetric information on detected transients simultaneously.

1 Introduction

The systematic study of night sky variability on subsecond time scales still remains an important, but practically unsolved problem. Its necessity for the search of non-stationary objects with unknown localization has been noted by Bondi (1970). Such studies have been performed (Schaefer 1985, 1987), but due to technical limitations it has only been possible either to reach high temporal resolution

¹ Special Astrophysical Observatory of Russian Academy of Sciences, Russia

² Institute for Precise Instrumentation, Russia

³ Bologna University, Italy

⁴ Astronomical Observatory of Bologna, INAF, Italy

⁵ National University of Ireland, Galway, Ireland

⁶ Kazan Federal University, Kazan, Russia

of tens of milliseconds in monitoring of $5' - 10'$ fields, or use 5–10 seconds time resolution in wider fields. The wide-field monitoring systems currently in operation, such as WIDGET, RAPTOR, BOOTES and π of the Sky, while having good sky coverage and limiting magnitude, lack temporal resolution, which significantly lowers their performance in the study of transient events of subsecond duration (as the detection limit degrades as a ratio of event duration to exposure time) or highly variable on subsecond time scales.

In (Karpov *et al.* 2005; Zolotukhin *et al.* 2004) we demonstrated that it is possible to achieve the subsecond temporal resolution in a reasonably wide field with small telescopes equipped with fast CCDs, to perform fully automatic searching and classification of fast optical transients. Moreover, a two-telescope scheme Beskin *et al.* (2005); Karpov *et al.* (2004), able to study such transients in a very short time after detection, has been proposed. According to these ideas, we created the prototype fast wide-field camera called FAVOR (Karpov *et al.* 2005) and the TORTORA camera as part of the TORTOREM (Molinari *et al.* 2006) two-telescope complex, and operated them over several years.

The discovery of the brightest ever GRB, GRB 080319B (the Naked-Eye Burst, Racusin *et al.* 2008), by several wide-field monitoring systems – TORTORA, RAPTOR and Pi of the Sky – and the subsequent discovery of its fast optical variability on time scales from several seconds down to a sub-second time scale (Beskin *et al.* 2010b) demonstrated that the ideas behind our efforts in fast temporal resolution wide-field monitoring are correct.

2 MegaTORTORA – multi-objective transforming instrument

The parameters defining the field of view size, detection limit and temporal resolution, are mutually exclusive, and are limited by the difficulties of constructing and using objectives with large relative apertures ($D/F \sim 1$ or greater). The only possible way to further improve them simultaneously is to design a multi-objective monitoring system, where detection limit is being improved by decreasing the angular pixel size (Beskin *et al.* 2007), and field of view – by pointing several identical channels towards different regions of the sky. To operate in a sky background dominated regime, the CCD read-out noise may be suppressed by a high quantum efficiency image intensifier, or by using low-noise EM-CCD or sCMOS as a detector.

Multi-objective design also gives a freedom in the regimes of operation, as fields of view of channels may be either separated or combined, either with the same photometric (or even polarimetric) filter or with combination of different ones.

The MegaTORTORA project Beskin *et al.* (2010a) we develop according to these lines utilizes the modular design and consists of a set of basic units, 9 objectives each, installed on a separate mounts. Each objective in a unit is placed inside the gimbal suspension with remotely-controlled micro-motors, and so may be oriented independently from others. Also, each objective possesses the set of color and polarization filters, which may be installed before the objective on the fly. It allows to change modes of observation on the fly, from routine wide-field

monitoring in the color band providing best signal-to-noise ratio (or in a white light, with no filters installed), to the narrow-field follow-up regime, when all objectives are pointed towards the same point, *i.e.* newly-discovered transient, and observe it in different colors and for different polarization plane orientations simultaneously, to acquire all possible kinds of information for the transient. Simultaneous observation of the transient by all objectives in white light is also possible to get better photometric accuracy by co-adding frames.

Each objective is equipped with the fast EM-CCD, which has a low readout noise even for a high frame rates when the internal amplification is in effect. The data from each channel of such a system, which is roughly 20 megabytes per second, is collected by a dedicated rackmount PC, which stores it in its hard-drive as well as performs its real-time data processing in a way similar to the current processing pipeline of FAVOR and TORTORA cameras, which currently operate under similar data flow rate. The whole system is coordinated by the central server which acquires the transient data from data-processing PCs and controls the pointing and mode of operation of all objectives in response to them.

3 Mini-MegaTORTORA as a MegaTORTORA prototype

As a limited realization of a MegaTORTORA concept we designed the prototype design – the Mini-MegaTORTORA, or MMT, which is basically a model of a 3×3 unit. Main design choice was to use the celostate in a gimbal suspension for a fast repointing of each channel. Such a decision allows to significantly loose the requirements for the structural, dynamical and precision parameters. We are building two variants of Mini-MegaTORTORA with different detectors (image intensifier with fast CCD for MMT-Spain and low-noise sCMOS for MMT-Kazan) and, therefore, slightly different parameters.

Both variants use the CANON EF85 F/1.2 lens as a main objective and celostate mirrors for a fast (faster than 0.3 s) repointing in the $\pm 20^\circ$ region of the sky. Optical design of a first variant is analogous to the one used in FAVOR (Karpov *et al.* 2005) and TORTORA (Molinari *et al.* 2006) systems but with the non-scaling image intensifier. For the second one, it is a bit simple and lacks the image intensifier and transmission optics.

Detector of the first variant is based on a fast Sony IX285AL CCD chip with $6.4 \mu\text{m}$ pixel and 0.13 s exposure in a continuous acquisition regime, which gives $7.5 \text{ } 1392 \times 1036$ frames per second with 12-bit depth. Non-scaling image intensifier has a quantum efficiency of about 25%, and amplified image from its output window is transferred to the CCD by a transmission optics which downscals it 1.7 times; resulting pixel scale is $25''$ per pixel and total field of view of a channel is about 100 square degrees. The high image intensifier amplification (of ~ 150) overcomes CCD read-out noise, but induces its own, spatially-correlated and highly non-poissonian, shot-noise due to ions hitting the photocathode events. Resulting limiting magnitude in differential imaging mode is about $B \sim 12^{\text{m}}$; it is somewhat worse in direct imaging regime due to spatial correlation of the dominant image intensifier noise. Also, direct imaging suffers from the non-uniform spatial

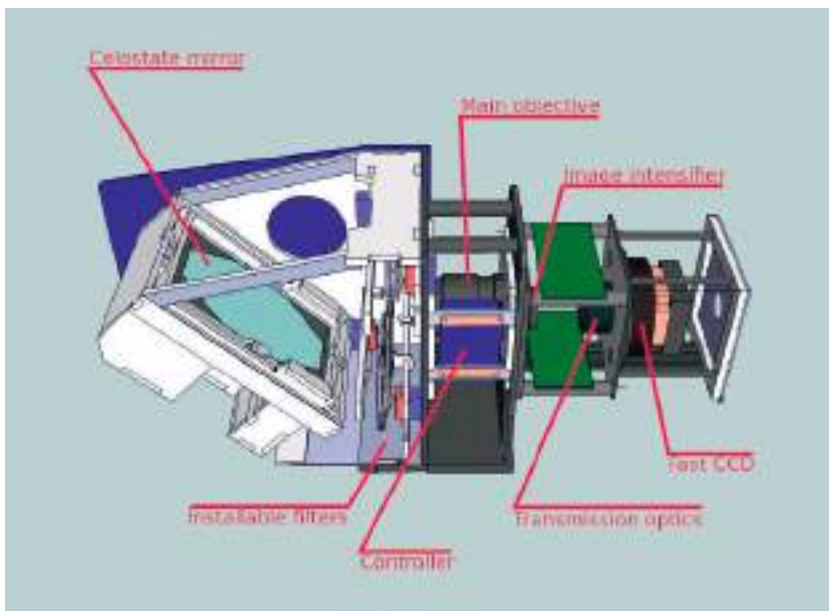


Fig. 1. Schematics of a single channel mechanical design of a MMT-Spain variant.

sensitivity of image intensifier microchannel plates, which drives it very important to perform a proper flat-fielding - and each channel therefore is equipped with its own flat-fielding module consisting of a dull surface on the inner part of a lid and dedicated photodiodes.

The mechanical scheme of a channel for this variant is shown in Figure 1.

MMT-Spain will be installed at El-Arenosillo atmospheric station in Huelva, Spain in fall 2013.

Second variant, MMT-Kazan, is equipped with Andor Neo sCMOS, which has 2560×2160 $6.4 \mu\text{m}$ pixels with 16-bit depth. Due to limitations of a PC processing power, as well as available harddrives space, we decided to operate it in a 10 frames per second regime, which still provides us with ~ 3 Tb of data per night. Quantum efficiency is about 55% with read-out noise as low as 1e^- . Pixel scale is about $15''$ per pixel, and the channel field of view is about 100 square degrees. The limiting magnitude of a channel will be about $B \sim 12.5^{\text{m}}$ in 0.1 s, in both differential and direct imaging.

MMT-Kazan will be installed at Engelgardt observatory of Kazan Federal University, Kazan, Russia in summer 2013.

Both variants of MMT will use custom fork mounts based on a Skywatcher EQ6 head, each carrying two channels simultaneously.

INTAS (04-78-7366), by the Presidium of the Russian Academy of Sciences Program, by the grant of President of Russian Federation for the support of young Russian scientists and by the grant of European Union (FP7 grant agreement number 283783, GLORIA project). The construction of MMT-Kazan is being financed by Kazan Federal University. S.K. has also been supported by a grant of Dynasty foundation. G.B. thanks Landau Network-Centro Volta and Cariplò Foundation for fellowship and Brera Observatory for hospitality. We thank Emilio Molinari, Stefano Covino and Cristiano Guidorzi for technical help organizing TORTORA observations and for discussions of the results.

References

- Beskin, G., Bad'in, V., Biryukov, A., *et al.*, 2005, Nuovo Cimento C, 28, 751
Beskin, G., Bondar, S., Karpov, S., *et al.*, 2010a, Adv. Astron., 2010
Beskin, G., de-Bur, V., Karpov, S., Plokhotnichenko, V., & Bondar, S., 2007, Bull. Spec. Astrophysical Observatory, 60-61, 217
Beskin, G., Karpov, S., Bondar, S., *et al.*, 2010b, ApJ, 719, L10
Bondi, H., 1970, Q.J.R. Astron. Soc., 11, 443
Karpov, S., Bad'in, D., Beskin, G., *et al.*, 2004, Astron. Nachr., 325, 677
Karpov, S., Beskin, G., Biryukov, A., *et al.*, 2005, Nuovo Cimento C, 28, 747
Molinari, E., Bondar, S., Karpov, S., *et al.*, 2006, Nuovo Cimento B, 121, 1525
Racusin, J.L., Gehrels, N., Holland, S.T., *et al.*, 2008, GRB Coordinates Network Circular, 7427, 1
Schaefer, B., 1985, AJ, 11, 1363
Schaefer, B., 1987, A&A, 174, 338
Zolotukhin, I., Beskin, G., Biryukov, A., *et al.*, 2004, Astron. Nachr., 325, 675

STATUS OF THE BOOTES-IR PROJECT AT OSN FOR GRB NEAR-IR FOLLOW-UP

R. Cunniffe¹, A.J. Castro-Tirado¹, M. Jelínek¹, J. Gorosabel^{1,2,3},
B. Moliné¹ and F. García-Segura⁴

Abstract. Bootes-IR (Castro-Tirado *et al.* 2005) is a robotic observatory based around a 60 cm alt-az telescope (dubbed T60) that can slew rapidly while carrying heavy instrumentation at the Nasmyth foci. Initially commissioned with an optical camera, with which the optical afterglow to GRB 060707 (<http://gcn.gsfc.nasa.gov/gcn3/5290.gcn3>) was discovered, we have concentrated our efforts on the near-IR (0.8–2.5 μm) camera (BIRCAM) for which the telescope was specifically designed. The telescope is installed at the Observatorio de Sierra Nevada near Granada in Spain, at an altitude of 3000 m and in an area of very low humidity. The telescope, dome, camera and liquid nitrogen generation and refilling systems have all been recently brought back into operation, and routine observations are expected to begin within the next few months.

1 BOOTES and BOOTES-IR

BOOTES (Burst Observer and Optical Transient Exploring System) (Castro-Tirado *et al.* 1999) is a worldwide network of robotic telescopes, begun in 1998 at Huelva in southern Spain with two small enclosures (BOOTES-1A & B). These were followed by the 60 cm ultra-fast and ultra-light BOOTES-2 telescope in Málaga, the alt-az BOOTES-IR telescope in Granada, and two clones of the

¹ Instituto de Astrofísica de Andalucía (IAA-CSIC), Glorieta de la Astronomía s/n, 18008 Granada, Spain

² Unidad Asociada Grupo Ciencia Planetarias UPV/EHU-IAA/CSIC, Departamento de Física Aplicada I, E.T.S. Ingeniería, Universidad del País Vasco UPV/EHU, Alameda de Urquijo s/n, 48013 Bilbao, Spain

³ Ikerbasque, Basque Foundation for Science, Alameda de Urquijo 36-5, 48008 Bilbao, Spain

⁴ Ovíjares, Granada, Spain

BOOTES-2 configuration: BOOTES-3 in Blenheim, New Zealand and BOOTES-4 in Lijiang, China. Locations for further telescopes are being explored, with the goal of complete north-south and 24-hour coverage. All telescopes and instruments are fully robotic (*i.e.* autonomous) under the RTS2 (Kubánek *et al.* 2004) observatory operating system.

1.1 *BOOTES-IR*

BOOTES-IR is the only near-IR instrument in BOOTES. The telescope is a fast-slewing, 0.6 m, f/8 Ritchey-Chrétien design able to reach any part of the sky in 10 seconds, with a typical slew time of 5 seconds. The Observatory of Sierra Nevada (www.osn.iaa.es) is situated 2986 m above sea level, where high altitude and desert climate provide exceptional NIR observing conditions. However, winter weather at OSN can be extremely severe, with peak windspeeds above 200 kph requiring not just a very strong dome, but also one that is well-sealed the slightest crack often results in a fog of tiny ice-crystals filling the dome and coating everything inside to later melt in inconvenient places. The first clamshell dome proved neither strong enough, nor well sealed enough, so a replacement dome was installed in 2007, of conventional two-door design and able to slew rapidly enough to match the telescope. However, on Christmas Day 2009, in extreme wind conditions, the upper door was physically blown off the dome, effectively destroying it as a working enclosure. A third dome has now been installed (since 2011), of much heavier construction, and it has survived two winters without damage.

1.2 *The NIR camera BIRCAM*

The NIR camera is based on a Rockwell HAWAII-1 array (1k × 1k HgCdTe hybrid detector), sensitive from 0.8 to 2.5 μm . The pixel scale is 0.7 for a field of view of 12×12 . The camera has an 8 position filter wheel, currently with Y, J, H and K filters, and a blank metal plate for dark frames. The camera is cooled via an internal LN2 tank, and although the original specifications called for a hold time of at least 24 hours, the finished camera does not quite meet this requirement, so in practice it must be filled twice per day rather than once, a significant imposition.

1.3 *Automated liquid nitrogen supply*

Given the the new twice-per-day requirement, and the severe weather that can prevent access to the dome, an automatic refilling system was envisaged, based around a dedicated liquid nitrogen plant as the most practical solution. However, the estimates of the effects of waste heat (6 kW) from the plant were optimistic, resulting in high temperatures directly under the T60 dome and adjacent to the pillar.

1.4 Building extension

In 2012, after a number of solutions were studied, the decision was taken to construct a small separate building adjacent to the existing dome. This was explicitly designed for high-volume ventilation, with double end-walls, separated by a 20 cm space and open at the bottom, with ventilation ducts piercing the inner wall near the top. The building was also raised 30 cm above the ground on steel pillars so that the wind could blow underneath providing extra cooling surface area and avoiding stagnation zones where snow could gather.

1.5 Control and refilling

Through practical experiment, it was determined feeding LN₂ from the ground floor up to the telescope required an operating pressure of 1 bar, which is higher than that of the LN₂ generating plant. Relying on the system's low duty cycle, the simplest solution was to install a 1 bar dewar that could be depressurised, refilled, and re-pressurised between filling operations. Rather than building a flexible feed system through the telescope mount, it is possible (and much simpler) to install a fixed arm outside the volume of rotation of the telescope, such that a downward pointing nozzle is just above a receiving cup when the telescope is in the parked position. Control of refilling is then achieved via electrically operated cryo-valves.

1.6 Safety

Liquid nitrogen is both a cryogenic and an asphyxiation hazard, particularly in enclosed spaces such as the T60 dome. As vented nitrogen gas will be cold, it will sink to the floor, where the intake of an active ventilation system can preferentially remove it. This system activates for 15 minutes of every hour, continuously if a human is detected by a burglar-alarm type passive infra-red sensor, and when the refilling system is active. The refilling system itself had to be designed fail-safe: the valves will close if electrical power is lost, a separate interlock will prevent LN₂ discharge unless the telescope is parked, and a control idiom is used that prevents a computer failure from leaving the system in a dangerous state (commands take effect for a short time only, and must be re-issued repeatedly for a longer effect).

2 Conclusion

The BOOTES-IR telescope is a fast and capable robotic instrument in an excellent (if challenging) site, which is expected to start operation with automatic refilling in the coming months.

We appreciate the financial support by the Spanish Ministry of Economy and Competitiveness through the research project AYA 2009-14000-C03-01 and AYA 2010-39727-C03-01. JG is supported by the Ikerbasque Foundation for Science and the IAA-CSIC Unidad Asociada at ETSI-UPV/EHU.

References

- Castro-Tirado, A.J., Soldán J., Bernas, M., *et al.*, 1999, A&AS, 138, 583
Castro-Tirado, A.J., de Ugarte Postigo, A., Jelínek, M., *et al.*, 2005, Il Nuovo Cimento
28, 715
Kubánek, P., Jelínek, M., Nekola, M., *et al.*, 2004, AIP Conf. Proc., 727

PHOTOMETRIC OBSERVATIONS OF GRB 080605 BY BOOTES-1B AND BOOTES-2

M. Jelínek¹, E. Gómez Gauna², A.J. Castro-Tirado¹ and
J. Gorosabel^{1,3,4}, on behalf of the BOOTES Collaboration

Abstract. BOOTES-1B and BOOTES-2 were first to follow-up the *Swift* GRB 080605. Observations started 44 s after the GRB trigger, discovering the optical afterglow with the brightness of $R = 14.7$. A power-law decay with an $\alpha = 1.27 \pm 0.04$ was observed during the first ~ 600 s after the trigger.

1 Introduction

The GRB in question was a long burst detected by Swift on June 5, 2008 at 23:43:57 UT Sbarufatti *et al.* (2008). The best known position is α (J2000) = 17:28:30.05, $\delta = +04:00:56.2$ from *HST* imaging. The host was found to be a metal enriched star forming galaxy at redshift 1.64 (Krühler *et al.* 2012). Zafar *et al.* (2012) analyzed the SED of GRB 080605 to show that its host galaxy exhibits the 2175 Å extinction feature.

In the vicinity of the afterglow location, there are several stars complicating the photometry with small and medium size telescopes Kann *et al.* (2008). From photometric points from *GROND* (Zafar *et al.* 2012), a power-law decay index of $\alpha_{\text{late}} = 0.72$ can be derived.

2 Observation by BOOTES

BOOTES-1B reacted to the burst trigger and started to take images 44 s after the GRB. A series of 2 s unfiltered exposures were acquired. The pixel scale

¹ Instituto de Astrofísica de Andalucía, IAA-CSIC, 18008 Granada, Spain

² Visitor at EELM-CSIC, 29750 Algarrobo, Spain

³ Unidad Asociada Grupo Ciencia Planetarias UPV/EHU-IAA/CSIC, Departamento de Física Aplicada I, E.T.S. Ingeniería, Universidad del País Vasco UPV/EHU, Alameda de Urquijo s/n, 48013 Bilbao, Spain

⁴ Ikerbasque, Basque Foundation for Science, Alameda de Urquijo 36-5, 48008 Bilbao, Spain

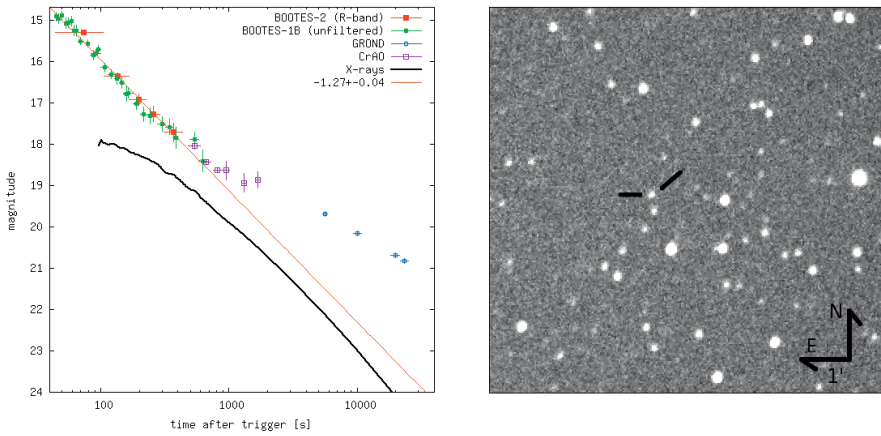


Fig. 1. *Left:* the optical and XRT lightcurve lightcurve of the GRB 080605, X-rays (Sbarufatti *et al.* 2008) have been scaled up by an arbitrary constant. *Right:* details of the surroundings of the optical afterglow of GRB 080605 as observed by BOOTES-1B. Image taken 45 s after the trigger.

of $2''/\text{pixel}$ does not permit us to spatially separate the optical transient from the nearby, 17.8 m star. About 10 minutes after the trigger, the OT+star flux is dominated by the star and getting the OT brightness from then on becomes impossible. To obtain photometry, images were combined, resulting in longer exposure times. Eventually, 28 photometric points were obtained between 45 and 630 s after the GRB trigger. By a simultaneous fit of the decay rate α and the nearby star brightness $m_{\text{measured}} = -2.5 \log_{10}(10^{-0.4m_*} + 10^{-0.4m_{\text{OT},t_0} + 2.5\alpha \log_{10} t/t_0})$ we obtained $\alpha = 1.27 \pm 0.04$ and the brightness $m_* = 17.81 \pm 0.03$. The photometric points obtained are in the Table 1 with the nearby star flux subtracted.

BOOTES-2/TELMA reacted in 44 s and obtained a series of 60 s R-band exposures. The images have the same problem as those from BOOTES-1B: it is impossible to distinguish the star and the OT. Five photometric points were obtained by flux subtraction of the star with $m_R = 17.42 \pm 0.07$.

3 Discussion

BOOTES-1B and BOOTES-2 data were independently fitted and both provided the same decay index $\alpha = 1.27$ during the first 10 minutes after the trigger. A nearby star prevented prolonged follow-up with the coarse spatial sampling provided by BOOTES. X-ray lightcurve (Sbarufatti *et al.* 2008), seems to undergo a transition from a plateau into a power-law decay with $\alpha_X = 1.47$. The optical lightcurve decay as seen by Zafar *et al.* (2012) between 1.5 and 6.5 h after the trigger is $\alpha_{\text{late}} = 0.72$. There might be some trace of a transition between the two

Table 1. Photometric observations of the GRB 080605 optical afterglow, as obtained by BOOTES-1B and BOOTES-2. The brightness shown is after subtracting the flux of the nearby star. The first column shows the time in seconds since the burst trigger.

T [s]	exp	mag	dmag	tel	T [s]	exp	mag	dmag	tel
44.7	2.0	14.68	0.11	B-1B	158.5	15.0	16.55	0.18	B-1B
47.3	2.0	14.73	0.11	B-1B	164.7	27.0	16.53	0.13	B-1B
49.6	2.0	14.65	0.10	B-1B	190.7	24.0	16.79	0.15	B-1B
53.3	2.0	14.84	0.13	B-1B	215.7	25.0	17.05	0.18	B-1B
55.9	2.0	14.83	0.12	B-1B	241.9	26.0	17.08	0.20	B-1B
59.3	2.0	14.79	0.12	B-1B	300.1	43.0	17.28	0.18	B-1B
61.9	2.0	15.02	0.13	B-1B	343.3	43.0	17.35	0.19	B-1B
64.5	2.0	15.02	0.14	B-1B	386.1	39.0	17.62	0.26	B-1B
69.8	7.0	15.27	0.08	B-1B	428.9	42.0	17.80	0.28	B-1B
78.9	6.0	15.34	0.09	B-1B	537.0	84.0	17.66	0.17	B-1B
87.4	8.0	15.61	0.12	B-1B	627.3	94.0	18.18	0.27	B-1B
91.8	16.0	15.57	0.08	B-1B					
95.8	8.0	15.47	0.10	B-1B	74.1	60.0	15.28	0.03	B-2
107.2	14.0	15.91	0.11	B-1B	135.5	60.0	16.35	0.08	B-2
121.1	13.0	16.08	0.12	B-1B	196.7	60.0	16.91	0.14	B-2
133.7	13.0	16.19	0.13	B-1B	258.0	60.0	17.27	0.19	B-2
146.2	11.0	16.28	0.15	B-1B	371.4	121.0	17.70	0.23	B-2

optical decay rates detected by Rumyantsev and Pozanenko (2008) at about 700 s after the trigger.

We appreciate the auspices of INTA, EELM-CSIC and UMA as well as the financial support by the Junta de Andalucía and the Spanish Ministry of Economy and Competitiveness through the research projects P07-TIC-03094, AYA 2009-14000-C03-01 and AYA 2010-39727-C03-01. This study was carried out in the framework of the Unidad Asociada IAA-CSIC at the group of planetary science of ETSI-UPV/EHU. This work was supported by the Ikerbasque Foundation for Science.

References

- Kann, D.A., Laux, U., & Ertel, S., 2008, GCN Circular, 7864, 2008
- Krühler, T., Fynbo, J.P.U., Geier, S., *et al.*, 2012, A&A, 546, A8
- Rumyantsev, V., & Pozanenko, A., 2008, GCN 7857
- Sbarufatti, B., Parsons, A., Sakamoto, T., *et al.*, 2008, GCN Report, 142, 1–4
- Zafar, T., Watson, D., Elíasdóttir, Á, *et al.*, 2012, ApJ, 753, 82

STATUS OF PI OF THE SKY TELESCOPES IN SPAIN AND CHILE

T. Batsch¹, H. Czyrkowski², M. Cwiok², R. Dabrowski², G. Kaspruwicz³,
A. Majcher¹, A. Majczyna¹, K. Malek^{4,5}, L. Mankiewicz⁴, K. Nawrocki¹,
R. Opiela⁴, L.W. Piotrowski², M. Siudek⁴, M. Sokolowski¹,
R. Wawrzaszek⁶, G. Wrochna¹, M. Zaremba² and A.F. Żarnecki²

Abstract. Pi of the Sky is a system of wide field-of-view robotic telescopes which search for short timescale astrophysical phenomena, especially for prompt optical GRB emission. The system is designed for autonomous operation, follows the predefined observing strategy and adopts it to the actual conditions. We describe the current status of telescopes located in Chile and Spain and prospects for future development.

1 Introduction

The “Pi of the Sky” (Burd *et al.* 2005) is a system of wide field of view robotic telescope designed for efficient search for astrophysical phenomena varying on scales from seconds to months, especially for prompt optical counterparts of Gamma Ray Bursts (GRBs). The design of the apparatus allows to monitor a large fraction of the sky with a range of 12^m – 13^m and time resolution of the order of 1 – 10 seconds. In order to ensure that all project requirements are met with full control over the detector design and construction, “Pi of the Sky” detectors are equipped with custom designed CCD cameras, built by project members. Each camera is equipped with Canon lenses $f = 85$ mm, $f/d = 1.2$ and covers $20^\circ \times 20^\circ$ of the sky.

¹ National Centre for Nuclear Research, Hoza 69, 00-681 Warsaw, Poland

² Faculty of Physics, University of Warsaw Hoza 69, 00-681 Warsaw, Poland

³ Institute of Electronic Systems, Warsaw University of Technology, Nowowiejska 15/19, 00-665 Warsaw, Poland

⁴ Centre for Theoretical Physics of the Polish Academy of Sciences, Al. Lotników 32/46, 02-668 Warsaw, Poland

⁵ Institute for Advanced Research, Nagoya University, Furo-cho, Chikusa-ku, 464-8601 Nagoya, Japan

⁶ Space Research Center of the Polish Academy of Sciences, Bartycka 18A, 00-716 Warsaw, Poland

The full “Pi of the Sky” system, which is under construction now will be capable of continuous observation of about 1.5 steradians, which is roughly corresponding to the field of view of the BAT instrument on board the Swift satellite (Gehrels *et al.* 2004). In October 2010 the first unit of the new Pi of the Sky detector system was successfully installed in the INTA El Arenosillo Test Centre in Spain. The first site of the ultimate system should be fully operational next year, in the same location.

2 Observations

2.1 *Observational strategy continuous observation of large part of the sky*

Observations of optical counterparts of GRBs during or even before the gamma-ray emission are crucial for understanding the nature of GRBs. The standard approach, which relies on waiting for an alert distributed by the GCN network (The Gamma Ray Burst Coordinates Network; Barthelmy *et al.* 1998) and subsequently moving the telescopes to the target as fast as possible, does not allow us to detect an outburst at the moment of or before the GRB explosion. Thus, the “Pi of the Sky” strategy is based on continuous observation of a large fraction of the sky which increases the chances that a GRB will occur in the observed area. Following the field of view of the Swift satellite, with the full “Pi of the Sky” system, will allow to eliminate a delay of the observation due to telescope re-pointing to the coordinates from GCN. Dead time, which arises from the decision process and signal propagation from the satellite to the GCN and from the GCN to the ground instruments is eliminated as well.

The search for GRB requires very fast data processing and identification of events in real-time. On the other hand, the search for transients and the analysis of variable star are based on precise photometry which requires detailed image analysis. To fulfill both requirements we developed two different sets of algorithms: for on-line and off-line data processing. Off-line analysis is to identify all objects in an image, and to add their measurements to the database. The on-line algorithm searches for flashes in real-time by comparing a new image with the stack of recently taken frames. Any observed difference is considered as possible candidate event. All events are processed through a multilevel triggering system similar to those known from high-energy physics experiments.

The observations of the famous “naked-eye” GRB 080318B (Racusin *et al.* 2008) have confirmed the usefulness of “Pi of the Sky” strategy. Wide-field telescopes performing continuous observations of large part of the sky are capable of detecting GRBs at the moment or even before explosion. GRB 080318B was recognized by the “Pi of the Sky” self-triggering system independently from the alert received from the GCN.

2.2 *The “Pi of the Sky” prototype*

Before constructing the final version, tests of hardware and software were performed with a prototype consisting of 2 custom-designed cameras placed on an equatorial mount. The detector is fully autonomous and operates without any

human supervision, although remote control via Internet is possible as well. Cameras work in coincidence and observe the same field of view with a time resolution of 10 s. The limiting magnitude for a single frame is 12^m and rises to 13.5^m for a frame stacked from 20 exposures. Till 2009 all observations were made in white light and no filter was used, except for an IR-cut filter in order to minimize the sky background. Since May 2009 we have had a Bessel-Johnson R-band filter installed on one of the cameras in order to facilitate absolute calibration of the measurements. The prototype had been working at Las Campanas Observatory in Chile since June 2004 till the end of 2009. In March 2011 the detector was moved to a new site in San Pedro de Atacama, approximately 750 km north from LCO (still in Chile) and about 2 400 meters above sea level.

During the period 2006–2009 the prototype has gathered over 2 billion measurements for almost 17 million objects. All measurements acquired by “Pi of the Sky” are publicly accessible through a user-friendly web interface on the Pi of the Sky Home Page. Effort on improving data quality is still ongoing. We have developed a system of dedicated filters to remove measurements from star light curve measurements, which could be affected by different factors due to detector imperfections or weather conditions. The measurement quality can be improved by an approximate color calibration algorithm based on the spectral type of reference stars and an uncertainty of the order of 0.013^m can be obtained.

3 New detector unit in Spain

The final detector consists of 4 custom-designed CCD cameras, which are improved versions of the cameras developed for the prototype. The cameras can operate in two operational modes thanks to specially designed equatorial mount. The mechanism for moving cameras against the main instrument axis enable to point all cameras at the same object (common-target mode, DEEP common field of view 20° × 20°) or cover adjacent fields (side-by-side, WIDE, total coverage 40° × 40°). Due to numerous improvements, the new design of the telescope mount provides much better pointing accuracy and a shorter reaction time than the prototype. New detector unit has been successfully operated in the INTA El Arenosillo test centre in Mazagón near Huelva, Spain, on the coast of the Atlantic Ocean from October 2010. The ultimate system, consisting of 4 such units, will be operational in 2013.

We are very grateful to G. Pojmanski for access to the ASAS dome and sharing his experience with us. We would like to thank the staff of the Las Campanas Observatory San Pedro de Atacama Observatory and the INTA El Arenosillo test centre in Mazagón near Huelva for their help during the installation and maintenance of our detector. This work has been financed by the Polish Ministry of Science and Higher Education in 2009–2012 as a research project.

References

- Barthelmy, S.D., Butterworth, P., Cline, T.L., *et al.*, 1998, AIPC, 428, 99
- Burd, A., Cwiok, M., Czyrkowski, H., *et al.*, 2005, New Astron., 10, 409
- Gehrels, N., Chincarini, G., Giommi, P., *et al.*, 2004, ApJ, 611, 1005
- Racusin, J.L., Karpov, S.V., Sokolowski, M., *et al.*, 2008, Nature, 455, 183

GLORIA - THE GLOBAL ROBOTIC TELESCOPES INTELLIGENT ARRAY FOR E-SCIENCE

L. Mankiewicz¹ on behalf of the GLORIA collaboration

Abstract. GLORIA stands for “GLObal Robotic telescopes Intelligent Array” GLORIA will be the first free and open-access network of robotic telescopes in the world It will be a Web 2.0 environment where users can do research in astronomy by observing with robotic telescopes and/or analyzing data that other users have acquired with GLORIA, or from other free access databases, like the European Virtual Observatory.

1 Introduction

Many Internet communities have already formed to speedup scientific research, to collaborate in documenting something or as social projects. Research in astronomy can only benefit by attracting many eyes to the sky - to detect something new in the sky requires looking in the right place and the right moment Our robotic telescopes can search the sky but the vast quantities of data produced are far greater than astronomers have time to analyze. Furthermore, even the most advanced and powerful algorithms used in automatic analysis pipelines have limitations that could lead to missing important discoveries. GLORIA will provide a way of putting thousands of eyes and minds on this problem It is intended to be a Web 2.0 structure with the possibility of doing real experiments The community will not only generate content as in most Web 2.0 but will control telescopes around the world both directly and via scheduled observations The community will take decisions for the network and that will give “intelligence” to GLORIA, while the drudge work (such as drawing up telescope schedules that satisfy various constraints) will be done by dedicated algorithms that are being developed for the purpose.

During the initial period, the GLORIA consortium consists with 13 institutions, operating 17 telescopes which will be integrated into the GLORIA network.

¹ Centre for Theoretical Physics of the Polish Academy of Sciences, Al. Lotników 32/46, 02-668 Warsaw, Poland

Some of them, like BOOTES, Pi of the Sky or Mini-MegaTORTORA have observations of optical activity associated with Gamma Ray Bursts as their principal scientific program. In the future, we plan to provide user required inputs so other users can integrate their telescopes into the network. GLORIA is also collaborating with the “Discover the COSMOS” EU funded project, which aims at innovative ways to involve teachers and students in eScience through existing infrastructures.

The GLORIA project will define free standards, protocols and methodologies for:

1. Controlling robotic telescopes and all related instrumentation such as cameras filterwheels domes etc..
2. Giving web access to the network: access to an arbitrary number of robotic telescopes via a web portal.
3. Conducting on-line experiments: users will be able to design specific web environments to control telescopes and perform observations aimed at studying some specific scientific issues.
4. Conducting off-line experiments: users will be able to design specific web environments for analyzing astronomical meta – data produced by GLORIA and other databases.

We are going to seek the collaboration of amateur astronomers and their telescopes. Some amateur astronomers are very active with excellent instrumentation and observing locations However they are frequently limited in their ability to properly exploit and interpret their data Interaction with professional astronomers and the use of powerful customized analysis tools will greatly improve the quantity, quality and reliability of the data that amateurs can collect with their instruments The GLORIA community will benefit from their telescopes the data they produce, and simply the extra knowledge, experience and ideas their presence will bring.

GLORIA associates with each user through a meritocratic parameter, called “Karma” in Web 2.0 environments This is correlated with the user’s activity and their performance of useful work In the context of GLORIA, it is the method whereby access to scarce resources (such as telescope time) is determined. Calculation of karma is done automatically, incorporating, for example, the votes of the community for the work of each user. This method has been successfully proven in many collaborative web sites such as YouTube.

2 GLORIA as a network

Technically, GLORIA aims to create a completely robotised and autonomous network of telescopes. For each target, the selection of instrument as well as exposure settings are to be decided automatically, without human intervention, based on information about telescopes and the time slots that each telescope offers for the network. Putting together 17 telescopes in one network offers significant potential



Fig. 1. Geographical location of the initial 17 telescopes of GLORIA. A star symbol means multiple telescopes.

for automatically triggered follow-up observations. Such observations are obviously useful for transients of all kinds, including GRB observations.

3 Experiments with GLORIA

GLORIA will provide a web interface that will allow users to perform specific astronomical research projects through “experiments”. Users will be guided through the different tasks each project requires. These experiments are of two kinds: those that require a telescope (which we have called “on-line” experiments) and “off-line” experiments, which work on data produced by the GLORIA network or derived from other databases, such as the European Virtual Observatory. Moreover, GLORIA will design a methodology documentation and software components to allow users to design new experiments. Advanced users will not only be able to design new experiments, but also to integrate them into the network, by following the open methodology, and make them usable by all.

During the lifetime of the GLORIA project there will be demonstrators for at least one online and one off-line experiment. At an early stage of the project the partners will decide on the exact astronomical topics to start investigating, including, for example: Exoplanets, Supernovae, Gravitational lenses, PHA (Potentially Hazardous Asteroids), Space debris, NEO (Near Earth Objects) etc..

4 Broadcasted astronomical events

To advertise the project and test P2P technologies, GLORIA had set the goal to broadcast live 5 astronomical events around the world. Three such broadcasts, the **Venus Transit** June 6th 2012, **Northern Lights from Greenland** August

24th-28th 2012, and **Solar Eclipse** November 13th 2012 have been successfully performed. Thanks to innovative P2P technology the GLORIA network delivered images and video streams taken in Japan, Australia and Norway live to more than 100 thousand viewers. In addition, some commercial TV stations took the GLORIA stream and broadcast it on their channel. Dedicated pedagogical materials were prepared and distributed prior to each event and off-line experiments were created using data and images collected during the event. For further information visit gloria-project.eu

GLObal Robotic telescopes Intelligent Array for e-Science (GLORIA) is a project funded by the European Union Seventh Framework Programme (FP7/2007-2012) under grant number 283783. I am grateful to A.J. Castro-Tirado, L. Hanlon, L. Nicastro and F.M. Sanchez for their remarks concerning the manuscript.

STATUS UPDATE OF THE WATCHER ROBOTIC TELESCOPE

M. Topinka¹, S. Meehan¹, L. Hanlon¹, P. Tisdall¹, H. van Heerden²,
P. Meintjes², M. Hoffman², M. Jelínek³ and P. Kubánek⁴

Abstract. The current status of the Watcher robotic telescope is presented in the light of a recent hardware and software upgrade. The latest gamma-ray burst rapid follow-up observations are discussed, with particular reference to GRB 120711A.

1 Introduction

The Watcher robotic telescope is located at Boyden observatory close to Bloemfontein in South Africa ($29^{\circ}02'20''$ S, $26^{\circ}24'17''$ E) therefore covering the southern hemisphere. The weather allows observations for ~ 200 nights per year. Its primary scientific activity is in gamma-ray burst follow-up observations. However, a monitoring programme of Fermi blazars has recently begun. The telescope consists of a 40 cm primary mirror in the Cassegrain configuration ($f/14.25$) and a Paramount ME mount (with ~ 60 s round-trip time, see Fig. 1). It is equipped with an Andor EMCCD camera, Optec filter-wheel (giving BVRI filters and clear) and Robofocus focuser. The site includes UPS power backup, web-cam, cloudmeter, rain sensor, robotized Zelio roof controller and a Davis weather station⁵. Watcher is controlled by the RTS2 software package⁶. Recently, the telescope has undergone a software upgrade, in which the astrometry package was embedded in the pipeline, as well as general hardware maintenance.

¹ University College Dublin, Ireland

² University of the Free State, South Africa

³ IAA-CSIC, Spain

⁴ FZÚ, Czech Republic

⁵The Watcher observational status and weather information for the site are tweeted from @WatcherTele

⁶The robotic telescope network software RTS2 is a live open source code provided at <http://rts2.org>

Table 1. A selection of interesting GRBs observed by Watcher. Δ shows delays between satellite GRB triggers and the beginning of the first exposure.

GRB	Triggered by	Δ [s]	Comments
GRB 060526	Swift	+36	Achromatic jet break in the afterglow
GRB 070610	Swift	+53	Suspected to be an optically flaring magnetar Swift J195509+261406
GRB 080905B	Swift	+43	Two peak afterglow as a signature of reverse and forward shock
GRB 120711A	INTEGRAL	+80	Extremely long lasting X-ray/ γ -ray tail

2 GLORIA

Watcher is a constituent member of the GLORIA project⁷. The acronym stands for “GLObal Robotic-telescopes Intelligent Array”. GLORIA will be the first free and open access network of robotic telescopes in the world. It will provide a Web 2.0 environment where users can do research in astronomy by observing with robotic telescopes, and/or by analyzing data that other users have acquired with GLORIA, or from other free access databases, such as the European Virtual Observatory. GLORIA is a network of heterogeneous telescopes with a scheduler that accepts telescope-neutral observing plans as input. A schedule for each telescope is then produced, optimized according to the available time and telescope capabilities. Additionally, GLORIA provides live web broadcasts of astronomical events (*e.g.* the Transit of Venus and the total solar eclipse in November 2012) and educational resources to engage the interest of students and the public in astronomy.

3 Early GRB afterglows and GRB 120711A

The main scientific goal of Watcher is the rapid follow-up observation of GRB afterglows. Slewing precision, enhanced by applying the T-point mount model correction and the corrections from successful astrometry⁸, is $\gtrsim 1'$. Rapid GRB follow-up is essential for observing the early stage of an optical afterglow and optical flashes. In the fireball scenario, the peak in a light curve can represent a forward shock passing the observational band or it can be a signature of a reverse shock (Piran 1999; Zhang & Kobayashi 2005). Propagating into the ejecta rather than into ISM, the reverse shock can reveal properties of the GRB outflow. Comparing the forward and reverse shock peaks, an estimate of the jet magnetization can be made (Harrison & Kobayashi 2012).

The latest achievement is an early observation ($\gtrsim 80$ s after the burst, Fig. 2) of GRB 120711A, an extremely bright and long GRB that was triggered by INTEGRAL (GCN 13434) and also observed by FERMI/LAT (GCN 13437). Most unusually, the burst also showed a long tail of emission, lasting at least

⁷For more information about GLORIA visit <http://gloria-project.eu>

⁸The details of the astrometry package can be found at <http://astrometry.net>

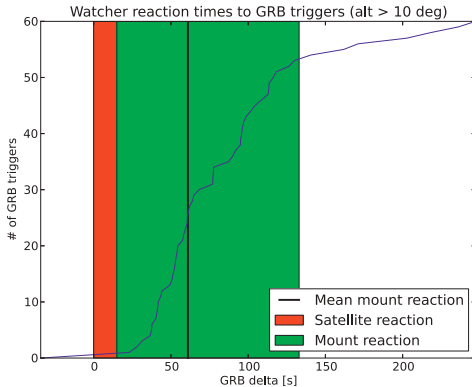


Fig. 1. Cumulative distribution of the number of bursts as a function of response time (Δ_{GRB}), considering only GRBs $> 10^\circ$ above the local horizon at the time of the GCN receipt. The plot shows the time elapsed between the GRB trigger and receipt of the GCN (red), the delay associated with the mount reaction (green), which is composed of two distributions attributable to slewing and executing a meridian flip, and delayed triggers or GRBs below the horizon (white).

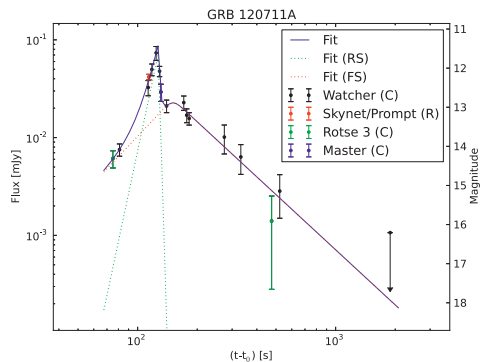


Fig. 2. Watcher light curve of GRB 120711A suggesting the presence of both a reverse and forward shock. t_0 refers to the trigger time. Data points from ROTSE-3 (GCN 13432), Master (GCN 13443) and Skynet/Prompt (GCN 13430) are also shown. A sum of two smoothly connected power-laws representing a forward and reverse shock fits the data.

up to ~ 1200 s after the trigger time and detected by both IBIS (GCN 13435) and SPI (GCN 13468) in the 20–50 keV energy range.

4 Discussion and conclusions

The optical light curve of GRB 120711A obtained predominantly from Watcher indicates a presence of a strong reverse shock. If t_0 is placed at the rise of the main burst determined from the INTEGRAL data, rather than at the precursor that raised the trigger ($t_0 - t_{\text{trigger}} \sim 67$ s) a reasonable forward shock and reverse shock model fits the observations: $\alpha_{RS} \sim -4.5$, $\beta_{RS} \sim 3.4$, $\alpha_{FS} \sim -0.6$, $\beta_{FS} \sim 1.4$.

GLObal Robotic telescopes Intelligent Array for e-Science (GLORIA) is a project funded by the European Union Seventh Framework Programme (FP7/2007-2012) under grant agreement number 283783.

References

- Harrison, R., & Kobayashi, S., 2012 [[arXiv:1211.1032v1](https://arxiv.org/abs/1211.1032v1)]
- Piran, T., 1999, Phys. Rev., 314, 575
- Zhang, B., & Kobayashi, S., 2005, ApJ, 628, 315

SWIFT PUBLICATION STATISTICS AND THE COMPARISON WITH OTHER MAJOR OBSERVATORIES

S. Savaglio¹ and U. Grothkopf²

Abstract. The gamma-ray bursts (GRB) *Swift* satellite was launched at the end of 2004 and is funded until 2014. Its γ -ray, X-ray, and optical-UV instruments discover and localize about 100 GRBs per year. We report on the success of this mission by counting the number of papers with *Swift* data and their impact (*i.e.*, number of citations to those papers) for the publication years 2005 to 2011. In the first year, the number of papers was 24, and it steadily increased to 287 in the year 2011, reaching Keck. If this trend continues, before the end of the mission *Swift* may be approaching XMM-Newton and Chandra, with \sim 400 publications. Science topics of Swift publications have widened over time, and in 2011 almost 3/4 of all publications were about other energetic targets, such as AGN, novae, supernovae, X-ray binaries, pulsars, massive and stellar black holes.

1 Introduction

Bibliometrics is one quantitative approach to evaluate the success for individual scientists, research institutes, or universities. It counts the number of papers of these entities, and their impact through the number of citations to their papers.

Here we present the first complete bibliometric investigation for the years 2005–2011 of the γ -ray burst (GRB) mission *Swift* (Gehrels *et al.* 2004). *Swift* was launched at the end of 2004, while the first paper appeared in 2005. Its bibliometrics is compared with major observatories. For a full description of the method and details, see Savaglio & Grothkopf (2012).

2 Methodology

For *Swift*, VLT, HST, Gemini and Subaru, papers are selected consistently. Only papers that use data are counted; theoretical papers are not included. Bibliometrics for XMM-Newton and Chandra is performed differently and their numbers are

¹ MPI f. Extraterrestrial Physics, Garching bei München, Germany

² European Southern Observatory, Garching bei München, Germany

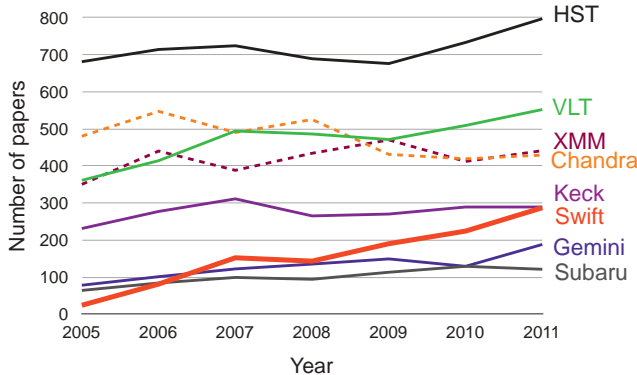


Fig. 1. Number of papers published based on data from different observatories, for the years 2005–2011. *Swift* data where first published in 2005 (thick red line), few months after its launch, in November 2004. Chandra and XMM-Newton are represented as dashed lines because here bibliometrics is measured using different criteria, which give a higher number of publications.

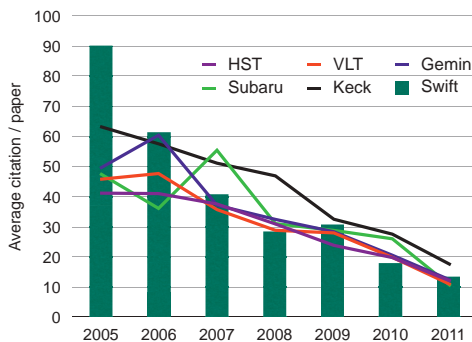


Fig. 2. Number of citations per paper for *Swift* (green histogram), HST, VLT, Gemini, Subaru and Keck, for the years 2005–2011.

generally higher than what we would get with our method. We used FUSE (Full-Text-Search tool), developed and maintained by the ESO Library (Erdmann & Grothkopf 2010; Grothkopf & Meakins 2012) to identify possible *Swift* papers. These are then carefully inspected to make sure that *Swift* data were used.

3 Number of publications and citations

The first *Swift* data papers were published in 2005, a few months after the launch (Fig. 1). With a steady and steep increase, the satellite produced 287 papers in 2011, many more than Gemini, twice those of Subaru, and reached Keck, one of the most successful observatories ever. After 7 years of operation, the plateau has

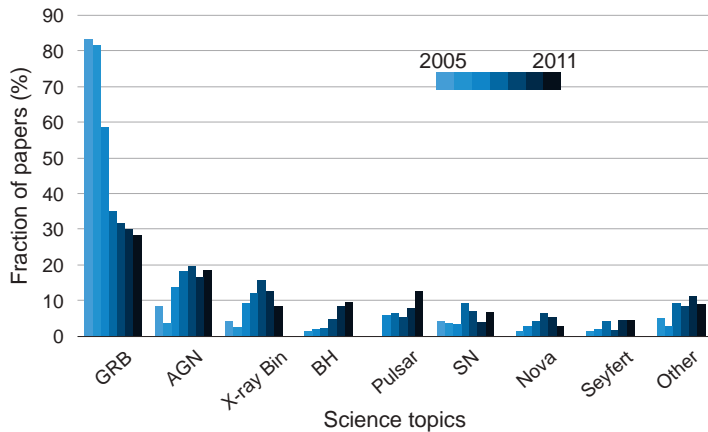


Fig. 3. Fraction of papers over the total for *Swift* ordered according to the science topic, for the years 2005–2011. An AGN paper is also dealing with distant QSOs, BL Lacs or blazars. BH indicates massive or stellar black holes. SN includes supernovae and supernova remnants.

not yet been reached; the total number of papers is 1101. We obtained citations to data papers for all these observatories, for publication years 2005–2011 (Fig. 2). *Swift* papers are on average cited as often or more frequently than papers from other major observatories. In November 2012, the average number is 28.3 citations per paper. Among the top 150 most cited *Swift* publications, 26 (~17%) were published in *Nature* and *Science*, much more than what is generally obtained by other observatories (5%–8%).

4 Science topics

While the main goal of *Swift* is to detect GRBs, the satellite also observes other energetic events (Fig. 3). In the first two years, over 80% of the publications were GRB papers, and almost 60% in 2007. During the past 4 years, 2008–2011, the science done by *Swift* was mostly non-GRB (which dropped to 28%–35%). A large fraction is dedicated to galactic sources: ~1/4 of the papers in 2008–2011 are about X-ray binaries, pulsars, supernovae. Very popular are AGNs, with almost 20% of all publications.

References

- Erdmann, C., & Grothkopf, U., 2010, in: Library and Information Services in Astronomy VI: 21st Century Astronomy Librarianship, From New Ideas to Action, ASP Conf. Ser., 433, 81
- Gehrels, N., Chincarini, G., Giommi, P., *et al.*, 2004, ApJ, 611, 1005
- Grothkopf, U., & Meakins, S., 2012, The Messenger, 147, 41
- Savaglio, S., & Grothkopf, U., 2012, PASP, submitted

ASTRONOMICAL HOSTING IN CENTRAL ASIA

A. Pozanenko¹, A. Volnova^{1,2}, S. Guziy³, N. Tungalag⁴, E. Klunko⁵
and I. Molotov⁶

Abstract. Networked projects *e.g.* Gamma-Ray Burst follow up optical observations require dense worldwide coverage. We are investigating potentially interesting sites for observatories in Central Asia where coverage by observatories is still poor. One of the most important parameter of a site is a number of clear night hours. We present first results of direct parameter measurements gathered with weather stations and our own observations in different sites of Mongolia.

1 Data analysis and results

Site selection. Our project was started from a selection of sites for investigation in Mongolia. The basic approach in the first step is to locate the sites with maximal number of clear sky night hours and minimal annual ground wind speed. We were inspired by early reports by Batsukh *et al.* (1995) about number of astronomical observational hours. To start our investigation we referred on the Atlas of the climate and ground water resources in the Mongolia (1985). The southern region of Mongolia has a maximal number of sunshine days, and at the same time west part of the region is high-mountain desert within spurs of Mongolian-Altai. This type of relief can be suitable for good quality of astronomical observations. We obtained data from several weather stations in the provinces (aimak) of Umnugovi, Govi-Altay, Bayanhongor. Usually weather stations are placed in the central settlement of area (sum). Additionally we use the data of our own monitoring in the site of Tavantalgoi (50 km west from Ulaanbaatar) and Sayan Solar Observatory (SSO) nearby Mondy settlement, Russia (Fig. 1 and Table 1).

¹ Space Research Institute, RAS, Moscow, Russia; e-mail: apozanen@iki.rssi.ru

² Sternberg Astronomical Institute of Lomonosov Moscow State University, Moscow, Russia

³ Mykolaiv National University, Mykolaiv, Ukraine

⁴ Research Centre of Astronomy & Geophysics of MAS, Ulaanbaatar, Mongolia

⁵ Institute of Solar-Terrestrial Physics, SB, RAS, Irkutsk, Russia

⁶ Keldysh Institute for Applied Mathematics, RAS, Moscow, Russia



Fig. 1. Map of the sites.

Data selection. In the first stage we use only data obtained during night time in 23 p.m., 2 a.m. and 5 a.m. of local time. Cloud amount parameter lies in the range 0–10, and was estimated by visual method. Also we used the ground wind speed and wind direction data. In the two sites, Tavantalgai and SSO we were able to use automatic digital cloudmeters and data from digital weather stations. However in this paper we restrict our investigations only to night measurements of the three parameters.

Data reduction. We define clear sky when cloud parameter is equal to zero. If for all three night measurements (23, 2 and 5) cloud parameter equals to zero, we suggest it as a whole clear night. Then we calculate the number of clear night hours as number of measurements with cloud parameter equals zero multiplied by 3, *i.e.* the time interval between successive measurements. Mean wind speed and direction is the average per three night measurements. In contrary, for Tavantalgai and SSO sites we use data of cloudmeters taken once per 10 minutes and the number of clear hours can be calculated more correctly. Calibration of the cloudmeters are performed in comparison with images of all sky cameras taken at the same time.

Results. In Table 1 we provide results of our calculations. First column is a name of the station, next columns represent, the international index of the weather station (or observatory code), coordinates and a height above sea level. The number of clear night hours, ground wind speed and wind direction is averaged for 3 years (Jan. 2009 – Dec. 2011). For Tavantalgai it is averaged for Nov. 2010 – Nov. 2012, and for SSO Mondy it is averaged for the period Oct. 2009 – Oct. 2012 (Fig. 2). Wind direction in degrees is presented for the Winter season.

Discussion and comparison with other sites. All of the sites have a maximum of clear nights and number of clear night hours in Fall and Winter seasons. Estimated number of clear night hours in general exceeds the same parameters for North Caucasus (*e.g.* Kornilov *et al.* 2010). In the station Ajbogd the number of clear

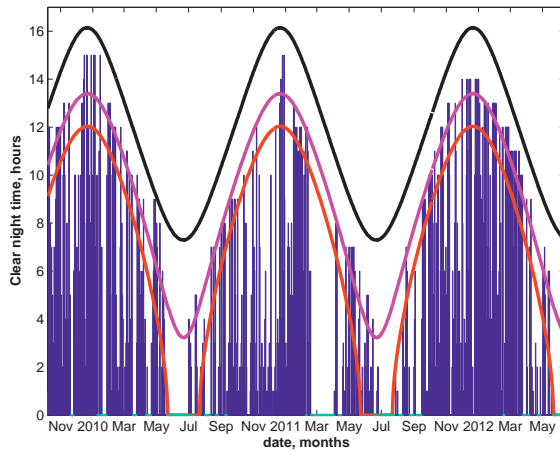


Fig. 2. Seasonal variations of number of clear sky hours in SSO (Mondy). Cyan on the X-axis denotes data gaps.

Table 1. Weather stations and results obtained in 2009–2012.

Station name	Index	Latitude (N)	Longitude (E)	Height, m	Clear night hours	Wind, m/s	Wind direction
Gurbantes	44374	43.20	101.00	1726	1390	4.1	180
Shinejinst	44329	44.53	99.27	2219	1410	3.4	225
Ajbogd	44324	44.91	94.96	1442	1960	2.2	90
Bayantsagan	44326	45.05	98.85	2030	1410	2.5	315
Bogd	44334	45.17	100.76	1280	1580	4.1	315
Bugat	44268	45.55	94.35	2000	1330	3.6	360
Tavantalgoi	n/a	47.88	106.33	1670	>1270	5.1	315
SSO Mondy	C48	51.61	100.92	2007	>1570	3.5	n/a

night hours is close to 2000, and this region we are planning to investigate more precisely. Our direct measurements of clear night hours is somewhat less than the same parameter estimated indirectly in early publications (Batsukh *et al.* 1995). Detailed results of our project will be presented in forthcoming publications.

The work was supported by RFBR grant 11-01-92202-Mong-a.

References

- Batsukh, D., Ganbaatar, D., Khaltar, D., *et al.*, 1995, A&AS, 113, 341
 Kornilov, V., Shatsky, N., Vozniakova, O., *et al.*, 2010, MNRAS, 408, 1233
 The atlas of the climate and ground water resources in the Mongolian's people republic, 1985, ed. D. Tuvdendorzh & B. Myagmarzhav (Ulaanbaatar, GUGMS of Mongolia)

Chapter XI.

Instrumentation & Techniques-II *(Lomonosov/UFFO)*

ULTRA-FAST FLASH OBSERVATORY: FAST RESPONSE SPACE MISSIONS FOR EARLY TIME PHASE OF GAMMA RAY BURSTS

I.H. Park¹, S. Ahmad², P. Barrillon², S. Brandt³, C. Budtz-Jørgensen³,
A.J. Castro-Tirado⁴, P. Chen⁵, J.N. Choi¹¹, Y.J. Choi⁶, P. Connell⁷,
S. Dagoret-Campagne², C. Eyles⁷, B. Grossan⁸, M.-H.A. Huang⁹,
A. Jung¹⁰, S. Jeong¹⁰, J.E. Kim¹⁰, M.B. Kim¹, S.-W. Kim¹¹,
Y.W. Kim¹, A.S. Krasnov¹², J. Lee¹, H. Lim¹, E.V. Linder^{10,13},
T.-C. Liu⁵, K.W. Min⁶, G.W. Na¹⁰, J.W. Nam⁵, M.I. Panasyuk¹²,
H.W. Park¹, J. Ripa¹, V. Reglero⁷, J.M. Rodrigo⁷, G.F. Smoot^{10,13},
S. Svertilov¹², N. Vedenkin¹², M.-Z. Wang⁵ and I. Yashin¹²

¹ Department of Physics, Sungkyunkwan University, Seobu-ro 2066, Suwon-si, 440-746, Korea

² LAL, University of Paris-Sud 11, Orsay, France

³ National Space Institute Astrophysics, Technical University of Denmark, 2800 Kgs. Lyngby, Denmark

⁴ Instituto de Astrofísica de Andalucía (IAA-CSIC), PO Box 03004, 18080 Granada, Spain

⁵ Department of Physics, National Taiwan University, 1 Roosevelt Road, Taipei, 106, Taiwan

⁶ Korea Advanced Institute of Science and Technology, 291 Daehak-ro, Yuseong-gu, Daejeon 305-701, Korea

⁷ Universidad de Valencia, GACE, Edif. de Centros de Investigacion, Burjassot, 46100 Valencia, Spain

⁸ Space Sciences Laboratory, University of California at Berkeley, USA

⁹ Department of Energy Engineering, National United University, 1, Lienda, Miaoli, Taiwan, 36003

¹⁰ Department of Physics, Ewha Womans University, 11-1 Daehyun-dong, Seoul 120-750, Korea

¹¹ Department of Astronomy, Yonsei University, 134 Shinchon-dong, Seoul 120-749

¹² Skobeltsyn Institute of Nuclear Physics of Lomonosov, Moscow State University, Leninskie Gory, 119234, Russia

¹³ Institute for the Early Universe, Ewha Womans University, 11-1 Daehyun-dong, Seoul 120-750, Korea

Abstract. One of the unexplored domains in the study of gamma-ray bursts (GRBs) is the early time phase of the optical light curve. We have proposed Ultra-Fast Flash Observatory (UFFO) to address this question through extraordinary opportunities presented by a series of small space missions. The UFFO is equipped with a fast-response Slewing Mirror Telescope that uses a rapidly moving mirror or mirror array to redirect the optical beam rather than slewing the entire spacecraft or telescope to aim the optical instrument at the GRB position. The UFFO will probe the early optical rise of GRBs with sub-second response, for the first time, opening a completely new frontier in GRB and transient studies. Its fast response measurements of the optical emission of dozens of GRB each year will provide unique probes of the burst mechanism and test the prospect of GRB as a new standard candle, potentially opening up the $z > 10$ universe. We describe the current limit in early photon measurements, the aspects of early photon physics, our soon-to-be-launched UFFO-pathfinder mission, and our next planned mission, the UFFO-100.

1 Introduction

In spite of the wide knowledge already acquired about GRBs mainly through *CGRO* [1], *BeppoSAX* [2], HETE-2 [3], *Integral* [4], *Swift* [5] and *Fermi* [6], there are still many opened questions about their progenitors and environment. Deeper understanding of GRBs requires not only more statistics of GRBs but also measurements of infrared (IR), polarization, early photons, and high- z GRBs, which can be realized with sensitive IR technology, large volume of crystal for X-ray and large aperture for ultraviolet (UV)/optical/IR, faster response or slewing telescopes, and large aperture with high sensitivity detector, respectively. Moreover, *Swift* is very unlikely able to extend its operations, much longer than its designed lifetime. Post-*Swift* missions are foreseen, as well as missions primarily dedicated to high- z GRBs, gamma polarimetry and early photons, *i.e.* SVOM [7] and JANUS [8], POLAR [9] and UFFO (Ultra-Fast Flash Observatory) series, respectively.

Thorough understanding of GRBs will be aided by multi-wavelength observations in the early emission phase. Hundreds of GRBs UV/optical light curves have been measured since the discovery of optical afterglow [10]. The *Swift* is the fastest high-sensitivity space observatory that has simultaneously measured X-ray and UV/optical signals in hundreds of GRBs [5]. However, even after nearly 7 years of operation of *Swift*, the immediate follow-up optical observation of the explosion is scarcely made, because the *Swift* telescope typically responds in ~ 100 seconds. Ground-based telescopes do occasionally respond faster, but only a handful of rapid detections have been made to date with heterogeneous sensitivities. Only a few short duration GRBs have been detected in the UV/optical/IR within the first minute after the gamma ray signal.

This lack of early observations and the blindness to the rise phase of many GRB optical light curves along with those of other rapidly variable transient sources, leaves many important physical questions arising at the short time scales unexplored. Rapid data collection is also essential for tests of fundamental physics such as constraints on Lorentz violations [11] and CPT [12] from the time delay between different energy photons, or between photons and neutrinos. Coincident or successive observations of the explosion event as an electromagnetic counterpart to a neutrino observatory or gravitational wave observatory signal would greatly improve our understanding of black holes, neutron stars, and strong field gravity.

We have developed methods, for the first time, for reaching sub-minute and sub-second time scales in a spacecraft observatory appropriate for launch on small satellites. We have proposed Slewing Mirror Telescope (SMT) that employs a rapidly moving mirror or mirror array to redirect the optical path at a telescope, instead of slewing the entire spacecraft or telescope to aim the optical instrument at the GRB position. We describe in the following the concept and development of a fast-response optical telescope, the early photon physics with the UFFO project, the current status of the first mission UFFO-pathfinder [13] onboard Lomonosov spacecraft to be launched in 2013, and a proposed full-scale mission of UFFO-100 as the next step.

2 Current limits of early photon measurements

The very large field of the Burst Alert Telescope (BAT) of *Swift* [14] produces a crude sky position via a coded mask technique. The entire observatory spacecraft then slews to point the UV/optical telescope (UVOT) and other instruments at the GRB position. Though the remarkable success of *Swift* in numerous detections of optical afterglows associated with GRB, only a handful of responses have occurred in less than 60 seconds. The response frequency falls off for response time below 100 sec with an almost complete cutoff by 60 sec. Due to finite mission lifetime, *Swift* is not expected to increase significantly this number of sub-minute responses.

The *Swift* broadcasts the position of GRB within $5 \sim 7$ seconds to ground-based observatories via the gamma-ray coordinate network (GCN). Although the response of some robotic telescopes on ground (to name a few: ROTSE-I-III [15], RAPTOR [16], PAIRITEL [17], Super-LOTIS [18], BOOTES [19]) is extremely rapid, *e.g.* 25 sec for ROTSE-III, the sensitivity is far less than that of the *Swift* UVOT. Due to their small size, and to the limitations of ground-based observing including daytime and weather, together these instruments have managed only a handful of rapid detections [20]. A concurrent optical and gamma observation of the prompt phase of GRB080319B [21] was achieved luckily by TORTORA [22] on REM telescope and by “Pi of the Sky” [23] when this GRB occurred in their field of view and in the field of view of the Konus/Wind instrument [24]. Because of atmospheric scattering or absorption, a 30 cm aperture space telescope compares favorably in sensitivity to a 4-m ground-based telescope [25]. The slower slew times

of such larger terrestrial telescopes makes them uncompetitive for the sub-1000 sec regime. The *Swift* limit of 60 sec response is therefore the practical minimum for sensitive UV/optical GRB studies for the near to mid-term future.

Figure 1 shows the domain of frequency and time accessible by space and ground experiments. The UFFO missions will explore the blank parameter space, the fast- and ultra-fast regimes below 60 sec and even below 1 sec, in a systematic survey and thus significantly enlarge the sample of such observations.

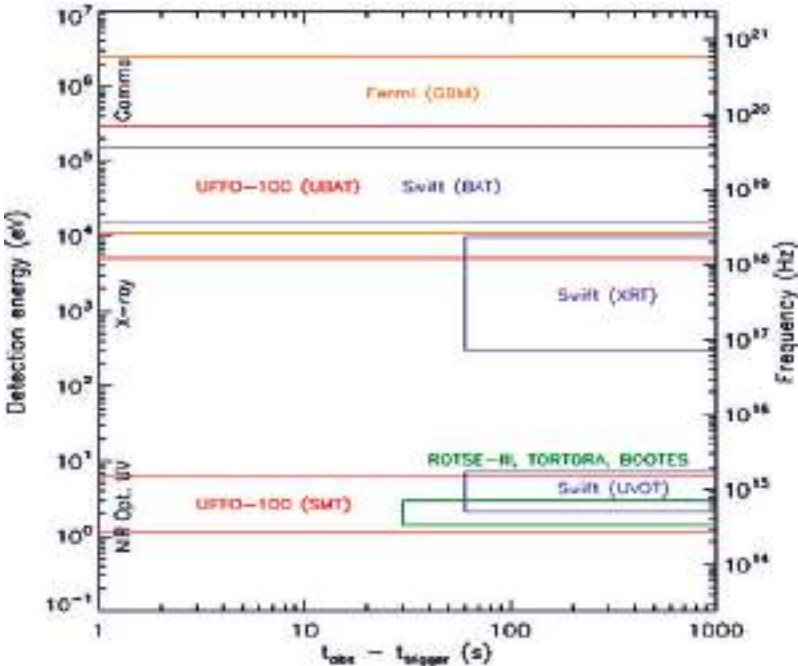


Fig. 1. The accessible frequency and time domain. The UFFO missions will make a systematic survey of the fast- and ultra-fast regimes below 60 sec and below 1 sec, respectively.

3 Slewling mirror telescope

On localizing or identifying GRB, conventional GRB observatories in space or on the ground must reorient their entire spacecraft or telescope to aim their narrow field instruments at the GRB. Our approach to accelerate the slew capabilities is to redirect the optical path at an astronomical telescope via a substantially more lightweight slewing mirror rather than move the entire payload or telescope [39]. The slewing system can be either a flat mirror or mirror arrays such as MEMS (Micro-Electro-Mechanical Systems) mirror array (MMA), mounted on a gimbal

platform. In either case, a large field of view (FOV) is accessible without the aberration inherent in wide-field optical systems.

Figure 2 illustrates the concept of SMT. The parallel rays from the distant source are directed on-axis with respect to the fixed optics by the moving mirror system. The net effect is to steer the UV/optical instrument beam, instead of moving the telescope or the spacecraft itself. The beam can be steered by two-axis rotation of the mirror plate, rotation of the individual MMA devices, or rotation of MMA and also gimbal afterward.

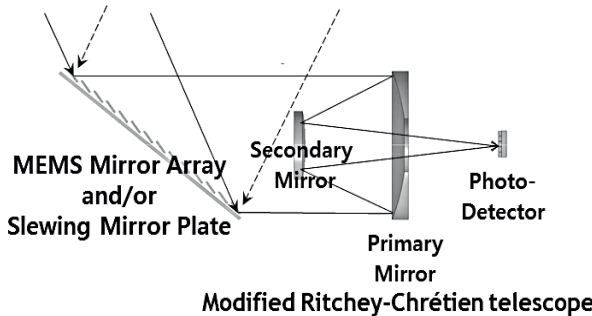


Fig. 2. Schematic of Slewing Mirror Telescope's beam re-direction system.

We find that various types of rotating mirrors move across the entire field of view wider than $180^\circ \times 180^\circ$, point, and settle in less than 1 sec. In order to build a telescope with milliseconds slew speed both for x- and y-directions at a time, our lab consortium has produced small mirror arrays driven by MEMS devices. Resembling mirror segments mounted on two-axis gimbals, MEMS micromirrors are fabricated in arrays using advanced silicon and integrated circuit technologies. These MEMS mirror arrays, fabricated like other microelectronics devices, can move, point, and settle in less than a few msec with rotation angle $\pm 15^\circ$ off axis and thus FOV of $60^\circ \times 60^\circ$. Only voltages are applied to tiny electric actuators for rapid pointing to observe bursts. These are extremely lightweight and low power devices that are well suited to the platform of a microsatellite. A series of small prototype MMA system have been developed in our group since 2004 [26]. We fabricated a small prototype of 3 mm caliber telescope to demonstrate the idea of fast slewing or tracking [27]. It was flown once in space on the ISS in 2008, and once on Tatiana-2 satellite in 2009, with excellent performance, both for nadir observation of transient luminous events occurring in the upper atmosphere [28].

4 Physics from prompt response UV/optical observations

Beyond the possible physics with GRBs, the SMT offers a unique opportunity to probe a new, very early emission parameter space to thoroughly investigate the

rise phase of GRB, which thus far has been observed only occasionally. A variety of rise time physics is as follows.

4.1 Early rise of light curves

The discovery of optical afterglows of GRB was a monumental event in modern astrophysics [29], ending the thirty-year mystery of the GRB distance scale. The study of GRB UV/optical afterglows and their host galaxies has led to knowledge of the origin of some types of GRB and the discovery of the most distant explosions known (*e.g.* GRB 090423 at $z = 8.2$) [30]. Much progress has been made in GRB science since the launch of the *Swift* observatory in 2004 [5]. The observations from *Swift* did not produce a simple picture of GRB, but rather documented the richness and complexity of this phenomenon. After some 370 UV/optical observations by *Swift* UV/optical telescope made, a huge variation in light curves has been observed, especially in the early rise time. There appear to be distinct classes of fast-rising ($t_{\text{peak}} < 102$ sec) and slow-rising bursts [31]. Additionally, the light curves are complex, with decays, plateaus, changes in slope, and other features that are not yet understood.

It is claimed [31] that among the population of GRB with fast-rising optical light curves, the optical luminosity correlates with the rise time, giving promise as a kind of “calibrated standard candle” much like Type Ia supernovae which would make GRBs useful as a cosmological probe of the very high redshift universe. In order to move this possibility to the status of a refined tool, a larger sample of such optically fast-rising GRBs is required, and in particular, better time resolution is required early on. Fastest-rising bursts often have none or just one measurement in their rising phase – hardly enough to understand the physics in this regime – and many other bursts have no early measurements at all. Less than 10 GRBs in this study were measured at less than 100 sec after their burst trigger and not a single measurement was made at less than 15 sec after trigger.

In this respect, several fundamental questions arise. Are there more features in the early light curve that have been missed by such sparse sampling? Does any feature of the rise correlate with the luminosity or a particular aspect of the physics? How many bursts are misclassified because the rapid rise was missed? The need for earlier measurements (faster UV/optical response after the initial gamma-ray burst) is clear and compelling.

4.2 Short duration GRBs

GRBs have a separation on the spectral hardness vs. duration plane, and can be classified into short and hard type (SHGRBs) and long and soft type (LSGRBs), according to the duration around 2 sec [32]. The short time scale of SHGRB emission, the associated lower luminosity and shorter time scale of the X-ray and optical afterglow lead to speculation that the two classes have fundamentally different physical origins [33]. LSGRBs are thought to originate from the collapse of massive stars, *e.g.* the collapsar model [34], and SHGRBs from the merger of

compact objects like neutron stars and black holes (for a review of SHGRBs, see *e.g.* [35]). Other types of classifications, including those with more of a physical than phenomenological motivation, have been proposed (*e.g.* [36]). Very short GRB (VSGRB) may originate from the evaporating Primordial Black Holes [37].

The recent progress in SHGRBs is extremely exciting. As of this writing, however, only about \sim 20 SHGRBs have had UV/optical measurements often with only one measurement above background, and thus suffer from poor time resolution in their light curves. Two measurements during the decay period are required to determine the most rudimentary decay time constant, assuming a power-law decay. The rise phase of SHGRB optical emission is not observed in most cases. What is the shape of the rise? Is the shape homogeneous? The rise time may give rich information including the size of the system and the surrounding environment. The physical origin of this type of burst remains an outstanding mystery, so any hints as to this origin would be extremely valuable. Is there any prompt UV/optical emission from such events? What would we see if we observed more of these events in the sub-minute or sub-second regime? Are there ultra-short events on the accretion disk dynamical time scale of compact objects (that are beamed so we can see them)? Earlier observations would answer these questions and open a new window probing compact object structure, populations, and evolution.

4.3 Dark GRBs

Dark GRBs are those that stand out as having a very faint optical signal compared to X-ray afterglow. Only recently, extinction has been found to be the dominant source of dark GRBs [38]. An alternative scenario, however, suggests that some dark GRBs are simply faded out faster for optical than X-ray emission [39]. In this scenario, the optical emission fades in less than \sim 102 sec, so that most observations would not detect the optical afterglow. Better short time scale observations would shed light on this two-mechanism model.

4.4 Physical time scales in compact objects

In a more general sense, resolving the light curve peak time at any epoch gives a hint of the most important physical processes in that epoch. Coalescence of neutron star and black hole systems are features of a number of GRB models, particularly models for the less understood short GRB. The light crossing time of outer accretion disk bounds, the dynamic time scales of large accretion disk systems, and other time scales are in the sub-minute regime, requiring rapid response for their measurement. The time scales of jet formation or deceleration in these smaller systems may also be in this time regime.

4.5 Emission processes by cross-correlations

Another general tool that rapid-response observations afford is the correlation of light curves from different bands. If complex light curves in different bands have a

clear correlation, this is a very strong argument for a physical linkage between the processes of emission in the two wave bands. The delay between the light curves gives further information about both processes [21]. Referring to the correlation of rapid-response light curves accidentally observed earlier, it is intriguing that early UV/optical light curves show good correlation to their X/ γ light curves (GRB 041219 [40], GRB 080319B [21]), yet others do not (GRB 990123 [40]). Is this a clue to additional processes, or a hint that the origin of these GRBs is quite different, *i.e.* SN Ia *vs.* Ib? What will we see if we can extend these correlations of early emission to SHGRB?

4.6 *Emission processes by spectral slope*

The broad-band spectra of GRBs can be modeled by power laws evolving in time. Chromatic and achromatic jet breaks are important predictions/distinguishing features of models. One feature is the well-known transition from relativistic to non-relativistic emission, the transition from “prompt” emission to afterglow. The change in spectral slope, and the time of this change, are therefore important diagnostics of the interaction of the jet and the surrounding medium, and/or injection of additional energy into the jet. The broad-band spectral slope itself is a discriminator of the electron energy distribution, magnetic field, and other features of the emission mechanism.

4.7 *Test of shock models with bulk lorentz factor*

Measurement of early UV/optical emission can serve as a probe of the physical conditions in the GRB fireball at short times. A simple, nearly model-independent argument [41] shows that the bulk Lorentz factor depends on the time of the early UV/optical emission peak. Measurement of the peak will therefore provide a measurement of the bulk Lorentz factor.

4.8 *Identification of internal shock via fast variability*

Currently, UV/optical emission at early times in typical bursts is believed to come from external shocks, and predicted to have a smooth, monotonic rise (*e.g.* see [42] and references therein). Observation of an early time UV/optical light curve that more closely resembles a gamma-X light curve, jagged, and with multiple peaks, would clearly indicate the presence of prompt optical emission produced by internal shock. Sub-minute measurements would be required to learn more about such prompt emission.

4.9 *Multi-messenger and fundamental physics*

The coming generation of gravitational wave observatories should regularly detect the coalescence of binary compact systems, the favored scenario for SHGRBs.

This will open an entirely new field of astronomy. Because of its novel nature, corresponding UV/optical measurements will be highly important to interpret the astrophysics of the event. Moreover, while gravitational wave signals from binary system inspirals have the potential to yield highly accurate distance measurements, they alone cannot break the degeneracy in parameters to yield the redshift – this requires observation of an electromagnetic counterpart such as the GRB. Fast-response optical observations can test Lorentz violations from the time delay between different energy photons, or between photons and neutrinos or early emission with GW. Such a fast-response would be essential for deep understanding of compact objects and cosmology [43].

5 The UFFO program

The UFFO will respond to initial photons within a fraction of a second, the hitherto unexplored time domain after the burst of GRB by using the concept of SMT's fast or ultra-fast slewing mirror technology. The UFFO project will be carried out in a series of relatively light payloads to be accommodated readily to micro or small satellites. The first is UFFO-pathfinder that will be flown aboard the *Lomonosov* spacecraft in 2013. Though the pathfinder is a small and limited, it could be the observational cornerstone of future mission development for rapid responses. The next upgrade version, UFFO-100 with its payload mass of 120 kg and 40 cm telescope aperture, is expected to launch in 2018. The UFFO-100 will extend its measurement capability to near-IR (NIR) using dichroic beam splitter on the SMT optics bench. We will demonstrate that such a small mass payload is useful to make major advances in GRB science.

5.1 UFFO-pathfinder

The main constraints for inclusion in *Lomonosov* are 20 kg total instrument mass and 800 cm maximum length. Therefore, the system of the UFFO-pathfinder was designed to (i) fit the constraints of the *Lomonosov* spacecraft, (ii) use all proven technologies and (iii) to be available for fast delivery. The payload consists of two instruments: SMT for rapid coverage of UV/optical sky and UBAT (UFFO Burst Alert and Trigger Telescope) for X-ray triggers and GRB localization. We have designed a small telescope to provide imaging measurements using a gimbal beam-steering system in SMT described above. UBAT is a wide-field coded mask camera similar to that of the *Swift* BAT scaled to fit the available mass and size requirements.

The UFFO-pathfinder has passed space environments test, including thermal, vacuum, shock, and vibrations, successfully at National Space Organization of Taiwan (NSPO) in August 2011. The final integration of the flight model to the *Lomonosov* spacecraft and space environments test is currently under way at a branch of Roscosmos (see Fig. 3).

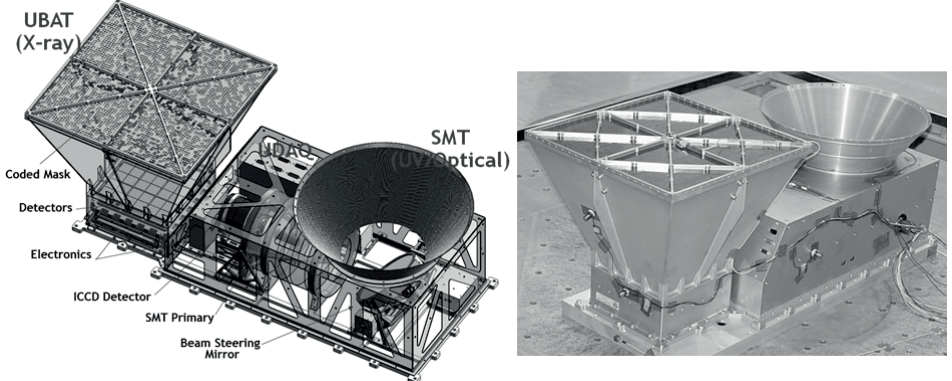


Fig. 3. A rendering of integrated UFFO Pathfinder (*left*) and fabricated flight model (*right*).

As a subsystem of UFFO-pathfinder, the SMT is designed for fast observation of the prompt UV/optical photons from GRBs. The SMT/UFFO-pathfinder uses a gimbal system which provides 1 sec response over the entire FOV of UBAT, $90.2^\circ \times 90.2^\circ$. Electric motors driving gimbal-mounted mirrors are a fundamentally simple and robust technology. For UFFO-pathfinder we used off-the shelf encoders and motors and have already obtained sub-arcsecond settling over $+/-90$ degrees with $t < 1$ sec travel + settle time. The SMT optics includes a Ritchey-Chretien telescope with a 100 mm diameter aperture. Its field of view is 17×17 arcmin 2 . The focal detector is an Intensified Charge-Coupled Device (ICCD) with a pixel size of 4×4 arcsec 2 and a wavelength sensitive to $200 \sim 650$ nm. The ICCD operates in photon counting mode and could observe faint objects up to ~ 19 magnitude B-star in white light per 100 sec, assuming the same performance as *Swift* and the background estimated by *Swift*. The SMT has the readout rate of 20 msec and can take 50 frames per second. Two identical flight models of SMT have been built and delivered. The details of SMT can be found in [44].

Numerous instruments have used coded-mask aperture shadow cameras (*e.g.* BATSE/*CGRO* [27], *BeppoSAX* [28], HETE-2 [29], *Integral* [30], and *Swift* [31]) to determine positions of GRBs. With the time constraint to meet the launch schedule as well as mass and power constraints for UBAT (only approximately 10 kg and 10 W), we adopted a well-established coded-mask technique similar to *Swift* BAT but scaled down for the localization of bright, transient X-ray sources. In order to respond over a wider energy range, *e.g.* $15 \sim 150$ keV, however, we used pixellated YSO scintillating crystal red out by 36 64-ch multi-anode photo-multiplier tubes (MAPMTs) with 36 64-ch SPACIROC ASICs. With only 191 cm 2 of detecting area, our collaboration has made a viable camera with which we expect to detect dozens of GRBs per year. The details of UBAT are described in [45].

The rate of burst trigger depends on the fluence of X-rays. The X-ray flux of typical burst would be one per sec per cm², while backgrounds are two or three per sec per cm². *Swift* can trigger (rate trigger) GRBs typically with 50 msec of X-rays collection. The UBAT detection area is smaller than BAT by factor 25, so it needs 25 times longer collection time for the same burst. The UBAT will require longer collection time up to 64 sec, depending on the brightness of GRBs. Therefore, our estimate is to observe 60% of BAT bursts typically with about 1.5 sec of collection time, if the orbit is same. On the other hand, larger detection area improves the localization accuracy, *i.e.* BAT can localize bursts at 90% probability to a region 1 ~ 4 arcmin. The UBAT will be able to localize bursts at the confidence level of 7σ to a region 10 arcmin across, thus contained fully within the FOV of the SMT. It is noted that it takes only less than a second to determine the position of GRB, using a dedicated FPGA (Field Programmable Gate Array) for “imaging trigger”.

The UFFO Data Acquisition (UDAQ) is in charge of central control of the payload not only with preset commands but upload commands from the ground; interfacing to the spacecraft; data collection from SMT and UBAT, storing in several NOR flash memories and transfer to the spacecraft. It is also responsible for monitoring of all housekeeping parameters; calculation of the orbit and recognition of day and night with its photosensors; arbitration and prioritization of triggers from UBAT and BDRG (another Fermi-like payload of Lomonosov); power management, etc.. All of these functions are implemented in an ACTEL FPGA for the low power consumption and fast real-time processing. As mentioned, trigger calculations with the data from UBAT, including rate trigger and imaging trigger, are also performed in another ACTEL FPGA, which reduces the latency significantly, *e.g.* below 1 sec.

5.2 UFFO-100

Awaiting the completion and launch of the UFFO-pathfinder, the UFFO collaboration has been exploring its next step, a more ambitious project: UFFO-100 (named indicating the mass of payload), based on the same design principle but with total mass larger than 100 kg.

The great instrumental challenge of the UFFO concept is to see changes in the optical light curve on short time scales, which requires short exposures. Therefore, the aperture size of the instrument is the fundamental limitation on both the total number of GRB that may be detected, and the time resolution. GRB gamma-ray light curves, even the longer-duration class, have high amplitude variability at every observed time scale. Comparison of the variability between the gamma-X bands and the optical bands can tell us a great deal about the emission physics at the source. Thus far, with the most rapid optical measurements available, it is not known whether gamma-X and optical emission correlates, has lags, or perhaps correlates only in certain types of bursts. There is simply not enough

short time scale data. The UFFO-100 will answer such an intriguing question of “What would *Swift* have seen if it could have responded faster?”, with the slewing mirror telescope of an aperture 40 cm as large as that of *Swift*, but with several enhancements to make it even more sensitive and productive, enabling detections at even shorter time resolution.

Though some enhancements may be restricted by the precise restrictions of payload, UFFO-100 would afford a 1024 cm² X-ray camera but improved detector technology. The goal is to finally integrate the MMA technology with the motorized slewing mirror and to add a NIR-sensitive camera and specific optical instrumentation to detect the distinguished bursts. The UV/optical and NIR cameras, both with 17 arcmin fields, use the incoming beam from the SMT after being split from a dichroic. Much of the instrumentation, particularly the electronics, will be built on the heritage of UFFO-pathfinder. The pathfinder basic telescope design, fast-mode beam steering, spacecraft bus interface, and data acquisition system architecture will be shared with UFFO-100. We expect UFFO-100. to be flown as one of the scientific payloads of the Russian Resurs-P3 satellite in 2018. The comparison of two payloads performance together with *Swift* is shown in Table 1.

6 Summary

We propose two space missions implementing the UFFO approach in order to investigate a new area of gamma-ray burst phase space both quantitatively and qualitatively. The UFFO equipped with SMT has an extraordinary capability by permitting the first ever systematic study of GRB UV/optical/NIR emission, for example 1 sec after trigger for UFFO-pathfinder and far earlier than 1 sec after trigger for UFFO-100. Our fundamental science objective is to use our ability to probe this new, very early emission parameter space to make measurements of and thoroughly investigate the rise phase of GRB, which is thus far only occasionally observed. In the time domain, this improves on *Swift*’s response by several orders of magnitude. In the spectral domain, we will improve on *Swift*’s sensitivity by ~ 2.5 mag (assuming the power-law light curve extends at very early times), and we expect to detect afterglow components that are invisible to *Swift* because of extinction.

The UFFO-pathfinder has now entered the final stage of completion, heading for launch onboard *Lomonosov* satellite in 2013. The pathfinder is a small and limited, yet remarkably powerful micro-observatory for rapid optical response within 1 sec after X-ray trigger to bright gamma-ray bursts. Its sub-minute measurements of the optical emission of dozens of GRB each year will result in a more rigorous test of current internal shock models, probe the extremes of bulk Lorentz factors, provide the first early and detailed measurements of fast-rise GRB optical light curves, and possibly test the prospect of GRB as extreme z cosmological probes. We foresee not only its exciting findings but the proof-of-principle of this new approach for future GRB telescopes.

Table 1. Major parameters and expected performance of UFFO payloads together with Swift.

	Parameter or performance	UFFO-pathfinder	UFFO-100	<i>Swift</i>
X-ray	Detector	YSO crystal + MAPMT	(Silicon strip) and (Crystal + MAPMT or SiPM)	CdZnTe
	UBAT Field of View (half coded)	$90.2 \times 90.2 \text{ degree}^2$ (1.8 sr)	$90.2 \times 90.2 \text{ degree}^2$ (1.8 sr)	$100 \times 60 \text{ degree}^2$ (1.4 sr)
	X-ray detection area	191 cm^2	1024 cm^2	5240 cm^2
	X-ray detection element	$48 \times 48 \text{ pixels}$	$64 \times 64 \text{ pixels}$	256×128
	X-ray pixel size	$2.8 \times 2.8 \text{ mm}^2$	$2 \times 2 \text{ mm}^2$	$4 \times 4 \text{ mm}^2$
	X-ray sensitivity	15 – 150 keV	5 – 300 keV	15 – 150 keV
	GRB localization error	10 arcmin	4 arcmin	$1 \sim 4 \text{ arcmin}$
UV/optical/NIR	X-ray collection time/ GRB position calculation time	1 – 64 sec / 1 sec	1 – 64 sec / 1 sec	1 – 64 sec / 5 – 7 sec
	Telescope type	Ritchey-Chrétien + Slewing mirror	Modified Ritchey-Chrétien + Slewing mirror	Modified Ritchey-Chrétien
	Telescope Aperture	10 cm	40 cm	30 cm
	Field of View	$17 \times 17 \text{ arcmin}^2$ over $70 \times 70 \text{ degree}^2$	$17 \times 17 \text{ arcmin}^2$ over $90 \times 90 \text{ degree}^2$	$17 \times 17 \text{ arcmin}^2$
	Wavelength range	200 nm – 650 nm	200 nm – 1100 nm	170 nm – 650 nm
	Number of pixels	256×256	256×256	256×256
	Physical pixel scale	4 arcsec	4 arcsec	4 arcsec
SMT	SMT data taking start time after trigger	1 sec	1 msec – 1 sec	40 – 200 sec, typically 80 sec

This work is supported by Creative Research Initiatives program (RCMST) of MEST/NRF. IP, EL, GS, HL are members of IEU, which is funded by the WCU program (R32-2009-000-10130-0). VL and ACT acknowledge the financial support from the Spanish MINECO project AYA 2009-14000-C03-01/ESP, and PC Taiwan's National Science Council Vanguard Program (100-2119-M-002-025), MP Program of development of Lomonosov Moscow State University. We thank Nauchno-issledovatel'skij institut elektromekhaniki (NIIEM) of Russia and the National Space Organization (NSPO) of Taiwan for their support in the numerous tests of our instruments for space qualification. Our special thanks to Dr. Yang of KRISS and H.K. Lee of Samsung Electronics for their assistance in the design and manufactures SMT mirrors.

References

- [1] Fishman, G.J., 1994, ApJS, 92, 229
- [2] Boella, G., Butler, R.C., Perola, G.C., *et al.*, 1997, A&AS, 122, 299
- [3] Ricker, G., Hurley, K., Lamb, D., *et al.*, 2002, ApJ, 571, L127
- [4] Winkler, C., Courvoisier, J.-L., Di Cocco, G., *et al.*, 2003, A&A, 411, L1
- [5] Gehrels, N., Chincarini, G., Giommi, P., *et al.*, 2004, ApJ, 611, 1005
- [6] Perna, R., Lazzati, D., Fiore, F., *et al.*, 2003, ApJ, 585, 775
Oates, S.R., Page, M.J., Schady, P., *et al.*, 2009, MNRAS, 395, 490
Perley, D.A., Bloom, J.S., Klein, C.R., *et al.*, 2010, MNRAS, 406, 2473
- [7] Paul, J., Wei, J., Basa, S., *et al.*, 2011, Comptes Rendus Physique, 12, 298
- [8] Roming, P.W.A., Bilen, S.G., Burrows, D.N., *et al.*, 2012, Memorie della Societa Astronomica Supplement, 21, 155
- [9] Produit, N., Barao, F., Deluit S., *et al.*, 2005, Nucl. Instr. Meth. A, 550, 616
- [10] Costa, E., Frontera, F., Heise, J., *et al.*, 1997, Nature, 387, 783
Kann, D.A., Klose, S., Zhang, B., *et al.*, 2011, ApJ, 734, 96
- [11] Ellis, J., Mavromatos, N.E., Nanopoulos, D.V., *et al.*, 2006, AP, 25, 402
- [12] Kostelecky, V.A., & Mewes, M., 2008, ApJ, 689, L1
- [13] Park, I.H., Grossan, B., Lim, H., *et al.*, 2009 [[arXiv:0912.0773](https://arxiv.org/abs/0912.0773)]
- [14] Barthelmy, S.D., 2004, Proc. SPIE, 5165, 175
- [15] Akerlof, C.W., Kehoe, R.L., McKay, T.A., *et al.*, 2003, PASP, 115, 132
- [16] Vestrand, W.T., Borozdin, K.N., Brumby, S.P., *et al.*, 2002, Proc. SPIE, 4845, 126
- [17] Bloom, J.S., Starr, D.L., Blake, C.H., *et al.*, 2006, ASP Conf. Ser., 351, 751
- [18] Williams, G.G., Park, H.S., Barthelmy, S.D., *et al.*, 2004, AIP Conf. Proc., 727, 723
- [19] Jelinek, M., Castro-Tirado, A.J., Postigo, A.U., *et al.*, 2010, Adv. Astron., 432172
- [20] Akerlof, C., Balsano, R., Barthelmy, S., *et al.*, 1999, Nature, 398, 400
- [21] Racusin, J.L., Karpov, S.V., Sokolowski, M., *et al.*, 2008, Nature, 455, 183
- [22] Beskin, G., Bondar, S., Karpov, S., *et al.*, 2010, Adv. Astron., 171569
- [23] Burd, A., Cwiok, M., Czyrkowski, H., *et al.*, 2005, New Astron., 10, 409
- [24] Aptekar, R.L., Frederiks, D.D., Golenetskii, S.V., *et al.*, 1995, Space Sci. Rev., 71, 265
- [25] Roming, P.W.A., Kennedy, T.E., Mason, K.O., *et al.*, 2005, Space Sci. Rev., 120, 95
- [26] Kim, M., Park, J.H., Jeon, J.A., *et al.*, 2009, J. Micromech. Microeng., 19, 035014
- [27] Park, J.H., Garipov, G.K., Jeon, J.A., *et al.*, 2008, Opt. Express, 16, 25, 20249

- [28] Nam, S., *et al.*, 2008, Nucl. Instr. Meth. A, 588, 197
Yoo, B.W., Park, J.H., Park, I.H., *et al.*, 2009, Opt. Express, 17, 5, 3370
- [29] van Paradijs, J., Groot, P.J., Galama, T., *et al.*, 1997, Nature, 386, 686
- [30] Tanvir, N.R., Fox, D.B., Levan, A.J., *et al.*, 2009, Nature, 461, 1254
- [31] Panaitescu, A., & Vestrand, W., 2008, MNRAS, 387, 497
- [32] Kouveliotou, C., Meegan, C.A., Fishman, G.J., *et al.*, 1993, ApJ, 413, L101
- [33] Zhang, F.-W., Shao, L., Yan, J.-Z., *et al.*, 2012, ApJ, 750, 88
- [34] MacFadyen, A.I., & Woosley, S.E., 1999, ApJ, 524, 262
- [35] Nakar, E., 2007, Physics Reports, 442, 166
- [36] Norris, J.P., & Bonnell, J.T., 2006, ApJ, 643, 266
- [37] Cline, D.B., Otwinowski, S., Czerny, B., *et al.*, 2011 [[arXiv:1105.5363](https://arxiv.org/abs/1105.5363)]
- [38] Perley, D.A., Cenko, S.B., Bloom, J.S., *et al.*, 2009, AJ, 138, 1690
- [39] Groot, P.J., Galama, T.J., Vreeswijk, P.M., *et al.*, 1998, ApJ, 502, L123
- [40] Vestrand, W.T., Wozniak, P.R., Wren, J.A., *et al.*, 2005, Nature, 435, 178
- [41] Molinari, E., Vergani, S.D., Malesani, D., *et al.*, 2007, A&A, 469, L13
- [42] Piran, T., 2004, Rev. Mod. Phys., 76, 1143
- [43] Stoldosky, L., 2000, Phys. Lett. B, 473, 61
- [44] Jeong, S., Nam, J.W., Ahn, K.B., *et al.*, 2013, Opt. Express, 21, 2, 2263
- [45] Jung, A., Ahmad, S., Ahn, K.B., *et al.*, 2011 [[arXiv:1106.3802](https://arxiv.org/abs/1106.3802)]
Kim, J.E., Lim, H., Jung, A., *et al.*, 2011 [[arXiv:1106.3803](https://arxiv.org/abs/1106.3803)]
Na, G.W., Ahn K.B., Choi, H.S., 2011 [[arXiv:1106.3804](https://arxiv.org/abs/1106.3804)]

THE ULTRA FAST FLASH OBSERVATORY PATHFINDER – UFFO-P GRB IMAGING AND LOCATION WITH ITS CODED MASK X-RAY IMAGER UBAT

P.H. Connell¹ and V. Reglero¹, on behalf of the UFFO collaboration

Abstract. The UFFO pathfinder mission will attempt to locate the optical afterglow of a GRB within seconds of its detection and location by a wide field X-ray imager. It will be mounted on the Lomonosov spacecraft for launch in 2013 and consists of a coded mask X-ray imager UBAT to detect a GRB and estimate a direction vector which will be passed to the SMT optical system which will rotate a moveable mirror to lock onto the GRB and direct the optical afterglow to a camera with a $\sim 17'$ wide aperture. We present the design geometry of the UBAT instrument only, with results of simulations for a range of GRB types to show probable photon integration times to be expected to extract a significant FOV image reconstruction and GRB location.

1 Introduction

The Ultra Fast Flash Observatory pathfinder is designed to observe GRB light curves within seconds, or minutes at most first with an X-ray imager to detect a GRB and estimate, within a $\pm 32 \times 32^\circ$ FOV, its local direction vector – which is then passed to a slewing optical camera SMT which will then record the subsequent GRB light curve. Construction and functional details of UBAT, SMT, their electronics and triggering have been described in other papers (Jung *et al.* 2012) from the UFFO collaboration and will not be discussed further – we present here only imaging methods and the theoretical imaging location performance to be expected from an instrument like UBAT.

2 UBAT detector-mask configuration and correlation imaging

UBAT has two principle components – a detector array and a coded mask – whose geometrical configuration is shown in Figure 2 (left). The detector is *logically*

¹ University of Valencia, Spain

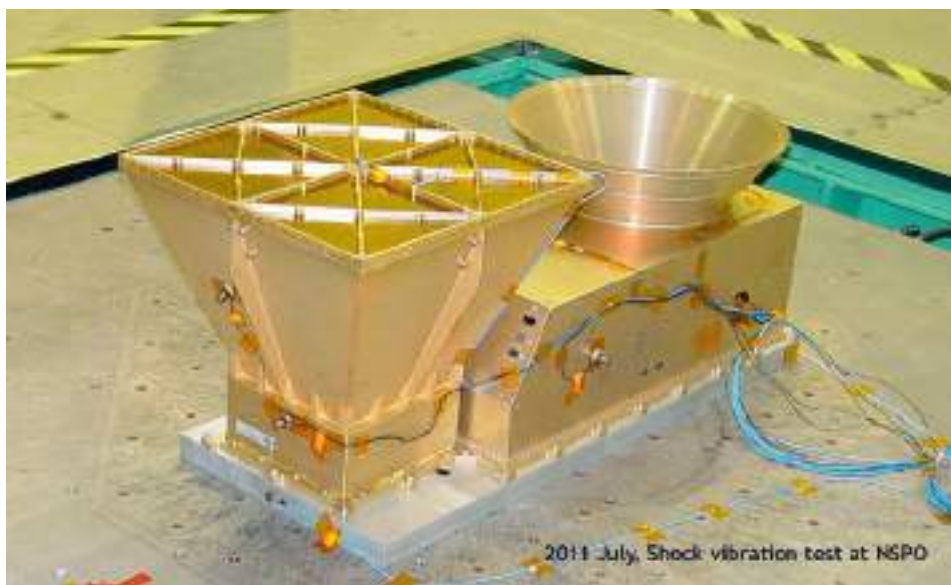


Fig. 1. The UBAT coded mask X/ γ -ray imager (*left*) and SMT optical camera (*right*) on UFFO.

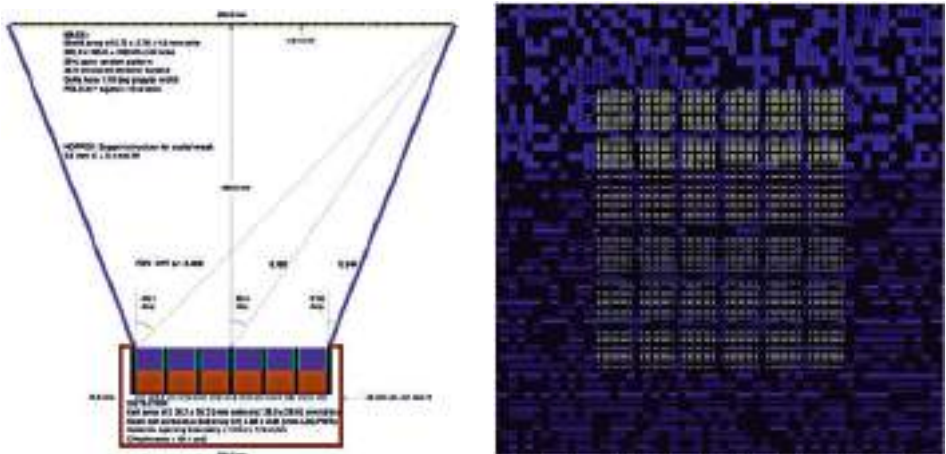


Fig. 2. The UBAT detector-mask configuration (*left*) and detector-mask shadow geometry (*right*).

a 48×48 array of 2.88×2.88 mm square YSO cells – but is *physically* a 58×58 array, with 5 pairs of inactive columns and rows.

The coded mask is a 68×68 array of $5.76 \times 5.76 \times 1.0$ mm square Tungsten elements in a random pattern, with a $\sim 50\%$ open fraction. It will cast a variable

illumination pattern (or shadowgram) on the detector array below it, depending on the location of a γ -ray or X-ray point source in the instrument field of view above. The mask pattern, and a subset of it which will illuminate the 58×58 detector array due to an on-axis source is shown in Figure 2 (right).

A source in the UBAT FOV will cast a unique random illumination pattern on the detector array, and its location – as a vector offset from the detector centre – can be found simply by moving the detector pattern over the mask hole pattern to find the best correlation as shown in Figure 3 (left).

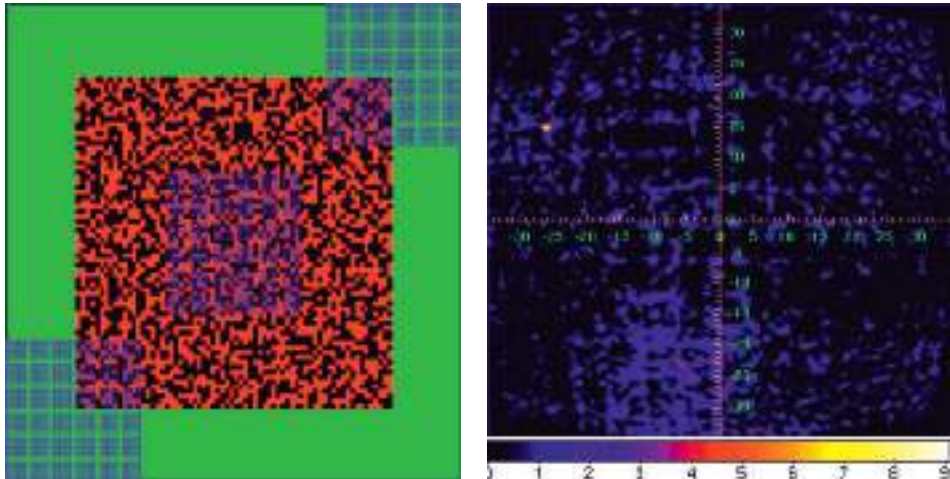


Fig. 3. Detector-mask correlation possibilities (*left*) typical correlation image extracted (*right*).

The location of a GRB must be done in real time and using Freely Programmable Gate Arrays (FPGA) imbedded in the onboard DPU – therefore the imaging algorithm used will require a fixed system of mask and image arrays to minimize processing time. Arrays used will have a pixel size of the detector cell dimensions of 2.88 mm to avoid any floating point calculations when correlating one array with another.

The array system used for image reconstruction is shown above in Figure 3 (left) where the 68×68 coded mask pattern pixels are embedded as a 136×136 array of (red-black) pixels – with values of (0,1) – in a 192×192 array of zeroes (green). To find a location where a 58×58 detector pattern (excluding dead columns/rows) has the best correlation with a 58×58 mask pattern subset, the detector-array is simply shifted stepwise on all possible locations within the 192×192 array, and at each step a correlation is made with the aim of finding that with a maximum signal-to-noise-ratio (SNR).

It can be seen that the 58×58 detector pattern has only one array of 135×135 possible correlation positions and this constitutes a ***raw correlation image*** made up of a quasi- uniform background (or DC-level) with an image peak, or

maximum, projecting out at the location corresponding to that of the GRB in the FOV.

The raw correlation image $C[i,j]$ can be calculated most simply as follows

$$C[i,j] = \sum_{d,e} M[i+d, j+e] * D[d, e]$$

$C[i,j]$ ($i,j = 0,134$) are correlation image pixel values

$M[m,n]$ ($m,n = 0,191$) are mask pattern values of (0,1)

$D[d,e]$ ($d,e = 0,57$) are detector array pixel values.

Another modification of this to subtract out any image background or DC-level is

$$C[i,j] = \sum_{d,e} \{ M[i+d, j+e] - O[i, j] \} * D[d, e]$$

where $O[i,j]$ is the open fraction, of detector pixels which correspond to a mask hole, and usually fluctuates around a value of 0.5. When $D[d,e]$ is uniform $C[i,j]$ is about zero.

The background in this image fluctuates - image noise - with some standard deviation and with this a second ***SNR correlation image*** can be created - this image is then scanned to find the pixel location of the peak with the largest SNR.

From this pixel location an offset vector from the centre of the image is calculated and with the addition of the height of the mask above the “detector interaction plane” a 3D direction vector for the GRB can finally be extracted. When this calculation is applied to each pixel in the raw SNR image a FOV zenith image shown in Figure 3 (right) can be created, showing clearly the angular location of the GRB.

It is to be noted the FOV-axis of UBAT will not be constant during the 10–100 seconds expected duration of GRB pulses – because the Lomonosov carrier spacecraft will be constrained to point its Z-axis along an earth radial, causing the FOV-axis of UBAT to rotate continuously at ~ 3.75 arcmin/sec. Therefore correlation imaging will be made in steps of 0.5 second intervals and each new correlation image will be given a spatial rotation to compensate for the FOV movement and accumulated in a **raw correlation image** which will be in a reference system of the time the GRB was triggered.

3 Evolution of image peak signal-to-noise-ratio with time

Correlation imaging takes place in intervals of 0.5 seconds to compensate for any FOV movement but also to examine the accumulated raw correlation image to decide if the SNR peak is significant enough to decide if the GRB has been located. Further imaging is then stopped, a more accurate centroid location of the correlation image SNR peak can be calculated and a final GRB direction can be passed to the SMT for slewing operations to record the GRB optical lightcurve.

It is therefore of interest to know how the SNR of the image peak in the accumulated raw correlation image evolves to decide on the correct criteria to

stop imaging and calculate a final GRB direction vector in the minimum possible time.

In Figure 4 below are plotted the results of four separate simulations of correlation imaging for UBAT observations of a GRB pulse of width 30 seconds (a mean value observed) and mean pulse flux values of 2,4,8,16 ph/cm²/sec to show how the SNR of the image peak varies with time. Each of the four colours plotted shows the repetition of 10 Monte Carlo simulations to show the statistical variance in any SNR curve.

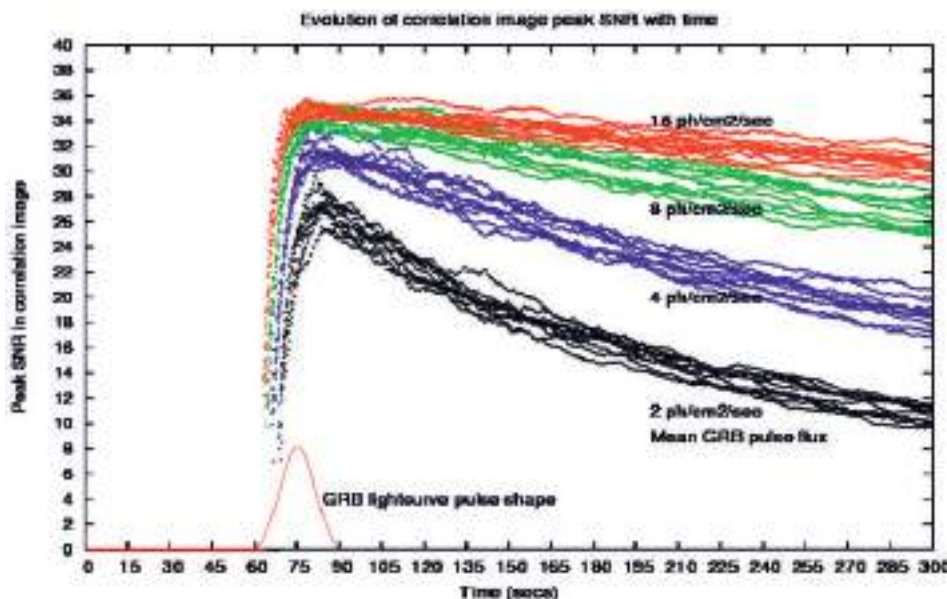


Fig. 4. Time evolution of the SNR of the correlation image peak for GRBs of different strength.

Each curve shows that the SNR increases to a maximum with a variable fall off to zero as no further GRB flux is accumulated in the correlation image – only background noise.

More important is that the maximum SNR asymptotes to a value of ~ 36 which is due to the fact UBAT uses a random coded mask pattern. In this case any 58×58 subset of the mask pattern will give a maximum correlation at one location on the mask and a lesser ($\sim 50\%$) flat but fluctuating value at all other mask locations. This means the ratio of the maximum correlation value to the standard deviation of the flat pixel fluctuations will be finite, ~ 37 in the case of the UBAT mask pattern – a systematic error so that the correlation image peak SNR will never increase uniformly with GRB flux strength.

4 GRB imaging location time as a function of pulse width

Examination of the image peak SNR evolution curves in Figure 4 above shows, for a 30 second pulse width an peak SNR of ~ 10 can be attained within 2–10 seconds of trigger time depending on the GRB flux strength.

Further simulations were made for a range of GRB pulse width values covering 2–120 seconds. In Figure 5 below is a plot showing the distribution of GRB “imaging location times” for each pulse width – for an image peak SNR threshold value of 10 – and repeated 10 times to show the statistical variation.

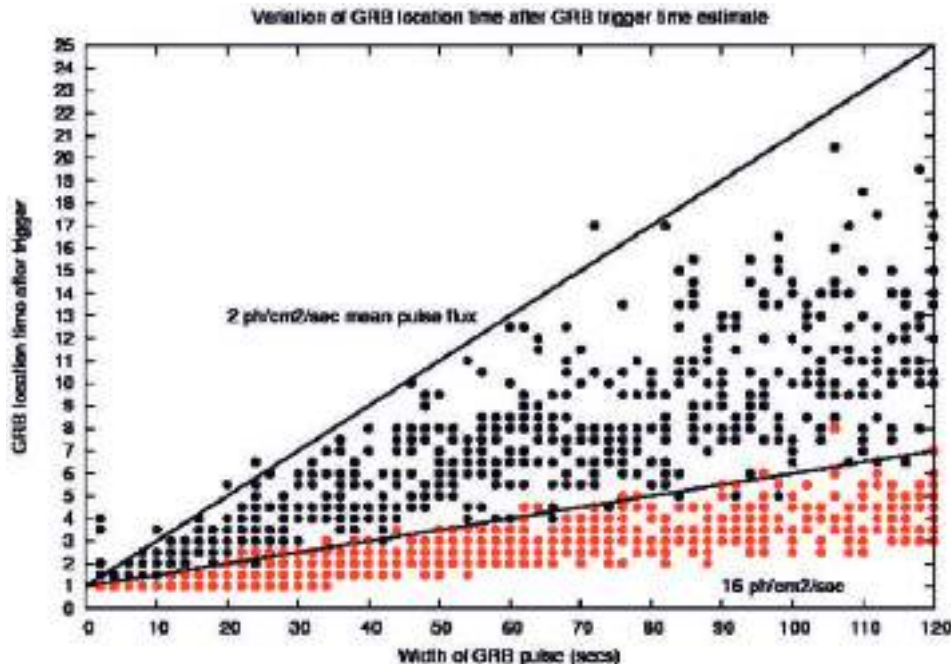


Fig. 5. The distribution of GRB imaging location time for weak and strong GRB flux values.

5 Conclusion

From repeated Monte Carlo simulations of the UBAT coded mask imager using the 0.5 second stepwise correlation imaging procedure described above we can derive its correlation image peak SNR evolution curves, as a function of GRB mean flux strength.

We can also estimate probable GRB “imaging location times”, depending on the GRB flux strength and pulse width. An example of the performance of UBAT for an expected weak GRB mean flux of $\sim 2 \text{ ph}/\text{cm}^2/\text{sec}$ shows a GRB location

time with an order of magnitude of $\sim 5 \pm 2$ secs for a pulse width of ~ 30 secs, and $\sim 16 \pm 9$ secs for longer pulse widths of ~ 120 secs.

This is still a work in progress and will be repeated in greater detail when the final UBAT detector response matrix at launch for UBAT becomes available.

References

- Jung, A., Ahamad, A.S., Barrillon, P., *et al.*, 2012, Design and implementation of electronics and data acquisition system for Ultra-Fast Flash Observatory, Proceedings GRB 2012 Symposium (Marbella, Spain, Oct. 2012)

DESIGN, CONSTRUCTION AND PERFORMANCE OF THE DETECTOR FOR UFFO BURST ALERT & TRIGGER TELESCOPE

J. Lee¹, S. Jeong¹, J.E. Kim¹, Y.W. Kim¹, G.W. Na¹, J.E. Suh¹,
M. Kim², H. Lim², I.H. Park², J. Ripa², J.N. Choi³, S.-W. Kim³,
Y.J. Choi⁴, K.W. Min⁴, P. Chen⁵, J.J. Huang⁵, T.-C. Liu⁵, J.W. Nam⁵,
M.-Z. Wang⁵, M.-H.A. Huang⁶, P. Connell⁷, C. Eyles⁷, V. Reglero⁷,
J.M. Rodrigo⁷ and A.J. Castro-Tirado⁸

Abstract. One of the key aspects of the upcoming Ultra-Fast Flash Observatory (UFFO) pathfinder for Gamma Ray Bursts (GRBs) identification is the UFFO Burst Alert & Trigger Telescope (UBAT). The scientific propose of UBAT is to detect and locate as fast as possible the GRBs in the sky. This is achieved by using a coded mask aperture camera scheme with a wide field of view (FOV) and selecting a X-ray detector of high quantum efficiency and large detection area. This X-ray detector of high quantum efficiency and large detection area is called the UBAT detector. The UBAT detector consists of 48×48 Yttrium Oxyorthosilicate (YSO) scintillator crystal arrays and Multi Anode Photomultiplier Tubes (MAPMTs), analog electronics equipped with ASIC chips, digital electronics equipped with Field Programmable Gate Array (FPGA) chips, and a mechanical structure that supports all components of the UBAT detector. The total number of the pixels in the UBAT detector is 2304, and the total effective detection area is 191 cm^2 . We will present the design and construction, and performance of the UBAT detector including the responses of the UBAT detector to X-ray sources.

¹ Department of Physics, Ewha Womans University, Seoul, Korea

² Department of Physics, Sungkyunkwan University, Suwon, Korea

³ Department of Astronomy, Yonsei University, Seoul, Korea

⁴ Department of Physics, Korea Advanced Institute of Science and Technology, Daejeon, Korea

⁵ LeCosPA, National Taiwan University, Taipei, Taiwan

⁶ National United University, Miao-Li, Taiwan

⁷ University of Valencia, Valencia, Spain

⁸ Instituto de Astrofisica de Andalucia, CSIC, Granada, Spain

Table 1. Specifications of the UBAT.

Mass	10 kg
Power consumption	10 W
Volume	400(L) \times 400(W) \times 382.5 (H) mm ³
Pixel size	2.88 \times 2.88 mm ²
Number of pixels	48 \times 48
Field of View	1.83 sr (90.2° \times 90.2°)
Energy range	15 – 150 keV
GRB location accuracy	\leq 10 arcmin for $>7\sigma$

1 Introduction

The prime scientific purpose of the Ultra-Fast Flash Observatory (UFFO) pathfinder is to observe the early UV/optical photons from GRBs (Park *et al.* 2013). The UFFO pathfinder was installed in the Russian Satellite *Lomonosov* which will be launched in 2013. The UFFO pathfinder has two key components. The one key component is the wide field of view X-ray telescope called the UFFO Burst Alert & Trigger Telescope (UBAT). The other key component is the UV/optical telescope equipped with a slewing mirror and also Ritchey-Chretien telescope. The UBAT is able to detect X-rays from GRBs, and then to determine the location of GRBs. The location of GRBs is passed to the SMT which rotates (*i.e. point*) its slewing mirror to the GRBs. The UV/optical lights will be directed to the on-axis of the Ritchey-Chretien telescope by the slewing mirror pointed to the GRBs which the source emitting the UV/optical lights. The UBAT telescope is described in this paper, and the description and detail of the SMT will be found elsewhere (Jeong *et al.* 2013).

2 Specification of the UFFO burst alert & trigger telescope

The UBAT will trigger GRBs and determine their locations by detecting X-rays from them. Its mass and power consumption is 10 kg and 10 W, respectively, due to the constraint given by the overall *Lomonosov* satellite mission. The specification of the UBAT is shown in Table 1.

3 Components and assembly of the UFFO burst alert & trigger telescope

The UBAT consists of the code mask, hopper and detector as shown in Figure 1. The coded mask is a tungsten plate with a random pattern of opens and blocks that transmit or stops X-rays from GRBs. The hopper, made of tungsten, supports the coded mask as well as the UBAT detector.

The UBAT detector consists of Yttrium Oxyorthosilicate (YSO) scintillator crystal arrays, Multi Anode Photomultiplier Tubes (MAPMTs), analog and digital

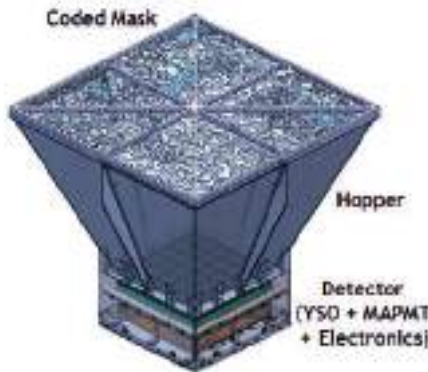


Fig. 1. The UFFO Burst Alert & Trigger Telescope.

electronics, and power board. Figure 2 shows the components of the UBAT detector. Either a YSO crystal array or a MAPMT has 64 pixels in the 8×8 array with the same pixel size of $2.88 \times 2.88 \text{ mm}^2$. The thickness of the YSO crystal is 3 mm. Each YSO crystal array is mounted on top of a MAPMT using optical glue. There are 36 pairs of the YSO crystal array and MAPMT in the 6×6 array in the UBAT detector. The YSO crystal array converts incident X-rays to the optical scintillating lights. The scintillating lights are then transmitted by refraction to the corresponding MAPMT where the lights are converted to photo-electrons in the photo-cathode. These photo-electrons are then multiplied by the factor of $\sim 10^6$ as the electrons travel along several dynodes inside the MAPMT. The multiplied electrons, *i.e.* charges, are fed to the analog Application Specific Integrated Circuit (ASIC) chips mounted on the analog board. The analog ASIC chips output the digitized photon counting and energy of X-rays. These digitized values of counting and energy of X-rays are transferred to the digital board, equipped with Field Programmable Gate Array (FPGA) chips, where the digital values are summed or subject to other digital operations. The power board produces the low voltage power for analog and digital electronics as well as the high voltage for MAPMTs. The UBAT detector, inside the full UBAT, after assembled with its components is shown in Figure 3.

4 Performance of the UFFO burst alert & trigger telescope

Am-241 radioactive sources emit X-rays of 60 keV energy. They also emits X-rays of low energy, and the average energy of these low energy X-rays is about 20 keV. Several Am-241 sources are placed upon the YSO crystal arrays to test the response of the UBAT detector. Figure 4 shows the clear response, *i.e.* photon counting, of the UBAT detector to eight collimated Am-241 sources. The accuracy in the X-ray source location of the UBAT is currently underway using an X-ray source at a far distance from the UBAT.

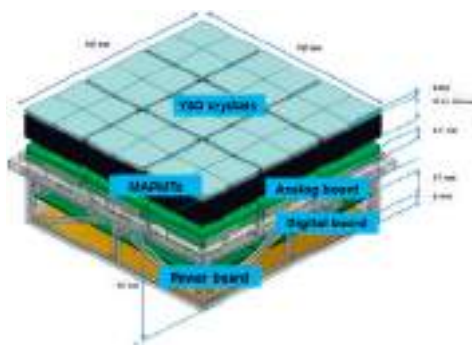


Fig. 2. The UBAT detector.



Fig. 3. The assembled UBAT and its detector.

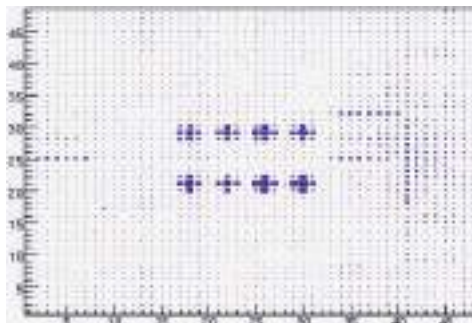


Fig. 4. The response of the UBAT detector to the collimated Am-241 X-ray source.

5 Conclusion

We have designed and constructed the UFFO Burst Alert & Trigger Telescope using a coded mask, Yttrium Oxyorthosilicate (YSO) scintillator crystal arrays,

Multi Anode Photomultiplier Tubes, and analog and digital electronics. The UBAT assembled with these components successfully demonstrated its X-ray detection capability for the energy range from 15 keV to 150 keV. It was integrated onto the Ultra-Fast Flash Observatory (UFFO) pathfinder, which was, in turn, installed onto the *Lomonosov* satellite. The UBAT is expected to detect X-rays from Gamma Ray Bursts and determine the location of tens of GRBs every year. The location of the GRBs will be passed to the SMT in the UFFO. The SMT will point its slewing mirror to the GRBs to detect the very early UV/optical photons from them, which is the unchartered area in the field of the GRB observation.

This research was supported by Basic Science Research Program through the National Research Foundation of Korea (NRF) funded by the Ministry of Education, Science and Technology (2010-0025056), Creative Research Initiatives (Research Center of MEMS Space Telescope) of MEST/KRF, and supported by World Class University (WCU) program through the National Research Foundation of Korea funded by the Ministry of Education, Science and Technology (R32-2009-000-10130-0) in Korea.

References

- Jeong, S., Nam, J.W., Ahn, K.B., *et al.*, 2013, Opt. Express, 21, 2263
Park, I.H., Brandt, S., Budtz-Jorgensen, C., *et al.*, 2013, New J. Phys., 15, 023031

THE CALIBRATION AND SIMULATION OF THE GRB TRIGGER DETECTOR OF THE ULTRA FAST FLASH OBSERVATORY

M.-H.A. Huang¹, S. Ahmad², P. Barrillon², S. Brandt³,
C. Budtz-Jørgensen³, A.J. Castro-Tirado⁴, S.-H. Chang⁵, Y.-Y. Chang⁶,
C.R. Chen⁵, P. Chen⁶, H.S. Choi⁷, Y.J. Choi⁸, P. Connell⁹,
S. Dagoret-Campagne², C. Eyles⁹, B. Grossan¹⁰, J.J. Huang⁶,
S. Jeong¹¹, A. Jung¹¹, J.-E. Kim¹¹, M.-B. Kim¹², S.-W. Kim¹³,
Y.-W. Kim¹², A.S. Krasnov¹⁴, J. Lee¹², H. Lim¹², C.-Y. Lin⁵,
E.V. Linder¹⁰, T.-C. Liu⁶, N. Lund³, K.W. Min⁸, G.-W. Na¹¹,
J.-W. Nam⁶, M.I. Panasyuk¹⁴, I.H. Park¹², V. Reglero⁹, J. Řípa¹²,
J.M. Rodrigo⁹, G.F. Smoot¹⁰, J.-E. Suh¹¹, S. Svertilov¹⁴, N. Vedenkin¹⁴,
M.-Z. Wang⁶ and I. Yashin¹⁴

¹ Department of Energy Engineering, National United University, Miao-Li, Taiwan;
e-mail: mahuang@nuu.edu.tw

² Laboratoire de l'Accélérateur Linéaire, University of Paris-Sud 11, Orsay, France

³ Technical University of Denmark, Copenhagen, Denmark

⁴ Instituto de Astrofísica de Andalucía, CSIC, Granada, Spain

⁵ National Space Organization, Taiwan

⁶ LeCosPA, National Taiwan University, Taipei, Taiwan

⁷ Korea Institute of Industrial Technology, Cheonan, Korea

⁸ Department of Physics, Korea Advanced Institute of Science and Technology, Daejeon, Korea

⁹ University of Valencia, Valencia, Spain

¹⁰ Institute for the Early Universe, Ewha Womans University, Seoul, Korea

¹¹ Department of Physics, Ewha Womans University, Seoul, Korea

¹² Sungkyunkwan University, Suwon, South Korea

¹³ Department of Astronomy, Yonsei University, Seoul, Korea

¹⁴ SINP, Moscow State University, Moscow, Russia

Abstract. The UFFO (Ultra-Fast Flash Observatory) is a GRB detector on board the Lomonosov satellite, to be launched in 2013. The GRB trigger is provided by an X-ray detector, called UBAT (UFFO Burst Alarm & Trigger Telescope), which detects X-rays from the GRB and then triggers to determine the direction of the GRB and then alerts the Slewing Mirror Telescope (SMT) to turn in the direction of the GRB and record the optical photon fluxes. This report details the calibration of the two components: the MAPMTs and the YSO crystals and simulations of the UBAT. The results shows that this design can observe a GRB within a field of view of $\pm 35^\circ$ and can trigger in a time scale as short as 0.2 – 1.0 s after the appearance of a GRB X-ray spike.

1 Introduction

The UFFO (Ultra-Fast Flash Observatory) is a GRB detector, designed to catch the optical photons as early as possible. The UFFO-path finder is the first detector, which consists of two sub-detectors: the Slewing Mirror Telescope (SMT) and the UFFO Burst Alert Telescope (UBAT) (Park *et al.* 2013). UBAT uses a coded mask detector to detect X-rays from a GRB (Kim *et al.* 2012). The triggered pattern is used to determine the direction from which the GRB arrives and then the location of the GRB is sent to the SMT. SMT consists of a slewing mirror in front of an optical telescope. By turning this mirror, the field of view can be extended from the $17' \times 17'$ of a telescope and CCD to almost $35^\circ \times 35^\circ$ (Jeong *et al.* 2013). It takes only approximately 1 s to move the mirror to the desired direction. The UFFO-path finder is installed on the Lomonosov satellite and is scheduled to be launched in 2013.

This study firstly constructs a complete model of UBAT in a GEANT4 simulation package and then studies several key characteristics of the UBAT. Section 2 describes UBAT geometry and the GEANT4 model. Section 3 presents the results from the calibration of the MAPMTs and the YSO crystals. Section 4 presents simulation results, including the active energy range for X-rays, the potential noises from charged particles and the determination of the direction of the GRB and the angular resolution.

2 UBAT structure and model

The top of UBAT is a 68×68 pixels coded mask, made from 1 mm thick Tungsten. In order to increase the mechanical strength, Kapton tapes are glued to the both sides of the coded mask. At the base of UBAT is an 6×6 array of X-ray detectors, which consists of YSO crystals coupled with Multi-Anode Photo-Multiplier Tubes (MAPMT) and readout electronics. The YSO crystals convert incoming X-rays into optical photons and then the MAPMTs convert the photons to photoelectrons and amplify the current to render it detectable. In order to isolate the optical

photons within one pixel, each YSO crystal is wrapped with a thin reflecting tape, except for the side facing the MAPMT.

3 MAPMT and YSO crystal calibration

The 64 channels MAPMT are custom made by Hamamatsu Photonics, with 8×8 pixels, 2.88 mm square, beneath a 0.8 mm thick frontal UV glass. The gain of each pixel of the MAPMT is defined as the DAQs (Data AcQuisition system) reconstructed voltage reading per photoelectron (PE) emitted from the photocathode. The NuTel DAQ system is used (Yeh *et al.* 2004), which is capable of simultaneously taking data from 512 channels, to calibrate the gain of the MAPMTs. A blue LED is used, which has the same wavelength as that has emitted by the YSO. This sends a pulsed light to test the MAPMT's responses at different high voltages. The DAQ records the data by synchronizing with the LED pulse, instead of the MAPMT signals. The signals $S(x)$ as a function of DAQ reading x in mV are then fitted by a Poisson functions, $S(x) = A \times \mu^{x/G} \times e^{-\mu}/\Gamma((x/G) + 1)$, to determine the gain G and mean number of photo-electrons μ . Figure 1 shows a typical light pulse histogram with its fitting result for one channel and the gain for all channels.

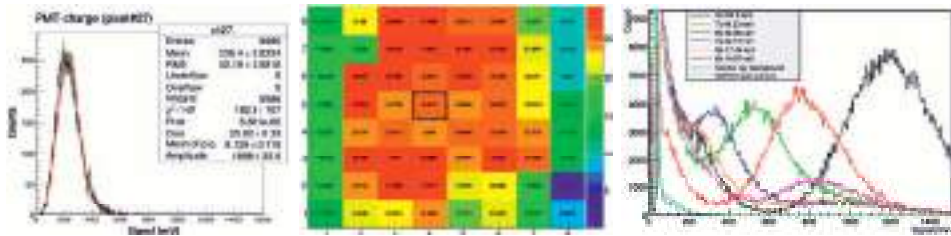


Fig. 1. The figure on the left side, shows a histogram of the data from channel 27. The figure on the center shows the Gain distributions of this MAPMT at 800V. Channel 27 is located at coordinate index (4, 5) and surrounded by a black dash square. The figure on the right side shows the energy calibration for the YSO crystals.

The scintillator is an array of 64 small YSO crystal blocks, each of size $2.65 \text{ mm} \times 2.65 \text{ mm} \times 3 \text{ mm}$ (thickness), which has the same dimensions as the MAPMT and which attaches to its frontal UV glass. For the calibration of the YSO crystals, a variable X-ray source is placed in front of the YSO and MAPMT assembly and the signals from each cell are recorded. Figure 1 shows a combination of several X-ray emission lines. The YSO photon yield is derived as 10.5 photons/keV and the light yield is linear in the test range, from 22.1 keV to 59.5 keV.

4 UBAT simulation

In order to simulate the operation of UBAT, a complete model of UBAT was constructed, using the GEANT4 simulation package. The coded mask, shown in

panel (a) of Figure 2, has an approximately 50% opening fraction and a crossing pattern of reinforcement rigs. The Kapton tape cuts off X-rays below approximately 5 keV and the Tungsten cuts off X-rays below approximately 200 keV. Between 5 keV and 200 keV, X-ray photons trigger UBAT and produce a certain pattern on 48×48 detector pixel array, which then can be used to determine the direction of arrival of the X-rays, using a reconstruction algorithm (Connel *et al.* 2013). Figure 2 shows the patterns for three directions, relative to the main axis of the UBAT.

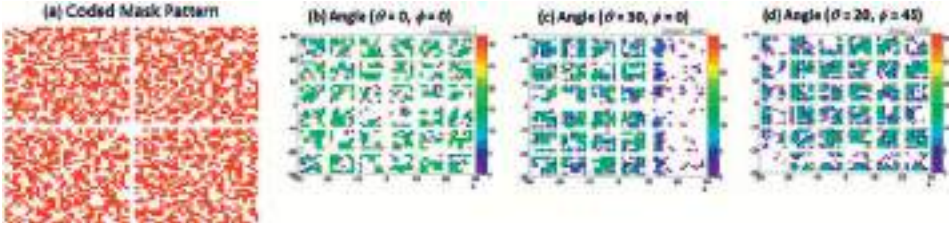


Fig. 2. Panel (a) shows UBAT coded mask pattern. Red represents open cells and white represents the blocked cells and the supporting rigs. The other three panels (b, c, d) show the patterns of triggered cells, from three directions. The color coding denotes the charge of the triggered pixels.

Several GRB light curves are used to study the trigger time. The mean X-ray count before the GRB is considered to be the background noise and counts above background are treated as a GRB signal. Simulations were performed at one frame per second and both photons from the background and/or GRB were generated independently. Each 1 s frame can be stack together to form 2 s, 4 s, 8 s, 16 s, 32 s image frame continuously. The trigger rate of those frames of different period are recorded and then the running mean and RMS values are calculated (Kim *et al.* 2012). If a frame has a rate greater than a predefined level, then it passes the first level trigger, called the rate trigger, and the pattern is then analyzed to determine the direction of the arrival. If the arrival direction can be determined above some predefined SNR, it then passes the second level trigger, called the image trigger. This simulation accounts for all the blockage from the supporting structure and for the stochastic nature of the background noise and the signal.

Apart from the astronomical X-ray background, the charged particles from cosmic rays and space radiation also contribute to noise. These effects are studied by injecting protons, electrons and gamma rays of various energy ranges, from 10 keV to 1 TeV. Low-energy charged particles cannot penetrate the 1 mm Tungsten coded mask, they could penetrate through the opening holes and trigger some pixels. However, electron flux are almost constant within minutes and will not pass the rate trigger, even a large random fluctuation may cause a rate trigger, their isotropic distribution may not pass the image trigger. Although high-energy particles can penetrate the sidewalls, their signals are concentrated in just one frame and their trails are mainly grouped in near-by pixels, which is inconsistent

with the pattern of the coded mask. Therefore, it is concluded that charged particles are not a major source of noise or can be excluded by identifying the particular abnormal detector pixel pattern they leave behind.

Approximately 300 GRB light curves from BATSE were used in the trigger simulation. For a strong GRB, UBAT can trigger 0.5 s after the GRB starts and an additional second is required to slew the SMT. The UFFO can record optical photons as early as 1.5 s. The exact time depends on the signal-to-noise ratio.

Once a rate trigger occurs, the image pattern is analyzed to determine the arrival direction of the X-ray source. The angular resolution is determined by comparing the input direction of the X-rays to the reconstructed direction. Figure 3 shows the angular error distribution in three energy ranges, assuming an isotropic distribution of X-ray sources. The mean angular errors are within $17'$ or 0.283° of the field of view of the SMT telescope and only a few percent of events are outside this limit, at a higher energy. The higher the photon energy, the larger is the mean angular error. However, in a realistic GRB spectrum, there are much less high-energy photons than low-energy photons. It is concluded that UBAT can localize GRB sources within the design values.

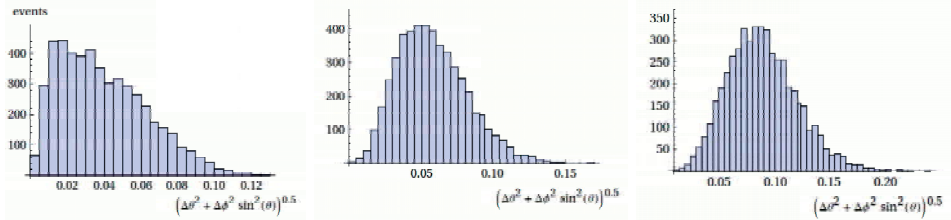


Fig. 3. The distributions of the angular error for 5, 50, and 100 keV photons are shown, from left to right. The horizontal axis represents the angular error, in degree. The input directions are isotropically distributed.

References

- Connell, P., Ahmad, S., Barrillon, P., *et al.*, 2013, for the UFFO collaboration, proc. 2012, Gamma Ray Burst Symposium (Marbella, Spain) (Oct. 8–12, 2012)
- Jeong, S., Nam, J.W., Ahn, K.B., *et al.*, 2013, for the UFFO collaboration, Opt. Express, 21, 2263
- Kim, J.E., Ahmad, S., Barrillon, P., *et al.*, 2012, for the UFFO collaboration, Proc. SPIE 8443, 84432R; doi:10.1117/12.926348
- Park, I.H., Ahmad, S., Barrillon, P., *et al.*, 2013, for UFFO collaboration, submitted to the New J. Phys.
- Yeh, P., Athar, A., La Barbera, N., *et al.*, 2004, Mod. Phys. Lett. A., 19, 1117

THE SLEWING MIRROR TELESCOPE AND THE DATA-ACQUISITION SYSTEM FOR THE UFFO-PATHFINDER

H. Lim¹, S. Ahmad², P. Barrillon², S. Brandt³, C. Budtz-Jørgensen³,
A.J. Castro-Tirado⁴, P. Chen⁵, Y.J. Choi⁶, P. Connell⁷,
S. Dagoret-Campagne², C. Eyles⁷, B. Grossan⁸, M.-H.A. Huang⁹,
A. Jung¹⁰, S. Jeong¹⁰, J.E. Kim¹⁰, M.B. Kim¹, S.-W. Kim¹¹,
Y.W. Kim¹, A.S. Krasnov¹², J. Lee¹, E.V. Linder^{8,10}, T.-C. Liu⁵,
N. Lund³, K.W. Min⁶, G.W. Na¹⁰, J.W. Nam⁵, M.I. Panasyuk¹²,
I.H. Park¹, J. Ripa¹, V. Reglero⁷, J.M. Rodrigo⁷, G.F. Smoot^{8,10},
J.E. Suh¹⁰, S. Svertilov¹², N. Vedenkin¹², M.-Z. Wang⁵ and I. Yashin¹²

Abstract. The Ultra-Fast Flash Observatory (UFFO) aims to detect the earliest moment of Gamma-Ray Bursts (GRBs) which is not well known, resulting into the enhancement of GRB mechanism understanding. The pathfinder mission was proposed to be a scaled-down version of UFFO, and only contains the UFFO Burst Alert & Trigger Telescope (UBAT) measuring the X-ray/gamma-ray with the wide-field of view and the Slewing Mirror Telescope (SMT) with a rapid-response for the UV/optical photons. Once the UBAT detects a GRB candidate with the position accuracy of 10 arcmin, the SMT steers the UV/optical photons from the candidate to the telescope by the fast rotatable mirror and provides the early UV/optical photons measurements with 4 arcsec

¹ Sungkyunkwan University, Suwon, Korea

² University of Paris-Sud 11, Orsay, France

³ Technical University of Denmark, Copenhagen, Denmark

⁴ Instituto de Astrofísica de Andalucía, CSIC, Granada, Spain

⁵ National Taiwan University, Taipei, Taiwan

⁶ Korea Advanced Institute of Science and Technology, Daejeon, Korea

⁷ University of Valencia, Valencia, Spain

⁸ University of California, Berkeley, USA

⁹ National United University, Miao-Li, Taiwan

¹⁰ Ewha Womans University, Seoul, Korea

¹¹ Yonsei University, Seoul, Korea

¹² Moscow State University, Moscow, Russia

accuracy. The SMT has a modified Ritchey-Chrétien telescope with the aperture size of 10 cm diameter including the rotatable mirror and the image readout by the intensified charge-coupled device. There is a key board called the UFFO Data Acquisition system (UDAQ) that manages the communication of each telescope and also of the satellite and the UFFO overall operation. This pathfinder is designed and built within the limited size and weight of ~ 20 kg and the low power consumption up to ~ 30 W. We will discuss the design and performance of the UFFO-pathfinder, and its integration to the Lomonosov satellite.

1 Introduction

Gamma-Ray Bursts (GRBs) are the most energetic events in the sky with the higher photon luminosities than any other objects in the universe and seen to the highest red-shift. They have been detected in random directions in the sky once or twice per day and have lasted from a fraction of seconds to hundred seconds.

Compared with X-ray observations of GRBs, the optical photons are observed in 40% of X-ray events. The *Swift* observatory detecting the multi-wavelength photons of GRBs and the ground-based fast robotic telescope rarely have observed the UV/optical photons in less than 60 sec after the GRB trigger. The Ultra-Fast Flash Observatory (UFFO) was proposed to detect the earliest explosion moments associated with GRBs and to study the GRBs emission mechanism, their progenitors etc.. The UFFO is designed to begin the UV/optical observation in less than a few seconds after trigger with the beam steering technology which is implemented in the Slewing Mirror Telescope (SMT). The UFFO-pathfinder, a pilot GRB mission is scheduled to launch into orbit in 2013 by the Lomonosov spacecraft to verify the early UV/optical measurements of GRBs with the fast rotatable mirror system. There are two telescopes and one data acquisition system: the UFFO Burst Alert & Trigger Telescope (UBAT) for the X-ray triggering, the SMT for the UV/optical measurement and the UFFO Data Acquisition System (UDAQ).

The UBAT is a coded-mask aperture X-ray camera with a wide field of view (FOV) of 1.8 sr and the detector module with effective active area of 191.1 cm^2 , localizing the GRBs within the accuracy of 10 arcmin diameter. The SMT slews the motorized mirror rapidly forward to the target triggered by UBAT within a second and measures UV/optical afterglow with a Ritchey-Chrétien telescope and a focal plane detector. The UDAQ controls the operation and communication of each telescope and also interfaces with the satellite. As shown in Figure 1 (left), the UFFO-pathfinder was designed and built with the constraints of the mass of 20 kg and the maximum length of 800 mm required by the spacecraft. The logic functions of UFFO's each readout system were implemented in the field programmable gate arrays (FPGAs) and are operated with the low power consumption and the fast signal processing.

In this paper, we will discuss the design, fabrication and performance test of the SMT and the UDAQ that are integrated in the UFFO-pathfinder.

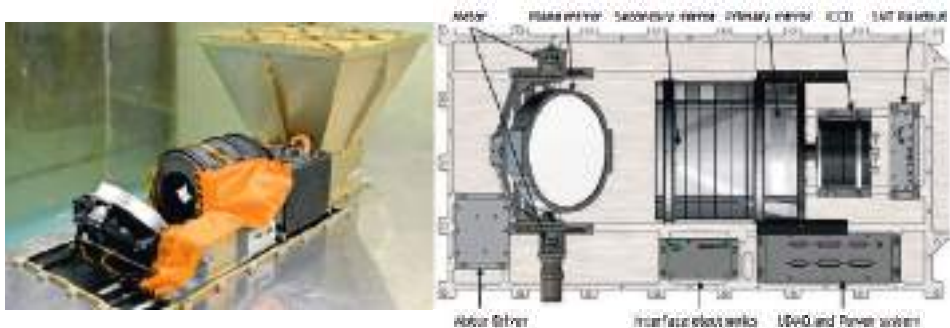


Fig. 1. *Left:* picture of UFFO-pathfinder without the SMT case. *Right:* schematic view of the SMT assembly.

2 Slewing mirror telescope

The SMT provides the fast pointing to the target with the narrow FOV using a fast steerable mirror plate. It is a Ritchey-Chrétien telescope with a 100 mm diameter aperture using a motorized mirror plate and with an f-number of 11.4. The FOV of SMT is 17×17 arcmin 2 and each pixel corresponds to the angular size of 4×4 arcsec 2 . The wavelength coverage is 200 \sim 650 nm. The overall size is 622.5(L) \times 400(W) \times 210(H) mm 3 . With the mass of 11.5 kg and the power of 10 W, the optics, the mechanical structure and the electronics were designed and fabricated. When the UBAT finds the GRB candidates and sends their location information to the SMT via the UDAQ interface, the SMT calculates the motor slewing angle, tilts the rotatable mirror to UBAT's detected target as following the angle and takes its UV/Optical data. This process is done within seconds after a GRB is triggered and consequently the UFFO can detect the early emission from GRBs.

2.1 Ritchey-Chrétien telescope



Fig. 2. Photograph of the assembled Ritchey-Chrétien Telescope with 10 cm of aperture.

As shown in Figure 2, this telescope consists of a primary mirror of 100 mm in diameter and -1.01 in conic coefficient and a secondary mirror of 20 mm in diameter and -1.83 in conic coefficient, located about 130 mm away. It has the good imaging performance in Modulation Transfer Function (MTF) of 0.77 at the Nyquist frequency of 22.52 mm^{-1} and an on-axis RMS spot radius of $2.48 \mu\text{m}$. The optical system is designed for sufficient stiffness within the tight mass budget and for the proper optical performance with the thermal stability. The obscuration ratio of the assembled telescope is 12.5%.

The optical alignment of SMT telescope was measured using an interferometer. With respect to the primary mirror, the secondary mirror was aligned by adjusting five movements of X&Y decenters, X&Y tilts and Z displacement. In order to satisfy with the required optics resolution, the RMS value of Wavefront Error (WFE) from the aligned optics should be less than 0.25 of the injected light source's wavelength. The measured error is less than $\lambda/20$ using He-Ne (632.8 nm) laser and shows the good alignment and integration of SMT optics [1].

2.2 Slewing mirror stage

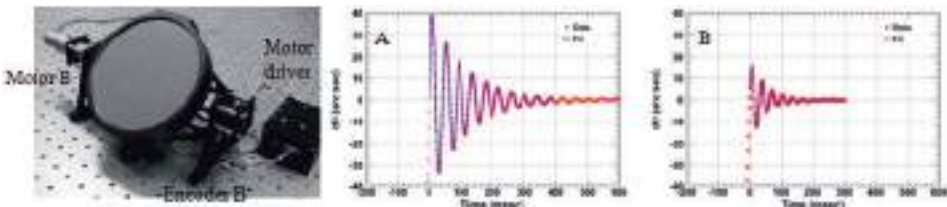


Fig. 3. Slewing mirror stage was shown (*left*). After slewing the mirror, the settling time measured less than 300 ms at A-axis (*center*) and at B-axis (*right*).

A slewing mirror (Fig. 3 (left)) with two-axis gimbal stage is located in front of a Ritchey-Chrétien telescope and points the target with the pointing accuracy of 1 arcmin. This tilting range is ± 35 deg in sky coverage which corresponds into the half-coded FOV of UBAT. The mirror is driven by the stepping motors and a harmonic drive gear with 100:1 reduction ratio, providing the minimum step size of 4.05 arcsec. After slewing the mirror, the settling time for two-axis motors was measured to be less than 300 ms (Fig. 3 (center) and Fig. 3 (right)). In order to cover the 10 cm diameter of SMT optics, the Zerodur mirror with 15 cm diameter was used and weighted to be 482 g with the light-weighting factor of 57% [1].

2.3 Focal plane detector and readout system

For the focal plane detector, an Intensified Charge-Coupled Device (ICCD) was chosen and consists of a photocathode, two Micro-Channel Plates (MCPs) for photoelectron multiplication, a phosphor screen, a tapered fiber-optics and a CCD readout system with the detectable pixels of 256×256 . For the customized ICCD,

an UV-enhanced S20 material for the photocathode is used to detect the photons of 200 – 650 nm. The photoelectrons from the photocathode are amplified by the gain of $10^4 \sim 10^6$ in MCPs stage. They are converted to photons in the phosphor screen. This screen uses the P46 material with the fast decay time of 300 ns and its output photons are readout by a fast interline CCD, Kodak KAI-0340 which provides a fast pixel-readout rate up to 40 MHz. The phosphor screen is coupled with the CCD by the tapered fiber-optics with the ratio of $3.2:1 \pm 3\%$. Therefore, the actual focal plane size of SMT is $6.062 \times 6.062 \text{ mm}^2$ and a pixel size is $23.7 \times 23.7 \mu\text{m}^2$.



Fig. 4. ICCD including the CCD-sensor board (*left*), the clok-generator board (*center*) and the SMT-DAQ board (*right*).

In order to build the SMT readout system within the limited space and power, the readout system consists of three parts; the ICCD including the CCD-sensor board for sensor readout, the clock-generator board for the operation of CCD sensor, and the SMT-DAQ board for overall SMT operations including motor control and interface with UDAQ [2]. The CCD output is digitized with 10bit ADC and the readout rate of one frame is 4 ms. When checking the integrated SMT using the parallel beam, we achieved the Point Spread Function of 4.8 arcsec.

2.4 Data-acquisition system

The UDAQ manages the overall operation of UFFO-pathfinder, and the interfaces with each telescope and also the satellite. The architecture of UFFO-pathfinder is shown schematically with the trigger flows, the data flows and the control flows in Figure 5. When the Satellite provides the power for UFFO-pathfinder, the UFFO power system produces the required voltages and first supports the voltages for UDAQ. The UDAQ automatically starts to run, controls to distribute the powers to SMT and UBAT and monitors the operation status and the hardware status, such as housekeeping data. All logic functions performed by the UDAQ are implemented in a field programmable gate arrays (FPGA) without a microprocessor. It supports the fast processing and the suitable operation for the sub-minute data observation [3]. Figure 6 shows the fabricated UDAQ board and the UFFO bus-interface board with the satellite.

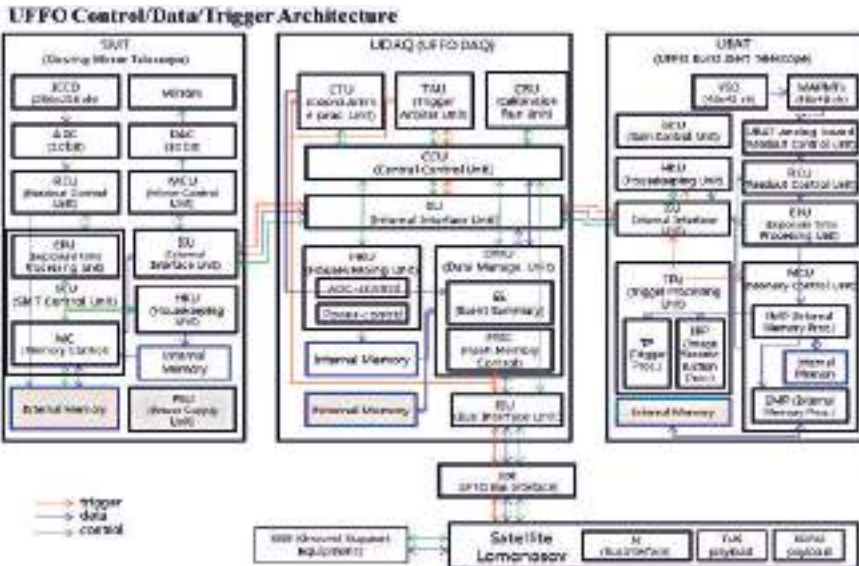


Fig. 5. Architecture of the UFFO-pathfinder including SMT, UDAQ, UBAT and satellite interface. There are the trigger flows (red line), the data flows (blue line), and the control flows (green line).

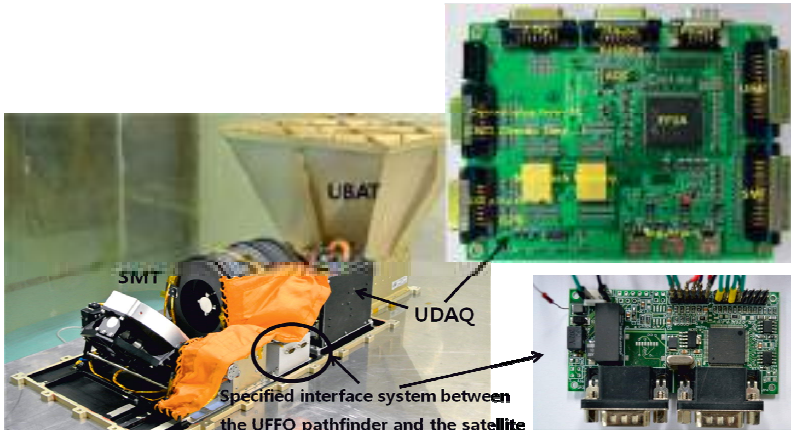


Fig. 6. UDAQ board (*top-right*) and the UFFO bus-interface board (*bottom-right*). The left picture shows the positions of these boards.

3 Conclusion

The Slewing Mirror Stage is a key instrument of UFFO and allows for us to detect the early UV/optical photons of GRBs. The Slewing Mirror Telescope

which consists of the telescope, the slewing mirror stage and the readout system, is designed, built and integrated in the UFFO-pathfinder. The integrated SMT system is successfully delivered to Russia. The UFFO data-acquisition System is the main control system for UFFO-pathfinder and has been tested with each telescope and the satellite.

This research was supported by Basic Science Research Program through the National Research Foundation of Korea (NRF) funded by the Ministry of Education, Science and Technology (2010-0025056), Creative Research Initiatives (RCMST) of MEST/KRF, and supported by World Class University (WCU) program through the National Research Foundation of Korea funded by the Ministry of Education, Science and Technology (R32-2009-000-10130-0) in Korea.

References

- [1] Jeong, S., Ahmad, S., Barrillon, P., *et al.*, 2012, Proc. SPIE, 8443, 84432S
- [2] Kim, J.E., Lim, H., Jung, A., *et al.*, 2011, Proceeding of 2011 ICRC
[arXiv:1106.3803]
- [3] Na, G.W., Ahmad, S., Barrillon, P., *et al.*, 2012, Proc. SPIE, 8443, 84432T

SPACE EXPERIMENTS ON-BOARD OF *LOMONOSOV* MISSION TO STUDY GAMMA-RAY BURSTS AND UHECRS

A.M. Amelushkin¹, V.V. Bogomolov¹, V.V. Benghin¹, G.K. Garipov¹,
E.S. Gorbovskoy², B. Grossan³, P.A. Klimov¹, B.A. Khrenov¹, J. Lee⁴,
V.M. Lipunov², G. Na⁴, M.I. Panasyuk¹, I.H. Park⁴, V.L. Petrov¹,
G.F. Smoot³, S.I. Svertilov¹, Yu. Shprits⁵, N.N. Vedenkin¹
and I.V. Yashin¹

Abstract. The number of experiments on-board Lomonosov spacecraft are preparing now at SINP MSU in co-operation with other organisations. The main idea of Lomonosov mission is to study extreme astrophysical phenomena, such as cosmic gamma-ray bursts and ultra-high energy cosmic rays. These phenomena connect with processes occurred in very distant astrophysical objects of the Early Universe and give us information about first stages of Universe evolution. Thus, the Lomonosov mission scientific equipment includes several instruments for gamma-ray burst observation in optics, ultra-violet, X-rays and gamma-rays and the wide aperture telescope for ultra-high energy particle study by detection of ionisation light along its tracks in the atmosphere. The main parameters and a brief description of these instruments are presented.

1 Introduction

Studies of extremely high energy and power processes such as ultra-high energy cosmic rays (UHECR) and cosmic gamma-ray bursts (GRB) are of great importance

¹ D.V. Skobeltsyn Institute of Nuclear Physics of M.V. Lomonosov Moscow State University, Leninskie Gory, 1/2, 119991 Moscow, Russia

² P.K. Shternberg Astronomical Institute of M.V. Lomonosov Moscow State University, Universitetskii prosp. 17, 119992 Moscow, Russia

³ Berkeley Center for Cosmological Physics, Berkeley, California, USA

⁴ Department of Physics, Sungkyunkwan University, Seobu-ro, Jangangu, Suwon-si, Gyeongido 440-746, Korea

⁵ Inst. of Geophysics and Planetary Physics, UCLA, 405 Hilgard Ave / 7127, Los Angeles, CA, USA

not only in order to understand these phenomena, but also to develop the theory of the Early Universe.

Gamma-ray bursts are observed as short (from dozens of milliseconds up to dozens of seconds) pulses of gamma-fluxes up to the energy of at least 10^9 eV. Discovered in 60 s years of 20th century they are still at the cutting edge of astrophysics. These phenomena being the most powerful in the Universe occur not only in gamma-range, but also in optics and UV. The power of the explosion of these bright astrophysical objects achieves $10^{51} - 10^{53}$ erg/s. GRB optical emission lasts up to several hours or even days as an afterglow, which appears after a giant explosion in the external shock wave expanding in the interstellar medium and stellar wind of the exploded star. Probably, it is due to the collapse of a fast-rotating very massive star to a black hole in the case of so-called long-duration (more than a few seconds) bursts or merging of neutron stars in tight binary system in the case of so-called short-duration (less than a second) bursts. However, these models are under discussion and the nature of these extraordinary phenomena is still unknown. Due unusually powerful brightness of GRBs, studying their properties allows the researchers to look in the epoch of the early Universe, *i.e.* to study evolution of the stars and the stellar populations within the wide range of redshifts from $z \sim 0.1$ up to $z \sim 15 - 20$, it is more than 98% of the age of our Universe.

The other extreme phenomena in the Universe are ultra-high energy cosmic rays, which are most likely produced by the Active galactic nuclei (AGN). The fundamental problem is to estimate maximal particle energy, to which they could be accelerated in such sources, and whether there is a maximum energy to which particles can be accelerated in the Universe. Because AGN are very distant objects, UHECR go a long way before coming to the Earth. During their propagation UHECR lose energy due to photo-production of secondary particles (mostly pions) on the microwave background photons. It leads to a natural limit of observable cosmic ray particle energy and to the UHECR energy spectrum cut-off at the photo-production energy threshold, *i.e.* about $5 \cdot 10^{19} - 10^{20}$ eV (GZK (Greisen-Zatsepin-Kuzmin) - cut-off). However, so far we have only limited and contradictory information about the energy spectrum and composition of the cosmic particles at extremely high energies. Thus, it is not possible to make any final conclusion about the nature of UHECR, their sources location and mechanism of acceleration.

2 Scientific objectives

The mentioned above problems of extreme phenomena studies dictate the scientific objectives of considerable space experiments and suggest a specific set of appropriate instruments.

The following problems should be studied during the Lomonosov mission:

- detection of GRBs within optical and gamma ranges especially in order to study the optical prompt emission and precursors;

- studies of UHECR ($5 \cdot 10^{19} - 10^{20}$ eV) near the GZK energy spectrum cut-off;
- studies of the transient luminous phenomena in the upper atmosphere, started during the previous MSU space projects “Universitetsky – Tatiana” and “Universitetsky – Tatiana – 2” (Garipov *et al.* 2005; Garipov *et al.* 2010);
- detection of the magnetospheric particles, which are the possible sources of transient and quasi-stationary phenomena in the upper atmosphere within the X-ray and optical ranges.

The objective of GRB studies during the Lomonosov mission is to accomplish simultaneous burst detection within the gamma-rays and optics ranges along with possibility of obtaining prompt emission as well as precursor light curves. This possibility provides unique information about GRB central engine functioning. On this way we plan to use the successive experience of ground-based systems of wide field cameras and robotic telescopes MASTER, which had detected the prompt emission of several GRBs in September, 2010 (Gorbovskoy *et al.* 2011). The point is to use the co-aligned GRB gamma-ray monitor detectors and wide field optical cameras, which should be operated continuously and store the data on trigger from the GRB gamma-ray monitor. In this case the field of view (FOV) of the optical camera will be inside the FOV of gamma-ray detector and there will not need to redirect the optical system. Thus, the time delay between optic and gamma-ray signals will be zero, and even the event pre-history including the possible precursors could be recorded. Another approach is based on fast re-orientation technique using MEMS technology or very fast (during less than 1 s) rotating mirror. In this case the source indication for the optical system is given by the trigger from X-ray imager.

Another goal of the Lomonosov mission is UHECR studies. The Earth’s atmosphere will be used as a “detector” of UHECR, which produce cascades of secondary particles, *i.e.* extensive air showers (EAS), which can provide us information about the primary particle parameters. The bulk of secondary particles in EAS ionize molecules and atoms of atmospheric nitrogen and oxygen and lead to the so-called ionization glow, which is most intensive along the EAS axis and looks like a point source moving with light velocity during very short time (tens microseconds). The ionization light intensity provides information about the energy of primary particle, while direction of EAS track follows arrival direction of primary particle. Thus, an instrument capable to image the UHECR ionization track is necessary.

Such instrument will be also able to detect so-called “transient luminous events” (TLEs) in the upper atmosphere. The nature of TLEs is probably associated with atmospheric electricity phenomena. During the high-altitude electric discharges between the clouds and ionosphere (at altitudes of 10–70 km) short-time (with duration 1–100 milliseconds) bursts of electromagnetic radiation within wide spectral range (from visual light up to UV and even X-rays and gamma-rays) are observed. Current experimental data about discharges in the upper atmosphere have shown that these phenomena are global, number of discharges and the energy released in

these discharges are so high that we can expect certain relations between discharge phenomena and other geophysical phenomena.

Studies of charge particle fluxes in the near-Earth space and especially the high energy magnetospheric electrons could be considered as an associated goal of the mission. Radiation environment at low altitudes (less than \sim 500–600 km) is basically determined by the fluxes of quasi-trapped and precipitated particles of the Earth's radiation belts and the solar particles penetrating mainly into the polar caps regions. The scientific payload of the "Lomonosov" satellite will include a complex of instruments for the studies of the processes of charged particles penetration into the upper atmosphere of Earth and for the analysis of the radiation conditions at low altitudes.

3 Instrumentation

Scientific equipment installed on-board the "Lomonosov" satellite includes a number of instruments intended to study the scientific cases mentioned above:

- set of instruments for GRB studies including gamma-ray monitor BDRG, optical wide-field cameras SHOCK and UFFO instrument consisting of UV and X-ray telescopes;
- optical wide aperture telescope TUS for imaging of the UHECR tracks in the atmosphere;
- set of instruments for studies of energetic particle fluxes in the near-Earth space including magnetometer, high energy electron detector ELFIN and charge and neutral particle monitor DEPRON.

3.1 Space telescope TUS

Orbital telescope TUS (Russian abbreviation for "Tracking Instrument") is intended for observations of UV (300–400 nm wavelength) bursts in the night atmosphere of Earth.

Detector consists of two main parts: mirror-concentrator with area of 1.8 m^2 (Fig. 2) and photo detector composed of 256 pixels, located at the mirror focus (Figs. 1 and 3). TUS technological parameters are: mass \sim 60 kg, power consumption \sim 65 W, data rate 250 Mbytes/day.

Mirror-concentrator is designed as sum of the central parabolic mirror and 11 parabolic rings focusing a parallel beam to one focal point. In this design thickness of the mirror construction is small (3 cm) which is important for mirror implementation into satellite construction. Mirror focal distance is 1.5 m. The mirror is cut to hexagonal segments with a diagonal of 63 cm. Mirror segments are made of carbon plastic strengthened by a honey comb aluminum plate so that the mirror construction is thermally stable in a wide range of temperatures. Mirror surface is obtained as plastic replicas of aluminum press forms (one for central mirror part and one for 6 lateral parts).

Plastic mirror surface is covered by an aluminum film and protected by a SiO₂ coat based on vacuum evaporation. Reflectivity of the mirror surface at wavelength 350 nm (average for the atmosphere fluorescence) is 85%. Expected life time of the mirror is not less than 3 years.

TUS mirror passed various space qualification and optical tests. These tests show stability of optical quality of the mirror in space conditions.

Photo detector pixels are photomultiplier tubes PMT R1643 of Hamamatsu with multi-alcali cathode of 13 mm diameter. Quantum efficiency of the PMT cathode is 20% for a wavelength of 350 nm. PMT's multi-alcali cathode (instead of the standard bi-alcali one used in ground-based fluorescence detectors) was chosen for operation in a wider range of temperatures where the cathode operates in a linear regime. To make the detector field of view (FOV) uniformly filled with pixels, light guides with square entrance (15 × 15 mm) and circle output adjusted to PMT cathode were used.

The principles of observations using the TUS instrument are illustrated in Figure 1.

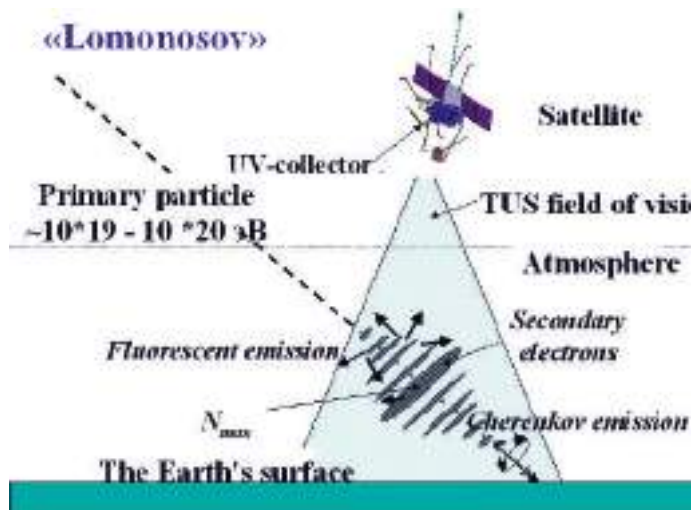


Fig. 1. Illustration of UHECR detection with TUS.

3.2 Gamma-ray burst monitor BDRG and wide-field optical cameras SHOKs

The BDRG instrument is intended for monitoring and locating gamma-ray sources at the celestial vault within the gamma-range and for the production of the trigger signal for the SHOCK wide-field optic cameras.

BDRG provides:

- monitoring of the transient astrophysical phenomena (GRBs, “X-ray novas”, “Soft gamma-ray repeaters”, etc.);
- timing of soft gamma-radiation of the X-ray double stars and pulsars;
- patrol of solar radiation within the gamma-range.

The BDRG instrument consists of three identical gamma-ray detector units BDRG-1...BDRG-3 with axes normally directed to each other. The system as a whole allows to observe a half of celestial sphere and to produce a rectangular co-ordinate system with the axes coinciding with the axes of the detectors. Each gamma-ray burst is detected by one of the detectors or by a combination of two or three detectors. In the last case directing cosines which set the location of the source against the detecting system can be determined by the ratio of the counting rate amplitude increases in each detector to the total amplitude (the counting rate) which characterises the total flux falling on the detecting system. This method provides accuracy of the localisation of gamma-ray burst source on the sky for the most powerful events $1^\circ - 4^\circ$ (Mazets & Golenetskii 1981).

The SHOCK instrument (Russian abbreviation for “Optical camera of super-wide field of vision”) consists of two stationary wide-angle fast cameras. Their field of view is situated within the area of gamma-bursts’ detection of other instruments onboard the “Lomonosov” satellite.

Each SHOK unit is an optical camera with a wide field of view, which must be within the field of view of the corresponding detector of the gamma-bursts monitor. Due to this feature it is possible to detect the burst within the optical and gamma-ray ranges simultaneously, and in the case of continuous observations a significant opportunity for measuring of optical curves of the gamma-ray burst prompt emission and their precursors’ detecting are provided.

Field of view of each camera is about 1000 square degrees, and maximum framing rate is about 5–7 frames/sec. In fact, cameras record “a movie” continuously, and in case of gamma-ray burst detection part of this movie can be transmitted to the Earth.

Among the bursts it is possible to process the images in order to find optical transients: supernova, novae, “orphan” bursts, asteroids and near-space objects and space debris.

It must be emphasized that the SHOK device will be the first orbital experiment with cameras of super-wide field. Development of detection methods of dangerous asteroids and space debris from space are of particular interest.

3.3 UFFO instrument

The UFFO instrument consists of 20-cm UV-optic telescope SMT with a fast rotating mirror and the wide-field X-ray imager UBAT.

The main goal of the observations by means of the UV-telescope SMT is the recording of the intrinsic radiation of gamma-ray bursts due to opportunity of very

fast (~ 1 s) rotation of the mirror focusing in the region of the burst localisation at the moment of the trigger of gamma-monitor or UBAT instrument which allows to obtain images within X-range (Chen *et al.* 2011). The UBAT instrument is based on the combination of a coding mask and the position-sensitive detector with pixels produced of LYSO scintillator.

3.4 Instruments for magnetosphere study: DEPRON and EIFIN-L

The DEPRON instrument (Dosimeter of Electrons, PROtons and Neutrons) is intended for measurements of the absorbed doses and linear energy transfer spectra from high-energy electrons, protons and nuclei of space radiation, and for detecting thermal and slow neutrons.

The instrument includes:

- Charged particles dosimeter based on semiconductor detector;
- Thermal neutrons detector based on gas-discharge counter SI13N;
- Circuits for analogous and digital processing of detectors' signals, for information storage and analysis;
- Power supply units for the detectors and electronics.

The ranges of the neutron flux density measured by means of SI13N counters for the neutrons within the energy range of 10^{-3} – 10^2 eV is 0.1 – 10^2 neutrons/($\text{cm}^2 \text{s}$).

The EIFIN-L (Electron Loss and Fields Investigator for the “Lomonosov” mission) instrument is a joint project of the Institute of Geophysics and Planetary Physics at the University of California, Los-Angeles (IGPP/UCLA) and Skobeltsyn Institute of Nuclear Physics of M.V. Lomonosov Moscow State University. It consists of a Flux Gate Magnetometer (FGM), an Energetic Particle Detector for Electrons (EPDE), and an Energetic Proton Detector for Ions (EPDI).

The main scientific objective of the MSU-UCLA collaboration is to understand the dominant mechanisms of the loss of energetic electrons and ions. Energetic particles create a hazardous environment for satellites and humans in space and cause a number of satellite failures.

3.5 The information unit (BI)

The Lomonosov on-board equipment also includes the information unit BI (Russian abbreviation for “Information unit”), which is needed in order to provide control of the scientific equipment complex onboard the “Lomonosov” satellite. It provides collection, storage and transmission of the telemetric information to Earth.

An information unit is developed in order to provide operation of the scientific equipment complex onboard the “Lomonosov” satellite and its operative and flexible control during the execution of the scientific program. The service systems of the basic satellite platform can not fit the requirements of the unique scientific

experiments – complicated scientific equipment, huge volume of scientific information storage, high-operative control of the equipment, therefore it was necessary to develop a special information unit.

4 Conclusion

The set of instruments installed on-board the “Lomonosov” satellite allow the study of a wide range of cases of modern astrophysics and space physics. The main of them are the studies of extreme events in sources placed on cosmological distances such as UHECRs and GRBs. To be launched in the nearest future the “Lomonosov” mission gives the scientists a good opportunity for solving the mentioned above problems.

This work was partially supported by funds from Megagranta № 11.634.31.0076.

References

- Chen, P., Ahmad, S., Ahn, K., *et al.*, 2011 (The UFFO Collaboration), Proc. 32nd ICRC Beijing (August 11-18)
- Garipov, G.K., Khrenov, B.A., Panasyuk, M.I., *et al.*, 2005, Astropart. Phys., 24, 400
- Garipov, G.K., Khrenov, B.A., Klimov, P.A., *et al.*, 2010, J. Geophys. Res., 115, doi:10.1029/2009JA014765
- Gorbovskoy, E.S., Lipunova, G.V., Lipunov, V.M., *et al.*, 2011, MNRAS, in press
- Mazets, E.P., & Golenetskii, S.V., 1981, Astrophys. Space Sci., 75, 47

BDRG AND SHOK INSTRUMENTS FOR STUDY OF GRB PROMPT EMISSION IN MICHAYLO LOMONOSOV SPACE MISSION

A.M. Amelushkin¹, V.V. Bogomolov¹, V.I. Galkin¹, B.V. Goncharov¹,
E.S. Gorbovskoy², V.G. Kornilov², V.M. Lipunov², M.I. Panasyuk¹,
V.L. Petrov¹, G.F. Smoot³, S.I. Svertilov¹, N.N. Vedenkin¹
and I.V. Yashin¹

Abstract. The study of GRB prompt emission (PE) is one of the main goals of the *Lomonosov* space mission, which is being prepared at Moscow State University. The GRB monitor (BDRG) and the wide-field optical cameras (SHOK) are intended for detection of GRB prompt emission as well as optical counterparts. The BDRG instrument consists of three identical NaI(Tl)/CsI(Tl) (13.0×2.0 cm \varnothing) phoswich detectors, whose axes determine the Cartesian coordinate system. This allows to localize any GRB source on the sky by means of the count rate seen by each detector with an accuracy of ~ 2 deg. The SHOK instrument consists of two identical wide-field cameras (WFC) directed in such a way that the field of view (FOV) of each WFC overlaps by the corresponding BDRG FOV, which produces a trigger on the WFC in case of a GRB detection. With this setup, the GRB prompt light curve will be obtained in the visible without any delay with respect to gamma-rays, which is crucial for a GRB central engine understanding.

1 Introduction

GRBs are one of the most energetic phenomena in the Universe. They appear as short (from dozens of milliseconds up to dozens of seconds) increases of fluxes of gamma radiation with typical energy of tens or hundreds of keV and sometimes are

¹ D.V. Skobeltsyn Institute of Nuclear Physics of M.V. Lomonosov Moscow State University, Leninskie Gory, 1/2, 119991 Moscow, Russia

² P.K. Shternberg Astronomical Institute of M.V. Lomonosov Moscow State University, Universitetskii prosp. 17, 119992 Moscow, Russia

³ Berkeley Center for Cosmological Physics, Berkeley, California, USA

observed in hard gamma-rays with energy of at least 10^9 eV. Over the last years, UV/optical telescopes follow-ups have allow to perform multiwavelength studies of afterglows (Gehrels *et al.* 2009).

Usually UV and optical observations start at several tens of seconds after the beginning of the burst in gamma-rays. This delay is caused by the delayed trigger as well as for the repointing of optical instrument towards the given GRB direction. Thus the optical radiation appearing during the first stages of the bursts (optical prompt emission) is not well studied yet.

The *Lomonosov* scientific program includes a multi-wavelength GRB study at different epochs (Sadovnichii *et al.* 2012). In particular, prompt emission measurements will be provided based on the direct observations by the wide field optical cameras and other instruments onboard *Lomonosov*, namely: a gamma-ray spectrometer (BDRG) and a wide field optical camera (SHOK) (which will be presented in this manuscript) besides a gamma-ray coded-mask detector and a fast reaction UV/optical telescope (UFFO-p, described elsewhere).

2 Design and characteristics of BDRG gamma-ray spectrometer

The BDRG gamma-ray spectrometer for the *Lomonosov* mission is designed in order to obtain temporal and spectral information about GRBs in energy range 10–3000 keV as well as to produce GRB trigger for the other instruments and missions.

The BDRG instrument consists of 3 similar detector boxes, connected to the data analysis box (see Fig. 1). The BDRG detectors axes are shifted 90° from each other. Detectors have cosine angular dependence of sensitive area (FWHM $\sim 60^\circ$) that allows one to determine the coordinates of GRB with accuracy of few degrees for bright GRBs by comparing the different detector countrates. The instrument is sensitivite to bursts with fluences down to 10^{-7} erg/cm². Each detector consists of optically coupled thin (3 mm) NaI(Tl) and considerably thick (17 mm) CsI(Tl) crystals. The thickness of NaI(Tl) is optimized for soft part of energy range. CsI(Tl) plays a role of active shield for soft radiation being the main detector for harder energy photons. Working ranges are 0.01–0.5 MeV for NaI(Tl) and 0.05–3 MeV for CsI(Tl) one. Detector boxes have mass ~ 5.5 kg and power consumption < 3 W (~ 15 W for the data analysis box).

2.1 Detector box electronics design and calibration principles

A pulse of current originates from the corresponding photomultiplier (PMT) leading to the amplitude discriminator generating an “event start” pulse. A sequence of control signals formed after the pulse is used for the change of “SPDT state” so the two parts of the primary PMT output pulse are integrated independently. The first one is proportional to the amount of light collected during the first 800 ns of the pulse (so called “Fast component”) and the second one is proportional to the amount of light collected during the next 2 μ s (the so called “Slow component”). Both fast and slow components are analyzed at the BDRG information box

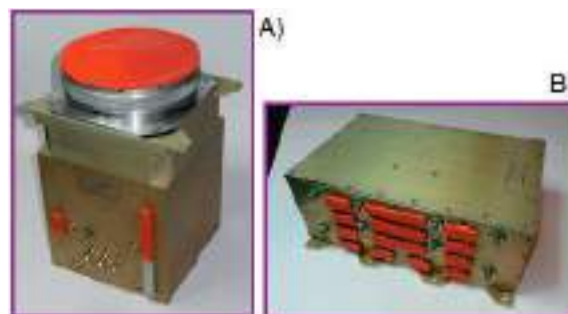


Fig. 1. The BDRG instrument: A) The detector box. B) The data analysis box.

(BA BDRG) in order to determine in which scintillator the interaction took place and the value of energy release. A sequence of output data frames is produced in the BA BDRG box allotting for the analysis of the GRB data.

The calibration procedure used for BDRG instrument can be explained using 2D-diagram where x and y values for each event represents its fast and slow component amplitudes. An example of such diagram for ^{137}Cs gamma-source is presented in Figure 2. One can see two straight lines for NaI(Tl) and CsI(Tl) events. The points between these lines correspond to the events when Compton interaction of a gamma-quantum took place so the energy was released in both crystals. The spots of events with energy release 662 keV correspondent to total energy absorption peak of ^{137}Cs source radiation as well as 1.46 MeV and 2.614 MeV events from background isotopes ^{40}K and ^{208}Tl (from ^{232}Th decay sequence) are seen.

One can see a spot of 32 keV X-rays on the detailed subpicture. These events are present only in NaI(Tl) part of detector because most of such X-rays interact with it and do not get to CsI(Tl) layer. A red cross shows a zero point correspondent to zero amplitude of the PMT pulse. This point is shifted from (0,0) by some small constant voltage level at ADC inputs. The energy release can be determined from the distance between the point of event and this zero point individually for each scintillator. One can see that events in NaI(Tl) and CsI(Tl) are well separated by an energy release greater than 10 keV.

2.2 Production of BDRG trigger

The BDRG monitoring readings demonstrate a fast increase of gamma-ray flux if the trigger is produced. Necessary conditions for trigger production are:

- Presence of fast rise of hard X-rays readings (channel 25–100 keV will be used in BDRG).
- Not too high rate in hard X-rays.
- GRB/imitation by electrons criterion based on NaI(Tl)/CsI(Tl) ratio (see below).

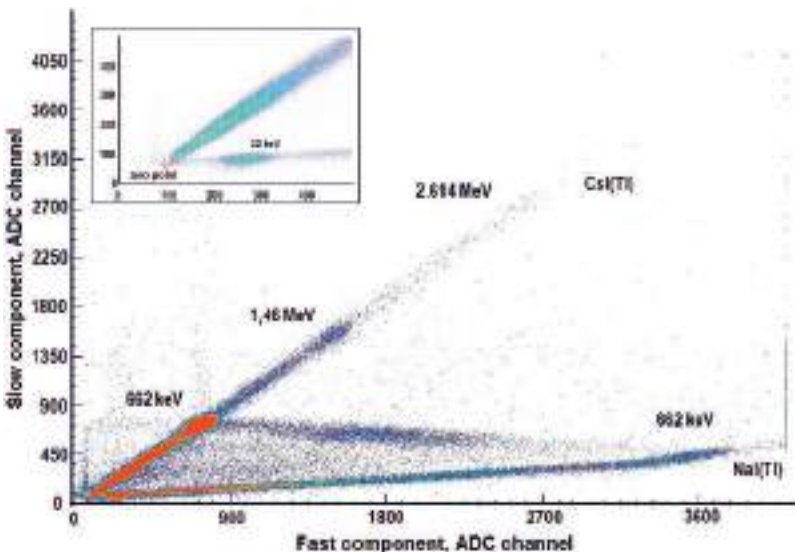


Fig. 2. Example of 2D-diagram (slow part of PMT pulse *vs.* fast one) for ^{137}Cs gamma-rays.

The algorithm for detecting a fast rise in the gamma-ray countrates is illustrated in Figure 3. Countrates are stored in memory with temporal resolution ΔT (temporal resolution of burst data to be transmitted to Earth) for $100 * \Delta T$ interval. The track record (the recording history) is divided into $5 * \Delta T$ bins (row N_{5i}) with the sums N_{100} and N_{50} being the numbers of events for the first and the second half of countrate history, which are properly determined (see Fig. 3). By means of linear regression, the expected value for the next $5 * \Delta T$ interval is calculated (named $N_{5\text{exp}}$). If $N_{50} < 30$, the mean value is used. Then, the standard deviation σ is calculated for the difference between the value of N_{5i} and the one obtained by the regression method. Then the values N_5 and $N_{5\text{exp}}$ are compared each other. Thus, a trigger is produced if:

$$\begin{cases} N_5 > N_{5\text{exp}} + N * \sigma \\ N_5 > 2 \end{cases}$$

N is the number of standard deviations when the increase is considered to be significant.

Several timescales will be used for independent triggering: 20 ms, 1 s and 20 s. The threshold (value N in formula above) can be chosen by analysis of empiric distribution of triggers. An example of such distribution for 20 ms and 1 s triggering is shown in Figure 4. The criterion for onboard triggering can be soft allowing one to have ~ 20 false bursts per day transferred to Earth but not to loose any real GRB with enough countrate. For the presented case it is set to $N_{\text{sigm}} > 9$ for 20 ms. The criterion used for the alerts distributed to world net must be harder. Proposed value is $N_{\text{sigm}} > 12$ or even greater.

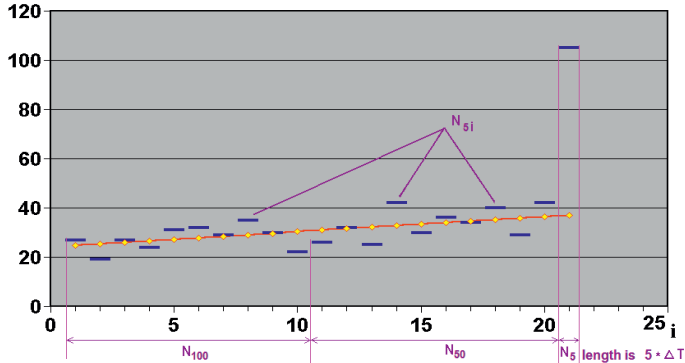


Fig. 3. Illustration for the algorithm of search for fast rise of gamma-ray countrates.

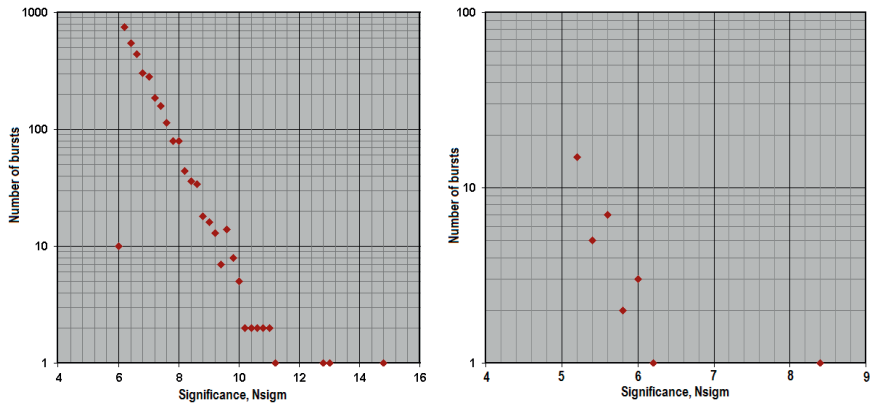


Fig. 4. Distribution of 20 ms (*left*) and 1 s (*right*) triggers from a 65 h background measurement.

It is necessary to be sure that the fast rise of BDRG readings was caused by true GRB gamma-rays and not by bremsstrahlung x-rays coming from the satellite when it some particles beam passes thru. The criterion used in BDRG is based on the comparison of countrates seen by NaI(Tl) and CsI(Tl) in different energy channels. The parameters of the criterion such as the limits of energy intervals and NaI(Tl)/CsI(Tl) threshold ratio were chosen by modelling using the Geant software. They can be also changed by commands during the space experiment.

2.3 *Estimation of GRB coordinates*

The GRB position can be estimated by comparing the countrates recorded at the 3 BDRG detectors due the having cosine (incident angle) effect. The 3 detectors are tilted 90° from each other so the GRB direction can be calculated from the formula $\cos \theta_i = N_i/\sqrt{N_1^2+N_2^2+N_3^2}$ where θ_i is the angle between the detector

axe and the burst direction and N_i is the number of events in the detector number i . The accuracy of GRB localization depends on GRB brightness, hardness and background level. The results of numeric modelling and preliminary laboratory tests with ^{241}Am radioactive source are presented in Figure 5.

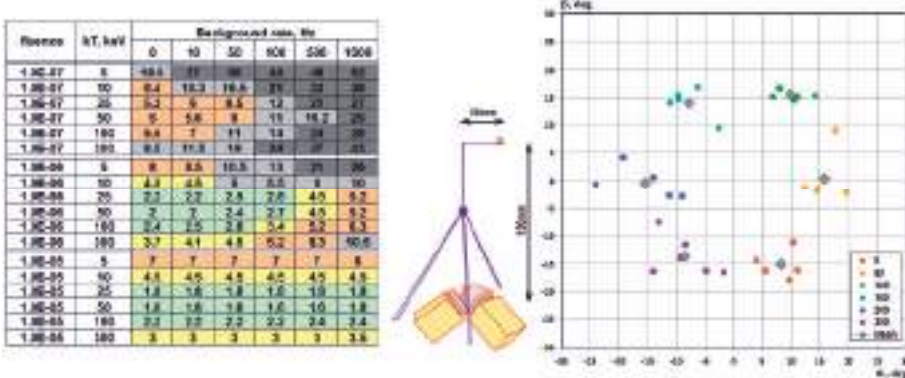


Fig. 5. Left: accuracy of GRB positioning (degrees) estimated by numeric simulations. Right: result of preliminary laboratory tests with ^{241}Am radioactive source as shown in the sketch. Depending on the distance of the source to the main axis (0 for on-axis, 60 mm, 120 mm, etc.) the localization in the (α, β) plane varies significantly.

3 SHOK wide field optical camera

The SHOCK instrument consists of two stationary wide-angle fast cameras. Their field of view is situated within the area of gamma-bursts' detection of other instruments onboard the "Lomonosov" satellite (see simplified FOV together with SHOK photo in Fig. 6). Each SHOK unit is an optical camera with a wide FOV about $20^\circ \times 40^\circ$, and maximum framing rate about 5–7 frames/sec with sensitivity ~ 11 mag. In fact, cameras record "a movie" continuously, and in case of gamma-ray burst detection part of this movie can be fixed and transmitted to the Earth. The amount of data is ~ 700 Mb/burst. GRB light curves will be fixed in the optical and gamma-ray ranges simultaneously, and a significant opportunity for measuring of optical curves of the gamma-ray burst prompt emission and their precursors' detecting are provided.

4 Conclusion

Expected numbers of GRBs were estimated taking into account the instruments FOV as well as the background conditions on low altitude orbit. Based on previous missions, one can expect ~ 150 GRB triggers per year from BDRG (but this number should be corrected due to the fact that high background is expected due to the high inclination of the orbit) and ~ 40 of them will be visible by all BDRG detectors

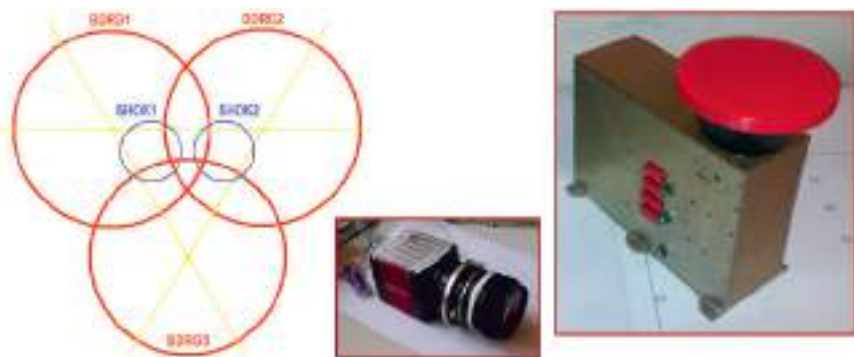


Fig. 6. *Left:* simplified FOV of SHOK and BDRG. *Center:* SHOK camera unit. *Right:* the SHOK camera unit embedded in its housing.

providing coordinate measurements. At most ~ 10 GRBs will appear in the FOV of SHOK cameras. For each trigger the light curve with 1ms resolution for gamma rays and 200 ms for optical range will be obtained including history, providing new results in multiwavelength study of GRB prompt emission.

This work was partially supported by funds from Megagrant N° 11.634.31.0076.

References

- Gehrels, N., Ramirez-Ruiz, E., & Fox, D.B., 2009, ARA&A, 47, 567
 Sadovnichii, V.A., Panasyuk, M.I., Amelushkin, A.M., *et al.*, 2012, J. Cosmology, 18, 799

DEVELOPMENT OF SLEWING MIRROR TELESCOPE OPTICAL SYSTEM FOR THE UFFO-PATHFINDER

S. Jeong¹, J.W. Nam², K.-B. Ahn³, I.H. Park⁵, S.-W. Kim^{3,4}, J. Lee⁵,
H. Lim⁵, S. Brandt⁶, C. Budtz-Jørgensen⁶, A.J. Castro-Tirado⁷,
P. Chen², M.H. Cho¹, J.N. Choi³, B. Grossan⁸, M.A. Huang⁹, A. Jung¹,
J.E. Kim¹, M.B. Kim⁵, Y.W. Kim¹, E.V. Linder^{8,11}, K.W. Min¹⁰,
G.W. Na¹, M.I. Panasyuk¹², J. Ripa⁵, V. Reglero¹³, G.F. Smoot^{8,11},
J.E. Suh¹, S. Svertilov¹², N. Vedenkin¹² and I. Yashin¹²

Abstract. The Slewing Mirror Telescope (SMT) is the UV/optical telescope of UFFO-pathfinder. The SMT optical system is a Ritchey-Chrétien (RC) telescope of 100 mm diameter pointed by means of a gimbal-mounted flat mirror in front of the telescope. The RC telescope has a 17×17 arcmin² in Field of View and 4.3 arcsec resolution (full width half maximum of the point spread function). The beam-steering

¹ Department of Physics, Ewha Womans University, 11-1 Daehyun-dong, Seoul 120-750, Korea

² Department of Physics, National Taiwan University, 1 Roosevelt Road, Taipei, 106, Taiwan

³ Department of Astronomy, Yonsei University, 134 Shinchon-dong, Seoul 120-749, Korea

⁴ Yonsei University Observatory, Yonsei University, 134 Shinchon-dong, Seoul 120-749, Korea

⁵ Department of Physics, Sungkyunkwan University, Seobu-ro, Jangangu, Suwon-si, Gyeongido 440-746, Korea

⁶ National Space Institute Astrophysics, Technical University of Denmark, 2800 Kgs, Lyngby, Denmark

⁷ Instituto de Astrofísica de Andalucía (IAA-CSIC), PO Box 03004, 18080 Granada, Spain

⁸ University of California at Berkeley, Space Sciences Laboratory, 7 Gauss Way, Berkeley, CA 94720, USA

⁹ Department of Energy Engineering, National United University, 1, Lienda, Miaoli, Taiwan, 36003

¹⁰ Korea Advanced Institute of Science and Technology, 291 Daehak-ro, Yuseong-gu, Daejeon 305-701, Korea

¹¹ Institute for the Early Universe, Ewha Womans University, 11-1 Daehyun-dong, Seoul 120-750, Korea

¹² Skobeltsyn Institute of Nuclear Physics of Lomonosov, Moscow State University, Leninskie Gory 119234, Russia

¹³ Universidad de Valencia, GACE, Edif. de Centros de Investigacion, Burjassot, 46100 Valencia, Spain

mirror enables the SMT to access a 35×35 degree region and point and settle within 1 sec. All mirrors were fabricated to about 0.02 wavelengths RMS in wave front error (WFE) and 84.7% average reflectivity over 200 nm \sim 650 nm. The RC telescope was aligned to 0.05 wavelengths RMS in WFE (test wavelength 632.8 nm). In this paper, the technical details of the RC telescope and slewing mirror system assembly, integration, and testing are given shortly, and performance tests of the full SMT optical system are reported.

1 Introduction

To measure the early photons from Gamma-Ray Bursts (GRBs), the Ultra-Fast Flash Observatory was proposed [1]. As the first step, the UFFO-pathfinder instrument has been developed and is scheduled to be launched 2013 as one of science payloads onboard the *Lomonosov* Russian satellite. The UFFO-pathfinder (Park *et al.* 2012) consists of two instruments, the UFFO Burst Alert and Trigger Telescope (UBAT) (Park *et al.* 2012; Jung *et al.* 2011; Nim *et al.* 2011; Na *et al.* 2011) for X-ray trigger and localization and Slewing Mirror Telescope (SMT; Jeong *et al.* 2013). When UBAT provides a trigger signal and approximate coordinates of a GRB to SMT, the SMT slewing mirror rotates quickly to the target coordinate and brings images of the UV/optical counter parts of GRB into the instrument FOV (Field of view) faster than the current GRB instruments in space and ground. The SMT optical system in UFFO-pathfinder is the first proof to realize such a measurement concept in GRB observation. In this paper, especially the technical details of SMT optical system, *i.e.* slewing mirror stage and RC telescope are presented shortly.

2 SMT RC telescope and slewing mirror assembly

The SMT optical system requirements are summarized in Table 1. The Ritchey-Chrétien (RC) telescope has a primary mirror (M1) of 100 mm in diameter and -1.01 in conic coefficient and a secondary mirror (M2) of 20 mm in diameter and -1.83 in conic coefficient. The telescope has 1.14 m effective focal length and fits within 200 mm SMT length budget in UFFO-pathfinder. It produces 17×17 arcmin 2 in instantaneous FOV (IFOV) on the detector and almost diffraction limited performance, with a Modulation Transfer Function (MTF) of 0.77 at 22.52 mm^{-1} Nyquist frequency and an on-axis RMS spot radius of $2.48\text{ }\mu\text{m}$. Its spot diagrams over the SMT FOV are well within the Airy disk of 400 nm in diameter. The optics design satisfies all the RC telescope performance requirements as listed in Table 1. To minimize the stress on the M1 caused by a mismatch in thermal expansion coefficient (CTE) between the Invar flexure and the aluminum support structure, the M1 is mounted to the M1 support plate via 3 bi-pod flexures with 12 mm long, 2 mm wide, and 1.5 mm thick. The M2 cell is then mounted to the M1 support plate by 4 spider arms. The M2 cell has an invar spider core with 3 flexure blades. The final resulting RMS system WFE of the RC telescopes was found to be 22.3 nm for 633 nm in wavelength that is well within WFE requirement of <0.15 waves.

Table 1. Requirements for SMT optics.

SMT optics	Slewing mirror and RC telescope
Aperture size	10 cm
Slewing coverage	70×70 arcdeg 2
Slewing speed	>30 deg / sec
Detector FOV	17×17 arcmin 2
Angular resolution	4 arcsec
Advanced resolution	0.5 arcsec (after centroiding)
Modulation Transfer Function	>0.4 at 22.52 mm $^{-1}$
Sensitive wavelength	200 – 650 nm
Mass	3 kg
Volume	600 (l) \times 320 (w) \times 200 (h) mm 3

The slewing mirror stage has an aluminum support ring and RTV566 pads are inserted between the ring and mirror around its peripheral, front and back surfaces. A two axes gimbal stage is constructed with stepper motors and rotary encoders. Using the harmonic drive gear, its step size is controlled with ~ 4 arcsec precision and the rotation angle can be controlled precisely to 2 arcmin in accuracy. The 2 axis stage can be rotated from $+22.25^\circ$ to -21.47° in inner axis and from $+66.26^\circ$ to -2.25° in outer axis on average. It allows for the full $\pm 35^\circ$ in sky coverage. The total mass of slewing mirror assembly is measured to about 1.85 kg, satisfying the mass requirement of <2 kg. All mirrors are made of *Zerodur* substrates, coated with $\text{SiO}_2 + \text{Al}$ for a reflexivity $R_{\text{avg}} > 85\%$. The slewing mirror *Zerodur* blank is light weighted 482 g to satisfy the mass budget <0.6 kg. The developed SMT optical system is presented in Figure 1.

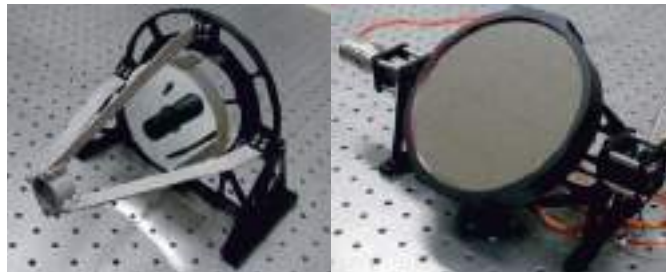


Fig. 1. Manufactured SMT optics system, RC telescope (*left*) and slewing mirror stage (*right*).

3 System validation test of SMT optics

The flight model SMT performance was validated in Russia. The pre-flight model of RC telescope was used as a collimator. A He-Ne laser beam with 635 nm

was focused on the PFM RC telescope focus point. It was then diverged before being collimated to a parallel beam to feed the slewing mirror that redirected it to the M1. The beam was subsequently reflected by M2, and then focused onto the focal plane. The resulting focal images of the 4.3 arcsec (Y-slice, Gaussian fit 1σ) PSF is presented in Figure 2.

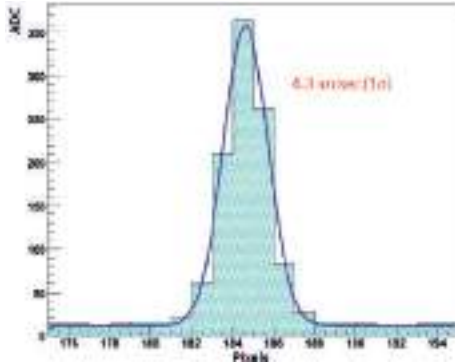


Fig. 2. Point spread function of flight model SMT [2].

4 Conclusion

The UFFO project has proposed for the first time the systematic exploration of UV/optical GRB light curves far earlier than 60 seconds after the localization of GRBs by X-ray observations. It is based on a novel concept of Slewing Mirror Telescope (SMT) that utilizes a fast slewing or tracking mirror, instead of controlling the attitude of a whole satellite or telescope body, to point and track the target GRB. It has 10 cm aperture and provides a \sim 4.3 arcsec (1σ width) PSF over 17×17 arcmin 2 in IFOV. And the angular resolution will be recovered up to 0.5 arcsec after the centroiding algorithm. This IFOV can be expanded to cover \pm 35 degrees in operational FOV within about 1 s after the trigger using slewing mirror. The SMT optical system has been designed, constructed at first time and its SMT flight instrument is now integrated in the *Lomonosov* satellite pending launch in 2013.

This research was supported by the Korean Creative Research Initiatives (RCMST) of MEST/NRF, the Basic Science Research program of MEST/NRF (2010-0025056), the World Class University program of MEST/NRF (R32-2009-000-10130-0), the Spanish MINECO project AYA-2009-14027-C05-01, AYA2011-29936-C05-01, AYA-2012-39727-C03-01 and AYA 2009-14000-C03-01/ESP, Taiwan's National Science Council Vanguard Program (100-2119-M-002-025) LeCosPA of National Taiwan University, Program of development of Lomonosov Moscow State University and Korean programs NRF 2012-0006632, 2010-0029390 and Yonsei-KASI joint research for the Frontiers of Astronomy and Space Science Program 2012. We thank Samsung Electronics (Super-precision Optics Lab., Imaging Division) for production of SMT mirrors, the National Space Organization (NSPO) of Taiwan and Nauchno-issledovatel'skij institut elektromehaniki

(NIIEM) of Russia for instrument space qualification, SCHOTT KOREA for consulting on the design of a light-weight mirror, and Dr. Yang of KRISS and H. K. Lee of Samsung for valuable discussions.

References

- Jeong, S., *et al.*, 2013, Opt. Express, accepted
Jung, A., Ahmad, S., Ahn, K.-B., *et al.*, 2011 [[arXiv:1106.3802](https://arxiv.org/abs/1106.3802)]
Kim, J.E., Lim, H., Jung, A., *et al.*, 2011 [[arXiv:1106.3803](https://arxiv.org/abs/1106.3803)]
Na, G.W., Ahn, K.-B., Choi, H.S., *et al.*, 2011 [[arXiv:1106.3804](https://arxiv.org/abs/1106.3804)]
Park, I.H., *et al.*, 2012, submitted to New J. Phys.

DESIGN AND IMPLEMENTATION OF ELECTRONICS AND DATA ACQUISITION SYSTEM FOR ULTRA-FAST FLASH OBSERVATORY

A. Jung^{1,2}, S. Ahmad³, P. Barrillon³, S. Brandt⁴, C. Budtz-Jørgensen⁴,
A.J. Castro-Tirado⁵, S.-H. Chang⁶, Y.-Y. Chang⁷, C.R. Chen⁶,
P. Chen⁷, H.S. Choi⁸, Y.J. Choi⁹, P. Connell¹⁰, S. Dagoret-Campagne³,
C. Eyles¹⁰, B. Grossan¹¹, J.J. Huang⁷, M.-H.A. Huang¹², S. Jeong^{1,2},
J.E. Kim^{1,2}, M. Kim¹³, S.-W. Kim¹⁴, Y.W. Kim¹³, A.S. Krasnov¹⁵,
J. Lee¹³, H. Lim¹³, C.-Y. Lin⁶, E.V. Linder^{2,11,16}, T.-C. Liu⁷, N. Lund⁴,
J.W. Nam⁷, K.W. Min⁹, G.W. Na^{1,2}, M.I. Panasyuk¹⁵, I.H. Park¹³,
V. Reglero¹⁰, J. Ripa¹³, J.M. Rodrigo¹⁰, G.F. Smoot^{2,11,16}, J.E. Suh²,
S. Svertilov¹⁵, N. Vedenkin¹⁵, M.-Z. Wang⁷ and I. Yashin¹⁵,
on behalf of the UFFO collaboration

Abstract. The Ultra-Fast Flash Observatory (UFFO) Pathfinder for Gamma-Ray Bursts (GRBs) consists of two telescopes. The UFFO Burst Alert & Trigger Telescope (UBAT) handles the detection and

¹ Institute of Basic Science, Sungkyunkwan University, Suwon, South Korea;
e-mail: erajung@gmail.com

² Department of Physics, Ewha Womans University, Seoul, South Korea

³ LAL, University of Paris-Sud 11, Orsay, France

⁴ Technical University of Denmark, Copenhagen, Denmark

⁵ Instituto de Astrofísica de Andalucía, CSIC, Granada, Spain

⁶ National Space Organization, Taiwan

⁷ LeCosPA, National Taiwan University, Taipei, Taiwan

⁸ Korea Institute of Industrial Technology, Cheonan, South Korea

⁹ Department of Physics, Korea Advanced Institute of Science and Technology, Daejeon, South Korea

¹⁰ University of Valencia, Valencia, Spain

¹¹ University of California at Berkeley, Space Sciences Laboratory, USA

¹² National United University, Miao-Li, Taiwan

¹³ Sungkyunkwan University, Suwon, South Korea

¹⁴ Department of Astronomy, Yonsei University, Seoul, South Korea

¹⁵ SINP, Moscow State University, Moscow, Russia

¹⁶ Institute for Early Universe, Ewha Womans University, Seoul, South Korea

localization of GRBs, and the Slewing Mirror Telescope (SMT) conducts the measurement of the UV/optical afterglow. UBAT is equipped with an X-ray detector, analog and digital signal readout electronics that detects X-rays from GRBs and determines the location. SMT is equipped with a stepping motor and the associated electronics to rotate the slewing mirror targeting the GRBs identified by UBAT. First the slewing mirror points to a GRB, then SMT obtains the optical image of the GRB using the intensified CCD and its readout electronics. The UFFO Data Acquisition system (UDAQ) is responsible for the overall function and operation of the observatory and the communication with the satellite main processor. In this paper we present the design and implementation of the electronics of UBAT and SMT as well as the architecture and implementation of UDAQ.

1 Introduction

Gamma-Ray Bursts (GRBs) are flashes of gamma ray flux originating from the most energetic events in the sky, with peak photon luminosities higher than that of any other object in the Universe (Jung *et al.* 2011). As such the early-stage observations of the light curves and emission spectrum are essential to the understanding of the nature of GRBs. However, the early-phase observations were often limited by the response time of the instruments operated in space. For example, in the case of the *Swift* observatory the entire spacecraft has to be maneuvered to point toward the GRB position after being triggered by the detection of γ -rays, which typically takes about a minute. Thus, it is difficult to obtain sub-minute ultraviolet (UV) and visible light curves with *Swift* (Park *et al.* 2013). The proposed Ultra-Fast Flash Observatory Pathfinder (UFFO-P) is designed to observe sub-minute GRB light curves by adopting the slewing mirror technology (Jeong *et al.* 2013). This removes the need to repoint the entire spacecraft.

2 Overview of Ultra-Fast Flash Observatory Pathfinder (UFFO-P)

One of the key aspects of the upcoming UFFO-P for GRBs identification is the electronics, which is based on a novel space telescope technique. The main goal of UFFO-P is to systematically measure early UV/optical photons from GRBs up to sub-second timescales, in order to gain a deeper understanding of GRB mechanisms. UFFO-P is planned to be launched by on the *Lomonosov* spacecraft in 2013 into a sun-synchronous orbit at an altitude of \sim 550 km. As shown in Figure 1, UFFO-P consists of two telescopes and one main data acquisition system: the UFFO Burst Alert & Trigger Telescope (UBAT) for the detection and location of GRBs, the Slewing Mirror Telescope (SMT) aimed at measuring the UV/optical afterglow, and the UFFO Data Acquisition (UDAQ) system for controlling the operations and communications with the telescopes.

2.1 UFFO Burst Alert & Trigger Telescope (UBAT)

UBAT is designed to detect the hard X-ray photons from GRBs in the energy range from \sim 15 to \sim 100 keV. UBAT is comprised of a mechanical assembly, a coded mask



Fig. 1. *Left:* manufactured UFFO-P. *Right:* drawing.

with a hopper and a detector. The detector includes the YSO crystals, MAPMTs, FPCB, analog and digital boards, high voltage boards, and the support structure, as can be seen in Figure 2 left.



Fig. 2. *Left:* UBAT and detector. *Right:* test set up and result of test [4].

The YSO scintillation crystal converts the γ /X-ray photons to UV photons, which eventually become electrical pulses through the chain of multi-anode photomultipliers (MAPMTs) and pulse-shaping electronics. These electrical pulses are measured and recorded with a period of 5 μ s (Jung *et al.* 2011). The 64-channel MAPMT is read out by SPACIROC (Spatial Photomultiplier Array Counting and Integrating Chip) ASIC (Ahmad *et al.* 2010). The data are transferred to a digital board built around an Actel A3PE3000L Field-Programmable Gate Array (FPGA) which provides the computing power for trigger decisions. The main components of UFFO-P are shown in Table 1. As seen in Figure 2 right, Americium-241 (Am241) is placed on the YSO crystal of one pixel. The radiation from the Am241 20 keV and 60 keV lines are observed.

2.2 Slewing Mirror Telescope (SMT)

As shown in Figure 3, SMT is an ultra-fast optical/UV telescope that can slew to a target within 1 sec. The detector is an intensified CCD with Micro-Channel Plates (MCPs). SMT has a readout rate of 4 ms and can acquire 250 frames per second. It takes only 1s to receive the trigger signal to slew the motorized mirror towards the target and collect UV/optical data (Kim *et al.* 2011). The CCD readout,



Fig. 3. SMT and UDAQ boards, test setup and test result.

mirror movement commands and data storage are managed by an Actel A3P1000 FPGA.

2.3 UFFO Data Acquisition (UDAQ)

Using an Actel A3P1000 FPGA, UDAQ acts as the central control system, which controls and manages the operation and communication of each telescope and is also in charge of the interface with the satellite. It will write the data taken by each telescope in the NOR flash memory and send them to the satellite via the Bus-Interface system (BI), as shown in Figure 3 left. All the operations between UFFO-P and the satellite have been tested (see Fig. 3 right). Interfaces between UDAQ and SMT/UBAT and between UFFO-P and the satellite have been tested too. As shown in Figure 3 right, when UDAQ receives a command for UBAT from the satellite, it first decodes the command and then sends it to UBAT. UBAT also generates and sends the trigger information to UDAQ. Finally UDAQ distributes the information to SMT and the satellite. These UDAQ interfaces including the command and the trigger information show good performance without errors (Na *et al.* 2011).

3 Conclusion

UFFO-P is planned to be launched in 2013 and is designed to measure the early phase in particular of short duration gamma ray bursts with a sub-minute response time. The effects of radiation in space on logic device and memory can disrupt performance, resulting in loss of data. Therefore UFFO-P electronics use rad-hard ASICs, military grade Actel FPGA and space grade 3D plus memory for the main components, as shown in Table 1. We are in the final stages of development and tests. So far, we have completed both the electronics and the telescope. The next step is to test perform UBAT- SMT cross calibration.

Table 1. Main components for each system.

	SMT	UDAQ	UBAT
FPGA (Military)	Actel A3P1000	Actel A3P1000	Actel A3PE3000L

This research was supported by Basic Science Research Program through the National Research Foundation of Korea (NRF) funded by the Ministry of Education, Science and Technology (2010-0025056), Creative Research Initiatives (RCMST) of MEST/KRF, and supported by World Class University (WCU) program through the National Research Foundation of Korea funded by the Ministry of Education, Science and Technology (R32-2009-000-10130-0) in Korea.

References

- Ahmad, S., Barillon, P., Blin-Bondil, S., *et al.*, 2010, JINST, 5, C12012
Jeong, S., Nam, J.W., Ahn, K.-B., *et al.*, 2013, Opt. Express, 21, 2263
Jung, A., Ahmad, S., Ahn, K.-B., *et al.*, 2011 [[arXiv:1106.3802](https://arxiv.org/abs/1106.3802)]
Kim, J.E., Ahmad, S., Barillon, P., *et al.*, 2012, ISBN: 9780819491442
Kim, J.E., Lim, H., Jung, A., *et al.*, 2011 [[arXiv:1106.3803](https://arxiv.org/abs/1106.3803)]
Na, G.W., Ahn, K.-B., Choi, H.S., *et al.*, 2011 [[arXiv:1106.3804](https://arxiv.org/abs/1106.3804)]
Park, I.H., Brandt, S., Budtz-Jørgensen, C., *et al.*, 2013, New J. Phys., 15, 023031

DEVELOPMENT OF MOTORIZED SLEWING MIRROR STAGE FOR THE UFFO PROJECT

J. Nam¹, for the UFFO Collaboration, K.B. Ahn², M. Cho³, S. Jeong³,
J.E. Kim³, S. Ahmad⁴, P. Barrillon⁴, S. Brandt⁵, C. Budtz-Jørgensen⁵,
A.J. Castro-Tirado⁶, C.-H. Chang⁷, C.-Y. Chang⁷, Y.Y. Chang¹,
C.R. Chen⁷, P. Chen¹, H.S. Choi⁸, Y.J. Choi⁹, P. Connel¹⁰,
S. Dagoret-Campagne⁴, C. Eyles¹⁰, B. Grossan³, J.J. Huang¹,
M.-H.A. Huang¹¹, A. Jung³, M.B. Kim¹², S.-W. Kim², Y.W. Kim¹²,
A.S. Krasnov¹³, J. Lee¹², H. Lim¹², E.V. Linder³, T.-C. Liu¹, N. Lund⁵,
K.W. Min⁸, G.W. Na³, M.I. Panasyuk¹³, I.H. Park¹², V. Reglero¹⁰,
J. Ripa¹², J.M. Rodrigo⁶, G.F. Smoot³, J.E. Suh³, S. Svertilov¹³,
N. Vedenkin¹³, M.-Z. Wang¹ and I. Yashin¹³

Abstract. The Ultra-Fast Flash Observatory (UFFO) is a space observatory for optical follow-ups of gamma ray bursts (GRBs), aiming to explore the first 60 seconds of GRBs optical emission. UFFO is utilized to catch early optical emissions from GRBs within few sec after trigger using a Gimbal mirror which redirects the optical path rather than slewing entire spacecraft. We have developed a 15 cm two-axis Gimbal mirror stage for the UFFO-Pathfinder which is going to be on board the Lomonosov satellite which is to be launched in 2013. The stage is designed for fast and accurate motion with given budgets

¹ National Taiwan University, Taipei, Taiwan

² Yonsei University, Seoul, Korea

³ Ewha Womans University, Seoul, Korea

⁴ LAL, University of Paris-Sud 11, Orsay, France

⁵ Technical University of Denmark, Copenhagen, Denmark

⁶ Instituto de Astrofísica de Andalucía, CSIC, Granada, Spain

⁷ National Space Organization, Hsinchu, Taiwan

⁸ Korea Institute of Industrial Technology, Cheonan, Korea

⁹ Korea Advanced Institute of Science and Technology, Deajeon, Korea

¹⁰ University of Valencia, Valencia, Spain

¹¹ National United University, Miao-Li, Taiwan

¹² Sungkyunkwan University, Suwon, Korea

¹³ Moscow State University, Moscow, Russia

of 3 kg of mass and 3 Watt of power. By employing stepping motors, the slewing mirror can rotate faster than 15 deg/sec so that objects in the UFFO coverage (60 deg \times 60 deg) can be targeted in \sim 1 sec. The obtained targeting resolution is better 2 arcmin using a close-loop control with high precision rotary encoder. In this presentation, we will discuss details of design, manufacturing, space qualification tests, as well as performance tests.

1 Introduction

Having a fast response of GRB telescope has been scientists' great dream from BeppoSAX (Boella *et al.* 1997) through SWIFT (Gehrels *et al.* 2004). Now, the dream has been realized by UFFO (Park *et al.* 2013; Chen *et al.* 2011) with a fast localization- and slewing-capability. For the first step, we have developed a pathfinder payload (UFFO-Pathfinder) with a mass of \sim 20 kg for launch in 2013, while a full scale mission with 100 kg mass, UFFO-100, is being planned for future.

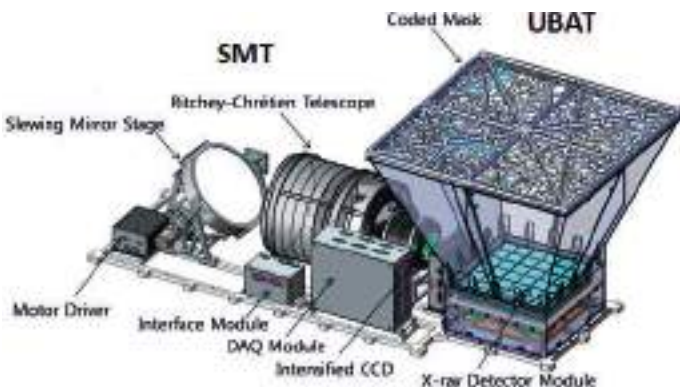


Fig. 1. A schematic view of UFFO-Pathfinder.

UFFO consists of two telescopes; the UFFO Burst Alert Telescope (UBAT) and the Slewing Mirror Telescope (SMT). UBAT is a $90^\circ \times 90^\circ$ wide Field Of View (FOV) coded mask X-ray camera to issue event triggers and to determine localizations. The localization can be obtained within a sec after the trigger using a fast imaging algorithm implemented in Field Programmable Gate Array (FPGA). The localization resolution is better than 10 arcmin in an energy range of X-rays 10–100 keV. More detailed information can be found in other references (Park *et al.* 2013; Jung *et al.* 2011).

SMT is the key concept of UFFO to capture early optical emissions from GRBs in the sub-minute regime (Jeong *et al.* 2013). SMT consists of three main instruments; Motorized Gimbal Mirror, Ritchey-Chrétien Telescope (RCT), and Intensified Charge-Coupled Device (ICCD) as a photo detector. The motorized

Gimbal mirror is located in front of RCT to redirect the beam path. The $D = 10\text{ cm}$ RCT has a narrow FOV ($17\text{ arcmin} \times 17\text{ arcmin}$), but the slewing capability further extends the SMT sky coverage up to $70\text{ arcdeg} \times 70\text{ arcdeg}$. The pixel size of ICCD is $4\text{ arcsec} \times 4\text{ arcsec}$. The Point Spread Function (PSF) of SMT is $\sim 1\text{ arcsec}$.

2 Motorized Gimbal mirror system

Figure 2 shows the motorized Gimbal mirror. In order to reduce the size, we designed a motor and the structure of the inner axis to be located below the mirror. A $D = 15\text{ cm}$ Zerodur substrate of the mirror was light-weighted to be 480 g with a light-weighting factor $\sim 60\%$. In order to minimize mechanical stress, Silicone pads were inserted at six points round the mirror in the gap between the mirror and the mount ring. It also helps reduce deformation of the mirror surface by non-uniform thermal expansion. The enhanced-aluminum coating on mirror surface provides $\sim 85\%$ of average reflectivity in a range of $200\text{--}700\text{ nm}$ wave length.

We used the unipolar type of stepper motors with a step size of 1.8 deg . Sufficient torque, as well as a fine size of step were obtained by employing a $100:1$ gear on the output axis of the motor. To reduce steering uncertainty, Harmonic Drive Gears with a small backlash (less than 2 arcmin) were used. The minimum step size was further reduced to 4 arcsec using the $1/16$ micro-stepping control technique. We used the close-loop control with a high precision rotary encoder placed on the mirror rotation axis at the opposite side from which the motor is located. The obtained targeting resolution was $\sim 2\text{ arcmin}$, limited by the accuracy of the rotary encoder. Maximum rotational speed of the mirror is faster than 15 deg/sec using a practical set of acceleration table. This corresponds to the optical targeting speed of 30 deg/sec .

The motor control logic was implemented in FPGA. In order to reduce the power consumption, a single FPGA chip integrated all functions for both ICCD readout and motor control logic (Kim *et al.* 2011). While waiting for the trigger, the mirror stays at the standby mode targeting the center of UFFO FOV, where the average slewing angle for upcoming GRB events is expected to be the minimum. When a GRB event trigger occurs, the logic sends the motor drivers the number of pulses according to the angle from the standby position to the target coordinates.

SMT also receives triggers from the other X-ray instrument on the Lomonosov satellite; the BDRG. However, the success probability in targeting to BDRG events is expected to be low due to its limited localization resolution. The motor control includes compensation logic for the drift of the spacecraft (SC) based on interpolation of SC altitude information issued every second by the satellite. When the payload is exposed in the sunlight, the system parks the mirror in the safety mode where the mirror faces toward the zenith direction to minimize reflection of the sunlight on the mirror to optical instruments. Maximum power consumption of the mirror system is about 3.5W including motors, drivers, and encoders. This power can be reduced to under 2W by releasing the holding torque of the

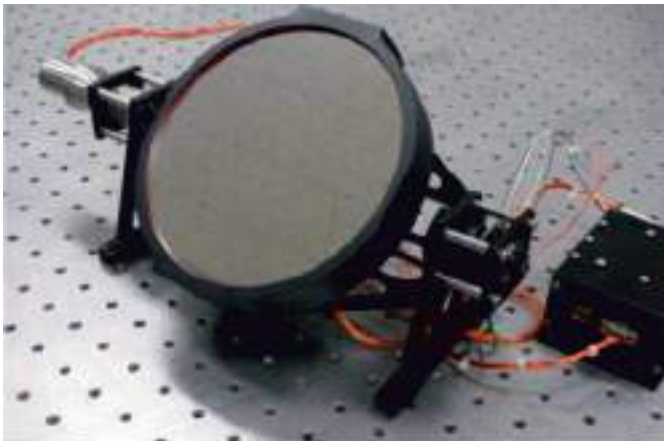


Fig. 2. Manufactured Motorized Gimbal Mirror System.

motors during the safety mode. Possible systematic errors such as optical axis mis-alignment and offsets of the rotary encoder can be corrected by parameters from calibrations during the flight.

3 Test results and readiness

The space qualification tests were performed with the fully integrated SMT system at the National Space Organization, Taiwan in Jul 2011. All devices including the motors, the encoders, the motor driver board, and the control board were found to be healthy under thermal vacuum conditions of the temperature range $-30 \sim 40^\circ\text{C}$ and the pressure of $\sim 10^{-7}$ mbar. No outgassing material was found to contaminate the optical instruments. Subsequent shock (45 g for 3 ms) and vibration (1–9.5 g in 5–2000 Hz) tests were also successfully carried out without showing any instrumental damages or functional degradations. The UFFO has been integrated together with other payloads onto Lomonosov at Istra, Russia in 2012. The full system validation tests during the integration demonstrated successful targeting and imaging taking capabilities. Further developments on the mirror control are still in progress to optimize the slewing speed and settling time.

4 Summary

We have successfully developed the slewing mirror system for the UFFO-pathfinder. The UFFO-pathfinder will demonstrate the new concept for fast response telescope design by employing a slewing mirror on a space-based instrument, which will open up the promising future of scientific discoveries from GRBs during the very early photon emission phase.

References

- Boella, G., Butler, R.C., Perola, G.C., *et al.*, 1997, A&AS, 122, 299
Chen, P., Ahmad, S., Ahn, K.B., *et al.*, 2011, Proceeding of ICRC [[arXiv:1106.3929](https://arxiv.org/abs/1106.3929)]
Gehrels, N., Chincarini, G., Giommi, P., *et al.*, 2004, ApJ, 611, 1005
Jeong, S., Nam, J.W., Ahn, K.B., *et al.*, 2013, Opt. express, 21, 2263
Jung, A., Ahmad, S., Ahn, K.B., *et al.*, 2011, Proceeding of ICRC [[arXiv:1106.3802](https://arxiv.org/abs/1106.3802)]
Kim, J.E., Lim, H., Jung A., *et al.*, 2011, Proceeding of ICRC [[arXiv:1106.3803](https://arxiv.org/abs/1106.3803)]
Park, I., Ahmad, S., Parrillon, P., *et al.*, 2013, New J. Phys., 15, 023031

IN-FLIGHT CALIBRATIONS OF UFFO-PATHFINDER

J. Řípa¹, S. Ahmad², P. Barrillon², S. Brandt³, C. Budtz-Jørgensen³,
A.J. Castro-Tirado⁴, S.-H. Chang⁵, Y.-Y. Chang⁶, C.R. Chen⁵,
P. Chen⁶, H.S. Choi⁷, Y.J. Choi⁸, P. Connell⁹, S. Dagoret-Campagne²,
C. Eyles⁹, B. Grossan¹⁰, J.J. Huang⁶, M.-H.A. Huang¹¹, S. Jeong¹²,
A. Jung¹², J.-E. Kim¹², M.-B. Kim¹, S.-W. Kim¹³, Y.-W. Kim¹,
A.S. Krasnov¹⁴, J. Lee¹, H. Lim¹, C.-Y. Lin⁵, E.V. Linder¹⁰, T.-C. Liu⁶,
N. Lund³, K.W. Min⁸, G.-W. Na¹², J.-W. Nam⁶, M.I. Panasyuk¹⁴,
I.H. Park¹, V. Reglero⁹, J.M. Rodrigo⁹, G.F. Smoot¹⁰, J.-E. Suh¹²,
S. Svertilov¹⁴, N. Vedenkin¹⁴, M.-Z. Wang⁶, I. Yashin¹⁴ and others from
the UFFO collaboration

Abstract. The Ultra-Fast Flash Observatory (UFFO), which will be launched onboard the *Lomonosov* spacecraft, contains two crucial instruments: UFFO Burst Alert & Trigger Telescope (UBAT) for detection and localization of Gamma-Ray Bursts (GRBs) and the fast-response Slewing Mirror Telescope (SMT) designed for the observation

¹ Sungkyunkwan University, Suwon, South Korea; e-mail: ripa.jakub@gmail.com

² Laboratoire de l'Accélérateur Linéaire, University of Paris-Sud 11, Orsay, France

³ Technical University of Denmark, Copenhagen, Denmark

⁴ Instituto de Astrofísica de Andalucía, CSIC, Granada, Spain

⁵ National Space Organization, Taiwan

⁶ LeCosPA, National Taiwan University, Taipei, Taiwan

⁷ Korea Institute of Industrial Technology, Cheonan, South Korea

⁸ Department of Physics, Korea Advanced Institute of Science and Technology, Daejeon, South Korea

⁹ University of Valencia, Valencia, Spain

¹⁰ Institute for the Early Universe, Ewha Womans University, Seoul, South Korea

¹¹ National United University, Miao-Li, Taiwan

¹² Department of Physics, Ewha Womans University, Seoul, South Korea

¹³ Department of Astronomy, Yonsei University, Seoul, South Korea

¹⁴ SINP, Moscow State University, Moscow, Russia

of the prompt optical/UV counterparts. Here we discuss the in-space calibrations of the UBAT detector and SMT telescope. After the launch, the observations of the standard X-ray sources such as pulsar in Crab nebula will provide data for necessary calibrations of UBAT. Several standard stars will be used for the photometric calibration of SMT. The celestial X-ray sources, *e.g.* X-ray binaries with bright optical sources in their close angular vicinity will serve for the cross-calibration of UBAT and SMT.

1 Methods

The UFFO-Pathfinder (Chen *et al.* 2011; Lim *et al.* 2012; Na *et al.* 2011; Park *et al.* 2012) consists of two scientific instruments. One is UBAT (Jung *et al.* 2011; Kim *et al.* 2012; Na *et al.* 2012; Rodrigo *et al.* 2012) for X-ray/gamma-ray observations of GRBs, and the second one is SMT (Jeong *et al.* 2011, 2012; Kim *et al.* 2011) of field of view $17' \times 17'$ for optical/UV observations of GRB afterglows. UBAT provides SMT positional information of a burst and SMT afterwards slews to this location to start collecting the optical/UV data. After the launch the positional accuracy of SMT will be checked and compared with the positional accuracy of UBAT on the real sky sources. We searched for the brightest X-ray/gamma-ray sources in the sky (see Table 1), which have bright optical sources (in filter V and/or B $< 10\text{--}5$ mag) in close angular vicinity ~ 5 arcmin and we intend to use them for UBAT-SMT positional cross-calibration and check up of the system (see Fig. 1).

By observing the Crab pulsar (Kirsch *et al.* 2005) we plan to carry out flux and positional accuracy calibrations of UBAT itself. After the launch we plan to take observations of several standard photometric stars in order to perform photometric calibration of SMT.

Table 1. An example of the brightest celestial X-ray sources, here the three brightest sources in the energy range 20–100 keV from the Fourth IBIS/ISGRI Soft Gamma-Ray Survey Catalog (Bird *et al.* 2010), which is the all sky catalogue compiled from the observations by the INTEGRAL satellite. Objects such as radio pulsars, high mass X-ray binaries (HMXRB) etc. will be used for cross-calibrations of SMT and UBAT.

Object	RA (deg)	dec (deg)	Flux at 20–100 keV ($\text{ph.s}^{-1}.\text{cm}^{-2}$)	Type
Crab	83.63	22.02	0.27	Radio Pulsar
Cyg X-1	299.60	35.20	0.21	HMXRB
4U 1700–377	255.99	−37.85	0.05	HMXRB

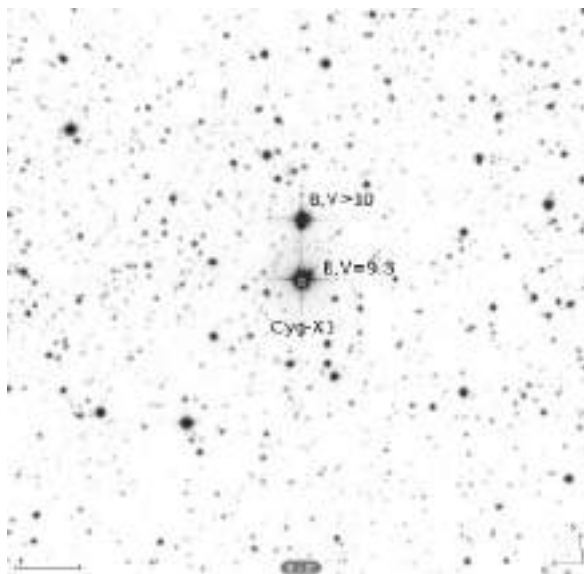


Fig. 1. An example of a bright celestial X-ray source (X-ray binary Cyg-X1) which is also bright in the optical range and also has a bright optical source, star V1674 Cyg, at a distance of 54 arcsec. X-ray source like this can be used for cross-calibration of SMT and UBAT.

This study was supported by Creative Research Initiatives (RCMST) of MEST/NRF.

References

- Bird, A.J., Bazzano, A., Bassani, L., *et al.*, 2010, ApJS, 186, 1
 Chen, P., Ahmad, S., Ahn, K., *et al.*, 2011, Proc. 32nd Int. Cosmic Ray Conf., 8, 240
 Jeong, S., Ahn, K., Nam, J., *et al.*, 2011, Proc. 32nd Int. Cosmic Ray Conf., 8, 238
 Jeong, S., Ahmad, S., Barrillon, P., *et al.*, 2012, Proc. SPIE, 8443, id. 84432S
 Jung, A., Ahmad, S., Ahn, K., *et al.*, 2011, Proc. 32nd Int. Cosmic Ray Conf., 8, 230
 Kim, J.E., Lim, H., Jung, A., *et al.*, 2011, Proc. 32nd Int. Cosmic Ray Conf., 8, 234
 Kim, J.E., Ahmad, S., Barrillon, P., *et al.*, 2012, Proc. SPIE, 8443, id. 84432V
 Kirsch, M.G., Briel, U.G., Burrows, D., *et al.*, 2005, Proc. SPIE, 5898, 22
 Lim, H., Ahmad, S., Barrillon, P., *et al.*, 2012, Proc. Int. Astron. Union, 279, 349
 Na, G.W., Ahn, K., Choi, H.S., *et al.*, 2011, Proc. 32nd Int. Cosmic Ray Conf., 8, 222
 Na, G.W., Ahmad, S., Barrillon, P., *et al.*, 2012, Proc. SPIE, 8443, id. 84432T
 Park, I.H., Ahmad, S., Barrillon, P., *et al.*, 2012, Proc. SPIE, 8443, id. 84430I
 Rodrigo, J.M., Macián, J.M., Biosca, J.T., *et al.*, 2012, Mem. Soc. Astron. Ital., 83, 370

Chapter XII.
Cosmology and Early Universe

GAMMA-RAY BURSTS AND THE FIRST STARS

V. Bromm¹

Abstract. Gamma-ray bursts (GRBs) triggered by the death of the first stars promise to provide a powerful probe into the state of the high-redshift universe. I will review the basic physics of how the first stars formed, evaluating whether they are suitable GRB progenitors. After providing estimates of the high-redshift GRB number density, I will discuss the utility of such bursts in probing the ionization state, and the degree of metal enrichment, of the early intergalactic medium. The prospects for these studies are bright, provided that we can fly a dedicated mission that combines a gamma-ray detector with on-board near-infrared capabilities.

1 Introduction

One of the key questions in modern cosmology is to understand how the first stars and galaxies ended the cosmic dark ages a few hundred million years after the Big Bang (Barkana & Loeb 2001; Bromm *et al.* 2009; Loeb 2010). Prior to their emergence, the universe exhibited a simple state, devoid of complex structure, of any elements heavier than lithium, and of high-energy radiation fields. Within Λ CDM cosmology, the first stars, the so-called Population III (Pop III), are predicted to form at $z \sim 20 - 30$ in dark matter minihalos of mass $\sim 10^6 M_{\odot}$. The formation of the first bona-fide galaxies, implying the presence of long-lived stellar systems, may be delayed until more massive host halos become available (Bromm & Yoshida 2011). Once the first sources of light have appeared on the cosmic scene, the universe was rapidly transformed through the input of ionizing radiation and heavy chemical elements. The character of this fundamental transition, as well as the assembly process of the first galaxies, crucially depended on the feedback exerted by Pop III stars (Ciardi & Ferrara 2005). The feedback in turn is determined by the initial mass function (IMF) of the first stars (Bromm & Larson 2004; Glover 2005). Although important uncertainties remain, the key prediction is that the Pop III IMF is biased towards high mass (top-heavy). At

¹ Department of Astronomy, University of Texas at Austin, USA

least a fraction of the first stars could therefore have collapsed into massive black holes (BHs) at the end of their short lives, and thus provide viable gamma-ray burst (GRB) progenitors.

Upcoming facilities such as the *James Webb Space Telescope (JWST)*, and the next generation of extremely-large telescopes on the ground (GMT, TMT, E-ELT) promise to open up a direct window into the first billion years of cosmic evolution (Gardner *et al.* 2006). Despite their exquisite sensitivity at near-IR wavelengths, even these observatories may not be able to directly probe the first stars, unless they formed in massive clusters (Pawlik *et al.* 2011), or were gravitationally lensed (Rydberg *et al.* 2012). The only opportunity to probe individual Pop III stars may be to catch them at the moment of their explosive death. This could involve extremely energetic supernova (SN) events, such as hypernovae or pair-instability SNe (Hummel *et al.* 2012; Pan *et al.* 2012), or GRBs. The latter fate depends on whether Pop III stars could give rise to suitable collapsar progenitors, involving rapidly rotating massive stars (MacFadyen & Woosley 1999). Since Pop III stars are predicted to fulfill both requirements (see the discussion below), GRBs are expected to be prevalent at very high redshifts. Indeed, GRBs may play a key role in elucidating primordial star formation, as well as the properties of the early intergalactic medium (IGM), given their extreme intrinsic brightness, both of the prompt γ -ray emission, as well as that of the prolonged afterglow.

A number of features render GRBs ideal probes of the epoch of first light (Loeb 2010): (*i*) Traditional sources to observe the high- z universe, such as quasars and Lyman- α emitting galaxies, severely suffer from the effects of cosmological dimming, whereas GRB afterglows, if observed at a fixed time after the trigger, exhibit nearly-flat infrared fluxes out to very high z (Ciardi & Loeb 2000). This counter-intuitive effect arises, because a fixed time interval in the observer frame translates into an increasingly early time in the source frame. Such earlier times in turn sample the rapidly decaying GRB lightcurve² at the moment of maximal brightness, thus compensating for the cosmological dimming (increasing luminosity distance). (*ii*) In the hierarchical setting of cosmic structure formation, earlier times are dominated by lower-mass host systems. The massive hosts required for quasars and bright galaxies therefore are “dying out” at the highest redshifts (Mortlock *et al.* 2011). GRBs, on the other hand, mark the death of individual stars, which can form even in very low-mass systems. (*iii*) Finally, Pop III GRBs would provide very clean background sources to probe the early IGM. Again reflecting the low masses of their hosts, any proximity effect should be much reduced, as ionized bubbles are confined to the immediate vicinity of the Pop III system; the IGM would thus largely remain unperturbed. In addition, since GRB afterglow spectra can be described as featureless, broken power-laws (Vreeswijk *et al.* 2004), any signature imprinted by absorption and emission events along a given line of sight can be easily discerned. The outlook for GRB cosmology, therefore, is bright.

²Note that this argument pre-supposes that the power-law afterglow decay has been established, and may not be valid at the earliest times.

Future missions, such as *JANUS*, *Lobster*, or *SVOM*, promise to fully unleash its potential.

2 Formation of the first stars

The longstanding consensus view has been that the conditions in the early universe favored the formation of predominantly massive stars, such that the Pop III IMF was top-heavy (Abel *et al.* 2002; Bromm *et al.* 2002; Bromm & Larson 2004). This expectation rests on the much less efficient cooling in pure H/He gas, where the only viable cooling agent is molecular hydrogen. The primordial gas can therefore reach temperatures of only ~ 200 K, compared to the 10 K reached in dust-cooled molecular clouds in the present-day Milky Way. The correspondingly enhanced thermal pressure is reflected in a Jeans mass that is larger by one to two orders of magnitude in the Pop III case. Another element of this “standard model” of primordial star formation has been that the first stars formed typically in isolation, one per minihalo.

Recently, beginning with work done in 2009, this traditional paradigm has been refined in important ways (Turk *et al.* 2009; Stacy *et al.* 2010; Clark *et al.* 2011; Greif *et al.* 2011, 2012). Supercomputing power, as well as algorithmic advances, now enable us to follow the protostellar collapse to densities, $n \sim 10^{22} \text{ cm}^{-3}$, where the initial hydrostatic core forms in the center of the cloud (Yoshida *et al.* 2008). Crucially, the computations can now also be extended into the main accretion phase. An important lesson has been that accretion is mediated through a near-Keplerian disk, similar to present-day star formation. The hot conditions in the surrounding cloud result in extremely large rates of infall onto the disk ($\dot{M} \propto T^{3/2}$); this rapid mass loading drives the disk inevitably towards gravitational instability, such that a small multiple of Pop III protostars emerges, often dominated by a binary system. It is not yet possible to extend such ab-initio simulations all the way to the completion of the protostellar assembly process; the final mass of Pop III stars and their final IMF are thus still subject to considerable uncertainty. However, first attempts to carry out the radiation-hydrodynamical calculations required to treat the late accretion phase, where protostellar feedback tends to limit further infall, have confirmed the basic prediction: the first stars were typically massive, with masses of a few $\sim 10 M_{\odot}$, although rarely very massive ($> 100 M_{\odot}$), as previously thought, forming as a member of small multiple systems (McKee & Tan 2008; Hosokawa *et al.* 2011; Stacy *et al.* 2012a).

2.1 Collapsar requirements

Are Pop III stars suitable GRB progenitors? To successfully trigger a collapsar event, the leading contender for long-duration GRBs (Woosley 1993; MacFadyen *et al.* 2001), a number of conditions have to be met. These are quite stringent, and often difficult to fulfill simultaneously (Zhang & Fryer 2004; Petrovic *et al.* 2005; Belczynski *et al.* 2007).

The first requirement for a collapsar central GRB engine, the emergence of BH remnants, is thus fulfilled. The binary nature of Pop III stars may also enable

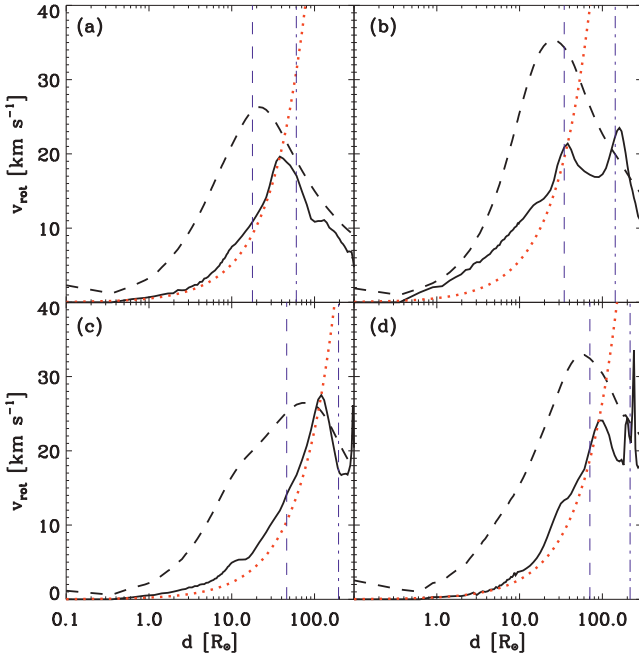


Fig. 1. Rotational velocities in Pop III protostars (from Stacy *et al.* 2012b). The panels show the situation in four statistically independent minihalos. *Solid lines*: the rotational velocity as a function of radial distance from the protostellar center. *Dashed lines*: Keplerian velocity *vs.* radius. *Dotted lines*: rotational velocity expected for solid-body rotation. In each panel the vertical lines mark the location of the protostellar “surface”, defined as the boundary of the hydrostatic core (dashed), or the radius of the photosphere (dot-dashed). It is evident that rotational velocities comprise sizable fractions of the maximal, Keplerian, values. The caveat here is that the simulations could follow the evolution only for ~ 10 yr after the formation of the initial hydrostatic core.

them, if the binary is sufficiently close to allow for Roche-lobe overflow and a common-envelope phase, to expel the extended hydrogen (and helium?) envelope. This may be crucial to prevent the quenching of the relativistic jet, launched by the central engine (Bromm & Loeb 2006; but see Suwa & Ioka 2011). What about the additional requirement that the collapsar progenitor retains enough angular momentum? This question ties in with the rate of rotation of Pop III stars, where almost nothing is known yet. A first attempt to address this within a fully cosmological context has recently been carried out (Stacy *et al.* 2011, 2012b), indicating that the first stars may have typically been very fast rotators, with surface rotation speeds of a few 10% of the break-up value (see Fig. 1). Such high rates of rotation would have important consequences for Pop III stellar evolution, possibly enabling strong mixing currents, and for the fate encountered at death

(Yoon *et al.* 2006). Thus, it is plausible that all requirements for a collapsar central engine were in place in the early universe. The next question now is: How common were Pop III GRBs, and do current or planned missions have a fair chance to detect them?

2.2 How frequent were Pop III bursts?

Briefly after the cosmological distance scale to GRBs had been established, it was realized that they provide a powerful probe of the cosmic star formation history, extending out to very high redshifts where the first stars are expected to form (Lamb & Reichart 2000; Bromm & Loeb 2002). As a case in point, we now have examples of such bursts at very high redshifts, with the spectroscopically confirmed GRB 090423 at $z \simeq 8.2$ (Salvaterra *et al.* 2009; Tanvir *et al.* 2009), and a photometrically constrained candidate at $z \sim 9.4$ (Cucchiara *et al.* 2011). In addition, the radio afterglow of GRB 090423 has been detected with the VLA (Chandra *et al.* 2010), providing useful constraints on the afterglow energetics and geometry, as well as on the circumburst density. From these observations, we have learned that the afterglow properties of the very high- z bursts are not significantly different from the more local sample.

To explore the likely space of discovery, it is important to construct models of the high-redshift GRB rate. Schematically, this involves the following framework (for details, see Bromm & Loeb 2006):

$$\frac{dN_{\text{GRB}}^{\text{obs}}}{dz} = \psi_{\text{GRB}}^{\text{obs}}(z) \frac{\Delta t_{\text{obs}}}{(1+z)} \frac{dV}{dz}, \quad (2.1)$$

where $dN_{\text{GRB}}^{\text{obs}}$ is the number of GRBs, as observed with a given instrument, from within a redshift interval dz , $\psi_{\text{GRB}}^{\text{obs}}$ the number of bursts per comoving volume, and the other symbols have their usual meaning. The connection between the burst number density and cosmic star formation rate density (SFRD) can be expressed via:

$$\psi_{\text{GRB}}^{\text{obs}}(z) = \eta_{\text{GRB}} \psi_*(z) \int_{L_{\text{lim}}(z)}^{\infty} p(L) dL, \quad (2.2)$$

where $\psi_*(z)$ is the cosmic SFRD, η_{GRB} the GRB formation efficiency, $p(L)$ the GRB luminosity function, and $L_{\text{lim}}(z)$ the minimum intrinsic luminosity required to detect the burst with a given instrument, from a given redshift.

Most of the intricacies come in when dealing with the efficiency factor. For simplicity, one could assign a constant value, possibly calibrating it to the observed Pop I/II value: $\eta_{\text{GRB}} \sim 10^{-9}$ bursts per unit solar mass (Bromm & Loeb 2006). Within such an idealized model, one typically estimates that of order 10% of all *Swift* GRBs should originate from $z > 5$, with of order 0.1 Pop III bursts per year. Detection of a Pop III burst may thus lie just outside of the *Swift* capabilities, unless we get lucky. However, the real situation is likely much more complicated. The GRB efficiency could well depend on redshift, or on environmental factors, such as the metallicity of the host system (Langer & Norman 2006). Since the early modeling of the GRB redshift distribution, significant refinements have been

added (Daigne *et al.* 2006; Campisi *et al.* 2011; deSouza *et al.* 2011; Ishida *et al.* 2011; Elliott *et al.* 2012). It is important, though, to not lose sight of the inherently very uncertain nature of this enterprise.

Among the most crucial uncertainties is the physical mechanism responsible for terminating the early mode of predominantly massive Pop III stars. Current thinking often posits that this Pop III to II transition is brought about by chemical feedback. The idea is that the cooling ability of star forming gas is greatly enhanced once it has been enriched with the first heavy elements beyond a threshold level, termed the “critical metallicity” (of order $Z_{\text{crit}} \sim 10^{-4} Z_{\odot}$). The underlying physics is complex. Some models claim that fine-structure lines of neutral oxygen and singly-ionized carbon may drive this transition (Bromm & Loeb 2003); others identify dust cooling as the key agent (Schneider *et al.* 2006). If dust were indeed responsible, predicted values of Z_{crit} are typically smaller by one to two orders of magnitude, compared with the fine-structure scenarios.

3 GRBs as probes of the early IGM

Assuming standard, shocked-synchrotron theory, the properties of Pop III afterglows have been worked out (Gou *et al.* 2004; Inoue *et al.* 2007). Consistently, across a wide range of wavelengths, from the near-IR to radio, as well as in the X-ray bands, flux levels are predicted that bring such Pop III bursts within reach of existing and planned instruments. A key uncertainty in such modeling is what to assume for the circumburst density (Wang *et al.* 2012). If we can identify these bursts through rapid follow-up in the near-IR, they will provide us with exquisite background sources to probe the early IGM. Firstly, we can place constraints on the ionized fraction of the high- z IGM, as a function of redshift. This would provide a much more discerning picture of the cosmic reionization history, compared to the integral constraint from *WMAP*. In the latter case, by measuring the optical depth to Thomson scattering along the travel path of a CMB photon from the surface of last scattering to $z = 0$, we cannot distinguish between models that can be quite different, but happen to yield the same line-of-sight integral. The basic idea is to exploit the absorption strength in the red damping wing of the Lyman- α resonance, which is very sensitive to any residual IGM neutral fraction (Barkana & Loeb 2004). This idea has been tested with the exquisite spectrum taken for GRB 050904 at $z \simeq 6.3$ (Totani *et al.* 2006). The problem there proved to be the strong local column in neutral hydrogen, which completely overwhelmed any contribution from the general IGM. Again, the hope is that if we go to Pop III bursts, such local contamination would not be a problem, given that the first stars are expected to form in low-mass host systems. Any local damping would then be small compared with the cosmological signal.

A second use of a Pop III GRB background source is to scrutinize the degree and nature of metal enrichment in the pre-galactic universe (see Fig. 2). The first stars are predicted to form in a highly biased region of the Gaussian random field of density fluctuations, such that their formation sites are strongly clustered. Any Pop III burst would then likely explode in a region that already may have been

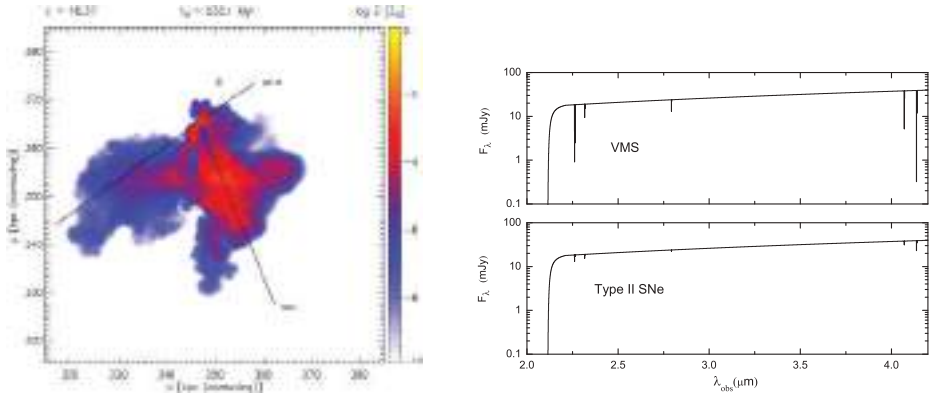


Fig. 2. Probing pre-galactic metal enrichment (from Wang *et al.* 2012). *Left panel:* metallicity distribution in a region of clustered Pop III star formation. The box size is 70 kpc (comoving), shown at $z \simeq 16.4$. A Pop III GRB explodes at the intersection of the two lines. *Right panel:* resulting near-IR absorption spectra. We consider two different cases for the Pop III SN enrichment, from conventional core-collapse (Type II) and from a very massive star (VMS) progenitor. The situation corresponds to 1 day (in the observer frame) after the GRB trigger. The lines are imprinted by low-ionization species of C, O, Si, and Fe. The sharp cutoff at lower wavelengths is due to the complete absorption of Ly α radiation in the neutral IGM. The VMS absorption-line signal should well be within the capabilities of the *JWST*.

enriched by a small number of SNe (Greif *et al.* 2010). The diagnostic provided by a high signal-to-noise, near-IR spectrum of a Pop III afterglow may allow us to not only measure the overall metallicity at a given redshift. Additionally, we may also be able to distinguish between the abundance pattern from different kinds of explosion, such as a pair-instability SN, a hypernova, or a more conventional core-collapse (Type II) event (Karlsson *et al.* 2013). A lower-redshift, $z \simeq 2$, example of this diagnostic is GRB 081008, where high-resolution spectroscopy with the Very Large Telescope has probed the host interstellar medium (D’Elia *et al.* 2011).

4 Signature of Pop III bursts

An important unsolved problem in GRB cosmology is how to uniquely identify possible Pop III bursts. High-redshift in itself is not sufficient, because different stellar populations will form contemporaneously, at least at $z \leq 15$. Attempts have been made to work out signatures that rely entirely on the gamma-ray emission, basically derived from the higher BH masses expected for Pop III remnants (*e.g.*, Mészáros & Rees 2010). However, such diagnostics appear very uncertain, not least because: How would we test or calibrate such gamma-ray-only markers? The commonly held notion that Pop III bursts could be unambiguously identified via the absence of any metal absorption lines in their afterglow spectra may not

work either (see the argument in the previous section). What are we then left with? The metal-bubbles discussed above would originate at distances exceeding a few (physical) kpc from the burst. The immediate “near-zone” of the Pop III GRB, however, would still be chemically pristine. A unique identifier for Pop III bursts may thus be an ensemble of H/He *emission* lines, possibly on top of the metal absorption signal originating farther away from the burst. The emission lines would arise as recombination radiation in the compact H II region powered by the UV-ionizing flux from the GRB afterglow. Such an emission line signature still needs to be worked out in detail, to see whether the line fluxes are sufficiently bright to render them detectable.

References

- Abel, T., Bryan, G.L., & Norman, M.L., 2002, *Science*, 295, 93
 Barkana, R., & Loeb, A., 2001, *Phys. Rep.*, 349, 125
 Barkana, R., & Loeb, A., 2004, *ApJ*, 601, 64
 Belczynski, K., Bulik, T., Heger, A., & Fryer, C.L., 2007, *ApJ*, 664, 986
 Bromm, V., Coppi, P.S., & Larson, R.B., 2002, 564, 23
 Bromm, V., & Larson, R.B., 2004, *ARA&A*, 42, 79
 Bromm, V., & Loeb, A., 2002, *ApJ*, 575, 111
 Bromm, V., & Loeb, A., 2003, *Nature*, 425, 812
 Bromm, V., & Loeb, A., 2006, *ApJ*, 642, 382
 Bromm, V., Yoshida, N., Hernquist, L., & McKee, C.F., 2009, *Nature*, 459, 49
 Bromm, V., & Yoshida, N., 2011, *ARA&A*, 49, 373
 Campisi, M.A., Maio, U., Salvaterra, R., & Ciardi, B., 2011, *MNRAS*, 416, 2760
 Chandra, P., Frail, D.A., Fox, D., *et al.*, 2010, *ApJ*, 712, L31
 Ciardi, B., & Ferrara, A., 2005, *Space Sci. Rev.*, 116, 625
 Ciardi, B., & Loeb, A., 2000, *ApJ*, 540, 687
 Clark, P.C., Glover, S.C.O., Smith, R.J., *et al.*, 2011, *Science*, 331, 1040
 Cucchiara, A., Cenko, S.B., Bloom, J.S., *et al.*, 2011, *ApJ*, 736, 7
 Daigne, F., Rossi, E.M., & Mochkovitch, R., 2006, *MNRAS*, 372, 1034
 D’Elia, V., Campana, S., Covino, S., *et al.*, 2011, *MNRAS*, 418, 680
 de Souza, R.S., Yoshida, N., & Ioka, K., 2011, *A&A*, 533, A32
 Elliott, J., Greiner, J., Khochfar, S., *et al.*, 2012, *A&A*, 539, A113
 Gardner, J.P., Mather, J.C., Clampin, M., *et al.*, 2006, *Space Sci. Rev.*, 123, 485
 Glover, S.C.O., 2005, *Space Sci. Rev.*, 117, 445
 Gou, L.J., Mészáros, P., Abel, T., & Zhang, B., 2004, *ApJ*, 604, 508
 Greif, T.H., Glover, S.C.O., Bromm, V., & Klessen, R.S., 2010, *MNRAS*, 387, 1021
 Greif, T.H., Springel, V., White, S.D.M., *et al.*, 2011, *ApJ*, 737, 75
 Greif, T.H., Bromm, V., Clark, P.C., *et al.*, 2012, *MNRAS*, 424, 399
 Hosokawa, T., Omukai, K., Yoshida, N., & Yorke, H.W., 2011, *Science*, 334, 1250
 Hummel, J.A., Pawlik, A.H., Milosavljević, M., & Bromm, V., 2012, *ApJ*, 755, 72
 Inoue, S., Omukai, K., & Ciardi, B., 2007, *MNRAS*, 380, 1715

- Ishida, E.E.O., de Souza, R.S., & Ferrara, A., 2010, MNRAS, 418, 500
- Karlsson, T., Bromm, V., & Bland-Hawthorn, J., 2013, Rev. Mod. Phys., in press
[arXiv:1101.4024]
- Lamb, D.Q., & Reichart, D.E., 2000, ApJ, 536, 1
- Langer, N., & Norman, C.A., 2006, ApJ, 638, L63
- Loeb, A., 2010, “How did the first stars and galaxies form?” (Princeton Univ. Press: Princeton)
- MacFadyen, A.I., & Woosley, S.E., 1999, ApJ, 524, 262
- MacFadyen, A.I., Woosley, S.E., & Heger, A., 2001, ApJ, 550, 410
- McKee, C.F., & Tan, J.C., 2008, ApJ, 681, 771
- Mészáros, P., & Rees, M.J., 2010, ApJ, 715, 967
- Mortlock, D.J., Warren, S.J., Venemans, B., *et al.*, 2011, Nature, 474, 616
- Pan, T., Kasen, D., & Loeb, A., 2012, MNRAS, 422, 2701
- Pawlak, A.H., Milosavljević, M., & Bromm, V., 2011, ApJ, 731, 54
- Petrovic, J., Langer, N., Yoon, S.-C., & Heger, A., 2005, A&A, 435, 247
- Rydberg, C.-E., Zackrisson, E., Lundqvist, P., & Scott, P., 2012, MNRAS, submitted
[arXiv:1206.0007]
- Salvaterra, R., Della Valle, M., Campana, S., *et al.*, 2009, Nature, 461, 1258
- Schneider, R., Omukai, K., Inoue, A.K., & Ferrara, A., 2006, MNRAS, 369, 1437
- Stacy, A., Greif, T.H., & Bromm, V., 2010, MNRAS, 403, 45
- Stacy, A., Bromm, V., & Loeb, A., 2011, MNRAS, 413, 543
- Stacy, A., Greif, T.H., & Bromm, V., 2012a, MNRAS, 422, 290
- Stacy, A., Greif, T.H., Klessen, R.S., Broom, V., & Loeb, A., 2012b, MNRAS, submitted
[arXiv:1209.1439]
- Suwa, Y., & Ioka, K., 2011, ApJ, 726, 107
- Tanvir, N.R., Fox, D.B., Levan A.J., *et al.*, 2009, Nature, 461, 1254
- Totani, T., Kawai, N., Kosugi, G., *et al.*, 2006, PASJ, 58, 485
- Turk, M.J., Abel, T., & O’Shea, B.W., 2009, Science, 325, 601
- Vreeswijk, P.M., Ellison, S.L., Ledoux, C., *et al.*, 2004, A&A, 419, 927
- Wang, F.Y., Bromm, V., Greif, T.H., *et al.*, 2012, ApJ, 760, 27
- Woosley, S.E., 1993, ApJ, 405, 273
- Yoon, S.-C., Langer, N., & Norman, C., 2006, A&A, 460, 199
- Yoshida, N., Omukai, K., & Hernquist, L., 2008, Science, 321, 669
- Zhang, W., & Fryer, C.L., 2004, in “Stellar Collapse”, ed. C.L. Fryer (Dordrecht: Kluwer), 327

A COMMON BEHAVIOR IN THE LATE X-RAY AFTERGLOW OF ENERGETIC GRB-SN SYSTEMS

L. Izzo^{1,2}, G.B. Pisani³, M. Muccino¹, J.A. Rueda^{1,2}, Y. Wang¹,
C.L. Bianco^{1,2}, A.V. Penacchioni³ and R. Ruffini^{1,2}

Abstract. The possibility to divide GRBs in different subclasses allow to understand better the physics underlying their emission mechanisms and progenitors. The induced gravitational collapse scenario proposes a binary progenitor to explain the time-sequence in GRBs-SNe. We show the existence of a common behavior of the late decay of the X-ray afterglow emission of this subclass of GRBs, pointing to a common physical mechanism of their late emission, consistent with the IGC picture.

It has been proposed that the temporal coincidence of a Gamma Ray Burst (GRB) and a supernova (SN) Ib/c emission (GRB-SN) can be explained by the concept of induced gravitational collapse (IGC) (Ruffini *et al.* 2001, 2007). This concept has been extended recently (Rueda & Ruffini 2012) and can be summarized as follows. In the IGC scenario the GRB-SN progenitor is a binary system composed by an evolved massive star and a Neutron Star (NS). The evolved star undergoes a SN explosion leading to a subrelativistic expansion of the SN core progenitor outer layers, while its high density core contracts, as it was shown in (Arnett & Meakin 2011). Since the SNe associated to GRBs are of type Ib/c, the SN core progenitor is very likely an evolved Wolf-Rayet, or a Carbon-Oxygen (CO) core. Part of the expelled material is accreted at a high rate by the NS companion, fastly increasing the NS mass. The NS can reach, in a few seconds, the critical mass and consequently gravitationally collapses to a Black Hole (BH). This gravitational collapse process leads to the emission of a canonical GRB. The SN emission may again be observed as an optical bump in the late afterglow emission.

These two distinct emissions, the early SN expansion that leads to the accretion process (Episode 1) and the actual GRB emission (Episode 2), have been

¹ Sapienza University of Rome, P.le Aldo Moro 5, 00185 Rome, Italy;
e-mail: luca.izzo@gmail.com

² ICRA Net, Piazza della Repubblica 10, 65122 Pescara, Italy

³ Erasmus Mundus Joint Doctorate IRAP PhD. Student, Université de Nice Sophia Antipolis, Nice Cedex 2, Grand Château Parc Valrose, France

called double emission episodes and were clearly identified in the gamma-ray energy range in GRB 090618 (Izzo *et al.* 2012a) and GRB 101023 (Penacchioni *et al.* 2012). Recent observations of the late ($t = 10^8 - 10^9$ s) emission of low energetic GRBs-SNe, or X-ray Flashes (XRFs), show a distinct emission in the X-ray regime consistent with temperatures $T \sim 10^7 - 10^8$ K. Similar features have been also observed in the two Type Ic SNe (SN 2002ap and SN 1994I) that are not associated to GRBs. It was shown (Negreiros *et al.* 2012) that this late decay emission in the X-rays of GRB 980425/sn1998bw, GRB 030329/sn2003dh and GRB 03123/SN2003lw might be explained as the luminosity coming from the cooling of the neo-NS from the remnant of the SN. In more energetic GRBs-SNe additional mechanisms, related either to the BH, formed from the IGC of the NS companion, or to the neo-NS left by the SN, could be at work. We will present elsewhere these other mechanisms in connection with the IGC scenario.

We turn now to the analysis of the late X-ray afterglow of our sample of GRBs-SNe. It consists of 6 GRBs, with redshift, for which a SN event was observed after about 10 days from the GRB trigger, or a SN was not observed but there is a double emission episode in the prompt emission of the GRB. We have also considered two additional GRBs, 101023 and 110709B, for which there is no a redshift observation, but their prompt emission shows evidence of a double emission episode. For these two GRBs there is an estimated redshift of 0.9 and 0.75 respectively (Penacchioni *et al.* 2012, 2013). The sample include GRB 090618 and GRB 060729, at redshift of 0.54, for which a photometric bump associated to a SN event was detected and reported in literature (Cano *et al.* 2011). GRB 091127 is associated with sn2009nz at a redshift of $z = 0.49$. We include also GRB 111228 for which a transient, associated with a SN event, was detected in the differential photometry of the optical emission in two epochs, 34 and 76 days after the GRB trigger (D'Avanzo *et al.* 2012). We made similar considerations for GRB 080319B, where the optical emission in the i' -band shows a decay unusual for a GRB afterglow and more related to an underlying SN emission (Kann *et al.* 2008). We include also GRB 061007, for which no SN event was detected, due to the lack of late optical observations, but for which a clear thermal first emission episode was reported in literature (Larsson *et al.* 2011). These GRBs have an isotropic energy larger than 10^{52} erg, which is at least two orders of magnitude larger than the energy emitted in the well-known cases of GRB 980425 and GRB 060218, which have a relative low-redshift and are not taken into account in this analysis.

We have compared the late X-ray emission of all GRBs in the sample. We developed a code which allows to transform this late GRB emission in a luminosity (0.3–10 keV) light curve computed in the rest-frame. In order to extrapolate any spectrum in a common rest-frame, we have corrected any GRB for a specific correction factor, proportional to the respective redshift. After the correction for the distance and for the time, we have included all the X-ray afterglow light curves in a common picture, see left panel in Figure 1. It is evident a common behavior at late times, $t > 10^4$ s. A fit with a simple power-law function, $L_{t_0} \propto t^\gamma$ of the emission after $t_0 = 2 \times 10^4$ s at $z = 1$, provides the values of the luminosity at the initial time t_0 and of the time decay index. We noted a clustering of the

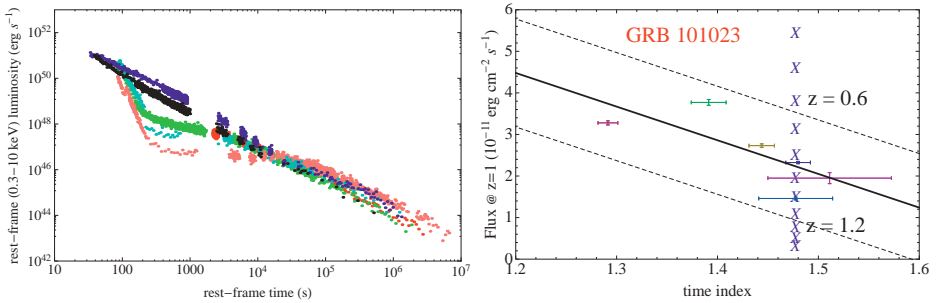


Fig. 1. The X-ray luminosity of the six GRBs with measured redshift in the 0.3–10 keV rest-frame energy range (*left panel*). The estimates of the redshift for GRB 101023. The solid black line is the best fit of the correlation $F_{obs,z=1}\gamma$ where $F_{obs,z=1}$ is the observed flux at $z = 1$ and at $t = 20\,000$ s in the rescaled light curve, γ is the power-law index decay of the late X-ray afterglow light curve. The dashed lines correspond to a deviation of $2\sigma_{ext}$ from the best fit line, where σ_{ext} is the extra scatter error computed using the method explained in D'Agostini (2005). The blue crosses represent the values of $(F_{obs,z=1}, \gamma)$ for GRB 101023 computed for different values of the redshift (*right panel*).

distribution of the luminosities for any GRB in the sample around a best-fit line, similar to other results in literature (Penacchioni *et al.* 2012, 2013). We then estimated the redshift for GRB 101023, $0.6 < z < 1.2$ with best value $z = 1.0$ (see right panel in Fig. 1), and GRB 110709B, $0.4 < z < 0.6$ with best value $z = 0.5$, by varying their redshift and computing the corresponding L_{t_0} and γ .

References

- Arnett, W.D., & Meakin, C., 2011, ApJ, 733, 78
- Bernardini, M.G., Margutti, R., Mao, J., *et al.*, 2012, A&A, 539, A3
- Cano, Z., Bersier, D., Guidorzi, C., *et al.*, 2011, MNRAS, 413, 669
- D'Agostini, G., 2005 [[arXiv:physics/0511182](https://arxiv.org/abs/physics/0511182)]
- D'Avanzo, P., Melandri, A., Palazzi, E., *et al.*, 2012, GCN 13609
- Dainotti, M.G., Willingale, R., Capozziello, S., *et al.*, 2010, ApJ, 722, 215
- Izzo, L., Rueda, J.A., & Ruffini, R., 2012, A&A, 548, L5
- Izzo, L., Penacchioni, A.V., Ruffini, R., *et al.*, 2012, A&A, 543, A10
- Kann, A., Schulze, S., & Updike, A.C., 2008, GCN 7627
- Larsson, J., Ryde, F., Lundman, C., *et al.*, 2011, MNRAS, 414, 2642
- Negreiros, R., Rueda, J.A., Bianco, C.L., *et al.*, 2012, A&A, 540, A12
- Penacchioni A.V., Ruffini, R., Izzo, L., *et al.*, 2012, A&A, 538, A58
- Penacchioni A.V., Ruffini, R., Bianco, C.L., *et al.*, 2013 [[arXiv:1301.6014](https://arxiv.org/abs/1301.6014)]
- Rueda, J.A., & Ruffini, R., 2012, ApJ, 758, L7
- Ruffini, R., Bianco, C.L., Fraschetti, F., *et al.*, 2001, ApJ, 555, L117
- Ruffini, R., Bernardini, M.G., Bianco C.L., *et al.*, 2007, ESA Sp. Pub., 622, 561

Chapter XIII.

Instrumentation & Techniques-III Future Projects

X-RAY AND GAMMA-RAY POLARIMETRY OF GRBS

E. Costa¹

Abstract. Polarimetry is expected to play a major role as a diagnostic tool for GRBs. Techniques and methods for X/Gamma ray polarimetry are reviewed including the specific problems related to the transient nature of the sources. Optical data do not encourage optimistic predictions on polarimetry of afterglows. I review some of the existing and proposed experiments for the prompt and discuss the existing results.

1 Introduction

Polarimetry is a powerful diagnostic tool in X-ray and Gamma-ray astronomy in more than one astrophysical context. Polarization may be intrinsic to the emission process, or introduced by the transfer of the radiation from the source to the observer, when the geometry highly deviates from spherical symmetry. GRB show non thermal spectra, where synchrotron likely plays an important role and evolve so fast that thermalization is unlikely. They could be beamed or, in any case, the so called relativistic collimation introduces a selection of emitting regions visible to the observer, preventing the large scale smearing of polarization. Therefore GRB have been candidate for polarimetry but measuring the polarization of X and Gama rays is not easy and needs dedicated instruments and observing strategies. X-ray polarimetry of afterglows is only a special case of the polarimetry of X-ray sources, that has not been attempted any more since 35 years. The polarimetry of the prompt emission has been performed as a byproduct of instruments, built for other purposes. The very first data from a dedicated instrument are now coming. I discuss the validity and the significance of these data.

2 How can we measure the polarization of hard X-rays and soft Gamma-rays

Every polarimeter is composed of an analyzer, where an interaction occurs, whose outcome angle depends on polarization, and a detector of the products of the

¹ Istituto di Astrofisica e Planetologia Spaziali, 031 INAF, via del Fosso del Cavaliere, 100, Roma, Italy

interaction, to measure their angular distribution. Polarimeters can be *dispersive* when each angle is sampled at each time and *not dispersive* where all the angles are measured simultaneously. Dispersive polarimeters require the rotation around the optical axis. Non dispersive polarimeters in principle do not need, but in most cases the instrument response is not symmetric around the axis and rotation is needed to compensate the systematic effects. Every measurement of polarization can be reduced to building a modulation curve, namely a histogram of counts as a function of the angle. If the beam is not polarized the curve is flat:

$$N(\varphi) = \text{constant} \quad (2.1)$$

if it is polarized to some degree the modulation curve can be represented with the equation

$$N(\varphi) = A + B\cos^2(\varphi) \quad (2.2)$$

where the constant term A accounts for both the unpolarized fraction and the non ideal performance of the device. We can therefore define the modulation as:

$$M = \frac{N_{max} - N_{min}}{N_{max} + N_{min}}. \quad (2.3)$$

With a beam 100% polarized the modulation depends only on the instrument and is named μ or *modulation factor*. Thence the measurement of the polarization is:

$$\Pi = \frac{1}{\mu} \times \frac{B}{B + 2A}. \quad (2.4)$$

The Equation (2.1) is in practice a series of counts distributed with poisson statistics around the expected values. The constant B in 2.2 can be seen as the second term of the power spectrum in the fourier expansion of this series. Π is a positively defined quantity following a χ^2 distribution with 2 d.o.f.. By integrating we can compute the so called Minimum Detectable Polarization, conventionally given for a 99% probability.

$$MDP = \frac{4.29}{\varepsilon \mu F} \times \sqrt{\frac{B + \varepsilon F}{ST}} \quad (2.5)$$

where, S is the collecting surface of the instrument, ε is the efficiency, B is the background for unit surface and T the observing time.

This gives what we need, in terms of flux, area and observing time, to reject the hypothesis that a source is unpolarized. For a measurement of the polarization at 3σ level the time required is around twice that needed for the MDP (Weisskopf *et al.* 2009).

2.1 X-rays

The Bragg diffraction at 45° was the process applied for polarimetry in the first 25 years of X-ray Astronomy. The device is dispersive and the crystal and the

detector (mounted at 90° from the optical axis) are rotated around the axis (historically the whole satellite was rotating). The modulation factor is 1 but the band width is limited to few eV and the background high, so that the measurement is reliable but the sensitivity is poor. This can be mitigated by using mosaic crystals, with a broader rocking curve, slightly bent to achieve a moderate focussing. This method was applied aboard OSO-8 for the only positive detection of polarization ever in the X-ray band (Weisskopf *et al.* 1976). In a telescope, a small flat crystal can be mounted at 45° before the focus and the photons, compliant with the Bragg condition, are focussed on a secondary plane in a newtonian mounting.

Around 10 years ago a big change occurred with the introduction of detectors based on photoelectric effect within a gas. The photoelectrons ejected from the K-shell (the large majority) have angular distribution of \cos^2 around the electric vector. This means that, were we able to measure this direction, the process would be a *perfect* analyzer of linear polarization. This was well known since the beginning of X-ray astronomy. The troubles derive from the fact that, in the range of X-rays, the electrons propagate in materials much less than photons of the equivalent energy. The newly produced electron ionizes the material and eventually is completely stopped. But it scatters as well, so that the information on the direction is quickly lost. To derive this direction one must be able to analyze the charge distribution within a layer of material which is a very small fraction of the thickness of material needed to stop a photon with a decent efficiency. As a consequence the method could be efficiently applied only with gas detectors and only after the progress in microelectronics allowed for the development of detectors finely subdivided. The first implementation was in Costa *et al.* (2001). A gas cell is polarized with a drift field parallel to the optical axis. The electrons of the track created in the gas by the photoelectron, are drifted by a constant field to a Gas Electron Multiplier, that amplifies the track while preserving the shape and the proportionality to the charge. The amplified track is collected by a read out plane finely pixellated. A further improvement came soon after (Bellazzini *et al.* 2004) when the readout plane was built as the top of an ASIC VLSI chip. The effect is that a single solid block includes the bottom of the detector, the read-out pad, an individual analog electronic chain for each of the 100 000 pads, a triggering system and a pre-selection electronics that allows to fetch out the content of only a frame around pixels that passed the threshold. The content of these pixels is A/D converted. From the analysis of the track the impact point, the direction angle and the total charge are derived. In the focus of a telescope this device, named Gas Pixel Detector can therefore perform at the same time images, spectroscopy, timing and polarization.

A different concept to exploit the same physical process was developed, a few years later, at GSFC (Black 2007). In a gas cell an electric field, perpendicular to the optical axis, drifts the electrons of the track to a GEM and then to a set of strips that make the one-dimensional projection of the track. The image in the drift direction is performed with the method of the Time Projection Chamber. This method looses the information on the absorption point and needs rotation because systematics heavily depend on the drift direction. The GPD polarimeter

is truly imaging, needs no rotation and minimizes background and systematics, while the TPC makes polarimetry of everything falls within a large field of view and needs rotation, but can be built thicker and, thence, more efficient.

The role of diffraction is not completely disappeared. Herman L. Marshall at MIT developed an instrument based on diffraction from multilayered artificial crystals (Marshall 2010) of photons collected by a telescope. The method is effective at very low energies.

2.2 Gamma-rays

The application of the photoelectric effect in gases in principle could be extended up to xenon but, in practice has not, due to the higher scattering/stopping ratio and to the highly non-diagonal response matrix. The technique of the photoelectron in gas has been so far limited to mixtures based on pressurized Argon, which restricts the application below 30 keV.

At higher energies the dominant interaction is the Compton effect. If we express E and E' the energy of the photon before and after the scattering respectively, the Klein Nishina cross section is

$$\frac{d\sigma}{d\Omega} = \frac{r_0^2}{2} \frac{E'^2}{E^2} \left(\frac{E}{E'} + \frac{E'}{E} - 2 \sin^2 \vartheta \cos^2 \varphi \right) \quad (2.6)$$

where r_0 is the classic radius of the electron, ϑ is the scattering angle and φ the azimuth scattering angle. Contrary to the photoelectric effect the modulation depends on the angle of scattering and decreases with the energy. Around 90° and at low energies the scattering is an almost ideal analyzer, while the forward and back scattering loose memory of polarization. A polarimeter based on this effect is always composed of one or more scatterer and one or more absorber, which is always a detector. They may be passive when the scatterer is an inert material of low Z (Li or Be) or active, when the scatterer is a detector itself, in coincidence with the absorber(s). The first are cheaper and easier to do but the background is high and the sensitivity is good for strong sources only.

Active polarimeters can be also focal plane instruments in the focus of multi-layer optics (Krawczynski *et al.* 2011; Fabiani *et al.* 2013).

The most studied configuration, without optics (McConnell 2010), is based on an array of detectors, to achieve a large collecting area. The radiation scattered on one detector is absorbed in another one and the time coincidence identifies the pair. To each pair of detectors corresponds a projected angle of the scattered photon. If the direction of the impinging photon is known the scattering angle is derived and the histogram (modulation curve) built. Two different concepts are there:

- one-phase. The scatterer and the absorber are detectors of the same material.
- two-phases. The array includes detectors of different atomic number. Typically organic (low Z) scintillator to act as a scatterer and inorganic (high Z) scintillator to act as absorbers, or a similar combination of solid state detectors (*e.g.* Si and CdTe).

Computations say that the two phases configurations are much more sensitive (Costa *et al.* 1995), especially because of the much wider bandwidth. Yet the one-phase ones are easier to build. Arrays of high Z detectors built as a part of a system based on coded masks can be also used as a one-phase polarimeter. This has given origin to another class of polarimeters: those giving polarimetry as a byproduct of an instrument designed and built to do something else. This is very important because many of the published results of GRB polarimetry derive from this kind of experiments.

2.3 *Polarimetry of GRBs*

All the techniques described so far have been conceived for source polarimetry. Are they suited for GRBs? The simpler case is that of the Afterglow. When you point you know where it is. The polarimetry of afterglows is the same of the polarimetry of any weak source but you can integrate for a limited time. Only a photoelectric polarimeter in the focus of a large telescope is able to perform polarimetry of the brightest early afterglows. Discussing the rationale of such a measurement is not the goal of this paper, but the low level of optical polarization and the role of synchrotron suggest that the expectation of polarization could be very low. The case for a telescope dedicated to GRB polarimetry is weak, when compared with the polarimetry of other sources but the case to give fast pointing capability to any future mission of polarimetry is strong enough.

The science case for the polarimetry of the prompt is stronger but the difficulties are significantly amplified for this specific application. You do not know where the source is and need a wide field which (so far) excludes the optics. Each burst is detected at a different direction, with a different response of the instrument. You need the position and the spectrum from the same experiment or from another one. The flux may be very bright (actually it must be to perform polarimetry) and detector must be fast with dead time under control. Serious problems arise from the control of systematic effects. A pair of detectors identifies a scattering angle but the different angles are covered in a very different manner and a simple histogram is more an illustration of this coverage than of the polarization of the beam. Moreover this asymmetry strongly depends on the impact point and on the inclination of the beam with respect to the axis of the instrument. The Equation (2.2) assumes a poisson distribution of counts in the phase histogram with constant mean value. In a polarimeter devoted to sources this could be solved by rotation around the axis but in a polarimeter devoted to GRBs this is not possible because the axis direction is unknown. Various methods have been proposed to subtract these effects but no rigorous evaluation of the residual systematic effects has been worked out. Monte Carlo simulations are nowadays very good, but nothing can substitute the experimental data. The response to polarized and unpolarized beams at various energies is needed to account for all the small effects that cannot be included in the mass model, or the effects of electronics such as equalization and stability of thresholds. In the design of instruments dedicated to polarimetry, one of the drivers is the prevention of systematics. Results

achieved with experiments that perform polarimetry as a byproduct science must be discussed with special caution.

3 The existing measurements

3.1 The RHESSI data

Coburn & Boggs (2003) analyzed data from GRB 021206 collected with RHESSI. By studying coincident signals from pairs of Ge detectors they found, $\Pi=(80\pm 20)\%$. This first detection was subsequently disconfirmed (Rutledge & Fox 2004; Wigger 2004) since it was found that a significant fraction of pairs were not really correlated events. This shows how pairs of events, not related, can produce a modulation curve that mimics a polarization. This an important lesson for future experiments, for which these affects should be discovered by proper diagnostics and accurate calibrations before the launch, with particular attention to those experiments that were not conceived as polarimeters.

3.2 The BATSE data

BATSE experiment aboard GRO localized GRBs by comparing the counts of detectors oriented toward different directions. At higher energies, the calculation is complicated by the contribution of photons scattered by the different masses aboard CGRO and those reflected (backscattered) by the Earth atmosphere (this with a few ms delay). McConnell *et al.* (1996) hypothesized that the polarization of gamma-rays could be detected as well by this method. Following this idea Willis *et al.* (2005) analyzed the data of 2 strong GRBs detected by BATSE. The polarization of the GRB flux was introduced as a fit parameter. Heavy systematics are present and discussed in the paper, but it is likely that the data can be interpreted with the presence of polarization ranging in 30%–100% for GRB 930131 and in 40%–100% in GRB 960624.

3.3 The INTEGRAL data

In various phases of its development INTEGRAL was declared also as a polarimeter. In practice the polarimetric function was activated after many years. By analyzing coincident events on pair of Ge detectors and comparing with the distributions simulated, Kalemci *et al.* (2007) searched for polarization in data of GRB 041219a, the brightest ever detected by INTEGRAL, collected with the Ge Spectrometer SPI. They find a polarization of $98\% \pm 33\%$, that they consider more like an upper limit, because of the limited sample. By using data on radioactive sources on ground, they exclude equivalent systematics. The same data were analyzed also by McGlynn *et al.* (2007) that found hints of high polarization, but with very poor significance. It is worth, at this point, a short discussion about polarimetry of sources. With a similar analysis of coincidences Dean *et al.* (2008) found a Linear polarization ($46 \pm 10\%$), between 0.1–1 MeV of the Crab

Nebula. Differently from the X-ray data the angle seems oriented with the jet. The polarization of the Crab has been also detected with IBIS, the other instrument of INTEGRAL, by analyzing the angular distribution of photons scattered from the first plane of detectors and absorbed by the second (Forot *et al.* 2008). The angles are compatible but the degree of polarization is very high ($>71\%$ in the off pulse) and significantly different from that detected by SPI. Subsequently, again with IBIS data, a high polarization ($67 \pm 30\%$) was detected on CygX-1 above 400 keV (Laurent *et al.* 2011). The analysis of SPI data on the same source at the same time, in a first moment seemed to contradict IBIS data for the flux (Jourdain *et al.* 2012). In a second time also SPI found the high polarization at higher energies (Jourdain *et al.* 2012a). A discrepancy with IBIS in the polarization angle was solved. The same analysis was performed on data collected by IBIS on GRB 041219a by Gotz *et al.* (2009). First they performed a separate analysis for the two main peaks. For the first peak they disconfirm the high polarization found by McGlynn *et al.*, while they find on the second peak a polarization of $43 \pm 25\%$. Then they divided the interval into 36 sub-intervals lasting 10s each overlapping the nearby one of 5 s, and searched for polarization in those where the signal in the image was stronger. In one of the interval (number 30) they find a high polarization and in a few other a certain level of polarization with different angles and with moderate significance. This suggests that polarization is fast varying during the burst. This fact, combined with the high and different impact of dead time on the two data sets can explain discrepancies between the two results. From data collected on ground with radioactive sources the authors set limits to systematic effects. A major problem is that Dean *et al.* in discussing their observations of the Crab, find that systematic effects, not accounted with simulations, prevail on statistical fluctuations. They divided the observation into 5 sub sets and derived an empirical statistics from the spread of results. Nothing like this was apparently applied by the other scholars that assume the poisson distribution as the basis of their analysis and, in some case, discuss the systematics as a limit to the detectable polarization but not a parameter of the estimation.

3.4 The IKAROS/GAP data

IKAROS (Interplanetary Kite-craft Accelerated by Radiation Of the Sun) harbors various scientific packages. One of them is The Gamma-Ray Burst Polarimeter (GAP). It is based on a block of plastic scintillator (12 cm diameter and 6 cm thick) read with a single photomultiplier. All around the block are 12 detectors of CsI, each with its own readout photomultiplier (Yonetoku 2011). The scatterer is one block with one signal only and the line connecting its center with each absorber is assumed as the direction of the scattered photon. This reduces the modulation but makes the mass model more simple ad reliable. The instrument has been calibrated at 80 keV with radiation of known degree of polarization normal to the instrument. The results are consistent with the simulations. With respect to a rigorous testing the calibrations at different angles and at different energies are missing. But the simple geometry of the scattering block, with one

PMT only, and the presence of independent calibration sources for each detector, allowing for threshold equalization, make the whole adequately reliable. The main limitation is the small area resulting in a limited sensitivity, but we can hope that with more bursts arriving with time GAP is going to provide the first frame of this GRB science. In the data of the strong burst GRB 100826a GAP detected a polarization of $27 \pm 11\%$ with a significance of 2.9σ (Yonetoku *et al.* 2011a) in the assumption that the angle changes during the burst. Later GAP detected on GRB 110301a polarization of $70 \pm 22\%$ with a statistical significance 3.7σ and on GRB 110721a a polarization of $84 + 16 - 21\%$ (Yonetoku *et al.* 2012). GAP results advocate for a high polarization of GRBs and increase the confidence on previous results.

4 Present and future experiments

No experiment of polarimetry of faint sources is presently approved. The most advanced is PolariS, a small satellite with two telescopes with a photoelectric detector and a scattering detector respectively (Hayashida *et al.* 2012). It is not clear how fast it can re-point to perform polarimetry of the early afterglow. It also includes 3 wide field polarimeters which are declared to be more sensitive than GAP. Various experiments for the polarimetry of the prompt afterglow are there. Tsubame is a small satellite of university class with a wide field instrument, a narrow field compton detector and re-pointing capability (Toizumi *et al.* 2011). Some of the designs proposed for polarimetry of sources have been also proposed, in a version without collimator. For a review of the scattering polarimeters see McConnell (2010). The most evolved, is POLAR a project developed by the University of Genève, to fly, in a short term, aboard the Chinese Space Station, in a joint effort with Beijing IHEP. It is based on moduli of wire like plastic scintillator ($6 \text{ mm} \times 6 \text{ mm} \times 200 \text{ mm}$) read out with a pixel photomultiplier. The assemble of 25 moduli results into a block of $40 \times 40 \times 20 \text{ cm}^3$ of finely subdivided plastic scintillator. This is what I call a *one-phase polarimeter*, all based on a single, in this case low Z, material. The long wires improve the efficiency at expenses of modulation. The most frequent interaction is compton-compton so that the energy of single photons is not determined. Ignoring the energy of the photon makes difficult to interpret the detected modulations, unless the spectrum of the GRB is known from an independent instrument. The team of POLAR has performed, beside simulations, long campaigns of testing with radioactive and synchrotron polarized and unpolarized sources. The effective threshold at 200 keV and the strong spurious effects for off-axis detections, are the two major problems but the team is working out methods to face them (Orsi 2011). POLAR will significantly increase the sample of GAP, with some uncertainty on the spectra deconvolution, but with a better statistics. It could be the first instrument calibrated in a complete way.

A Compton telescope is itself a polarimeter, but the only one flown so far (COMPTEL) selected only forward angles and higher energies, where the modulation is negligible (Schoenfelder *et al.* 1993). The future Compton telescopes,

based on finely subdivided detectors, will operate at lower energies and will accept scattering angles closer to 90°. Unfortunately the only one approved, aboard ASTRO-H, has a collimator that is good for sources but makes it useless for GRBs.

References

- Bellazzini, R., Angelini, F., & Baldini, L., 2004, Nucl. Instr. Meth. Phys. Res. A, 535, 477
- Black, J.K., Baker, R.G., & Deines-Jones, P., 2007, Nucl. Instr. Meth. Phys. Res. A, 581, 755
- Coburn, W., & Boggs, S.E., 2003, Nature, 423, 415
- Costa, E., Cinti, M.N., Feroci, M., *et al.*, 1995, Nucl. Instr. Meth. Phys. Res. A, 366, 161
- Costa, E., Soffitta, P., Bellazzini, R., *et al.*, 2001, Nature, 411, 662
- Fabiani, S., Campana, R., Costa, E., *et al.*, 2013, to be published in Astropart. Phys. [[arXiv:1301.1161v1](https://arxiv.org/abs/1301.1161v1)]
- Forot, M., Laurent, P., Grenier, I.A., *et al.*, 2008, ApJ, 688, L29
- Götz, D., Laurent, P., Lebrun, F., *et al.*, 2009, ApJ, 695, L208
- Hayashida, K., Yonetoku, D., & Gunji, S., 2012, SPIE, 8443
- Jourdain, E., Roques, J.P., & Malzac, J., 2012, ApJ, 744, 64J
- Jourdain, E., Roques, J.P., Chauvin, M., *et al.*, 2012, ApJ, 761, 27J
- Kalemci, E., Boggs, S.E., Kouveliotou, C., Finger, M., *et al.*, 2007, ApJS, 169, 75
- Krawczynski, A., Garson, Q., Guo, *et al.*, 2011, Astropart. Phys., 34, 550
- Laurent, P., Rodriguez, J., Wilms, J., *et al.*, 2011, Science, 332, 438
- Marshall, H.L., Heilmann, R., Schulz, N.S., & Murphy, K.D., 2010, SPIE, Vol. 7732
- McConnell, M., Forrest, D., Vestrand, W.T., & Finger, M., 1996, AIP Conf. Proc., 384, 851
- McConnell, M., 2010, in X-ray Polarimetry: A New Window in Astrophysics, Ronaldo Bellazzini, Enrico Costa, Giorgio Matt & Gianpiero Tagliaferri (Cambridge University Press), 11
- McGlynn, S., Clark, D.J., Dean, A.J., *et al.*, 2007, A&A, 466, 895
- Orsi, S., Haas, D., Hajdas, W., *et al.*, 2011, Nucl. Instr. Meth. Phys. Res. A, 648, 139
- Rutledge, R.E., & Fox, D.B., 2004, MNRAS, 350, 1288
- Schoenfelder, V., Aarts, H., Bennett, K., *et al.*, 1993, ApJS, 86, 657
- Toizumi, T., Enomoto, T., Yatsu, Y., *et al.*, 2011, Physica E, 43, 685
- Weisskopf, M.C., Cohen, C.G., Kestembbaum, H.L., *et al.*, 1976, ApJ, 208, L125
- Weisskopf, M.C., Elsner, R.F., Kaspi, V.M., *et al.*, 2009: X-ray Polarimetry and Its Potential Use for Understanding Neutron Stars, ed. W. Becker, Neutron Stars and Pulsars, Ap&SS Library (Springer-Verlag Berlin Heidelberg 2009), 357
- Wigger, C., Hajdas, W., Arzner, K., Güdel, M., & Zehnder, A., 2004, ApJ, 613, 1088
- Willis, D.R., Barlow, E.J., Bird, A.J., *et al.*, 2005, A&A, 439, 245
- Yonetoku, D., Murakami, T., Gunji, S., *et al.*, 2011, PASJ, 63, 625
- Yonetoku, D., Murakami, T., & Gunji, S., 2011, ApJ, 743, L30
- Yonetoku, D., Murakami, T., & Gunji, S., 2012, ApJ, 758, L1

GRBS AND LOBSTER EYE X-RAY TELESCOPES

R. Hudec^{1,2}, L. Pina³, V. Marsikova⁴ and A. Inneman⁴

Abstract. A large majority of GRBs exhibit X-ray emission. In addition, a dedicated separate group of GRB, the XRFs, exists which emission dominates in the X-ray spectral range. And the third group of GRB related objects (yet hypothetical) are the group of off-axis observed GRBs (orphan afterglows). These facts justify the consideration of an independent experiment for monitoring, detection and analyses of GRBs and others fast X-ray transients in X-rays. We will present and discuss such experiment based on wide-field X-ray telescopes of Lobster Eye type. We show that the wide field and fine sensitivity of Lobster Eye X-ray All-Sky Monitor make such instruments important tools in study of GRBs.

1 Introduction

The X-ray sky is highly variable, rich in variable and transient sources of both galactic as well as extragalactic origin. Among physically most important transient sources, the detection of Gamma Ray Bursts (GRBs) in X-rays confirms the feasibility of monitoring, detecting and study of these phenomena by their X-ray emission (either prompt or afterglow, *e.g.* Amati *et al.* 2004 & Fontera *et al.* 2004). For classical GRBs, the X-ray afterglows are detected in $\sim 90\%$ of the cases (De Pasquale *et al.* 2003). Moreover, there are X-ray rich GRBs, (hypothetical) orphan GRBs (detectable in X-rays but not in gamma-rays due to different beaming angle) and XRFs which can be detected and studied in X-rays. However, since these events cannot be predicted, and are relatively rare, very wide-field instruments are required. They must achieve high sensitivities and provide precise

¹ Astronomical Institute, Academy of Sciences of the Czech Republic, 251 65 Ondřejov, Czech Republic

² Czech Technical University in Prague, Faculty of Electrical Engineering, Prague, Czech Republic

³ Czech Technical University in Prague, Faculty of Nuclear Science, Prague, Czech Republic

⁴ Rigaku Innovative Technologies Europe, Prague, Czech Republic

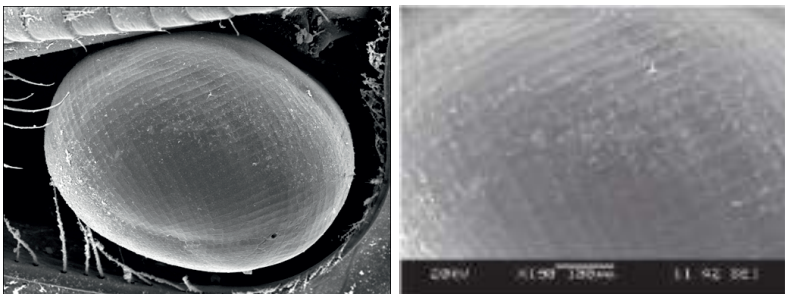


Fig. 1. The crayfish eye under optical microscope. On the picture right the surface square cells (covered by protecting membrane) are clearly visible.

localizations in order to effectively study the objects. Novel wide field X-ray telescopes with imaging optics are expected to represent an important tool in future space astronomy projects in general, especially those for deep monitoring and surveys in X-rays over a wide energy range. The Lobster-Eye (LE) wide field X-ray optics has been suggested by Schmidt (Schmidt 1975, orthogonal stacks of reflectors) and by Angel (Angel 1979, array of square cells). Up to 180 deg FOV may be achieved with these devices. This X-ray optics offers an opportunity to achieve very wide fields of view (FOV, 1000 square degrees and more) while the widely used classical Wolter grazing incidence mirrors are limited to roughly 1 deg FOV (Priedhorsky *et al.* 1996; Inneman *et al.* 2000).

2 Lobster eye X-ray telescopes

The LE telescopes in Schmidt arrangements are based on perpendicular arrays of double-sided X-ray reflecting flats. In the first prototypes developed and tested, double-sided reflecting flats produced by epoxy sandwich technology as well as gold coated glass foils have been used (Inneman *et al.* 1999). More recently, micro Schmidt lobster eye arrays with foils thickness as low as 30 microns have been developed and tested in order to confirm the capability of these systems to achieve fine angular resolutions of order of a few arcmin (Fig. 1). The thin foils are separated by 70 microns gaps in these prototypes. On the other hand, large lobster eye systems with Schmidt geometry have been designed and constructed, achieving dimensions up to $300 \times 300 \times 600$ mm (Fig. 1). Their optical and X-ray optical tests (Fig. 2) have confirmed the expected performance according to calculations (computer ray-tracing). The calculations and the measurement results indicate that the lobster eye telescope based on multi array of modules with thin and closely spaced glass foils (analogous to those already assembled and tested) can meet the requirements *e.g.* of the ESA ISS Lobster mission (including the angular resolution and with better transmission) and can hence represent an alternative to the recently suggested MCP technique (Fraser *et al.* 2002).

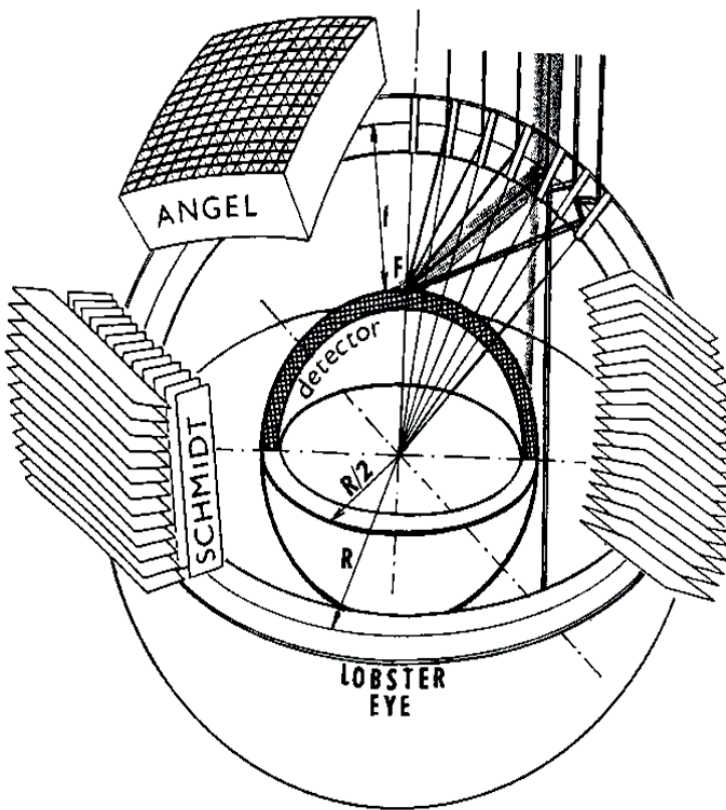


Fig. 2. The two arrangements of the LE X-ray optics.

The Angel LE systems consist of numerous square cells of very small size (about 1×1 mm or less at lengths of order of tens of mm, *i.e.* with the length/size ratio of 30 and more) are to be produced. Test modules with LE Angel cells have been successfully produced. The linear test module has 47 cells 2.5×2.5 mm, 120 mm long (*i.e.* length/size ratio of almost 50), surface microroughness 0.8 nm, $f = 1300$ mm. Another test module is represented by a L-shaped array of $2 \times 18 = 36$ cells of analogous dimension. The surface microroughness of the replicated reflecting surfaces is better than 1 nm.

3 Astrophysics with LE X-ray monitor

Deep (limiting flux of 10^{-12} erg $\text{cm}^{-2} \text{s}^{-1}$ can be easily achieved for daily scanning observation) X-ray sky monitoring with large FOVs (*e.g.* FOV of 6×180 deg can be easily assembled on the space vehicles) is expected to contribute significantly to various fields of modern astrophysics (2009). A few most important examples are listed below.

MODULE	size	plate thickness	distance	length	eff. angle	focal length	resolution	field of view	energy
	d(mm)	t(mm)	a(mm)	l(mm)	a/l	f(mm)	r(arcmin)	(°)	(keV)
macro	300	0.75	10.80	300	0.036	6000	7	16	3
middle	80	0.3	2	80	0.025	400	20	12	2
mini 1	24	0.1	0.3	30	0.01	900	2	5	5
mini 2	24	0.1	0.3	30	0.01	250	6	5	5
micro	3	0.03	0.07	14	0.005	80	4	3	10

Fig. 3. The LE laboratory samples assembled and tested in the Czech Republic.

(1) Gamma Ray Bursts (GRBs). Detection rates of nearly 20 GRBs/year can be obtained for the prompt X-ray emission of GRBs, taking into account the expected GRB rate 300/year. (2) X-ray flashes. Detection rates of nearly 8 X-ray flashes/year are expected, assuming XRF rate of 100/year. (3) X-ray binaries. Because of their high variability in X-rays they will be one of major targets in LE observations. LE will be able to observe their short-time outbursts by long-term extended monitoring. Almost all galactic XRB are expected to be within the detection limits. (4) Stars. Because of the low X-ray luminosity of ordinary stars, only nearby stars are expected to be observable. We estimate the lower limit of ordinary stars observable by the LE telescope as 600. The sampling rate of LE observations will be sufficient enough to observe sudden X-ray flux increases during flares while still having the capability of monitoring the variability on time scales of years. (5) Supernovae. The LE telescope should be able to detect the theoretically predicted thermal flash lasting for \sim 1000 sec for the first time. Together with the optical SNe detection rate and estimates of the LE FOV we estimate the total number of SNe thermal flashes observed by the LE experiment to \sim 10/year. More details on the advantages of LE X-ray telescopes in scientific analysis of SNe are given in Sveda *et al.* 2005. (6) AGNs. Active Galactic Nuclei will surely be one of the key targets of the LE experiment. LE will be able to monitor the behavior of the large (\sim 1000) sample of AGNs providing long-term observational data with good time sampling (hours). (7) X-ray transients. The LE experiment will be ideal to observe X-ray transients of various nature due to its ability to observe the whole sky several times a day for a long time with a limiting flux of about 10^{-12} erg cm $^{-2}$ s $^{-1}$. More and fainter X-ray transients are expected to be detected by the LE sky monitor enabling the detailed study of these phenomena. (8) Cataclysmic Variables. Cataclysmic Variables (CVs) are very active galactic objects, often showing violent long-term activity in both the optical and X-ray passband (outbursts, high/low state transitions, nova explosions) as well as rapid transitions between the states of activity. Search for the relation of the optical and X-ray activity is very important – monitoring of a large number of CVs is necessary to catch them in various states of activity.

4 Conclusions

The various prototypes of both Schmidt as well as Angel arrangements have been produced and tested successfully, demonstrating the possibility to construct these

lenses by innovative but feasible technologies. Both very small Schmidt lenses (3×3 mm) as well as large lenses (300×300 mm) were developed, constructed, and tested (1999, 2000). Promising results were obtained in studies of LE X-ray monitors for small satellites and related tests (2009, 2009, 2011). This makes the proposals for space projects with very wide field lobster eye optics possible for the first time. The LE All Sky Monitor is capable to detect around 20 GRBs and 8 XRFs yearly and this will surely significantly contribute to the related science. Another LE application may be the investigation of X-ray emission from atmospheric triggers such as Terrestrial Gamma-Ray Flashes (TGF).

This study and related scientific considerations were partly supported by the grants 102/09/0997 and 13-33324S *Lobster Eye X-Ray Monitor* provided by the Grant Agency of the Czech Republic. The microscopic images of crayfish eye were kindly provided by Petr Jan Juračka and Adam Petrušek, Charles University, Faculty of Natural Sciences in Prague.

References

- Amati, L., Frontera, F., in't Zand, J.J.M., *et al.*, 2004, A&A, 426, 415
 Angel, J.R.P., 1979, ApJ, 364, 233
 De Pasquale, M., Piro, L., Perna, R., *et al.*, 2003, ApJ, 592, 1018
 Fraser, G.W., Brunton, A.N., Bannister, N.P., *et al.*, 2002, Proc. SPIE, 4497, 115
 Frontera, F., Amati, L., in 't Zand, J.J.M., *et al.*, 2004, ApJ, 616, 1078
 Gorenstein, P., 1998, Proc. SPIE, 3444, 382
 Inneman, A., Hudec, R., & Pina, L., 2000, Proc. SPIE, 4138, 94
 Inneman, A., Hudec, R., Pina, L., *et al.*, 1999, Proc. SPIE, 3766, 72
 Priedhorsky, W.C., Peele, A.G., & Nugent, K.A., 1996, MNRAS, 279, 733
 Schmidt, W.K.H., 1975, Nucl. Instr. Meth., 127, 285
 Sveda, L., Hudec, R., Pina, L., *et al.*, 2005, in Cosmic Explosions, Springer Proceedings in Physics, Vol. 99, ed. J.M. Marcaide & K.W. Weiler, 197
 Sveda, L., Hudec, R., Pina, L., *et al.*, 2009, in EUV and X-Ray Optics: Synergy between Laboratory and Space, ed. R. Hudec & L. Pina, Proceedings of the SPIE, Vol. 7360, p. 73600F, 10
 Tichy, V., Sveda, L., Marsik, J., *et al.*, 2009a, Baltic Astron., 18, 369
 Tichy, V., Hromcik, M., Hudec, R., *et al.*, 2009b, Baltic Astron., 18, 362
 Tichy, V., Barbera, M., Collura, A., *et al.*, 2011, Nucl. Instr. Meth. Phys. Res. A, 633, id. 169

OBSERVING GRBS WITH THE *LOFT* WIDE FIELD MONITOR

S. Brandt¹, M. Hernanz², M. Feroci^{3,4}, L. Amati⁵, Alvarez²,
P. Azzarello⁶, D. Barret⁷, E. Bozzo⁶, C. Budtz-Jørgensen¹,
R. Campana^{3,4}, A. Castro-Tirado⁸, A. Cros⁷, E. Del Monte^{3,4},
I. Donnarumma³, Y. Evangelista^{3,4}, J.L. Galvez Sanchez², D. Götz⁹,
F. Hansen¹, J.W. den Herder¹⁰, A. Hornstrup¹, R. Hudec^{11,12},
D. Karelina², M. van der Klis¹³, S. Korpela¹⁴, I. Kuvvetli¹, N. Lund¹,
P. Orleanski¹⁵, M. Pohl¹⁶, A. Rachevski¹⁷, A. Santangelo¹⁸, S. Schanne⁹,
C. Schmid¹⁹, L. Stella²⁰, S. Suchy¹⁸, C. Tenzer¹⁸, A. Vacchi¹⁷,
J. Wilms¹⁹, N. Zampa¹⁷, J.J.M. in't Zand¹⁰
and A. Zdziarski²¹

¹ National Space Institute, Technical University of Denmark, Elektrovej Bld 327, 2800 Kgs Lyngby, Denmark

² IEEC-CSIC-UPC-UB, Carrer del Gran Capità, 2, 08034 Barcelona, Spain

³ IAPS-INAF, via del Fosso del Cavaliere 100, 00133 Rome, Italy

⁴ INFN, Sez. Roma Tor Vergata, via della Ricerca Scientifica 1, 00133 Rome, Italy

⁵ INAF-IASF-Bologna, via P. Gobetti, 101, 40129 Bologna, Italy

⁶ ISDC, Geneve University, Chemin d'Ecogia 16, 1290 Versoix, Switzerland

⁷ IRAP, avenue du Colonel Roche, 9, BP. 44346, Toulouse, France

⁸ Instituto Astrofísica de Andalucía, Glorieta de la Astronomía, s/n., 18008 Granada, Spain

⁹ CEA Saclay, DSM/IRFU/SAp, 91191 Gif-sur-Yvette, France

¹⁰ SRON, Sorbonnelaan 2, 3584 CA Utrecht, The Netherlands

¹¹ Astronomical Institute of the Academy of Sciences of the Czech Republic, Fricova 298, 251 65 Ondrejov, Czech Republic

¹² Czech Technical University in Prague, Zikova 1903/4, 166 36 Praha 6, Czech Republic

¹³ Astronomical Institute Anton Pannekoek, University of Amsterdam, Science Park 904, 1098 XH Amsterdam, The Netherlands

¹⁴ Department of Physics, Division of Geophysics and Astronomy, PO Box 48, 00014 University of Helsinki, Finland

¹⁵ Space Research Centre, Warsaw, Bartycka 18A, Warszawa, Poland

¹⁶ DPNC, Geneve University, Quai Ernest-Ansermet 30, 1205 Geneva, Switzerland

¹⁷ INFN, Trieste, via A. Valerio 2, 34127 Trieste, Italy

¹⁸ IAAT University of Tuebingen, Sand 1, 72076 Tuebingen, Germany

¹⁹ University of Erlangen-Nuremberg, Schlossplatz 4, 91054 Erlangen, Germany

²⁰ INAF-OA Roma, via Frascati, 33, 00040 Monte Porzio Catone, Italy

²¹ Copernicus Astronomical Center, Bartycka 18, Warsaw, Poland

Abstract. LOFT (Large Observatory For X-ray Timing) is one of the four candidate missions currently under assessment study for the M3 mission in ESAs Cosmic Vision program to be launched in 2024. LOFT will carry two instruments with prime sensitivity in the 2–30 keV range: a 10 m^2 class large area detector (LAD) with a $<1^\circ$ collimated field of view and a wide field monitor (WFM) instrument. The WFM is based on the coded mask principle, and 5 camera units will provide coverage of more than 1/3 of the sky. The prime goal of the WFM is to detect transient sources to be observed by the LAD. With its wide field of view and good energy resolution of $<500 \text{ eV}$, the WFM will be an excellent instrument for detecting and studying GRBs and X-ray flashes. The WFM will be able to detect ~ 150 gamma ray bursts per year, and a burst alert system will enable the distribution of ~ 100 GRB positions per year with a ~ 1 arcmin location accuracy within 30 s of the burst.

1 Introduction

LOFT (Large Observatory For X-ray Timing) [1, 2], is one of the four missions selected in 2011 for assessment study for the ESA M3 mission [3]. The final mission selection will be done in early 2014. LOFT will, if selected, carry two science instruments, both based on Silicon drift detectors (SDDs), with a primary energy range of 2–30 keV. A schematic view of the LOFT spacecraft and payload is shown in Figure 1.

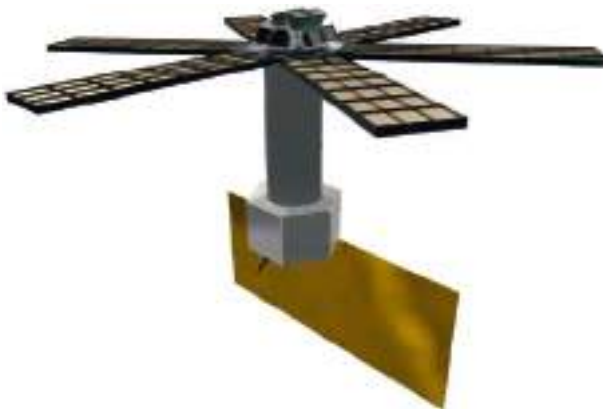


Fig. 1. Schematic views of the LOFT spacecraft showing the deployed Large Area Detector (LAD) panels attached to the optical bench. The Wide Field Monitor (WFM) is placed on the optical bench at the top. The direction of maximum response of the WFM is co-aligned with the viewing direction of the LAD.

The Large Area Detector (LAD) is a collimated instrument with an effective area of $\sim 10 \text{ m}^2$ designed for X-ray timing with a better than 250 eV energy

resolution and a $10 \mu\text{s}$ time resolution [4]. The second instrument on LOFT is a Wide Field Monitor (WFM) based on the coded mask principle, and with a detector plane based on Silicon Drift Detectors, much similar to the LAD detectors, but with a design optimized for position determination of the incoming X-rays [5]. The WFM is primarily needed to detect interesting targets for the LAD, but with exciting and unique capabilities on its own. In order to optimize for the detection of weak sources in a background dominated by cosmic diffuse emission and other X-ray sources the coded mask has a 25% open fraction. We note that for GRBs an open fraction of 50% is normally used, when the signal is dominating the background. A single WFM camera and the full WFM camera assembly on the spacecraft is shown in Figure 2.

The mission duration will be 4 years, and is mainly driven by the statistics of the occurrence of the bright black hole transients, which are a class of prime targets for the LAD. The orbit for LOFT is nearly equatorial with an altitude of ~ 550 km.

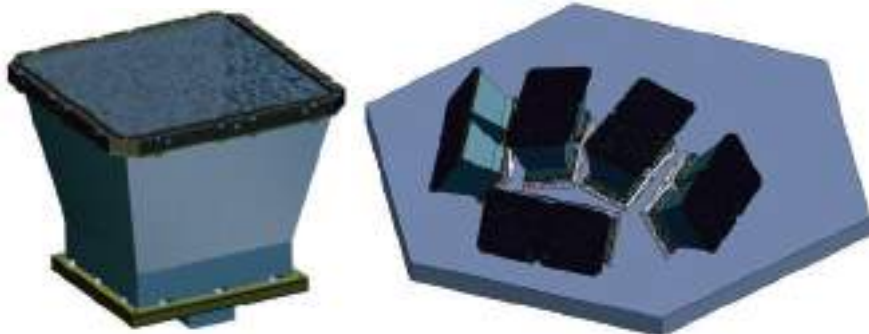


Fig. 2. *Left:* one WFM coded mask camera. The angular resolution is highly asymmetric at $5' \times 5'$. A pair of cameras oriented at a relative rotation of 90° offers a $5' \times 5'$ combined resolution and a source position accuracy of $1' \times 1'$. *Right:* the WFM assembly mounted on the LOFT optical bench consisting of 5 co-aligned camera pairs, for a total of 10 cameras.

2 The WFM science goals

The main goal for the WFM is to detect new transients and state changes of known sources suitable for observation with the LAD. However, the WFM will be able to do important science on its own. With a very large field of view, covering more than 1/3 of the sky, the WFM offers a high duty cycle compared to other X-ray monitors with a scanning mode of operation, like the past RXTE/ASM and the current MAXI monitor.

The LOFT-WFM is ideally suited to study the physics of prompt, explosive events, such as gamma-ray bursts, bursts and intermediate flares from magnetars, and X-ray bursts. The low-energy threshold at 2 keV [1, 2] is well below that of

current and foreseen monitors such as Swift-BAT, and SVOM or UFFO and the energy resolution <500 eV (and a goal of <300 eV) is unique. The soft response and good energy resolution of the WFM will allow the detection of spectral features in the soft prompt X-ray emission, where observations are still very limited. The source location accuracy is better than 1 arcmin for burst with sufficient counting statistics.

Table 1. Summary of the performance parameters of the LOFT WFM. The energy resolution is required to be better than 500 eV, but the goal is to achieve 300 eV or better.

Parameter	One Camera	One Camera Unit = 2 crossed cameras	Overall WFM
Energy Range	2–30 (30–80) keV	2–30 (30–80) keV	2–30 (30–80) keV
Active Detector Area	182 cm ²	364 cm ²	1820 cm ²
Peak Effective Area (on-axis, through 25% open mask)	>40 cm ²	>80 cm ²	>80 cm ²
Energy Resolution FWHM	<500 eV	<500 eV	<500 eV
Field of View at Zero Response	90° × 90°	90° × 90°	210° × 90° + 45° × 90°
Field of view at 20% response	60° × 60°	60° × 60°	180° × 60° + 60° × 60°
Angular Resolution	5' × 5°	5' × 5'	5' × 5'
Point Source Location Accuracy (10σ signal)	<1' × 30'	<1' × 1'	<1' × 1'
On-axis sensitivity at 5σ in 3 s, in Galactic Center	380 mCrab	270 mCrab	270 mCrab
On-axis sensitivity at 5σ in 58 ks (1 day Galactic Center pointing)	3.0 mCrab	2.1 mCrab	2.1 mCrab

Our simulations show that in the first year of the mission, LOFT-WFM will detect more than 50 gamma-ray bursts at redshifts >2 and the LOFT WFM will be able to contribute to the study of high z GRBs. Over a four-year mission, even conservative models predict that WFM will detect 15–30 GRB at $z > 5$ and $\sim 5\text{--}10$ GRB at $z > 6$, which will be promptly localized and followed-up in multi-wavelength campaigns. These discoveries may shed light on fundamental topics such as the formation of population III stars, the star formation rate and the evolution of the interstellar medium of galaxies from the epoch of re-ionization.

We emphasize that no past, present, or planned GRB experiment has such a combination of low energy threshold, energy resolution, and wide field of view as the LOFT WFM.

3 The WFM sky coverage

The WFM will be placed on the optical bench on top of the spacecraft. The WFM configuration consisting of 5 camera pairs (a total of 10 cameras) each with a field of view of $90^\circ \times 90^\circ$ at zero response. The WFM baseline configuration is illustrated in Figure 2. This configuration will cover ~ 5.5 steradian or $\sim 44\%$ of the sky at zero response, and ~ 4.2 steradian or $1/3$ of the sky at 20% response relative to on-axis.

Four of the five units are arranged such that their viewing axes lies in the plane of the solar panel of the LOFT spacecraft, and the fifth unit is tilted out of this plane, away from the Sun, by 60° . The viewing directions of the four units are off-set by $\pm 15^\circ$ and $\pm 60^\circ$ relative to the LAD pointing direction, which also lies in the solar panel plane (see Fig. 1). The effective area of the full WFM assembly is shown in the right hand panel of Figure 3. With this arrangement, the two central units have the LAD target in their field, where the detectors are fully illuminated, providing the maximum WFM coverage, with $\sim 160 \text{ cm}^2$ effective area. The zero response field of view of the 4 units is $210^\circ \times 90^\circ$. However, depending on the configuration of the LAD panels and the placement of the WFM units on the optical bench, only an unobstructed field of view of $180^\circ \times 90^\circ$ can be assured. The 60° tilt of the two outer units with respect to the LAD pointing direction is preferred in order to have a reasonable response at the edge defined by the plane of the optical bench. In this configuration, the WFM nominally covers half of the sky that is accessible to LAD pointings. The WFM may therefore in just 2 LOFT pointings cover all the sky accessible to the LAD, or an area corresponding to at least 75% of the sky.

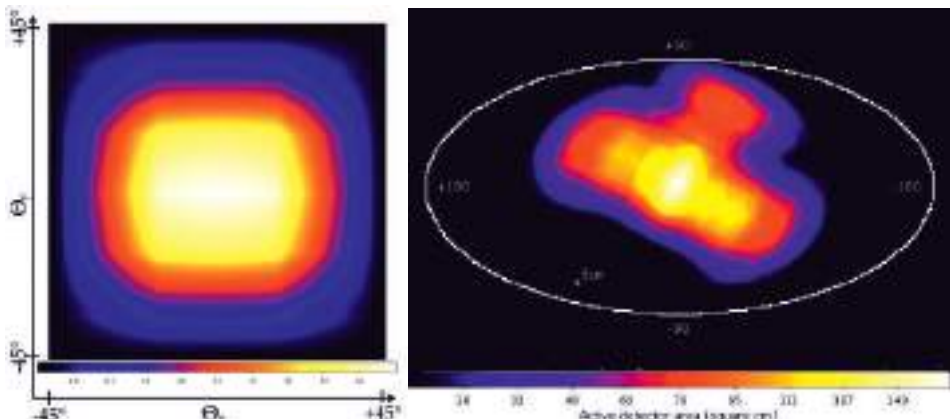


Fig. 3. *Left panel:* map of the single camera sensitive area expressed in cm^2 , with a maximum of $\sim 45 \text{ cm}^2$ of a single camera. *Right panel:* map in Galactic coordinates of the active detector area for an example observation of the Galactic center. The effective area has its maximum of $\sim 160 \text{ cm}^2$ in the direction of the LAD pointing.

4 The LOFT burst alert system

The WFM is estimated to be able to detect \sim 150 Gamma Ray Bursts per year and we expect to be able to distribute near real time positions for \sim 100 burst per year. Scientifically it is highly desirable to do follow-up observations of these sources with other telescopes and instruments as soon as possible after (or even during) the event. Therefore LOFT will employ a VHF transmission capability to send a short message about the occurrence of such events with minimum delay to a network of VHF receiving stations on the ground for further distribution to interested observatories. The LOFT burst alert system will distribute the location of a transient event with \sim 1 arc minute accuracy to end users within 30 s (goal 20 s) of the onboard detection of the burst in at least 2/3 of the cases.

For a coded mask instrument, the deconvolution of the detector image into a sky image is computationally very demanding. The deconvolution will be done onboard by cross correlation of the mask pattern with the background subtracted detector image by discrete Fast Fourier Transform (DFFT) algorithm. The position is initially defined relative to the camera coordinate system, but is then, based on the pointing information, transformed into a position on the sky, which is compared with a catalog of known X-ray sources. If the position does not correspond to a known source and the calculations meet a certain set of quality/reliability criteria the software will send a short message with brief information about the event to the onboard data handling in order for it to be transmitted immediately to the ground via the spacecraft VHF transmitter system. The message will contain information on burst time, burst location, duration, and a set of quality flags for the use of the ground based users.

The LOFT burst alert system ground segment will be based on the network based on the equatorial subset of the VHF stations planned for the SVOM mission, or a similar dedicated network, in case the SVOM network will not be realized. The typical data rate for this system is 600 bits/s, which allows a short message containing the basic burst information, to be transmitted in less than 2 seconds. The requirements of a maximum delay between the burst trigger and the delivery of the burst information packet of <30 s is very conservative. A realistic goal will be a delay less than 20 s, and we expect the system in many cases performing significantly better. The number of VHF ground stations needed to ensure continuous coverage is limited to 12 ideally placed stations. However, the placement of the stations will eventually be determined by available land based sites with sufficient infrastructure (see Fig. 4). The VHF ground station will be managed by a central LOFT Alert Center, having the responsibility of validating the burst alerts and distributing the alerts to the end users.

We note that the LOFT mission does not include any capability for the satellite to do automated reorientations to observe the GRB afterglows with the LAD, as this would impose significant and costly requirements on the spacecraft autonomy.

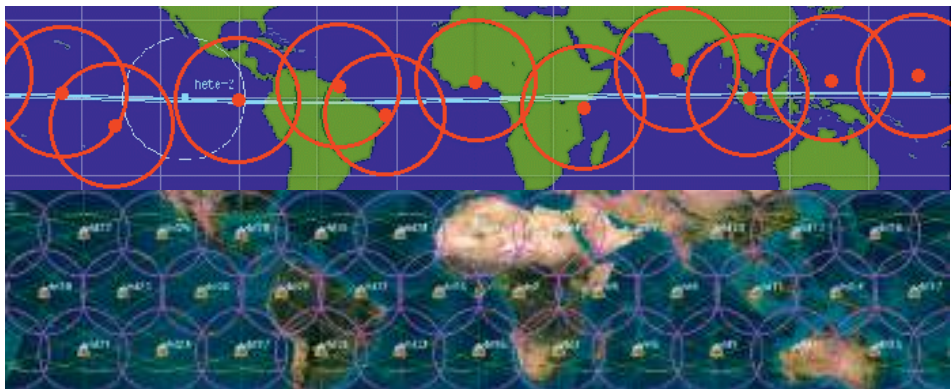


Fig. 4. The location of VHF stations for the former GRB mission HETE-II (*top*) and the theoretical SVOM network (*bottom*). The ideal LOFT burst alert system network consists of the 12 central/equatorial stations of the planned SVOM system.

5 Conclusion

Although LOFT is not designed to be a GRB mission, the WFM is expected to provide significant, independent contributions to the field of the gamma ray burst studies through the near real time burst alert system.

According to the current ESA selection schedule, it will be known by early 2014, if LOFT will move ahead from the assessment phase and be implemented for an expected launch in 2024.

References

- [1] Feroci, M., Stella, L., van der Klis, M., *et al.*, 2012, Exper. Astron., 34, 415
- [2] Feroci, M., den Herder, J.W., Bozzi, E., *et al.*, 2012, SPIE Conf. Ser., 8443-85
- [3] “Cosmic Vision: Space Science for Europe 2015-2025”, ESA Brochure, Vol. BR-247, 1-111 (15 Oct. 2005)
- [4] Zane, S., Walton, D., Kennedy, T., *et al.*, 2012, SPIE Conf. Ser., 8443-87
- [5] Brandt, S., Hernanz, M., Alvarez, L., *et al.*, 2012, SPIE Conf. Ser., 8443-88

A-STAR: THE ALL-SKY TRANSIENT ASTROPHYSICS REPORTER

J.P. Osborne¹, P. O'Brien¹, P. Evans¹, G.W. Fraser¹, A. Martindale¹,
J.-L. Atteia^{2,3}, B. Cordier⁴ and S. Mereghetti⁵

Abstract. The small mission A-STAR (All-Sky Transient Astrophysics Reporter) aims to locate the X-ray counterparts to ALIGO and other gravitational wave detector sources, to study the poorly-understood low luminosity gamma-ray bursts, and to find a wide variety of transient high-energy source types, A-STAR will survey the entire available sky twice per 24 hours. The payload consists of a coded mask instrument, Owl, operating in the novel low energy band 4–150 keV, and a sensitive wide-field focussing soft X-ray instrument, Lobster, working over 0.15–5 keV. A-STAR will trigger on \sim 100 GRBs/yr, rapidly distributing their locations.

1 Introduction

Responding to the 2012 call from the European Space Agency for a new type of small scientific mission for launch in late 2017, a consortium of institutes⁶ proposed A-STAR: the All-Sky Transient Astrophysics Reporter. The mission call had a cost cap of €50M to ESA (including launch). Despite the severe cost limit, A-STAR is excitingly capable; it has three objectives:

1. Precisely locate the high-energy photon sources of gravitational-wave and neutrino transients and transients located by the new generation of astronomical facilities.

¹ Dept of Physics & Astronomy, University of Leicester, LE1 7RH, UK

² UPS-OMP, Université de Toulouse, IRAP, Toulouse, France

³ CNRS, IRAP, 14 avenue Edouard Belin, 31400 Toulouse, France

⁴ CEA, IRFU, Service d'Astrophysique, 91191 Gif-sur-Yvette, France

⁵ INAF-IASF Milan, via Bassini 15, 20133 Milano, Italy

⁶UK: Univ. Leicester, ISIC; F: IRAP, LAM, ARTEMIS, CEA, IAP, APC; DK: DTU, SSC; I: IASF-Milan, IASF-Rome; B: Univ. Liège; CH: ISDC; PL: SRC (PAS).

2. Reveal the physics underlying the variety in the population of gamma-ray bursts, including high-luminosity high-redshift bursts, low-luminosity bursts and short bursts.
3. Discover new high-energy transient sources over the whole sky, including supernova shock break-outs, black hole tidal disruption events, magnetar flares, and monitor known X-ray sources with daily observations.

2 Scientific objectives

2.1 Gravitational wave sources

The launch of A-STAR will coincide with the true dawn of the era of multi-messenger astronomy during the second half of the current decade. The upgrading of the LIGO and VIRGO GW detectors (ALIGO/AVirgo) will revolutionize astronomy by permitting the detection and localization of GWs at a rate of perhaps dozens per year. IceCube and KM3NeT will likewise revolutionize neutrino astrophysics, routinely detecting cosmological neutrinos. Several of the most powerful sources of GWs predicted by general relativity, *e.g.* NS-NS or NS-BH mergers and core-collapse SNe, and neutrino sources such as GRBs produce powerful electromagnetic (EM) signals. ALIGO is planned to be operational by 2016–2018 and will be capable of identifying a randomly oriented NS-NS (NS-BH) merger out to ~ 450 (~ 900) Mpc, with a combined predicted rate of 50 yr^{-1} (Abadie *et al.* 2010), but with relatively poor sky localizations of $\sim 10\text{--}1000$ sq. degrees (Klimenko *et al.* 2011). IceCube and KM3NeT can localize to an accuracy of better than a few degrees but within a smaller volume of the Universe (the IceCube Collaboration 2011; Kappes 2007). To maximize the science return of the multi-messenger era requires an in-orbit trigger and search facility that can either simultaneously detect the event or rapidly observe the large error boxes provided by the GW and neutrino facilities with good sensitivity to the EM signal. This combined requirement is uniquely provided by A-STAR, which is able to trigger using Owl or Lobster and observe a very large fraction of the GW/neutrino error boxes within an orbit due to the large grasp of the Lobster instrument compared to current generation X-ray facilities, *e.g.* Lobster has a grasp 40 times that of Swift/XRT. For events triggered on-board with Owl or Lobster, GW searches can also be carried on the resultant known sky locations with lower ALIGO/AVirgo signal-to-noise thresholds and hence an increased search distance.

2.2 Gamma-ray bursts

In recent years GRBs have become essential in the study of stellar explosions, the evolution of massive stars (*e.g.* Pian *et al.* 2006), the extreme physics of relativistic jets and particle acceleration (*e.g.* Racusin *et al.* 2008), and as light-houses illuminating the distant Universe (*e.g.* Tanvir *et al.* 2009). In the future we expect GRBs to provide a powerful probe of the epoch of reionization of the Universe (*e.g.* Tanvir *et al.* 2012), constrain the properties of the first stars, and will revolutionize GW astrophysics by associating GW signals with GRBs.

In this context, it is striking that so little is known about the origin of GRBs and the conditions needed for their production. Many basic questions remain unresolved: Why do only a few percent of Type Ibc supernovae produce long GRBs? What is the role of metallicity and binarity in LGRB production? Are some LGRBs powered by proto-neutron stars, at least initially? What is the range of beaming angles of long and short GRBs? What progenitor systems produce short GRBs? Why do some nearby long GRBs have no accompanying supernova (Fynbo *et al.* 2006; Gal-Yam *et al.* 2006)? Having a functioning orbiting high-energy facility to address these issues is essential, particularly when we consider the advent of future large observatories such as the European ELT and the JWST at visible and infrared wavelengths, the full ALMA interferometer in the sub-mm, SKA and its precursors in radio, and CTA and HAWC at very high energies, that will revolutionize our vision of GRBs and their host galaxies. Other time-domain surveys such as Pan-STARRS and LSST will bring the power of multi-wavelength observations to time domain astronomy, possibly revealing the elusive orphan afterglows of GRBs, permitting an accurate measure of GRB beaming.

2.3 Discovering new high-energy transients

Magnetars, young NS with external magnetic fields of 10^{13} – 10^{15} G, are among the most powerful and spectacular high-energy transients in the sky. About twenty sources believed to be magnetars are currently known in our Galaxy and in the Magellanic Clouds, but since most of them are transients with long quiescent periods, the total population waiting to be discovered is certainly much larger (Mereghetti 2008). Magnetars can produce Giant Flares thought to be due to star crustal fractures, we predict that A-STAR will see more than 2 per year. Intermediate flares are more frequent; the wide field of view and the frequent sky coverage of A-STAR will, for the first time, allow detection of a large number of flares and obtain a reliable estimate of the frequency of such events.

The birth of a new SN is revealed by a burst of high-energy emission as the shock breaks out of the star. This has been spectacularly captured in a serendipitous Swift XRT observation of SN2008D (Soderberg *et al.* 2008): SNe are usually found only days to weeks after the explosion as radioactive heating powers optical brightening. Few observations exist early in a SN evolution: SN2008D remains

Table 1. A-STAR detection rates for different astrophysical transients and variables.

Transient type	Rate
GW sources	$2\text{--}3 \text{ yr}^{-1}$
GRB	100 yr^{-1}
Magnetars	2 yr^{-1}
SN shock breakout	1 yr^{-1}
TDE	15 yr^{-1}
AGN+Blazars	100 day^{-1}
Thermonuclear bursts	10 day^{-1}
Novae	1
Dwarf novae	day^{-1}
SFXTs	10 yr^{-1}
Stellar flares	$\sim 100 \text{ yr}^{-1}$
Stellar super flares	1 week^{-1}

the only non-GRB SN to be detected in X-rays at the time of first radiation escape from the star. A-STAR will significantly advance our understanding of the SN explosion mechanism, detecting SNe at the very moment of emergence, gathering comprehensive, prompt data and alerting follow-up communities to these landmark events.

Tidal disruption events (TDEs) offer a unique probe of the ubiquity of BH in galaxies, accretion on timescales open to direct study, and the nature and dynamics of galactic nuclei. Such events are expected to be visible as luminous, roughly Eddington limited objects with hot, UV and soft X-ray emission (*e.g.* Komossa *et al.* 2004; Gezari *et al.* 2012). The recent discovery by Swift of two highly luminous outbursts from galactic nuclei implies that at times a fraction of this energy is deposited in a new relativistic jet outflow (Levan *et al.* 2011; Bloom *et al.* 2011; Burrows *et al.* 2011), offering a new route to their identification and an opportunity to study newly-born jets. A-STAR is ideal for both the discovery and characterization of TDEs, opening new windows on numerous astrophysical questions.

3 A-STAR instruments

3.1 Owl

Owl is a coded mask telescope operating in the 4–150 keV energy range. It has a wide field of view ($\sim 1.44 \text{ sr}$) and a $10'$ source error radius (90% confidence) for the faintest sources (7σ detection), improving to $2'$ for the brightest ($>30\sigma$).

The Owl detector plane is made of 3840 Schottky CdTe detectors ($4 \times 4 \text{ mm} \times 1 \text{ mm}$ thick) yielding a geometrical area of 614 cm^2 . The new generation ASICs developed at CEA Saclay, together with the careful detector selection and the optimized hybridization done at IRAP Toulouse allow to lower the detection threshold with respect to former CdTe detectors by about 10 keV, reaching $\sim 4 \text{ keV}$.

A coded aperture mask, made of a 0.6 mm thick tantalum sheet, placed 46 cm above this detection plane, defines a coded field of view of $\approx 60^\circ \times 88^\circ$. In order to optimize the sensitivity for short bursts the mask aperture was set at 40%. Taking into account the geometrical parameters, and the materials present along the optical axis, the effective area is estimated to 104 cm^2 at 4 keV.

Data are continuously analyzed on board in order to detect bursts, by first detecting a count rate increase (in several energy bands) on time scales from 10 ms to 20 s followed by the formation of the image in the triggered time window in



Fig. 1. The Owl coded mask instrument.

which a new source is searched, or by systematic searches for new sources in images built on time scales from 20 to 1200 s. Triggers are sent to the A-STAR service module to request a slew maneuver.

By decreasing its low energy threshold in the soft X-ray domain, while keeping a large field-of-view, Owl will open a new window on the Universe. It will detect almost all of the GRB population seen by Swift, and is especially sensitive to highly red-shifted bursts and to the poorly understood low energy bursts.

3.2 Lobster

Lobsters and other crustaceans focus by grazing incidence reflection off curved square pore optic arrays. This technique uniquely provides X-ray focussing over a very wide field, and is ideally suited to the A-STAR goals as it enables efficient detection of a large number of GRBs in a new low energy regime.

Lobster comprises 3 modules, each with a $17.3 \times 17.3^\circ$ field of view. These form a single 900 square degree FOV, centred on that of Owl. Each Lobster module has an array of 7×7 40×40 mm Micro-Channel Plate optics, mounted onto a titanium front end, supported by a carbon fibre mechanical structure. The optics have a spherical radius of 600 mm, focusing onto the detector at 300 mm. The camera contains an MCP detector which is curved to match the 300 mm curvature of the focal plane, an anti-coincidence system, a thin aluminized polyimide optical/UV blocking filter, and the readout and analogue electronics. This configuration has a position resolution FWHM of $25 \mu\text{m}$ over the $\sim 93 \times 93$ mm imaging area of the detector, sufficient to significantly oversample the PSF.

Lobster provides un-vignetted and uniform resolution imaging across a very wide FOV, while maintaining the imaging advantage in sensitivity over collimating and coded mask systems. The point spread function of a Lobster optic is cruciform, 25% of the counts fall in the central peak, 50% in the arms and 25% in a diffuse centred pyramid. The detector performance is well matched to the optic capabilities and allows source position centroiding to $<1.8'$ for 90% of GRBs, $<0.5'$ for 50% and 10% better than $<0.17'$ for 10% (determined by Monte-Carlo simulation of Lobster observation of Swift GRBs).

The position and trigger algorithm maximises sensitivity by employing two stages: the first projects the image in two perpendicular 1D histograms, and a candidate detection is when a 2.5σ event is seen above background in both axes. The second stage takes a cross shaped patch centred on the candidate and integrates over time, the transient is confirmed if the signal exceeds a specifiable higher statistical significance (*e.g.* $\sim 6.3\sigma$ to achieve a false trigger rate of 1 in 10^{10}). At this level the 30-minute sensitivity is $3 \times 10^{-11} \text{ erg.cm}^{-2}.\text{s}$ (0.15–5 keV). The two-stage approach maximises sensitivity to faint transients and minimises false alerts.

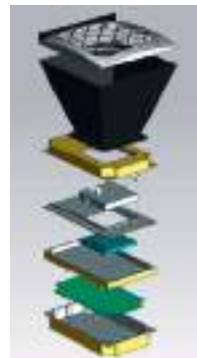


Fig. 2. A single Lobster module.

4 Mission profile

A-STAR carries two wide-field X-ray imagers and a fast communication system. The payload is designed to operate with the mass and power resources provided by a microsatellite platform. We have performed detailed accommodation studies, which have demonstrated that the Myriade Evolutions and Proba satellites fit within a standard Vega piggyback volume. The operational mission life is 3 years.

The scientific return of A-STAR depends crucially upon the ability of the satellite to point the instruments at the open sky for 15–30 min long exposures; the ability to compute the positions of detected transients on-board and to transmit alerts quickly to the ground; and a fast reaction on reception of Targets of Opportunity. Key to success is the number of transients detected; the mission profile is optimized to maximize this number. We have therefore chosen an orbit with an altitude of 650 km and an inclination $i < 30^\circ$ in order to minimize the time spent unusefully in a high radiation environment. This orbit can be reached with a Vega launch as a passenger (A-STAR fits within the standard piggyback volume).

The survey strategy is an essential ingredient of the mission. A-STAR will cover a significant fraction of the sky twice a day, perform long exposures taking full advantage of Lobster sensitivity, and observe Owl-detected transients with Lobster within 1–2 minutes. The A-STAR strategy relies on three ~ 1500 sec long dwells per orbit, two in the day side and one in eclipse, respecting the 90° sun avoidance angle required by Owl and Lobster. The eclipse dwells will detect transients in the night hemisphere, allowing a prompt response by ground-based facilities.

The need to transmit alerts quickly (within 1 minute) from the spacecraft to the ground calls for a dedicated system. We have studied two possible systems: in the first option, the consortium provides a network of VHF ground stations, as studied by CNES for the SVOM mission. An alternative is to use the COM Dev (Europe) SB-Sat system to send short messages via Inmarsat.

5 Concluding remarks

ESA announced that A-STAR was not selected on October 15, 2012. We believe that the science case for a wide-field high-cadence X-ray survey is very strong, and in particular that the promise of the new generation of gravitational wave detectors is best realised by such a survey. We intend to pursue future new mission opportunities vigorously.

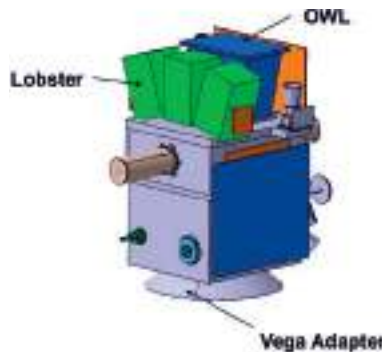


Fig. 3. A-STAR on Myriade Evolution.

We thank the 29 Co-Is and 62 associate scientists for their valuable input to the A-STAR proposal. JPO & PE acknowledge the support of the UK Space Agency.

References

- Abadie, J., Abbot, B.P., Abbot, R., *et al.*, 2010, Class. Quantum Grav., 27, 173001
Klimenkon, S., Vedovato, G., Drago, M., *et al.*, 2011, PhRvD, 83, 102001
The IceCube Collaboration, 2011 [[arXiv:1111.2741](https://arxiv.org/abs/1111.2741)]
Kappes, A., 2007 [[arXiv:0711.0563](https://arxiv.org/abs/0711.0563)]
Pian, E., Mazalli, P.A., Masetti, N., *et al.*, 2006, Nature, 442, 1011
Racusin, J.L., Karpov, S.V., Sokolowski, M., *et al.*, 2008, Nature, 455, 183
Tanvir, N.R., Fox, D.B., Levan, A.J., *et al.*, 2009, Nature, 461, 1254
Tanvir, N.R., Levan, A.J., Fructer, A.S., *et al.*, 2012, ApJ, 754, 46
Fynbo, J.P.U., Watson, D., Thöne, C.C., *et al.*, 2006, Nature, 444, 1047
Gal-Yam, A., Fox, D.B., Price, P.A., *et al.*, 2006, Nature, 444, 1053
Mereghetti, S., 2008, A&ARv, 15, 225
Soderberg, A.M., Berger, E., Page, K.L., *et al.*, 2008, Nature, 453, 469
Komossa, S., Halpern, J., Schartel, N., *et al.*, 2004, ApJ, 603, L17
Gezari, S., Chornock, R., Rest, A., *et al.*, 2012, Nature, 485, 217
Levan, A.J., Tanvir, N.R., Cenko, S.B., *et al.*, 2011, Science, 333, 199
Bloom, J.S., Giannios, D., Metzger, B., *et al.*, 2011, Science, 333, 203
Burrows, D.N., Kennea, J.K., Ghisellini, G., *et al.*, 2011, Nature, 476, 421

FEASIBILITY OF A SMALL, RAPID OPTICAL/IR RESPONSE, NEXT GENERATION GAMMA-RAY BURST MISSION

B. Grossan^{1,2}, G.F. Smoot^{1,4}, V.V. Bogomolov¹, S.I. Svertilov¹,
N.N. Vedenkin¹, M. Panasyuk¹, B. Goncharov³, G. Rozhkov³,
K. Saleev³, E. Grobovskoj¹, A.S. Krasnov¹, V.S. Morozenko¹,
V.I. Osedlo¹, E. Rogkov¹, T.V. Vachenko¹ and E.V. Linder^{1,2}

Abstract. We present motivations for and study feasibility of a small, rapid-optical/IR response gamma-ray burst (GRB) space observatory. By analyzing existing GRB data, we give realistic detection rates for X-ray and optical/IR instruments of modest size under actual flight conditions. Given new capabilities of fast optical/IR response (~ 1 s to target) and simultaneous multi-band imaging, such an observatory can have a reasonable event rate, likely leading to new science. Requiring a *Swift*-like orbit, duty cycle, and observing constraints, a *Swift*-BAT scaled down to 190 cm^2 of detector area would still detect and locate about 25 GRB yr^{-1} for a trigger threshold of 6.5σ . About 23% of X-ray located GRB would be detected optically for a 10 cm diameter instrument ($\sim 6 \text{ yr}^{-1}$ for the 6.5σ X-ray trigger).

1 Introduction

Swift has been spectacularly productive in the study of gamma-ray bursts (GRBs), but is past its design lifetime. A new GRB observatory with new capabilities would be welcome. No obvious replacement is on the horizon: the SVOM mission is now uncertain, and other upcoming observatories described as “GRB-capable” lack: (i) high GRB rates, (ii) an on-board optical instrument, and (iii) optical-quality positions. Without (i), you cannot do statistical studies; without (ii) & (iii) you cannot apply ever-evolving techniques in follow-up observations that make *Swift* so productive. Here we study a small post-*Swift* GRB observatory with the following

¹ Extreme Universe Laboratory, Moscow State University, Russian Federation

² University of California at Berkeley Space Sciences Laboratory, USA

³ Moscow State University, Russian Federation

⁴ University of California at Berkeley, USA

requirements: small, due to limited resources in the current world economy; high GRB rate, to enable statistical studies; new capabilities, to investigate new science; optical quality locations, to enable the most varied possible follow-up science. Is this feasible? How small could a GRB observatory instrument really be?

2 The GRB rate for a “mini-BAT”

From Beppo-Sax to Swift-BAT, coded mask X-ray cameras have yielded high GRB rates & localizations smaller than optical telescope fields. In Burrows *et al.* (2012), the wide field of view of coded mask cameras dominated energy range & sensitivity for maximum GRB rate. Consider a BAT scaled down in detector area, but with the same field of view (FOV), for GRB location. Such a scaled-down BAT can still achieve a relatively high detection rate: for steady sources, rate depends on SNR (signal to noise ratio), $\text{SNR} \sim A^{1/2}$ for steady sources, and so rate must be *weakly* dependent on detector area, A . GRBs are transient, however; their detected light curve, fluence & duration change with background noise, therefore A , so the SNR relation can be more complex. We therefore used actual BAT light curves to predict performance of a smaller BAT, to determine how small an instrument would still locate GRBs at a high rate.

2.1 Method: Rate estimate from BAT data SNR_{peak} measurements

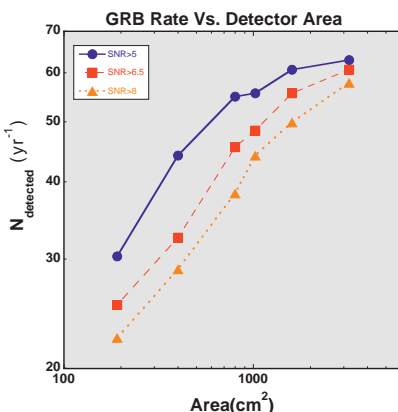


Fig. 1. GRB Detection Rate *vs.* Detector Area for *Swift* BAT-Like instruments.

fluctuations $>$ threshold (in σ) over background (the trigger and detection criteria). The trailing average background ($t-19.2$ to $t-6.4$ s) was used. All triggers were checked by eye for false triggers (only 1 found). (BAT also has a long time window image data trigger, rarely triggered; we had no such trigger, as the benefit for a small instrument would likely be very small.) We analyzed 94 GRB light curves 2010 Nov. – 2012 Mar to find the SNR_{peak} in each window. We then scaled

The peak SNR time segment of a GRB light curve determines the smallest instrument collecting area, A_{collect} required for its detection. GRB rate as a function of A_{collect} was determined by (i) finding the peak SNR segment in BAT light curves, (ii) scaling to get $\text{SNR}_{\text{peak}}(A_{\text{collect}})$, then (iii) counting the number of bursts with $\text{SNR}_{\text{peak}} >$ threshold to determine the detection rate.

We used a very simple SNR_{peak} “Trigger”, specified as follows: We used the sum of 64 ms data channels 1–3 (15–100 kev, the highest S/N combination). Integration time windows of 0.25, 0.5, 1, 2, 4, 8 s were examined for

the SNR for instruments of smaller collecting area, and reported the number of bursts over trigger threshold in the smaller instruments.

Pre-selecting only burst data, as we did, begs the question of false alarm rate. This pre-selection is acceptable because in a real mission, known tools are available to control excessive false alarms: trigger parameter tuning, cutoff rigidity maps, and others.

2.2 Analysis results

Our simplified trigger detected 91% of BAT bursts (86 detections, 1 fail, 7 image trigger non-detects). For only 190 cm^2 of collecting area, $<1/25$ th of *Swift*, 22 GRB/yr would still have $\text{SNR}_{\text{trig}} > 8$; this number increases to 25 and 30 for SNR_{trig} of 6.5 and 5.0, respectively⁵.

Imaging/location consistent with triggering analysis. After triggering, an image is made, with location uncertainty $\sim 1/\text{SNR}_{\text{image}}$. Is the correlation noise of coded-mask imaging, the dominant noise in $\text{SNR}_{\text{image}}$, a problem? In a simulation by Connell (2012), all triggers with $\text{SNR}_{\text{peak}} > 5$ yielded $\text{SNR}_{\text{image}} > 8$, the typical coded mask design threshold. Localization quality is therefore not a problem.

Robust result. We recognize this approach is valid only for BAT-like instruments with similar orbit, operations & observing constraints. Background depends on instrument & spacecraft construction, via activation & secondary emission. The BAT background is $\sim 1.9 \text{ cts s}^{-1} \text{ cm}^{-2}$ 15–150 keV (`bat_desc.html`). The ESA MXGS coded mask camera, with similar CZT detectors (5 mm thick) and shielding, on the International Space Station (copious mass & solid angle for secondaries), has estimated background = $2.1 \text{ cts s}^{-1} \text{ cm}^{-2}$ 15–200 keV (Renzi 2009). The results are therefore not sensitive to spacecraft platform; orbital inclination and altitude dominate the background considerations.

3 New science from follow-up optical/IR

A “mini-BAT” would sample the brightest of the known *Swift* GRB population. How then, do we get new science? *Swift* optical follow-up is hardware-limited to >60 s after trigger. Telescope pointing has been achieved with beam-steering mirrors in ~ 1 s over similar sized fields by the upcoming Ultra-fast Flash

⁵The Ultra-Fast Flash Observatory-pathfinder X-ray camera (UFFO-p; Kim *et al.* 2012) has 190 cm^2 collecting area, but is planned to fly in a polar orbit (89° inclination) with high background regions, losing substantial useful observing time. We roughly estimate a duty cycle of 20% of that of BAT (from the time in high background regions and a 1000 s background decay after).

From this, and a field of view 84% that of BAT’s, we find that UFFO-p’s X-ray rates are ~ 0.17 of those above, (4.3 yr^{-1} , $\text{SNR}_{\text{trig}} = 6.5$) assuming all else identical to BAT. We then expect ~ 1 detection yr^{-1} for the 10 cm UVOT-like optical instrument on UFFO-p (see Sect. 3.1).

Observatory-Pathfinder (Jeong *et al.* 2012). Such rapid-response on-orbit optical follow-up would take advantage of the shorter communication time and lack of weather of ground-based rapid follow-up. Such an instrument would yield new information: optical or IR bulk Lorentz factors from the time of opt/IR peak (Molinari *et al.* 2007); a much better sample of GRB optical rise times (these rise times are often less than the >60 s *Swift* UVOT response, and so are infrequently measured); the first dust evaporation detection via time-resolved simultaneous multi-band colors (all of which occurs in <60 s, too fast for most telescopes; see Grossan *et al.* 2012 for details & additional science topics).

We did not consider a focused X-ray telescope (XRT) for a small observatory, as such instruments are large, expensive, & complex. An IR/optical imager would still yield a precise position for its detections, partially replacing an XRT.

3.1 Aperture size vs. rate

The brightest *Swift* UVOT V fluxes for each GRB (Fig. 2) show a detection rate strongly dependent on sensitivity. Sensitivity, dominated by non-instrument background, scales as 1/aperture diameter, D (for same exposure time and pixel size). For typical conditions, rate decreases by a factor of 0.8 for 2X smaller D (blue line); by 0.7 for a 3X smaller D (pink line). For a 190 (or 1000) cm² mini-BAT, *Swift* orbit & constraints, the GRB Rate plot (Fig. 1), gives 25 (or 48) GRB X-ray locations/yr (6.5 σ trigger). Conservatively neglecting any correlation of V *vs.* X, for DUVOT/2, ~7 (or 13) optical detections/yr are predicted. However, these rates can be significantly increased. Earlier optical acquisition *may* catch many bursts when brighter. A near-IR detector *will* get up to 50% more extinguished GRB (Perley *et al.* 2009). Detector quantum efficiency (QE) improvement will also boost rate (a CCD has ~4–5X UVOT’s QE).

4 Discussion & summary

Our conservative analysis using *Swift* data firmly supports the feasibility of small GRB missions: small instruments with good orbits and high duty cycle can produce GRB locations at useful rates for follow-up studies. Improving on *Swift* technology can boost these rates by improving detector sensitivity: *e.g.*, SVOM-like 5–150 keV detectors give ~2.7X BAT (15–150 keV) source photon flux. Better optical QE and IR sensitivity would increase optical/IR rates.

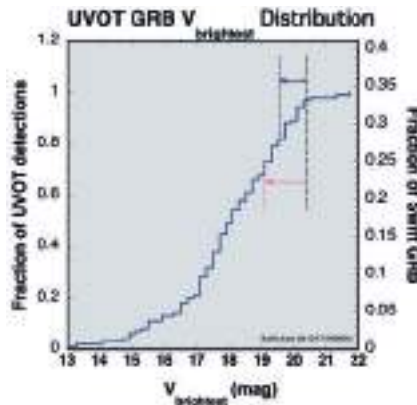


Fig. 2. *Swift* UVOT Maximum Brightness *vs.* Rate.

Rapid acquisition for prompt optical emission enables new lines of inquiry. An additional IR channel would yield the first prompt IR measurements and permit the study of dynamic extinction. Additional bands would give more information for small mass cost.

Smaller X-ray cameras can roughly measure GRB durations & spectra, but will have poor Short GRB rates, and greater uncertainty in E_{peak} and flux. We find that new science, even limited to the brightest GRBs of the already known *Swift* population, outweighs these disadvantages. In the future, we will extend this work to investigate the performance of more types of X-ray, optical, IR detectors, spacecraft, and orbits.

We gratefully acknowledge the support of the Russian Federation Ministry of Education and Science, Agreement No. 11.G34.31.0076.

References

- bat_desc.html: http://heasarc.nasa.gov/docs/swift/about_swift/bat_desc.html
Burrows, D.N., Fox, D., Palmer, D., *et al.*, 2012, Mem. Suppl. Soc. Astron. Ital., 21, 59
Connell, P., 2012, presentation, this conf., and priv. comm.
Grossan, B., Park, I.H., Ahmad, S., *et al.*, 2012, SPIE Astronomical Telescopes +
Instrumentation (Amsterdam RAI, The Netherlands, July 1-6), 8443, 84432R
Jeong, S., Ahmad, S., Barrillon, *et al.*, 2012, SPIE Astronomical Telescopes +
Instrumentation (Amsterdam RAI, The Netherlands, July 1-6), 8443, 84432S
Kim, J.E., Ahmad, S., Barrillon, P., *et al.*, 2012, SPIE Astronomical Telescopes +
Instrumentation (Amsterdam RAI, The Netherlands, July 1-6), 8443, 84432V
Molinari, E., Vergani, S.D., Malesani, D., *et al.*, 2007, A&A, 469, 13
Perley, D.A., Cenko, S.B., Bloom, J.S., *et al.*, 2009, AJ, 138, 1690
Renzi, F., 2009, 6th GEANT 4 Space Users Workshop, Madrid (http://www.inta.es/g4suw2009/docs/Presentations/20_Wed_May_2009/G4SUWS_2009_Renzi_BackgroundEstimationInMXGS.pdf)

GRB POTENTIAL OF ESA GAIA

R. Hudec^{1,2} and V. Šimon¹

Abstract. The potential of GRB analyses (including highly redshifted objects) with ESA mission Gaia is briefly addressed.

1 Introduction

ESA Gaia satellite, with expected launch date in 2013, is an ambitious mission to chart a three-dimensional map of our Galaxy, the Milky Way, in the process revealing the composition, formation and evolution of the Galaxy (Perryman 2005, 2006). Gaia will provide unprecedented positional and radial velocity measurements with the accuracies needed to produce a stereoscopic and kinematic census of about one billion stars in our Galaxy and throughout the Local Group. This amounts to about 1 per cent of the Galactic stellar population. Combined with astrophysical information for each star, provided by on-board multi-colour photometry, these data will have the precision necessary to quantify the early formation, and subsequent dynamical, chemical and star formation evolution of the Milky Way Galaxy. Additional scientific products include detection and orbital classification of tens of thousands of extra-solar planetary systems, a comprehensive survey of objects ranging from huge numbers of minor bodies in our Solar System, through galaxies in the nearby Universe, to some 500 000 distant quasars. It will also provide a number of stringent new tests of general relativity and cosmology (<http://gaia.esa.int>).

The payload consists of a single integrated instrument the design of which is characterised by: A dual telescope concept, with a common structure and a common focal plane. Both telescopes are based on a three-mirror anastigmat (TMA) design. Beam combination is achieved in image space with a small beam combiner. Silicon-carbide (SiC) ultra-stable material is used for mirrors and telescope

¹ Astronomical Institute, Academy of Sciences of the Czech Republic, 25165 Ondřejov, Czech Republic

² Czech Technical University in Prague, Faculty of Electrical Engineering, Prague, Czech Republic

structure A highly robust measurement system for the Basic Angle between the two telescopes' pointing directions A large common focal plane with an array of 106 CCDs. The large focal plane also includes areas dedicated to the space-craft's metrology and alingment measurements. The satellite will be placed on the Lissajous-type orbit around L2 (<http://gaia.esa.int>).

To study the optical counterparts of gamma-ray bursts (GRBs), Gaia will have several advantages. First, it will be a deep limiting magnitude of 20 mag (Jordi & Carrasco 2007), much deeper than most of the previous studies and global surveys. Secondly, the time period covered by Gaia observations, *i.e.* 5 years, will also allow some studies requiring long-term monitoring. The most important advantage of Gaia for GRB studies will be the color (spectral) resolution. This will allow some detailed studies involving analysis of the color and spectral changes not possible before. The details of studies of the optical counterparts of high-energy sources are described in detail in the dedicated sub-workpackages within the workpackage Specific objects studies within the Gaia CU7 (Hudec & Šimon 2007a,b).

2 Photometry

The Optical Transients (OTs) and Optical Afterglows (OAs) of GRBs usually reach their peak optical luminosity in the initial phase, shortly (several minutes) after the gamma-ray emission which typically lasts from a fraction of second to several minutes. In the later, much longer phase which can last for several (even more than 10) days, the OAs usually display a characteristic power-law fading profile (if a logarithm of the time interval between the start of the GRB and the given observation is used, and the brightness is measured in magnitudes). A sequence of observations mapping this OA light curve is therefore necessary. According to Zhang (2007), most of OAs are fainter than about 18 mag already about 1 day after the GRB, although some of them can be even brighter than 14 mag in the early phase. Gaia is therefore definitely able to detect these OAs in their early phase. However, the sampling provided by Gaia is not optimal, hence only rarely we can expect detection of OA of GRB based only on this type of data.

3 Spectro-photometry/low-dispersion spectroscopy

The Gaia instrument consists of two low-resolution fused-silica prisms dispersing all the light entering the field of view (FOV). Two CCD strips are dedicated to photometry, one for blue photometer (BP) and one for red photometer (RP). Both strips cover the full astrometric FOV in the across-scan direction. All BP and RP CCDs are operated in TDI (time-delayed integration) mode. CCDs have 4500 (for BP) or 2900 (for RP) TDI lines and 1966 pixel columns (10×30 micron pixels). The spectral resolution is a function of wavelength as a result of the natural dispersion curve of fused silica. The BP and RP dispersers have been designed in such a way that BP and RP spectra have similar sizes (on the order

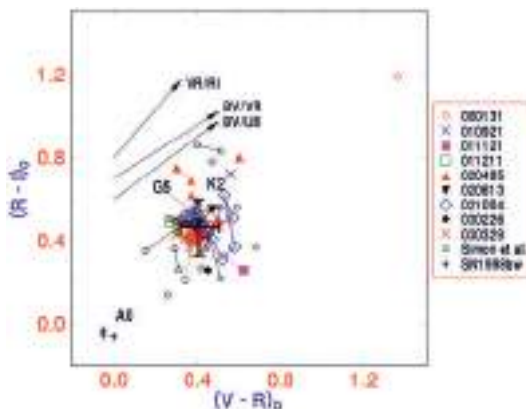


Fig. 1. Example of the color-color diagram of OAs of long GRBs. The data for the time interval <10.2 d after the burst in the observer frame and corrected for the Galactic reddening are displayed. Multiple indices of the same OA are connected by the lines for convenience. The mean colors (centroid) of the whole ensemble of OAs (except for GRB 000131 and SN 1998bw) are marked by the large cross. The representative reddening paths for $E_{B-V} = 0.5$ mag and positions of the main-sequence stars are also shown. Adapted from Šimon *et al.* (2001, 2004a).

of 30 pixels along scan). BP and RP spectra will be binned on-chip in the across-scan direction; no along-scan binning is foreseen. RP and BP will be able to reach the object densities in the sky of at least $750\,000$ objects deg^{-2} . Albeit the dispersion is low, the major strength of Gaia for many astrophysical fields will be the spectrophotometry, as the low dispersion spectra may be transferred to numerous well-defined color filters. We have shown (Šimon *et al.* 2001, 2004) that the individual OAs of GRBs display quite specific and remarkably similar color indices with negligible changes during the first several days after the GRB (an example of such a color-color diagram is shown in Fig. 2). This feature is important for distinguishing OAs from other types of astrophysical objects. This suggests that although OAs possess a large range of redshifts z , they display very similar spectra in the observer frame for $z < 3.5$. This gives us a hope to resolve whether an optical event is related to a GRB even without available gamma-ray detection.

4 Strategy and detection rate

The Gaia instruments will map the entire sky with deep limits. The duration of most of OA is about 10–20 days in the observer frame, hence they are likely to be detected by Gaia during its scans even without rapid pointing at the GRB position. However, this assumes that they will occur in the FOV of Gaia telescopes. As already indicated, the OA can be recognized according to several features even

without information on the time profile. The following features appear to be important: (1) unique color indices, (2) rapid rise (a new object appears between two scans), (3) host galaxy of the GRB at the position of OA – this galaxy can be detected by ground-based observations later. We note that even search for orphan afterglows will be possible with Gaia. The missing gamma-ray emission, with only an OA remaining, can also suggest this important event. Gamma-ray emission from many GRBs remains unobservable because the jet is not pointing to the observer, but the late-time OA is less beamed and can reach us (Rhoads 1997; Rossi *et al.* 2008). Also failed GRBs are possible contributors to the population of orphan afterglows (Huang *et al.* 2002).

The estimated Gaia detection rate for OAs of GRBs, including orphans, is expected to be up to ~ 100 in the whole Gaia lifetime (5 years). This low rate is due to small FOV of the Gaia telescopes ($\sim 0.36 \text{ deg}^2$ each). Higher detection rate is expected in plate Low-Dispersion Spectroscopy (LDS) surveys (due to much larger FOV) in which analogous strategies (*e.g.* high-redshift triggers) can be applied.

5 Highly redshifted Universe

Some GRBs may be at large distances and hence highly redshifted. The Gaia mission will be able to study highly redshifted triggers. The redshifted Lyman alpha line/break can be used to measure the value of z . This was *e.g.* the idea of the proposed Joint Astrophysics Nascent Universe Satellite (JANUS) Small Explorer (SMEX) Space Mission (Fox 2010) with coverage range of 0.7–1.7 microns (Gaia RP has a coverage of 0.65–1.0 microns). GRBs are located at cosmological distances, often with $z > 0.5$ (*e.g.* Robertson & Ellis 2012). The Lyman break is therefore shifted to the optical band for the objects at z larger than about 3.5. This break manifests itself as a sharp decrease of the flux in the blue part of the spectrum. Such a feature is prominent in the smooth spectral profile of OA. This OA will therefore appear shifted from its true position because of the lack of its blue part of the spectrum. A comparison of the accurate position of the OA obtained by Gaia in the astrometric mode with the blue edge of its spectrum can be used for an easy resolving the objects occurring in our Galaxy from those located at cosmological distances. Also the determination of z , hence of its distance necessary for the determination of its luminosity, will be possible.

6 Conclusions

We conclude that the ESA Gaia satellite will contribute to scientific investigations of GRBs. In the field of GRB study, Gaia advantages can be briefly summarized as follows. (1) Unique chance to provide early or simultaneous LDS for GRBs (so far LDS mostly late) (2) Chance to recognize/classify OAs and OTs of GRBs using LDS and/or color information even in their later phases and without known

GRB (3) Chance to detect/study orphan OAs of GRBs and (4) Chance of redshift estimation up to ~ 7 .

The Czech participation in the ESA Gaia project was supported by the PECS project 98058. The scientific part of the study is related to the grant 102/09/0997 provided by the Grant Agency of Czech Republic (GA CR). The analyzes of spectral plates are supported by GA CR grant *Digitizing Astronomical Plate Archives and Investigation of Celestial Sources in Digitized Plate Archives* 13-39464J.

References

- Fox, D., 2010, BAAS, 42, 573
Huang, Y.F., Dai, Z.G., & Lu, T., 2002, MNRAS, 332, 735
Hudec, L., 2007, Algorithms for spectral classification of stars, BSc. Thesis (Charles University, Prague)
Hudec, R., & Šimon, V., 2007a, Specific object studies for cataclysmic variables and related objects ESA Gaia Reference Code GAIA-C7-TN-AIO-RH-001-1
Hudec, R., & Šimon, V., 2007b, Specific object studies for optical counterparts of high energy sources. ESA Gaia Reference Code GAIA-C7-TN-AIO-RH-002-1
Jordi, C., & Carrasco, J.M., 2007, ASP Conf. Ser., 364, 215
Perryman, M., 2005, ASP Conf. Ser., 338, 3
Perryman, M., 2006, Gaia overall science goals, <http://sci.esa.int/gaia/>
Rhoads, J., 1997, ApJ, 487, L1
Robertson, B.E., & Ellis, R.S., 2012, ApJ, 744, 95
Rossi, E.M., Perna, R., & Daigne, F., 2008, MNRAS, 390, 675
Šimon, V., Hudec, R., Pizzichini, G., & Masetti, N., 2001, A&A, 377, 450
Šimon, V., Hudec, R., Pizzichini, G., & Masetti, N., 2004, AIP Conf. Proc. 727, 487
Zhang, B., 2007, ChJAA, 7, 1

Chapter XIV.
Non Electromagnetics, VHE and UHE Emission

CONSTRAINING GRB AS SOURCE FOR UHE COSMIC RAYS THROUGH NEUTRINO OBSERVATIONS

P. Chen^{1,2}

Abstract. The origin of ultra-high energy cosmic rays (UHECR) has been widely regarded as one of the major questions in the frontiers of particle astrophysics. Gamma ray bursts (GRB), the most violent explosions in the universe second only to the Big Bang, have been a popular candidate site for UHECR productions. The recent IceCube report on the non-observation of GRB induced neutrinos therefore attracts wide attention. This dilemma requires a resolution: either the assumption of GRB as UHECR accelerator is to be abandoned or the expected GRB induced neutrino yield was wrong. It has been pointed out that IceCube has overestimated the neutrino flux at GRB site by a factor of ~ 5 . In this paper we point out that, in addition to the issue of neutrino production at source, the neutrino oscillation and the possible neutrino decay during their flight from GRB to Earth should further reduce the detectability of IceCube, which is most sensitive to the muon-neutrino flavor as far as point-source identification is concerned. Specifically, neutrino oscillation will reduce the muon-neutrino flavor ratio from $2/3$ per neutrino at GRB source to $1/3$ on Earth, while neutrino decay, if exists and under the assumption of normal hierarchy of mass eigenstates, would result in a further reduction of muon-neutrino ratio to $1/8$. With these in mind, we note that there have been efforts in recent years in pursuing other type of neutrino telescopes based on Askaryan effect, which can in principle observe and distinguish all three flavors with comparable sensitivities. Such new approach may therefore be complementary to IceCube in shedding more lights on this cosmic accelerator question.

¹ Department of Physics and Leung Center for Cosmology and Particle Astrophysics (LeCosPA), National Taiwan University, Taipei, 10617 Taiwan;
e-mail: pisinchen@phys.ntu.edu.tw

² Kavli Institute for Particle Astrophysics and Cosmology, SLAC National Accelerator Laboratory, Menlo Park, CA 94025, USA

1 Introduction - neutrino as cosmic messenger

Ultra-high energy cosmic rays (UHECR) with energies beyond 10^{19} eV have been observed (HiRes 2009; Auger 2010; ANITA 2010). Their origin, however, has not been clear. This challenge has been considered as one of the eleven science questions for the new century by the well publicized white-paper prepared for the US National Research Council by the Turner Committee in 2003 (Turner 2003). Gamma ray bursts (GRB), the most violent explosions in the universe second only to the Big Bang, has long been considered as a promising candidate site for the “cosmic accelerator” where UHECRs, primarily protons, are generated. Since proton trajectory can be bent by inter- and intra- galactic magnetic fields on its way to Earth, its incoming angle cannot reveal its origin. It happens that a necessary by-product of UHECR on or near the cosmic accelerator, such as GRB, site are the neutrinos at comparable energy (UHECN). Being charge-neutral and weakly interacting, neutrinos so produced can propagate straight-forwardly to Earth. The detection of such neutrinos would therefore provide a useful means to address the cosmic accelerator puzzle.

There are multiple channels where such conversion can happen. We assume that the UHECRs are primarily protons. First, such protons can interact with the intense GRB background within the GRB fireball, possibly comoving, and neutrinos are generated through photo-pion production. Such interaction is particularly pronounced in the Δ -resonance process:

$$p + \gamma \rightarrow \Delta \rightarrow n + \pi^+ \rightarrow n + \{\mu^+ + \nu_\mu\} \rightarrow n + \{[e^+ + \nu_e + \bar{\nu}_\mu] + \nu_\mu\}. \quad (1.1)$$

The resulting UHECN spectrum should peak at several hundred TeV (Waxman & Bahcall 1997). Such UHECNs are produced strictly on the GRB site. Second, the UHECR protons may instead collide with the cosmic microwave background (CMB) on their flight to Earth, and turn into UHECNs under the same process in Equation (1). This is the so-called GZK process (Greisen 1966; Zatsepin & Kuzmin 1966; Berezinsky & Zatsepin 1969). For this channel to happen, it would require a much higher UHECR proton energy since CMB photons are much softer than that of GRB (but may collide head-on). The associated neutrino spectrum has a flat top ranging from 10^{15} eV to 10^{20} eV (see Fig. 1). Though such UHECNs are produced offsite from the cosmic accelerator, it generally occur very near the source. For example, at redshift $z \sim 1$ the mean-free-path for a UHECR proton above the GZK threshold energy is < 6 Mpc. A neutrino so produced would arrive at Earth with an incoming angle that is within 5 arc second around the GRB where the UHECR proton was accelerated. The point-back ability of UHECN to the cosmic accelerator is thus not so compromised even through this channel.

2 Non-observation of GRB neutrinos at IceCube

Giving the importance of the issue as described above, the recent IceCube announcement of the non-observation of GRB neutrinos (Abbasi *et al.* [IceCube Coll.] 2011; Ahlers *et al.* 2011) came as a disappointment to many. IceCube

calculated the expected prompt neutrino spectrum in the internal shock scenario of the fireball model following Guetta *et al.* (2004), which is based on Waxman & Bahcall (1997). As far as point-source observations are concerned, IceCube is most sensitive to muons for two reasons (Karle *et al.* [IceCube Coll.] 2003): 1.) Muons allow a very good angular resolution of 0.7° over a wide range of energy; 2.) The effective volume for muons exceeds the geometric volume of the detector by factors of 10–50, depending on energy. Following IceCube and for the rest of this paper, we shall neglect the contributions from the other two flavors in IceCube’s sensitivity to address the GRB connection with cosmic accelerator.

IceCube’s starting point is to express the GRB neutrino flux in terms of its UHECR proton flux:

$$\frac{\mathcal{F}_\nu^{\text{IC}}}{\mathcal{F}_p} = \frac{1}{8} f_{\pi,b}, \quad (2.1)$$

where $f_{\pi,b} \equiv f_\pi(E = E_b)$ is the fraction of proton energy carried by the pion as a result of proton-GRB photon collision, with a spectral-break energy ϵ_b at Δ -resonance:

$$E_b = 1.3 \times 10^{16} \Gamma_{2.5}^2 \epsilon_{b,\text{MeV}}^{-1} \text{eV}, \quad (2.2)$$

where $\Gamma = 10^{2.5} \Gamma_{2.5}$ is the Lorentz factor of the bulk flow and $\epsilon_b = 1 \epsilon_{b,\text{MeV}}$. On the other hand, the proton flux can be normalized by the gamma-ray flux through

$$\mathcal{F}_p = \frac{1}{f_e} \mathcal{F}_\gamma, \quad (2.3)$$

where f_e is the ratio of accelerated proton to electron energies. By 2011 with half of its detector completed, IceCube has reached the sensitivity that is comparable to the expected neutrino flux from GRBs. Based on 117 GRB events, IceCube searched for neutrino emission from these sources over a wide range of energies and emission times, but produced no evidence for such, excluding prevailing models at 90% CL.

3 Over-estimation of neutrino flux at source

It has been pointed out, however, that the IceCube Collaboration might have over-estimated the neutrino flux at GRB source by as much as a factor 5 (Zhuo Li 2012). If so, then the IceCube results have not yet ruled out the GRB candidacy for the cosmic accelerator. Here we review Li’s argument and correction to the GRB neutrino flux. His main points are as follows.

1. For a flat proton distribution with the index given above and the Band-function parameters, $\alpha = -1$ and $\beta = -2.2$, so chosen by IceCube, the assumption of $f_\pi(E) = f_{\pi,b}$ is valid only for protons with energy $E > E_b$. For $E < E_b$, f_π is no longer a constant but instead proportional to the energy: $f_\pi \propto E$. The physical reason for this is simple: the higher energy target photons are harder to find to match with the lower energy protons. Thus by applying constant f_π to all proton energies, Equation (1) has overestimated the initial neutrino flux.

2. Equation (3.1) has also ignored the suppression of neutrino production at high energies due to the radiative cooling of secondary pions/muons. The synchrotron cooling timescale is shorter than that for the secondary decay, and therefore the neutrino production will be suppressed, when the pion/muon energy is above the cooling energy E_c .

Thus the neutrino production is mainly contributed by the primary protons with an energy window $E_b < E < E_c$, which is only a fraction of the total number of GRB accelerated UHE protons. Let the maximum and minimum accelerated proton energies be E_{max} and E_{min} , respectively, with ratio $E_{max}/E_{min} \sim 10^9$, and let $E_c/E_b \sim 10^2$. One then finds, for a proton energy spectrum $E^2 dn_p/dE \propto E^{2-p}$, with $p \approx 2$,

$$\mathcal{F}_\nu = \frac{\mathcal{F}_\nu^{\text{IC}}}{\mathcal{F}_p} \int_{E_b}^{E_c} E \frac{dn_p}{dE} dE \approx \mathcal{F}_\nu^{\text{IC}} \frac{\ln(E_c/E_b)}{\ln(E_{max}/E_{min})} \sim 0.22 \mathcal{F}_\nu^{\text{IC}}. \quad (3.1)$$

Thus the correction to the IceCube assumption of the neutrino flux is the reduction of $\mathcal{F}_\nu^{\text{IC}}$ by roughly a factor 5. With this correction, Li found that the IceCube data is still consistent with the assumption of GRB as the origin for UHECR.

It should be reminded that there exist additional corrections to the neutrino flux due to various uncertainties in the fundamental physics parameters such as f_π and f_e , as well as in the GRB and UHECR acceleration models.

4 Evolution of neutrino flavors in flight

Having discussed the conversion factor from UHE protons to neutrinos at GRB site, which is GRB model and cosmic accelerator model dependent, in this section we turn our attention to the impact on the GRB-neutrino connection due to neutrino properties in-flight from GRB to Earth. While the notion of neutrino oscillation is by now well-known and has been incorporated into data analysis, it appears that the implication of possible neutrino decay has thus far not been taken into active consideration.

4.1 Neutrino oscillation

As we know, neutrinos oscillate among their three different flavors (Fukuda *et al.* [Super-Kamiokande Collaboration] 1998). From Equation (2.1) we see that every proton-photon interaction will produce one electron neutrino and two muon neutrinos. So the ratio between different neutrino flavors at source, per out-coming neutrino, is

$$\text{At Source: } f_e^S : f_\mu^S : f_\tau^S = 1/3 : 2/3 : 0. \quad (4.1)$$

Being produced at cosmic distance, which is much much larger than the neutrino oscillation length, the GRB induced ultra-high energy neutrinos flavors will reach an equilibrium when arriving at Earth with a uniform distribution (see, for example, Wang *et al.* 2013):

$$\text{In Flight: } f_e^E : f_\mu^E : f_\tau^E = 1/3 : 1/3 : 1/3. \quad (4.2)$$

As mentioned earlier, although IceCube is able to detect all neutrino flavors, in its search for point sources such as neutrino emission from GRB, muon-neutrino has the highest sensitivity and best angular resolution. This, however, necessarily reduces the effective neutrino flux to 1/3 of the total flux emitted from GRB.

4.2 Neutrino decay

Another major discovery about neutrinos in the last two decades is that neutrinos have mass. This, together with additional assumption of the decay process based on notions beyond the standard model of particle physics, leads to the prediction of neutrino decay, from the higher mass eigenstates to the mass ground state. One can envision at least two possible mass hierarchies: the normal hierarchy, *i.e.*, $m_3 \gg m_2 > m_1$, and the inverted hierarchy, *i.e.*, $m_2 > m_1 \gg m_3$. It has been shown that under normal hierarchy the eventual flavor ratio on Earth, again normalized to number of neutrinos produced at GRB site, is (Beacom *et al.* 2003; Maltoni & Winter 2008)

$$\text{Normal Hierarchy:} \quad f_e^E : f_\mu^E : f_\tau^E = 2/3 : 1/8 : 5/24, \quad (4.3)$$

or

$$\text{Inverted Hierarchy:} \quad f_e^E : f_\mu^E : f_\tau^E = 0 : 2/5 : 3/5. \quad (4.4)$$

So for the IceCube search for GRB emission of neutrinos, which is most sensitive to ν_μ , its detector sensitivity would be further reduced from 1/3 (based on pure oscillation) to 1/8 of the total neutrino flux for the case of normal hierarchy, but would gain slightly from 1/3 for the purely oscillating scenario to 2/5 if the neutrino mass eigenstates follow the inverted hierarchy.

In summary, at the GRB site every UHECR proton that collides with the background GRB or CMB photons would generate 3 neutrinos, among them 2 are muon neutrinos, *i.e.*, the ν_μ contributes 2/3 of the total population. By the time these neutrinos arrive on Earth, the ν_μ contribution reduces to 1/3, due to neutrino oscillations. When the neutrino decay is considered, in particular with the assumption of normal hierarchy, then its contribution will become 1/8 when arriving on Earth, a factor 3/8 reduction from that under pure oscillation. On the contrary, if the neutrino mass eigenstates follow the inverted hierarchy, then the ν_μ population rises from 1/3 to 2/5. We should caution, however, that the notion of neutrino decay is not a direct consequence of the standard model and is not yet experimentally verified.

5 Detecting GZK neutrinos with askaryan effect

While the estimate of the GRB induced UHE proton and neutrino fluxes at the GRB site are GRB model and acceleration mechanism dependent, we see that the evolution of the neutrino flavor ratio during their flight to Earth depends on neutrino's fundamental properties. Among them neutrino oscillation is well-established, while neutrino decay still awaits experimental evidence. Based on the

discussion in the previous section, however, it should be fair to conclude that, as far as the issue of UHECR cosmic accelerator is concerned, it would be more advantageous if a neutrino observatory can be sensitive to *all* flavors. In this regard, an idea proposed by Askaryan in the 1960 s (Askaryan 1962, 1965), can in principle detect all neutrino flavors with comparable sensitivities due to the vastness of the typical detection volume involved in such approach.

As was proposed by Askaryan, high energy cosmic neutrino can be detected by observing the radiowave band of the Cherenkov radiation emitted by the neutrino-induced shower in a large solid target. The neutrino induced shower, though inherently charge neutral, will develop a charge disparity by the time when the shower reaches its maximum, with $\sim 20\%$ more electrons than positrons due to the shorter stopping distance of the positrons propagating in ordinary matter. Since all particles travels near the speed of light, the shower remains compact and thus the emitted Cherenkov radiation is a sharp impulse and therefore is wide-band in the frequency domain, where the radiaowave portion is enhanced due to the coherence of emission. This effect has been validated in a series of experiments in sand, salt and ice performed at SLAC (Gorham 2000).

Several ongoing and proposed experiments, *e.g.*, GLUE (Gorham *et al.* 2004), RICE (Kravchenko *et al.* 2006), ANITA (2009), LUNASKA (James *et al.* 2010), ARIANNA (Barwick 2007; Gerhardt *et al.* 2010), and ARA (Chen & Hoffman 2009; Allison *et al.* [ARA Coll.] 2011), are based on the Askaryan effect. In particular, the balloon-borne ANITA has so far completed two successful missions in Antarctica with exciting results. With an average altitude of 30 km, it tends to detect neutrinos at the higher energy end of the GZK spectrum. So far one candidate neutrino event has been identified from ANITA-2 (Gorham *et al.* 2010). An upgraded ANITA-3 has been scheduled to launch in December 2013 with the expectation of detecting multiple neutrinos. Two new ground-based projects, ARIANNA and ARA, are both at the proof-of-principle stage. For the case of ARA, it is envisioned to cover 200 km^2 area at South Pole with 37 antenna stations. To date (Jan. 2013) 3 stations have been successfully deployed about 200 m under ice at Pole. Figure 1 shows the projected ARA37 detector sensitivity in comparison with other projects.

Focusing on the issue of GRB as a candidate site for UHECR production and its connection to UHE cosmic neutrino detection, what is important for a neutrino telescope is the angular resolution and the *total* flux of incoming neutrinos; the composition of neutrino flavors within the total flux does not *a priori* matter. That said, it would be advantageous if a neutrino telescope for this purpose has indeed the capability of distinguishing neutrino flavors. IceCube can distinguish all three flavors based on different characteristics of their tracks. What about Askaryan effect-based observatories such as ARA? Recent investigations indicate that flavor identification in ARA37 is in principle feasible (Chen *et al.* 2013; Wang *et al.* 2013). On the other hand, due to the vastness of the detector's geometric volume and sparseness of antenna stations (2 km separation), as a trade-off for its higher sensitivity the angular resolution of Askaryan effect-based observatories tend not to be as good as that for IceCube. For example the angular resolution for

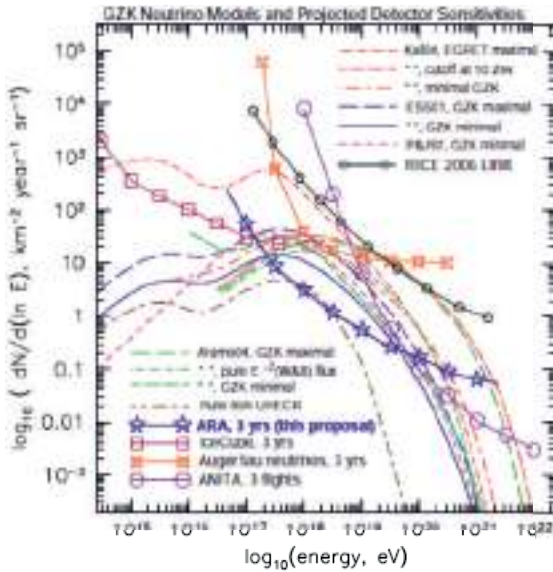


Fig. 1. ARA37 sensitivity in comparison with other contending projects plotted against different GZK neutrino models.

ARA37 is $\sim 6^\circ$, which is about an order of magnitude worse than that of IceCube muon-neutrino detection.

6 Conclusion

We have shown that in addition to the over-estimation by IceCube of the GRB included neutrino flux at-source by a factor ~ 5 as pointed out by Zhou Li, there are additional impacts to the neutrino flux in-flight as they traverse the cosmos. While the effect due to neutrino oscillations is well-known and has been incorporated into analysis, that due to a possible neutrino decay has received less attention. If neutrinos do decay and their mass eigenstates follow the normal hierarchy, then the net effect is that the flux for muon-neutrino would further reduce from 1/3 under the pure oscillation scenario to 1/8, which would be quite a sizable impact on the IceCube detector sensitivity, assuming that IceCube solely relies on muon-neutrinos in its investigation of the cosmic accelerator question. There are, however, new types of neutrino observatories based on Askaryan effect that are less sensitive to neutrino flavors and would therefore provide almost one order of magnitude improvement in neutrino detection sensitivity. As a trade-off, their angular resolution, on the other hand, will not be as good as that with muon-neutrino at IceCube. If such detector can in addition distinguish different flavors, then the measured flavor ratio would provide a crucial information on the nature of UHECR production, or the inner-workings of cosmic accelerator, at source such as GRB. In conclusion the new type of neutrino observatories based on Askaryan effect maybe

complementary to IceCube in shedding lights on this very acute question about the origin of cosmic accelerators.

The author thanks Francis Halzen, Zhou Li, Tsung-Che Liu, and Jiwoo Nam for helpful discussions. This work is supported by Taiwan National Science Council under Project No. NSC100-2119-M-002-025 and by US Department of Energy under Contract No. DE-AC03-76SF00515.

References

- Abbasi, R., Abu-Zayyad, T., Al-Seady, M., *et al.* [High Resolution Fly's Eye Collaboration], 2009, *Astroparticle Phys.*, 32, 53
- Abbasi, R., Abdou, Y., Abu-Zayyad, T., *et al.* [IceCube Collaboration], 2011, *Phys. Rev. Lett.*, 106, 141101
- Abraham, J., Abreu, P., Aglietta, M., *et al.* [Pierre Auger Collaboration], 2010, *Phys. Lett. B*, 685, 239
- Ahlers, M., Gonzalez-Garcia, M.C., & Halzen, F., 2011, *Astroparticle Phys.*, 35, 87
- Allison, P., Auffenberg, J., Bard, R., *et al.* [ARA Collaboration], 2012, *Astroparticle Phys.*, 35, 457
- Askaryan, G.A., 1962, *JETP*, 14, 441
- Askaryan, G.A., 1965, *JETP*, 21, 658
- Barwick, S.W., 2007, *J. Phys.: Conf. Ser.*, 60, 276
- Beacom, J.F., Bell, N.F., Hooper, D., *et al.*, 2003, *Phys. Rev. Lett.*, 90, 181301
- Berezinsky, V., & Zatsepin, G., 1969, *Phys. Lett. B*, 28, 423
- Chen, P., & Hoffman, K.D., 2009, "Origin and Evolution of Cosmic Accelerators – The Unique Discovery Potential of a Neutrino Telescope: Astronomy Decadal Survey (2010-2020) Science White Paper [[arXiv:0902.3288](https://arxiv.org/abs/0902.3288)]
- Chen, C.-C., Chen, P., Hu, C.-Y., *et al.*, 2013, *Mod. Phys. Lett. A*, 28, 1340009
- Fukuda, Y., Hayakawa, T., Ichihara, E., *et al.* [Super-Kamiokande Collaboration], 1998, *Phys. Rev. Lett.*, 81, 1158
- Gerhardt, L., Klein, S., Stezelberger, T., *et al.* [ARIANNA Collaboration], 2010, *Nucl. Instr. Meth. Phys. Res. A*, 624, 85
- Gorham, P., Allison, P., Barwick, S., *et al.* [ANITA Collaboration], 2009, *Phys. Rev. Lett.*, 103, 051103
- Gorham, P.W., Allison, P., Bauhman, B.M., *et al.* [ANITA Collaboration], 2010, *Phys. Rev. D*, 82, 022004
- Gorham, P.W., Hebert, C.L., Liewer, K.M., *et al.* [GLUE Collaboration], 2004, *Phys. Rev. Lett.*, 93, 041101
- Greisen, K., 1966, *Phys. Rev. Lett.*, 16, 748
- Guetta, D., Hoper, D., Alvarez-Muniz, J., *et al.*, 2004, *Astroparticle Phys.*, 20, 429
- Hoover, S., Nam, J., Gorham, P.W., *et al.* [ANITA Collaboration], 2010, *Phys. Rev. Lett.*, 105, 151101
- James, C.W., Ekers, R.D., Alvarez-Muniz, J., *et al.* [LUNASKA Collaboration], 2010, *Phys. Rev. D*, 81, 042003
- Karle, A., Ahrens, J., Bahcall, J.N., *et al.* [IceCube Collaboration], 2003, *Nucl. Phys. B - Proc. Suppl.*, 118, 388

- Kravchenko, I., Cooley, C., Hussain, S., *et al.* [RICE Collaboration], 2006, Phys. Rev. D, 73, 082002
- Li, Z., 2012, Phys. Rev. D, 85, 027301
- Maltoni, M., & Winter, W., 008, JCAP 0807.064
- Saltzberg, D., Gorham, P., Walz, D., *et al.*, 2001, Phys. Rev. Lett., 86, 2802
- Turner, M., ed. "Connecting Quarks with the Cosmos: Eleven Science Questions for the New Century", 2003 (US National Research Council Publication)
- Wang, S.-H., Chen, P., Huang, M.-L., *et al.*, "Feasibility of Determining Diffuse Ultra-High Energy Cosmic Neutrino Flavor Ratio through ARA Neutrino Observatory", 2013 [[arXiv:1302.1586](https://arxiv.org/abs/1302.1586)] [[astro-ph.HE](#)], submitted to JCAP
- Waxman, E., & Bahcall, J., 1997, Phys. Rev. Lett., 78, 2292
- Zatsepin, G., & Kuzmin, V., 1966, JETP Lett., 4, 114

FERMI GBM CAPABILITIES FOR MULTI-MESSENGER TIME-DOMAIN ASTRONOMY

V. Connaughton^{1,2}, V. Pelassa¹, M.S. Briggs^{1,2}, P. Jenke¹, E. Troja³,
J.E. McEnery³ and L. Blackburn³

Abstract. Owing to its wide sky coverage and broad energy range, the *Fermi* Gamma-ray Burst Monitor (GBM) is an excellent observer of the transient hard X-ray sky. GBM detects about 240 triggered Gamma-Ray Bursts (GRBs) per year, including over 30 which also trigger the *Swift* Burst Alert Telescope (BAT). The number of GRBs seen in common with *Swift* is smaller than expected from the overlap in sky coverage because GBM is not as sensitive as the BAT and the GBM GRB population is thus skewed to the brighter, closer bursts. This population includes about 45 short GRBs per year, giving GBM an excellent opportunity to observe the electromagnetic counterpart to any gravitational wave candidate resulting from the merger of compact binary members. The same characteristics make GBM an ideal partner for neutrino searches from nearby GRBs, and for the elusive Very-High Energy (VHE) counterparts to GRBs. With the deployment of the next-generation gravitational-wave detectors (Advanced LIGO/VIRGO) and VHE experiments (CTA and HAWC) potentially within the lifetime of the *Fermi* Gamma-ray Space Telescope, the prospects for breakthrough observations are good.

1 Introduction

The Gamma-ray Burst Monitor (GBM) on-board the *Fermi* Gamma-ray Space Telescope covers the entire unocculted sky using 12 thin (1.27 cm) Sodium Iodide (NaI) detectors with different orientations placed around the spacecraft and covering an energy range from 8 keV to 1 MeV, and two bismuth germanate (BGO) scintillators placed on opposite sides of the spacecraft with energy coverage from 200 keV to 40 MeV (Meegan *et al.* 2009). In four years of operation,

¹ CSPAR, University of Alabama in Huntsville, AL 35805, USA

² Department of Physics, University of Alabama in Huntsville, AL 35805, USA

³ NASA GSFC, USA

Fermi has opened a new window to the world of Gamma-Ray Burst (GRB) spectroscopy. Observations by the GBM between 8 keV and 40 MeV and the Large Area Telescope (LAT, Atwood *et al.* 2009) from 100 MeV to tens of GeV have provided a high-energy view over an unprecedentedly long energy baseline. Follow-up observations of LAT-detected GRBs have revealed the distance to 10 GRBs. Typically the *Swift* X-Ray Telescope (XRT) observes the LAT error circle in one or a small number of pointings beginning from 11 to 48 hours after the GBM trigger, after ground-processing of the LAT data. This is followed by optical observations of any fading XRT afterglow candidates. In three LAT-detected GRBs, the latency was much smaller because the GRB also triggered the *Swift* BAT, and in two LAT-detected GRBs the LAT position was accurate enough to permit optical follow-up without the intermediate stage of the *Swift* XRT pointing. The impact of GBM on afterglow observations has been less dramatic owing to the limitations of the uncollimated GBM detectors, which provide good spectral coverage but no imaging localization capabilities. GRB 090902B was observed by ROTSE (Pandey *et al.* 2010) an hour after the GBM trigger, with ROTSE tiling the GBM prompt emission error circle. A source was detected by ROTSE at the position of the burst hours before a better localization was obtained using LAT prompt and *Swift* afterglow data, providing the earliest measurement of the GRB afterglow. The MASTER wide-angle robotic telescope regularly observes GBM error boxes looking for prompt optical emission, but has not found any candidates down to between 8th and 12th magnitude (Tyurina *et al.* 2009). In general, the small fields-of-view of the most sensitive follow-up telescopes have prevented regular afterglow observations of the degrees-scale error circles resulting from GBM localizations and GRB 090902B is the only GBM GRB for which an optical counterpart was detected without localization by an imaging instrument or the InterPlanetary Network.

2 GBM localization of GRBs

Source localization is achieved using the relative rates recorded in the 12 NaI detectors to estimate the most likely arrival direction given the angular and spectral response of the detectors. In addition to background rates which average above 1000 counts/sec over the *Fermi* orbit and vary by a factor of about 2 depending on geomagnetic latitude, the recorded rates from the source of gamma rays contain three elements: direct flux from the source, flux scattered in the spacecraft, and flux scattered from the atmosphere. The contributions from each of these components depend on the observing geometry as well as the spectrum of gamma rays from the source. We construct our response to a particular GRB by adding two model terms, the direct response which depends only on the source-spacecraft geometry, and the atmospheric response which depends on the source-spacecraft-Earth geometry. We compare the observed rates to the expected rates from a GRB coming from each position on the 1° resolution sky grid with one of three typical input GRB spectra - soft, medium and hard - selecting the position and spectral shape that minimize χ^2 . Using a sample of 200 reference GRB positions

from instruments with good localizing capabilities such as the *Swift* BAT, *Fermi* LAT, INTEGRAL, MAXI, SuperAGILE, and the InterPlanetary Network (IPN), we estimate that in addition to the statistical uncertainty associated with this process, there is a 3° systematic uncertainty (1σ) that applies to most GRBs, with about 10% of GBM-detected GRBs having a much larger systematic effect extending beyond 10° (Connaughton *et al.*, in prep.).

Because of on-board computing limitations, the locations produced by the Flight Software (FSW) use a coarser 5° grid, a single spectral shape, and assume the Earth is directly beneath the spacecraft. The ground automated (GA) locations and the final human-in-the-loop (HiTL) locations use the full-resolution grid and Earth-*Fermi* geometry, but the GA location sees only a snippet of source and background data provided by the FSW, whereas the HiTL location requires a longer data downlink and interaction by the burst advocate on duty to select both a good background and an optimized source interval. All three location types are distributed as notices to the GRB Coordinates Network (GCN). Both the FSW and GA notices arrive within seconds of data receipt, or about 30 s following the trigger, and the HiTL notice can arrive as soon as 20–30 minutes up to several hours after the trigger. A HiTL notice is not sent if another instrument has detected the GRB and provided a more precise location, but the FSW and GA notices appear automatically.

3 Who should follow up GBM-detected GRBs?

3.1 TeV community

After 20 years of looking for Very High Energy (VHE) photons from GRBs, beginning in the BATSE era with the Whipple 10-m telescope (Connaughton *et al.* 1997), the field is still without a VHE GRB counterpart or even a meaningful upper limit. A photon with energy E_1 will interact with a photon of energy E_2 to produce an electron-positron pair if $E_1 E_2 * (1 - \cos\theta) > 2(m_e c^2)^2$, where θ is the angle between the two photons, m_e the rest-mass of an electron and c the speed of light. This results in the attenuation of gamma-ray signals above a few tens GeV owing to the presence of intervening Extragalactic Background Light (EBL) photons, and limits the visible horizon so that the higher the energy of a photon, the closer the source must be in order to detect it, with the exact horizon depending on the model assumed for EBL as a function of energy and redshift. Observations of photons above 10 GeV from GRB 080916C by the LAT from a redshift of 4.4, without noticeable attenuation, excluded some proposed EBL models (Abdo *et al.* 2009) but the remaining viable models predict that detections above a few hundred GeV will be possible only within redshift unity. VHE observations of GRBs are also difficult because the duty cycle of the Imaging Atmospheric Cherenkov Telescope (IACT) is low (10–13%) owing to the need for dark, moonless nights, and the slew time to reach a GRB is typically tens of seconds to over a minute. With an energy threshold of 400 GeV, the pioneering IACT, the Whipple 10-m, had a very limited source horizon owing to EBL absorption. The lower energy threshold (100 GeV) of the current-generation IACT arrays such as VERITAS means

that more GRBs lie within the detectable VHE horizon compared to the Whipple era. The most recent results from VERITAS (Acciari *et al.* 2011) show that VHE observations have occurred within the duration of the prompt emission, but not for GRBs known to be within the VERITAS EBL horizon. The next-generation IACT, the Cherenkov Telescope Array (CTA) will be much more sensitive, with three telescope types including the Large Size Telescope (LST) which will have an energy threshold of tens GeV, bringing all but the most distant GRBs within the detection horizon of CTA. The field-of-view of the LST will be $3.5 - 4^\circ$ so that a tiling strategy for following GBM GRBs will be adopted. Estimates of the annual detection rate of GBM GRBs by CTA, taking into account this tiling necessity, the average slew rate of the telescope, and the average spectral and duration properties and distance distribution of GBM-detected GRBs, are a few tenths of a GRB per year, comparable to the expected overlap with the *Swift*-detected GRB sample (Gilmore *et al.* 2013). With broad sky coverage and high duty cycle, the High Altitude Water Cherenkov (HAWC) will be sensitive to bright nearby GRBs without slewing, but with lower sensitivity than CTA. Annual detection rates have yet to be published.

3.2 Neutrino experiments

Neutrinos are expected through the delta resonance from $p\gamma$ interactions in the fireball, and subsequent decay of the delta resonance pion into leptons and neutrinos. For bright GRBs with Lorentz factors of around 100, this flux should be detectable with IceCube (Dermer & Atoyan 2006). A lack of neutrino detection constrains (i) how much energy is in protons relative to electrons in the fireball or (ii) how low the Bulk Lorentz factor of the fireball can be. The lack of neutrino detection by IceCube from a set of over 200 GRBs (a mixture of *Fermi* and *Swift* GRBs) (Abbasi *et al.* 2012) constrains the parameter space in at least one of these directions: either the fireball has such a high bulk Lorentz factor (greater than 400) that the true energy of the protons at the source is too low for the $p\gamma$ interaction, or the amount of energy in protons is much less than 1/10 the energy in electrons. For an individual GRB, the detectability of its neutrino signal depends on (i) the observed gamma-ray fluence of the GRB - the neutrino flux scales with the gamma-ray flux (ii) the Lorentz factor of the GRB - lower is better. Given that GBM is a prolific detector of bright GRBs, it is an ideal partner for neutrino searches from individual bursts in the IC59-or-beyond configurations of IceCube.

3.3 Next-generation gravitational wave experiments

Neutron Star - Neutron Star (NS-NS) and Neutron Star - Black Hole (NS-BH) mergers are believed to be likely sources of detectable gravitational waves. They are also the preferred model for short GRBs (SGRB). Searches for GW signals from 154 GRBs using past science runs from LIGO and VIRGO were not fruitful (Abadie *et al.* 2012), but LIGO was sensitive to SGRBs only within 33 Mpc from NS-NS, 70 Mpc from NS-BH systems, closer than any SGRBs with measured redshift. The expected signal from long GRBs is uncertain. The Advanced

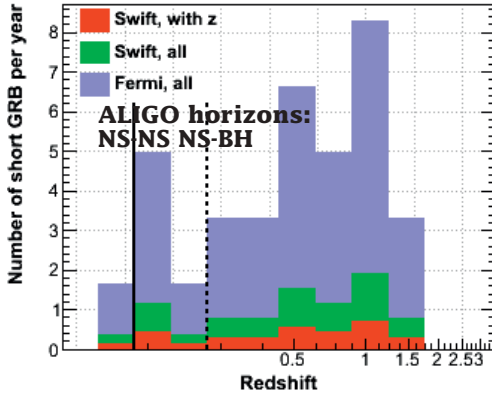


Fig. 1. SGRB rate as a function of redshift for *Fermi* and *Swift*. ALIGO horizons for NS-NS and NS-BH mergers are shown as black vertical lines (Pelassa *et al.* 2012).

configurations of both LIGO and VIRGO will have horizons of $z = 0.11$ (445 Mpc) and 0.22 (927 Mpc) for NS-NS and NS-BH mergers, respectively (Abadie *et al.* 2010). Estimates of annual SGRB detection within these horizons are shown in Figure 1 (Pelassa *et al.* 2012). The SGRBs with known redshift in the *Swift*-detected population are assumed to form part of the same population as those with unknown redshift so that the number of SGRBs detected by *Swift* per year, N_{Swift} , as a function of redshift is presented as the number of SGRBs with measured redshift in each bin divided by the fraction of SGRBs with known redshift. The same assumption about the underlying redshift distribution of GBM-detected SGRBs yields the number of SGRBs per year seen by GBM, N_{GBM} , as a function of redshift. Given that $N_{GBM}/N_{Swift} = 4.5$ we show the expected SGRB detection for GBM as a function of redshift by multiplying the Swift SGRB distribution by this factor. Bromberg *et al.* (2012) suggest that because of the greater sensitivity of *Swift* to short collapsar events relative to GBM, the *Swift* SGRB sample may be contaminated by collapsar events and one can be confident that *Swift* SGRBs are merger events only in the sub-sample of SGRBs lasting less than 0.6 s. For this reason, N_{GBM}/N_{Swift} may be larger for merger SGRBs and the number of merger events seen by GBM within the ALIGO horizon could also be larger than suggested by Figure 1. ALIGO localization of detected GW events can produce large non-contiguous sky regions covering up to 100 sq degrees, so that in addition to providing the electromagnetic counterpart to a GW candidate, the moderate localization capability (10 s sq degrees) of GBM is useful in eliminating some of these regions for follow-up by X-ray or optical instruments. In the absence of a convincing GW event, GBM can also provide useful seed sky positions for sub-threshold offline ALIGO searches.

4 The future

Even with no improvement in localization capabilities over the *Fermi* mission, GBM is an ideal partner for neutrino and GW searches, particularly in the era

of ALIGO/VIRGO and the deployment of new IceCube configurations with more strings. A modest improvement would really help the case for CTA, removing the need to tile the error box, and thus increasing the joint GBM-CTA GRB detection rate from a few tenths to 1 per year. Efforts to improve GBM GRB localization include: (i) characterization of systematic errors to either identify GRBs with low systematic uncertainties or refine the localization based on GRB or geometrical properties that might lead to a large but measurable systematic effect (ii) moving to a real-time GA location that uses more data and is not limited by statistics (iii) improving our detector response database by identifying its deficiencies through our study of localization errors and (iv) reducing the statistical uncertainty of GBM locations through finer grid resolution, gradient searches within the existing grid, or other algorithmic techniques.

References

- Abadie, J., Abbott, B.P., Abbott, R., *et al.*, 2010, *Class. Quant. Grav.*, 27, 173001
Abadie, J., Abbott, B.P., Abbott, R., *et al.*, 2012, *ApJ*, 760, 12
Abbasi, R., Abdou, Y., Abu-Zayyad, T., *et al.*, 2012, *Nature*, 484, 351
Acciari, V., Aliu, E., Arlen, T., *et al.*, 2011, *ApJ*, 743, 62A
Atwood, W.B., Abdo, A.A., Ackermann, M., *et al.*, 2009, *ApJ*, 697, 1071
Abdo, A., Ackermann, M., Arimoto, M., *et al.*, 2009, *Science*, 323, 1688
Bromberg, O., Nakar, E., Piran, T., & Sari, R., 2012 [[arXiv:1210.0068](https://arxiv.org/abs/1210.0068)]
Connaughton, V., Akerlof, C.W., Barthelmy, S., *et al.*, 1997, *ApJ*, 479, 859
Dermer, C.D., & Atoyan, A., 2006, *New J. Phys.*, 8, 122
Gilmore, R., Bouvier, A., Connaughton, V., *et al.*, 2013, to appear in *Exp. Astron.*
Greiner, J., Clemens, C., Kruehler, T., *et al.*, 2009, *A&A*, 498, 89
Meegan, C., Lichti, G., Bhat, P.N., *et al.*, 2009, *ApJ*, 702, 791
Pandey, S., Swenson, C.A., Perley, D.A., *et al.*, 2010, *ApJ*, 714, 799
Pelassa, V., Connaughton, V., Troja, E., *et al.*, 2012, eConf Fermi Symposium 2012
Tyurina, N., Lipunov, V., Kornilov, V., *et al.*, 2009 [[arXiv:0907.1036](https://arxiv.org/abs/0907.1036)]

COSMIC-RAYS AND GAMMA RAY BURSTS

A. Meli¹

Abstract. Cosmic-rays are subatomic particles of energies ranging between a few eV to hundreds of TeV. These particles register a power-law spectrum, and it seems that most of them originate from astrophysical galactic and extragalactic sources. The shock acceleration in super-alfvenic astrophysical plasmas, is believed to be the main mechanism responsible for the production of the non-thermal cosmic-rays. Especially, the importance of the very high energy cosmic-ray acceleration, with its consequent gamma-ray radiation and neutrino production in the shocks of the relativistic jets of Gamma Ray Bursts, is a favourable theme of study. I will discuss the cosmic-ray shock acceleration mechanism particularly focusing on simulation studies of cosmic-ray acceleration occurring in the relativistic shocks of GRB jets.

1 Overview

Cosmic Rays (CRs) are subatomic particles and radiation of extra-terrestrial origin. They are believed to originate from galactic, and extra-galactic sources. CRs gain vast amounts of energy through shock acceleration, and extragalactic relativistic objects such as GRBs seem to be one of the most promising source candidates for the production of very high energy (VHE) CRs and consequent radiation. Work progress on the subject in the late 1970 s, see *e.g.* Krymskii (1977), based on the original Fermi acceleration mechanism, see Fermi (1949), and since then the so-called first-order Fermi or diffusive acceleration mechanism by astrophysical shock waves was established. Meanwhile considerable analytical and numerical investigations have been performed, shedding light into the details of the CR acceleration mechanism and particle kinematics at highly relativistic shocks in extragalactic sources such as GRBs.

In more detail, the theory of diffusive shock acceleration, is about a mechanism where CRs gain an amount of energy by crossing a shock front -formed in

¹ IFPA, Institut of Astrophysics and Geophysics, University of Liège, Belgium & Web Institute of Physics; e-mail: www.wiph.org

a super-Alfvénic plasma flow- in consecutive cycles, while they scatter off the irregularities of the magnetic field frozen-into the plasma. It is analytically shown that non-relativistic shocks, in the diffusive approach, produce particle momentum distributions as: $f(p) \propto p^{-\sigma}$ with spectral index σ , which depends only on the compression ratio of the shock, $r = V_1/V_2$, that is: $\sigma = 3r/(r - 1)$ (Drury 1983). Nevertheless, for the relativistic shocks the effect of shock speed, $V \rightarrow c$, to the spectral index σ , or the inclination ψ of the shock to the magnetic field, as well as the different scattering modes play a significant role to the particle energy distributions, *e.g.* see Meli *et al.* (2008), Meli (2011).

GRB sources are sources of extragalactic origin and observations have shown that their host galaxies have a redshift z ranging between 0.008 and 8.2. The so called fireball-model, is a scenario where it is assumed that the formation of a GRB begins either with the merger of a binary neutron star or with the collapse of a massive star (*i.e.* Hypernova $\sim 40 M_{sol}$), see Meszaros (2002). Both scenarios create a black hole with a disk of material around it. The hole-disk system consequently pumps out a jet of material at close to the speed of light. Relativistic shock waves within this material form which in turn give off radiation. The magnetic field is very large in these jets ranging from 10^3 to 10^{12} Gauss. It has been theorized that in the so-called pre-burst phase, a faster blob of material collides with a slower blobs creating an internal shock wave, with an estimated Lorentz factor Γ of 100–1000. In that phase an intense gamma-ray emission is observed, and is believed that it originates from accelerated electrons and/or protons. As the jet material expands very fast, it eventually collides with the ambient cooler and slower medium, creating an external shock wave with an estimated Γ speed between 2 and 50. This is the so called afterglow phase of the GRB event, where X-rays, visible light, and radio waves are emitted.

Here I will discuss numerical studies for CR acceleration as this may occur in relativistic internal and external shocks of GRB jets.

2 Simulation studies

Here I use the established test-particle Monte Carlo codes, described in Meli *et al.* (2008), for calculating differential spectra, spectral indices and acceleration rates, using the appropriate parameters for simulating shocks in GRB jets environments (*i.e.* relativistic parallel and perpendicular shocks). A large number of relativistic test-particles (*i.e.* of negligible mass), $N_i = 10^6$, is injected upstream a shock, in a Cartesian system xyz , allowing different shock inclinations and Lorentz speed factor values of $10 \leq \Gamma \leq 1000$. A pitch-angle scattering of the particle is allowed such as $\theta \leq 1/\Gamma$ -assuming high turbulence- for both upstream and downstream shock regions. For a detailed discussion on numerics and kinematics in relativistic shocks see Meli *et al.* (2008) and references therein.

Fully relativistic Lorentzian transformations (reference frames *i.e.* shock-rest frame, fluid-rest frame, E=0 frame) are applied. The code-runs were set for a series of various conditions as application to external or internal shocks in GRB jets. The simulations calculate differential spectra, spectral indexes, and acceleration

rates, *versus* shock Lorentz factors, for parallel or perpendicular shock inclinations and these are compared to their non-relativistic shock counterparts. It is most prominently shown that a wide range of spectral indices is possible for the different inclinations and different shock velocities, and moreover speed-up of the acceleration was evident. In particular, the simulation study results are summarized as follows:

1) Relativistic shocks can generate a multitude of spectral forms (smooth power-law, structured power-laws or concave spectra), in contrast to their non-relativistic counterparts, where the spectrum is always a power-law with a constant spectral index value. 2) Spectral index is not universal, as it depends on gamma flow speed and shock inclination. 3) In the simulations it was evident that faster shocks generate flatter distributions: Subluminal (*i.e.* quasi-parallel) shocks seem to be very efficient accelerators. Superluminal (*i.e.* quasi-perpendicular) shocks are not as efficient. Specifically, it was prominently seen that quasi-parallel shocks are very efficient in terms of maximum attained CR energies registering values to about 10^{19} eV, assuming protons, while quasi-perpendicular shocks do not seem to be candidates responsible for the VHE CR origin in GRB jets. This means that internal shocks being faster by more than an order of magnitude than the external ones, can generate flat spectra if they are quasi-parallel, but they can be steeper if the shocks are quasi-perpendicular ones. 4) Finally, a considerable speed-up of the acceleration process was observed, mostly evident for the quasi-perpendicular shocks. This can be explained due to the large inclination of the magnetic field vector to the relativistic shock surface, intersecting it, which strongly affects the particle kinematics and consequently its trajectory intersections with the shock, as it was firstly shown in Meli and Quenby (2003b).

3 Conclusions

The relativistic shocks in the jets of GRBs are a favorable accelerator candidate for the VHECRs and consequent radiation. We discuss here that relativistic shocks of different inclinations can alter dramatically the CRs spectral form, spectral indices, acceleration efficiency, as well as the acceleration rates. The results of this study can give insights into understanding the radiation and also a potential neutrino emission from GRBs.

References

- Drury, L. Oc., 1983, RPPh, 46, 973
- Fermi, E., 1949, PhRv, 75, 1169
- Krymskii, G.F., 1977, Akademiiia Nauk SSSR, 234, 1306
- Meli, A., & Quenby, J.J., 2003b, APh, 19, 649
- Meli, A., Becker, J., & Quenby, J.J., 2008, A&A, 492, 323
- Meli, A., 2011, AstrSpSc, 7, 287
- Meszaros, P., 2002, ARA&A, 40, 137

CONCLUDING REMARKS

L. Mankiewicz¹

I was really afraid when Alberto asked me to give concluding remarks at this conference. Particle theorist by education, with most of the career spent on calculating Feynmann diagrams for hard processes in QCD, what could I really contribute? But then I realized that if I, in a sense outsider and allien, can be convinced and impressed by the results presented at the conference, it speaks for itself.

And indeed, you have convinced and impressed me. I started my adventure with GRB in 2003, convinced by Bohdan Paczyński to drop QCD and start building small robotic telescopes. I understood that GRBs carry a promise of fundamental discoveries – today I would say that GRBs have made it into the history of science as a unique context, unique tool to study fundamental physics and the Universe at the same time.

We have heard an impressive account how the field was born and how clever (and persistent) people designed the first detectors and flew them on board on early satellite missions. We could follow the technological progress which finally led to the most advanced instruments on board of *Swift*, *Integral*, *Fermi* and other satellites.

The importance of adequate technology is very much visible in the context of observations of GRB emissions, both prompt and afterglow. An enormous amount of high-quality data has been collected so far. Discovery of precursors to short GRBs raised the question of to which extent the classification of GRB into short and long ones makes sense at all. High quality, time- and energy-resolved data pose a real challenge to the theory. We have seen quite a number of models and numerical simulations. I have seen similar situation in particle physics many times – as a rule, extending range of observations, in this case improving time and energy resolution poses serious difficulties to models, even if undergoing

¹ Centre for Theoretical Physics of the Polish Academy of Sciences, Al. Lotników 32/46, 02-668 Warsaw, Poland

physics of radiation and dynamics of relativistic plasma is very well understood piece-wise. Here, the key factor is probably the complicated environment in which all these processes coexist and interact with each other. In my personal opinion model fitting could profit from consideration and a better understanding of a more general physical picture.

It might be also useful to develop meaningful tools to analyze common, averaged over the certain subsample of events features of GRB radiation rather than apply modeling to each event separately. Clearly, better data, with time resolved multiband spectrometry, photometry, polarization, and radio will further constrain our thinking about mechanisms of emission. I think that we are still in the phase when theorists need to be inspired by the data in the first place, so theorists, please go back to the data and try to understand them.

I would very much like to see that our understanding of GRBs dynamics is extended towards progenitor/central engine mechanism. Here, GRB physics overlap with another very “hot” topic, namely ongoing effort for detection of gravitational waves. If gravitational waves originate in a sudden change of space-time geometry caused by a progenitor explosion, a source of gravitational waves might be also a source of strong electromagnetic emission. Hence, understanding of the central engine mechanism is not only interesting because of fascination about relativistic physics in strong gravitational fields which governs these events, but also because of the first gravitational waves detection – which would be a potentially Nobel prize discovery.

Another very interesting topic has been the host galaxies study. Most of these galaxies would never attract observer’s attention, and yet as it follows from the data, the population of GRB hosts galaxies is different from *e.g.* population of “supernova” galaxies. Large – z GRBs have also emerged as a unique tool to probe the very early Universe. It has been proven in a few cases that because of these observations we can indeed successfully reach back in time to the onset of observable Universe and gather information about its evolution. It is a mind-blowing development, isn’t it?

From the side of detectors and satellites, the situation looks very good. *Swift*, *Fermi*, *Integral* and other telescopes forming the IPN and the ground-based telescopes gathered in GCN form together an example of a very successfull, perhaps the most successfull ever observational campaign. We have also witnessed a whole series of talks and poster contributions about new ideas and new developments aiming at improving time resolution and extending robotic networks in ordet to facilitate 24h/day coverage and fast, automatic response to alerts.

In particular, new satellite detectors, like *UFFO-Pathfinder* or *LobsterEye*, or new ground-based installations, like *MegaTORTORA* were presented at the very last day of the conference. These projects use innovative technology in order to achieve a much faster response to alerts combined with a higher spacial or time resolution. Their success will soon bring us even more very interesting and significant data.

It has been a very fruitful conference. I am honoured to be able to thank wholeheartedly Alberto and other members of LCO and SOC for such an inspiring event. But I would like to extend these thanks to you all. We are all living on the stage, somewhat at a corner place, of the enormous theatre, the Universe. The script is full of unexpected and violent events. As, I believe, Richard Feynman put it, humans are the only known species which show interest in understanding of this script, as far as it goes. Truth to tell, during last couple of years I have observed that this interest is waning, at least officially. The Polish Minister of Science told me a few months ago that if the government debt is going to raise too fast "we will take money from science". And yet I am convinced that this quest is absolutely crucial for survival of homo sapiens. Hence, GRBs are special and you, people who study them, you are very special. Thank you and come safely home.

Index

- Afonso P.M.J., 325
Ahmad S., 501, 531, 537, 567, 573, 579
Ahn K.-B., 561, 573
Allen W., 251
Alvarez, 617
Amati L., 617
Amelushkin A.M., 545, 553
Aptekar R.L., 27, 71, 459
Asano K., 115
Atteia J.-L., 625
Axelsson M., 53
Azzarello P., 617
- Bagoly Z., 65
Bai J.-M., 91
Barkov M., 319
Barret D., 617
Barrillon P., 501, 531, 537, 567, 573, 579
Barthelmy S., 459
Bartolini C., 465
Baryshev Yu.V., 435
Batsch T., 479
Batta A., 153
Benghin V.V., 545
Bersten M.C., 367
Beskin G., 241, 465
Bhat N.P., 45
Bianco C.L., 595
Blackburn L., 657
Bloom J.S., 391
Bogomolov V.V., 545, 553, 633
Bondar S., 465
Bond I., 251
- Boynton W., 459
Bozzo E., 617
Brandt S., 501, 531, 537, 561, 567, 573, 579, 617
Bravo Calle O.J.A., 435, 439
Breeveld A.A., 211
Bremer M., 279
Bret A., 295, 135
Briggs M.S., 459, 657
Bromm V., 585
Budtz-Jørgensen C., 501, 531, 537, 561, 567, 573, 579, 617
- Campana R., 617
Campana S., 229, 359
Cannizzo J.K., 449
Castillo-Carrión S., 251
Castro Cerón J.M., 251, 279
Castro-Tirado A.J., 65, 235, 251, 267, 275, 279, 345, 471, 475, 501, 525, 531, 537, 561, 567, 573, 579, 617
Chang C.-H., 573
Chang S.-H., 531, 567, 579
Chang Y.-Y., 531, 567, 573, 579
Chen C.R., 531, 567, 573, 579
Chen P., 95, 501, 525, 531, 537, 561, 567, 573, 579, 647
Chernenko A., 337
- Chochol D., 255
Choi E.J., 177
Choi H.S., 531, 567, 573, 579
Choi J.N., 501, 525, 561
Choi Y.J., 501, 525, 531, 537, 567, 573, 579
Cho M.H., 561, 573
Christie G., 251
Cline T., 71, 459
Connaughton V., 459, 657
Connell P.H., 501, 517, 525, 531, 537, 567, 573, 579
Cordier B., 625
Costa E., 601
Covino S., 229, 375
Cros A., 617
Cui C., 251
Cummings J., 459
Cunniffe R., 251, 471
Cwiok M., 479
Czyrkowski H., 479
- Dabrowski R., 479
Dagoret-Campagne S., 501, 531, 537, 567, 573, 579
Daigne F., 185, 331
D'Avanzo P., 229
Díaz Andreu J., 251
de Gregorio Monsalvo I., 267
de la Morena Carretero B., 251
D'Elia V., 247
Del Monte E., 459, 617

- den Herder J.W., 617
 De Pasquale M., 211, 217
 de Ugarte Postigo A., 235, 251, 267, 279, 345
 Donnarumma I., 617
 Dutan I., 177
 Elenin L., 259
 Elliott J., 325
 Erofeev A., 259
 Evangelista Y., 617
 Evans P., 625
 Eyles C., 501, 525, 531, 537, 567, 573, 579
 Fan Y.-Z., 83
 Fan Y., 251
 Farinelli R., 129
 Fellows C., 459
 Fernández-Muñoz R., 251
 Feroci M., 459, 617
 Ferrero P., 325, 345, 431
 Filgas R., 223, 325
 Fishman G.J., 5
 Fiuzo F., 295
 Fraija N., 301
 Fraser G.W., 625
 Frederiks D.D., 27, 71, 275, 459
 Frederiksen J.T., 177
 Fruchter A.S., 413
 Fugazza D., 229
 Fukazawa Y., 459
 Fynbo J.P.U., 267, 397
 Galkin V.I., 553
 Galvez Sanchez J.L., 617
 Garcia-Appadoo D., 267
 García-Segura F., 471
 García-Segura G., 371
 Garipov G.K., 545
 Gehrels N., 449, 459
 Ghirlanda G., 229
 Ghisellini G., 229
 Giannios D., 165
 Goldsten J., 459
 Golenetskii S.V., 27, 71, 459
 Golovin D., 459
 Gómez Gauna E., 475
 Goncharov B.V., 553, 633
 González M.M., 301
 Gorbovskoy E.S., 545, 553
 Greiner J., 267
 Gorosabel J., 65, 235, 251, 267, 275, 279, 345, 471, 475
 Götz D., 617
 Granot J., 141
 Greco G., 241, 465
 Grebenev S., 75
 Greiner J., 325, 431
 Gremillet L., 295
 Grobovskoj E., 633
 Grossan B., 501, 531, 537, 545, 561, 567, 573, 579, 633
 Graham J.F., 413
 Grothkopf U., 491
 Gu W.-M., 341
 Guarneri A., 465
 Guziy S., 65, 235, 251, 279, 345, 495
 Hajdas W., 459
 Hanabata Y., 459
 Hancock P., 267
 Hanlon L., 487
 Hansen F., 617
 Hardee P.E., 173, 177
 Harshman K., 459
 Hartmann D.H., 177
 Hernández-Cervantes L., 371
 Hernández-García L., 345
 Hernanz M., 617
 Higuera J., 371
 Hjorth J., 397
 Hoffman M., 487
 Holland S.T., 211
 Hornstrup A., 617
 Huang J.J., 525, 531, 567, 573, 579
 Huang M.-H.A., 501, 525, 531, 537, 561, 567, 573, 579
 Hudec R., 271, 251, 611, 617, 639
 Hurley K., 459
 Inasaridze R., 259
 Inneman A., 611
 Ivanov A., 259
 Ivanov E., 465
 Ivanov V., 259
 Izzo L., 595
 Jakobsson P., 397
 Jelínek M., 65, 235, 251, 279, 471, 475, 487
 Jenke P., 657
 Jeong S., 501, 525, 531, 537, 561, 567, 573, 579
 Jung A., 501, 531, 537, 561, 567, 573, 579
 Kamble A., 267
 Kann D.A., 217, 267, 275, 309, 325, 431
 Karelín D., 617
 Karpov S., 241, 465
 Kasprowicz G., 479
 Kawai N., 59
 Kheyfets I., 251
 Khrenov B.A., 545
 Kim J.-E., 501, 525, 531, 537, 561, 567, 573, 579
 Kim M.-B., 501, 525, 531, 537, 561, 567, 573, 579
 Kim S.-W., 501, 525, 531, 537, 561, 567, 573, 579

- Kim Y.-W., 501, 525, 531, 537, 561, 567, 573, 579
 Klimov P.A., 545
 Klose S., 325, 431, 443
 Klunko E., 495
 Komarova V.N., 403, 439
 Kong A.K.H., 83
 Kopylov A.I., 439
 Kornilov V.G., 553
 Korpela S., 617
 Kouprianov V., 259
 Krasnov A.S., 501, 531, 537, 567, 573, 579, 633
 Krimm H., 459
 Krugly Yu., 259
 Krühler T., 325, 397, 431
 Kubánek P., 251, 487
 Kuin N.P.M., 211, 267
 Kuvvetli I., 617
 Kvaratskhelia O., 259
 Lara-Gil O., 251
 Lee W.H., 153, 301
 Lee J., 501, 525, 531, 537, 545, 561, 567, 573, 579
 Lim H., 501, 525, 531, 537, 561, 567, 573, 579
 Lin C.-Y., 531, 567, 579
 Linder E.V., 501, 531, 537, 561, 567, 573, 579, 633
 Lipunov V.M., 545, 553
 Litvak M.L., 459
 Litvinenko E., 259
 Liu T., 341
 Liu T.-C., 501, 525, 531, 537, 567, 573, 579
 López-Cámara D., 159
 Lundgren A., 267
 Lund N., 15, 531, 537, 567, 573, 579, 617
 Lu J.-F., 341
 Majcher A., 479
 Majczyna A., 479
 Makishima K., 459
 Malanushenko V., 255
 Malek K., 479
 Malesani D., 397
 Mankiewicz L., 483, 479, 667
 Marisaldi M., 459
 Marshall F.E., 211
 Mazets E.P., 27
 Moliné B., 471
 Marsikova V., 611
 Martindale A., 625
 Martín S., 267
 Mateo Sanguino T. de J., 251
 Matkin A., 259
 Milvang-Jensen B., 397
 Matsuoka M., 59
 Mazets E., 71, 459
 Medvedev M., 177
 Meegan C., 459
 Meehan S., 487
 Meintjes P., 487
 Melandri A., 229
 Meli A., 663
 Mereghetti S., 625
 Mészáros A., 79
 Metzger B.D., 165
 McEnergy J.E., 657
 Mihara T., 59
 Mimica P., 165
 Minaev P., 75, 275
 Min K.W., 177, 501, 525, 531, 537, 561, 567, 573, 579
 Mitrofanov I.G., 459
 Mizuno Y., 173, 177
 Molkov S., 75
 Molotov I., 259, 495
 Morii M., 59
 Morozenco V.S., 633
 Moskvitin A.S., 403
 Muccino M., 595
 Murakami T., 459
 Murphy T., 267
 Na G., 545
 Na G.-W., 501, 525, 531, 537, 561, 567, 573, 579
 Nakahira S., 59
 Narayan R., 295
 Nam J.-W., 501, 525, 531, 537, 561, 567, 573, 579
 Nardini M., 325
 Nava L., 229
 Nawrocki K., 479
 Negoro H., 59
 Nevski V., 259
 Nicastro L., 263
 Nishikawa K.-I., 173, 177
 Nicuesa Guelbenzu A., 325, 431
 Niemiec J., 173, 177
 Niino Y., 427
 Nishimura Y., 59
 Nordlund A., 177
 Norris J.P., 345
 Oates S.R., 211, 217, 267
 O'Brien P.T., 351, 625
 Oganesyan G., 241
 Ohno M., 459
 Oleynik P., 71
 Olivares E., F., 325
 Omodei N., 123
 Opiela R., 479
 Orleanski P., 617
 Osborne J.P., 625
 Osedlo V.I., 633
 Ogawa Y., 59
 Page M.J., 211
 Palmer D., 459
 Palshin V.D., 27
 Pal'shin V., 71, 459
 Panasyuk M.I., 501, 531, 537, 545, 553, 561, 567, 573, 579, 633
 Pandey S.B., 203, 279

- Parijskij Yu.N., 439
 Park H.W., 501
 Park I.H., 79, 251, 501, 525, 531, 537, 545, 561, 567, 573, 579
 Pavlenko E., 255
 Pe'er A., 105
 Pelassa V., 657
 Penacchioni A.V., 595
 Pérez-Álvaro E., 135, 295
 Pérez del Pulgar C., 251
 Pérez-García M.A., 331
 Pérez-Ramírez D., 65, 235, 251, 279, 345
 Pérez-Rendón B., 371
 Perkov A., 465
 Perley D.A., 275, 391
 Petrov V.L., 545, 553
 Pina L., 611
 Piotrowski L.W., 479
 Piron F., 123
 Pisani G.B., 595
 Pohl M., 173, 177, 617
 Pozanenko A., 75, 259, 275, 319, 495
 Pizzichini G., 271
 Prochaska J.X., 391
 Rabaza-Castillo O., 251
 Rachevskii A., 617
 Ramirez J.L., 301
 Rau A., 325, 459
 Razzaque S., 123
 Reglero V., 501, 517, 525, 531, 537, 561, 567, 573, 579
 Ricci D., 263
 Ripa J., 501, 525, 537, 561, 567, 573
 Řípa J., 79, 531, 579
 Rodrigo J.M., 501, 525, 531, 537, 567, 573, 579
 Rogkov E., 633
 Rossi A., 325, 431
 Rowlinson A., 351
 Rozhkov G., 633
 Rueda J.A., 595
 Ruffini R., 595
 Rumyantsev V., 275
 Ruyer C., 295
 Sabau-Graziati L., 251
 Sacahui J.R., 301
 Sakamoto T., 59
 Saleev K., 633
 Salvaterra R., 229
 Sánchez-Ramírez R., 65, 235, 251, 267, 279, 345
 Sanin A.B., 459
 Santangelo A., 617
 Santillán A., 371
 Sapountzis K., 181
 Sasyuk V., 465
 Savaglio S., 381, 491
 Sbarufatti B., 229
 Schady P., 211, 325
 Schanne S., 617
 Schmid C., 617
 Schmidl S., 217, 325
 Serino M., 59
 Shearer A., 465
 Shprits Yu., 545
 Shugarov S., 255
 Silk J., 331
 Silva L.O., 295
 Šimon V., 271, 639
 Sinyakov E., 259
 Siudek M., 479
 Smith D.M., 459
 Smoot G.F., 501, 531, 537, 545, 553, 561, 567, 573, 579, 633
 Sokolov I.V., 435, 439
 Sokolov V.V., 403
 Sokolowski M., 479
 Sol H., 177
 Starr R., 459
 Stella L., 617
 Stockem A., 295
 Suchý S., 617
 Sudilovsky V., 325
 Sugizaki M., 59
 Suh J.-E., 525, 531, 537, 561, 567, 573, 579, 579
 Svertilov S.I., 501, 531, 537, 545, 553, 561, 567, 573, 579, 633
 Svinkin D., 71, 459
 Tagliaferri G., 229
 Takahashi T., 459
 Takahashi Y., 95
 Tajima T., 95
 Tam P.H.T., 83
 Tanvir N.R., 397, 421
 Tashiro M., 459
 Tello J.C., 65, 235, 251, 279, 345
 Temirova A.V., 439
 Tenzer C., 617
 Terada Y., 459
 Thomasson P., 439
 Thöne C.C., 235, 267
 Tisdall P., 487
 Titarchuk L., 129
 Topinka M., 487
 Troja E., 39, 657
 Tsvetkova A., 71
 Tungalag N., 259, 495
 Ulanov M., 71
 Updike A., 431
 Vacchi A., 617
 Vachenko T.V., 633
 van der Klis M., 617
 van Heerden H., 487
 Varda D., 259
 Vasileiou V., 123
 Vedenkin N.N., 501, 531, 537, 545, 553, 561, 567, 573, 579, 633
 Veres P., 65, 79

- Vergani S.D., 229, 407
Vianello G., 123
Vitek S., 251
Vlahakis N., 181
Volnova A., 259, 275, 495
von Kienlin A., 459
- Wang M.-Z., 501, 525,
531, 537, 567, 573, 579
Wang Y., 595
Wawrzaszek R., 479
Wiersema K., 195
- Wilms J., 617
Winters J.M., 279
Wrochna G., 479
Xue L., 341
Yamaoka K., 459
Yashin I.V., 501, 531, 537,
545, 553, 561, 567, 573,
579
Yock P., 251
Yoshida A., 59
- Zampa N., 617
Zand J.J.M. in't, 617
Zaremba M., 479
Zarnecki A.F., 479
Zdziarski A., 617
Zhang B., 173, 177, 217,
285
Zhang F.-W., 87
Zhang X., 459
Zhao X.-H., 91
Zhelenkova O.P., 439
Zheng W., 203